13 May 2005

Science

Vol. 308 No. 5724
Pages 909–1072 $10

CASSINI REVEALS TITAN

125 YEARS OF GLOBAL Science

AAAS

High-performance features come standard.

The best real-time PCR system just got better.

Stratagene's Mx3005P™ Real-Time PCR System sets the next benchmark in real-time PCR with new high-performance features, increased flexibility to support more applications and chemistries, and affordable pricing for the individual researcher (€29,900 list price*).Real-time PCR systems starting at €24,950 list price*.

- **The *only* instrument with five (5) color multiplex capability and user-selected filters**
- **Novel custom filter path selection for FRET probe chemistries**
- **Includes Beacon Designer™ oligo design software**

Need More Information? Give Us A Call:

Stratagene USA and Canada
Order: (800) 424-5444 x3
Technical Services: (800) 894-1304

Stratagene Europe
Order: 00800-7000-7000
Technical Services: 00800-7400-7400

Stratagene Japan K.K.
Order: 03-5159-2060
Technical Services: 03-5159-2070

www.stratagene.com

STRATAGENE®

DNA Sequencing Services

SNP Discovery/Resequencing/ Variant Discovery	**$0.01 per base, per direction**
High throughput sequencing	**$5 per reaction**
cDNA sequencing	**$5 per reaction**
S.A.G.E. sequencing	**$5 per reaction**

Custom Genomic Services

Custom Gene synthesis	**$1 per base pair**
PCR	**$1 per amplicon**
Real Time PCR	**$500 per assay**
Whole genome scanning	**$5 per locus, per sample**
Nucleic acid extraction/ purification	**$2.50 per mini-prep**
Mutagenesis	**$400 any mutation within 5 bp frame**
Subcloning	**$400 per clone**
Library construction: Genomic, cDNA, BAC	**Please inquire for pricing**

POLYMORPHIC
Polymorphic DNA Technologies, Inc.℠

www.polymorphicdna.com
info@polymorphicdna.com

1125 Atlantic Ave., Ste. 102
Alameda, CA 94501

888.362.0888

For more information please visit www.polymorphicdna.com

Amersham Biosciences

Part of GE Healthcare

Before you put our radionucleotides to the test

We put them to the test

Radionucleotides from GE Healthcare are made to perform. Our ^{32}P and ^{33}P nucleotides are tested in DNA-labeling experiments before shipping, so you can be confident they'll work in your application. But what's more, they're manufactured frequently and dispensed from local sites, so you can always rely on rapid delivery of the freshest material. For your convenience, they're available in a variety of pack sizes and formats, which can be customized to your specific needs. All of which adds up to a refreshingly easy way to ensure the best results in your research.

Visit www.amershambiosciences.com/radiochemicals

imagination at work

Science

Special Issue

Cassini Reveals Titan

A 170-km-wide region of Saturn's largest moon, Titan, revealed in synthetic aperture radar imaging from the Titan Radar Mapper instrument onboard the Cassini Orbiter. North is to the right. A complex and geologically young surface is revealed, with few impact craters but many features that may have been formed by cryovolcanism. [Image: NASA/Jet Propulsion Laboratory/U.S. Geological Survey]

Volume 308
13 May 2005
Number 5724

940

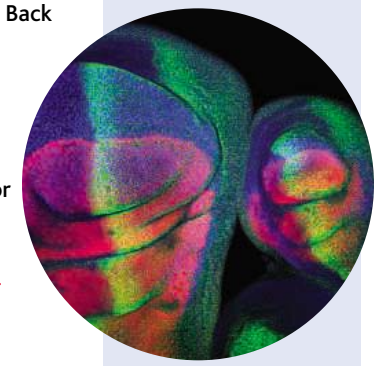

955

Contents continued

Integrated Solutions — Automated Nucleic Acid Prep

A new generation of lab automation, as easy as A, B, C!

A: Insert an EZ1 Card containing the appropriate nucleic acid purification protocol.

B: Set up processing quickly and safely using pre-filled and sealed reagent cartridges.

C: Complete automation; from opening reagent cartridges to elution of highly pure nucleic acids.

The BioRobot® EZ1 purifies DNA, RNA, or viral nucleic acids from clinical and pathology samples for a range of sensitive downstream applications.

The BioRobot EZ1 system offers:

- **Safe and simple operation** — easily set protocols using pre-programmed EZ1 Cards and quickly set up processing with pre-sealed reagent cartridges
- **Reliable and flexible purification** — get high-quality genomic and viral nucleic acids from various sample types, such as blood, tissues, swabs, and paraffin-embedded sections
- **Rapid results** — purify 1 to 6 samples in 15–20 minutes
- **Affordable, slimline automation** — save space with the small footprint and no external PC

Discover the benefits of walkaway nucleic acid purification at www.qiagen.com/goto/EZ1 !

QIAGEN

Perspectives continued

Science Express www.sciencexpress.org

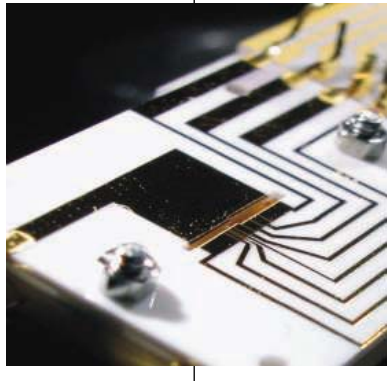

997

Brevia

Reports

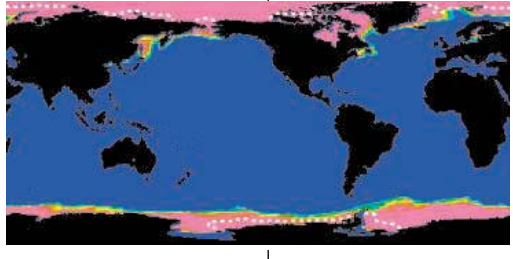

1003

Contents continued

The odds of a compound making it from an initial screening hit to an approved drug are roughly 1 in 10,000. That's represented in years of work and hundreds of millions of dollars that go into bringing a blockbuster drug to market.

accelerate > news at ten

In the grand scheme of things, conducting the early phases of drug discovery isn't headline news. But science dictates that success is found through the combination of a sound hypothesis and the methodical scrutiny of data — both essential parts of the long and arduous process of drug discovery.

Ever wonder what might happen if someone made the process easier and faster? We did. And we built a business around doing just that. By supplying you with the widest array of high-activity kinases, sub-proteomic scale human protein microarrays (ProtoArray™), and innovative GeneBLAzer® cell-based assays, Invitrogen's Drug Discovery Solutions allow you to maximize your discovery resources without adding layers of internal cost.

It's a better, smarter way to work that saves time, money, and resources. And ultimately, it increases your odds of getting a drug to market today that might hold the promise of a better tomorrow.

It's a long shot, we know, but no one ever said changing the world would be easy. Perhaps we can make it a little easier.

Schedule your free consultation with a Drug Discovery Solutions Specialist. E-mail us at drugdiscovery@invitrogen.com or visit us at www.invitrogen.com/drugdiscoverysolutions

invitrogen™

drug discovery solutions

Reports continued

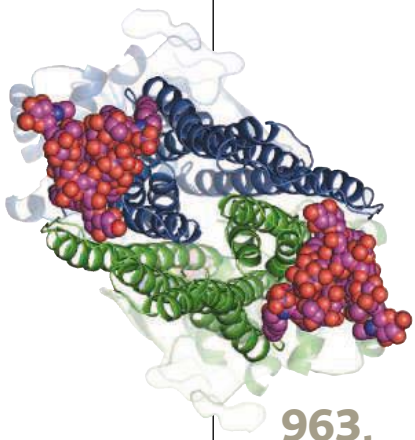

963, 1023, & 1028

1046

AAAS
ADVANCING SCIENCE, SERVING SOCIETY

SCIENCE (ISSN 0036-8075) is published weekly on Friday, except the last week in December, by the American Association for the Advancement of Science, 1200 New York Avenue, NW, Washington, DC 20005. Periodicals Mail postage (publication No. 484460) paid at Washington, DC, and additional mailing offices.

Domestic individual membership and subscription (51 issues): $135 ($74 allocated to subscription). Domestic institutional subscription (51 issues): $550; Foreign postage extra: Mexico, Caribbean (surface mail) $55; other countries (air assist delivery) $85. First class, airmail, student, and emeritus rates on request. Canadian rates with GST available upon request, GST #1254 88122. Publications Mail Agreement Number 1069624. **Printed in the U.S.A.**

Change of address: allow 4 weeks, giving old and new addresses and 8-digit account number. **Postmaster:** Send change of address to *Science*, P.O. Box 1811, Danbury, CT 06813–1811. **Single copy sales:** $10.00 per issue prepaid includes surface postage; bulk rates on request. *Science* is indexed in the *Reader's Guide to Periodical Literature* and in several specialized indexes.

Contents continued

The MJ Line of Amplification Products

The perfect combination.

Bio-Rad doubles your capacity for real-time PCR

The Chromo4™ real-time detector now offers even more flexibility. Now you can mount two Chromo4 modules on the dual-bay Dyad Disciple™ thermal cycler, doubling experimental options and output. With the Disciple base, two different protocols can be run simultaneously, so you can get results sooner. Best of all, any combination of swappable Chromo4 modules and Alpha™ sample blocks can be operated in parallel, for the utmost in economy and flexibility.

- Twice the flexibility
- Twice the throughput
- Four-color multiplexing capability
- Thermal gradient feature
- Relative gene expression analysis software

Two Chromo4 real-time detectors on the Dyad Disciple thermal cycler

For more information, visit us on the Web at **www.mjr.com**

Visit us on the Web at **discover.bio-rad.com**
Call toll free at 1-800-4BIORAD (1-800-424-6723);
outside the US, contact your local sales office.

BIO-RAD

sciencenow www.sciencenow.org Daily News Coverage

A Nose for Sexual Preference
Homosexual men and heterosexual women have similar response to male scent molecule.

Mars Crash Site Identified?
Five-year-old photos may show the resting place of a doomed lander.

Living to Eat Cheese Another Day
Mice that make lots of a particular antioxidant live longer, healthier lives.

Reviewing grant proposals.

science's next wave www.nextwave.org Career Resources for Young Scientists

Career Development Center: To Fund or Not to Fund? *S. Eckert and J. Boss*
Is it worth it to suffer through reviewing grant proposals, or should you concentrate on your own research?

Career Development Center: Program Officers Behaving Badly *GrantDoctor*
Get tips on what to do when your program officer still won't call you back.

Europe: East Coast Researcher Takes the Plunge *H. Cullup*
Immunologist Hannah Cullup took the plunge and left the UK to do her postdoc in Brisbane, Australia.

MiSciNet: Concha Gómez—A Math Guru for Women and Minorities *E. Francisco*
A University of Wisconsin professor helps retain minorities in science, math, and engineering.

MiSciNet: My Grand Slam *M. Piñon*
Monica Piñon discusses her path from a community college to the UC Berkeley School of Optometry.

GrantsNet: International Grants and Fellowships Index *Next Wave Staff*
Here's the latest list of research funding, scholarships, fellowships, and internships offered outside the U.S.

science's sage ke www.sageke.org Science of Aging Knowledge Environment

Perspective: Keep Time, Stay Healthy *G. Block*
Is sleep-cycle disruption the reason altered circadian rhythm causes metabolic syndrome?

News Focus: Death in the Dirt *M. Leslie*
Long-lived in the petri dish, mutant worms bite the dust in soil.

News Focus: Heart, Heal Thyself *M. Leslie*
Researchers turn on possible heart-repair mechanism.

Heart cell division is not just for kids.

bHLH heterodimer transcription factor bound to DNA.

science's stke www.stke.org Signal Transduction Knowledge Environment

Perspective: A Rationally Designed Small Molecule That Inhibits the HIF-1α–ARNT Heterodimer from Binding to DNA in Vivo *C. Vinson*
Small molecules that specifically block transcription factor binding may hold promise as therapeutics.

Review: Regulating Inducible Transcription Through Controlled Localization *E. C. Ziegler and S. Ghosh*
Modulation of transcription factor localization is an important mechanism for gene regulation.

Separate individual or institutional subscriptions to these products may be required for full-text access.

PIERCE

Grasp the Proteome™

Protein Staining

Imperial™ Protein Stain

A fast, sensitive and robust Coomassie protein stain; 20 minutes to detect 6-12 ng of protein/band

Imperial™ Protein Stain is a ready-to-use Coomassie stain for detecting protein bands in SDS-PAGE and 2-D gels. The stain is a unique formulation of Coomassie R-250 that delivers substantial improvements in protein-staining performance compared to homemade or other commercially available stains.

Highlights:

- **Fast** – detects as little as 6 ng protein/band in just 20 minutes
- **Sensitive** – detects as little as 3 ng protein/band and less with the enhanced protocol
- **Compatible** – with mass spec analysis and protein sequencing
- **Easy-to-use** – no methanol/acetic acid fixation and destaining required

Ordering Information

Product #	Description	Pkg. Size
24615	Imperial™ Protein Stain *Sufficient reagent to stain up to 50 mini gels*	1 L
24617	Imperial™ Protein Stain *Sufficient reagent to stain up to 150 mini gels*	3 x 1 L

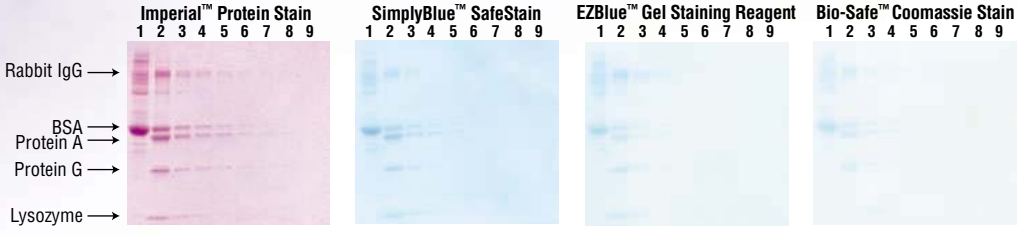

Imperial™ Protein Stain is fast and sensitive. Proteins were separated on Novex 4-20% Tris-glycine gels, stained for 5 minutes and destained 3 x 5 minutes in water. **Lane 1:** BSA only (6 µg), Lanes 2-9 contained the indicated proteins at the following concentrations: **Lane 2:** 1,000 ng, **Lane 3:** 200 ng, **Lane 4:** 100 ng, **Lane 5:** 50 ng, **Lane 6:** 25 ng, **Lane 7:** 12 ng, **Lane 8:** 6 ng and **Lane 9:** 3 ng.

www.piercenet.com/impst22e

PIERCE

Tel: 815-968-0747 or 800-874-3723 • Fax: 815-968-7316 • Customer Assistance E-mail: CS@piercenet.com

Outside the United States, visit our web site or call 815-968-0747 to locate your local Perbio Science branch office (below) or distributor

Belgium & Dist.:	China:	France:	Germany:	Hong Kong:	The Netherlands:	United Kingdom:	Switzerland:
Tel +32 53 85 7184	Tel +86 10 8049 9033	Tel 0800 50 82 15	Tel 0228 9125650	Tel 852 2753 0686	Tel 076 50 31 880	Tel 0800 252185	Tel 0800 56 31 40
euromarketing@perbio.com	support@perbio.com.cn	euromarketing@perbio.com	de.info@perbio.com	SalesHK@perbio.com	euromarketing@perbio.com	uk.info@perbio.com	euromarketing@perbio.com

PERBIO

edited by Stella Hurtley and Phil Szuromi

Flipping Across the Membrane

ATP binding cassette transporters pump hydrophobic compounds across the cell membrane and include the efflux pumps implicated in bacterial antibiotic resistance and cancer drug resistance in humans. Hydrolysis of adenosine triphosphate provides the energy for structural changes that mediate substrate transport, but the mechanism remains unclear. Two studies provide insight into the transport cycle of MsbA, a bacterial transporter that transports lipid A and lipopolysaccharide across the bacterial inner membrane (see the Perspective by **Davidson and Chen**). **Dong *et al.*** (p. 1023) used electron paramagnetic resonance to map conformational changes during the ATP cycle of MsbA, and **Reyes and Chang** (p. 1028) determined the x-ray structure of MsbA in a transition state complex with magnesium, adenosine diphosphate, vanadate, and lipopolysaccharide. Both studies are consistent with a mechanism in which ATP hydrolysis drives flipping of amphipathic substrates.

Qubit Version of Fourier Transforms

Interest in quantum computing exploded after Shor developed an algorithm for factoring large numbers in 1994. A key component of that algorithm requires the ability to carry out a quantum Fourier transform on a set of quantum "qubits" that are the analog of binary digits in classical computations. **Chiaverini *et al.*** (p. 997) report their experimental demonstration of a semiclassical quantum Fourier transform using trapped beryllium ions as qubits. The results show the possibility of performing a version of the Fourier transform that requires only single-qubit operations conditioned on the measurements of other qubits in a system that can be scaled up to a large number of qubits.

Coordinating Plant Defenses

Pathogen invasion at one site in a plant triggers defensive reactions throughout the rest of the plant. This systemic acquired resistance is mediated by salicylic acid and the regulatory protein NPR1, and involves the activation of a suite of pathogenesis-related genes. **Wang *et al.*** (p. 1036) found that another group of genes is activated and encodes the cellular secretory machinery. The same regulatory triggers set in motion production of anti-pathogen proteins, as well as enhance the means to deliver them to where they can do the most damage.

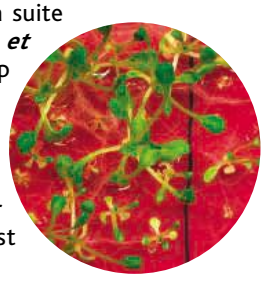

Lichen in the Mists of Time

Fungi form a major branch of the tree of life and also provide important symbiotic relations with other organisms, commonly phototropic bacteria. These relations in part form "lichens"—essentially fungi that practice agriculture using bacteria. Fungi in turn release nitrogen for plants in human agriculture. **Yuan *et al.*** (p. 1017) now describe a lichen-like association between fungi and cyanobacteria or algae from the Doushantou Formation, China, dating to about 600 million years ago. The lichen (and fungi) occur in a shallow marine setting, which suggests that such symbioses were established well before the rise of terrestrial plants.

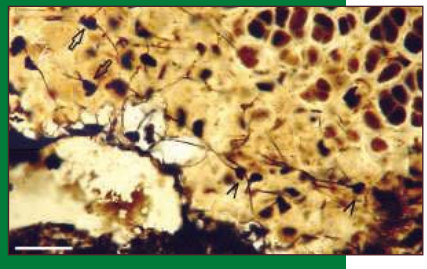

Marine Nitrogen Pools

Nitrogen is an essential and sometimes limiting nutrient in marine ecosystems whose role in controlling productivity is well-understood. It exists in the surface ocean mostly as dissolved organic nitrogen (DON), but despite decades of research, only a small fraction of the DON in surface ocean waters has been chemically characterized. **Aluwihare *et al.*** (p. 1007) used solid-state ^{15}N nuclear magnetic resonance to characterize two distinct pools of high-molecular-weight (HMW) DON, which comprise about 30% of the total. One pool, which makes up approximately half of the DON near the surface, is more readily hydrolyzed, whereas the deep ocean contains mostly forms that are resistant to chemical hydrolysis and biological degradation. The authors describe how these pools produce the vertical profile of HMWDON that is observed and discuss the chemical transformations that might transfer nitrogen to the deep ocean.

How Hydrogen Hung Around

Hydrogen is lost permanently from our atmosphere as it leaks slowly into space. The atmosphere of early Earth was much richer in hydrogen than it is now, and until recently, it was generally thought that its escape rate was so rapid that prebiotic organic compounds must have formed in a relatively oxidized environment. **Tian *et al.*** (p. 1014, published online 7 April 2005; see the Perspective by **Chyba**) report calculations that show that the escape of hydrogen from early Earth occurred 100 times more slowly than previously thought. The hydrogen mixing ratio of the early atmosphere was more than 30%, two orders of magnitude greater than formerly predicted. An atmosphere so rich in hydrogen would have facilitated greatly the formation of prebiotic organic compounds.

Out of Africa Revisited

The route of human colonization of Asia after dispersing out of Africa 60,000 years ago has remained unresolved. DNA sequence analysis of existing populations can provide phylogenies that can be mapped onto geographic distribution (see the Perspective by **Forster and Matsumura**). **Macaulay *et al.*** (p. 1034) tested alternative models for the settlement of Eurasia by modern humans using complete mitochondrial (mt) DNA genomes (which provide the highest possible resolution of the maternal genealogical tree) by studying the "missing link" of Southeast Asian aboriginal populations. Only one model—a single, rapid dispersal along the coat from East Africa to India and thence to Southeast Asia and Australasia—can explain the phylogenetic patterns observed. Moreover, all subsequent peopling of Europe and Asia can be explained by this initial dispersal event. **Thangaraj *et al.*** (p. 996)

CONTINUED ON PAGE 923

CREDITS (TOP TO BOTTOM): YUAN *ET AL.*; WANG *ET AL.*

Traditional Mini Preps are Over.

Start automating with the latest in plasmid DNA purification. The Mini Prep 96 can perform up to 96 preps in 1 hour of processing time. Up to 8 µg of plasmid DNA per lane at less than $1 a prep.

Start with easy operation. Disposable cassettes allow for direct loading of culture with no centrifugation.

Start the Mini Prep 96 with the push of a button. Remove high purity DNA and use in most microbiology protocols — including sequencing and cell transfection.

Start saving time and money with the Mini Prep 96.

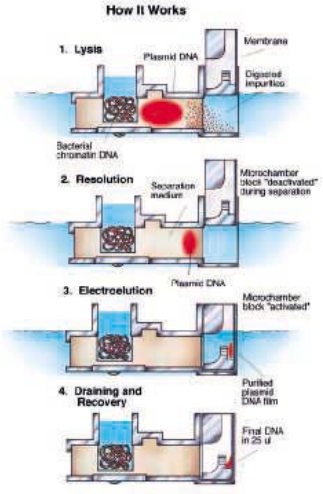

Four Easy Steps to Plasmid DNA Purification

Stop Manual Mini Preps START ENTER Start the Mini Prep 96™

1-800-466-7949
www.macconnell.com

Mini-Preps at the Push of a Button.
6195 Cornerstone Court, San Diego, California 92121, Fax: 858-452-6753

MacConnell Research

identified M31 and M32 mtDNA types among indigenous Andaman islanders which show that these populations became genetically isolated about 50,000 to 70,000 years ago, apparently after their initial migration from Africa.

pH Makes the Switch

Adenylyl cyclases (AC) synthesize the second-messenger cyclic AMP (cAMP). **Tews *et al.*** (p. 1020) have characterized an AC from *Mycobacterium tuberculosis* that produces cAMP in a pH-dependent manner. The enzyme consists of two complementary monomers, and high-resolution structures show that interaction between the catalytic and regulatory domains prevents formation of the active site in the inhibited (high pH) state. Two molecular switch regions mediate structural rearrangement of the catalytic domains so that they are positioned to form the active site at their interface. Mutagenesis results support the idea that a pH-dependent structural transition regulates activity.

Leprosy Migrations

Leprosy is a puzzling disease caused by a slowly developing infection with *Mycobacterium leprae*. **Monot *et al.*** (p. 1040; see the news story by **Grimm**) examined the distribution of rare single nucleotide polymorphisms of several isolates of the leprosy bacillus collected from around the world. The pathogen has a very stable genome, and it appears that a single clone has spread north and east from East Africa or the Middle East with successive waves of human migration, reaching West Africa and the Americas from Eurasia within the past few hundred years.

Tropical Degassing

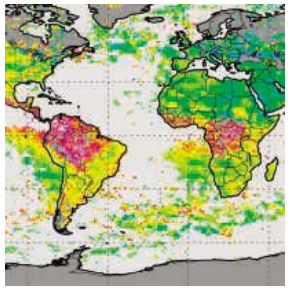

Methane is the second most important trace greenhouse gas, accounting for 20% of their collective absorption of solar radiation, but its sources and sinks are not well understood. **Frankenberg *et al.*** (p. 1010, published online 17 March 2005) present results from SCIAMACHY, an instrument onboard the ENVISAT satellite, which reveal the global distribution of tropo spheric methane. Methane concentrations are unexpectedly high over terrestrial tropical regions, indicating that it is produced in amounts much greater than previously had been assumed. This discovery could help reconcile the disagreement between various estimates of the global methane budget.

CREDIT: FRANKENBERG *ET AL.*

Round-the-Clock Metabolism

The behavior of most organisms is organized around a 24-hour cycle. One of the key molecular regulators of this circadian rhythmicity is a transcription factor called CLOCK. Mice carrying a mutation in the *Clock* gene show profound disturbances in circadian behavior. **Turek *et al.*** (p. 1043, published online 21 April 2005) now show that these *Clock* mutant mice also overeat, become overweight, and develop features of metabolic syndrome, including elevated serum levels of glucose and lipids. The metabolic disturbances were accompanied by alterations in the expression of neuropeptides implicated in appetite control and energy balance.

The Maturing Repertoire of Canary Songs

A canary's song is made up of units of sound organized with syntax and phrasing. **Gardner *et al.*** (p. 1046) have now distinguished some of the forces that shape the adult bird's song. When young canaries were isolated from other birds' songs, they showed remarkable ability to mimic synthetic songs that were far from the normal canary song. However, as these birds matured, their songs became more typical of normal adult canaries, despite having never heard such songs. Thus, with maturity in the canary comes a loss of vocal flexibility, and increasing dominance of an innate program of song structure.

DyNAmo™

qPCR and qRT-PCR Kits

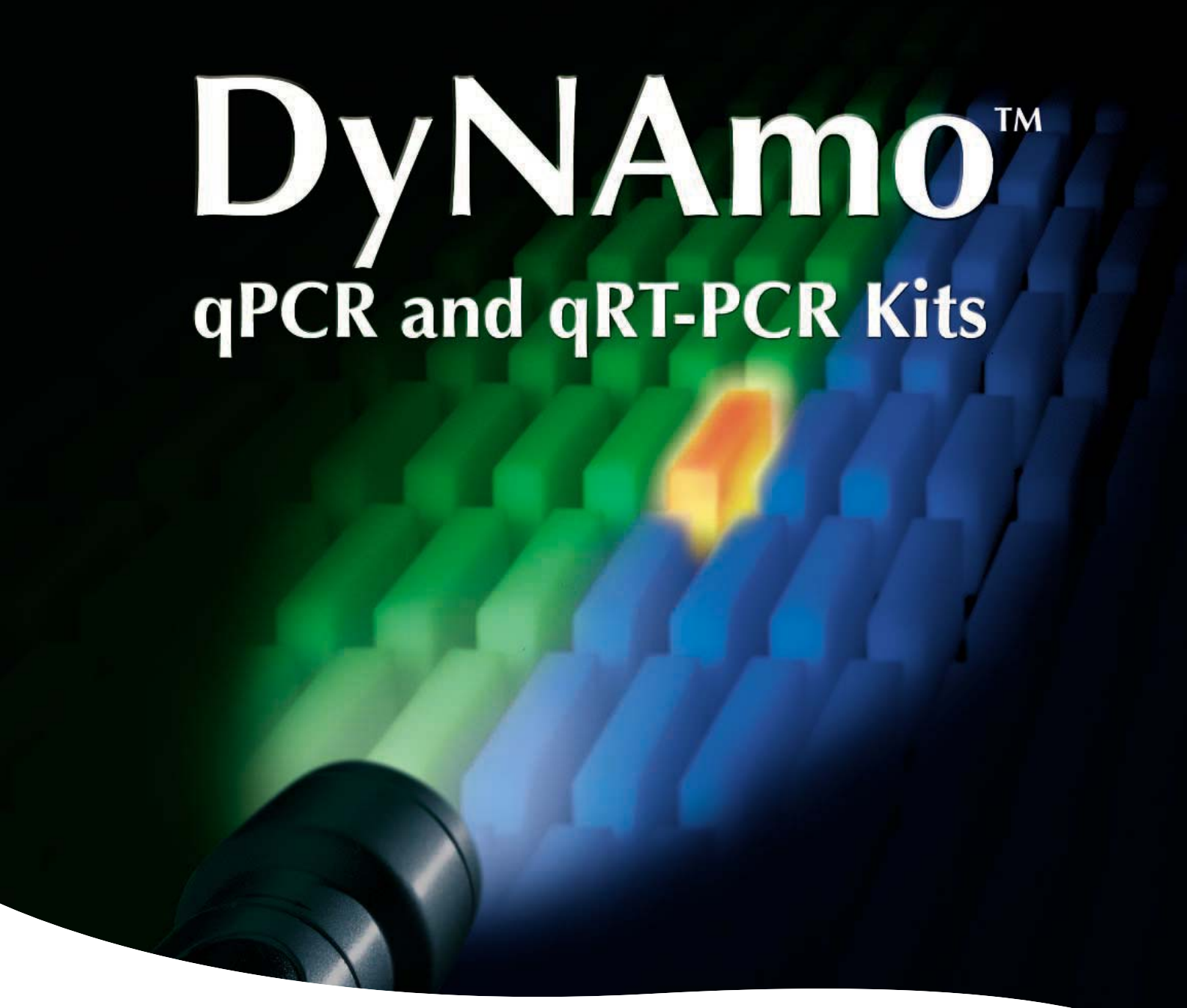

Finnzymes' DyNAmo™ qPCR and qRT-PCR Kits:

SYBR® Green Chemistry

- **DyNAmo™ HS SYBR® Green qPCR Kit** (F-410S/L)
- **DyNAmo™ Capillary SYBR® Green qPCR Kit** (F-420S/L)
- **DyNAmo™ SYBR® Green 2-step qRT-PCR Kit** (F-430S/L)
- **DyNAmo™ Capillary SYBR® Green 2-Step qRT-PCR Kit** (F-440S/L)

Probe Chemistry

- **DyNAmo™ Probe qPCR Kit** (F-450S/L)
- **DyNAmo™ Probe 2-Step qRT-PCR Kit** (F-460S/L)

Engineered for qPCR

Finnzymes' DyNAmo™ qPCR Kits are a superior choice for quantitative real-time analysis. These kits offer excellent performance in detection and quantification of DNA and RNA sequences from various sources. DyNAmo qPCR Kit family contains optimized kits for both SYBR® Green and probe chemistries with various platforms. For more information visit **www.finnzymes.com**

NEW ENGLAND BioLabs® Inc.

Distributed in the US and Canada by New England Biolabs.
Other countries visit www.finnzymes.com

FINNZYMES
TOOLS FOR MOLECULAR BIOLOGY

Finnzymes Oy • Keilaranta 16 A, 02150 Espoo, Finland • Tel. +358 9 584 121 • Fax +358 9 5841 2200 • fz@finnzymes.fi • www.finnzymes.com

Living Laboratory in Peril

The name Galapagos conjures up images of giant tortoises, Darwin's finches, and a remote pristine archipelago that is rightly described as "a living laboratory of evolution." But that picture of this World Heritage site is seriously flawed by current events, including wholesale violations of the Special Law for Galapagos passed by the Ecuadorian government in 1998. That law, which followed a series of conflicts generated by immigration and illegal fishing, was a consensus of island and national opinion and was greeted with delight by scientists and conservationists. Alas, it isn't working.

The law excluded even Ecuadorians from moving to the Galapagos unless they had been born there or had family on the islands. Unfortunately, much immigration had already occurred. The Special Law's goal was to promote the conservation of biodiversity jointly with sustainable development: a dream uniting incompatible goals. The Galapagos population has grown a remarkable 10-fold in 30 years, to over 27,000 in 2005. Consumption has grown even faster: In contrast to a mere three vehicles in the 1970s, over 350 taxis now create pollution and congestion on Santa Cruz Island.

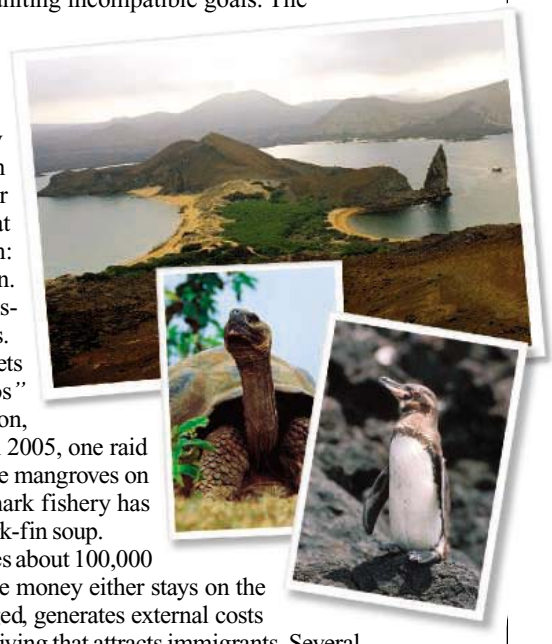

The threat to endemic species on the Galapagos is significant. A viability workshop conducted by the Darwin Initiative and the World Conservation Union (IUCN) in February of this year found that the Galapagos penguin was under serious threat, with the probability of extinction in the next century estimated at about 30%. Terrestrial ecosystems have a growing invasive species problem: Blackberries, introduced in the 1980s, now shade and smother native vegetation. Old invaders, such as goats, pigs, rats, and cats, continue to destroy native ecosystems and affect the function, species composition, and restoration of the islands.

The islands' fishery, small in the early 1970s, is now an industry, serving markets in Asia and elsewhere. The sea cucumber fishery, in the 1990s, involved "pepineros" from off-island who periodically took over the Charles Darwin Research Station, holding it hostage to protest fishing restrictions. They're still around: In March 2005, one raid found 7000 sea cucumbers, of a species illegal for harvest, in crates hidden in the mangroves on Fernandina Island; 100,000 were also captured on Isabela. An international shark fishery has already decimated that population in its effort to supply the Asian market for shark-fin soup.

Tourism is currently capped at 120,000 tourists a year, and an average year sees about 100,000 tourists visit the islands. They generate an annual $150 million, but most of the money either stays on the mainland or goes to where the tours originate. Tourism, even when well managed, generates external costs through waste disposal and also by encouraging development and a standard of living that attracts immigrants. Several immediate actions are needed to help the Galapagos archipelago remain a poster child for evolution and conservation. The islands need a nonextractive marine park around the westernmost islands of Fernandina and Isabela to protect the two endemic bird species (the Galapagos penguin and flightless cormorant) that are concentrated there. Policies limiting human population growth and consumption on the islands should be encouraged. Conservation measures are needed to prevent the introduction of diseases such as West Nile Virus and avian malaria. Fishing rights could also be bought out. New regulations must control illegal fishing and prohibit fishing techniques with unacceptable bycatch. Alternative work for genuine fishermen must be found. Galapagos tour costs should also include the external environmental costs of tourism.

How will such changes come about, and who will exact them? The organization charged with running the Galapagos, the National Park, lacks stability at the top. Ten park directors have been terminated in the past 2 years. Their demise was the result of constant political intervention to ignore exploitation of the islands. That leaves the solution in the hands of others. How can scientists help? Through scientific and professional organizations, we can call on establishments such as the IUCN to help the Ecuadorian government carry out science-based conservation, acquire worldwide financial support, and devise and enforce new laws that work. Our responsibility as scientists is to alert institutions, governments, and the public to the de-evolution of the Galapagos Islands. The international science community must garner strong global political support for the natural wonders of the Galapagos. Only then will this laboratory of evolution have a chance to persist for another 100 years.

P. Dee Boersma, Hernan Vargas, Godfrey Merlen

P. Dee Boersma is the Wadsworth Endowed Chair of Conservation Science at the University of Washington, Seattle, WA. Hernan Vargas is a D. Phil. student and a member of the Wildlife Conservation Research Unit at the University of Oxford, Oxford, UK. Godfrey Merlen is director of WildAid Galapagos, Santa Cruz, Galapagos.

10.1126/science.1114395

“THE FASTEST GROWING CROP IN IOWA IS NOT WHAT YOU EXPECT.”

MORE AND MORE BIOSCIENCE COMPANIES PLANNING TO EXPAND ARE TAKING A LOOK AT IOWA. And for good reason. Iowa leads the nation in the production of raw biomass at roughly 2.75 billion bushels. The state is home to three public universities that are world-renowned for their research in plant, animal and human bioscience. And to date there are more than 1,800 Iowa establishments already involved in the bioscience industry. To learn more about expanding your business in Iowa, visit iowalifechanging.com. Because the closer you look, the more Iowa grows on you.

www.iowalifechanging.com

IOWA
life | changing™

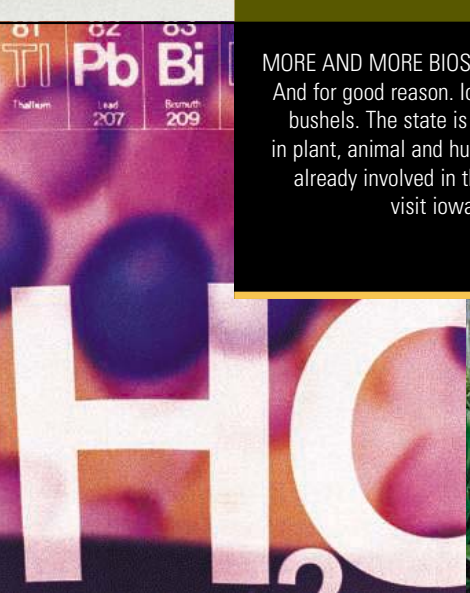

EDITORS' CHOICE

edited by Gilbert Chin

ECOLOGY/EVOLUTION

Competition Begins at an Early Age

The nestlings of brood parasites such as cuckoos and cowbirds, even if unsuccessful at ousting outright the eggs or nestlings of the host bird, compete with the host nestlings for provisioning by the parents. As a consequence of this competition, host nestlings frequently do not survive to fledge.

Song sparrow (*Melospiza melodia*) parent and fledgings.

In a study of brown-headed cowbirds that parasitized song sparrow nests in Canada, Zanette *et al.* find that such mortality can result in sex-biased survival. The sex ratios of song sparrow nestlings and fledglings in parasitized nests differed significantly from those in unparasitized nests, with a much lower proportion of female chicks surviving in the former. In mixed-sex broods in unparasitized nests, female song sparrow chicks are already at a developmental disadvantage compared to females in single-sex broods, and the presence of cowbird chicks appears to exacerbate this intraspecific, intersexual competition. Thus, in areas where cowbirds are common, the brood parasites have the potential to affect song sparrow demography and sex ratio. These findings confirm recent theories that suggest that parasites and predators can alter the sex ratio of their host and prey populations. — AMS

Ecology **86**, 815 (2005).

VIROLOGY

Retooling Degradation Factories

After breaching the outer defenses and establishing themselves inside a eukaryotic cell, viruses subvert existing cellular machinery in order to produce their progeny. When human cells are infected by poliovirus, new viruses are manufactured on cytoplasmic vesicles that are bounded by a double membrane. Jackson *et al.* examined the origin of these virus factories and found that they appear to be derived from autophagosomes, cellular compartments that ordinarily are used in the disposal of defunct organelles. It seems that after cellular invasion, the incoming virus becomes associated with membranes that mature into autophagosomes. Stimulation of autophagy in infected cells actually increased poliovirus yield, whereas inhibition reduced it. Although autophagy is known to be important in the cellular clearance of some microbes (such as *Mycobacterium tuberculosis*), for poliovirus and for related rhinoviruses, these destructive organelles are actually exploited to increase the efficiency of viral replication. — SMH

PLoS Biol. **3**, e156 (2005).

CHEMISTRY

Correlating Continua

Surface-enhanced Raman scattering (SERS) occurs on certain noble metal surfaces that are rough or have high curvature, such as colloidal particles. Moore *et al.* have probed the nature of the broad continuum states that usually accompany the sharp, highly enhanced molecular vibrations by performing a two-dimensional covariance and correlation analysis of single-molecule SERS spectra. Vibrational modes for the species on the native silver particles prepared in citrate solution are correlated with a continuum that peaks at 3000 cm^{-1}, but when the same particles were exposed to rhodamine 6G, the vibrational features correlated to a continuum that peaks at 1600 cm^{-1}. Neither continuum has sharp features of its own and thus appears to be associated with the particles, either as active sites or a surface species, that have molecular specificity. — PDS

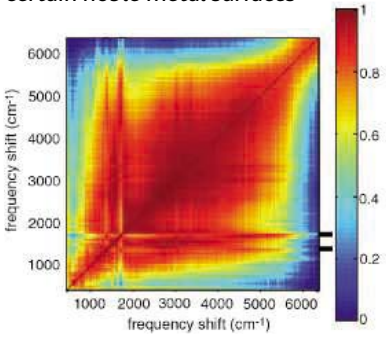

Two-dimension correlation map for the native silver particles.

J. Am. Chem. Soc. 10.1021/ja043651u (2005).

GEOPHYSICS

Sliding Under Lake Tahoe

The Great Basin of the United States is called that because, over the past 40 million years, the crust has been extending broadly. The locus of extension, which is characterized by faulting and volcanism, has moved from the center of the basin to its eastern and western margins, notably forming Death Valley, California. Along the western margin, the extension is complicated by its interaction with the San Andreas fault, a major strike-slip fault, and is now impinging on the Sierra Nevada Mountains (which have some of the highest elevations in North America).

Kent *et al.* have determined the recent extension at the margin in the Lake Tahoe area (on the border between California and Nevada) by dating and mapping offset shorelines and ancient avalanches into the lake. This history implies that the region is extending by about 0.5 mm/year, enough to produce a magnitude 7 earthquake approximately once every 3000 years. Such a quake could generate waves in Lake Tahoe approaching 10 m, or even much higher waves if the earthquake were to induce a slide into the lake as has happened in the past. — BH

Geology **33**, 365 (2005).

EVOLUTION

Coming Up for Air

The emergence of organisms from the ocean onto land was made possible by a suite of adaptations, not least of which were the integrated biomechanical changes that were required for bodily support and locomotion in a 1*g* world, as compared to a buoyant and

CONTINUED ON PAGE 929

incompressible aquatic environment. Sensory systems also had to adapt, and Niimura and Nei have examined the evolutionary dynamics of the genes encoding olfactory receptors in a phylogenetic analysis based on draft genome sequences from fish, frog, and chicken, along with already available genome data from mouse and human. They find that the most recent common ancestor (MRCA) of fishes and tetrapods carried at least nine distinct groups of olfactory receptors. Present-day fish have inherited eight of

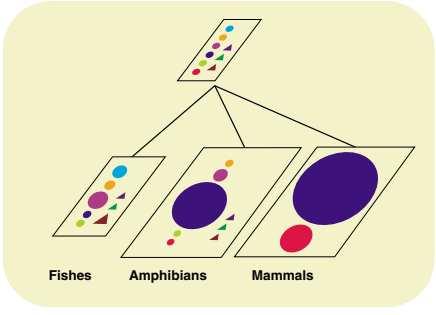

Ancestry of mammalian olfactory receptor groups α (red) and γ (blue).

these, but have lost group α, which is one of two groups extant in mammals and birds, the other being group γ. The number of olfactory receptors in groups α and γ has expanded enormously (numbering about 1000 in mouse), and they are proposed to have become specialized for the detection of airborne molecules, whereas olfactory receptor genes (presumed to have retained their competence for sensing water-soluble odorants) in the other groups were discarded. — GJC

Proc. Natl. Acad. Sci. U.S.A. **102**, 6039 (2005).

CHEMISTRY

Bimetallic Bases

The typical notion of a chemical base is a reactive molecular anion bound to a charge-balancing metal cation. Although the influence of anion structure on reactivity has long been appreciated, the metals are often regarded as interchangeable bystanders. Recent work suggests that the cations can play a strong role, however, particularly when two of them cooperate.

Andrikopoulos *et al.* prepared a hybrid base of butyl sodium and magnesium bis(tetramethylpiperidide). The butyl anion in the complex strips a proton from the *meta*-carbon in toluene, three carbons away from the more acidic methyl group. The origins of this unexpected reactivity were clarified by determining a crystal structure and by performing density functional calculations. The Mg cation stabilizes the deprotonated *meta*-carbon, whereas the Na cation interacts with π electrons above the phenyl ring.

Similarly, García *et al.* treated aminophenylphosphine (a phenyl ring bearing adjacent NH_2 and PH_2 groups) successively with butyl lithium and bis(dimethylamido)tin. In the resulting product, which is not produced by either base alone, all four protons have been stripped from the N and P centers. Crystallography revealed a complex structure in which four of the amido phosphide molecules are stabilized by a network of six Sn and four Li cations. — JSY

Angew. Chem. Int. Ed. 10.1002/anie.200500379; 10.1002/anie.200500340 (2005).

PSYCHOLOGY

Learning About Bias at an Early Age

Interpreting what someone else says can involve making an assessment of what that person believes or wants. In the former kind of situation, adults and children (from about 3 years of age onward) are capable of appreciating that what the speaker knows may not be an accurate representation of reality—that is, what is said appears to be true from the speaker's point of view, but is in fact not true because the speaker holds a false belief. In the latter type of situation, adults are aware that self-interest can lead one to make statements that are outright lies (motivated, intentional errors), reflect biases (motivated but unintentional errors), or simply are plain old mistakes.

Mills and Keil have examined how children evaluate these kinds of statements. In the first setting, where the outcome of a footrace was ambiguous, second- and fourth-graders, unlike kindergartners, were less apt to believe contestants who claimed to have won as compared to those who admitted defeat. In another setting in which the outcome was unambiguous, kindergartners, second-graders, and fourth-graders all were inclined to label erroneous claims aligned with the speaker's self-interest as lies and those aligned against as mistakes; however, sixth-graders demonstrated the beginnings of an awareness of how self-interest might unintentionally induce a misstatement and hence identified some of the erroneous claims as the products of bias. — GJC

Psychol. Sci. **16**, 385 (2005).

CREDITS: NIIMURA *ET AL.*, *PROC. NATL. ACAD. SCI. U.S.A.* **102**, 6039 (2005)

www.sciencemag.org

Science

1200 New York Avenue, NW
Washington, DC 20005
Editorial: 202-326-6550, FAX 202-289-7562
News: 202-326-6500, FAX 202-371-9227

Bateman House, 82-88 Hills Road
Cambridge, UK CB2 1LQ
+44 (0) 1223 326500, FAX +44 (0) 1223 326501

SUBSCRIPTION SERVICES For change of address, missing issues, new orders and renewals, and payment questions: 800-731-4939 or 202-326-6417, FAX 202-842-1065. Mailing addresses: AAAS, P.O. Box 1811, Danbury, CT 06813 or AAAS Member Services, 1200 New York Avenue, NW, Washington, DC 20005

INSTITUTIONAL SITE LICENCES please call 202-326-6755 for any questions or information

REPRINTS Ordering/Billing/Status 800-635-7171; Corrections 202-326-6501

PERMISSIONS 202-326-7074, FAX 202-682-0816

MEMBER BENEFITS Bookstore: AAAS/BarnesandNoble.com bookstore www.aaas.org/bn; Car purchase discount: Subaru VIP Program 202-326-6417; Credit Card: MBNA 800-847-7378; Car Rentals: Hertz 800-654-2200 CDP#343457, Dollar 800-800-4000 #AA1115; AAAS Travels: Betchart Expeditions 800-252-4910; Life Insurance: Seabury & Smith 800-424-9883; Other Benefits: AAAS Member Services 202-326-6417 or www.aaasmember.org.

science_editors@aaas.org (for general editorial queries)
science_letters@aaas.org (for queries about letters)
science_reviews@aaas.org (for returning manuscript reviews)
science_bookrevs@aaas.org (for book review queries)

Published by the American Association for the Advancement of Science (AAAS), *Science* serves its readers as a forum for the presentation and discussion of important issues related to the advancement of science, including the presentation of minority or conflicting points of view, rather than by publishing only material on which a consensus has been reached. Accordingly, all articles published in *Science*—including editorials, news and comment, and book reviews—are signed and reflect the individual views of the authors and not official points of view adopted by the AAAS or the institutions with which the authors are affiliated.

AAAS was founded in 1848 and incorporated in 1874. Its mission is to advance science and innovation throughout the world for the benefit of all people. The goals of the association are to: foster communication among scientists, engineers and the public; enhance international cooperation in science and its applications; promote the responsible conduct and use of science and technology; foster education in science and technology for everyone; enhance the science and technology workforce and infrastructure; increase public understanding and appreciation of science and technology; and strengthen support for the science and technology enterprise.

INFORMATION FOR CONTRIBUTORS

See pages 135 and 136 of the 7 January 2005 issue or access www.sciencemag.org/feature/contribinfo/home.shtml

EDITOR-IN-CHIEF **Donald Kennedy**
EXECUTIVE EDITOR **Monica M. Bradford**
DEPUTY EDITORS **R. Brooks Hanson, Katrina L. Kelner**
NEWS EDITOR **Colin Norman**

EDITORIAL SUPERVISORY SENIOR EDITORS Barbara Jasny, Phillip D. Szuromi; SENIOR EDITORS Gilbert J. Chin, Lisa D. Chong, Pamela J. Hines, Paula A. Kiberstis (Boston), Beverly A. Purnell, L. Bryan Ray, Guy Riddihough (Manila), H. Jesse Smith, Valda Vinson, David Voss; ASSOCIATE EDITORS Marc S. Lavine, Jake S. Yeston; ONLINE EDITOR Stewart Wills; CONTRIBUTING EDITOR Ivan Amato; ASSOCIATE ONLINE EDITOR Tara S. Marathe; BOOK REVIEW EDITOR Sherman J. Suter; ASSOCIATE LETTERS EDITOR Etta Kavanagh; INFORMATION SPECIALIST Janet Kegg; EDITORIAL MANAGER Cara Tate; SENIOR COPY EDITORS Jeffrey E. Cook, Harry Jach, Barbara P. Ordway; COPY EDITORS Cynthia Howe, Alexis Wynne Mogul, Sabrah M. n'haRaven, Jennifer Sills, Trista Wagoner; EDITORIAL COORDINATORS Carolyn Kyle, Beverly Shields; PUBLICATION ASSISTANTS Chris Filiatreau, Joi S. Granger, Jeffrey Hearn, Lisa Johnson, Scott Miller, Jerry Richardson, Brian White, Anita Wynn; EDITORIAL ASSISTANTS Ramatoulaye Diop, E. Annie Hall, Patricia M. Moore, Brendan Nardozzi, Michael Rodewald; EXECUTIVE ASSISTANT Sylvia S. Kihara; ADMINISTRATIVE SUPPORT Patricia F. Fisher

NEWS SENIOR CORRESPONDENT Jean Marx; DEPUTY NEWS EDITORS Robert Coontz, Jeffrey Mervis, Leslie Roberts, John Travis; CONTRIBUTING EDITORS Elizabeth Culotta, Polly Shulman; NEWS WRITERS Yudhijit Bhattacharjee, Jennifer Couzin, David Grimm, Constance Holden, Jocelyn Kaiser, Richard A. Kerr, Eli Kintisch, Andrew Lawler (New England), Greg Miller, Elizabeth Pennisi, Charles Seife, Robert F. Service (Pacific NW), Erik Stokstad; Amitabh Avasthi (intern); CONTRIBUTING CORRESPONDENTS Marcia Barinaga (Berkeley, CA), Barry A. Cipra, Adrian Cho, Jon Cohen (San Diego, CA), Daniel Ferber, Ann Gibbons, Robert Irion, Mitch Leslie (NetWatch), Charles C. Mann, Evelyn Strauss, Gary Taubes, Ingrid Wickelgren; COPY EDITORS Linda B. Felaco, Rachel Curran, Sean Richardson; ADMINISTRATIVE SUPPORT Scherraine Mack, Fannie Groom BUREAUS: Berkeley, CA: 510-652-0302, FAX 510-652-1867, New England: 207-549-7755, San Diego, CA: 760-942-3252, FAX 760-942-4979, Pacific Northwest: 503-963-1940

PRODUCTION DIRECTOR James Landry; SENIOR MANAGER Wendy K. Shank; ASSISTANT MANAGER Rebecca Doshi; SENIOR SPECIALISTS Vicki J. Jorgensen, Jessica K. Moshell; SPECIALISTS Jay R. Covert, Stacey Ferebee; **PREFLIGHT** DIRECTOR David M. Tompkins; MANAGER Marcus Spiegler; SPECIALIST Jessie Mudjitaba;

ART DIRECTOR Joshua Moglia; ASSOCIATE ART DIRECTOR Kelly Buckheit; ILLUSTRATOR Katharine Sutliff; SENIOR ART ASSOCIATES Holly Bishop, Laura Creveling, Preston Huey, Julie White; ASSOCIATE Nayomi Kevitiyagala; PHOTO RESEARCHER Leslie Blizard

***SCIENCE* INTERNATIONAL**

EUROPE (science@science-int.co.uk) EDITORIAL: INTERNATIONAL MANAGING EDITOR Andrew M. Sugden; SENIOR EDITOR/PERSPECTIVES Julia Fahrenkamp-Uppenbrink; SENIOR EDITORS Caroline Ash (Geneva: +41 (0) 222 346 3106), Stella M. Hurtley, Ian S. Osborne, Peter Stern; ASSOCIATE EDITOR Stephen J. Simpson; EDITORIAL SUPPORT Emma Westgate; Deborah Dennison ADMINISTRATIVE SUPPORT Janet Clements, Phil Marlow, Jill White; NEWS: INTERNATIONAL NEWS EDITOR Eliot Marshall DEPUTY NEWS EDITOR Daniel Clery; CORRESPONDENT Gretchen Vogel (Berlin: +49 (0) 30 2809 3902, FAX +49 (0) 30 2809 8365); CONTRIBUTING CORRESPONDENTS Michael Balter (Paris), Martin Enserink (Amsterdam and Paris); INTERN Mason Inman

ASIA Japan Office: Asca Corporation, Eiko Ishioka, Fusako Tamura, 1-8-13, Hirano-cho, Chuo-ku, Osaka-shi, Osaka, 541-0046 Japan; +81 (0) 6 6202 6272, FAX +81 (0) 6 6202 6271; asca@os.gulf.or.jp JAPAN NEWS BUREAU: Dennis Normile (contributing correspondent, +81 (0) 3 3391 0630, FAX 81 (0) 3 5936 3531; dnormile@gol.com); CHINA REPRESENTATIVE Hao Xin, + 86 (0) 10 6307 4439 or 6307 3676, FAX +86 (0) 10 6307 4358; haoxin@earthlink.net; SOUTH ASIA Pallava Bagla (contributing correspondent +91 (0) 11 2271 2896; pbagla@vsnl.com); CENTRAL ASIA Richard Stone (+7 3272 6413 35, rstone@aaas.org)

EXECUTIVE PUBLISHER **Alan I. Leshner**
PUBLISHER **Beth Rosner**

FULFILLMENT & MEMBERSHIP SERVICES (membership@aaas.org) DIRECTOR Marlene Zendell; MANAGER Waylon Butler; SENIOR SPECIALIST Pat Butler; SPECIALISTS Laurie Baker, Tamara Alfson, Karena Smith, Andrew Vargo; MARKETING ASSOCIATE Deborah Stromberg

BUSINESS OPERATIONS AND ADMINISTRATION DIRECTOR Deborah Rivera-Wienhold; BUSINESS MANAGER Randy Yi; SENIOR FINANCIAL ANALYST Lisa Donovan; BUSINESS ANALYST Jessica Tierney; FINANCIAL ANALYST Farida Yeasmin; RIGHTS AND PERMISSIONS: ADMINISTRATOR Emilie David; ASSOCIATE Elizabeth Sandler; MARKETING: DIRECTOR John Meyers; MEMBERSHIP MARKETING MANAGER Darryl Walter; MARKETING ASSOCIATE Julianne Wielga; RECRUITMENT MARKETING MANAGER Allison Pritchard; ASSOCIATES Mary Ellen Crowley, Amanda Donathen, Catherine Featherston; DIRECTOR OF INTERNATIONAL MARKETING AND RECRUITMENT ADVERTISING Deborah Harris; INTERNATIONAL MARKETING MANAGER Wendy Sturley; MARKETING/MEMBER SERVICES EXECUTIVE: Linda Rusk; JAPAN SALES AND MARKETING MANAGER Jason Hannaford; SITE LICENSE SALES: DIRECTOR Tom Ryan; SALES AND CUSTOMER SERVICE Mehan Dossani, Catherine Holland, Adam Banner, Yaniv Snir; ELECTRONIC MEDIA: INTERNET PRODUCTION MANAGER Lizabeth Harman; ASSISTANT PRODUCTION MANAGER Wendy Stengel; SENIOR PRODUCTION ASSOCIATES Sheila Mackall, Amanda K. Skelton, Lisa Stanford; PRODUCTION ASSOCIATE Nichele Johnston; LEAD APPLICATIONS DEVELOPER Carl Saffell

PRODUCT ADVERTISING (science_advertising@aaas.org); MIDWEST Rick Bongiovanni: 330-405-7080, FAX 330-405-7081 • WEST COAST/W. CANADA B. Neil Boylan (Associate Director): 650-964-2266, FAX 650-964-2267 • EAST COAST/E. CANADA Christopher Breslin: 443-512-0330, FAX 443-512-0331 • UK/SCANDINAVIA/FRANCE/ITALY/BELGIUM/NETHERLANDS Andrew Davies (Associate Director): +44 (0)1782 750111, FAX +44 (0) 1782 751999 • GERMANY/SWITZERLAND/AUSTRIA Tracey Peers (Associate Director): +44 (0) 1782 752530, FAX +44 (0) 1782 752531 JAPAN Mashy Yoshikawa: +81 (0) 33235 5961, FAX +81 (0) 33235 5852 ISRAEL Jessica Nachlas +9723 5449123 • TRAFFIC MANAGER Carol Maddox; SALES COORDINATOR Deiandra Simms

CLASSIFIED ADVERTISING (advertise@sciencecareers.org); U.S.: SALES DIRECTOR Gabrielle Boguslawski: 718-491-1607, FAX 202-289-6742; INTERNET SALES MANAGER Beth Dwyer: 202-326-6534; INSIDE SALES MANAGER Daryl Anderson: 202-326-6543; WEST COAST/MIDWEST Kristine von Zedlitz: 415-956-2531; EAST COAST Jill Downing: 631-580-2445; LINE AD SALES Emnet Tesfaye: 202-326-6740; SENIOR SALES COORDINATOR Erika Bryant; SALES COORDINATORS Rohan Edmonson, Christopher Normile, Joyce Scott, Shirley Young; INTERNATIONAL: SALES MANAGER Tracy Holmes: +44 (0) 1223 326525, FAX +44 (0) 1223 326532; SALES Christina Harrison, Suitlana Barnes; SALES ASSISTANT Helen Moroney; JAPAN: Jason Hannaford: +81 (0) 52 789 1860, FAX +81 (0) 52 789 1861; PRODUCTION: MANAGER Jennifer Rankin; ASSISTANT MANAGER Deborah Tompkins; ASSOCIATE Amy Hardcastle; SENIOR TRAFFICKING ASSOCIATE Christine Hall; SENIOR PUBLICATIONS ASSISTANT Robert Buck; PUBLICATIONS ASSISTANT Natasha Pinol

AAAS BOARD OF DIRECTORS RETIRING PRESIDENT, CHAIR Shirley Ann Jackson; PRESIDENT Gilbert S. Omenn; PRESIDENT-ELECT John P. Holdren; TREASURER David E. Shaw; CHIEF EXECUTIVE OFFICER Alan I. Leshner; BOARD Rosina M. Bierbaum; John E. Burris; John E. Dowling; Lynn W. Enquist; Susan M. Fitzpatrick; Richard A. Meserve; Norine E. Noonan; Peter J. Stang; Kathryn D. Sullivan

AAAS
ADVANCING SCIENCE, SERVING SOCIETY

New!
Applied Biosystems 9800 Fast PCR System.

PCR in just 25 minutes.

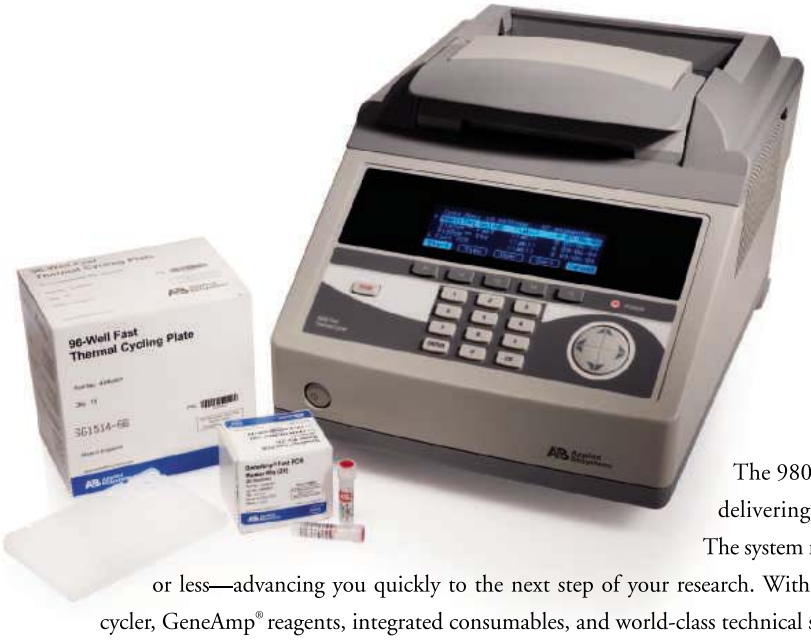

The 9800 Fast PCR System is the first fully integrated solution delivering fast PCR performance in a standard 96-well format. The system reduces PCR reaction time from two hours to 25 minutes or less—advancing you quickly to the next step of your research. With the fast-optimized system including the 9800 thermal cycler, GeneAmp® reagents, integrated consumables, and world-class technical support, you can count on fast, reliable results. Put your trust in the 9800 Fast PCR System for faster PCR performance—visit http://info.appliedbiosystems.com/**9800**

iScience. Applied Biosystems provides the innovative products, services, and knowledge resources that are enabling new, integrated approaches to scientific discovery.

Applied Biosystems

NetWatch

edited by Mitch Leslie

RESOURCES

Liquid Assets

Whether it's the Everglades or just a seasonal pool, a wetland is a haven for life. Find out where these habitats are located across much of the United States with the Wetlands Mapper* at this U.S. Fish and Wildlife Service site. The tool lets you zoom in to a scale of just a few meters. The site also lists wetland plant species and reports on how fast wetlands are vanishing (23,000 hectares a year in 2000). The U.S. Geological Survey's National Wetlands Research Center† offers fact sheets on topics such as mangroves and climate change as well as the nutria, a ratlike invasive species chomping its way through Louisiana's dwindling swamps. An online library includes reports documenting the ecology and habitat needs of more than 100 coastal wetland residents, from the black abalone to the yellowtail snapper.

* wetlands.fws.gov

† www.nwrc.usgs.gov

IMAGES

The Earth in Your Computer

Few of us will ever gaze down at Earth from space. With the free program World Wind, though, even chairbound adventurers can swoop past Japan's Mount Fuji (right), trace the fractures in a Greenland iceberg, or zoom in on their houses from high altitudes. The software from NASA's Ames Research Center knits together satellite images and elevation data, letting users chart spectacular virtual trips. For more than 30 major U.S. cities, the program features 25-centimeters-per-pixel color images—a resolution that allows viewers to pick out cars on the Golden Gate Bridge. Black-and-white aerial photographs and topographic maps capture the rest of the country. Users can also overlay the latest temperature and cloud-cover measurements and summon data on fires, floods, storms, and volcanic activity. You'll need Windows, a 3-D graphics card, and a 1.4 gigahertz or faster processor.

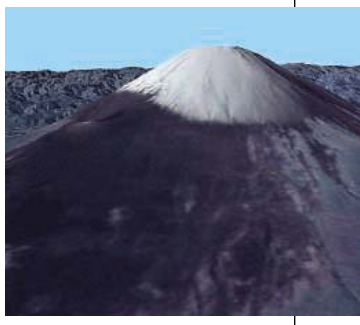

worldwind.arc.nasa.gov

RESOURCES

Still in the Crosshairs

The Cold War may be long over, but the threat of nuclear annihilation remains. To drive home the point, the nonprofit Federation of American Scientists provides its Nuclear Weapon Effect Calculator, a Java applet that lets visitors see how far the zone of destruction would stretch if an atomic bomb of a specific size exploded in Washington, D.C., or in one of 24 other American cities. "This is just a very graphic way to let anyone see what the effect of a bomb on his city would be," says Ivan Oelrich, director for the federation's strategic security project.

The foundation's Web site offers scientific guidance on issues from energy-efficient housing to biomedical computing, but its focus is nuclear arms control. You'll find tutorials on timely questions such as how a gas centrifuge could help a rogue nation amass the uranium necessary to make a bomb. Reports also apply technical expertise to policy analysis, arguing for instance that an adversary could evade the U.S.'s proposed earth-boring "bunker buster" bomb simply by tunneling deeper.

www.fas.org

EXHIBITS

A Killer Remembered

Americans were so worried about polio in the early and middle 20th century that some towns forbade travelers under 16 years old from entering, fearing they might be carrying the disease. At Whatever Happened to Polio? you can look back at those nervous days and learn about the vaccines that helped stamp out polio in the United States.

The new Web site, which accompanies an exhibit at the Smithsonian Institution, marks the 50th anniversary of the polio vaccine. It offers period photos, audio clips from polio survivors, and other resources that chart the disease's wrenching impact on society and families. For instance, newly diagnosed children were often quarantined for up to 14 days, followed by several weeks of limited contact with their parents. Technologies of the day included these cumbersome iron lungs that helped paralyzed patients breathe (left). You can also learn about Jonas Salk's and Albert Sabin's vaccines. Salk introduced his vaccine first, but Sabin's, which relied on a weakened virus rather than an inactive one, was more widely used. A final section looks at current efforts to eradicate polio from the few countries where it remains.

americanhistory.si.edu/polio

Send site suggestions to netwatch@aaas.org. Archive: www.sciencemag.org/netwatch

CREDITS (TOP TO BOTTOM): BILL GILL/USFWS; NASA; SMITHSONIAN INSTITUTION

This Week

PAGE 936
Leprosy and human migration

938
What price security?

FUSION REACTOR

ITER Rivals Agree to Terms; Site Said to Be Cadarache

CAMBRIDGE, U.K., AND TOKYO—The contenders to host the $11 billion ITER fusion project—Japan and the European Union—finally appear to have made a deal. After 16 months of negotiations, the two parties have agreed on a package to compensate the runner-up. The only thing left is to name the winner, which must be done by the end of June. And if European politicians and Japanese newspapers are to be believed, the most expensive science experiment on Earth will be built in France.

The original schedule for building the International Thermonuclear Experimental Reactor (ITER) called for a siting decision to be made in December 2003 between Cadarache in southern France or Rokkasho in northern Japan. But the project's six partners split down the middle: The United States and Korea supported the Japanese site, whereas Russia and China backed the E.U. site in France. Technical studies early last year failed to produce a clear favorite. Since then, European and Japanese officials have been chalking up frequent-flyer points in lobbying their partners.

The aim of ITER is to recreate the power of the sun on Earth. Hydrogen isotopes in a superhot plasma fuse rapidly enough to generate roughly 10 times more heat than the reactor needs to keep running. This would ensure that a future fusion power plant will produce excess electricity. Building such a reactor is a huge undertaking: Construction costs alone are projected at $5 billion over 10 years, and another $6 billion will be spent on operating the reactor and decommissioning it at the end of the 30-year project.

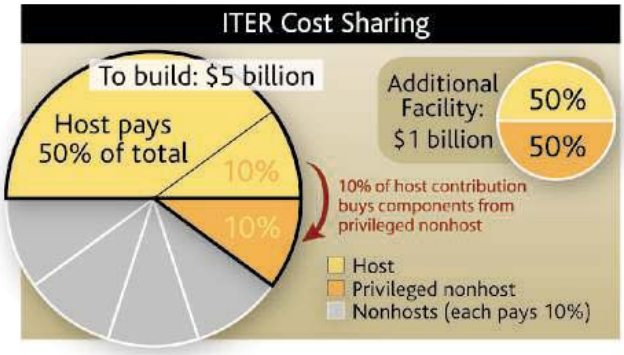

Rebaking the pie. To compensate the runner-up, ITER's host will place 10% of its contracts there. The host will also pay for half of a new facility in that country.

Much of this money will be spent in the host country, so the competition for this prize has been fierce and protracted. But during an E.U. delegation visit to Tokyo on 12 April, the two sides resolved to settle the site issue before the 6 July start of the G8 economic summit of industrialized nations in Scotland (*Science*, 15 April, p. 337). After an apparently productive discussion between Japanese Prime Minister Junichiro Koizumi and E.U. officials at a 2 May meeting in Luxembourg, *The Yomiuri Shimbun*, one of Japan's leading daily papers, quoted government sources as saying Japan might be willing to give up its bid for ITER if it won a lucrative role in building the reactor. And late last week, at a meeting on earth observation in Geneva, Japanese and E.U. officials finally worked out a formula that was acceptable to both sides.

The details have not been made public, but E.U. officials have told *Science* that ITER's host will be expected to foot 50% of the bill. The other five partners would contribute 10% each. Most of these contributions will be in the form of components built in their own countries and shipped to the site. But the unsuccessful contender will have a "privileged" position in the project, producing 20% of ITER's components but only paying for 10%, with the extra funding coming from the successful host. E.U. sources say the payment will be low-key, made through industrial contracts.

That's not all the runner-up will get. Its nationals will be guaranteed a minimum share of ITER's staff—20%, according to Japanese newspapers. And it will get to host a new parallel research effort to help commercialize fusion, with one possibility a materials testing center to assess whether reactor linings can stand up to decades of neutron bombardment. E.U. sources say that this facility could cost as much as $1 billion, divided evenly between Japan and the E.U.

The formula must still be approved by all six ITER partners. Shuichiro Itakura, head of the Office of Fusion Energy at Japan's education ministry, says the formula is simply a "common view" between the two negotiators. "It still needs to be reviewed within the [Japanese] government," he adds. But in ▶

SOURCE: ITER

STEM CELL RESEARCH

California Institute Picks City by the Bay

After a heated competition akin to selecting a venue for the Olympics, San Francisco has been chosen as headquarters for the California Institute for Regenerative Medicine (CIRM).

Ten California cities vied to host the 50-person managerial hub of the $3 billion, 10-year research program created by passage of Proposition 71 last November. Bidders offered a splendid array of perks from free office space to health club memberships to access to private jets.

A search committee accorded points to each city on the basis of qualities such as research environment, office space, and conference facilities. San Francisco led Sacramento and San Diego in the technical rankings that went to the 29-member oversight committee, which chose San Francisco over San Diego by a vote of 16 to 11.

Some observers worried about regional bias on the oversight panel, headed by Bay Area financier Robert Klein. Indeed, the committee was split almost equally between northern and southern Californians, and all voted accordingly except for two members from Los Angeles, notes Jane Signaigo-Cox of the San Diego Regional Economic Development Corporation. But she thought the vote was "fair."

Pushed aggressively by Mayor Gavin Newsom, San Francisco's bid was worth about $18 million. Delayed by lawsuits alleging conflict-of-interest violations and inadequate state oversight, CIRM hopes to award its first research grants by November.

–CONSTANCE HOLDEN

Europe, some are boldly predicting that ITER will be built in France, in line with the E.U.'s position that it's Cadarache or nothing. Going even further, President Jacques Chirac said on French television on 4 May that France was "on the verge of getting ITER sited at Cadarache."

E.U. officials are more reticent than the French. One senior official says he is "confident of a resolution," but it is still "a very delicate situation." Japan's Ministry of Education put out a statement strongly denying it has given up trying to bring ITER to Rokkasho. Researchers are staying quiet for fear of jeopardizing the deal, but the politicking appears to have added a fusion development facility that was not originally on the negotiating table. "I think it's important that an additional facility is now included, because ITER alone is not going to provide all the data we need to move toward commercialization," says Yoshikazu Okumura of the Japan Atomic Energy Research Institute.

Politicians from the six ITER partners are now looking to wrap things up at a late June meeting in Moscow. The venue is symbolic: It was here in 1985 that Soviet researchers persuaded President Mikhail Gorbachev to approach Western leaders with the idea of working together on a global fusion research project that would benefit society and reduce international tensions. For a while, ITER seemed more likely to do the opposite. But the injured feelings may soon pass into history.

–Daniel Clery and Dennis Normile

NASA ASTRONOMY

New Space Telescope May Be Scaled Back

Faced with a $1 billion cost overrun, NASA managers last week began to search for cheaper designs for the $3.5 billion James Webb Space Telescope (JWST). But astronomers say the initial attempt to scale back the complexity of the spacecraft and its instruments is a nonstarter for the mission slated for a 2011 launch as a follow-on to the Hubble Space Telescope.

The crisis comes just as the decision not to send a space shuttle servicing mission to Hubble seems likely to be overturned by NASA's new chief Michael Griffin. Some scientists worry that extending the life of Hubble into the next decade could add to the pressure to scale back Webb, which is the top priority in the astronomy community's decadal plan put together under the auspices of the National Academies.

Named for one of NASA's first administrators, Webb will use its 6.5-meter mirror and four major instruments to observe primarily the infrared portion of the spectrum, peering back in time to the era of galaxy formation and piercing interstellar dust to get close-up views of other planetary systems. It may also provide clues to the elusive nature of dark matter. The telescope's science team includes Europeans, Americans, and Canadians.

Until just a few weeks ago, astronomers thought the telescope was on track despite a budget request this year from NASA to trim $55 million from its account over the next 5 years. That's before its prime contractor, Northrop Grumman, wrote NASA that the telescope would cost $309 million above the previous estimate, according to John Mather, NASA's JWST project director. The largest chunk of that increase was a shift in the spacecraft testing from a facility operated by NASA's Lewis Research Center in Cleveland, Ohio, to Johnson Space Center in Houston, Texas. The Lewis facility proved inadequate for handling the full spacecraft, and alterations would have been too costly. Additional technical changes to the design have added nearly $100 million to the cost.

It's also going to cost more to launch the telescope. It was originally slated to fly on a U.S. rocket before the European Space Agency (ESA) offered an Ariane 5 as its major contribution to the program. The offer provoked complaints from U.S. industry and other government agencies, but after months of wrangling, the White House has given Griffin authority to use the European rocket, which he is expected to do shortly. Accommodating Webb on Ariane, combined with a likely 1-year launch delay, bumps up its price, as does an increased reserve fund ordered by NASA. New rules that require NASA projects to include all costs associated with the program mean another $100 million. When you add it all up, according to JWST program scientist Eric Smith, the total overrun is approximately $1 billion.

To reduce JWST costs, NASA managers last week suggested returning to a scaled-back version proposed in the mid-1990s. Under that plan, JWST's mirror would be only 4 meters in diameter, and its ability to detect certain wavelengths would be significantly reduced. As a result, data on some objects would take as much as 25 times longer to gather than with the current design. The telescope's expected lifetime also would be halved, to 5 years.

"It would not be scientifically sensible to fly that mission," says Peter Jakobsen, ESA's study scientist for JWST. Other scientists agree. In a meeting last week with NASA officials, the JWST science team rejected the alternative as unacceptable. "It is clear to scientists that almost all science would be lost" in this plan, says Mather.

CREDIT: TRW AND BALL AEROSPACE

Webb woes. NASA's next-generation telescope has suddenly gotten $1 billion more expensive.

NASA managers have given scientists a couple of weeks to come up with a better alternative. But their job won't be easy. "If the funding is not compatible with breakthrough science, then [more] money needs to be moved to JWST, or it should be canceled," says George Rieke, an astronomer at the University of Arizona in Tucson who is a co–principal investigator on one instrument. Adds Mather: "It's a scary moment."

–Andrew Lawler

With reporting by Govert Schilling.

MICROBIOLOGY

Global Spread of Leprosy Tied to Human Migration

Long before the Black Death or AIDS ravaged society, there was leprosy. But for a disease that has devastated humans for millennia, leprosy remains enigmatic. Where did it originate, and how has it followed people seemingly everywhere they've gone?

The first comprehensive genetic comparison of the bacterial strains that cause the disease is providing some answers. On page 1040, molecular microbiologist Stewart Cole of the Pasteur Institute in Paris and colleagues use rare DNA differences among leprosy strains culled from various corners of the world to infer an East African or Near East origin of the disease. Their findings also challenge popular theories of how leprosy spread and indicate that colonialism and the slave trade helped bring the sickness to West Africa and much of the New World.

"It's very interesting work that should help us fill in the picture of how human migration is tied to the dissemination of leprosy," says Daniel Hartl, a population geneticist at Harvard University in Cambridge, Massachusetts.

Confirmed reports of leprosy first appear around 600 B.C.E. in sacred Indian texts that describe a victim's loss of finger and toe sensation—a hallmark of the damage the bacterium *Mycobacterium leprae* inflicts on the nervous system. By medieval times, cultures around the globe were familiar with the deforming lesions and decaying flesh that resulted in lepers being burned at the stake or carted off to die in remote colonies. Antibiotics helped bring the disease under control in the 1940s, but it persists in poor regions, and there are more than 500,000 new cases reported each year.

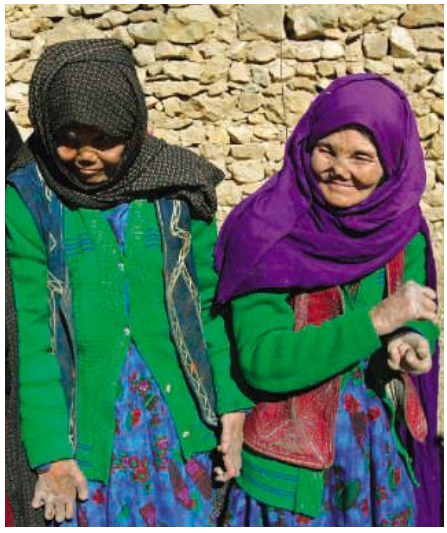

Worldwide toll. Leprosy persists among people in poor regions, such as these women in Afghanistan.

Scientists rely on genetic differences among strains to trace the history of a microbe, but seven strains of the leprosy bacterium, collected by Cole's group from an array of countries, had practically identical genomes. "*M. leprae* has the lowest level of genetic diversity of any bacterium I'm aware of," says Cole. "One clone has infected the whole world."

The intense similarity between strains compelled the researchers to take a closer look at their samples. Eventually they found subtle DNA sequence mutations called single nucleotide polymorphisms that allowed them to break a total of 175 worldwide strains into four types. Most Central Asian strains were of the type-1 variety, whereas type 2 predominated in Ethiopia, type 3 in Europe, North Africa, and the Americas, and type 4 in West Africa and the Caribbean.

The mutation patterns among the strains suggest that leprosy originated in either Central Asia or East Africa, says Cole, who favors the latter location because type 2 is the rarest and, thus, likely the oldest. "India has been stigmatized as the cradle of leprosy," Cole says. "But the disease could have just as likely arisen in East Africa."

The data also challenge the theory that Alexander the Great's soldiers brought leprosy to Europe when returning from their Indian campaign. "That would have required a transition from type 1 to 2 to 3," says Cole. It's more likely, he argues, that the soldiers contracted the bug in the Near East.

Another striking finding is the apparent effect of European emigration and the West African slave trade on the spread of leprosy. *M. leprae* types 3 and 4 are more similar to each other than they are to type 1, indicating that ▶

DOE WEAPONS LAB

Los Alamos Appoints Interim Director

George "Pete" Nanos has stepped down as director of Los Alamos National Laboratory on the eve of a competition to manage the New Mexico weapons lab.

The University of California (UC), which operates Los Alamos for the Department of Energy (DOE), announced last week that nuclear weapons physicist Robert W. Kuckuck, 65, will become interim director on 16 May. Nanos, a retired Navy admiral, joined the laboratory in January 2003, pledging to right the ship after a series of security lapses. But tough reforms, a decision to shut the lab down last year after a laser accident, and his brash style—he called scientists "cowboys" during the shutdown—earned him harsh reviews from lab scientists. A series of suspensions following the disappearance of classified disks—later found never to have existed—led to outrage in New Mexico and Washington, D.C., alike. Massachusetts Institute of Technology historian Hugh Gusterson calls Nanos "the most unpopular director the lab has ever had." Nanos is taking a job with the Pentagon's Defense Threat Reduction Agency.

Moving on. Nanos had a rocky tenure at Los Alamos.

"Nanos was between a rock and a hard place," says Pete Stockton, an investigator with the Project on Government Oversight, a Washington, D.C., watchdog group. Last week, Defense Nuclear Facilities Safety Board acting Chair A. J. Eggenberger told Congress that the shutdown—which is estimated to have cost more than $120 million—"resulted in the identification of numerous corrective actions." But at the same hearing, DOE's Inspector General Gregory Friedman reviewed a litany of lingering management problems.

Nanos's rocky tenure, insiders say, underscores the risk facing UC's Board of Regents. "Some think UC might walk away" from the competition, says Doug Roberts, the Los Alamos computer scientist who runs a Web site for anonymous comments from lab employees. Last month, Sandia National Laboratories operator Lockheed Martin recruited Sandia's former director, Paul Robinson, for its bid (*Science*, 15 April, p. 339). The National Nuclear Security Administration is expected to release final contract language shortly.

Oak Ridge National Laboratory Director Jeff Wadsworth calls Kuckuck (pronounced "cook-cook") a "terrific team builder." A physicist and former deputy director of Lawrence Livermore National Laboratory in California, he is not expected to be part of UC's management team if it competes for the Los Alamos contract. —ELI KINTISCH

CREDITS (TOP TO BOTTOM): AHMAD MASOOD/REUTERS; JEFF GEISSLER/AP PHOTO

these activities, rather than human passage from Asia via the Bering Strait, brought the disease to the New World. "Leprosy has clearly migrated with human populations in orderly patterns," says Cole. "And in places like the Americas, where the disease is relatively new, you're really seeing the negative side of colonialism."

Molecular anthropologist Connie Mulligan of the University of Florida, Gainesville, says the data tying colonialism to the spread of leprosy are "really good," but she's not convinced there's enough evidence to favor type 2 over type 1 as the original leprosy strain. Still, Mark Achtman, a microbial population geneticist at the Max Planck Institute for Infection Biology in Berlin, says that this new study is bringing us closer to understanding leprosy's past. "As humans, we want to know where we came from," he notes. "The same goes for our diseases." –DAVID GRIMM

ECOLOGY

Fish Moved by Warming Waters

Climate change has fish populations on the move. In Europe's intensively fished North Sea, the warming waters over the past quarter-century have driven fish populations northward and deeper, according to a study by conservation ecologist John D. Reynolds of the University of East Anglia in Norwich, U.K., and his colleagues. Such warming could hamper the revival of overfished species and disrupt ecosystems, they assert. The warming is expected to continue in the North Sea, and although fish species living to the south will likely move north and replace departing ones, the forecast for the region's fisheries will depend on whether the species that succeed are marketable.

"This is another clear indication that warming is playing a role" in ocean ecosystems, says physical oceanographer Ken Drinkwater of the Institute of Marine Research in Bergen, Norway. Although there have been many studies looking at the effects of climate change on marine species, "no one has looked in detail at changes in distributions of commercial and noncommercial species," says fish biologist Paul Hart of the University of Leicester in the United Kingdom. Similar climate-induced shifts in fish populations, he adds, might happen in other temperate seas, including those around Europe and much of the United States.

The study, published online this week by *Science* (www.sciencemag.org/cgi/content/abstract/1111322), used extensive records of fishing catches made by research vessels between 1977 and 2001, a period during which the North Sea's waters warmed by 1ºC at the sea floor. Reynolds's team cast a wide net, compiling data on the sea's 36 most common bottom-dwelling fish. They found that two-thirds of the populations moved toward cooler waters—either going north or to deeper waters, or both. "We saw shifts in both commercial and noncommercial species, and across a broad set of species," says conservation ecologist Allison Perry of the University of East Anglia. The fish species whose distribution have shifted tend to be smaller and mature earlier, she and her colleagues noted.

"Those fish that didn't shift raise interesting questions," adds Perry. Such species might be more closely tied to particular habitats or might not spread as quickly because of longer generation times. Because species are redistributing at different rates or not at all, the shifts could rend ties within ecosystems. Species are often adapted to each other and have developed mechanisms for avoiding certain predators or catching specific prey, Hart says: "If suddenly faced with new predators or prey, this could change the balance." Moreover, if the timing of development shifts differently among various species, "this could affect the match or mismatch between the fishes' food and predators," Drinkwater says.

Gone fish. Warming waters in the North Sea may make it harder for commercial fishers to find their normal catch.

CREDIT: CATHERINE KARNOW/CORBIS

Heavy commercial fishing has already pushed some species in the North Sea to the edge of extinction, and some researchers worry that the changing climate will exacerbate those problems. "Fishing is undoubtedly the most important factor for all the commercial species," says fisheries biologist Niels Daan of the Netherlands Institute for Fisheries Research in IJmuiden. "But it is possible the warming could prevent the recovery of stocks." –MASON INMAN

ScienceScope

No Stemming the Tide

New York state legislators have so far failed to pass a stem cell research bill, but private donors are busy making sure the state stays abreast of California in the stem cell stakes.

Last week, Mount Sinai School of Medicine in New York City announced a $10 million donation from financier Leon D. Black for the Black Family Stem Cell Institute. The new institute becomes the latest work outside the federal government's stem cell guidelines. Last year, Weill Medical College of Cornell University, also in New York City, was given $15 million by Houston philanthropists Shahla and Hushang Ansary to establish the Ansary Center for Stem Cell Therapeutics.

The Black Institute will be led by stem cell biologist Gordon Keller, who plans to hire six more researchers. "Yes, the private gifts are flowing," says Keller. "There'll be a lot happening in New York." Keller acknowledges that he's had some nibbles from California but that the new gift "allows us to build a very strong stem cell program here at Mount Sinai."

–CONSTANCE HOLDEN

ALS-Vet Linkage Pursued

The ALS Association is pushing for more research into why U.S. military veterans seem more prone to amyotrophic lateral sclerosis (ALS), also known as Lou Gehrig's disease, than the general population.

The reasons aren't clear. Last year, a Department of Veterans Affairs (VA) report by an outside panel of veterans and scientists concluded that there was a "probable link" between neurotoxins and Gulf War illnesses, some of which resemble ALS symptoms. That finding was criticized by a number of researchers (*Science*, 1 October 2004, p. 26).

At least two studies have found that veterans of the 1990–91 Gulf War were roughly twice as likely to develop ALS. But because ALS usually strikes in the 40s and 50s, those samples were relatively small. A much broader study was published in January in *Neurology*: There, a team of Harvard epidemiologists reported that men in the military had a roughly 50% greater chance of contracting ALS—meaning their lifetime risk rose from 2 to 3 in 1600.

This week the association called for additional funding to tackle the apparent link between ALS and military service and also asked Congress to respond to the VA report's recommendations.

–JENNIFER COUZIN

SENSITIVE TECHNOLOGY

Schools Fear Impact of Proposed License Changes

Academic and industry scientists are fighting proposed changes to export-control rules that could restrict some foreign nationals from using sensitive equipment when they do research in the United States. But federal officials say opponents are vastly overestimating the impact of the changes on the research enterprise.

The rules, enforced by the Commerce Department's Bureau of Industry and Security (BIS), apply to persons from countries that the U.S. government says pose national security threats. The list includes China, India, and Russia, which are major sources of U.S. scientific talent. Universities have traditionally believed that an exemption for basic research in the rules applied to them. But in March 2004, the Department of Commerce Inspector General (IG) noted that the use of export-controlled equipment for research was not exempt, meaning that universities would need licenses to employ foreign nationals in certain research projects.

Based on the IG's recommendations, the bureau clarified the license requirement. It also proposed changing the criterion for granting a so-called deemed export license from the foreign national's country of citizenship to his or her country of birth. That change is intended to block foreign nationals from subverting the rules by establishing citizenship in another country not on the danger list. The changes, which were published in the 28 March *Federal Register*, are open for public comment until 27 May.

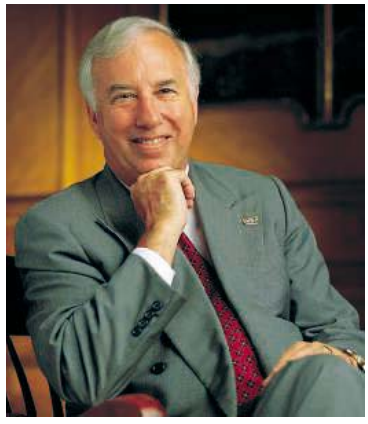

The price of security. Maryland's Daniel Mote says rule changes could cost his university $1.5 million.

BIS officials predict that the number of researchers requiring licenses will be very small. But Daniel Mote, president of the University of Maryland, College Park, says his school will need to spend $1.5 million to find out, that is, to classify research equipment on campus into different categories of export-controlled items and monitor their use. For practical reasons, he says, institutions may decide "when in doubt, apply for a license." One way for the government to reduce the regulatory burden on campuses, Mote said at a 6 May meeting at the National Academies, would be to grant international students and postdoctoral scholars a deemed export license when they receive visas. ▶

MICROBIOLOGY

Détente Declared on NIH Biodefense Funding

Microbiologists concerned that the buildup of biodefense research could be hurting basic research are celebrating a small victory after meeting with top National Institutes of Health (NIH) officials last week. Both sides agreed they should stop quibbling over grants data, and instead, NIH and the microbiology community should look at what scientific areas are falling through the cracks. "These are positive developments," says Richard Ebright, a microbiologist at Rutgers University in Piscataway, New Jersey, and a leading critic of NIH's biodefense spending.

The meeting marked a change in tone for NIH officials, who until now have defended funding decisions that more than 700 microbiologists questioned in a open letter (*Science*, 4 March, pp. 1396 and 1409). The letter claimed that giving the National Institute of Allergy and Infectious Diseases (NIAID) $1.5 billion more for biodefense has diverted microbiologists from studies of model organisms and nonbiodefense pathogens. As proof, the authors noted a sharp drop since 2000 in grants funded by the two main study sections reviewing those proposals.

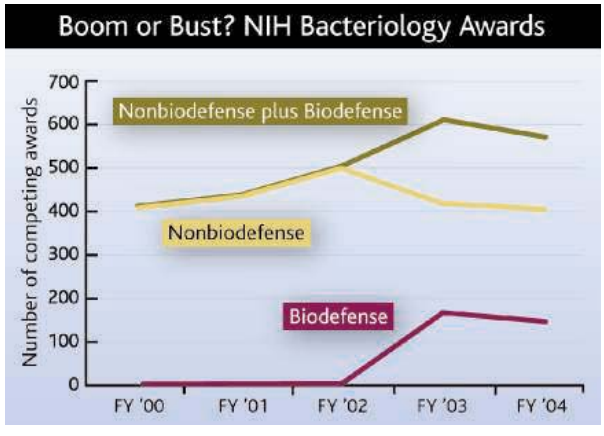

Numbers game. Some scientists blame a drop in nonbiodefense bacteriology grants on the rise in biodefense funding. NIH disagrees.

NIH Director Elias Zerhouni and NIAID Director Anthony Fauci initially said that nonbiodefense grants rose through 2003 at NIAID (*Science*, 1 April, p. 49). Since then, NIH has analyzed bacteriology grants across all 27 institutes, and NIH's Sally Rockey presented the data last week at a closed meeting with a half-dozen outside scientists including leaders from the American Society for Microbiology (ASM) in Washington, D.C. The new data show a roughly 17% drop in nonbiodefense grants in 2003, the first year of the influx of biodefense funding (see graph, above).

Ebright, who has calculated a 40% drop for 2003, points out that NIH found a decline even though it used an "extremely inclusive" definition that picked up grants in areas such as psychosocial research. But NIH extramural research chief Norka Ruiz Bravo insists that the drop coincides with a reduction in all disciplines as NIH's budget growth slowed after a 5-year doubling. "Without biodefense, the picture would be much bleaker" for microbiologists, Ruiz Bravo says. Even NIH's critics agree that it's hard to say if there has been a tradeoff. "The numbers are all so convoluted, it's like the blind guys feeling the elephant," says Stanley Maloy of San Diego State University in California, another meeting participant.

NIH and ASM are now planning a workshop to probe further. "The bigger issue is, what are the trends in the field, the gaps, what needs to be done," says Ruiz Bravo. That idea pleases ASM, which has worried about a "perceived decline in interest" in basic microbiology for 10 years, says ASM president James Tiedje of Michigan State University in East Lansing. "This workshop is an important goal for us."

The microbiologists' letter suggested broadening the definition of biodefense to include work on model organisms. But one signer, Barry Bloom of Harvard University, says Congress will expect NIH to spend its money on potential bioterror agents. As for where the money will come from, Bloom says, "it's a matter of priorities" for the entire NIH budget. –JOCELYN KAISER

CREDITS (TOP TO BOTTOM): JOHN CONSOLI/UNIVERSITY OF MARYLAND; SOURCE: NIH

Peter Lichtenbaum, assistant secretary of commerce for export administration, suggested another approach: Universities could apply for a deemed export license when enrolling international students and employing foreign researchers. "BIS grants 99% of applications," he says. Instead of classifying every piece of research equipment at the institution, he says, schools could identify technologies used by foreign nationals and then decide which ones needed a license.

Rachel Claus, a Stanford University attorney who specializes in export-control regulations, says BIS visited the campus last month and determined that "virtually none" of the equipment at a materials science and a nanofabrication lab would require a license. That's because instruction manuals "were publicly available for all of the items," she says. "But making that determination for the entire campus would certainly be a big undertaking," she adds.

The proposed shift in the demographic criterion for determining the need for a license also drew flak. Basing license requirements on country of birth would be a turnoff to researchers born in "countries of concern" who come to the United States as citizens or permanent residents of a third country such as Canada, says Cynthia Johnson, director of government relations at Texas Instruments. The fallout from that rule would "make it difficult for industry to retain them," she says.

–YUDHIJIT BHATTACHARJEE

GAMMA RAY ASTRONOMY

Signs Point to Neutron-Star Crash

Astronomers think they have witnessed their first colossal crash of two neutron stars, an event that has tantalized theorists for decades.

Shortly after midnight EDT on 9 May, a NASA satellite detected a sharp flare of energy, apparently from the fringes of a distant galaxy. The news from Swift, launched in November 2004, was quickly disseminated to ground-based astronomers, triggering hours of intense research. As *Science* went to press, exhausted observers verified that their early observations look a lot like a neutron-star merger. "Prudence would say that we need a strong confirmation, but we're very excited by it," says astronomer Joshua Bloom of the University of California, Berkeley.

Colliding neutron stars would help explain a puzzling variety of the titanic explosions called gamma ray bursts (GRBs). Astronomers are confident that "long" bursts, lasting from seconds to a few minutes, arise from gigantic stars that explode when their dense cores collapse and create black holes. But "short" bursts, emitting pulses of gamma rays in fractions of a second, have been utterly mysterious. The most popular theory holds that each member of a massive binary-star pair could explode as supernovas, leaving neutron stars that spiral inward and eventually merge in a cataclysmic flash.

The new midnight burst fits that picture. Picking up a 0.05-second spike of gamma rays from the constellation Coma Berenices, Swift took less than a minute to swivel and point its x-ray telescope at the GRB. It detected 11 photons—an extremely faint signal, but enough to notify ground-based telescopes of the approximate location.

Hours later, two telescopes—the 3.5-meter WIYN Telescope at Kitt Peak, Arizona, and the 10-meter Keck I Telescope at Mauna Kea, Hawaii—saw a faint patch of light within the search area, aligned with the outskirts of a galaxy about 2.7 billion light-years away. The galaxy is a massive blob in which no new stars have formed for billions of years.

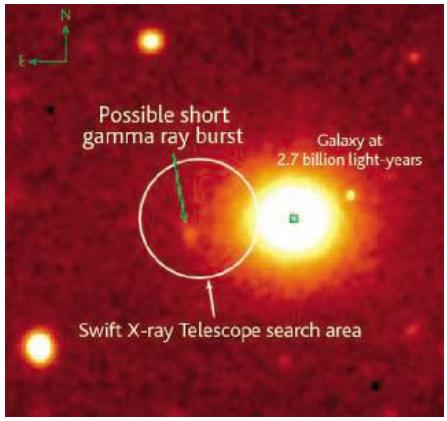

Neutron-star cataclysm? A faint patch of light (green arrow) may mark the spot where two neutron stars collided.

Such a location is exactly where astronomers expect to see neutron stars collide, says Swift lead scientist Neil Gehrels of NASA's Goddard Space Flight Center in Greenbelt, Maryland. Fierce kicks from supernova explosions should expel the neutron-star pair far from its native galaxy. Perhaps billions of years later, the stars coalesce in a brief fury of energy—probably forming a new black hole. "Everything seems to fit," Gehrels says. "It's the most interesting possibility for short bursts."

Other telescopes were set to scour the site of the GRB this week, including the Chandra X-ray Observatory. Confirmation that the burst's afterglow is indeed related to the old galaxy would solidify the discovery, says astrophysicist Shri Kulkarni of the California Institute of Technology in Pasadena: "I think we're seeing a faint supernova from the dead stuff in the neutron stars."

–ROBERT IRION

CREDIT: ADAPTED FROM J. BLOOM *ET AL.*/UC BERKELEY/WIYN TELESCOPE

ScienceScope

U.S. Funds Innovation Summit

Lawmakers worried about science and the future of U.S. industry are planning a fall conference to examine the problem. Provisionally dubbed the Innovation Summit, the event is the brainchild of Representative Frank Wolf (R–VA), chair of an appropriations panel that oversees several science agencies. After hearing a colleague, Vernon Ehlers (R–MI), lament the state of U.S. competitiveness, Wolf inserted $1 million for the event into a 2005 supplemental funding bill that passed Congress this week.

–ELI KINTISCH

Sex Differences at NIH

The National Institutes of Health (NIH) isn't paying enough attention to biological differences between the sexes, according to an advocacy group.

Only 3% of recent grants include a hypothesis about sex or gender differences, says the Society for Women's Health Research in a report released this week. Institutes that study behavioral and mental health research, such as the National Institute on Alcohol Abuse and Alcoholism (at 8%), are doing a better job. But the society found that the topic barely registers at the big five institutes, including those for heart disease and cancer.

The group's report doesn't say what the proportion should be, but "5% to 8% would be fabulous," says Sherry Marts, vice president for scientific affairs at the society.

–JOCELYN KAISER

Student-Friendly Visas

Foreign graduate students and postdocs seeking U.S. visas should not be required to prove they plan to return home, says a new report from the National Academies. The change is needed for the country to attract and retain sufficient scientific talent, says the report, which also recommends two new visa categories for graduate students and postdocs to help the government track them.

Under the U.S. Immigration and Nationality Act, most applicants for nonimmigrant visas have to convince consular officials that they intend to return home. The requirement is "a frequent basis for denial of visas in many countries including China, India, and Russia," says Norman Neureiter, who served on the academies' panel and directs the Center for Science, Technology, and Security Policy at AAAS (publisher of *Science*). The change would require congressional approval.

–YUDHIJIT BHATTACHARJEE

As advocacy groups in the orphan disease world plunge into clinical trials, they're faced with a delicate balancing act

Advocating, the Clinical Way

The idea gelled at the Havana Club in New York City, over Cuban food and heated conversation. Gathered at the Manhattan restaurant were trustees of a patient advocacy group, the Foundation Fighting Blindness (FFB) in Owings Mills, Maryland, and one of its founders, a wealthy New Jersey businessman, Gordon Gund. Gund lost his vision at age 30 from an inherited disease.

The group was grappling with a question confronting more and more advocacy organizations, particularly those fighting rare "orphan" diseases. One hundred sixty million dollars of research funding from FFB, spread across more than 3 decades, had helped uncover upward of 150 disease genes for retinal disorders. But it had failed to yield treatments for thousands of children whose sight was fading. Pharmaceutical companies were hesitant to enter a field that promised hefty risks and relatively low payoffs.

Out of that luncheon 3 years ago emerged a new scheme: FFB would fund its own costly clinical trials of therapies for retinal diseases. The foundation isn't alone as it tries to bridge the gap between basic and clinical science. Advocacy groups have long voiced frustration with the pace of therapy development. But the abundance of new basic research findings, particularly in genetics, is supplying advocates from Connecticut to California with ammunition to press forward with treatments.

For instance, the discovery 7 years ago of a gene linked to Batten disease, a fatal neurological disorder, prompted a family with two affected sons to help launch a gene-therapy trial. Fed up with the lack of new therapies since the 1989 discovery of the cystic fibrosis gene, the Cystic Fibrosis (CF) Foundation in Bethesda, Maryland, has inked agreements with 38 biotechnology companies and is pouring tens of millions of dollars into drug development. Advocates in more common disease areas, such as type 1 diabetes and prostate cancer, are also increasingly funding clinical research (see table, p. 941), as is the American Cancer Society.

But the challenges are perhaps most acute in the orphan disease world. Many of these conditions lack treatments altogether, and because of a paucity of patients, groups may have trouble raising large sums of money and attracting corporate and scientific interest, all needed to support clinical trials. Groups like the CF Foundation and FFB unabashedly say they're modeling themselves after biotechnology companies. But as advocacy groups adopt corporate principles and plunge into clinical trials, they find themselves navigating the sometimes hazy borders separating business, advocacy, and science.

Farsighted. Gene therapy restored Lancelot the dog's vision. Advocate Gordon Gund hopes treatments supported by his foundation will do the same for people.

One of the biggest questions is whether to seek a return on investment—which some, like the CF Foundation, have chosen to do—and how to do so without letting go of the original goal: finding potentially unprofitable treatments for small numbers of patients. Complicating matters is that several trials favored by orphan disease groups involve gene therapy, an endeavor tainted by deaths and complications that have left companies leery.

Shifting from a fundraising to a corporate mindset can also set off tensions: Late last month, FFB's board of directors, composed of affected individuals and their families, fired its new chief executive officer, a Stanford business school graduate named Ritchie Geisel, according to the departing executive. He'd been hired in part to push the foundation to think like a biotechnology company, but his approach apparently didn't mesh with that of longtime FFB donors.

"You've got a little foundation playing pharmaceutical company," says Alan Laties, an ophthalmologist at the University of Pennsylvania in Philadelphia and longtime chair of FFB's scientific advisory board. Therapy development is "very, very difficult" for novices venturing in, says Laties.

Still, these foundations and the scientists supporting them say they have little choice but to forge ahead. "We're looking at … just 200 kids in the world," says Ronald Crystal of Cornell Weill Medical Center in New York City, who's running the gene therapy trial for a form of Batten disease. "Do we abandon them?" he asks. "The answer is obviously no."

Filling a gap

The National Organization of Rare Disorders counts 6000 orphan diseases, defined as those affecting fewer than 200,000 people in the United States—not a big draw for pharmaceutical companies. The 1983 passage of the U.S. Orphan Drug Act, designed to entice companies with extra patent protection, improved the situation somewhat. Genzyme, a Cambridge, Massachusetts, biotech, has enjoyed financial success by focusing on rare lysosomal storage disorders such as Fabry disease, which causes blood vessel and organ complications. Genzyme charges about $200,000 for a year's worth of Fabrazyme, approved in the United States in 2003 and

CREDITS (TOP TO BOTTOM): FITZGERALD/CUSTOM MEDICAL STOCK PHOTO; COURTESY OF FOUNDATION FIGHTING BLINDNESS

Stolen sight. Retinitis pigmentosa destroys photoreceptors in the eye, gradually erasing vision.

earlier in Europe. By and large, though, the Orphan Drug Act "doesn't reduce [cost] enough to get companies to go over that hurdle," says Robert Greenberg, president and CEO of Second Sight, a Sylmar, California, company that's developing retinal prostheses.

One of the first advocacy groups to step in where companies declined to tread was the CF Foundation, a well-heeled nonprofit with a $157 million annual budget. CF patients produce excess mucus that clogs their lungs and pancreas. Most die of lung infections by their 30s.

In 2000, the foundation set up a grant-distributing subsidiary, Cystic Fibrosis Foundation Therapeutics, which has since helped establish a "pipeline" of experimental CF drugs. In 2004, the foundation funneled $36 million into the program, which includes clinical trials, screening to identify new drug targets, and animal testing. It distributed $11 million for basic research. The foundation is currently helping fund 21 clinical trials, up from six in 1999, says president and CEO Robert Beall.

Like pharmaceutical companies, the CF Foundation includes stringent conditions in its partnership agreements, such as linking payments to research milestones. Foundation contracts demand that intellectual-property rights for a drug revert to the foundation if a company drops the program. "You have to structure these deals to hold people accountable," says Beall. "It's a business relationship, not necessarily a charitable one."

And like a company, the foundation seeks a return on clinical investments that reach the market. This has happened just once so far, with an aerosolized antibiotic called TOBI. The CF Foundation invested $1.8 million in TOBI in the early 1990s and reaped $17 million in royalties after TOBI was approved in 1997, money it plowed back into its research program. (The foundation does not collect royalties long-term, although it sometimes controls drug patents.)

The CF Foundation has also had some high-profile failures. In March, it announced that a phase II gene-therapy trial by Targeted Genetics in Seattle, Washington, had flopped. "We've been funding them for years," says Suzanne Pattee, vice president of public policy and patient affairs at the CF Foundation. Such failures highlight the risk of financing therapies: They cost far more than basic research grants, and disappointments are common.

PHOTO CREDIT: CHIRON

New directions

Last fall, when Gund was weighing similar issues for FFB, he traveled to Beall's Bethesda office for advice. By then, FFB had laid out its new strategy with its scientists, patients and families, drug companies, and venture capitalists—encountering a dubious response at first.

How in the world would they raise the tens of millions of dollars needed to fund clinical work? Could they count on partnerships with industry? Would basic research fall by the wayside?

"I thought, 'Oh God, there goes the money' " for basic science, says Stephen Daiger, a geneticist at the University of Texas Health Science Center in San Antonio who has long received grants from FFB, which funds about $10 million a year in basic research. He studies retinitis pigmentosa (RP), the disease from which Gund suffers and the original focus of the foundation. Even though scientists such as Daiger say they're eager for FFB's new direction to pan out, Daiger wonders whether the foundation can keep funding basic research at the same level—which it promises it will do—while ramping up a new clinical program.

To date, FFB has supported research into gene therapy, cell transplants, and prosthetics that have slowed or reversed the effects of retinal disease in at least six animal models. Those affiliated with FFB talk enthusiastically of Lancelot, a shaggy, cream-colored briard born blind whose sight was partially restored by gene therapy and whose picture, with Gund and his wife Lulie, graces the FFB offices. A clinical trial of that gene therapy, for a form of RP called Leber congenital amaurosis, is slated to start this year. FFB plans to contribute funds. "If there was ever a time to move to humans, this is it," says Daiger.

Not everyone agrees, however. "The mechanisms [of disease] are known; the mechanisms for treatment are not as evident," says Joe Hollyfield, director of ophthalmic research at the Cleveland Clinic Foundation in Ohio. He questions how "100 genes and 100 pathways" can be translated into therapies.

Sound investment. The Cystic Fibrosis Foundation garnered $17 million after TOBI, a CF drug, hit the market.

Nonetheless, FFB is proceeding apace. Last year it launched the National Neurovision Research Institute (NNRI), a subsidiary that will fund clinical trials and act like a broker, helping garner financing for researchers pursuing promising therapies for retinal diseases. It will focus on areas in which intellectual property is undisputed.

"We're moving toward developing a venture fund" of $20 million to $50 million, with money raised largely from venture capitalists and possibly the government, says Edward Gollob, a New Jersey businessman and FFB's president. His daughter began losing her sight to RP at around age 8.

Picking and choosing

For FFB, going clinical could be a rocky ride. In January 2004, the foundation hired Geisel to replace its CEO of 18 years, whose expertise lay in fundraising, not business. Last month, Geisel says he was abruptly asked to leave. "It was very unexpected," he says, citing "issues with the board" as a reason for his departure. In an earlier interview, Geisel noted that FFB "still has elements of the family foundation" and explained that he was brought on to provide "more proactive leadership."

Last week, the foundation announced the appointment of a new CEO, William Schmidt, who starts next month. Unlike Geisel, Schmidt doesn't hold an MBA, although he has extensive experience in nonprofit management.

Meanwhile, plans for NNRI are chugging along. The institute will in some ways be like any start-up company: result-oriented with strict deadlines. It will expect a return on its

Moving Dollars Toward the Clinic

Advocacy Groups	2004 Budget (in millions)	No. of ongoing clinical trials
ALS Therapy Development Foundation	$4	1
Cystic Fibrosis Foundation	$157	21
Foundation Fighting Blindness	$16	none yet
Juvenile Diabetes Research Foundation	$147	17
Multiple Myeloma Research Foundation	$11	6
Myelin Repair Foundation (multiple sclerosis)	$1.25	none yet
Nathan's Battle Foundation (Batten disease)	$1	1
Prostate Cancer Foundation	$26	N/A

In-house mouse. The ALS Therapy Development Foundation runs its own mouse labs for drug research.

investment for products that reach the market. "We've got to" make a return to keep NNRI viable over the long term, says Gund, a venture capitalist himself.

But specific plans remain in flux. Key questions include what to fund, how to raise money, and how to structure agreements with companies. One underlying tension is balancing a therapy's benefits against the size of the market it could serve: Should a treatment that could help just hundreds of patients get funding over one that might potentially benefit many more patients with a common disease such as macular degeneration?

Suggestions about what NNRI should finance are guided by Morton Goldberg, an ophthalmologist at Johns Hopkins University in Baltimore, Maryland, who chairs NNRI's board of directors and who helps juggle advice from affected family members, scientists, and companies. In his Hopkins office, where a smiling portrait of himself hangs on the wall behind his desk, Goldberg says that in addition to gene therapy, promising approaches for retinal diseases include growth factors that protect nerve cells behind the eyes; retinal prosthetics, which have been tested in small clinical trials; some nutritional agents; and retinal cell transplants. Nearly all these therapies will require company funds at later stages of development.

A particularly vexing question is to what extent corporate interest should govern NNRI's funding decisions. Many ophthalmologists consider retinal gene therapies among the most promising potential treatments. But from a business perspective, gene therapy may not be the best investment. Recent disasters in the field—including three cases of leukemia among children with an immune disorder who received gene therapy—have raised red flags for companies.

Another issue is the size of the market for a particular gene therapy. After the first RP gene was pinpointed in 1990, more than 50 others followed, each of which causes retinal disease in just a fraction of RP patients. "It's so hard to say" whether retinal gene therapy makes sense as a business strategy, says Daniel Lubin, a venture capitalist advising NNRI. The gene therapy closest to clinical testing could help 2000 people. Lubin, managing partner and co-founder of Radius Ventures in New York City, argues that "what you want to do is identify orphan situations where the science is potentially a platform that's applicable to other" disorders, such as macular degeneration, for which there is a much larger market.

Although FFB's executives agree that a "larger platform" is ideal, Stephen Rose, the foundation's chief research officer, notes that a potential cure for even a subset of patients "would be 1000 people who have had their sight restored." After all, NNRI was formed in the first place because FFB's longtime constituents, a fractured market of roughly 200,000 patients, were being neglected by pharmaceutical companies.

Balancing act

Having a hand in therapy development is so new for most advocacy groups that almost none have seen a treatment through from start to finish. Even so, some advocates recognize that they risk becoming overly entwined with the drug industry, with whom they must partner, and with the treatments they help develop, whether or not their group profits. In theory, that could mean highlighting a therapy that's no better than another, or no longer offering the kind of dispassionate treatment advice that advocacy groups strive to supply.

The 7-year-old Multiple Myeloma Research Foundation (MMRF) in New Canaan, Connecticut, has chosen not to reap a return on its investments. Cofounder Kathy Giusti, a former pharmaceutical executive with this blood cancer, says that a quarter of the group's funds come from drug companies, but she doesn't intend to let that fraction rise. "We don't want to rely on them," she says of pharmaceutical companies, because that could disrupt MMRF's efforts to be balanced in describing treatment options to its constituents.

Money aside, objectivity can be tough for advocates devoted to seeking new medical therapies. "You form your own biases; you need to be honest with yourself about that," says Jamie Heywood, an engineer who launched the ALS Therapy Development Foundation 6 years ago after his 29-year-old brother Stephen was diagnosed with amyotrophic lateral sclerosis (ALS). Two of the drugs Heywood's foundation tested in mice have advanced to human trials, which the group is helping fund. But Heywood believes biases can be overcome. We "all have people we love dearly with this disease," he says. "There's a very strong bias corrector there."

One way to avoid bias is by leaving the fine print about trial design and enrollment up to companies and scientists, who often insist on this. Phil Milto recalls the anxiety of not knowing whether his sons would be part of the Batten disease trial that his group, Nathan's Battle Foundation, had pushed forward. (Both boys were admitted.)

FFB's chief operating office Randy Hove agrees that FFB's board of directors, made up of affected individuals and family members, "will not make any decisions" about trial design and enrollment. All trials are vetted by the Food and Drug Administration before a therapy is tested in humans—regardless of who funds it.

How advocacy groups pursue therapy development may ultimately reflect their allegiance to the corporate mindset many are embracing. As FFB welcomes a new party, the venture capitalists, to the table, its original "shareholders" will remain: wealthy benefactors with retinal disease in their families, who over the years have contributed millions in donations and who are impatient to realize the fruits of their gifts. Coaxing new factions to cooperate with longstanding ones will call for deft handling from FFB's newest leader.

—JENNIFER COUZIN

CREDIT: ALS THERAPY DEVELOPMENT FOUNDATION

Centers of Attention: NSF Takes Fresh Look at Their Proliferation

Faced with a shrinking budget, NSF's new director says it's time to "weed our garden" of centers. But will pruning stunt the growth of science?

Oceanographer David Karl was thrilled when National Science Foundation (NSF) officials told him in January that his proposed $20 million center on microbial diversity in the oceans had been selected for its next class of six Science and Technology Centers (STC). The approval capped Karl's 2-year quest for a spot in a flagship program, launched in 1987, that promotes multisite, interdisciplinary research on important scientific questions that affect society.

Then came the bad news: NSF was scaling back its plans, officials told him, and could make only two awards this spring. That left Karl and three other would-be center directors in a limbo that will likely extend until next year, after Congress approves NSF's 2006 budget and the agency decides whether it can afford any more of the centers, which typically operate for 10 years. And NSF officials aren't making any promises.

NSF's indecision has sent Karl scrambling to keep his multiuniversity team intact and to explore alternative sources of funding if NSF doesn't come through. (A pledge from the state of Hawaii to pick up all of the mandatory 30% outside contribution assumes that NSF would fund the project.) At 55, having spent his entire scientific career at the University of Hawaii, Manoa, Karl is also taking a fresh look at some tempting job offers from other universities in case the NSF center falls through. For researchers who flooded NSF with 159 proposals back in 2003, the status of the latest STC competition is a depressing reminder that big-ticket items are increasingly vulnerable in a budget that is contracting rather than doubling over 5 years, as Congress and President George W. Bush had promised in 2002.

The cutback also reflects a rethinking of NSF's current $350 million annual investment in nearly 200 centers of various sizes and shapes (see table, right). "We need to weed our garden," NSF Director Arden Bement told Congress this spring about the agency's portfolio of centers. "Perhaps they need to be more narrowly defined, to make sure that they are closer to the core mission of each directorate and the agency as a whole."

Bement says he doesn't plan to pull the plug on any existing centers, but he expects to take a "very hard look" at any future competition. NSF's oversight body, the National Science Board, has begun to ask similar questions and has asked NSF staff for a briefing on the topic at its meeting later this month.

The modern version of an NSF center was developed by then-Director Erich Bloch in the mid-1980s. Shrugging off complaints that the centers would eat into NSF's bread-and-butter grants to principal investigators (PIs) and tarnish the foundation's reputation for supporting bottom-up science, Bloch created a new vehicle, called Engineering Research Centers (ERC), and later, STCs. Funded at $2 million to $4 million a year for up to 10 years, the centers were intended to tackle emerging scientific challenges that also affect people's lives. The inaugural class of STCs, for example, includes centers on superconductivity and the prediction of storms. NSF has "graduated" 40 such centers and is currently supporting 19 ERCs and 11 STCs.

Fears that the centers would devour PI grants proved groundless; NSF typically devotes about 7% of its overall budget in any given year to them. Once that was clear, centers of various sizes, scopes, and durations began popping up like toadstools after a rainstorm. In 2003, NSF created a third, cross-agency vehicle on a par with the STCs and ERCs, called the Science of Learning Centers (SLC). By next year NSF hopes to be supporting seven such centers, with annual individual budgets approaching $5 million a year.

Although most NSF managers hold individual awards to be sacrosanct—"I call them our great discovery machine," says Joe Dehmer, who heads the physics division—they also see centers as an excellent way to tackle major questions that require a concentration of resources. "The CLTS [Centers for

NSF's Current Lineup of Centers

Name	Begun	No. of centers	Budget (in millions)
ACROSS THE FOUNDATION			
Engineering Research Centers	1985	19	$61
Science and Technology Centers	1987	11	$49
Science of Learning Centers	2003	3	$20
WITHIN A DIRECTORATE			
Centers for Analysis and Synthesis	1995	1	$7
Centers for Learning and Teaching	2000	17	$28
Chemistry Centers	1998	32	$13
Earthquake Engineering Research Centers	1988	3	$6
Long Term Ecological Research Network	1980	26	$23
Materials Centers	1994	35	$57
Mathematical Sciences Research Institutes	1982	6	$17
Nanoscale Science and Engineering Centers	2001	14	$34
Physics Frontier Centers	2001	10	$19
Plant Genome Virtual Centers	1998	25	$36
SBE Centers	N/A	11	$8

SOURCE: *SCIENCE*, WITH DATA FROM NSF

Optimizing the Discovery & Development Interface to *Improve Productivity*

Enhance Safety & Efficacy

Develop New Business

Explore New Markets

10th Anniversary DRUG DISCOVERY TECHNOLOGY® & Development

Keynote Sessions

Lester M. Crawford, D.V.M., Ph.D.
Acting Commissioner, FDA

John L. LaMattina, Ph.D.
President, Pfizer Global R&D

Keynote Panel Discussion

Exploring the Industry and Regulatory Interface in Drug Development

Moderator:

Robert R. Ruffolo, Jr., Ph.D.
President, R&D, Wyeth

The Boston Convention & Exhibition Center, Boston, MA

Conference: **August 8-11, 2005**

Exhibition: **August 9-11, 2005**

For more information and to register,
visit www.drugdisc.com

Presidential Sponsors:

Executive Sponsor:

Supporting Publications:

Assocation Sponsor:

Organized by:

Learning and Teaching] were developed when it became clear that in addition to training new science and math teachers for the public schools, we also had to address the need to train the next generation of the teachers of those teachers," explains Judith Ramaley, the former head of Education and Human Resources (EHR) who in July assumes the presidency of Winona State University in Minnesota. Dehmer says the 10 Frontier Physics Centers "have also turned out to be great magnets for talent."

That autonomy has led some NSF managers to continue proposing centerlike mechanisms. In chemistry, for example, division director Art Ellis last year gave $500,000 awards to three chemical bonding centers "to show us why they should grow into an NSF-like center." If they can't, Ellis says, the money will likely flow back into the pot for individual investigators. The materials science division, which has a long history of supporting centers, is in the midst of a recompetition for roughly half of its 28 centers. The solicitation was open to anyone, says division director Tom Webber, adding that it's typical for newcomers to best incumbents for a few of the prestigious slots.

For other programs, however, the chillier climate for centers is translating into stricter rules for the next competition. Next year, half of the physics centers that Dehmer assembled in 2001 will compete for another 5 years' worth of funding. But outsiders need not apply. "Typically, we like to have an open competition," Dehmer says, with the option of enlarging the program if the proposals are sufficiently strong. But under the new regime, Dehmer says, "there will be no centers [added] and no substitutes" if one or more existing centers fail to make the grade. "You could say we're taking a pause."

The same diet of budget cuts and upper management scrutiny has devastated EHR's learning and teaching centers, says Ramaley, who left NSF in December. "They were a wonderful attempt to address several pressing needs, from developing future [academic] faculty to collaborating with local school districts to preparing [public school] teachers," she says. "I considered them at the core of the EHR research portfolio." Ramaley anticipated supporting as many as 20 centers, from preschool to the doctoral level and covering all aspects of science and math education. But this year, after making 17 awards in 2000–04, NSF canceled a new, smaller competition that would also have given incumbents a chance for a second, 5-year award. The announcement has raised fears among science educators that the CLT program might expire quietly once existing grants run out.

Bement says that centers still play an important role in NSF's portfolio and that he isn't questioning the value of any particular initiative. At the same time, he says he got the message last summer when House appropriators attempted to remove funding for the entire 2005 class of STCs. The full Congress rescinded the move in the fall, giving him the authority to fund as many STCs as he saw fit. But he read the House language as a signal to proceed with caution.

For Karl, that policy means more administrative headaches. His proposed Center for Microbial Oceanography: Research and Education features activities to be carried out by teachers moving to Hawaii from the mainland, as well as work by young tenure-track scientists who are counting on the center to advance their careers. "I'm not complaining," he says, "and I'm confident that in the end we will be able to proceed. But in the meantime, it's very frustrating." –JEFFREY MERVIS

Neuroscience

Reflecting on Another's Mind

Mirror mechanisms built into the brain may help us understand each other

In the 1962 James Bond film *Dr. No*, the suave British secret agent awakens to find that someone has slipped a tarantula into his bed. It's an uncomfortable scene. As the hairy arachnid creeps up 007's arm, horrified viewers can almost feel their own arms tingle. Bond's fear and discomfort are contagious, as he squirms and maneuvers to shake the thing off.

Most people can tell what's going through Bond's mind without giving it any thought, says Christian Keysers, a neuroscientist at the University of Groningen in the Netherlands who incorporated the tarantula scene into his recent presentation at the annual meeting of the American Association for the Advancement of Science (AAAS) in Washington, D.C. Aside from aiding our enjoyment of movies, this instinctive ability to put ourselves in another's place is an important, real-life social skill that helps us size up potential friends, foes, and mates and enables us to learn from watching others, Keysers says. But how does the brain accomplish this type of mind reading?

Keysers and many of his colleagues suspect that the answer has something to do with "mirror" mechanisms in the brain that translate the observed movements and experiences of others into the patterns of neural activity that normally underlie our own motion and experience. In other words, if you get the creeps watching the spider crawl up James Bond's arm, it may because the scene fires up the same neurons that would be active were the spider making its way up your arm.

In recent years, neuroscientists have documented just this type of brain activity. Following the discovery of monkey neurons that mirror observed movements, researchers have turned to the human brain and found neural activity that mirrors not only the movements but also the intentions, sensations, and emotions of those around us.

The study of the brain's mirror systems will do for psychology what the study of DNA has done for biology, predicts Vilaya-

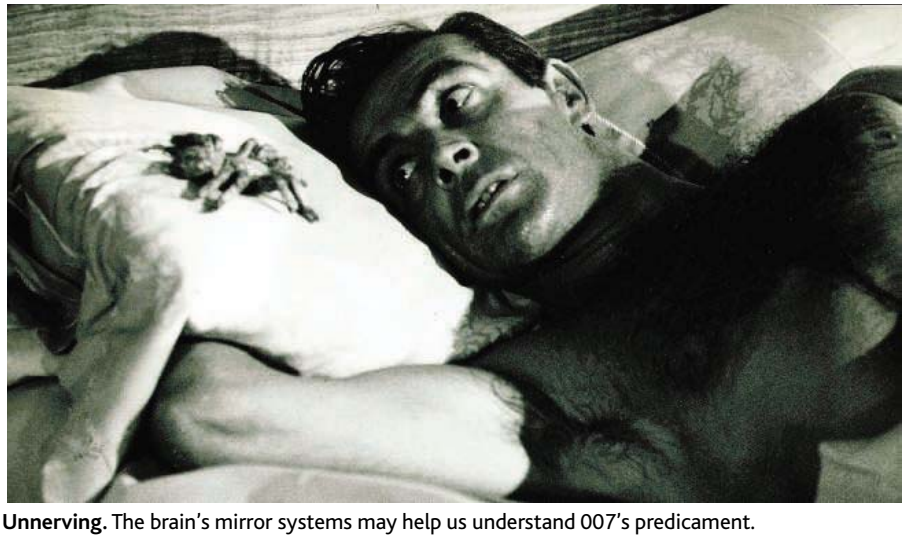

CREDIT: DANJAQ/EON/UA/THE KOBAL COLLECTION

Unnerving. The brain's mirror systems may help us understand 007's predicament.

nur Ramachandran, a neuroscientist at the University of California, San Diego. "It's opening doors into new realms like empathy," he says.

Others are more tempered in their enthusiasm, but many cognitive neuroscientists agree with Ramachandran that mirror systems in the brain represent a potential neural mechanism for empathy, whereby we understand others by mirroring their brain activity. That idea is bolstered by new evidence of abnormalities in the mirror systems of people with autism and other disorders that impair the ability to empathize with and understand the behavior of others.

Monkey see, monkey do

In the early 1990s, Giacomo Rizzolatti and colleagues at the University of Parma in Italy encountered a surprise while investigating a region of the macaque monkey brain that is important for planning movements. Neurons in this region of frontal cortex, known as F5, become active before a monkey reaches out with its arm—to grasp a peanut, for example. The team noticed that a small subset of F5 neurons also responded when a monkey happened to see a researcher reach for a peanut—even if the monkey never moved a muscle.

"We didn't believe it," Rizzolatti says. The team's skepticism dissipated with repeated experiments, however. The finding was exciting, Rizzolatti says, because it fit with ideas that were coming together at the time in philosophy and cognitive science, such as the hypothesis that understanding the behavior of others involves translating actions we observe into the neural language of our own actions. The monkey mirror neurons seemed to do just that, providing a potential neural mechanism to support that proposal.

Subsequently, researchers used functional magnetic resonance imaging (fMRI) and other techniques to investigate brain activity as people made—and observed others making—hand movements and facial expressions. These studies identified mirrorlike activity in several regions of the human brain, including a region of frontal cortex homologous to F5.

This human frontal region, known as Broca's area, is also involved in speech production—a connection that snared the attention of researchers studying the evolution of language (*Science*, 27 February 2004, p. 1316). Rizzolatti and others have argued that mirror neurons could facilitate the imitation of skilled movements like the hand and mouth movements used for communication. A paper published by his team last year in *Neuron*, for example, suggests that the mirror system in the frontal cortex is active as novices learn to play chords on a guitar by watching a professional guitarist.

Tea time. These images of a mock tea party helped reveal that a person's brain can discern whether another person intends to drink tea or clean up a mess.

Similar learning by imitation is a key feature of language acquisition in infants and is widely considered a prerequisite for language evolution.

Although no one has looked for mirror activity in babies imitating their mothers' speech, another team recently described mirror activity related to speech in adults. Last June, Marco Iacoboni of the University of California, Los Angeles, and colleagues reported in *Nature Neuroscience* that listening to speech cues up activity in regions of the frontal cortex that are active during speech production.

Good intentions

The brain's mirror systems may also decipher the intentions and future actions of others, according to recent work. In one study, Iacoboni and colleagues, including several members of the Parma team, scanned the brains of 23 volunteers as they watched short video clips that depicted scenes from before and after a mock tea party. The "before" clip featured a steaming cup and a teapot alongside a plate of edible goodies. In the "after" clip, volunteers saw the messy aftermath, including crumbs and a used napkin. At the end of both clips a hand reached in from offscreen and grabbed the teacup. The grasping movement was identical in each clip, but the context suggested different intentions: drinking tea in the "before" clip versus cleaning up in the "after" clip.

The volunteers' mirror systems registered the difference, the research team reported in the March issue of *PLoS Biology*. An area of the right frontal cortex previously shown to have mirrorlike responses to hand movements was more active during observation of the grasping movement when the implied intention was drinking, compared to when it was cleaning up. Both clips elicited more neural activity in this brain area than did a clip of a hand grabbing a teacup from an empty background. The findings indicate that neurons in this region are interested not only in the motion but also the motivation behind it, Iacoboni says. Knowing what others intend to do is extremely valuable in social situations, he adds. If John sees Katie reach for a cup of hot tea, for instance, he'd like to know whether she intends to drink it or throw the contents in his face.

In the 29 April issue of *Science* (p. 662), Rizzolatti's team reports similar findings in monkeys. The researchers first trained the monkeys to grasp a piece of food from a table and either eat it or place it in a cylinder on the table. Then they recorded the activity of individual neurons in the monkeys' inferior parietal lobule—a region of cortex distinct from F5 that also has mirror neurons. About two-thirds of the parietal mirror neurons tested responded differently during the reach movement when the goal of the action was different. Three-quarters of these brain cells responded more vigorously when the goal was eating; the rest responded more vigorously when the goal was placing.

Next, the researchers recorded from a subset of these parietal neurons while the monkeys watched a person do the same task. The person's reach and grasp movements were identical in both conditions—only the presence or absence of the cylinder at the start of each trial revealed whether the grasp would be followed by eating or placing. Even so, most of the parietal neurons showed the same preferences during the observed reach that they'd shown when the monkeys did the task themselves: Neurons that responded more strongly when the monkey reached to eat responded more strongly when the monkey observed a person reaching to eat. Rizzolatti says the findings suggest that the mirror neurons can, based on context, predict the next action in a series of actions.

Mutual feelings

Purists insist that the term "mirror neuron" applies only to the F5 and parietal movement-related neurons in monkeys, the only individual neurons whose mirror properties have been studied. But there's evidence that humans have multiple mirror systems, including ones that have nothing to do with planning movement.

Last year in *Neuron*, Keysers and colleagues described mirrorlike responses in a part of the brain involved in the sense of touch. Volunteers wearing shorts slid into an fMRI scanner, and researchers gently brushed the sub-

CREDIT: MARCO IACOBONI

jects' bare legs. At the same time, the scanner revealed the brain regions that responded. While inside the scanner, the subjects also viewed several video clips that showed an actor's legs being stroked by a rod or brush.

Both conditions—the actual touch and the observed touch—elicited similar activity in the subjects' secondary somatosensory cortex, an area involved in processing touch. This area was not activated, however, when the subjects viewed videos in which the brush approached the actor and slid back and forth without actually making contact. It's as if the brain translates vision into sensation, Keysers says. He proposes that this process is why the tarantula scene in *Dr. No* gives people the heebie-jeebies, and why we flinch when we see someone cut her finger with a kitchen knife.

But in the case of pain, the shared feeling may be more emotional than visceral. In a study reported last year, Tania Singer of University College London and colleagues used fMRI to measure how the brains of 16 women responded when they either received a painful shock or saw their romantic partner get shocked (*Science*, 20 February 2004, p. 1121 and 1157). The two situations elicited activity in many of the same brain regions, but the shared responses were limited to areas that process the emotional content of pain. Regions of the somatosensory cortex that register the location and nature of painful stimuli remained quiet when the women simply observed a shock. Women who scored higher on a written test of empathy showed greater brain responses while observing their partners' shock. Two similar studies by other teams have subsequently produced comparable findings.

Other types of emotional empathy may also invoke neural systems involved in experiencing an emotion directly. In 2003, Iacoboni and colleagues reported in the *Proceedings of the National Academy of Sciences* that regions of frontal cortex are active when subjects either observe or imitate emotional facial expressions. Later that year, Keysers and colleagues reported in *Neuron* that a brain region called the insula responds when people experience disgust or witness it in others. In this study, subjects inside an fMRI scanner donned a mask through which the researchers could pipe various odors. The smell of rotten eggs and rancid butter evoked activity in brain regions such as the anterior insula, a region associated with experience of disgust. That particular area also became active when the subjects simply watched a video in which an actor sniffed a glass and signaled by his facial expression that he'd gotten a whiff of something foul. Observing someone else's expression of disgust apparently activates our own neural representation of disgust, says Keysers. His team is now investigating whether this concept extends to other emotions, such as fear.

Keysers's report in *Neuron* meshes with case studies of people who, as a result of a stroke or other causes, suffer damage to their insula, says Ralph Adolphs, a cognitive neuroscientist at the California Institute of Technology in Pasadena. He and others have found that such people are unable to detect disgust in the facial expressions of others and are impaired in their ability to experience disgust themselves. In general, Adolphs says, people with impaired emotional experience are also impaired at recognizing and judging emotions in others. That suggests that one strategy for empathizing with others is by simulating aspects of their presumed emotional state within ourselves, he says.

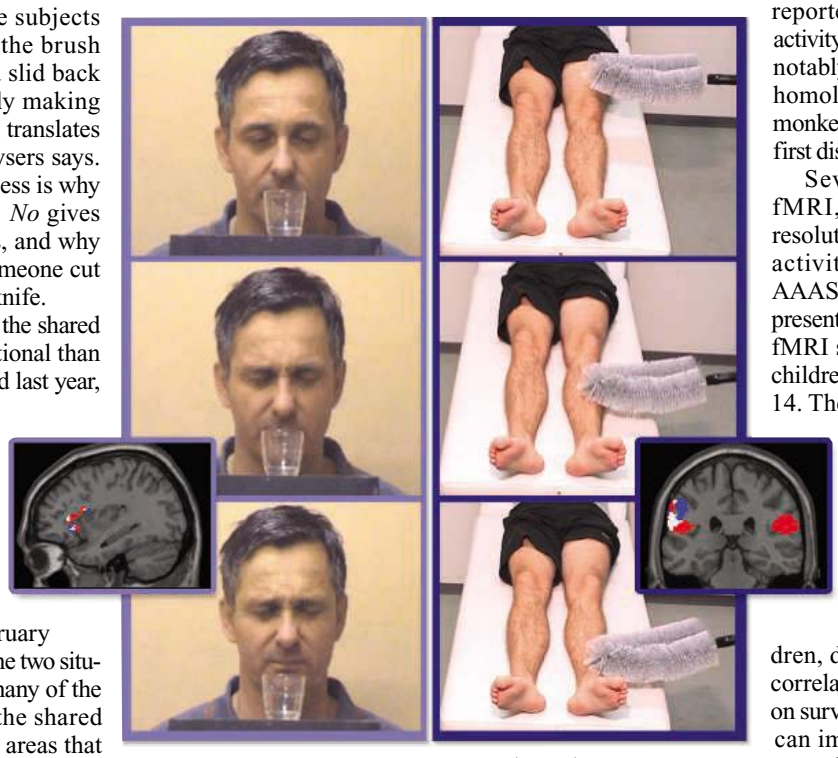

Shared experience. Certain brain areas (white) are active during both the experience and observation of disgust (*left*) or touch (*right*).

CREDIT: CHRISTIAN KEYSERS

Broken mirrors

People with autism and related disorders tend to have abnormalities in several behaviors linked to mirror neurons, including imitation, language development, and the ability to interpret the actions and emotions of others. A process that derails the brain's mirror systems—perhaps due to some miscue during brain development—could explain why these complex symptoms appear together, says Justin Williams, who studies autism at the University of Aberdeen, United Kingdom. A handful of recent reports hint at exactly that. For example, a study by Finnish researchers, published last year in the *Annals of Neurology*, used magnetoencephalography to compare the brain activity of eight people with the autism-related disorder Asperger syndrome to that of 10 healthy subjects while each imitated facial gestures shown in a series of still pictures. The team reported weak and sluggish neural activity in the Asperger patients, most notably in Broca's area, the human homolog of F5, the brain region in monkeys where mirror neurons were first discovered.

Several teams are now using fMRI, with its higher spatial resolution, to better pinpoint mirror activity in autistic people. At the AAAS meeting in February, Iacoboni presented preliminary results from an fMRI study of autistic and normal children between the ages of 10 and 14. The children observed and imitated emotional facial expressions. In the autistic children, mirror activity in the frontal cortex was reduced relative to that seen in normal children the same age, Iacoboni reported. Even among the normal children, differences in mirror activity correlated with the children's scores on surveys that gauge how easily they can imagine another person's perspective and how readily they empathize with the problems of others.

Still, most researchers say there's more to empathy than mirror mechanisms. In Keysers's view, such mechanisms provide only an intuitive, gut-level feeling that underlies empathy. "It's what gives you the richness of empathy, the fundamental mechanism that makes seeing someone hurt really hurt you," says Keysers. But he adds that there are other cognitive processes, at least in humans, that put information from the mirror systems into context. After all, without such checks and balances, we would be unable to spot someone faking an emotion, Keysers says.

We're also able to understand what someone is experiencing without experiencing it ourselves, adds Michael Arbib, a computational neuroscientist at the University of Southern California in Los Angeles: "If you see someone behaving badly, a sadist, you hopefully don't share their joy." A full account of the neural basis of empathy, Arbib and others say, will require understanding how the brain deciphers the information it gets from the mirror systems—in other words, finding out what's behind all the mirrors. **–GREG MILLER**

Random Samples

Edited by Constance Holden

Cultivating the Third Eye

The zoology laboratory of Dungar College in the small town of Bikaner in the Indian state of Rajasthan has some strange inmates: more than 50 three-eyed frogs. The amphibians have confirmed a long-held suspicion of developmental biologists that pineal glands retain the ability to respond to light and even to form into eyes.

Zoologist Om Prakash Jangir and his colleagues earlier found that if they removed tadpoles' eyes and raised the animals in a medium enriched with vitamin A, a new eye developed within 10 days over the site of the pineal gland. The researchers then transplanted tadpole pineal glands between the eyes of month-old frogs. With the help of some vitamin A, most of the amphibians developed third eyes within 15 days, the scientists report in the May issue of the *Indian Journal of Experimental Biology*.

"In lower vertebrates, the pineal organ had a visual role which got lost during evolution. Our experiments show that this vestigial organ can be activated in vertebrates," says Jangir. Both the eyes and the pineal organ depend on similar developmental signals in the embryo and express the same homeobox gene, he says. Ramesh Ramachandra Bhonde of the National Center for Cell Science in Pune calls the achievement "an important milestone" that contributes to the value of the pineal gland as a model in studies of both evolution and development.

Counting by Gates

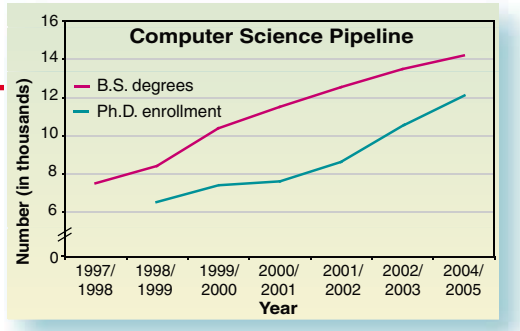

Microsoft Chair Bill Gates may know how to add up the profits of his software giant, but his math is a bit shaky on the labor power front. Microsoft has many vacant positions because "there just aren't as many [U.S.] graduates with a computer science background," Gates lamented last month at a forum on innovation and education at the Library of Congress in Washington, D.C. The shortage of grads "creates a dilemma for us, in terms of how we get our work done," noted the world's richest man.

But the data tell a different story. A newly published survey by the Computing Research Association (CRA) of top university departments show that the number of U.S. bachelor's degrees awarded in computer science rose by 85% from 1998 to 2004; a similar rise has occurred in doctoral programs since 1999 (see graph, above). The annual number of new undergrad majors has admittedly fallen off since the dot.com bust in 2000, notes CRA's Jay Vegso. "But these numbers have always been cyclical," he says. "I don't see any reason to panic."

Mating for Autism?

If cases of autism are on the increase, as some believe, here's one provocative explanation: Blame the rise on marriages between like-minded people, whom psychologist Simon Baron-Cohen of Cambridge University in the U.K. calls "systemizers."

Baron-Cohen argues that autism and related conditions like Asperger's are manifestations of what he calls the "extreme male brain": one with weak social skills and a strong tendency to "systemize," or think according to rules and laws. In a study of 1000 U.K. families, he has reported that the fathers as well as the grandfathers of children with autism spectrum conditions are more likely to work in professions such as engineering. And the mothers are also likely to be systemizers "with male-typical interests," he says.

Baron-Cohen, whose theory is in press at the journal *Progress in Neuropsychopharmacology and Biological Psychiatry*, says he and colleagues are performing genetic studies, collecting subjects, and conducting population surveys in systemizer-heavy areas, such as Silicon Valley, to test the idea that techies marrying each other is raising autism rates.

Some balk at the idea. Psychologist Elizabeth Spelke of Massachusetts Institute of Technology says there's no good evidence for an "inborn, male predisposition for systemizing." But psychiatrist Herbert Schreier of Children's Hospital in Oakland, California, believes the intermarriage of techies "probably does account for why you have pockets of high autism around Stanford and MIT." Drawing on his own practice, he adds that fathers of children with learning disabilities have a disproportionate tendency to be engineers or computer scientists.

Egyptian Beauty

Last week, archaeologists in Cairo unveiled a well-preserved, newly discovered 2300-year-old mummy—which Egyptian Antiquities chief Zahi Hawass says "may be the most beautiful mummy ever found in Egypt." The unidentified figure has a golden mask and is covered in brilliantly colored images of gods and goddesses as well as illustrations of the mummification process. It was found 2 months ago in the Saqqara pyramids complex, 20 kilometers south of Cairo, in the necropolis of King Teti. Scientists plan to do computed tomography studies of the mummy before it goes on display.

CREDITS (TOP TO BOTTOM): SOURCE: CRA; P. JANGIR; REUTERS

PEOPLE

Edited by Yudhijit Bhattacharjee

NONPROFIT WORLD

Norway's Nobels. Sweden's Nobel Prizes just got a little neighborly competition. Last week, Norwegian-born philanthropist Fred Kavli announced three $1 million prizes for research in astrophysics, neuroscience, and nanotechnology. The Norwegian Academy of Science and Letters will make the biennial selections beginning in 2008.

The fields were chosen because they are ripe for important breakthroughs, says David Auston, president of the Kavli Foundation, which supports 10 research foundations worldwide (*Science*, 21 January, p. 340), and may be revised over the years.

Kavli, who made his fortune selling sensors for automobiles and aircraft, wants the new prizes to recognize "more daring" discoveries than the Nobels. Auston says: "If a major development occurred in the last 5 to 10 years, we want to acknowledge that."

Got any tips for this page? E-mail people@aaas.org

PIONEERS

Housekeeping fellowships. Nobelist Christiane Nüsslein-Volhard says she is tired of watching young women scientists struggle to balance family and career. So the developmental geneticist has launched an initiative to help pay for household help.

The Christiane Nüsslein-Volhard Foundation will give roughly $600 a month to a handful of top-notch, early-career scientists who are mothers. Nüsslein-Volhard, director of the Max Planck Institute for Developmental Biology in Tübingen, Germany, says the money is not primarily intended for daycare but to pay someone to help with cleaning and cooking.

It's maddening "when a top woman scientist can't make it to a seminar because she has to go home and do the laundry," says Maria Leptin, a developmental biologist at the University of Cologne in Germany and a member of the foundation, which has so far raised over $500,000. "She should concentrate on what is most important—doing her work and spending time with her family—and nothing else." The first awards, lasting 1 to 3 years, will be made later this year and then annually.

DEATHS

Hazard-meister. After a career spent helping protect fellow Filipinos from natural hazards, the former head of the Philippine Institute of Volcanology and Seismology has fallen victim to a more mundane hazard of his profession.

On 28 April, Raymundo Punongbayan, 68, died in a helicopter crash that also claimed the lives of four staffers from the institute that he elevated to international prominence. The group was returning from a landslide hazard survey.

In 1991, Punongbayan won acclaim for an effort that moved 80,000 people from harm's way before Mount Pinatubo erupted. "Ray brought Philippine natural-hazard efforts into the modern world," says volcanologist Christopher Newhall of the U.S. Geological Survey in Seattle, Washington. "He was a good scientist and a masterful public relations person and politician."

Integration pioneer. Social psychologist Kenneth Clark, whose work on the negative effects of school segregation was instrumental in the historic 1954 Supreme Court ruling outlawing the practice, died on 1 May at his home in Hastings-on-Hudson, New York. He was 90.

Clark belonged to a pioneering generation of African-American scholars. He was the first to earn a doctorate in psychology from Columbia University (his wife and collaborator Mamie Phipps Clark was second); the first to become tenured in the City College system of New York; the first elected to the New York State Board of Regents; and the first black to be president of the American Psychological Association (APA).

Clark and his wife are remembered for a famous study using black and white dolls that showed that children in a segregated school thought the black dolls were bad. As APA president, he created a Board of Social and Ethical Responsibility that brought problems of social justice within psychology into greater prominence. "Clark was a deeply compassionate person committed to racial equality," says psychologist George Albee, a former president of the association. "He was a quiet, scholarly man but persistent and unwavering."

SIDELINES

Loud and clear. Physicists can filibuster, too. That was the message from string theorist Ed Witten, who read from a particle physics textbook during a mock filibuster at Princeton University begun late last month to protest a Republican threat to eliminate the filibuster by changing the rules of the U.S. Senate. The student-organized protest was held outside a campus building named for its donors, the family of Senate Majority Leader Bill Frist (R–TN).

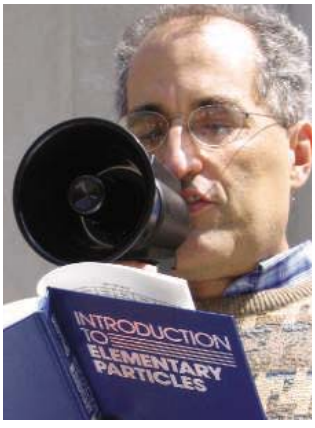

Listening to physics—Nobelist Frank Wilczek joined the protest—was a welcome change from a steady diet of novels and phone books offered up by other speakers, says Princeton sophomore Asheesh Siddique, one of the organizers: "We thought it was very cool."

CREDITS (TOP TO BOTTOM): PIEL PATRICK/GAMMA; CHRIS NEWHALL; JAYATRI DASS; ROBERT MAASS/CORBIS

An Open Mind Is a Trojan Horse?

GEORGE ANDERSON APPARENTLY MISUNDERstands the real issue regarding the anti-evolution stickers that have been put into biology textbooks in Georgia ("Keeping an open mind?," Letters, 22 Apr., p. 495). He seems to think that the creationism-evolution discussion is similar to a political debate, where different viewpoints from different people are equally valuable and important. The creationism-evolution discussion is not such a debate.

The question is whether the scientific evidence for evolution is greater or less than the scientific evidence for divine creation. There is no middle ground in this debate, unlike in political debates; it is a scientific question that can only be answered with scientific methodology. Stating that one side is correct and the other side is wrong may be perceived as dogmatism and arrogance in a political debate, but it is the ultimate goal of a scientific discussion, because science proceeds by the removal of erroneous ideas through critical experiments and observations. The highest level one can hope to achieve in the scientific domain is to formulate a theory, which is some set of hypotheses that have been confirmed by empirical evidence. In that sense, evolutionary theory does not differ from other scientific theories in chemistry or physics—for example, the general theory of relativity.

Why not put warning stickers about theories in chemistry and physics textbooks? The reason should be obvious to most scientists: The stickers in the biology textbooks are there for ideological reasons, not because those who have pushed for them are particularly interested in education of children. Rather, they want to question the scientific evidence for a well-established theory (evolution) because they oppose it from a religious viewpoint. We should fight against this special treatment of evolutionary theory and avoid letting creationist propaganda and antiscientific attitudes permeate schools and textbooks.

ERIK I. SVENSSON
Department of Animal Ecology, Lund University, Lund S-22362, Sweden.

Letters to the Editor

Letters (~300 words) discuss material published in *Science* in the previous 6 months or issues of general interest. They can be submitted through the Web (www.submit2science.org) or by regular mail (1200 New York Ave., NW, Washington, DC 20005, USA). Letters are not acknowledged upon receipt, nor are authors generally consulted before publication. Whether published in full or in part, letters are subject to editing for clarity and space.

Terrestriality and Tool Use

IN THEIR BREVIA "CAPUCHIN STONE TOOL use in Caatinga dry forest" (10 Dec. 2004, p. 1909), A. C. de A. Moura and P. C. Lee report that in the dry Caatinga habitat of Piauí (northeastern Brazil), capuchin monkeys (*Cebus libidinosus*) dig for tubers and use stones to crack open embedded food. Because tool use may allow monkeys to survive periods of food scarcity, they argue that its occurrence is related to energy bottlenecks. However, this argument is weakened by the frequent observations of spontaneous tool use by capuchins in captivity and in semi–free-ranging, provisioned groups, and by the absence of tool use in wild groups facing energy bottlenecks in many habitats (*1*). Moreover, according to Moura (*2*), the group that he observed was provisioned. Thus, food scarcity seems an unlikely explanation for tool use by capuchin monkeys.

A foraging capuchin monkey.

CREDIT: A. C. DE A. MOURA AND P. C. LEE

We propose instead that terrestriality, promoted by foraging on the ground, is the key factor promoting the emergence of tool use in capuchins. Spending time collecting or searching for food on the ground, rather than in trees, increases an individual's chances of attempting to collect or process foods where potential tools are also present. Food that requires removal from the ground or other strong embedding matrix, such as a husk, is particularly likely to elicit tool use as a natural extension of species-typical foraging actions that combine objects and surfaces (*1*). This hypothesis leads us to predict that tool use in wild capuchins will be more strongly associated with time spent on the ground foraging, particularly for encased foods, than with energy bottlenecks. If the hypothesis is correct, the possibility that terrestrial foraging habits supported the discovery of tools in human ancestors deserves attention.

ELISABETTA VISALBERGHI,[1] DOROTHY MUNKENBECK FRAGASZY,[2] PATRÍCIA IZAR,[3] EDUARDO B. OTTONI[3]
[1]Istituto di Scienze e Tecnologie della Cognizione, Consiglio Nazionale delle Ricerche, via Aldrovandi 16B, Rome 00197, Italy. [2]Department of Psychology, University of Georgia, Athens, GA 30602, USA. [3]Department of Experimental Psychology, University of São Paulo, Avenida Prof. Mello Moraes, 1721, Cidade Universitaria, São Paulo 05508-20, Brazil.

References
1. D. Fragaszy, E. Visalberghi, L. Fedigan, *The Complete Capuchin* (Cambridge Univ. Press, Cambridge, 2004).
2. A. C. de A. Moura, thesis, University of Cambridge (2004).

Response

VISALBERGHI *ET AL.* RAISE AN INTERESTING and important point; terrestriality provides significant tool use opportunities for primates. We proposed that the use of embedded resources was associated with habitual food scarcity and that the energetically expensive use of stones and other tools was a vital mechanism for food acquisition. Visalberghi *et al.* suggest that these capuchins were not energy limited because one group was partially provisioned, and they provide other examples of tool use by provisioned groups. In contrast, tool use has been seen in three unprovisioned groups (our Brevia), and palm nut cracking was suggested to be habitual for capuchins in Caatinga in nearby Piauí (*1*). Terrestriality, tool use, and food limitations are potentially linked, but we would place a priority on energy requirements being met in this habitat through extractive foraging with tools. First principles suggest that the foraging strategy is a consequence of what is available in the habitat rather than a secondary consequence of changing substrate or mode of locomotion.

If terrestriality is essential for the appearance of tool use, why is tool use rarely, if ever, seen in terrestrial capuchins in richer wild habitats? Defler (*2*) observed *Cebus albifrons* in Colombian semideciduous forest and did not see a single event of tool use in over 500 contact hours. Stones were common, palm nuts were available and consumed by the monkeys, and the monkeys spent up to 50% of time on the ground. In contrast, capuchins in the harsh Caatinga spend less than 23% of time on

the ground (*3*). Dry forests have lower diversity and lower net productivity than do rainforests (*4*), and the Caatinga is impoverished in comparison to other Neotropical dry forests (*3*, *5*); thus, energy bottlenecks are severe. Capuchins in this habitat frequently use twigs as probing tools, unassociated with terrestriality. Although the use of digging stones is obviously related to the exploitation of subterranean resources, we suggest that this technology is both more diverse and more complex than the link to ground foraging suggested by Visalberghi *et al*.

PHYLLIS C. LEE AND ANTONIO C. DE A. MOURA
Department of Biological Anthropology, University of Cambridge, Downing Street, Cambridge CB2 3DZ , UK.

References

1. D. Fragaszy *et al*., *Am. J. Primatol.* **64**, 359 (2004).
2. T. R. Defler, *Primates* **20**, 475 (1979).
3. A. C. de A. Moura, thesis, University of Cambridge (2004).
4. P. G. Murphy, A. E. Lugo, *Annu. Rev. Ecol. Syst.* **17**, 67 (1986).
5. G. Ceballos, in *Seasonally Dry Tropical Forests*, S. H. Bullock *et al*., Eds (Cambridge Univ. Press, Cambridge 1995), pp. 195–220.

Consensus About Climate Change?

IN HER ESSAY "THE SCIENTIFIC CONSENSUS on climate change" (3 Dec. 2004, p. 1686), N. Oreskes asserts that the consensus reflected in the Intergovernmental Panel on Climate Change (IPCC) appears to reflect, well, a consensus. Although Oreskes found unanimity in the 928 articles with key words "global climate change," we should not be surprised if a broader review were to find conclusions at odds with the IPCC consensus, as "consensus" does not mean uniformity of perspective. In the discussion motivated by Oreskes' Essay, I have seen one claim made that there are more than 11,000 articles on "climate change" in the ISI database and suggestions that about 10% somehow contradict the IPCC consensus position.

But so what? If that number is 1% or 40%, it does not make any difference whatsoever from the standpoint of policy action. Of course, one has to be careful, because people tend to read into the phrase "policy action" a particular course of action that they themselves advocate. But in the IPCC, one can find statements to use in arguing for or against support of the Kyoto Protocol. The same is true for any other specific course of policy action on climate change. The IPCC maintains that its assessments do not advocate any single course of action.

So in addition to arguing about the science of climate change as a proxy for political debate on climate policy, we now can add arguments about the notion of consensus itself. These proxy debates are both a distraction from progress on climate change and a reflection of the tendency of all involved to politicize climate science. The actions that we take on climate change should be robust to (i) the diversity of scientific perspectives, and thus also to (ii) the diversity of perspectives of the nature of the consensus. A consensus is a measure of a central tendency and, as such, it necessarily has a distribution of perspectives around that central measure (*1*). On climate change, almost all of this distribution is well within the bounds of legitimate scientific debate and reflected within the full text of the IPCC reports. Our policies should not be optimized to reflect a single measure of the central tendency or, worse yet, caricatures of that measure, but instead they should be robust enough to accommodate the distribution of perspectives around that central measure, thus providing a buffer against the possibility that we might learn more in the future (*2*).

ROGER A. PIELKE JR.
Center for Science and Technology Policy Research, University of Colorado, UCB 488, Boulder, CO 80309–0488, USA.

References

1 D. Bray, H. von Storch, *Bull. Am. Meteorol. Soc.* **80**, 439 (1999).
2. R. Lempert, M. Schlesinger, *Clim. Change* **45**, 387 (2000).

Response

PIELKE SUGGESTS THAT I CLAIMED THAT there are no papers in the climate literature that disagree with the consensus. Not so. I simply presented the research result that a sample based on the keywords "global climate change" did not reveal any, suggesting that the existing scientific dissent has been greatly exaggerated and confirming that the statements and reports of leading scientific organizations—including the U.S. National Academy of Sciences—accurately reflect the evidence presented in the scientific literature.

Pielke is quite right that understanding the results of scientific research does not implicate us in any particular course of action, and the purpose of my Essay was not to advocate either for or against the Kyoto accords or any other particular policy response. A full debate on the moral, social, political, ethical, and economic ramifications of possible responses to climate change—as well as the ramifications of inaction—would be a very good thing. But such a debate is impeded by climate-change deniers. In this respect, I am in complete agreement with Pielke's conclu-

sion, which was precisely the point of my Essay: Proxy debates about scientific uncertainty are a distraction from the real issue, which is how best to respond to the range of likely outcomes of global warming and how to maximize our ability to learn about the world we live in so as to be able to respond efficaciously. Denying science advances neither of those goals.

NAOMI ORESKES
Department of History and Science Studies Program, University of California at San Diego, La Jolla, CA 92093, USA.

Interpreting Correlation as Causation?

THE BRIEF ITEM "GAMBLING AS ADDICTION" (Random Samples, 21 Jan., p. 349) typifies the serious problems of interpretation that modern imaging techniques seem to have magnified many times.

In the study discussed, gamblers were subjected to functional magnetic resonance imaging (fMRI) scans while playing a simple game. Upon winning, the gamblers showed a less pronounced increase in ventral striatal activity than did control subjects (*1*). A simple interpretation would be that jaded gamblers had become less reactive to winning, and the research team had observed neurological underpinnings of this habituation. Instead, the researchers are described as having uncovered "abnormalities," and that gamblers may "compensate for deficiencies in their brain reward systems…"

Any behavioral difference is presumably correlated with a difference in neurological activity. However, the dangers of leaping to causal conclusions involving brain abnormalities can be seen by applying the same logic to the posterior hippocampus enlargement found in London cab drivers (*2*). Rather than concluding that the enlargement results from spatial demands, we might conclude that this "abnormality" creates an insatiable need for spatial stimulation, chaining its victims to potentially dangerous employment with limited executive prospects.

It is always tempting to treat physiological correlates of behavior as causing behavior, but that should make us doubly vigilant about overlooking the well-known limitations in the information that correlations are capable of providing.

JAMES W. ALDRIDGE
Departments of Psychology and Anthropology, University of Texas–Pan American, Edinburg, TX 78541, USA.

References

1. J. Reuter *et al.*, *Nat. Neurosci.* **8**, 147 (2005).
2. E. Maguire *et al.*, *Proc. Natl. Acad. Sci. U.S.A.* **97**, 4398 (2000).

EVOLUTION AND DEVELOPMENT

A Long and Winding Road

Denis Duboule

The love affair between development and evolution has not always been easy. The emergence of causal embryology in the late 19th century triggered developmental biologists to focus on their favorite animal or piece thereof (at the expense of a wider consideration of animal forms), whereas evolutionists have understandably shown little interest in the complex mechanisms underlying variation. The passion in this old couple was nevertheless revived in the early 1980s, following several revolutionary discoveries that led to the novel discipline of "evo-devo." *Endless Forms Most Beautiful*, as its subtitle indicates, is about this "new science," a qualification somewhat at odds with a major concept Sean Carroll develops in the book: that novel forms are always modifications of preexisting ones. This likely also applies to the history of ideas and disciplines.

It is admittedly difficult for today's young biologists to imagine the impact of these discoveries on our conceptual frameworks, and we all wonder how people could possibly have thought differently before. Carroll (a developmental geneticist at the University of Wisconsin, Madison) takes us for a journey into the early days of the field, introducing the fundamentals of evo-devo through a historical perspective. This is not always the simplest way to give a state-of-the-art account of a particular field of research, yet the author succeeds in the task. The book opens with a clear introduction of both the context and the basic tenets of evo-devo. Carroll explains the relevance of developmental mechanisms as sources of evolutionary innovation. He presents evo-devo as a science of inference, in which molecular features such as gene expression or regulatory specificities observed in two distinct animals are postulated to have existed in their common ancestor. This really is the modus operandi of the discipline, and throughout the book he offers many illuminating examples to validate this approach.

So what was the evo-devo revolution about? We can recognize several key claims. First, genes control development. Second, all animals develop by using the same set of genes. Third, the basic genetic principles underlying animal development are shared. That is, the same genes are used in much the same way, and they participate in the same networks, which in turn interact with each other in a rather generic fashion throughout the animal kingdom. Last, various parts of the same animal are built following the same logic, again by using similar modules and networks of genes. Nature is parsimonious, and things that work in particular functions are often subsequently recruited in parallel with the emergence of evolutionary innovations. Tinkering, multifunctionality, redundancy, and modularity are the key words of the discipline; also crucial is the notion of a genetic "tool kit" for animal development, a notion that is used throughout the text. As one would expect, arthropods occupy a large share of this description, which reflects both the history of the field and the expertise of the author. Carroll discusses the impact of sequencing the entire DNA of species, which has revealed great similarities among the genomes of different species, and the concurrent change in paradigm that leaves us wondering why then are we so different from other animals. The chapter dealing with primate evolution (subtitled "The Making of *Homo sapiens*") is especially thought-provoking in this respect.

Endless Forms Most Beautiful
The New Science of Evo Devo and the Making of the Animal Kingdom
by Sean B. Carroll

Norton, New York, 2005. 371 pp. $25.95, C$38. ISBN 0-393-06016-0.

Among the various tool kits, the *Hox* gene family receives special attention because of its importance in the development of these new concepts. Yet no explanation, not even a tentative one, is offered as to why this group of genes had (have) such a high epistemic value. Carroll shows how modifications in *Hox* gene regulation are associated with changes in forms—how minor causes can lead to major morphological effects such as the presence or absence of legs and wings. Nonetheless, among the various examples Carroll provides to illustrate this basic principle, I most enjoyed the chapters dealing with phenomena where these latter genes have little if any importance: the questions of butterfly eyespots, mammalian coat colors, and mimicry. These are discussed at some length, but anyone interested in knowing how butterflies can display such a variety of splendid wings will enjoy the details.

Evo-devo bears great hopes, but the approach also carries significant drawbacks. This is one aspect of the field that may have deserved more attention in the book. Carroll indeed tells us the best of evo-devo, discussing case studies in which developmental genetics, often backed up by functional assays, is associated with both molecular biology and a good knowledge of systematics and evolution. Not all studies are so comprehensive, and overly bold hypotheses are not rare in the field. At times, researchers take the "one P–one T" approach (one polymerase chain reaction to one theory), through which a mere expression domain can generate grandiose theories.

Another second aspect is perhaps of a more epistemological nature. To begin, development cannot explain evolution. Understanding developmental mechanisms

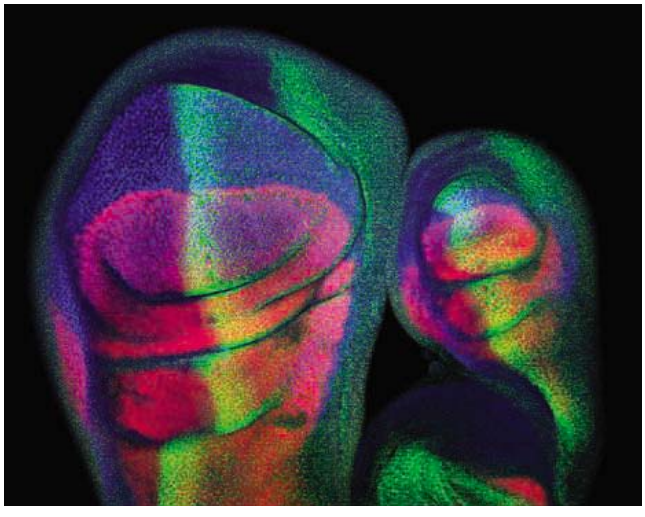

Produced with a common tool kit. Although of different sizes, *Drosophila* forewings and hindwings are subdivided by the same tool kit proteins (compare purple, red, and green-yellow patterns between the two wings).

CREDIT: JIM WILLIAMS, STEVE PADDOCK, AND SEAN CARROLL/HHMI, UNIVERSITY OF WISCONSIN

The reviewer is at the Department of Zoology and Animal Biology, National Research Centre Frontiers in Genetics, Sciences III, 30 Quai Ernest Ansermet, 1211 Geneve 4, Switzerland. E-mail: denis.duboule@zoo.unige.ch

can give us some hints as to how modifications thereof may have led to what we see today. But all animals available for such experimentation, regardless of their apparent levels of complexity, are themselves the result of millions of years of evolutionary tinkering, following a roadmap that we cannot possibly understand since it bears no intrinsic logic other than what is possible to do. In addition, the question of model systems deserved some attention, as these species are chosen because they often display a highly adapted feature, such as the wings of butterflies or the cell lineage of nematodes. One may thus wonder how many (if not all) of such systems will be necessary to fully understand the core of the universal rules at work.

A fundamental question raised by evo-devo—what is the impact of this discipline on our thinking about the evolutionary theory?—is addressed at the end of the book. Here, I must admit, I was hoping for some more provocative thoughts. Carroll's orthodoxy in his belief in Darwinism is sometimes awkwardly close to that expressed by creationists when arguing the opposite. Evo-devo is presented as an explanatory framework for gradualism—as a demonstration of the critical importance of selection in the emergence and maintenance of new forms and patterns. There is nothing wrong with this framework of course, and a more critical view is understandably difficult to express (even for a reader of Descartes) when disputes about aspects of evolutionary processes are so often used by creationists to argue against evolution itself.

Nonetheless, the best way to defend a theory is to criticize its unavoidable weaknesses, and the question of how evo-devo may help in this endeavor deserved a few paragraphs. "Endless forms most beautiful," the quotation from Charles Darwin used as the book's title, is by itself a source of confusion. Does "endless" mean the never-ending production of novel forms within a limited set of possibilities (in the past, present, and future)? Or does it imply that nature can produce a potentially infinite number of forms, which are then reduced by natural selection? This consideration is not merely philological, as it touches on the realm of possibilities wherein the "chance" of Jacques Monod or the "tinkering" of François Jacob could take place. Given that the same genes, modules, and mechanisms are at work throughout developing animal bodies, in many parts and at different times, can we still think of variation as affecting single parts of an otherwise unchanged organism? Carroll briefly addresses this fundamental issue, mentioning the difficulty in transferring concepts from microevolution to macroevolution. However, he does not discuss evo-devo's potential impact in readjusting the balance from an indefinite variation (the power of selection) to a perhaps more restricted number of possible variations imposed by the now-apparent internal constraints of developmental systems.

The book is somewhat difficult to classify. It is obviously neither a textbook nor a historical or epistemological essay about the relation between development and evolution. The field it describes is itself evolving, and if a revised edition is ever prepared some parts will stay as they are, some may disappear, and some will be modified along the way. *Endless Forms Most Beautiful* offers an excellent introduction to the still-young discipline of evo-devo. Readers will find an enjoyable account by a scientist who for more than 20 years has not only witnessed but contributed to the ongoing saga. Anyone interested in animal development and evolution will appreciate the book. I particularly recommend it to students and junior scientists still wondering about what to do in their future careers. They will quickly grasp the enormous potential of this field. The genuine passion Carroll has for the beauty of nature may also show them how fun science can be.

10.1126/science.1109964

ASTRONOMY

Going On from Observation

E. Margaret Burbidge

Sir Fred Hoyle will be remembered as the British scientist who, above all others, brought astronomy into the world of 20th century physics. It is fitting that *Conflict in the Cosmos* has been written by a scientist whose high-school fascination with astronomy led to a career in the field. Through that career, Simon Mitton gained both the scientific knowledge needed to follow Hoyle's life from birth in 1915 to death 86 years later and the experiences necessary to follow the intricacies of Cambridge University politics. Mitton also possesses several other advantages: access to Hoyle's correspondence, manuscripts, and other papers maintained at St. John's College, Cambridge, and the help and friendship of Lady Barbara Hoyle, whom Fred married in December 1939 and with whom he shared a loving and supportive marriage.

The reviewer is at the Center for Astrophysics and Space Sciences, University of California San Diego, 9500 Gilman Drive, Mail Code 0424, La Jolla, CA 92093–0424, USA. E-mail: mburbidge@ucsd.edu

Conflict in the Cosmos
Fred Hoyle's Life in Science
by Simon Mitton

Joseph Henry, Washington, DC, 2005. 398 pp. $27.95, C$37.95. ISBN 0-309-09313-9.

Fred Hoyle
A Life in Science

Aurum, London, 2005. 320 pp. £18.99. ISBN 1-85410-961-8.

After a prologue that sets the stage for the account of Hoyle's lifetime of achievements and battles, Mitton begins his narrative at teatime in Cambridge University's Institute of Theoretical Astronomy (IOTA), the institute Hoyle created. It is August 1972, IOTA has recently been merged with the historic Cambridge Observatories, and Hoyle is about to leave for good. Mitton takes us on Hoyle's last tour of the institute before turning to his subject's family background and early life in England's west Yorkshire. The account conforms to Hoyle's own description in his autobiographical books (*1*, *2*).

Life in west Yorkshire in the 1920s was not easy, and one can see the effects that Hoyle's childhood had in building the stamina and independent thinking that supported him all his life. As Mitton describes, Hoyle's father served as a machine gunner in World War I and lived through those years of slaughter before returning to the rigors of life in the wool trade. Hoyle's mother, an accomplished pianist, earned a little to supplement the pittance the government supplied to veteran soldiers' families by playing the piano at the town's cinema. Her son always loved music, especially that of Bach and Beethoven. As a young boy, Hoyle studied the locks of the local canal and used his father's old chemistry textbook to conduct gunpowder experiments in the scullery. Mitton offers a vivid account of Hoyle's early school days, during the hard years of the failing wool industry. After his dismal experiences at the local "dame school" (where one teacher taught all children up to age 11 in a single room), Hoyle's budding intellectual ability was recognized, treated with respect, and fostered at Bingley Grammar School. Its head played a crucial role in shaping his future: "Without the encouragement and determination of Alan Smailes, I would never have reached Cambridge."

Undergraduate studies in Cambridge and the beginning of his career in research led to one of Hoyle's most important friendships,

that with Raymond Lyttleton. The book describes their early research on the accretion mechanism for the capture by stars of matter from interstellar space. But World War II started, and the emerging importance of radar and the wartime need for mathematical physicists took Hoyle away from Cambridge into the pastures of Sussex where secret work on radar was conducted. In this work, he was joined by two of the many young emigré scientists who escaped from Hitler's persecution in Germany and Austria, Thomas Gold and Hermann Bondi. The chapter "Hoyle's Secret War," which describes this work on radar, also includes several recollections from Bondi and an account of Hoyle's first visit to the United States. Hoyle made the trip in order to attend a meeting on radar research held in Washington, D.C., but in typical fashion he turned it into an opportunity to travel west and visit the Mount Wilson Observatory. There he made the acquaintance of Walter Baade, the German-born astronomer who discovered that stars come in populations defined by their ages and their location in the Milky Way. Hoyle enjoyed this introduction to the excitement of observational astronomy, so far beyond the dull stuff going on in Cambridge. Those who have had the good fortune to know Baade personally can understand the effect the meeting had on Hoyle's emerging ideas about the lifetime of stars and the implications of observations by Edwin Hubble and Milton Humason of the recession velocities of galaxies.

This same period saw Hoyle's emergence as a gifted communicator to the general public in talks for the British Broadcasting Corporation and in popular books. In the years immediately after the war, Bondi, Gold, and Hoyle collaborated on their "steady-state cosmology," in which the recession velocities of galaxies are balanced by a slow creation of new matter. Mitton's account of the ensuing encounters at the Royal Astronomical Society meetings in London gives full documentation of the animosity that this theory engendered, a response I still find hard to comprehend.

The steady-state theory was one point of contention between Hoyle and the radio astronomer Martin Ryle, whose group worked in Cambridge's Cavendish Laboratory. Mitton discusses the antagonism and rivalry between the two researchers, which continued through the 1950s, in the appropriately named chapter "Clash of Titans."

In the early 1950s, Hoyle developed his fruitful collaboration and lifetime friendship with William Fowler, an experimental nuclear physicist at Caltech. During a sabbatical year at Cambridge, Fowler introduced my husband, Geoffrey (who had a research fellowship in Ryle's group), and me to Hoyle. Geoffrey and I were working on abundance of elements in stellar atmospheres. A decade earlier, Hoyle had begun to ponder how the mix of chemical elements observed in the Sun's spectrum could have formed. His work on nuclear reactions in stars had now led him to an explanation for the synthesis of elements up to iron. Fowler brought the four of us together to develop our comprehensive theory of these processes (*3*). Mitton's detailed account of Hoyle's achievements in these years amply demonstrates the genius of his subject.

CREDIT: COURTESY E. M. BURBIDGE

Hoyle in his prime. Hoyle, Fowler, and the Burbidges continued their work on the origin of the chemical elements far beyond their classic B^2FH (*3*). At this gathering at Caltech in about 1970, the four are ordered, left to right, BFHB.

Hoyle envisioned IOTA as a place where serious work in theoretical astronomy would attract visitors from all over the world and where the bright students and postdocs in Cambridge could mix in a free atmosphere of ideas, research, and discussions. Mitton describes the many years of effort that Hoyle expended to establish the institute, which opened in 1965. Characteristically, Hoyle had a great deal to say about the architecture of the building and the needs for a good lecture room and an accessible electronic computer.

After five successful years of astronomical research at IOTA, Hoyle's life in Cambridge entered a dark period that this biography does not dodge. Inevitable professional jealousies and the problem of obtaining continued funding for IOTA intruded. Mitton describes the events that precipitated Hoyle's abrupt 1972 resignation from the university that had been his scientific home since his entry as an undergraduate in 1933. Hoyle had always preferred occupying his mind with interesting puzzles, problems, and scientific concerns rather than with academic politics. He did not adequately deal with the threat posed by one of his Cambridge colleagues who, in Ray Lyttleton's picturesque phrase, was "rusted in" to what had been planned as a rotating position. While Hoyle was engaged in the last stages of the important work on the design and construction for the Anglo-Australian Telescope and the southern 48-inch Schmidt telescope, his position at Cambridge was successfully attacked. When he was not chosen to direct the new Institute of Astronomy, he made a rapid and characteristic decision: he resigned the Plumian professorship, departed from Cambridge, and found a new home in the Lake District.

Through arrangements made by his friends and colleagues, Bernard Lovell at the University of Manchester and Chandra Wickramasinghe at Cardiff University, he spent his following years as a visiting professor at their institutions. He finally retired to an apartment in Bournemouth, which remained a base where he and Barbara could welcome visiting friends. A tragic fall during a visit to his sister back in his childhood home in Yorkshire led to a long treatment for a broken shoulder, during which he continued to work on cosmology. He died three years later.

Conflict in the Cosmos successfully captures the remarkable breadth of a fascinating and influential scientist. I knew Hoyle for some 50 years and was continuously amazed by the many different areas he got into, always with new and interesting ideas. He tackled the riddle of Stonehenge, he wrote plays and science fiction novels [including *The Black Cloud* (*4*), now considered a classic], he penned opera lyrics with composer Leo Schmitt, and he worked on theories of panspermia to explain the origin of life on Earth. These are among the many diverse topics covered in the book's last chapter. Anyone interested in the development of 20th century astronomy and cosmology should read and enjoy Mitton's account of Hoyle's life and accomplishments.

References

1. F. Hoyle, *The Small World of Fred Hoyle: An Autobiography* (Michael Joseph, London, 1986).
2. F. Hoyle, *Home Is Where the Wind Blows: Chapters from a Cosmologist's Life* (University Science, Berkeley, CA, 1994).
3. E. M. Burbidge, G. R. Burbidge, W. A. Fowler, F. Hoyle, *Rev. Mod. Phys.* **29**, 587 (1957).
4. F. Hoyle, *The Black Cloud* (Heinemann, London, 1957).

10.1126/science.1111602

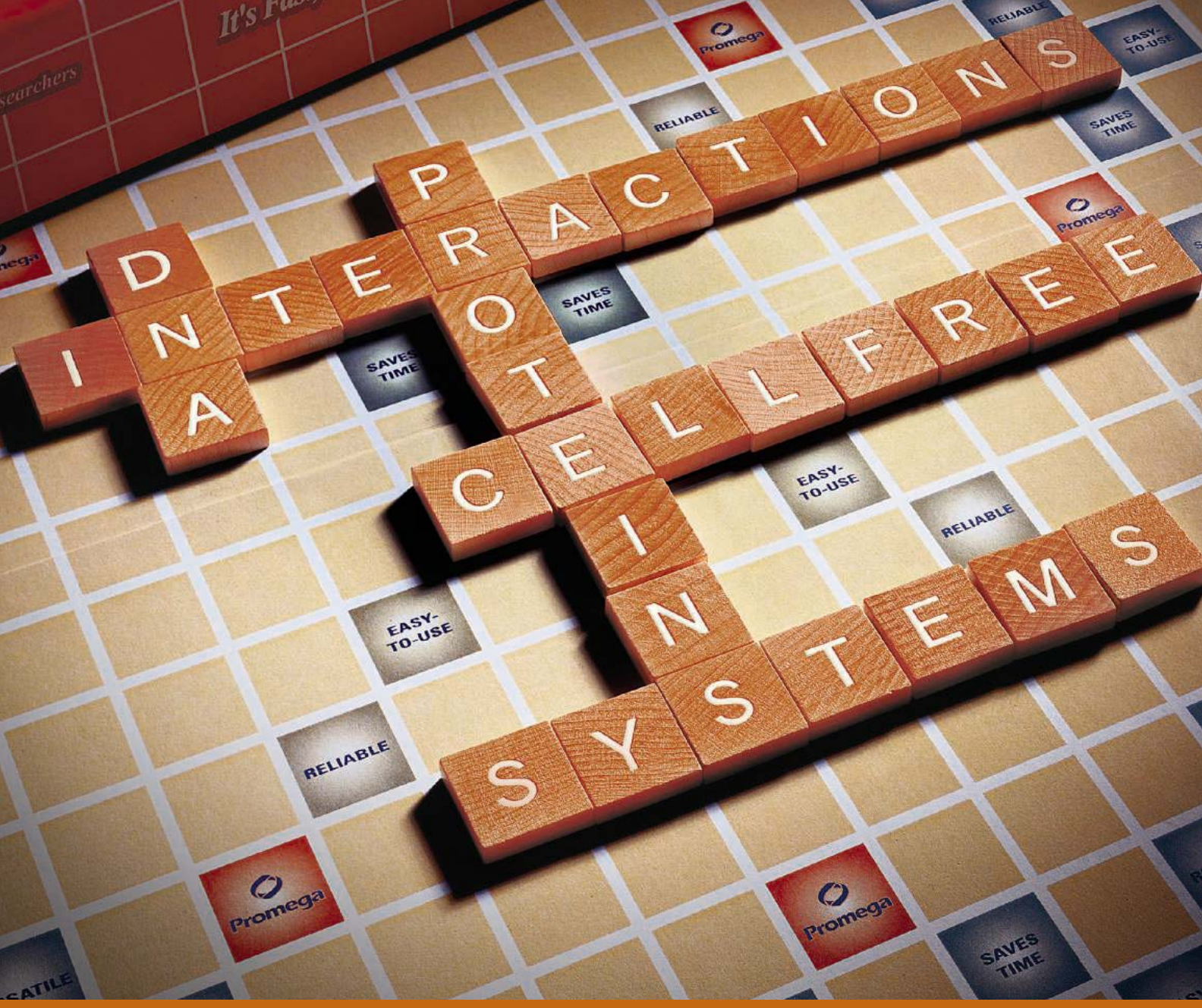

TNT® Cell-Free Protein Expression. Build on it!

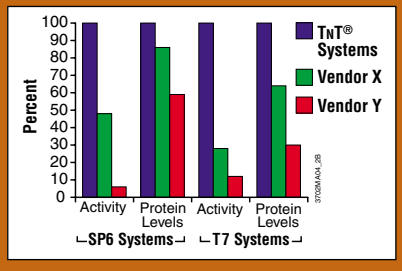

Generate more functional protein with Promega.

Easy, one-step protocols provide quick and accurate results. Use Promega TNT Coupled Transcription/Translation Systems. Generate more functional protein than you'll find in other available eukaryotic-based systems.

Ideal for:

- Protein:protein interactions
- Protein:nucleic acid interactions
- In vitro expression cloning

To learn more visit **www.promega.com/cellfree**

PROMEGA CORPORATION • www.promega.com

Promega

PUBLIC HEALTH

Increasing International Gaps in Health-Related Publications

Guillermo Paraje, Ritu Sadana,* Ghassan Karam

Do scientists in countries with the greatest burden of disease or weakest health systems contribute to science-related improvements in health? National scientific outputs reflect not only new knowledge, but also capacities to adapt and benefit from research conducted globally.

Although we recognize that evidence of scientific activity is found beyond the articles indexed by internationally recognized reference databases (*1*), we base our analysis on the Thomson Scientific databases, which include the addresses of all collaborating authors, during a 10-year period. Although there have been many studies of international research output (*2*–*5*), they have been broader in describing the scope of research across nonmedical fields, yet narrower in their definition of health-related research. Unlike previous studies, we do not confine scientific outputs addressing health to biomedical research only. We note that the knowledge required to address physical, mental, and social components of health and to organize and provide preventive, curative, and palliative services within any country must draw on many more scientific disciplines and research outputs. Therefore, we include fields and journals that cover a wider range of health topics, primarily referenced within the Science Citation Index (SCI), as well as health-related journals from the Social Sciences Citation Index (SSCI). Major categories in addition to biomedical sciences include clinical medicine, pharmacology, public health and health systems, social sciences and social welfare, environmental sciences, and food sciences related to health (*6*). Expanding our analysis beyond biomedical research and including a broader range of scientific outputs relevant to health increased by 15% the number of countries represented, primarily the low-income countries. The total number of journals included during the period 1992 to 2001 was 4061, with more than 3.47 million peer-reviewed publications (i.e., articles, notes, and reviews) analyzed, and with collaborating authors residing in 190 countries (*7*). Although 23 languages were represented by at least one publication in 2001, about 96% of publications were in English.

Scientific publications on health topics were disproportionately distributed and highly concentrated among the world's richest countries (see table, this page). More than 90% of the publications were produced by scientists in 20 countries. The top seven countries are also the G7 countries, which has not changed in the last decade (*2*). The United States was the most prolific, with its authors contributing to more than a third of worldwide production. Another third was shared by authors with affiliations in the United Kingdom, Japan, Germany, France, Canada, and Italy. The remaining third came from authors residing in 183 countries, 13 of which constituted the bulk of them. These proportions have been relatively stable over the 10-year period except for a clear upward trend in Brazil, China, and, in particular, the Republic of Korea—more than a ninefold increase. The contribution to scientific publications on health differs by country-income groups, as defined by the World Bank in 2001 (see figure, this page, and table, page 960). High-income (HI) countries had a relatively constant share of worldwide publications between 1992 and 2001. Upper-middle-income (UMI) countries, by contrast, increased their contribution by about 30%, although their overall share remains at 3% of worldwide production. Scientists residing in lower-middle-income (LMI) countries have also increased their contribution by more than 20%, with over a 6% share of worldwide production in 2001. This growth is largely due to increased publications indexed from Brazil, China, and Turkey, which together have overcompensated for the decrease in publications indexed from the Russian Federation. The low share of publications (less than 2% of the total) indexed from low-income (LI) countries declined by about 10% (*8*). Only one-fifth of the total for these 63 countries is produced in Sub-Saharan Africa (46 countries), whereas the bulk was mainly from Southeast Asia. India contributed 73% of the research outputs of LI countries in 2001, up from 66% in 1992.

These results provide further evidence that the gap in scientific publications between LI countries and the rest of the world has widened (*9*, *10*). Although the causes are not simple to understand, this decreasing proportion for LI countries (especially in Sub-Saharan Africa) in contrast to gains by LMI countries, underlines ongoing calls to improve capacities and networks, to intensify equitable research partnerships, to increase public funding for research and innovation strategies addressing national health priorities, and to increase the visibility of

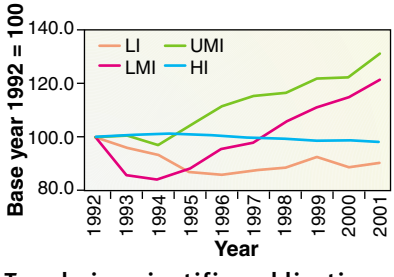

Trends in scientific publications. Countries are classified as LI, low income; LMI, lower-middle income; UMI, upper-middle income; HI, high income. Trends in scientific publications (63 LI, 54 LMI, 31 UMI, and 42 HI countries). Publication shares are indexed at 100 in 1992.

TOP 20 HEALTH-RELATED PUBLICATION PRODUCERS

Top 20 producers	Average Global Share 1992–2001
USA	36.68
United Kingdom	8.57
Japan	8.11
Germany	6.63
France	5.19
Canada	4.02
Italy	3.54
Netherlands	2.33
Australia	2.27
Spain	2.06
Sweden	1.93
China	1.63
Switzerland	1.39
India	1.16
Israel	1.04
Belgium	1.03
Denmark	0.90
Finland	0.89
Brazil	0.73
Republic of Korea	0.59
Rest of the world	9.32
Total	100.00

The authors are at the World Health Organization CH-1211 Geneva 27 Switzerland.

*Author for correspondence. E-mail: sadanar@who.int

research undertaken in these countries (*10–14*).

Within each economic category, two tiers of countries appear to exist, with publications highly concentrated in a few. Thus, national income does not fully explain differences in the share of scientific publications on health topics.

What enables or hinders conducting and publishing research within each group of countries should be further explored and understood from a systems perspective (*15, 16*). China's increasing proportion of worldwide outputs addressing health topics can be attributed to specific changes in research policies during the past two decades, including an increasing value on the assessment of research outputs (*17, 18*). The government has implemented break-through policies that provide intensive financial support to key laboratories and institutions, as well as leading disciplines, including those related to health. That China was the only developing country participating in the Human Genome Project provides evidence of these investments (*19*). Having at least one article indexed in a Thomson Scientific database is now required for most academic promotions, and each article is financially rewarded. Efforts to increase the quality of research include stronger institutional and peer-review mechanisms, more international cooperation, and major government-sponsored foreign education programs. To reduce "brain drain," expatriate Chinese researchers are being lured back with strong incentives (known as the "tortoise policy" introduced in the late 1990s) including high wages, housing, and a research environment that includes good facilities, flexible work schedules, and fostering and maintaining close collaborations with foreign research institutions, as well as among national universities, public institutions, and private companies (*17, 20*).

Rapid and steady economic and social development provides the backdrop to the Republic of Korea's gains. The government remains the main player behind the enormous increase in the country's research and development expenditures over the last 30 years, reflecting a jump from 0.31% of GDP to nearly 3% of GDP, with GDP itself increasing substantially. In 1994, seven ministries signed a pact to transform the Republic of Korea into one of the top countries in biotechnology by 2010 (*21*). The government has also initiated financing mechanisms and programs for technology transfers from academic institutions, where almost all research is conducted, to private-sector firms (*21*). Collaborations and exchanges with foreign institutions on other health topics are also rising, as evidenced by the opening of a new Institut Pasteur in Seoul in 2003. Some top institutions have started awarding points for publications as a means for promotion (*18*).

A more worldwide research base is likely to increase the relevance of and access to scientific outputs for countries with overburdened health systems, as well as ultimately to enlarge the impact of scientific activities on health status. Given the mounting gap in the share of worldwide scientific publications addressing health topics between low-income countries and the rest of the world and a highly concentrated production pattern within each economic category of countries, strategies to enhance scientific capacities need to reflect the heterogeneity found across countries; to require support at national, regional, and international levels for extending benefits to a greater number of countries; and to involve a wide range of actors beyond those traditionally working on biomedical or even clinical research. A key area for action is to understand and support what pushes and pulls scientists in diverse low-income countries to contribute to worldwide publication on a broad range of health topics and to integrate them into the global science community. Meanwhile, general policies need to recognize the enormous heterogeneity that is found within countries commonly grouped together. In addition, donor policies need to be consistent with these approaches and to be backed up by the political, financial, and social support required for longer-term gains without imposing priorities that are not in countries' interests. Increasing capacity must also be coupled with increasing demand and the use of relevant health research in low-income countries. Since 2000, the African Capacity Building Foundation broadened its mandate to strengthen analytical capacity in the African region beyond macroeconomic policy analysis to include core public-sector and training and research institutional development and to increase its portfolio to cover health issues. In 2004, it committed $37.5M for national and regional programs in Sub-Saharan Africa, on top of $250M disbursed in the region since 1991 (*22*). These and similar efforts should be strongly supported.

PUBLICATION BY AND WITHIN ECONOMIC GROUPINGS

	Average Global Share 1992-2001
LI (63 countries)	1.7
Top 5	1.4
Top 5 /Total LI (%)	82.0
LMI (54 countries)	5.4
Top 5	4.4
Top 5 /Total LMI (%)	81.1
UMI (31 countries)	2.5
Top 5	1.6
Top 5 /Total UMI (%)	64.1
HI (42 countries)	90.4
Top 5	65.6
Top 5 /Total HI (%)	72.5

The top five producers in order are as follows: (LI): India, Nigeria, Kenya, Pakistan, Bangladesh; (LMI): China, Russian Federation, Brazil, Turkey, South Africa; (UMI): Poland, Argentina, Mexico, Hungary, Czech Republic; (HI): USA, United Kingdom, Japan, Germany, France.

References and Notes

1. R. Sadana *et al.*, *BMJ* **328**, 826 (2004).
2. R. M. May, *Science* **275**, 793 (1997).
3. D. L. Hill, "InfoBrief" (NSF 04-336, Division of Science Resources Statistics, National Science Foundation, Arlington, VA, 2004).
4. European Commission, "Indicators for benchmarking of national research policies: Key figures 2001" (Unit for Competitiveness, Economic Analysis and Indicators, Research Directorate General, Brussels, 2001).
5. D. A. King, *Nature* **430**, 311 (2004).
6. For a complete listing of ISI categories and journals, see www.who.int/rpc/health_research/bibliometrics.
7. When collaborating authors resided in more than one country, we allocated credit for each paper by attributing a fraction to each country in proportion to the number of institutional addresses and authors. Using other counting methods or other internationally recognized reference databases, such as the National Library of Medicine's MEDLINE or the French National Center for Scientific Research's PASCAL, would yield similar results.
8. The average annual growth rate in the articles indexed by Thomson Scientific during the 10-year period is 1.75%; this means that even if the proportion of articles with addresses from LI countries has decreased over the period, the actual number of articles indexed has increased. Specifically, if one only compares the annual numbers of articles indexed in 1992 with those in 2001, for each income group of countries, the percentage increase differs: about 6% for LI, 42% for LMI, 53% for UMI, and 15% for HI countries.
9. C. Perez-Iratxeta, M. A. Andrade, *Science* **297**, 519 (2002).
10. W. W. Gibbs, *Sci. Am.* **12**, 92 (August 1995).
11. J. Gaillard, *Scientometrics* **23**, 57 (1992).
12. J. Keiser *et al.*, *BMJ* **338**, 1229 (2004).
13. Global Forum for Health Research (GFHR), *Monitoring Financial Flows for Health Research* (GHFR, Geneva, 2004), vol. 2.
14. D. Maselli, J. A. Lys, J. Schmid, "Improving impacts of research partnerships" (Swiss Commission for Research Partnerships with Developing Countries, Bern, Switzerland, 2004).
15. T. Pang *et al.*, *Bull. WHO* **81**, 777 (2003).
16. M. Rahman, T. Fukui, *Int. J. Technol. Assess. Health Care* **19**, 249 (2003).
17. J. Chen, X. Ying, National Institutes of Health Technology Assessment, Shanghai, personal communication, 17 January 2005.
18. D. Sinbanks, R. Nathan, R. Triendl, *Nature* **389**, 113 (1997).
19. L. Zhenzhen *et al.*, *Nature Biotechnol.* **22** (suppl.), DC13 (2004).
20. "Tortoise" in Chinese is the homophone for "overseas researcher returns to China."
21. J. Wong *et al.*, *Nature Biotechnol.* **22** (suppl.), DC42 (2004).
22. See www.acbf-pact.org.

23. We appreciate logistic support from Thomson Scientific in setting up the databases; training on bibliometric analyses from G. Lewison; and comments and suggestions from M. Abdullah, J. Chen, C. D'Souza, J. Dzenowagis, T Evans, S. P. Lee-Martin, G. Lewison, H. Momen, T. Pang, J. Whitworth, and X. Ying, as well as from anonymous reviewers.

Supporting Online Material
www.sciencemag.org/cgi/content/full/308/5724/959/DC1

10.1126/science.1108705

ECOLOGY

25 Years of Ecological Change at Mount St. Helens

V. H. Dale, C. M. Crisafulli, F. J. Swanson

18 May 2005 marks the 25th anniversary of the massive eruption of Mount St. Helens. This eruption involved diverse geological processes (*1*) that disturbed forests, meadows, lakes, and rivers (*2*) (see the figure). A huge landslide and searing flows of hot gases and pumice fragments (pyroclastic flows) inundated 60 km^2 of land, obliterating preexisting ecosystems and landforms. A steam-driven blast left blown-down forest and scorched standing forest over more than 500 km^2, but deposited generally <1 m of new material. A gentle rain of tephra (airborne volcanic rock fragments) fell from the sky and blanketed >1000 km^2 of live forest and aquatic systems with >5 cm of deposits (*2*). The initial impression of a lifeless landscape quickly changed as surviving plants and animals reemerged.

Survival of organisms was strongly influenced by characteristics of disturbance processes, local site conditions, and biological factors (*2*). In areas of pyroclastic flow and avalanche debris, almost no organisms survived; but elsewhere, diverse refuges facilitated survival. In the blast area, survivors included plants with underground buds, burrowing animals, and organisms protected by snow, topography, or other features (*2*). In the area of thin tephra fall, organisms that were able to stand above or penetrate the deposits had a greater potential for survival. Certain life-history attributes also favored survival; for example, some anadromous fish (which return from the sea to rivers to reproduce) and migratory bird populations were not present during the eruption. Organism size also proved important: Large species and individuals suffered greater mortality than did small ones. Surviving organisms included all of the primary trophic groups—herbivores, predators, scavengers, and decomposers. Thus, complex foodwebs quickly developed in the emerging ecosystems. Surviving species provided source populations, ameliorated site conditions, processed dead biological legacies (such as toppled trees) of the pre-eruption system, and established ecological interactions.

The timing of the eruption—that is, time of day, time of year, and the stage of development (succession) of plant and animal communities—strongly influenced patterns of survival and succession (*2*). The early morning eruption allowed nocturnal animals to be protected in their subterranean retreats. The early spring eruption meant that snow and ice created refuges and that plants had not yet broken winter dormancy at high elevations. The early successional stage of many recently harvested forest sites led to a profusion of wind-dispersed seeds of pioneer plant species. The importance of timing underscores the significance of chance in survival and successional pathways.

Key successional processes after any major disturbance include dispersal, site amelioration, establishment of organisms, species accrual, biotic interactions, and changing community structure (*2*). Dispersal pattern and rate were influenced by distance from source populations, wind patterns, landscape permeability, and mobility of seeds, spores, and organisms. Site amelioration was critical: The new volcanic substrates had low nutrient status, little moisture holding capacity, and limited shade, but differed from lava flow substrates common in other volcanic terranes in that they were readily penetrated by plants and animals. Site amelioration occurred via weathering, decomposition, addition of nutrients to soils, microbial activity, mixing of soils by animals, and clearing of suspended particulates from lakes. Over time, community structure increased across all disturbance zones as species accrued, individuals and populations grew and spread, and interactions developed.

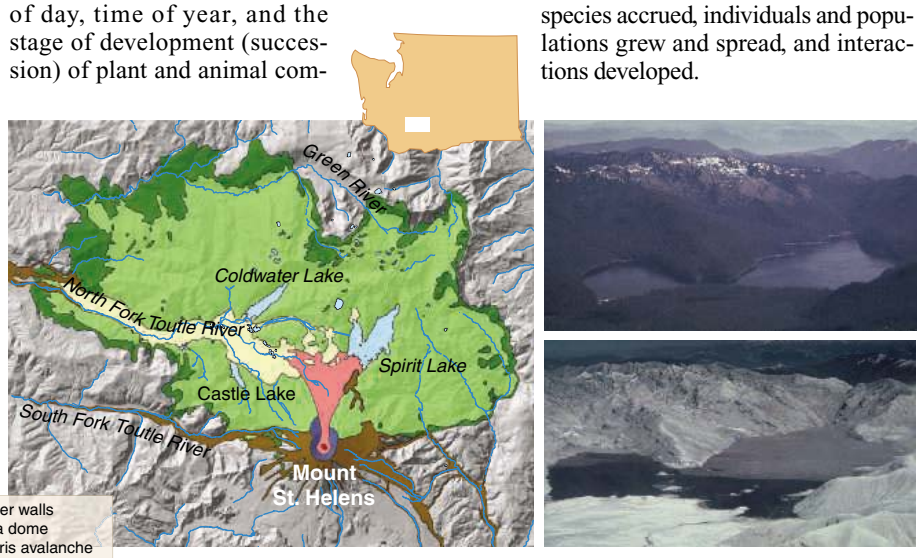

The diversity of geophysical disturbances. Views north from the summit of Mount St. Helens across Spirit Lake to Mount Rainier before (**top**) and after (**bottom**) the eruption of Mount St. Helens on 18 May 1980. (**Left**) This eruption involved several landscape-modifying processes: a massive landslide (debris avalanche), a lateral blast that blew down forest and scorched standing forest, pyroclastic flows, and mudflows down rivers that drained the volcano.

The rate of ecological response varied greatly among the different environments. In the quarter century since the 1980 eruption, lakes and most streams have largely returned to ecological conditions typical of forested areas of the region. Throughout the vast blast area, the terrestrial landscape has transformed from barren gray to mostly green with vegetation dominated by herbs, shrubs, and small patches of surviving trees. On the debris-avalanche and pyroclastic-flow deposits, vegetation is lush around ponds and wetlands, but sparse herb and shrub cover characterizes uplands and actively eroding sites. The number of verte-

V. H. Dale is at the Oak Ridge National Laboratory, Oak Ridge, TN 37831–6036, USA. C. M. Crisafulli is with the U.S. Department of Agriculture (USDA) Forest Service, Pacific Northwest Research Station, Forestry Sciences Laboratory, Olympia, WA 98512, USA. F. J. Swanson is at the USDA Forest Service, Pacific Northwest Research Station, Forestry Sciences Laboratory, Corvallis, OR 97331, USA. E-mail: dalevh@ornl.gov

brate species and their population sizes have increased dramatically since 1980. Birds have colonized in lock-step with increased habitat structure, but assemblages remain limited by the lack of forest structure. Yet even in the most disturbed areas, nearly all species of small mammals associated with undisturbed forests have returned. Secondary disturbances have modified pathways of succession. Shifting river channels, small landslides, and mudflows have repeatedly reset succession, enhancing the heterogeneity of vegetation patterns over the volcanic landscape.

Human activities have greatly altered natural ecological processes in many areas affected by the eruption. However, the U.S. Congress established a 43,300-ha National Volcanic Monument where natural processes can proceed unimpeded. Environmental scientists have provided advice concerning protection of natural features; management of erosion, floods, and natural resources; and development of interpretive programs and educational opportunities. During the decision-making process, potential risks to human life or property often outweighed ecological concerns.

A quarter century of ecological studies at Mount St. Helens has produced important lessons. First, living and dead biological legacies (for example, dead trees and rotten logs) are integral to the ecological response, even after severe disturbances. Second, ecological succession is very complex, proceeding at varying paces along diverse paths, and with periodic setbacks through secondary disturbances. Consequently, no single, overarching succession theory provides an adequate framework to explain ecological change. Third, chance factors, such as timing of the disturbance at various scales, can strongly influence survival and the course of succession. Finally, environmental scientists have provided a long-term and broad-scale view of how human actions can affect ecological systems, a requisite but not always integral component of decision-making.

The future at Mount St. Helens will be one of continuing change. The pace of ecological change will be determined by complex processes of ecological succession influenced by landscape position, topography, climate, and further biotic, human, and geophysical forces. The current volcanic activity at Mount St. Helens attests to its dynamic character (*3*). Even so, many biotic, landform, and soil legacies of the 1980 eruption will influence ecological processes for centuries to come.

References and Notes

1. P. W. Lipman, D. R. Mullineaux, Eds., *U.S. Geol. Surv. Prof. Pap.* **1250**, 844 (1981).
2. V. H. Dale, F. J. Swanson, C. M. Crisafulli, Eds., *Ecological Responses to the 1980 Eruption of Mount St. Helens* (Springer, New York, 2005).
3. D. Dzurisin *et al.*, *Eos* **86**, 25 (2005).
4. We thank J. Antos, D. Druckenbrod, J. Franklin, R. Parmenter, and A. Wallace for helpful comments. Support was provided by the USDA Forest Service, Pacific Northwest Research Station; Gifford Pinchot National Forest, Mount St. Helens National Volcanic Monument; National Geographic Society; EarthWatch; and Oak Ridge National Laboratory, which is managed by the University of Tennessee–Battelle for the U.S. Department of Energy under contract DE-AC05-00OR22725.

10.1126/science.1109684

ATMOSPHERIC SCIENCE

Rethinking Earth's Early Atmosphere

Christopher F. Chyba

In 1952, Stanley Miller, working with Harold Urey, simulated the atmosphere of early Earth with a gas mixture of methane (CH_4), ammonia (NH_3), molecular hydrogen (H_2), and water. When he introduced an electrical spark to represent lightning, he observed the formation of amino acids, the building blocks of proteins (*1*). Miller later showed that the amino acids were the result of reactions in liquid water (representing Earth's ocean) of simple organic molecules such as hydrogen cyanide (HCN) and formaldehyde (H_2CO) formed in the gas mixture (*2*). His experiment turned the study of the origin of life into an experimental science.

However, by the 1960s, the validity of hydrogen-rich (and hence reducing) model atmospheres for early Earth, such as the CH_4-NH_3 atmosphere used by Miller and Urey, was under attack (*3*). Since the 1970s, carbon dioxide (CO_2)–rich atmospheres have been favored (*4*). Miller has shown that the production of amino acids and other organic molecules is orders of magnitude less efficient in such atmospheres (*5*). For this and other reasons, the Miller-Urey approach to the origin of life has fallen out of favor with many researchers. But on page 1014 of this issue, Tian *et al.* (*6*) argue that the early-Earth atmosphere might have been hydrogen-rich after all.

In early models of Earth's evolution, the planet's iron-rich core was assumed to have formed slowly over hundreds of millions of years. Prior to core formation, metallic iron would have been abundant in Earth's mantle, in effect providing a huge oxygen sink. As a result, carbon and nitrogen compounds emitted ("outgassed") into the atmosphere—for example, in volcanic eruptions—would have been saturated with hydrogen (CH_4 and NH_3). Early life would have used the abundant organic molecules produced by Miller-Urey synthesis for energy and raw materials. Core formation would have freed the oxygen, leading to outgassing of CO_2 rather than CH_4 (*7*). Abiotic organic production would have plummeted, whereupon life would have evolved to cope with this change. It was an elegant picture—but probably largely wrong.

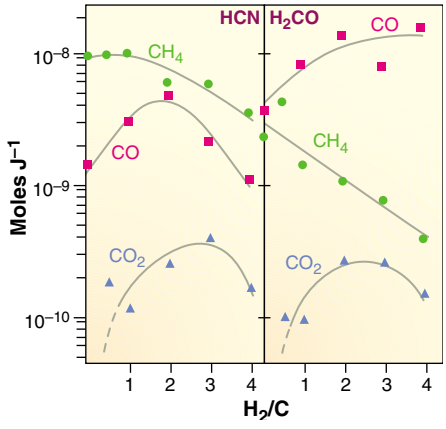

Hydrogen lends a helping hand. Yields (in moles produced per joule of input spark discharge energy) of organic molecules thought to be key for the origin of life are lower in CO_2-rich atmospheres than in CH_4-rich ones, although H_2/C ratios >1 maximize organic production in the former case. [Adapted from (*5*)]

It now appears that Earth was hot at the time of its formation, because it accreted from fast-colliding planetesimals. It seems unavoidable that the core formed virtually simultaneously with Earth itself. If the iron was largely sequestered in the core from the start, then there never was a Miller-Urey atmosphere. Even if there ever had been such an atmosphere, modeling suggested that it would be quickly destroyed by solar ultraviolet light. However, this problem would be circumvented by the formation of a high-altitude organic haze, similar to that in the atmosphere of Saturn's moon Titan (*8*). Thus, if Earth ever had a Miller-Urey atmosphere, it could be sus-

The author is at the SETI Institute, Mountain View, CA 94043, and in the Department of Geological and Environmental Sciences, Stanford University, Stanford, CA 94305, USA. E-mail: chyba@seti.org

tained. But it remains unclear how to form such an atmosphere to begin with.

Tian *et al*. (*6*) may have found a way to sidestep these problems. In their model, the atmosphere is CO_2-rich, not CH_4-rich, but contains as much as 30% H_2. The model uses the current hydrogen outgassing rate, increased by at most a small factor to account for the geologically more active early Earth. What is new is their transonic hydrodynamic escape model: For an atmosphere rich in H_2, the escape of hydrogen to space is hydrodynamic and limited by the availability of extreme ultraviolet light from the Sun. The model yields an escape rate that is much lower than previously found. Because less H_2 escapes, if Earth ever had an H_2-rich atmosphere, it could be sustained.

The figure shows why this matters for the origin of life. HCN and H_2CO are produced at much lower yields in CO_2-rich atmospheres than in CH_4-rich ones, but production is particularly low in CO_2-rich atmospheres when H_2/C ratios fall below 1 or rise above 5 to 10 (*5*). Tian *et al*. (*6*) suggest that they can keep $H_2/C > 1$ in their model, although this also depends on the poorly known CO_2 abundance. Their H_2-CO_2 atmosphere is less favorable for organic production than a Miller-Urey one, but far better than previously preferred model atmospheres with $H_2/C \sim 0.001$.

Many uncertainties and problems remain. Tian *et al*. focus on the oceans as the "birthplace of life," but polymerization of amino acids into proteins (or nucleotides into RNA) is thermodynamically unfavorable in liquid water. Furthermore, in an early ocean as saline as that of today, the salt inhibits key prebiotic reactions (*9*). The bulk ocean may thus have been one of the worst places to try to originate life. After making life's building blocks in the ocean, one needs to look elsewhere to carry the chemistry further. Some authors have abandoned this heterotrophic picture of the origin of life in favor of an autotrophic model, in which metabolic reactions that can fix their own carbon are the first steps on the road to life (*10*).

How does prebiotic organic production in the atmosphere of Tian *et al*. compare to other sources of organic molecules on early Earth? Because of uncertainties in the hydrogen content of the early atmosphere, examinations of this question have considered a range of H_2/C ratios (*11*). As model atmospheres become more hydrogen-rich, production of organic molecules through electrical discharges or ultraviolet light becomes increasingly important relative to delivery of organic molecules by meteorites or comets. Yet shock-tube experiments suggest that in Miller-Urey atmospheres, atmospheric shocks from meteors and impacts could be a dominant energy source for organic synthesis (*11*). Impactors may also have been a major driver of organic production in an early H_2-rich atmosphere.

These are tumultuous times in the study of the origin of life. The early ocean may have been even less hospitable for prebiotic chemistry than previously thought (*9*), and claimed evidence for the earliest signatures of life on Earth is being strongly challenged (*12*). Now a 30-year, albeit shaky, consensus on the nature of the early atmosphere may have to be reexamined, and the geochemical implications of an H_2-rich early atmosphere will need to be scrutinized. This turmoil makes it a great time for young scientists to enter the field, but it also reminds us that some humility regarding our favorite models is in order. As Jacob Bronowski noted, "Science is a tribute to what we can know although we are fallible" (*13*).

References

1. S. L. Miller, *Science* **117**, 528 (1953).
2. S. L. Miller, *Ann. N.Y. Acad. Sci.* **69**, 260 (1957).
3. P. H. Abelson, *Proc. Natl. Acad. Sci. U.S.A.* **55**, 1365 (1966).
4. J. C. G. Walker, *Evolution of the Atmosphere* (Macmillan, New York, 1977).
5. R. Stribling, S. L. Miller, *Origins Life* **17**, 261 (1987).
6. F. Tian, O. B. Toon, A. A. Pavlov, H. De Sterck, *Science* **308**, 1014 (2005); published online 7 April 2005 (10.1126/science.1106983).
7. H. D. Holland, in *Petrologic Studies: A Volume to Honor A. F. Buddington*, A. E. J. Engel *et al.*, Eds. (Geological Society of America, Washington, DC, 1962), pp. 447–477.
8. C. Sagan, C. Chyba, *Science* **276**, 1217 (1997).
9. P.-A. Monnard *et al.*, *Astrobiology* **2**, 139 (2002).
10. G. Wächtershäuser, *Microbiol. Rev.* **52**, 452 (1988).
11. C. Chyba, C. Sagan, *Nature* **355**, 125 (1992).
12. S. Moorbath, *Nature* **434**, 155 (2005).
13. J. Bronowski, *The Ascent of Man* (Little Brown, Boston, 1973), p. 374.

10.1126/science.1113157

STRUCTURAL BIOLOGY

Flipping Lipids: Is the Third Time the Charm?

Amy L. Davidson and Jue Chen

Gram-negative bacteria such as *Escherichia coli* are defined by the presence of a second or outer membrane bilayer that serves as a unique protective coat. While all cells have a membrane bilayer that forms a barrier to the passage of hydrophilic (water-soluble) compounds, the outer membrane is an asymmetric bilayer whose outer layer (or leaflet) contains a special lipid known as lipopolysaccharide (LPS). LPS decreases membrane fluidity, thereby creating a barrier to the diffusion of potentially toxic hydrophobic compounds (*1*). LPS is synthesized as a precursor known as Ra-lipid A in the inner leaflet of the inner membrane bilayer (*2*). Before it moves to the outer membrane, Ra-lipid A is flipped to the outer leaflet of the inner membrane, where a polysaccharide O-antigen chain is added to form mature LPS.

Two papers by Dong *et al*. (*3*) on page 1023 and Reyes *et al*. (*4*) on page 1028 of this issue shed light on this flipping mechanism. These studies elucidate the structure and dynamics of MsbA, an adenosine triphosphate (ATP)–binding cassette (ABC) transporter believed to accomplish this flipping event. ABC transporters, such as the homodimer MsbA consist of two helical membrane-spanning domains and two nucleotide-binding domains. Two ATP molecules bind along the dimer interface, interacting with residues in two conserved motifs, the Walker A motif from one nucleotide-binding domain and the ABC family signature motif from the opposing domain. Conformational changes in the nucleotide-binding domains, induced by binding and hydrolysis of ATP along the dimer interface, are coupled to conformational changes in the membrane-spanning domains that then mediate transport of substrate. One paper describes the x-ray crystal structure at 4.2 Å of MsbA from *Salmonella typhimurium* and is the third in a series of structures of MsbA from different organisms determined by the Chang laboratory (*4*). Although the first two structures have been criticized as nonphysiologic on the basis of aberrant behavior of the nucleotide-binding domains, it looks as though the third one may be the charm (see the figure). In the new structure, the nucleotide-binding domains appear correctly folded. They face each other across the dimer with an orientation similar to that seen in the ATP-bound dimers observed in the earlier structures (*5*, *6*), except that the dimer interface is more open. In addition, both nucleotide and Ra-lipid A are bound in a configuration suggestive of a "post-hydrolysis" state: Adenosine diphosphate (ADP) is present in one of the two nucleotide-binding domains, and Ra-lipid A

A. L. Davidson is in the Department of Molecular Virology and Microbiology, Baylor College of Medicine, Houston, TX 77030, USA. E-mail: davidson@bcm.tmc.edu J. Chen is in the Department of Biological Sciences, Purdue University, West Lafayette, IN 47907, USA. E-mail: chenjue@purdue.edu

appears to have already been flipped to the outer leaflet of the inner membrane. The location of Ra-lipid A in the structure adds credence to the hypothesis that the lipid is flipped from one leaflet to the other, rather than being expelled directly into the periplasmic space that lies between the outer and inner membranes.

In the first MsbA structure, the "open-apo" form (no ligands bound), the ABC family signature motif faces away from the two-fold axis of symmetry, contrary to our understanding that ATP is hydrolyzed at the dimer interface (*7*). Also, 40% of the residues in the nucleotide-binding domain are "missing" and presumably disordered. Comparison of the second structure, the "closed-apo" form, with the newest structure reveals dramatic differences in folding of the nucleotide-binding domains. The Walker A motif is located too far away from other conserved motifs in the "closed-apo" structure to form an active ATP-binding site at the interface. The three structures also reveal three very different ways by which the membrane-spanning domains interact at the dimer interface. Given the unusual flexibility exhibited by the nucleotide-binding domains in these three structures, one must proceed with caution in drawing conclusions about the actual mechanism of translocation when comparing the structures of the attached membrane-spanning domains. Translocation by ABC transporters requires conformational changes in the nucleotide-binding domains that are induced by ATP binding and hydrolysis. These are thought to control conformational changes in the membrane-spanning domains. In the second structure, the anomalous packing of the nucleotide-binding domains into a tightly closed but nucleotide-free dimer may have influenced the conformation and dimeric interaction of the membrane-spanning domains in a nonphysiologic way. Clearly, independent means are required to assess the relevance of each of these unique configurations to the translocation cycle. The great value of these structures for the larger transporter community is that they offer a framework for formulating and testing hypotheses.

The accompanying paper by Dong *et al.* comprehensively takes on this challenge by attaching more than 100 spin-labeled probes to different amino acids in the membrane-spanning domain of MsbA to define the structure and dynamics of this transporter during ATP hydrolysis (*3*). This electron paramagnetic resonance (EPR)–based approach, known as site-directed spin labeling, can define secondary structure elements in a protein and determine whether a given amino acid side chain is buried in the protein or is exposed to the lipid or to the aqueous environment. It is made all the more powerful by the structural coordinates for MsbA that provide a model to test. Moreover, transport proteins can be studied in the membrane, a more physiologic condition. Although several aspects of the MsbA structure are confirmed by the EPR analysis, discrepancies are also apparent. One notable example is how the extracellular loops of the dimer pack together. Substrate is proposed to pass through this interface during transport, and EPR suggests that these loops are more mobile and accessible to the aqueous environment in apo-MsbA than in either the open- or closed-apo structures. Furthermore, the distances between identical residues in the two loops, as measured by EPR, are not consistent with these structures either. Intriguingly, this region of MsbA is clearly more open in the new structure. The EPR constraints from this paper can now be applied to the new structure to see how well they match.

Vanadate is frequently used to trap ABC transporters in the catalytic transition state for ATP hydrolysis (*8*, *9*). Although it is used for this purpose in both papers, some clarification is in order. Vanadate acts as an analog of the γ-phosphate of ATP, forming a complex with Mg and ADP that mimics the transition state of ATP during hydrolysis. Trapping actually occurs after ATP hydrolysis when vanadate replaces phosphate in the active site. The authors of the EPR paper conservatively refer to this condition as a "post-hydrolysis" state even though it may mimic the transition state with MgADP and vanadate tightly bound between subunits (*10*). To analyze the dynamics of MsbA during the translocation cycle by EPR, the authors examined the effect of nucleotide binding and hydrolysis in the nucleotide-binding domains on the conformation of the membrane-spanning domains. They observed rigid body motion of membrane-spanning domains that could alternate the exposure of a central chamber to each side of the membrane. Residues in the inner leaflet and the intracellular domain come closer together, possibly to close the chamber, while residues at the periplasmic surface simultaneously move farther apart. This picture concurs nicely with EPR work showing that closure of the nucleotide-binding domains upon ATP binding and hydrolysis coincides with substantial opening at the periplasmic surface in a bacterial importer (*11*). The concept of closure of the cytoplasmic chamber emerges from comparison of the two apo MsbA structures, although perhaps not for the same reason; changes in distance between specific residues, as measured by EPR, are not compatible with an overlay of the two structures.

MgATP and vanadate were also added to MsbA during crystallization in the hope of obtaining the structure of MsbA trapped in the catalytic transition state. The structure does indicate ADP and vanadate at just one of the two nucleotide-binding sites, consistent with biochemical experiments (*8*, *9*). However, the signature motif from one nucleotide-binding domain is disengaged from nucleotide bound to the

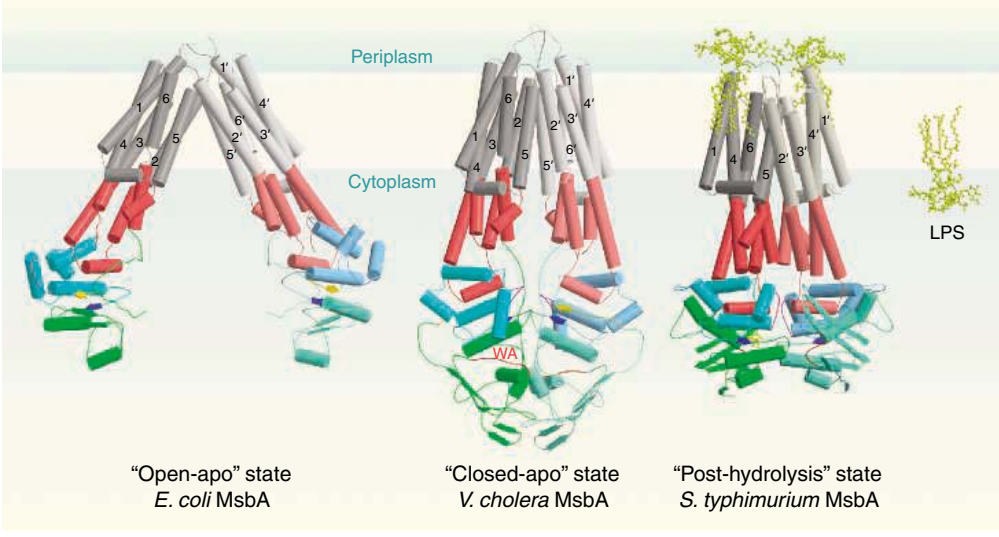

Three structures of MsbA. The membrane-spanning domains are gray, the intracellular domains are orange, and the nucleotide-binding domains are green (RecA-like domain) and cyan (helical domain). Conserved segments present at the active site in the nucleotide-binding domains: red, Walker A motif (WA); magenta, ABC family signature motif; blue, Walker B motif; yellow, Q loop. ADP and LPS are represented as ball-and-stick models. [Adapted from (*7*)]

Walker A motif of the second nucleotide-binding domain, creating an open dimer interface. This conformation is not consistent with biochemical characterization of the catalytic transition state. Vanadate-induced cleavage of both the Walker A and family signature of the maltose transporter demonstrates the close proximity of both motifs in the vanadate-trapped species (*10*), and mutagenesis experiments highlight the importance of the family signature in catalysis (*12*, *13*). The MsbA structure is characterized as a "post-hydrolysis" ADP-vanadate state rather than the catalytic transition state specifically because of this open nucleotide-binding site dimer configuration. These results raise the question of why ADP and vanadate are asymmetrically "trapped" in just one of the two sites if the dimer has opened. Low resolution prevents an answer here. Perhaps, at 4.2 Å, there are not enough data to reveal differences between the two monomers within the dimer. The authors forced the monomers to be identical by imposing strict noncrystallographic symmetry. In the end, we are presented with a less than satisfying symmetric solution to the structure of what may be an asymmetric dimer in the crystal. This data set does not allow us to draw specific conclusions about side-chain interactions and, more important, protein-nucleotide interactions. That awaits atomic resolution.

References and Notes

1. H. Nikaido, *Microbiol. Mol. Biol. Rev.* **67**, 593 (2003).
2. C. R. Raetz, in Escherichia coli *and* Salmonella*: Cellular and Molecular Biology*, F. C. Neidhardt *et al.*, Eds. (ASM Press, Washington, DC, 1996), vol. 1, pp. 1035–1063.
3. J. Dong, G. Yang, H. S. Mchaourab, *Science* **308**, 1023 (2005).
4. C. L. Reyes, G. Chang, *Science* **308**, 1028 (2005).
5. P. C. Smith *et al.*, *Mol. Cell* **10**, 139 (2002).
6. J. Chen, G. Lu, J. Lin, A. L. Davidson, F. A. Quiocho, *Mol. Cell* **12**, 651 (2003).
7. A. L. Davidson, J. Chen, *Annu. Rev. Biochem.* **73**, 241 (2004).
8. I. L. Urbatsch, B. Sankaran, J. Weber, A. E. Senior, *J. Biol. Chem.* **270**, 19383 (1995).
9. S. Sharma, A. L. Davidson, *J. Bacteriol.* **182**, 6570 (2000).
10. E. E. Fetsch, A. L. Davidson, *Proc. Natl. Acad. Sci. U.S.A.* **99**, 9685 (2002).
11. M. I. Austermuhle, J. A. Hall, C. S. Klug, A. L. Davidson, *J. Biol. Chem.* **279**, 28243 (2004).
12. G. Tombline, L. Bartholomew, K. Gimi, G. A. Tyndall, A. E. Senior, *J. Biol. Chem.* **279**, 5363 (2004).
13. G. Verdon *et al.*, *J. Mol. Biol.* **334**, 255 (2003).

14. We thank C. Reyes and G. Chang of (*4*) for sharing the coordinates of their structure.

10.1126/science.1113414

EVOLUTION

Did Early Humans Go North or South?

Peter Forster and Shuichi Matsumura

By analyzing the DNA of living humans from different locations, geneticists are able to assemble a detailed reconstruction of prehistoric human colonization of the world. This research endeavor was championed by the late Allan Wilson and his colleagues (*1*, *2*), who led the way with their studies of maternally inherited mitochondrial DNA (mtDNA). Their work led to the proposal of a recent African origin for modern humans, some 5000 generations ago. Anthropologists and geneticists have since joined forces to create a broad framework of possible prehistoric human migration routes and time scales (*3*–*6*). The two latest additions to this framework are described by Thangaraj *et al.* (*7*) on page 996 and Macaulay *et al.* (*8*) on page 1034 of this issue.

Enhanced online at www.sciencemag.org/cgi/content/full/308/5724/965

Our current understanding is that modern humans arose ~150,000 years ago, possibly in East Africa, where human genetic diversity is particularly high. Subsequent early colonization within Africa is supported by old genetic mtDNA and Y chromosome branches (often called "haplogroups") in the Bushmen or Khoisan of the Kalahari Desert, and in certain pygmy tribes in the central African rainforest. Early humans even ventured out of Africa briefly, as indicated by the 90,000-year-old Skhul and Qafzeh fossils found in Israel. The next event clearly visible in the mitochondrial evolutionary tree is an expansion signature of so-called L2 and L3 mtDNA types in Africa about 85,000 years ago, which now represent more than two-thirds of female lineages throughout most of Africa. The reason for this remarkable expansion is unclear, but it led directly to the only successful migration out of Africa, and is genetically dated by mtDNA to have occurred some time between 55,000 and 85,000 years ago. Studies of the paternally inherited Y chromosome yield time estimates for the African exodus that are in broad agreement with those derived from mtDNA.

It is at this point in the narrative that the studies by Thangaraj *et al.* (*7*) and Macaulay *et al.* (*8*) come into the picture. Which route did the first Eurasians take out of Africa? Most obvious, perhaps, is the route along the Nile and across the Sinai Peninsula leading into the rest of the world (see the figure). But if that were so, why was adjacent Europe settled thousands of years later than distant Australia? In Europe, Neanderthals were replaced by modern humans only about 30,000 to 40,000 years ago, whereas southern Australia was definitely inhabited

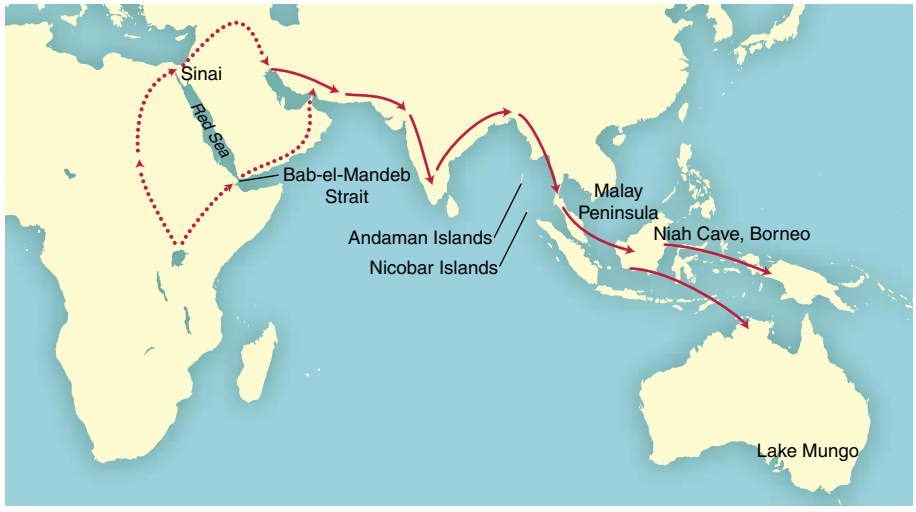

How did they get there? Hypothetical routes along the Indian Ocean coastline that could have been taken by early humans emigrating out of Africa. The oldest human traces outside of Africa and the Levant are at Lake Mungo in Australia (>46,000 years old) and in the Niah Cave of Borneo (>45,000 years ago). New mtDNA data, from Malaysians and aboriginal Andaman islanders, suggest that human settlements appeared along the Indian Ocean coastline 60,000 years ago (*7*, *8*).

The authors are at the McDonald Institute for Archaeological Research, University of Cambridge, Cambridge CB2 3ER, UK. E-mail: pf223@cam.ac.uk

46,000 years ago and northern Australia and Southeast Asia necessarily even earlier (*9*, *10*). Or did our ancestors instead depart from East Africa, crossing the Red Sea and then following the coast of the Indian Ocean (*11*)? A purely coastal "express train" would conveniently explain the early dates for human presence in Australia, but would require that humans were capable of crossing the mouth of the Red Sea some 60,000 years ago. Why, then, was this feat not repeated by any later African emigrants, particularly when the Red Sea level dropped to a minimum about 20,000 years ago?

Ideally, these questions would be answered by investigating ancient fossils and DNA from the Arabian Peninsula. But because this option is currently not available, Thangaraj *et al.* and Macaulay *et al.* have centered their investigation on the other side of the Indian Ocean, in the Andaman Islands and Malaysian Peninsula. Both groups used genetic studies of relict populations known to differ substantially from their Asian neighbors to estimate the arrival time of the first humans in these locations. Thangaraj and colleagues sampled the Andamanese, who were decimated in the 19th century by diseases imported by the British and then suffered displacement by modern Indian immigration (*12*). Macaulay and co-workers sampled the native tribal people of Malaysia, called the Orang Asli ("original people").

Fortunately, the two teams arrived at compatible conclusions. In the Andaman Islands, Thangaraj *et al*. identified the M31 and M32 mtDNA types among indigenous Andamanese. These two mtDNA types branched directly from M mtDNA, which arose as a founder 65,000 years ago. This time estimate for the arrival of M founder mtDNA is matched by that of Macaulay and co-workers. These investigators found mtDNA types M21 and M22 in their Malaysian data set. These M types are geographically specific branches of M that branched off from other Asian mtDNA lineages around 60,000 years ago. Thus, the first Eurasians appear to have reached the coast of the Indian Ocean soon after leaving Africa, regardless of whether they took the northern or the southern route. Interestingly, the adjacent Nicobar Islands do not harbor any old mtDNA branches specific to the islands. Instead, their mtDNA has a close and hence recent genetic relationship (on the order of 15,000 years or less) with the mtDNA of other Southeast Asian populations. This is not unexpected given the more Asian appearance of the Nicobar islanders.

Macaulay and colleagues go two steps further and estimate the prehistoric migration speed of early humans along the coast of the Indian Ocean; they also estimate the likely population size of the emigrant population. Comparing genetic dates of founder types between India and Australia, and assuming a 12,000-km journey along the Indian Ocean coastline, they suggest a migration speed for the first Eurasians of 0.7 to 4 km per year. This value is of the same order of magnitude as genetically dated inland journeys of migrant populations during the last Ice Age, 60,000 to 10,000 years ago (*6*).

One intriguing question is the number of women who originally emigrated out of Africa. Only one is required, theoretically. Such a single female founder would have had to carry the African L3 mtDNA type, and her descendants would have carried those mtDNA types (M, N, and R) that populate Eurasia today. Macaulay *et al*. use population modeling to obtain a rough upper estimate of the number of women who left Africa 60,000 years ago. From their model, they calculate this number to be about 600. Using published conversion factors, we can translate this estimate into a number between 500 and 2000 actual women. The authors' preferred estimate is several hundred female founders. All such estimations are influenced by the choice of parameters and by statistical uncertainty; hence, it is understood that the true number could have been considerably larger or smaller. Improved estimates will involve computer simulations based on informed scenarios using additional genetic loci.

Time is short if researchers wish to secure data on dwindling indigenous populations such as the Andamanese and the Orang Asli. The studies by Macaulay *et al*. and Thangaraj *et al*., which are devoted to the peoples inhabiting the "southern route" along the Indian Ocean, are therefore very welcome. We hope that the new findings will inspire archaeological exploration between the Arabian Peninsula and Southeast Asia in search of the remains of the first Eurasians 50,000 to 100,000 years ago.

References

1. R. L. Cann, M. Stoneking, A. C. Wilson, *Nature* **325**, 31 (1987).
2. L. Vigilant, M. Stoneking, H. Harpending, K. Hawkes, A. C. Wilson, *Science* **253**, 1503 (1991).
3. P. Endicott *et al.*, *Am. J. Hum. Genet.* **72**, 178 (2003).
4. R. Cordaux, M. Stoneking, *Am. J. Hum. Genet.* **72**, 1586 (2003).
5. P. A. Underhill, *Cold Spring Harbor Symp. Quant. Biol.* **68**, 487 (2003).
6. P. Forster, *Philos. Trans. R. Soc. London B Biol. Sci.* **359**, 255 (2004).
7. K. Thangaraj *et al.*, *Science* **308**, 996 (2005).
8. V. Macaulay *et al.*, *Science* **308**, 1034 (2005).
9. G. Barker, *Asian Perspect.* **44**, 90 (2005).
10. J. M. Bowler *et al.*, *Nature* **421**, 837 (2003).
11. S. Oppenheimer, *Out of Eden* (Constable, London, 2003).
12. S. Venkateswar, *Sci. Am.* **280**, 82 (May 1999).

10.1126/science.1113261

GEOPHYSICS

Past and Future Earthquakes on the San Andreas Fault

Ray J. Weldon, Thomas E. Fumal, Glenn P. Biasi, Katherine M. Scharer

The San Andreas fault is one of the most famous and—because of its proximity to large population centers in California—one of the most dangerous earthquake-generating faults on Earth. Concern about the timing, magnitude, and location of future earthquakes, combined with convenient access, have motivated more research on this fault than on any other. In recent years, an increasing number of sites along the fault have provided evidence for prehistoric earthquakes (*1*, *2*).

Damaging earthquakes are generated by rupture that can span hundreds of kilometers on a fault. Data from many sites must therefore be integrated into "rupture scenarios"—possible histories of earthquakes that include the date, location, and size (length of fault rupture) of all earthquakes on a fault during a period of time. Recently, rupture scenarios for the southern San Andreas fault have stimulated interest in how different scenarios affect interpretations of seismic hazard and underlying models of earthquake recurrence behavior.

Large earthquakes occur infrequently on individual faults. Scientists therefore cannot test recurrence models for damaging earthquakes by waiting for a series of large earthquakes to occur or by consulting instrumental records, which span at most 100 years. Records of large earthquakes must be dug out of the geologic record to characterize earthquakes that predate the instrumental record.

Such studies tend to provide samples of the date and ground displacement at isolated sites along the ruptures, hundreds of kilometers long, caused by large paleoearthquakes. Key insights into fault recurrence behavior have been gained from site-specific data on

R. J. Weldon and K. M. Scharer are in the Department of Geological Sciences, University of Oregon, Eugene, OR 97403, USA. E-mail: ray@ uoregon.edu; kscharer@ uoregon.edu T. E. Fumal is with the Earthquake Hazards Team, U.S. Geological Survey, Menlo Park, CA 94025, USA. E-mail: tfumal@usgs.gov G. P. Biasi is at the Seismological Laboratory, University of Nevada, Reno, NV 89557, USA. E-mail: glenn@seismo.unr.edu

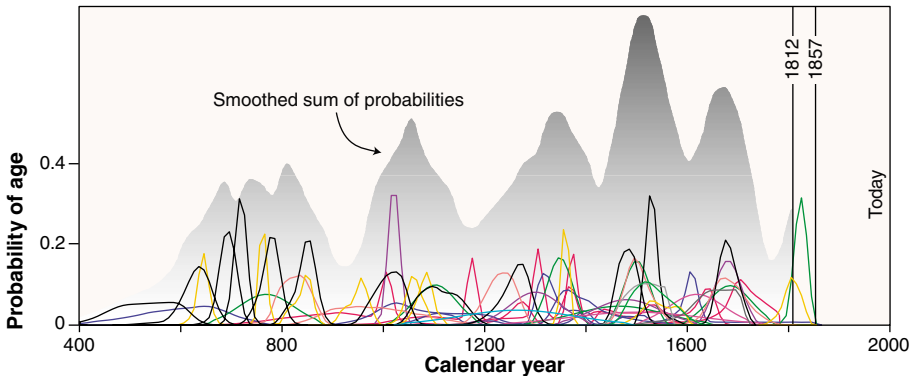

Ruptures on the southern San Andreas fault. Lines are probability density functions for the dates of individual earthquakes, colored by site; the 1812 and 1857 earthquakes have exact dates. Peaks and valleys in the smoothed sum of the individual probability density functions suggest that large parts of the fault rupture every ~200 years in individual large earthquakes or series of a few earthquakes. See (*2*) for site locations and data sources.

the southern San Andreas fault (*3*, *4*). However, measurements of the date and displacement often vary considerably between sites. Further advances in understanding the San Andreas fault will require the construction of rupture scenarios. Given the large body of data and recent advances in interpretive methodology, this goal is now within reach for the southern San Andreas fault.

To date, 56 dates of prehistoric earthquakes have been published, based on data from 12 sites on the southern 550 km of the San Andreas fault. There are also about 10 paleoseismic records for the earthquakes of 1857 and 1812. Analysis of these data (*4*, *5*) yields probability density functions of the dates of the earthquakes (see the first figure). These date distributions provide the raw material for correlating ruptures from site to site and the first step toward constructing a history of large earthquakes.

Unfortunately, rupture scenarios based on earthquake date alone are poorly constrained and support a wide range of earthquake models. The existing data can be explained by highly periodic overlapping ruptures (see the second figure, top panel), randomly distributed ruptures (middle panel), and even repeated ruptures spanning the entire southern San Andreas fault (bottom panel). Each model implies a different level of hazard to the Los Angeles region (see the figure legend, second figure) and supports a different physical model of faulting (*2*).

Strong overlap of event dates (see the first figure) may occur when many sites along the fault record the same earthquake or a sequence of earthquakes occur within years or decades. Poor or no overlap may indicate earthquakes with lesser rupture extent or errors in the dating and interpretation of paleoseismic data. Given the rupture lengths of the 1812 and 1857 earthquakes (~150 and 300 km, respectively) and the lack of substantial rupture in the 148 years since 1857, most scientists doubt the possibility of frequent small ruptures on the southern San Andreas fault. Three recent developments strengthen the hypothesis that the fault breaks in relatively infrequent, large earthquakes.

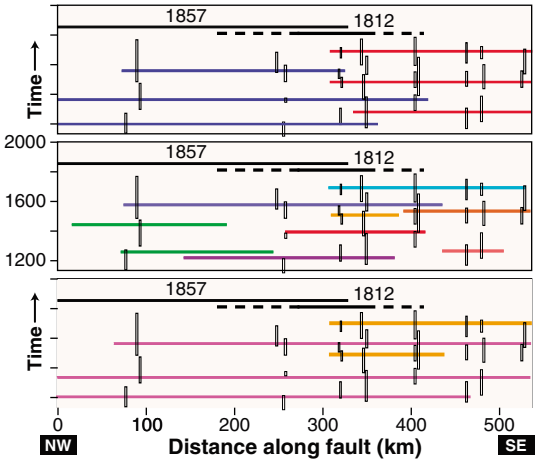

Cartoon of rupture scenarios. Black boxes denote paleoearthquake dates at sites along the fault. Black horizontal bars show the extents of the 1857 and 1812 ruptures. Three scenarios accommodate all dates. (**Top**) Ruptures spanning the northern two-thirds of the fault (like the 1857 earthquake) alternate with shorter ruptures centered on the southern third. This model yields a conditional probability of earthquake recurrence of ~70% in the next 30 years, largely due to the long time since a southern event. (**Middle**) Ruptures of variable length recur randomly. This model yields a conditional probability of ~40% in the next 30 years assuming Poisson behavior. (**Bottom**) Long ruptures (violet) span most of the fault, with small additional ruptures (like the 1812 earthquake) (orange) to satisfy all dates. This model yields a conditional probability of ~20% in the next 30 years, assuming quasi-periodic behavior of short and long events.

First, the relationship between a displacement observed at a site and the probability of seeing the same rupture at the next site along the fault has been quantified (*6*). Commonly observed displacements of 4 to 7 m (*7*, *8*) imply rupture lengths of more than 100 km (*9*), much more than the distances between paleoseismic sites. Date ranges from nearby sites that overlap poorly are thus likely in error. Second, different chemical, physical, and biological fractions of materials such as peat and charcoal yield very different radiocarbon dates (*10*–*12*). Because the type of material varies between sites, overlap of dates may be imperfect even if a single rupture spans the sites. Third, careful documentation of evidence from multiple excavations (*8*, *10*–*12*) shows a wide range in the quality of event evidence from excavation to excavation and site to site. Thus, the evidence for some paleoearthquakes may have been misinterpreted.

A much clearer picture of earthquakes on the southern San Andreas fault should emerge in the next 5 to 10 years. The groups of earthquake date ranges seen every ~200 years in the first figure will probably withstand this reevaluation. Some of these groups contain a single earthquake that ruptured through many sites and may have ruptured large parts of the southern San Andreas fault. Others contain multiple earthquakes at individual sites and could be multiple earthquakes with overlapping ruptures, like the 1812 and 1857 earthquakes (see the second figure). The current 148-year hiatus is probably not exceptional. However, no lull in the past 1600 years appears to have lasted more than ~200 years, and when the current hiatus ends, a substantial portion of the fault is likely to rupture, either as a single long rupture or a series of overlapping ruptures in a short time interval.

References and Notes

1. L. Grant, W. R. Lettis, Eds., Special issue on The Paleoseismology of the San Andreas Fault, *Bull. Seismol. Soc. Am.* **92** (2002).
2. R. J. Weldon, K. M. Scharer, T. E. Fumal, G. P. Biasi, *GSA Today* **14**, 4 (September 2004).
3. K. Sieh, M. Stuiver, D. Brillinger, *J. Geophys. Res.* **94**, 603 (1989).
4. G. P. Biasi, R. J. Weldon, T. E. Fumal, G. G. Seitz, *Bull. Seismol. Soc. Am.* **92**, 2761 (2002).
5. At four further sites, no exact dates can be determined for individual earthquakes, but the data can be related to other paleoearthquakes and thus help constrain the overall rupture scenarios (*2*).
6. G. P. Biasi, R. J. Weldon, *Bull. Seismol. Soc. Am.*, in press.
7. J. Liu, Y. Klinger, K. Sieh, C. M. Rubin, *Geology* **32**, 649 (2004).
8. R. J. Weldon *et al.*, *Bull. Seismol. Soc. Am.* **92**, 2704 (2002).
9. L. Wells, K. J. Coppersmith, *Bull. Seismol. Soc. Am.* **84**, 974 (1994).
10. T. E. Fumal *et al.*, *Bull. Seismol. Soc. Am.* **92**, 2726 (2002).
11. G. G. Seitz, thesis, University of Oregon (1999).
12. K. M. Scharer, thesis, University of Oregon (2005).

10.1126/science.1111707

INTRODUCTION

First of Many Returns

Titan, Saturn's largest moon, and Earth are the only two bodies in our solar system with nitrogen-rich atmospheres. Although Earth's atmosphere has evolved partly under the influence of life (and includes carbon dioxide as the main carbon species), Titan's remains more primitive, reducing, and rich in methane, and may resemble that hypothesized for the early Earth. Our first close view of Titan came from Pioneer and the two Voyager spacecraft, which flew by in the late 1970s and early 1980s. These spacecraft provided a taste of Titan's atmosphere and its structure, determined Titan's size and density (a mixture of rock and organic ices), and showed that the moon lacked a significant magnetic field, although it is affected greatly by its orbit in and out of Saturn's magnetic field. Detailed study of Titan, however, has been limited because its atmosphere is so thick that, like those of Venus, Jupiter, and Saturn, it is difficult to see the surface beneath the haze.

Cassini is equipped with a variety of instruments to both sample the haze and reveal the surface beneath it, and observations of Titan were a primary goal of the mission. Cassini also carried and released the Huygens probe, which successfully sampled Titan's atmosphere and landed on its solid surface late last year. The papers in this issue, including a summary by Mahaffy (p. 969), describe results from the first two passes of Cassini by Titan, including through its uppermost atmosphere.

To see through the haze, Cassini carries a radar mapper that with each pass will build up a map of Titan's surface. The initial flyby has already revealed much (see the cover); as discussed by Elachi *et al*. (p. 970), Titan apparently has a relatively young flat surface with only a few large and degraded impact craters, but with a striking variation in the deposits. Together these features seem to indicate that there has been active resurfacing, likely through some form of ice volcanism.

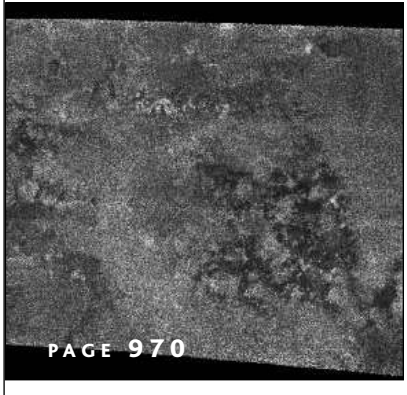
PAGE 970

A variety of other spectrometers on Cassini sampled and viewed Titan's atmosphere, providing new information on its composition and structure and showing some parallels with Earth's atmosphere [see Waite *et al*. (p. 982), Shemansky *et al*. (p. 978), and Flasar *et al*. (p. 975)]. Methane is abundant close to the surface, and Cassini has revealed several complex hydrocarbon species higher in the atmosphere. A tantalizing result is that although radiogenic argon is present (probably produced by outgassing of the moon's interior), the other argon isotopes that should have been present in an initial atmosphere are absent.

Cassini also measured the effects of Titan's passage through Saturn's magnetic field [see Wahlund *et al*. (p. 986), Mitchell *et al*. (p. 989), and Backes *et al*. (p. 992)]. It found and passed through a magnetic ionopause in Titan's atmosphere, below which the field strength dropped to zero, confirming Voyager's observation that Titan lacks a magnetic field.

Cassini is planning to revisit Titan more than 40 times during its mission, repeating many of these analyses and mapping different parts of the moon's surface. Together with the Huygens data, these data should help us understand the origin and evolution of Saturn's largest moon and, by analogy, Earth's early history.

–BROOKS HANSON

CONTENTS

Science

CREDIT: NASA/JET PROPULSION LABORATORY/U.S. GEOLOGICAL SURVEY

Intensive Titan Exploration Begins

Paul R. Mahaffy

The Cassini Orbiter spacecraft first skimmed through the tenuous upper atmosphere of Titan on 26 October 2004. This moon of Saturn is unique in our solar system, with a dense nitrogen atmosphere that is cold enough in places to rain methane, the feedstock for the atmospheric chemistry that produces hydrocarbons, nitrile compounds, and Titan's orange haze. The data returned from this flyby supply new information on the magnetic field and plasma environment around Titan, expose new facets of the dynamics and chemistry of Titan's atmosphere, and provide the first glimpses of what appears to be a complex, fluid-processed, geologically young Titan surface.

More than two decades ago, the Voyagers 1 and 2 spacecraft encountered Saturn on their grand tour of the solar system. In the summer of 2004, the Cassini mission—a sophisticated, heavily instrumented robotic platform—returned from Earth for a more systematic study of this gas giant with its complex system of satellites and icy rings. The mission had Titan (Fig. 1), Saturn's biggest moon, firmly in its sight.

The European Space Agency (ESA) and the Italian Space Agency collaborated with NASA on the Cassini mission. NASA's Jet Propulsion Laboratory led the development of the Cassini Orbiter and the ESA, that of the Huygens Probe of Titan's atmosphere. Instruments from both sides of the Atlantic were developed for both the Orbiter and Probe payloads. After a 7-year interplanetary cruise, the Huygens Probe was finally released from the Orbiter and successfully parachuted into Titan's atmosphere on 14 January 2005. During descent, it transmitted data back to the Orbiter and even continued to send back data for some time after it landed on Titan's surface. The Huygens data are still being analyzed, but data collected from several instruments on the Cassini Orbiter before, during, and after the first Titan flyby on 26 October 2004 are published in this issue (*1*–*7*); some reports include data from the second Titan flyby on 13 December 2004.

The orbital tour of a distant giant planet system is an ambitious undertaking. The first such endeavor, the Galileo mission, orbited Jupiter from 1995 to 2003 and sent a probe into its atmosphere. The mission demonstrated that such an in-depth study could provide astonishing discoveries, such as the likely existence of an ocean beneath the surface ices of the jovian moon Europa (*8*).

The Cassini spacecraft was launched in 1997 to study Saturn and its icy rings and at least 34 moons. From the start, the mission put a special focus on the moon Titan. This satellite is a unique object in our solar system (*9*), with a surface pressure 1.5 times as high as that at the surface of Earth and near-surface atmospheric temperatures below 100 K. The nominal mission length of 4 years should allow more than 70 orbits about Saturn; the resulting 44 close flybys of Titan will allow extensive study of its atmosphere and its surface. Close flybys of the moons Enceladus, Phoebe, Hyperion, Dione, Rea, and Iapetus are also part of Cassini's grand saturnian tour (*10*).

Voyager imaged Titan and obtained ultraviolet and infrared spectra from its atmosphere, but was unable to penetrate the orange hydrocarbon haze to get a clear view of the surface. Voyager measurements and stellar occultations suggested that the atmosphere might be cold enough to turn even its highly volatile methane into rain droplets, but

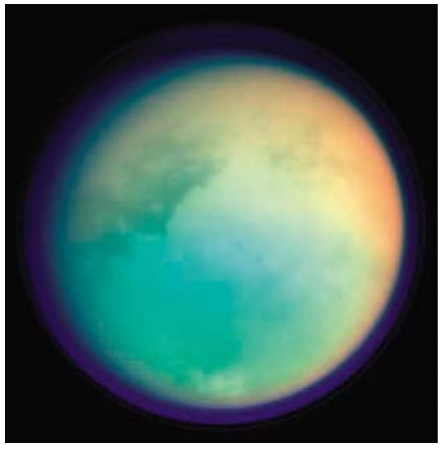

Fig. 1. A false-color view of Titan. This false-color image of Titan, derived from multiple wavelengths, was acquired during the first close flyby. Red and green colors (denoting infrared wavelengths) highlight methane, whereas the blue color (ultraviolet) shows the high atmosphere and detached hazes. Clouds are apparent near Titan's South Pole. [Credit: NASA/JPL]

speculation regarding possible hydrocarbon lakes or even a global hydrocarbon ocean awaited future validation. Eventually, both the Hubble space telescope and Earth-based radar were able to penetrate the haze and demonstrate that Titan's surface is heterogeneous. But it was left to the Cassini mission to examine this surface in detail.

About 1% of Titan's surface was imaged by the Cassini radar on the first flyby. On page 970, Elachi *et al.* (*1*) report a complex, crater-poor surface with evidence of surface flows. Based on these early results, the authors argue that Titan may be cryovolcanically active. The radar is not the only tool available from the Orbiter to view the Titan surface. Future comparison of radar data with imaging data, using spectral bands that penetrate the haze, will facilitate interpretation of surface features. The high-resolution images of the surface obtained by the Huygens Probe just before landing provide ground truth to the Orbital data at one surface location.

The primary constituent of the Titan atmosphere is nitrogen, with several percent of methane and trace amounts of stratospheric hydrocarbons and nitriles. Such a reducing environment may resemble that on early Earth, before microbial activity transformed Earth's atmosphere into a more oxidized state. The simple chemical building blocks of life, such as the amino acids that form proteins, contain both carbon and nitrogen, and knowledge of the prebiotic chemistry on Titan may help to elucidate chemical processes related to early life on Earth. The simplest molecule that contains both nitrogen and hydrogen (HCN) and heavier nitriles are found in Titan's atmosphere.

On page 975, Flasar *et al.* (*2*) derive temperature and wind profiles and provide a refined value for the abundance of CH_4 and CO in the atmosphere, based on data from the Cassini Fourier Transform Infrared Spectrometer. They also demonstrate seasonal variations in several trace hydrocarbon and nitrile species (such as C_2H_4, C_3H_4, C_4H_2, HCN, HC_3N, and C_2N_2) by comparison with abundances of the same species measured at a different time of year during the Voyager flyby. The interplay of atmospheric dynamics and heterogeneous or gas-phase chemistry that produce seasonal effects such as the terrestrial Antarctica ozone hole can now be systematically studied in another atmosphere with Cassini instruments.

Three other papers report imaging of energetic neutral atoms surrounding Titan [Mitchell *et al.*, page 989 (*4*)], measurements of magnetic fields along the path of the spacecraft [Backes *et al.*, page 992 (*3*)], and cold-plasma measurements in Titan's ionosphere [Wahlund *et al.*, page 986 (*5*)]. Together, these highly complementary data sets can be used to model the response of Titan's atmosphere to the input of energetic particles, primarily from the rapidly rotating Saturn magnetosphere. This process not only sends material from Titan into the magnetospheric system; it also provides one energy source for the continuous production of complex hydrocarbons, nitriles, and aerosols from the N_2 and CH_4 feedstock. On page 978, Shemansky *et al.* (*6*) describe the composition of Titan's upper atmosphere, derived from Cassini ultraviolet spec-

Solar System Exploration Division, NASA, Goddard Space Flight Center, Greenbelt, MD 20771, USA. E-mail: paul.r.mahaffy@nasa.gov

trometer data using stellar occultations after the 13 December flyby. The chemical composition of the upper atmosphere of Titan along the spacecraft track, derived from mass spectrometer measurements, is reported by Waite *et al.* on page 982 (*7*).

The desire to understand the formation and evolution of extrasolar planetary systems also motivates the detailed study of the Saturn system. Cassini observations will not only test and validate models of the processes that shaped the saturnian system into its collection of rings, satellites, and plasma; they will also provide an improved theoretical basis for understanding the conditions necessary for the emergence of planetary systems around young stars.

The in situ measurements provided by Cassini's flight through the upper atmosphere of Titan may constrain models of how this moon formed (*11*). For example, if CO and N_2 were dominant in the formation region of Saturn, clathrates (inclusion compounds within a host lattice such as water) of these molecules, together with the primordial and chemically inert ^{36}Ar and ^{38}Ar that were present during Titan's formation, might be incorporated into the planet. Alternatively, the source of the present N_2 atmosphere might be NH_3 that was later transformed into nitrogen. Measurements of the ^{36}Ar and ^{38}Ar argon isotopes relative to the radiogenic ^{40}Ar (released later into this atmosphere from the decay of ^{40}K) may distinguish between these alternatives. Likewise, tests of how much of Titan's atmosphere may have been lost over its history can come from measurements of the isotope ratios $^{15}N/^{14}N$, because loss to space fractionates these isotopes, with preferential loss of the lighter ^{14}N. The Cassini Orbiter mass spectrometer data (*7*), combined with Huygens Probe mass spectrometer (*12*) measurements of these same isotope ratios in the deep atmosphere, will provide better observational constraints on models of Titan formation.

The Cassini Orbiter/Huygens Probe mission provides an extraordinary example of a successful international collaboration in space exploration. The navigation (*9*) of this sophisticated science platform precisely to its targeted destination in Titan's upper atmosphere, the successful deployment and entry of the Huygens Probe, the solid performance from the large number of instruments, and the demonstration of the ability to flawlessly plan and execute complex measurement sequences are a tribute to the skill, dedication, and perseverance of the multinational Cassini team. Future Titan flybys will incrementally build up the map of Titan's surface and sample the atmosphere at different locations and seasons. The data from the first flyby reported here (*1*–*7*) provide a preview of the insights that can be expected from the next several years of exploration and are the first steps toward a substantially deeper understanding of this distant world.

References

1. C. Elachi *et al.*, *Science* **308**, 970 (2005).
2. F. M. Flasar *et al.*, *Science* **308**, 975 (2005).
3. H. Backes *et al.*, *Science* **308**, 992 (2005).
4. D. G. Mitchell *et al.*, *Science* **308**, 989 (2005).
5. J. E. Wahlund *et al.*, *Science* **308**, 986 (2005).
6. D. E. Shemansky *et al.*, *Science* **308**, 978 (2005).
7. J. H. Waite Jr. *et al.*, *Science* **308**, 982 (2005).
8. M. G. Kivelson *et al.*, *Science* **289**, 1340 (2000).
9. R. D. Lorenz, J. Mitton, *Lifting Titan's Veil* (Cambridge Univ. Press, Cambridge, UK, 2002).
10. A. A. Wolf, *Space Sci. Rev.* **104**, 101 (2002).
11. T. Owen, D. Gautier, *Space Sci. Rev.* **104**, 347 (2002).
12. H. B. Niemann *et al.*, *Space Sci. Rev.* **104**, 551 (2002).

10.1126/science.1113205

REPORT

Cassini Radar Views the Surface of Titan

C. Elachi,[1] S. Wall,[1]* M. Allison,[2] Y. Anderson,[1] R. Boehmer,[1] P. Callahan,[1] P. Encrenaz,[3] E. Flamini,[4] G. Franceschetti,[5] Y. Gim,[1] G. Hamilton,[1] S. Hensley,[1] M. Janssen,[1] W. Johnson,[1] K. Kelleher,[1] R. Kirk,[6] R. Lopes,[1] R. Lorenz,[7] J. Lunine,[7] D. Muhleman,[8] S. Ostro,[1] F. Paganelli,[1] G. Picardi,[9] F. Posa,[10] L. Roth,[1] R. Seu,[9] S. Shaffer,[1] L. Soderblom,[6] B. Stiles,[1] E. Stofan,[11] S. Vetrella,[5] R. West,[1] C. Wood,[12] L. Wye,[13] H. Zebker[13]

The Cassini Titan Radar Mapper imaged about 1% of Titan's surface at a resolution of ~0.5 kilometer, and larger areas of the globe in lower resolution modes. The images reveal a complex surface, with areas of low relief and a variety of geologic features suggestive of dome-like volcanic constructs, flows, and sinuous channels. The surface appears to be young, with few impact craters. Scattering and dielectric properties are consistent with porous ice or organics. Dark patches in the radar images show high brightness temperatures and high emissivity and are consistent with frozen hydrocarbons.

Saturn's largest satellite, Titan, is the only moon and one of only four solid bodies in the solar system to host a thick atmosphere, uniquely distinguished by nitrogen and methane and a complex suite of organic products of these molecules. Its primitive chemistry may reveal clues about the prebiotic origin of materials that ultimately gave birth to life in our solar system. The mapping of Titan is an especially challenging puzzle because the most likely constituent materials (e.g., water-ammonia and other ices, hydrocarbons, tholins) in this chemical and temperature regime are likely to exhibit different scattering properties than at Earth and Venus, the only other worlds mapped by spaceborne radar (*1*–*3*).

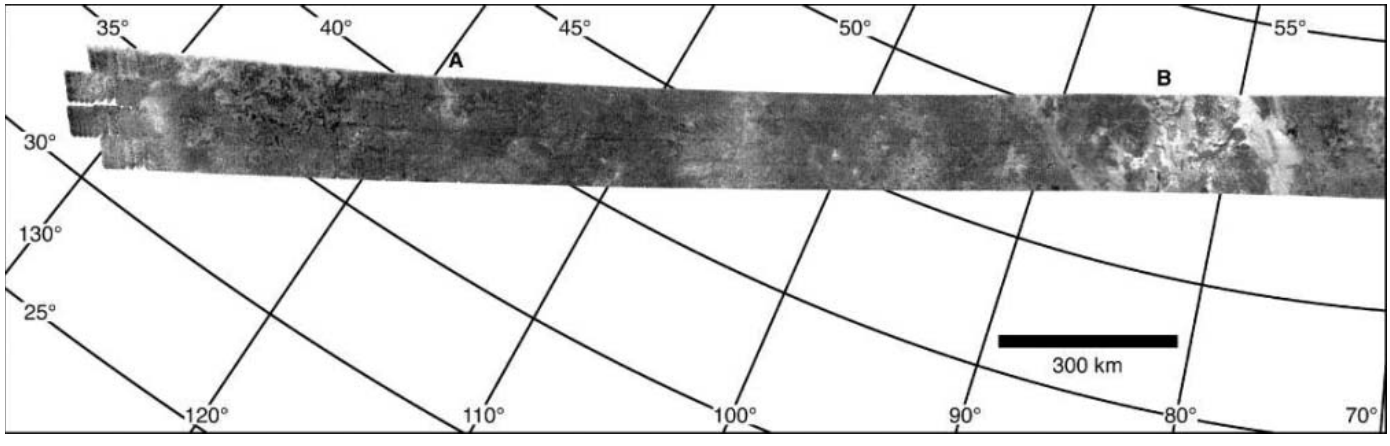

The Cassini mission's Titan Radar Mapper operates in four modes: radiometry, scatterometry, altimetry, and synthetic aperture radar (SAR) imaging (*4*). SAR mode requires ranges less than ~4000 km; high-resolution SAR (~500 m/pixel) can be collected only below ~1500 km. Data reported here are from the first close flyby, designated T_A, which occurred on 26 October 2004 at a minimum range of 1174 km, the first of 45 planned close flybys (*4*). Inbound full-disk radiometry and scatterometry scans of large regions, including the Huygens probe landing site (*5*, *6*), were acquired from ~25,000 km at differing angles. SAR coverage extending through closest approach over an arc of ~100° was followed immediately by an altimetry track covering an arc of ~10°. Scatterometry scans and radiometry scans in orthogonal linear polarizations were collected outbound. Observation geometries and details, coverage diagrams, and higher resolution images are available in (*4*).

The SAR image strip (Fig. 1; Fig. 2 in detail) reveals a variable surface with distinct units and features. On the basis of brightness, texture, and morphology, we define five units, two of regional scale and three of local scale. About one-quarter of the swath is composed of a regional-dark, homogeneous unit with relatively low backscatter (see the bottom half of Fig. 2A and parts of Fig. 2, D and E), which includes regions of variable backscatter with indistinct boundaries and scattered SAR-bright spots that may be small topographic features. Most of the rest of the swath consists of a higher backscatter, regional-mottled unit that is gradational at its boundaries with the darker, homogeneous unit. Two discrete SAR-bright units are distinguished. A bright lobate unit (Fig. 2E) occurs in several locations across the swath. The lobate boundaries range from distinct to gradational, with variable brightness across the unit. Both sheet-like and more digitate examples appear, sometimes associated with quasi-circular features. A bright, lineated unit exhibits sharp boundaries and bright, lineated interiors (Fig. 2C). The lineations are parallel and are spaced 1 to 2 km apart. This unit appears similar to grooved terrains seen at several scales on Ganymede (*7*, *8*). The fifth unit is SAR-dark and occurs as isolated patches a few tens of kilometers or less across (Fig. 2, B to D). One such dark patch is near the western end of the swath. These patches tend to be irregular, with sharp boundaries; many are interconnected by narrow sections, giving the impression that their distribution is topographically controlled, perhaps by depressions, valleys, and channels.

A large, roughly circular feature about 180 km in diameter is prominent in the SAR strip, centered near 50°N, 87°W (Fig. 2B, at left). The International Astronomical Union (IAU) has provisionally approved the name Ganesa Macula for this feature. It has suggestions of a volcanic construct, possibly a dome; it could also occupy an old impact scar. Along its edges are SAR-bright flanks; at its center, instead of a central peak, is an apparent central depression, about 20 km in its longest dimension, that resembles a volcanic crater. Several sinuous channels and/or ridges radiate from the central feature; these appear to carry material from the center. The 90-km sinuous features trending southeast could be responsible for transport of material to the SAR-bright regions along the flank. The terrain along the eastern margin is complex, exhibiting multiple lobate forms that may be flows.

A plot of the scatterometry backscatter cross section versus incidence angle shows both specular and diffuse-scattering echoes (Fig. 3A). The region where specular reflections could be observed was restricted by the Titan-spacecraft geometry to the central part of the inbound scatterometer raster map, but diffuse scattering was observable over a larger area, and the plot indicates considerable heterogeneity. Figure 3B shows a crude classification of the scatterometer measurements into high, medium, and low diffuse cross-section classes, with their locations plotted on Cassini Imaging Science Subsystem (ISS) imagery (*9*). This model-independent classification shows cross sections clearly correlated with the near-infrared (near-IR) albedo observed by ISS. Figure 4A shows a map of the cross section normalized to constant incidence angle by a simple cosecant model, revealing a strong correlation with the ISS image (Fig. 4C) in the low incidence angle region as well. Xanadu, the bright, continent-sized region at 90° to 150°W, shows the strongest backscatter, including a particularly bright spot near 120°W that is undistinguished in the near-IR.

The passive radiometer mode acquired an inbound unresolved disk brightness measurement and two low-resolution outbound microwave brightness maps. Disk-averaged brightness temperatures from these observations are 85 K, 85 K, and 86 K (each ±5 K), respectively, consistent with Earth-based measurements (*10*, *11*). Assuming a physical surface temperature of 94 K, these data

[1]Jet Propulsion Laboratory, California Institute of Technology, Pasadena, CA 91109, USA. [2]Goddard Institute for Space Studies, National Aeronautics and Space Administration, New York, NY 10025, USA. [3]l'Observatoire de Paris, 75014 Paris, France. [4]Agenzia Spaziale Italiana, 00198 Rome, Italy. [5]Facoltá di Ingegneria, 80125 Naples, Italy. [6]U.S. Geological Survey, Flagstaff, AZ 86001, USA. [7]Lunar and Planetary Laboratory, University of Arizona, Tucson, AZ 85721, USA. [8]Division of Geological and Planetary Sciences, California Institute of Technology, Pasadena, CA 91125, USA. [9]Universitá La Sapienza, 00184 Rome, Italy. [10]INFM and Dipartimento Interateneo di Fisica, Politecnico di Bari, 70126 Bari, Italy. [11]Proxemy Research, Laytonsville, MD 20882, USA. [12]Planetary Science Institute, Tucson, AZ 85719, USA. [13]Stanford University, Stanford, CA 94305, USA.

*To whom correspondence should be addressed. E-mail: steve.wall@jpl.nasa.gov

Fig. 1 (on facing pages). SAR image strip acquired by Cassini's Titan Radar Mapper during the Titan T_A flyby, with 5° latitude × 10° west longitude graticule. Resolution is ~500 m at image center, increasing to ~1400 m at eastern end. The image has been corrected to constant incidence angle with the use of the backscatter model shown in Fig. 3A and logarithmically scaled. Letters indicate regions enlarged in Fig. 2.

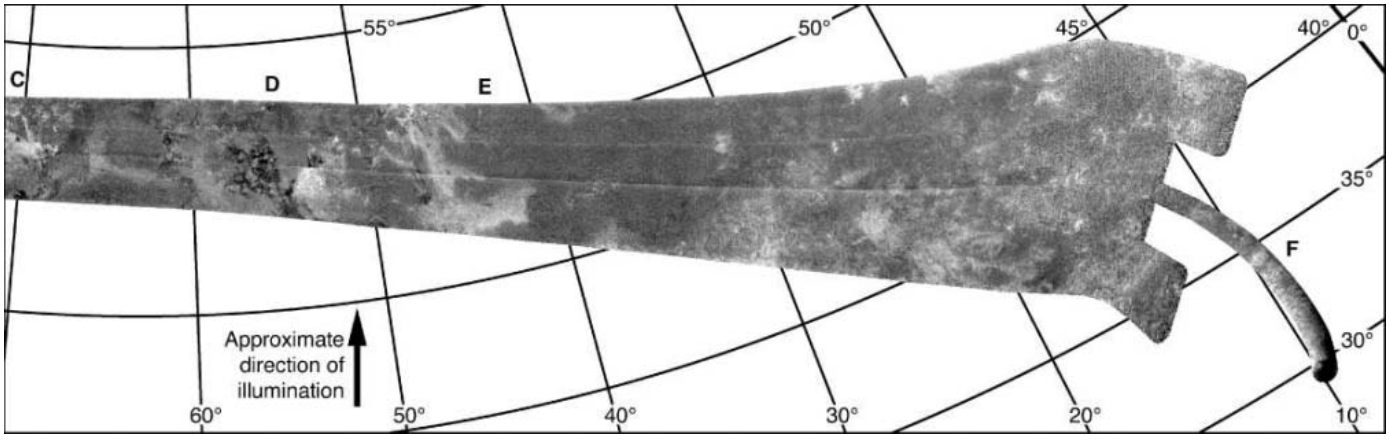

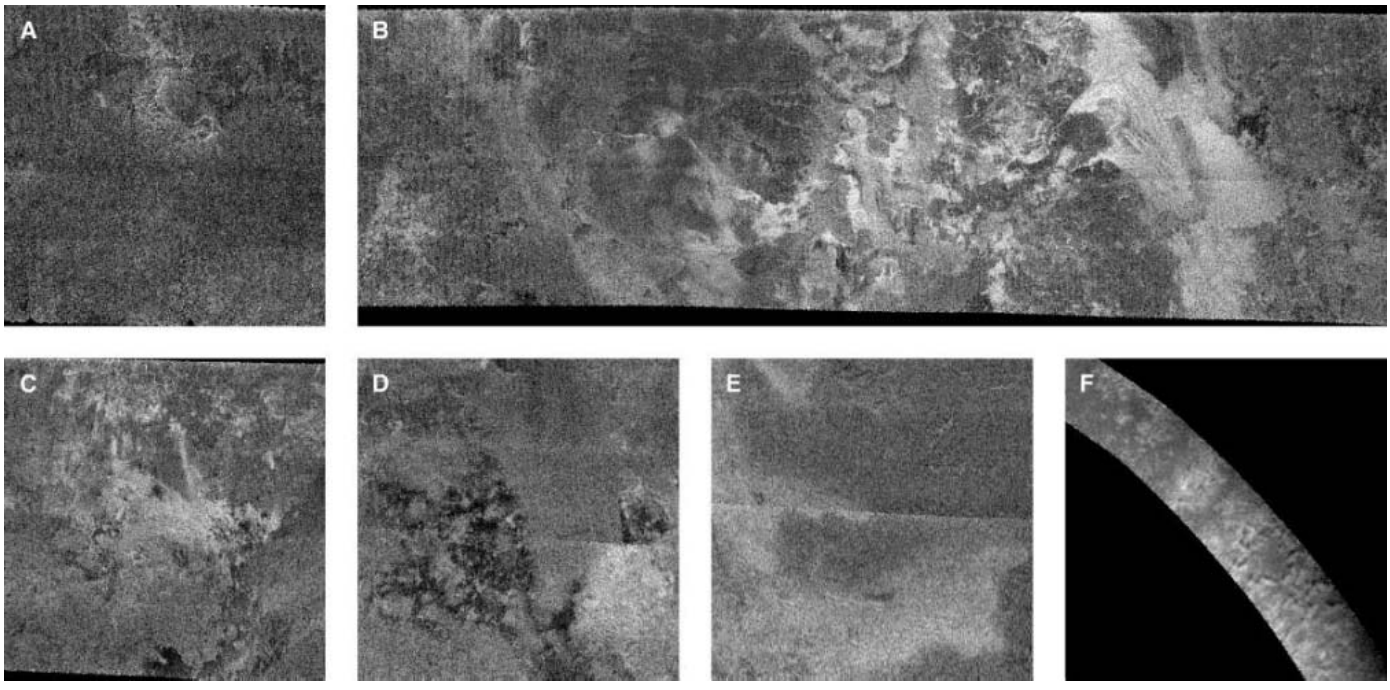

Fig. 2. Enlargements of the Cassini SAR image shown in Fig. 1. The letters correspond to the locations shown along the edge of the SAR strip in Fig. 1. Each image covers an area ~175 km high, with north approximately at top and illumination approximately from bottom. See text.

correspond to an overall surface emissivity of ~0.9. For a dielectric surface that can be characterized by the Fresnel equations, this is consistent with a dielectric constant of 2 to 3. The polarization and center-to-limb brightness distributions of the full-disk radiometer images are consistent with a uniform surface temperature and a bulk dielectric constant $\varepsilon = 2$, and are inconsistent with solid water ice ($\varepsilon = 3.1$) or ammonia ice ($\varepsilon = 4.5$). In particular, the polarization differences yield broadly uniform solutions for $\varepsilon = 2.1$ and 1.6, respectively, in northern and southern mid-latitude regions. The radiometry maps show considerable brightness temperature variations ≤10 K between regions ≤500 km in extent that can be attributed to emissivity variations (Fig. 4B). These variations are negatively correlated with those of the backscatter cross section.

Altimetry data were analyzed by a simple threshold algorithm and reduced to elevations relative to a sphere (Fig. 5); absolute radii are awaiting more accurate trajectory data. Relief along the altimetry track covered in this northern region is quite low, varying only ~150 m over 400 km. This is a small sample (0.02% of the surface) and does not currently coincide with SAR or optical coverage. However, Cassini radiometry and scatterometry maps of the outbound hemisphere (*4*) and ISS images (*9*) indicate that the altimetry does not cross any notable terrain boundaries. The SAR images also provide information about topographic relief of resolved geologic features, but without the geometric rigor of the altimetry. A few features in the SAR swath exhibit the close bright-dark downrange pairing that is characteristic of topographic shading. Radarclinometric analysis allows crude estimates of heights. The strongest sense of relief is given by small apparent hills, 5 to 10 km in width (Fig. 2F). Many of these show bright-dark pairing in the downrange direction, making it unlikely that they are flat surfaces of variable scattering. They were imaged at a lower incidence angle relative to most of the strip, maximizing topographic modulation. We estimate that the relief is only ~100 m and slopes are ~3° to 5° (*12*). Applying this approach to a flow-like feature at 41°W, 47°N indicates a height of ~250 m, bounding slopes of ~7°, and a flat top.

The potential pitfalls of overinterpreting brightness as slopes may be illustrated by the

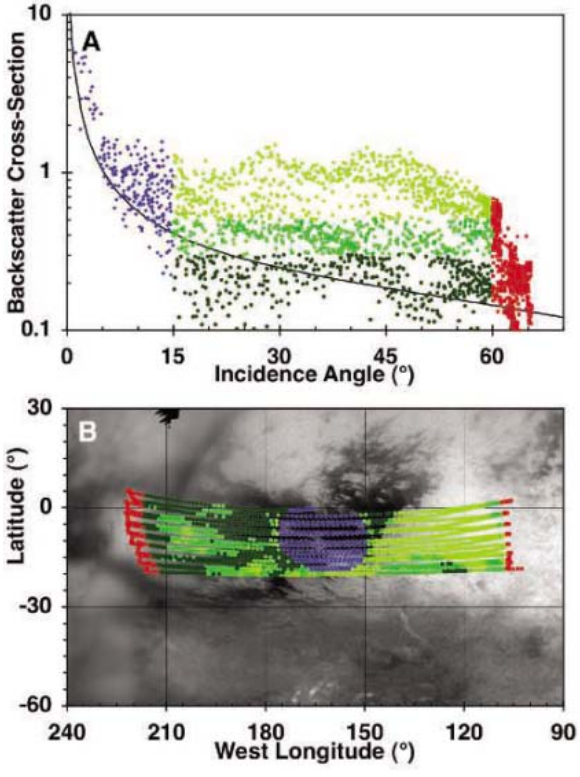

Fig. 3. Angular and spatial dependence of Cassini Titan T_A inbound scatterometer data. (**A**) Plot of backscatter cross section versus incidence angle shows specular behavior at small incidence angles (blue) and dropoff at largest incidence angles (red). Data at intermediate angles (green) show multiple populations (i.e., surface units) with distinct and only weakly incidence-dependent cross section. Data have been classified into low, medium, and high cross section (dark to light green). Curve is simple cosecant (incidence) backscatter model used to normalize images in Figs. 1 and 2 and scatterometry in Fig. 3A. (**B**) Map of scatterometer measurements overlaid on Cassini ISS image map (*9*), colored according to incidence angle and backscatter classification as in (A). High- and low-incidence classes are geographically restricted because of observation geometry, but cross-section classes at intermediate angles correlate clearly with near-IR albedo.

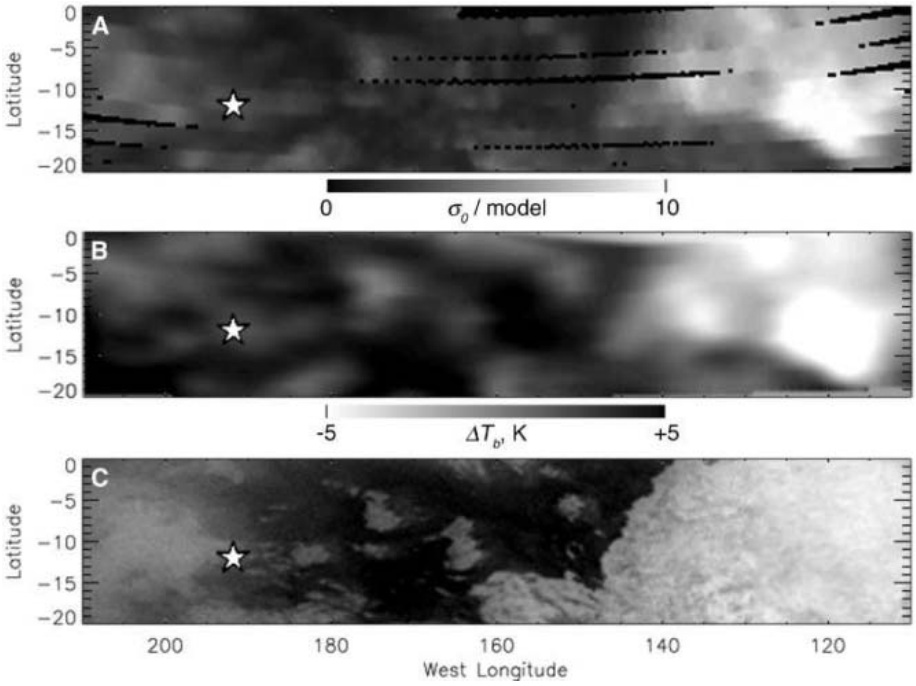

Fig. 4. Comparison of radar scatterometry and radiometry with near-IR albedo for a subset of the region in Fig. 3. Simple cylindrical projection is shown, with north at top. Star indicates approximate landing site of Huygens probe. **(A)** Backscatter cross section σ_0 normalized to constant incidence angle according to model curve from Fig. 3A. Black indicates data gaps where scan raster separation exceeded beam width. **(B)** Deviation of brightness temperature T_0 from model, plotted with reversed grayscale to facilitate comparison. **(C)** Portion of ISS image mosaic (*9*). Negative correlation between scatterometry and radiometry is near-perfect, given slightly coarser resolution of latter. Radar-ISS correlation is also strong but has noteworthy exceptions such as extremely radar-bright, low-emissivity spot within Xanadu Regio at 120°W, which is undistinguished optically.

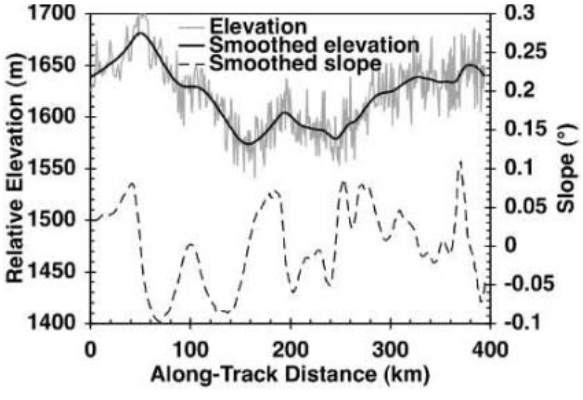

Fig. 5. Cassini radar altimetry profile. Leftmost data shown are near 10°W, 29°N, trending south-southeast. Raw elevations relative to a 2575-km sphere (gray) have been smoothed by convolution with a Gaussian function with standard deviation ~7 km (solid black line) to suppress the point-to-point variations (root mean square ~20 m) due to noise; bi-directional slopes were calculated from the smoothed elevations. Horizontal resolution is limited by beam width to ~25 km. Only elevation changes within the profile are significant, given current errors in trajectory information used to reduce the data.

large, bright, flow-like feature shown in Fig. 2E. Backscatter varies linearly across this feature, so if it is topographic, it is roughly parabolic in cross section, with maximum slopes of ±4°; the height of the 70-km–wide eastern part is ~1000 m. These dimensions are comparable to thick flows on Ariel (*13*) and would require an implausibly large amount of geothermal heat to be expressed over time as cryomagma. An alternative interpretation that we prefer, given the diffuse appearance of the feature, is that brightness is related to a compositional or textural gradient on the surface of a much thinner flow.

Given Titan's unique combination of atmosphere and temperature, the interpretation of these data is necessarily speculative until coverage is increased and is obtained from multiple instruments. Most notable is the lack of unambiguous impact craters visible in the SAR strip. Objects producing craters smaller than ~20 km would be screened by Titan's present atmosphere (*14*, *15*). Heavily cratered terrains on other large saturnian satellites typically have 200 to 400 craters per 10^6 km^2 larger than ~20 km (*16*); we should expect to find 100 to 200 craters here if this were an ancient surface. With no fresh craters and only a few degraded candidates, the resurfacing rate must be considerably higher than the impact cratering rate. We conclude, therefore, that this part of Titan's surface is geologically young. Crater obliteration may be due to burial, either by deposition of stratospheric photochemical debris or direct accretion and windblown deposition; pluvial erosion or deposition; tectonic processes; or cryovolcanism. The lobate units, channels, and other flow-like features suggest pluvial or volcanic processes; the presence of apparent volcanic constructs and a simple calculation of available resurfacing materials (*17*) favor cryovolcanism.

The SAR and scatterometer observations are consistent with previous Earth-based data, even though the wavelengths and the specific areas observed differ. Arecibo (wavelength = 13 cm) observations of Titan show a diffusely scattered component, with a weak specular component present for about 75% of the observation (*18*), indicating smooth surfaces with slopes as shallow as 0.2° and Fresnel reflectivities of several percent. The specular component has not been seen in radar observations of other icy solar system bodies; it requires the existence of regions that are nearly flat at subcentimeter scales. However, diffuse reflection of most of the echo power requires near-surface structural complexity (e.g., roughness or fractures and voids) at scales ≥0.5 cm. Surface roughness alone from geochemically plausible minerals would be too weak to produce the observed echoes. Therefore, although surface roughness per se may contribute to variations in the radar brightness, we concur with Campbell and co-workers (*18*) and attribute the bulk of Titan's radar echo (away from the specular peak in Fig. 3) to volume scattering, in which case multiple scattering in icy materials is known to be able to produce strong returns.

Titan's scatterometry, with both specular and diffuse components, in some ways resembles those of the Moon and the inner planets (*19*), albeit at a much higher magnitude. Such large variations in radar brightness in both components suggest that Titan's near-surface structure and composition are heterogeneous. Volume scattering depends critically on the transparency of the medium (*20*, *21*) and would be much greater for nearly pure water ice [as on the icy Galilean satellites (*22*)] than if absorbing material such as ammonia or silicates were present, as may be the case for Iapetus (*23*) and comets (*24*). Therefore, variability in composition remains an important candidate to explain variations in radar reflectivity, although we believe volume scattering in low-loss media to be an important effect, particularly in the SAR-bright regions.

At global scale, Titan differs from cold, icy surfaces such as Europa and Ganymede, where microwave emissivities of 0.5 to 0.6 and high radar reflectivity indicate the dominance of

volume scattering from the subsurface rather than from a simple dielectric half space (*25*). A much more complicated model for Titan, involving multiple surface layers and compositional heterogeneities, may be required to reconcile the Cassini scatterometry and radiometry observations. All materials posed as candidates for Titan's surface other than those containing ammonia are expected to have very low microwave absorption at temperatures ~100 K, and would have to be tens of meters deep to produce the observed emission.

The strong correlation between radiometry and optical data (Fig. 4, B and C) is not understood. The strong correlation between the SAR-bright and SAR-dark features and radiometrically cold and warm regions, respectively (Fig. 4, A and B), also suggests that volume scattering is one cause of the SAR-bright regions. If the SAR brightness were solely due to slopes, the correlation with brightness temperature would be positive. Surface roughness alone would have a small effect on thermal emission at the SAR viewing angle. A possible hypothesis is that (i) the optically brighter and colder areas are fractured or porous ice, producing volume scattering and resulting low emissivity, as on the surfaces of Europa and Ganymede; and (ii) the optically darker, warmer, high-emissivity areas have a lower average dielectric constant, being composed of either an organic sludge (*26*, *27*) or a porous material of high dielectric constant, such as water ice.

The location of reservoirs of organic liquid is unclear, although patches of SAR-dark material occupy ~1% of the swath and may well represent concentrations of organics. So far, these patches have been too small to resolve with radiometry. Shallow deposits of liquid hydrocarbons could, however, be transparent to microwaves, as is the case for cold and pure water ice (*28*). Alternatively, the liquid hydrocarbons could be masked by floating solids. All materials likely on Titan would sink in liquid ethane and methane, with the exception of the polymerized product of acetylene (polyacetylene), itself the most abundant solid product of stratospheric photolysis (*29*). Some forms of polyacetylene exhibit microporous structures with density ~0.4 g/cm^3, lower than any expected combination of methane, ethane, and nitrogen in surface liquid form (*28*, *29*). This material is a weak semiconductor and, if suspended or floating on liquids, it could appear relatively bright to radar and optical sensing and would contribute enough small-scale roughness to suppress the specular reflection at optical wavelengths.

From even this limited view of its smallest details, it is clear that Titan's surface is complex and young, although we note again that only 1% of it has been imaged by SAR. As we progress through the mission, we expect SAR coverage of more than 25% of the planet, near-global radiometry and scatterometry coverage, and tens of altimetric profiles, providing increasingly instructive information about the processes at work on Titan.

References and Notes

1. B. Campbell, *Radar Remote Sensing of Planetary Surfaces* (Cambridge Univ. Press, Cambridge, 2002).
2. J. McCauley *et al.*, *Science* **218**, 1004 (1982).
3. R. Saunders *et al.*, *J. Geophys. Res.* **97**, 13067 (1992).
4. Instrument detail, observation geometries and details, resurfacing rate, radarclinometry methods, a coverage diagram, and related references are available as supporting material on *Science* Online.
5. The Huygens probe descended on 14 January 2005, reaching the surface at about 10.5°S, 192°W. See (*30*).
6. Titan geographical coordinates are per the IAU (*31*): In general terms, the equator is roughly Titan's orbital plane, and zero longitude is the subsaturn point, with a libration of ±3° due to orbital eccentricity.
7. R. T. Pappalardo *et al.*, in *Jupiter: The Planet, Satellites, and Magnetosphere*, F. Bagenal Ed. (Cambridge Univ. Press, Cambridge, 2004), pp. 363–396.
8. J. G. Patel *et al.*, *J. Geophys. Res.* **104**, 24,057 (1999).
9. C. C. Porco *et al.*, *Nature* **434**, 159 (2005).
10. B. J. Butler, M. Gurwell, *Bull. Am. Astron. Soc.* **36**, 1075 (2004).
11. A. Grossman, D. Muhleman, *Bull. Am. Astron. Soc.* **24**, 954 (1992).
12. This apparent asymmetry could result from the actual backscatter behavior departing from the assumed 1/sin(i) form at small incidence angles and/or from the finite resolution of the images. Even allowing for these effects, the relief is likely not much more than 100 m, and slopes do not approach the incidence angle, so that the features are not severely distorted by layover.
13. D. G. Jankowski, S. W. Squyres, *Science* **244**, 1322 (1988).
14. J. Lunine, N. A. Artemieva, R. D. Lorenz, E. Flamini, paper presented at the 36th Annual Lunar and Planetary Science Conference, League City, TX, 14–18 March 2005, abstract 1504.
15. S. Engel, J. I. Lunine, W. K. Hartmann, *Planet. Space Sci.* **43**, 1059 (1995).
16. R. Lorenz, *Planet. Space Sci.* **45**, 1009 (1997).
17. R. Lorenz, *Planet. Space Sci.* **44**, 1021 (1996).
18. Campbell *et al.* (*32*) conducted observations with the Arecibo and Goldstone radio telescopes in November and December 2001 and late in 2002, obtaining disk-integrated echo spectra at longitudes 23° apart at 26°S.
19. S. Ostro, *Rev. Mod. Phys.* **65**, 1235 (1993).
20. K. Peters, *Phys. Rev. B* **46**, 801 (1992).
21. G. Black, D. Campbell, P. Nicholson, *Icarus* **151**, 167 (2001).
22. S. Ostro *et al.*, *J. Geophys. Res.* **97**, 18227 (1992).
23. G. J. Black, D. B. Campbell, L. M. Carter, S. J. Ostro, *Science* **304**, 553 (2004).
24. J. Harmon, D. Campbell, S. Ostro, M. Nolan, *Planet. Space Sci.* **47**, 1409 (1999).
25. D. Muhleman, A. Grossman, B. Butler, *Annu. Rev. Earth Planet. Sci.* **23**, 337 (1995).
26. We refer to the complex mix of nitriles and liquid and solid hydrocarbons produced by Titan's atmospheric photochemistry as "sludge." Dielectric constants vary, increasing with increasing mass density, from about 1.6 for methane to 3 or more for higher molecular weight materials, but 2.0 to 2.4 is a representative range for the mix. See (*33*).
27. R. Thompson, *Icarus* **86**, 336 (1990).
28. Models for liquid compositions on Titan's surface are discussed in (*34*).
29. The density of polyacetylene is discussed in (*35*).
30. M. Tomasko *et al.*, *Nature*, in press.
31. P. K. Seidelmann *et al.*, *Celest. Mech. Dynam. Astron.* **82**, 83 (2002).
32. D. B. Campbell, G. J. Black, L. M. Carter, S. J. Ostro, *Science* **302**, 431 (2003).
33. R. Lorenz *et al.*, *Planet. Space Sci.* **51**, 353 (2003).
34. J. Lunine, *Rev. Geophys.* **31**, 133 (1993).
35. D. Bott, in *Handbook of Conducting Polymers*, T. Skotheim, Ed. (Dekker, New York, 1986), pp. 1191–1232.
36. We gratefully acknowledge the many years of work by many hundreds of people in the development and design of the Cassini mission that have culminated in the results presented herein. The Cassini Project is a joint endeavor of NASA, the European Space Agency (ESA), and the Italian Space Agency (ASI). Cassini is managed by the Jet Propulsion Laboratory, California Institute of Technology, under a contract with NASA.

Supporting Online Material

www.sciencemag.org/cgi/content/full/308/5724/970/DC1
Materials and Methods
Figs. S1 to S4
Table S1
References

18 January 2005; accepted 25 April 2005
10.1126/science.1109919

Titan's Atmospheric Temperatures, Winds, and Composition

F. M. Flasar,[1]* R. K. Achterberg,[2] B. J. Conrath,[3] P. J. Gierasch,[3] V. G. Kunde,[4] C. A. Nixon,[4] G. L. Bjoraker,[1] D. E. Jennings,[1] P. N. Romani,[1] A. A. Simon-Miller,[1] B. Bézard,[5] A. Coustenis,[5] P. G. J. Irwin,[6] N. A. Teanby,[6] J. Brasunas,[1] J. C. Pearl,[1] M. E. Segura,[7] R. C. Carlson,[2] A. Mamoutkine,[2] P. J. Schinder,[3] A. Barucci,[5] R. Courtin,[5] T. Fouchet,[5] D. Gautier,[5] E. Lellouch,[5] A. Marten,[5] R. Prangé,[5] S. Vinatier,[5] D. F. Strobel,[8]† S. B. Calcutt,[6] P. L. Read,[6] F. W. Taylor,[6] N. Bowles,[6] R. E. Samuelson,[4] G. S. Orton,[9] L. J. Spilker,[9] T. C. Owen,[10] J. R. Spencer,[11] M. R. Showalter,[12] C. Ferrari,[13] M. M. Abbas,[14] F. Raulin,[15] S. Edgington,[9] P. Ade,[16] E. H. Wishnow[17]

Temperatures obtained from early Cassini infrared observations of Titan show a stratopause at an altitude of 310 kilometers (and 186 kelvin at 15°S). Stratospheric temperatures are coldest in the winter northern hemisphere, with zonal winds reaching 160 meters per second. The concentrations of several stratospheric organic compounds are enhanced at mid- and high northern latitudes, and the strong zonal winds may inhibit mixing between these latitudes and the rest of Titan. Above the south pole, temperatures in the stratosphere are 4 to 5 kelvin cooler than at the equator. The stratospheric mole fractions of methane and carbon monoxide are (1.6 ± 0.5) × 10^{-2} and (4.5 ± 1.5) × 10^{-5}, respectively.

Unlike other moons in the solar system, Titan has a substantial atmosphere and offers an interesting comparison with Earth and the other planets. Its pressure at the surface is 1.5 times Earth's, but its temperature is much colder, 90 to 94 K (*1*–*3*). Like Earth, Titan's atmosphere is primarily N_2, but CH_4 (not O_2) is the next–most abundant constituent. Dissociation of CH_4 and N_2 by ultraviolet sunlight and energetic electron impact leads to a rich mixture of organic compounds (*4*–*6*). Titan's winter polar atmosphere may be analogous to the terrestrial Antarctic ozone hole but with different chemistry. Infrared observations from the Voyager spacecraft indicated cold stratospheric temperatures, strong circumpolar winds, and an enhanced concentration of several organic compounds in the north-polar region, which was coming out of winter in 1980 to 1981 (*7*–*9*). This enhanced concentration suggests that the winter polar atmosphere was isolated from that at low latitudes. Titan has a 16-day period and rotates slowly, like Venus. Both have atmospheres that rotate globally much faster than their surfaces. Unlike Venus, however, Titan has a large seasonal modulation in its stratospheric temperatures and winds (*2*, *7*).

Here we summarize results from early Cassini orbiter observations of Titan by the Composite Infrared Spectrometer (CIRS). The observations were made on 2 July 2004 (flyby T0), shortly after Cassini was inserted into orbit around Saturn, and on 13 December 2004 (flyby TB). CIRS consists of two Fourier-transform spectrometers, which together measure thermal emission from 10 to 1400 cm^{-1} (wavelengths 1 mm to 7 μm) at an apodized spectral resolution selected between 0.5 and 15.5 cm^{-1} (*10*, *11*). The far-infrared interferometer (10 to 600 cm^{-1}) has a 4-mrad field of view on the sky. The mid-infrared interferometer consists of two 1 × 10 arrays of 0.3-mrad pixels, which together span 600 to 1400 cm^{-1}.

Like Earth, Titan has a well-defined stratosphere. It has been well characterized at altitudes up to ~225 km by Voyager radio-occultation and infrared observations (*1*, *7*, *8*) and also by the Infrared Space Observatory (*12*). Titan stellar occultations have been used to probe the mesosphere at altitudes of 300 to 500 km (*13*, *14*). In this region, the retrieved temperature profiles show great variability, possibly because of the influence of vertically propagating waves. The accuracy of the retrieved temperatures decreases at altitudes below ~300 km because of the uncertain contribution of aerosol absorption to the signal. None of these observations defined the stratopause, which is the maximum in the temperature profile separating the mesosphere from the underlying stratosphere. The stratopause temperature and its location are determined by the vertical variation of aerosol heating, infrared cooling to space by C_2H_6, and, to a lesser extent, heating of CH_4 in its near-infrared bands (*15*). At these altitudes, CH_4 is well mixed, but the aerosols tend to decrease with altitude and C_2H_6 increases slowly with altitude (*6*). The spatial resolution of the mid-infrared detector arrays allowed CIRS to observe Titan's atmosphere on the limb, where the line of sight extends through the atmosphere to deep space. In this mode, the altitude coverage and vertical resolution was determined by the array pixels (*11*). Figure 1A shows that vertical profiles up to the 0.01-mbar level (410 km) are feasible. At 15°S, a well-defined stratopause is evident near 0.07 mbar (310 km) with a temperature of 186 K.

CIRS mapped stratospheric temperatures over much of Titan (Fig. 1, B and C) in the second half of 2004, with its mid-infrared arrays in the nadir-viewing mode. This corresponded to early southern summer (solstice was in October 2002). The warmest temperatures were near the equator. Temperatures were moderately colder at high southern latitudes (by 4 to 5 K near 1 mbar), but they were coldest at high latitudes in the north, where it was winter. The thermal wind equation relates the variation of zonally averaged temperatures with latitude to the variation of the mean zonal winds along cylinders parallel to Titan's rotation axis (*16*). The derived zonal winds (Fig. 1D) were weakest at high southern latitudes and increased northward. The maximum winds were at low and mid- northern latitudes, reaching 160 m s^{-1} between 20°

[1]NASA/Goddard Space Flight Center, Code 693, Greenbelt, MD 20771, USA. [2]Science Systems and Applications, 5900 Princess Garden Parkway, Suite 300, Lanham, MD 20706, USA. [3]Department of Astronomy, Cornell University, Ithaca, NY 14853, USA. [4]Department of Astronomy, University of Maryland, College Park, MD 20742, USA. [5]Laboratoire d'Études Spatiales et d'Instrumentation en Astrophysique (LESIA), CNRS–Unité Mixte de Recherche (UMR) 8109, Observatoire de Paris, 5 place Jules Janssen, F-91925 Meudon Cedex, France. [6]Atmospheric, Oceanic, and Planetary Physics, Clarendon Laboratory, Parks Road, University of Oxford, Oxford OX1 3PU, UK. [7]QSS Group, 4500 Forbes Boulevard, Suite 200, Lanham, MD 20706, USA. [8]Department of Earth and Planetary Science, Johns Hopkins University, Baltimore, MD 21218, USA. [9]Jet Propulsion Laboratory, 4800 Oak Grove Drive, Pasadena, CA 91109, USA. [10]University of Hawaii, Institute of Astronomy, 2680 Woodlawn Drive, Honolulu, HI 96822, USA. [11]Department of Space Studies, Southwest Research Institute, 1050 Walnut Street, Suite 400, Boulder, CO 80302, USA. [12]Search for Extraterrestrial Intelligence (SETI) Institute, 515 North Whisman Road, Mountain View, CA 94043, USA. [13]Commissariat de l'Énergie Atomique, Saclay, Service d'Astrophysique, 91191 Gif-sur-Yvette Cedex, France. [14]NASA/Marshall Space Flight Center, SD50 NSSTC, Huntsville, AL 35812, USA. [15]Laboratoire Interuniversitaire des Systèmes Atmosphériques, Université de Paris 7 and 12, CNRS-UMR 7583, 61 Avenue General de Gaulle, 94010 Creteil Cedex, France. [16]Department of Physics and Astronomy, University of Cardiff, 5 The Parade, Cardiff CF24 3YB, UK. [17]Lawrence Livermore National Laboratory and Space Sciences Laboratory, University of California, Berkeley, L-041, Livermore, CA 94551, USA.

*To whom correspondence should be addressed. E-mail: f.m.flasar@nasa.gov

†Present address: LESIA, CNRS-UMR 8109, Observatoire de Paris, 5 place Jules Janssen, F-91925 Meudon Cedex, France.

and 40°N. The zonal winds at the 10-mbar level in Fig. 1D, which are not known, were set to zero. The errors from this assignment should not materially affect the displayed winds where they were strong, at low latitudes and in the north. The largest relative errors are likely to be at high southern latitudes, where the derived winds were smallest (*16*).

The CIRS observations, taken with earlier studies, indicate that the strongest zonal winds migrate seasonally in the stratosphere. Voyager infrared observations, taken in 1980 shortly after the northern spring equinox, indicated that the strongest winds were at mid- and high northern latitudes, and also at high southern latitudes (*8*). Subsequent stellar-occultation central-flash data provided information on the winds on the 0.25-mbar isobar in the upper stratosphere. An occultation of Sgr 28 in 1989, during northern summer, showed a strong jet (175 m s^{-1}) centered at 65°S (*13*, *17*). A more complex wind structure was observed in December 2001, a few months before northern winter solstice; a 220-m s^{-1} jet was centered near 60°N, and a somewhat weaker jet had a maximum near 20°S, with strong winds extending to 60°S (*18*). The CIRS data indicate that the southern-hemispheric winds have weakened and the strongest northern-hemispheric winds have migrated toward the equator (Fig. 1D). This is not a simple hemispheric reflection of the high-latitude jet observed during the Sgr 28 occultation, which occurred approximately one-half–Titan year earlier (*13*).

The lower temperatures at the south pole of Titan during early summer are in marked contrast to the south-polar warming seen in Saturn's stratosphere (*19*). A radiative explanation by itself is not straightforward, because the radiative relaxation time in Titan's upper stratosphere is so short (~1 year, compared with Saturn's orbital period of 29.5 years). Time-dependent radiative models of Titan, which assume opacities that are uniform in latitude, predict that the south pole near 1 mbar is 16 to 17 K warmer than the equator at the current season (*20*). Instead, it is 4 to 5 K colder. The gaseous opacity in the stratosphere

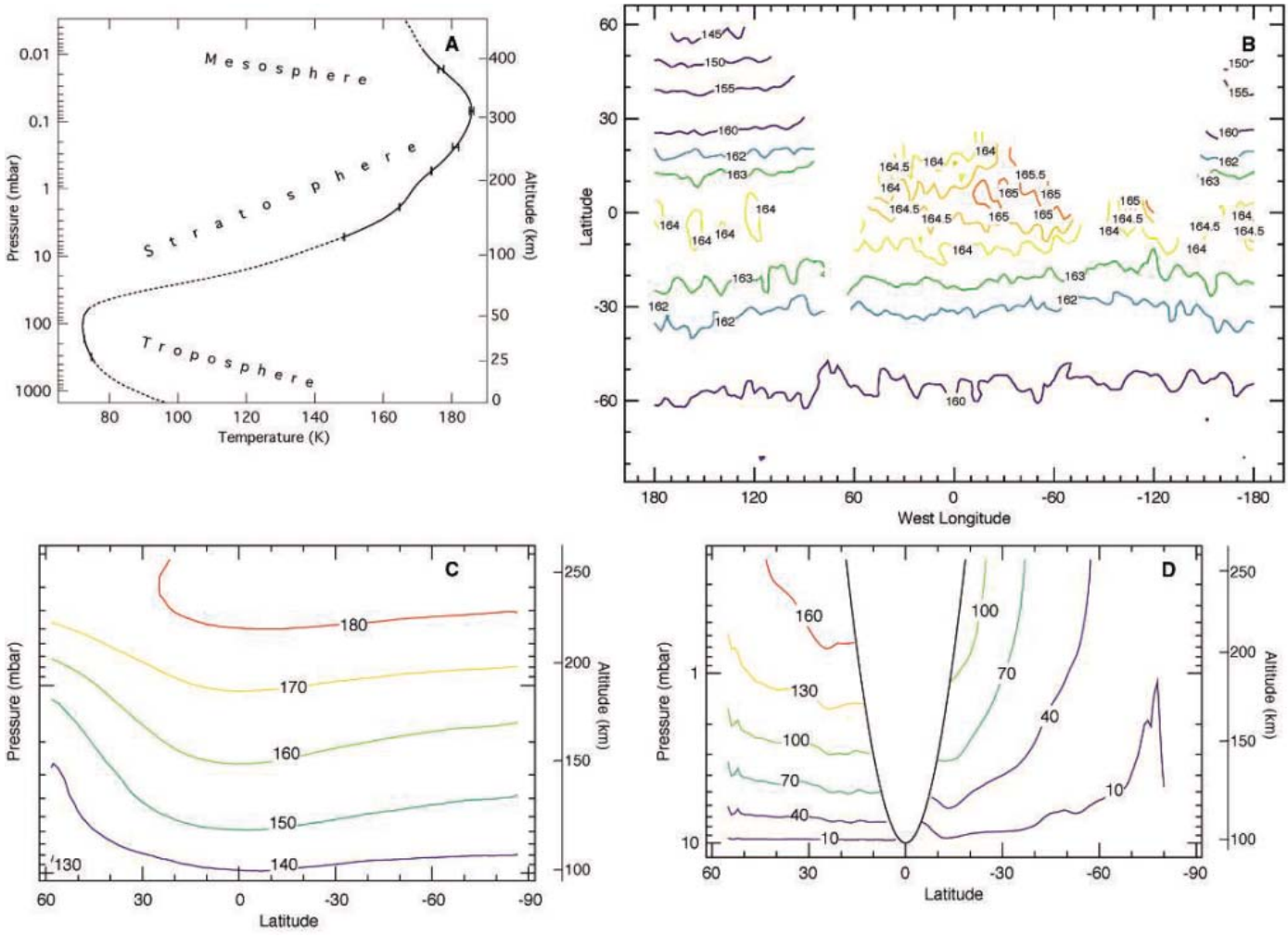

Fig. 1. Temperatures and zonal winds in Titan's atmosphere. (**A**) Vertical temperature profile near 15°S, retrieved from a combination of nadir- and limb-viewing spectra (*16*). The dashed portions of the curve represent the regions where temperatures are not well constrained by the spectra and are more influenced by the Voyager radio-occultation profiles (*1*) and radiative mesospheric models (*15*) used as the initial estimate. (**B**) Temperatures (K) on the 1.8-mbar isobar, obtained from nadir-viewing spectra at 3-cm^{-1} resolution. The map is a combination of observations taken on 2 July 2004, which were primarily in the southern hemisphere at longitudes centered near 0°, and observations on 13 December 2004, which were in both hemispheres at longitudes centered near 146°W. The horizontal resolution is 5° of great-circle arc. The temperature errors from instrument noise are 0.2 K at most locations, increasing to ~0.4 K at high northern latitudes, where there are fewer data. (**C**) Meridional cross section of stratospheric temperatures (K) averaged over available longitudes [see (B) for horizontal coverage], with latitude as the horizontal coordinate and pressure as the vertical coordinate (altitude is indicated on the right). The errors in zonal-mean temperature from noise range from 0.03 to 0.1 K. (**D**) Zonal winds (m s^{-1}), calculated from the temperatures in (C) using the thermal wind equation for a thick atmosphere (*16*). Positive numbers indicate eastward velocities. Winds at the 10-mbar level have been set equal to zero. At low latitudes within the parabola, this boundary condition is insufficient for calculating the winds, and they have been omitted (*16*). At 15° latitude, the noise in temperatures propagates into errors of 6 and 9 m s^{-1} at the 5- and 0.5-mbar levels, respectively; at higher latitudes the error decreases roughly as 1/tan (latitude).

could be heterogeneously distributed so that it cools less at low latitudes than at high latitudes, whereas fewer aerosols at the south pole could lead to less solar heating there (*21*).

The colder south pole may also be a manifestation of a lagged stratospheric cross-equatorial circulation (*8*). Although the radiative relaxation time is short compared with seasonal time scales, temperatures and zonal winds are coupled because of the thermal wind equation. The need to transport axial angular momentum from the hemisphere going into summer, where meridional temperature gradients are weakening, to that going into winter, where the gradients are strengthening, adds an inertia to the system that causes a phase lag of about one full season. It may be that the circulation is transporting angular momentum northward in early southern summer, with an attendant upwelling at high southern latitudes and adiabatic cooling. The vertical velocities required are small, about 0.05 cm s^{-1} (*16*). Two-dimensional coupled radiative-dynamical models with parameterized eddy mixing, which simulate the transport of radiatively active gaseous constituents and aerosols, have been developed to predict Titan's seasonal behavior. Although these models have been tuned to reproduce the stratospheric temperatures observed by Voyager reasonably well, they fail to account for the cooler south-polar temperatures observed now, instead predicting temperatures ~10 K warmer than at the equator (*22*).

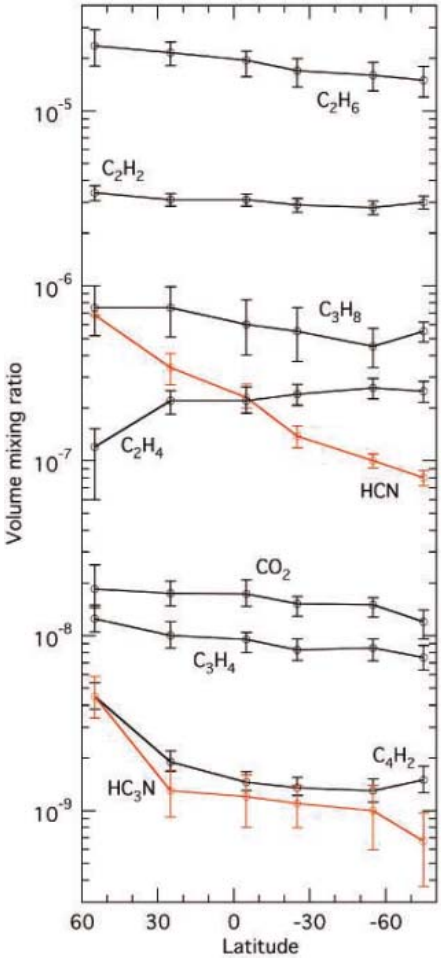

Fig. 2. Meridional distribution of several hydrocarbons and nitriles, retrieved from the spectral regions displayed in fig. S3, but at a resolution of 3 cm^{-1} (*16*). The vertical distribution of the gases was assumed to be uniform above the condensation level in the lower stratosphere. The temperature profile in Fig. 1A was used as an initial estimate, and the stratospheric temperatures were retrieved at different latitudes from radiances in the ν_4 band of CH_4. The errors indicated include those from noise in the spectral region containing the emission lines of the individual molecules, as well as from noise in the retrieved stratospheric temperatures.

Titan's atmosphere is rich in organics: hydrocarbons and nitriles (figs. S1 to S3). Hydrocarbons form from the photolytic and catalytic dissociation of CH_4. Nitriles are created by dissociation of N_2 from ultraviolet sunlight and impacts by energetic electrons from photoionization and the magnetosphere, followed by reactions with hydrocarbon radicals (*4*–*6*). Voyager 1 infrared data (*9*), which were obtained during Titan's early northern spring, showed that the concentrations of nitriles (HCN, HC_3N, and C_2N_2) and the more photochemically active hydrocarbons (C_2H_4, C_3H_4, and C_4H_2) were enhanced at high northern latitudes by factors of 10 to 100, compared with the concentrations at low latitudes. The CIRS observations in early northern winter show an enhancement of several of the same constituents at northern latitudes (Fig. 2), but by a smaller amount. Indeed, C_2H_4 now shows not an enhancement, but a twofold depletion at high northern latitudes. If the Voyager results are typical, then one can expect a build-up of the relative concentrations of these organic compounds through the winter into early spring. Numerical simulations suggest that the enhancement of these species is associated with an axisymmetric meridional circulation that subsides in the polar region during winter and early spring (*22*, *23*). Most of the enhanced species have larger mixing ratios at higher altitudes, where they are photochemically formed. Subsidence brings these enriched parcels of atmosphere down to the levels of the observed emission, ~1 to 10 mbar (*9*). Subsidence also brings the species into winter shadow, where they are shielded from further photodissociation (*24*). For the enhancements to persist at high northern latitudes, lateral mixing with the atmosphere at other latitudes must be inhibited, compared with the transport by the meridional circulation.

Titan's strong circumpolar winds (Fig. 1D) may facilitate this isolation, which is also a critical ingredient of the terrestrial Antarctic polar vortex during winter (*25*). There, the concentrations of species such as CH_4 and HF imply strong descent from the mesosphere well into the stratosphere, and these gases have sharp gradients across the polar vortex (*26*). Indeed, the whole process leading to the ozone hole within the vortex—the cold polar temperatures leading to the formation of stratospheric clouds, which denitrify the polar atmosphere by heterogeneous chemistry, liberating gaseous Cl_2; its photodissociation in the spring into Cl, which in turn irreversibly destroys O_3—requires the polar air to be isolated from the warmer, lower-latitude air that contains reactive nitrogen compounds (*25*). Planetary waves, which normally efficiently mix air masses, are unable to penetrate the polar vortex until later in spring, when polar temperatures rise and the circumpolar winds weaken. Planetary-scale waves on Titan have not been well characterized yet. The CIRS observations indicate that any thermal contrasts associated with waves are small at present. The maximum zonal variation in temperature observed in the available coverage shown in Fig. 1B is <1 to 1.5 K.

In the southern hemisphere, where it was summer, the hydrocarbons and nitriles were more uniformly distributed with latitude (Fig. 2). The numerical simulations (*23*) attribute such flat structure to rising motions in the summer hemisphere, bringing material impoverished in the trace organics from altitudes below their condensation level in the lower stratosphere. An interesting result pertains to C_2H_4. Recent analysis of Keck broad-band filter observations acquired from 1999 to 2002 suggests that C_2H_4 was 12 to 20 times as abundant in the south-polar region as at the equator (*27*). The CIRS data show little enhancement at the south pole. The relevant C_2H_4 photolysis rate [from (*28*), adapted for full illumination and $\lambda > 160$ nm] is 2×10^{-7} s^{-1}, or a 60-day lifetime for an individual molecule. Although a 12- to 20-fold enhancement in C_2H_4 could be removed in 150 to 180 days photochemically, it is not clear what caused the enhancement reported from the Keck data, because the period of observation was already middle to late spring in the southern hemisphere, a period when rising motions are predicted (*23*), and the diurnally averaged solar illumination changes slowly.

CH_4 is a condensable gas in Titan's troposphere. Analysis of Voyager's far-infrared and radio-occultation data indicate that its mole fraction near the surface ranges from 0.06 at low latitudes to 0.02 at high latitudes (*3*). The lifetime of CH_4 in Titan's atmosphere is only 4×10^7 years (*29*), and it requires a surface or interior source if the current inventory is typical of Titan's long-term history. The distribution of stratospheric CH_4 is probably uniform (*17*). Analyses of Voyager's infrared observations (in the ν_4 band of CH_4 near 1300 cm^{-1}) and radio-occultation soundings led to estimates of the CH_4 stratospheric mole fraction in the range 0.005 to 0.045 (table S1). Part of this uncertainty resulted because the CH_4 ν_4-band line-formation region is near 1 mbar, where Voyager radio-occultation data have large

errors. Uncertainties in the argon abundance and the cold-trapping constraint applied in the tropopause region also contributed to the errors in the estimated CH_4 mole fraction. The use of the pure rotational lines of CH_4 in the far-infrared (fig. S2B) eliminates many of these ambiguities. The line-formation region is in the stratosphere between 3 and 20 mbar (140 to 80 km altitude), which mostly lies between the two regions accessible to direct-temperature sounding, the upper troposphere and tropopause region between 500 and 50 mbar (20 to 60 km), and the upper stratosphere between 5 and 0.5 mbar (130 to 230 km). Nevertheless, interpolation between the two altitude ranges constrains the temperatures sufficiently to make an improved determination of the stratospheric CH_4 abundance. The optically thick ν_4 band is not too sensitive to the CH_4 abundance, but is more sensitive to the stratospheric temperatures, because it is on the Wien tail of the Planck function. The rotational lines are almost optically thin, and therefore they are more sensitive to the stratospheric CH_4 abundance but less sensitive to temperature, because they lie at wave numbers below those at the peak emission (fig. S1) (*30*). Figure S4 illustrates fits for synthetic spectra with different CH_4 mole fractions. The best fit in a least-squares sense to all the rotational lines corresponds to a mole fraction of $(1.6 \pm 0.5) \times 10^{-2}$. This is comparable to the mole fraction determined at 1000- to 1200-km altitude from remote-sensing and in situ measurements (table S1), indicating that CH_4 is fairly well mixed up to these altitudes.

In addition to containing CH_4, the far-infrared contains rotational lines of stratospheric emission from CO and HCN (fig. S2A). The rotational line-formation region of CO is similar to that of CH_4. We find from a least-squares fit of all the lines observed in independent selections of spectra from the T0 and TB flybys that the CO mole fraction is $(4.5 \pm 1.5) \times 10^{-5}$, assuming that it is uniform with altitude (*31*). This is consistent with the determination $[(5.0 \pm 1.0) \times 10^{-5}]$ by Gurwell and Muhleman (*32*), and marginally consistent with what Hidayat *et al*. (*33*) inferred below the 1-mbar level from disk-averaged heterodyne millimeter observations $[(2.5 \pm 0.5) \times 10^{-5}]$. Within the errors, it is also consistent with the tropospheric value $[(3.2 \pm 1.0) \times 10^{-5}]$ derived from 5-μm spectra (*34*), although one cannot rule out that the stratosphere has a higher concentration. One might expect the mole fractions of CO in the stratosphere and troposphere to be more or less equal, because CO does not condense at the temperatures and abundances observed, and the time constant for photochemical adjustment under current conditions is $\sim 10^9$ years (*4*).

References and Notes

1. G. F. Lindal *et al.*, *Icarus* **53**, 348 (1983).
2. D. M. Hunten *et al.*, in *Saturn*, T. Gehrels, M. S. Matthews, Eds. (Univ. of Arizona Press, Tucson, AZ, 1984), pp. 671–759.
3. R. E. Samuelson, N. R. Nath, A. Borysow, *Planet. Space Sci.* **45**, 959 (1997).
4. Y. L. Yung, M. Allen, J. P. Pinto, *Astrophys. J. (Suppl.)* **55**, 465 (1984).
5. D. Toublanc *et al.*, *Icarus* **113**, 2 (1995).
6. E. H. Wilson, S. K. Atreya, *J. Geophys. Res.* **109**, E06002, 10.1029/2003JE002181 (2004).
7. F. M. Flasar, R. E. Samuelson, B. J. Conrath, *Nature* **292**, 693 (1981).
8. F. M. Flasar, B. J. Conrath, *Icarus* **85**, 346 (1990).
9. A. Coustenis, B. Bézard, *Icarus* **115**, 126 (1995).
10. V. Kunde *et al.*, in *Cassini/Huygens: A Mission to the Saturnian Systems*, L. Horn, Ed. (SPIE Proceedings, The International Society for Optical Engineering, Bellingham, WA, 1996), pp. 162–177.
11. F. M. Flasar *et al.*, *Space Sci. Rev.* **115**, 169 (2004).
12. A. Coustenis *et al.*, *Icarus* **161**, 383 (2003).
13. W. B. Hubbard *et al.*, *Astron. Astrophys.* **269**, 541 (1993).
14. B. Sicardy *et al.*, *Icarus* **142**, 357 (1999).
15. R. V. Yelle, *Astrophys. J.* **383**, 380 (1991).
16. Materials and methods are available as supporting material on *Science* Online.
17. F. M. Flasar, *Planet. Space Sci.* **46**, 1125 (1998).
18. A. Bouchez, thesis, California Institute of Technology (2004); available at www.gps.caltech.edu/~antonin/thesis/.
19. F. M. Flasar *et al.*, *Science* **307**, 1247 (2005).
20. F. Hourdin *et al.*, *Icarus* **117**, 358 (1995).
21. B. Bézard, A. Coustenis, C. P. McKay, *Icarus* **113**, 267 (1995).
22. F. Hourdin, S. Lebonnois, D. Luz, P. Rannou, *J. Geophys. Res.* **109**, E12005, 10.1029/2004JE002282 (2004).
23. S. Lebonnois, D. Toublanc, F. Hourdin, P. Rannou, *Icarus* **152**, 384 (2001).
24. Y. L. Yung, *Icarus* **72**, 468 (1987).
25. M. R. Schoeberl, M. R. Hartman, *Science* **251**, 46 (1991).
26. J. T. Bacmeister, M. R. Schoeberl, M. E. Summers, J. R. Rosenfeld, X. Zhu, *J. Geophys. Res.* **100**, 11669 (1995).
27. H. G. Roe, I. de Pater, C. P. McKay, *Icarus* **169**, 440 (2004).
28. J. I. Moses *et al.*, *Icarus* **143**, 244 (2000).
29. D. Strobel, *Planet. Space Sci.* **30**, 839 (1982).
30. A. Coustenis *et al.*, *Icarus* **102**, 240 (1993).
31. To fit the CO rotational lines, we also had to fit the HCN lines. To do so, we used the vertical profile derived by Marten *et al.* (*35*) from disk-averaged millimeter observations, but scaled by a constant factor, $2.5^{+1.5}_{-1.1}$ (where +1.5 and –1.1 are the error values) for a selection of T0 spectra centered at 7°S and 2.8 ± 1 for a selection of TB spectra centered at 17°N.
32. M. A. Gurwell, D. O. Muhleman, *Icarus* **117**, 375 (1995).
33. T. Hidayat, A. Marten, B. Bézard, D. Gautier, *Icarus* **133**, 109 (1998).
34. E. Lellouch *et al.*, *Icarus* **162**, 125 (2003).
35. A. Marten, T. Hidayat, Y. Biraud, R. Moreno, *Icarus* **158**, 532 (2002).
36. S. Albright, M. H. Elliott, and J. S. Tingley assisted with instrument commanding and data processing; D. Crick, M. de Cates, and S. Brooks assisted with observation designs; and N. Stone helped with data analysis. We acknowledge support from the NASA Cassini Project, the British Particle Physics and Astronomy Research Council, the Centre National d'Études Spatiales (CNES), and the Institut National des Sciences de l'Univers (CNRS/INSU).

Supporting Online Material
www.sciencemag.org/cgi/content/full/308/5724/975/DC1
Materials and Methods
Figs. S1 to S4
Table S1
References

16 February 2005; accepted 14 April 2005
10.1126/science.1111150

REPORT

The Cassini UVIS Stellar Probe of the Titan Atmosphere

Donald E. Shemansky,[1]* A. Ian F. Stewart,[2] Robert A. West,[3] Larry W. Esposito,[2] Janet T. Hallett,[1] Xianming Liu[1]

The Cassini Ultraviolet Imaging Spectrometer (UVIS) observed the extinction of photons from two stars by the atmosphere of Titan during the Titan flyby. Six species were identified and measured: methane, acetylene, ethylene, ethane, diacetylene, and hydrogen cyanide. The observations cover altitudes from 450 to 1600 kilometers above the surface. A mesopause is inferred from extraction of the temperature structure of methane, located at 615 km with a temperature minimum of 114 kelvin. The asymptotic kinetic temperature at the top of the atmosphere determined from this experiment is 151 kelvin. The higher order hydrocarbons and hydrogen cyanide peak sharply in abundance and are undetectable below altitudes ranging from 750 to 600 km, leaving methane as the only identifiable carbonaceous molecule in this experiment below 600 km.

On 13 December 2004, the Cassini UVIS observed the occultation of two stars, Shaula (λ Sco) and Spica (α Vir) near the end of the second Titan flyby (labeled T_B). Both measurements of atmospheric transmission were obtained in egress: Spica was in the northern hemisphere over a range of latitudes and Shaula at a southern latitude, –36° (fig. S1). Observations were made with the extreme ultraviolet (EUV) and the far ultraviolet (FUV) UVIS channels (*1*). Data from Spica were compromised by spacecraft pointing drift but provide useful comparative atmospheric structural information at lower altitudes (*2*). The spectral range of the FUV observations (110 nm to 190 nm) is effective for the identification and determination of the hydrocarbon species abundances. These complement and extend solar occultation results from Voyager 1 and 2 in 1980 to 1981 (*3*, *4*) into the range 900 to 1200 km for CH_4. Our data

cover altitudes of 450 to 1600 km, showing the presence of a mesopause at 615 km. The distribution of higher order hydrocarbons and HCN in the results reported here shows a distinct divergence from inferences in the recent reanalysis (*4*) of the Voyager data.

We begin the description of the properties of the photon transmission at low altitudes, where the stellar photons are first detected in egress. Although the Spica results were affected by pointing drift at high altitude, a useful comparison can be made with Shaula at low altitudes (*2*), where transmission properties of species, other than the N_2, hydrocarbons, and HCN identified here, determine the observed photon flux. In the spectral region 180 to 190 nm defined as *c* (*2*), extinction by the carbonaceous species (and N_2) considered here is negligible. The Spica occultation occurred in the northern hemisphere over a latitude range of 70° to –30°, whereas Shaula occurred at a nearly constant –36° latitude (fig. S1). Measurable signal begins (first light) in *c* at 293 km in Shaula data and 279 km in Spica (fig. S2). The extinction of radiation in region *c* below 300 km and extending to below 200 km is attributed to species other than those identified in the UVIS spectra. The altitude difference (14 km) in first light between Shaula and Spica is attributed to global nonuniformity in atmospheric structure, because the asymptotic scale heights in the two data sets differ by 50% (11.1 and 7.5 km), with extinction a factor of 4 to 5 deeper for Shaula compared with Spica at 360 km (fig. S2), whereas the transmission curves match almost exactly above 500 km. The species in this region of the atmosphere do not have an identified spectral signature but are important components affecting the thermal and dynamic structure (*5*, *6*) that constitutes a major target of the Cassini Program. Aerosols are probably responsible for the extinction in this region. The narrow feature at 510 km in the Shaula profile may be the scattering haze seen in reflected sunlight in the Cassini Imaging Science Subsystem (ISS) (*7*). The data analyzed here are composed of sets of five contiguous exposure records that contain the spectral signals integrated over intervals of approximately 20 km of vertical atmospheric structure. The effective impact parameter altitude for analysis of each group of five measurements is determined by weighting against the estimated atmospheric scale height. The minimum scale height in the CH_4 data is ~40 km.

The reduction process to obtain species line-of-sight (LOS) abundances, by necessity, was carried out by simulation of the instrument response to modeled spectra, because of substantial internal scattering effects in the combined optical and detector system. The absorption structures of the six species recognized in the data have distinctive spectral shapes, but they are heavily overlapped. The data-reduction process was therefore carried out by iterative fitting of each of the observed absorption spectra by forward synthesis (*2*). Figure 1 shows the derived altitude distribution of abundance (molecules cm^{-2}). Uncertainties in the derived values, including a large component attributed to problems with the experimental cross sections of the higher hydrocarbons and HCN discussed in the supplementary online materials (*2*), are shown in Fig. 1. The photoabsorption cross sections (*8*–*20*) used here are the most recently available. The absorption spectra allow measurement of six species in the Titan upper atmosphere: CH_4, C_2H_2, C_2H_4, C_2H_6, HCN, and C_4H_2 (methane, acetylene, ethylene, ethane, hydrogen cyanide, and diacetylene) (Fig. 1).

The most important properties of the derived abundances from the present experiment plotted in Fig. 1 are the presence of a distinct change in slope in all of the species near 800 km altitude and the sudden leveling off of the LOS abundances of the higher hydrocarbons and HCN below 750 and 600 km. Model calculations fitting the CH_4 abundance data are shown plotted over the data in Fig. 1. The model fit to the data provides an extraction of the density, fundamental scale height, and temperature profiles of this species. This detailed model calculation, described below, was limited to CH_4 in the present work. The leveling off in the abundances of the higher order hydrocarbons and HCN below 750 and 600 km is an indicator that these species are not measurably present below these altitudes. The latter result is strongly divergent from the recent reanalysis of the Voyager solar occultation (*4*). The observed changes in the profiles of the higher order hydrocarbon and HCN distribution indicate that these species are subject to strong photochemical source-and-sink processes. Figure 1 includes abundance values for CH_4 from the Voyager experiment (*4*) and calculated LOS values from the Cassini Ion Neutral Mass Spectrometer (INMS) experiment inbound density measurements from the first Titan flyby (labeled T_A) provided by Yelle (*21*).

We obtain values of species number densities from the abundances shown in Fig. 1 by assuming that the atmosphere is hemispherically uniform, because the observations are intrinsically an integration along the LOS through the extent of the atmosphere. The derivation of the density, scale height, and temperature distribution of CH_4 is obtained assuming a hydrostatic atmosphere. The transmission of the stellar flux through the atmosphere is developed through the relations

$$\ln\left(\frac{I_\nu}{I_\nu^0}\right) = -2\int_0^\ell k_\nu d\ell \quad (1)$$

$$k_\nu = \sigma_\nu n(\ell) \quad (2)$$

$$\tau_\nu = k_\nu \bar{\ell} \quad (3)$$

$$\eta = \bar{n}(\ell)\bar{\ell} \quad (4)$$

where ℓ (cm) is location along the path of the flux through the atmosphere, k_ν is the absorption coefficient (cm^{-1}), τ_ν is optical depth, $n(\ell)$ (cm^{-3}) is gas number density, σ_ν (cm^2) is the scattering or absorption cross section, I_ν^0 is the incident differential stellar flux, and I_ν is the emergent differential flux observed by the spectrograph. The quantity $\eta_i(h)$ (cm^{-2}) is the abundance for species *i*, and the bar quantities are effective values.

We based our analysis on the quantity I_ν/I_ν^0 so that no absolute values of stellar flux are required. An example of a $\ln(I_\nu/I_\nu^0)$ spectrum containing observed data compared with the model simulation used to extract absorber

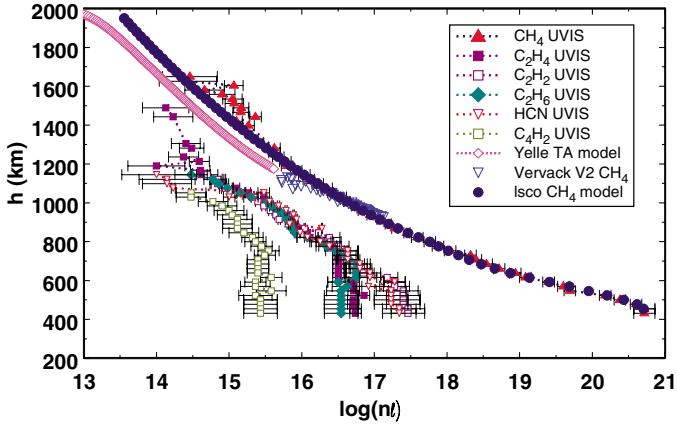

Fig. 1. Derived abundances of hydrocarbon species and HCN identified in the UVIS occultation of Shaula at Titan flyby T_B. The data are plotted in base 10 logarithm of abundance (cm^{-2}) against line-of-sight impact parameter *h*. A model fit to the CH_4 data is shown superimposed, which has allowed derivation of temperature, scale height distribution, and number density as functions of altitude. The calculated abundance of CH_4 derived from the INMS data (*21*) from flyby T_A (fig. S1) is also included. The Vervack *et al.* (*4*) derivation of CH_4 abundance from the Voyager encounter is also plotted, indicating close conformance with the INMS-derived values (*21*).

[1]Department of Aerospace Engineering, University of Southern California, University Park, Los Angeles, CA 90089, USA. [2]University of Colorado, Laboratory for Atmospheric and Space Physics, Boulder, CO 80303, USA. [3]Jet Propulsion Laboratory, Pasadena, CA 91109, USA.

*To whom correspondence should be addressed. E-mail: dons@hippolyta.usc.edu

abundances, $\eta_i(h)$, is shown in Fig. 2. Reducing the values of $\eta_i(h)$ to atmospheric vertical density distribution requires, effectively, differentiation of $\eta_i(h)$ as a function of LOS impact parameter, h, the minimum vertical altitude in the atmosphere. Direct differentiation of $\eta_i(h)$ is not practical, and in practice the density must be derived through an iterative forward-modeling process. The fundamental equation connecting pressure P and mass density $\rho_i(h)$ at altitude h is

$$dP = -g\rho dh \quad (5)$$

$$\frac{dP}{P} = -\frac{1}{H(h)}dh \quad (6)$$

$$H(h) = \frac{kT(h)}{\bar{m}(h)g(h)} \quad (7)$$

$$\rho_i(h) = n_i(h)m_i(h) \quad (8)$$

where H is scale height, and $g(h)$, $m(h)$, and $T(h)$ (gravitational acceleration, effective mass, and temperature, respectively) are altitude-dependent quantities, as indicated. The number density $n_i(h)$ is obtained from

$$\rho_i(h) = \frac{\rho_i(h_0)T(h_0)}{T(h)} exp\left[\int_{h_0}^{h} - \frac{\bar{m}(h)}{k}\frac{g(h)dh}{T(h)}\right] \quad (9)$$

$n_i(h)$ must then be derived from $\eta_i(h)$ through the relation

$$\eta(h) = 2.\int_0^{\ell} n(\ell, h)d\ell \quad (10)$$

These equations relate to a hydrostatic atmosphere and for this reason are limited in applicability to the globally nonuniform Titan atmosphere. If the atmosphere is not simple, as is the case for Titan, Eq. 10 must be solved iteratively on the distribution of $\eta_i(h)$ to extract $n_i(h)$, $m(h)$, $T(h)$, and ultimately $H(h)$ [$g(h)$ is, of course, a known quantity]. The quantity $m(h)$ has a complex dependence on atmospheric dynamics in this case (*22*), but there are constraints that limit behavior. Low in the atmosphere, it is safe to assume a fully mixed structure, so $m(h \ll)$ is fixed to the value 28 atomic mass units (amu), determined by the dominant N_2 component. It is this factor that constrains $T(h)$ for CH_4 in our analysis at altitudes up to 700 km. The derived temperature and scale height distribution for CH_4 is given in Fig. 3. Solutions to higher altitude then involve a collision frequency and bulk motion (diffusion) dependent transition to the asymptotic diffusive-separation value of $m(h) =$ 16 amu for CH_4. The departure from a mixed to diffusively separated atmosphere is indicated in Fig. 3 in the plot of the inferred N_2 scale height profile, shown as open triangles above 800 km, to be compared to the closed triangles. This result does not coincide with the analysis of the Cassini INMS experiment (*23*) but does agree approximately with recent model calculations (*24–26*).

The atmospheric kinetic temperature extracted from the derived CH_4 abundance declines rapidly with increasing altitude from 173 K at 450 km to 114 K at 615 km and rises at higher altitudes to 151 K at the top of the atmosphere. The location of the minimum temperature coincides approximately with the location of maximum abundance of HCN and the higher order hydrocarbons and marks the location of maximum infrared radiative cooling to space (Fig. 1). The kinetic temperature at the top of the atmosphere is, within 5%, in agreement with the results of the in situ Cassini INMS (*23*) (149 K) at the first Cassini encounter (T_A). Above 1200 km, the scale height depends on altitude according to the variation in $g(h)$, with constant $m(h \gg) = 16$ amu and kinetic temperature rising from 148 K to a terminal 151 K. The modeled values of CH_4 abundance shown in Fig. 1 are based on the iteratively determined CH_4 scale heights and temperatures given in Fig. 3. The sharp decline in temperature from an altitude of 450 km to 615 km required to fit the Shaula CH_4 abundance distribution has a temperature lapse rate of –1 K/km at 450 km and a mean of –0.37 K/km to the mesopause (for Earth, –6 K/km between stratopause and mesopause), compared with a predicted adiabatic lapse of –0.94 K/km. Figure 3 includes a plot of the Voyager results from the radio occultation (*27*) measurements showing the derived lower atmosphere temperature structure from ground level to 200 km, leaving a gap between 200 km and 450 km with the present results. The Yelle *et al.* (*28*) recommended and minimum engineering models of vertical temperature distribution are also shown in Fig. 3.

The solution of Eq. 10, confined by the abundance values derived from the observations, to obtain the temperature and scale height profiles proceeds through the integra-

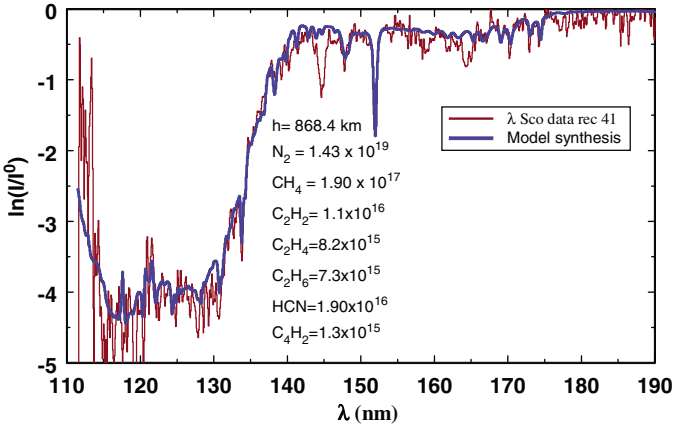

Fig. 2. Example of observed Shaula transmission spectrum from the Cassini UVIS FUV spectrograph, compared with a model synthesis of the absorbers CH_4, C_2H_2, C_2H_4, C_2H_6, HCN, and C_4H_2 at weighted mean impact parameter h = 868.4 km. Abundance values of the absorbers (cm^{-2}) are given. A distinct deficiency in the fit to the observed transmission spectrum appears at 144.5 nm and 164.5 nm, identified as Rydberg resonances in C_4H_2. The experimental data for C_4H_2 are saturated in these features and cannot reproduce the observed spectrum at these locations. At deeper locations in the atmosphere, modeled C_2H_2 resonances that are satisfactory in the spectrum shown here are no longer adequate because of temperature dependence in the absorption properties. Structure near the H Lyα line in the stellar spectra is caused by the dominance of internal instrumental scattering where the stellar flux is negligible.

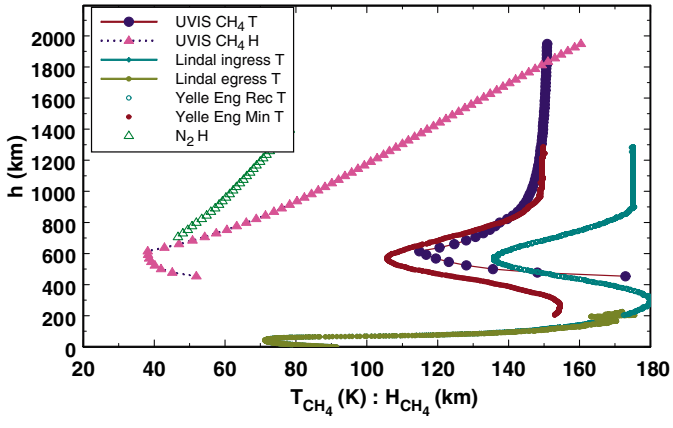

Fig. 3. Scale height (H) and temperature (T) derived for CH_4 from a model fit to the UVIS FUV abundance data shown in Fig. 1. The inferred scale height for N_2 is shown, indicating the location of departure from a mixed atmosphere in this analysis. The Voyager radio occultation results (*27*), giving temperature distribution from 0 to 200 km, are included for comparison, along with the Yelle *et al.* (*28*) recommended and minimum engineering models. The recommended model (*28*) is based on the original analysis of the Voyager Titan occultation, which reported a top-of-atmosphere temperature of 178 K.

tion of Eq. 9, directly provides an extraction of the species density distribution. The densities for CH_4 obtained in this way are shown in Fig. 4. The densities of the remaining species are estimated by rough approximation to the modeling process described here for CH_4. The densities at selected altitudes for the measured species, compared with recent model calculations (*24*), are shown in Table 1. The analysis from the Vervack *et al.* (*4*, *29*) work on the Voyager encounter data is included in Fig. 4. A model fit to the INMS (*23*) data, beginning at 1174 km, is also shown in Fig. 4, extended through the post-T_A model calculations by Yelle (*21*). The INMS (*23*) densities fall below the present values by a factor of 2 at 1200 km. Important aspects of the comparison of these results are that the INMS-Yelle CH_4 densities parallel the present values above 1200 km (which indicates both to be diffusively separated distributions at essentially the same temperature) and that below 1200 km, the Vervack *et al.* and INMS-Yelle results show smaller CH_4 scale heights than the present work (Fig. 4). This trend is consistent with the high-altitude transition to a mixed atmosphere in the former inferred isothermal structure, compared with the downwardly decreasing temperature in the present results with a significantly lower homopause. It is plausible that these differences are driven by atmospheric dynamics (*30*, *31*), because the Voyager and INMS observations were obtained across the terminator and the UVIS LOS was primarily in the dark southern hemisphere atmosphere (fig. S1). We regard this difference as probably driven by global nonuniformity in atmospheric structure rather than reflecting actual differences in data extraction in the two experiments, but there is certainly room for error on either side of this issue. The Voyager ingress and egress results straddle Shaula at 900 km (Fig. 4). Model (*24*) calculations agree within uncertainty with our determination of CH_4 density at the lower altitudes, but the model shows a trend (Fig. 4 and Table 1) from low to high altitude consistent with differences in applied temperature structure. In contrast, our data show greater densities than the model (*24*) for the higher hydrocarbons and HCN by factors of at least 2 (Table 1). The consistently larger derived densities for all of these species suggest that the differences are physically real. The Cassini UVIS data also imply that the lower atmosphere is layered (Fig. 1) in the higher order hydrocarbons and HCN. Below 600 km, the density of these species drops precipitously to undetectable levels, to mixing ratios four to six orders of magnitude below that of CH_4. This result is in strong disagreement with inferred measured densities of higher order hydrocarbons and HCN from the Voyager experiment (*4*) below 600 km. The implied lack of efficient radiators below 600 km provides a primary reason for the rise in the derived kinetic temperature below 615 km shown in Fig. 1.

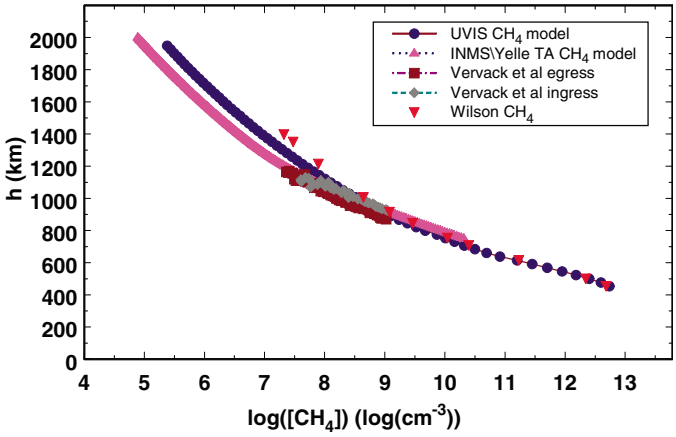

Fig. 4. The density distribution of CH_4 derived from the reduction of the UVIS Shaula occultation data is compared with the INMS (*21*) inbound values and the ingress-egress extraction by Vervack *et al.* (*4*, *29*) from the Voyager occultation. The CH_4 densities in the Wilson and Atreya (*24*) model are also plotted at selected altitudes. (See Table 1.)

This structure is different from that implied in photochemical models of the Titan atmosphere, in large part because atmospheric hazes are the least understood components of the Titan atmosphere. No published models to date directly address the thermal, radiative, and collisional accommodation properties of the haze in constraining the atmospheric thermal structure (*24*, *26*, *32*).

The UVIS occultation experiment at the Titan T_B flyby thus shows the presence of a mesopause with a relatively deep minimum in temperature in the dark south latitude atmosphere. The inference is that this is a structure similar to Earth's mesopause, where the effect of radiative cooling in reducing atmospheric temperature is balanced by the downward flow of heat from the thermosphere. Normalizing to the density of N_2 established at 1174 km by the INMS experiment, our predicted density of N_2 at 615 km using the UVIS temperature profile is 4×10^{13} cm^{-3}. This is a high value, and it remains to be seen whether this is compatible with the density profile from the surface up to 200 km determined by the Voyager radio occultation or whether atmospheric dynamics seriously affects vertical distribution in local time (*30*, *31*). Sicardy *et al.* (*31*) report the presence of a strong 200 m s^{-1} jet at northern latitudes, tapering to zero in south latitudes, and a well-confined inversion layer with a temperature increase of more than 15 K in a span of 6 km near 510 km, in ground-based stellar occultation observations spanning the altitude range 250 to 550 km. A layer of the reported subscale height size (*31*) would be attenuated in the UVIS T_B experi-

Table 1. Derived species densities at selected altitudes from the Cassini UVIS experiment compared with model calculations by Wilson and Atreya (*24*).

Altitude (km)		Number density (cm^{-3})					
h		CH_4*	C_2H_2†	C_2H_4†	C_2H_6†	C_4H_2†	HCN†
454	‡	5.5×10^{12}	‖	‖	‖	‖	‖
	§	5.5×10^{12}	3.6×10^{9}	1.3×10^{8}	6.0×10^{9}	4.9×10^{6}	7.4×10^{8}
500	‡	2.5×10^{12}	‖	‖	‖	‖	‖
	§	2.2×10^{12}	1.8×10^{9}	1.4×10^{8}	2.7×10^{9}	6.9×10^{6}	4.1×10^{8}
615	‡	1.6×10^{11}	1.4×10^{9}	‖	‖	‖	3.1×10^{8}
	§	1.7×10^{11}	3.2×10^{8}	1.2×10^{8}	3.6×10^{8}	6.5×10^{6}	1.0×10^{8}
707	‡	2.1×10^{10}	3.9×10^{8}	‖	2.8×10^{8}	‖	3.3×10^{8}
	§	2.6×10^{10}	9.9×10^{7}	8.5×10^{7}	1.1×10^{8}	2.4×10^{6}	4.3×10^{7}
753	‡	1.0×10^{10}	¶	¶	2.2×10^{8}	1.4×10^{7}	2.1×10^{8}
	§	1.1×10^{10}	5.9×10^{7}	7.1×10^{7}	6.7×10^{7}	1.4×10^{6}	3.0×10^{7}
845	‡	2.4×10^{9}	1.7×10^{8}	6.9×10^{7}	6.8×10^{7}	9.7×10^{6}	5.3×10^{7}
	§	2.7×10^{9}	2.3×10^{7}	4.1×10^{7}	2.3×10^{7}	4.0×10^{5}	1.7×10^{7}
914	‡	9.6×10^{8}	5.1×10^{7}	4.6×10^{7}	4.1×10^{7}	9.4×10^{6}	4.1×10^{7}
	§	1.2×10^{9}	1.2×10^{7}	2.3×10^{7}	9.0×10^{6}	1.4×10^{5}	1.1×10^{7}
1006	‡	3.3×10^{8}	2.0×10^{7}	2.5×10^{7}	2.6×10^{7}	4.3×10^{6}	3.2×10^{7}
	§	4.5×10^{8}	4.5×10^{6}	8.8×10^{6}	2.4×10^{6}	3.5×10^{4}	5.4×10^{6}
1213	‡	4.3×10^{7}	‖	¶	‖	‖	‖
	§	8.0×10^{7}	4.9×10^{5}	8.0×10^{5}	1.4×10^{5}	9.5×10^{2}	6.2×10^{5}
1350	‡	8.3×10^{7}	‖	9.3×10^{6}	‖	‖	‖
	§	3.0×10^{7}	1.2×10^{5}	1.7×10^{5}	2.6×10^{4}	7.3×10^{2}	1.4×10^{5}
1397	‡	1.3×10^{7}	‖	¶	‖	‖	‖
	§	2.2×10^{7}	7.2×10^{4}	1.0×10^{5}	1.5×10^{4}	3.1×10^{2}	8.3×10^{4}

*UVIS values estimated uncertainty < ±20%. †UVIS values column systematic uncertainties as large as 100%. Point-to-point uncertainties ~30%. ‡UVIS data values. §Wilson and Atreya model (*24*). ‖Densities too low to measure. ¶Densities not calculated.

ment. It is clear that the atmosphere in the range up to 600 km is a very complex system that will have to be examined over latitude and season to be understood.

References and Notes

1. L. W. Esposito *et al.*, *Science* **307**, 1251 (2005).
2. Materials and methods are available as supporting material on *Science* Online.
3. G. R. Smith *et al.*, *J. Geophys. Res.* **87**, 1351 (1982).
4. R. J. Vervack Jr., B. R. Sandel, D. F. Strobel, *Icarus* **170**, 91 (2004).
5. F. M. Flasar, *Planet. Space Sci.* **46**, 1109 (1998).
6. F. M. Flasar, *Planet. Space Sci.* **46**, 1125 (1998).
7. C. C. Porco *et al.*, *Nature* **434**, 159 (2005).
8. G. H. Mount, H. W. Moos, *Astrophys. J.* **224**, L35 (1978).
9. G. H. Mount, E. S. Warden, H. W. Moos, *Astrophys. J.* **214**, L47 (1977).
10. H. Sun, G. L. Weissler, *J. Chem. Phys.* **23**, 1160 (1955).
11. H. Okabe, *J. Chem. Phys.* **75**, 2772 (1981).
12. C. Y. R. Wu, F. Z. Chen, D. L. Judge, *J. Geophys. Res.* **106**, 7629 (2001).
13. F. Z. Chen, C. Y. R. Wu, *J. Quant. Spectrosc. Radiat. Transf.* **85**, 195 (2004).
14. C. Y. R. Wu, F. Z. Chen, D. L. Judge, *J. Geophys. Res. Planets* **109** (E7), E07S15, doi:10.1029/2003JE002180 (2004).
15. G. Cooper, G. R. Burton, C. E. Brion, *J. Electron Spectrosc. Relat. Phenom.* **73**, 139 (1995).
16. J. W. Au, G. Cooper, G. R. Burton, T. N. Olney, C. E. Brion, *Chem. Phys.* **173**, 209 (1993).
17. J. A. Nuth, S. Glicker, *J. Quant. Spectrosc. Radiat. Transfer* **28**, 223 (1982).
18. T. Nagata, T. Kondow, Y. Ozaki, K. Kuchitsu, *Chem. Phys.* **57**, 45 (1981).
19. J. A. R. Samson, G. N. Haddad, *J. Opt. Soc. Am.* **64**, 47 (1974).
20. J. A. R. Samson, G. N. Haddad, T. Masuoka, P. N. Pareek, *J. Chem. Phys.* **90**, 6925 (1989).
21. R. V. Yelle, personal communication.
22. D. F. Strobel, M. E. Summers, X. Zhu, *Icarus* **100**, 512 (1992).
23. J. H. Waite Jr. *et al.*, *Science* **308**, 982 (2005).
24. E. H. Wilson, S. K. Atreya, *J. Geophys. Res.* **109**, E06002; doi:10.1029/2003JE002181 (2004).
25. Y. L. Yung, M. Allen, J. P. Pinto, *Astrophys. J.* (suppl. **55**), 465 (1984).
26. A. J. Friedson, Y. L. Yung, *J. Geophys. Res.* **89**, 85 (1984).
27. G. F. Lindal *et al.*, *Icarus* **53**, 348 (1983).
28. R. V. Yelle, D. F. Strobel, E. Lellouch, D. Gautier, Eur. Space Agency Spec. Publ., *ESASP* **1177**, 243 (1997).
29. D. F. Strobel, personal communication.
30. I. C. F. Muller, R. V. Yelle, *Geophys. Res. Lett.* **29**, 2139 (2002).
31. B. Sicardy *et al.*, *AAS/DPS* **36.2206S** (2004).
32. E. Lellouch, D. M. Hunten, G. Kockarts, A. Coustenis, *Icarus* **83**, 308 (1990).
33. The authors thank H. Waite and R. Yelle of the INMS team, D. Strobel for useful comments and for providing data and calculations, E. Wilson for useful discussion and model densities, and L. Bloom for work on the manuscript. This work is one part of the Cassini UVIS investigation supported by the NASA/Jet Propulsion Laboratory Cassini mission.

Supporting Online Material

www.sciencemag.org/cgi/content/full/308/5724/978/DC1
Materials and Methods
Figs. S1 and S2

3 March 2005; accepted 14 April 2005
10.1126/science.1111790

REPORT

Ion Neutral Mass Spectrometer Results from the First Flyby of Titan

J. Hunter Waite Jr.,[1] Hasso Niemann,[2] Roger V. Yelle,[3] Wayne T. Kasprzak,[2] Thomas E. Cravens,[4] Janet G. Luhmann,[5] Ralph L. McNutt,[6] Wing-Huen Ip,[7] David Gell,[1] Virginie De La Haye,[1] Ingo Müller-Wordag,[8] Brian Magee,[1] Nathan Borggren,[3] Steve Ledvina,[5] Greg Fletcher,[1] Erin Walter,[1] Ryan Miller,[1] Stefan Scherer,[1] Rob Thorpe,[9] Jing Xu,[1] Bruce Block,[1] Ken Arnett[1]

The Cassini Ion Neutral Mass Spectrometer (INMS) has obtained the first in situ composition measurements of the neutral densities of molecular nitrogen, methane, molecular hydrogen, argon, and a host of stable carbon-nitrile compounds in Titan's upper atmosphere. INMS in situ mass spectrometry has also provided evidence for atmospheric waves in the upper atmosphere and the first direct measurements of isotopes of nitrogen, carbon, and argon, which reveal interesting clues about the evolution of the atmosphere. The bulk composition and thermal structure of the moon's upper atmosphere do not appear to have changed considerably since the Voyager 1 flyby.

This Report documents neutral composition measurements made with the INMS during the first low-altitude pass through Titan's upper atmosphere by the Cassini-Huygens spacecraft on 26 October 2004. During the ±15 min before and after its closest approach, INMS acquired a rich data set of information on Titan's atmospheric composition and structure covering an altitude range from 3000 to 1174 km. The closest approach occurred at 38.774° latitude, 88.45° west longitude at a solar local time of 16.753 hours. The highest priority objective of the Cassini orbiter during the first flyby was to measure the densities of the major atmospheric constituents N_2 and CH_4 and the inferred thermal structure between 1174 and 2000 km, because these data were important in planning the Huygens probe insertion and subsequent Cassini orbiter flybys. However, these measurements and subsequent analysis yielded substantial scientific results, including (i) the existence of large-amplitude (~10 K) and large–spatial scale (~180 km) atmospheric waves between 1100 and 1500 km, (ii) the identification of a suite of carbon-nitrile compounds at higher altitudes than anticipated (~1200 km), and (iii) the determination of the isotopic ratios of nitrogen in N_2, carbon in CH_4, and the abundance of ^{40}Ar as well as an upper limit for the mixing ratio of ^{36}Ar. We begin with a brief description of the instrument, then present the data set, and finish with a discussion of the major results enumerated above.

INMS is a dual–ion source quadrapole mass spectrometer covering the mass range of 0.5 to 8.5 and 11.5 to 99.5 daltons (*1*, *2*). The dual-source design combines classic closed and open ionization source configurations designed to measure inert species and reactive species and ions, respectively. The primary data reported in this paper were obtained with the closed source, which is designed to measure nonreactive atmospheric gases. In the closed source, the neutral gas flows into a spherical antechamber where it thermally accommodates with the walls of the antechamber before flowing through a transfer tube to an electron ionization source; there, the gas is ionized by an electron impact at 70 eV. The high flyby velocity of the Cassini spacecraft with respect to Titan (~6 km s^{-1}) produces a dynamic pressure enhancement in the antechamber, which increases sensitivity (*1*, *2*). Reactive species are not measured in this configuration.

Ionization of the primary constituents N_2 and CH_4 by the electron ionization source produced not only the primary ions N_2^+ and CH_4^+ but also dissociative fragments (over-

[1]Department of Atmospheric, Oceanic, and Space Sciences, University of Michigan, Ann Arbor, MI 48109–2143, USA. [2]NASA Goddard Space Flight Center, Greenbelt, MD 20771, USA. [3]Lunar and Planetary Laboratory, University of Arizona, 1629 East University Boulevard, Tucson, AZ 85721–0092, USA. [4]Department of Physics and Astronomy, University of Kansas, Lawrence, KS 66045, USA. [5]Space Sciences Laboratory, University of California, Berkeley, CA 94720, USA. [6]Applied Physics Laboratory, Johns Hopkins University, Laurel, MD 20723, USA. [7]Institute of Astronomy, National Central University, Chung-Li 32054, Taiwan. [8]Space and Atmospheric Physics Group, Imperial College, London SW7 2BW, UK. [9]Southwest Research Institute, Post Office Drawer 28510, San Antonio, TX 78228–0510, USA.

bars in Fig. 1). It also measured a host of ions and fragments due to minor atmospheric species (H_2, C_2H_2, C_2H_4, C_2H_6, C_3H_4, and Ar).

All of the measurable product channels were determined during the flight unit and engineering unit calibrations (with the exception of C_2N_2, C_3H_4, C_4H_2, HCN, and HC_3N, which were obtained from National Institute of Standards and Technology tabulations) and are subsequently used in the deconvolution of the spectra. The spectrum displayed in Fig. 1 (acquired every 4.6 s between the altitudes of 1230 and 1174 km and which can be co-added to enhance the signal-to-noise ratio) includes a mass scan covering the range from 1 to 99 daltons. This altitude range was chosen to be within approximately one atmospheric scale height of the Cassini closest approach (CA) altitude. The signal in each mass bin is a combination of the signals from the ionization or dissociative ionization of several species. Calibration data provide the sensitivity and the distribution of the dissociation products. Spacecraft velocity and altitude are used to compute the ram flow enhancement. From this data, a matrix is constructed relating instrumental response for various mass channels to the atmospheric composition. An inversion of this matrix with suitable numerical methods (*3*) yields abundances for a range of species. The measurements (and matrix elements) are weighted by the reciprocal measurement error.

Using two independent methods, we found the derived volume-mixing ratio of methane to be between 2.2 and 2.7% (for the first and second method, respectively) in the upper atmosphere. For the first method, we calculated the average ratio from the mass deconvolution of the average spectra between 1230 and 1180 km in the ingress data set as described above; for the second method, we used a diffusion model containing CH_4 and H_2 with an altitude-independent eddy diffusion coefficient and temperature as free parameters to fit the data in the altitude range of 1174 to 1500 km. The temperature structure between 1174 and 1500 km was found to be isothermal with a temperature (±SD) of 149 ± 3 K for the combined ingress and egress N_2 and CH_4 data sets (Fig. 2). A weak horizontal temperature gradient (~2 K/1000 km) was seen between ingress (145.8 K) and egress (151.8 K). From Fig. 2 we also note the close agreement of the present observations with the Voyager ultraviolet spectrometer data [reanalysis by Vervack (*4*)]. The extension of the INMS density profile (solid line) to lower altitudes in this case is with the assumption of a 149 K isothermal profile down to 900 km.

Some other important atmospheric quantities can also be derived from the density measurements. An eddy coefficient of $K = 4.2 \times 10^9$ cm^2 s^{-1} was determined by fitting the combined set of ingress and egress data ($K = 1.6 \times 10^9$ cm^2 s^{-1} was found for ingress data alone and $K = 8.3 \times 10^9$ cm^2 s^{-1} for egress data). Adequate fits were obtained assuming constant K with altitude. These values imply a homopause altitude defining the boundary between the well-mixed and diffusively separated portions of the atmosphere; the altitude was calculated by finding the intersection between K and the N_2-CH_4 binary diffusion coefficient profiles. We found the homopause at 1195 ± 65 km. Finally, the exobase above which the mean free path of a particle is equal to the atmospheric scale height was calculated from the measured densities to be at an altitude of 1429 ± 5 km.

We observed strong temperature perturbations superimposed on the isothermal profile derived from altitude analysis of the combined ingress and egress N_2 and CH_4 data sets. These perturbations along the spacecraft track can be mapped either horizontally or vertically and appear to represent either a vertically propagating oscillation or an intrinsic harmonic of the atmosphere. Only the vertical mapping case is presented in Fig. 3, suggesting a wave amplitude of 10 K and a vertical wavelength of 180 km. The origin of these waves in Titan's upper atmosphere could be an energy or momentum source located at lower altitudes in the

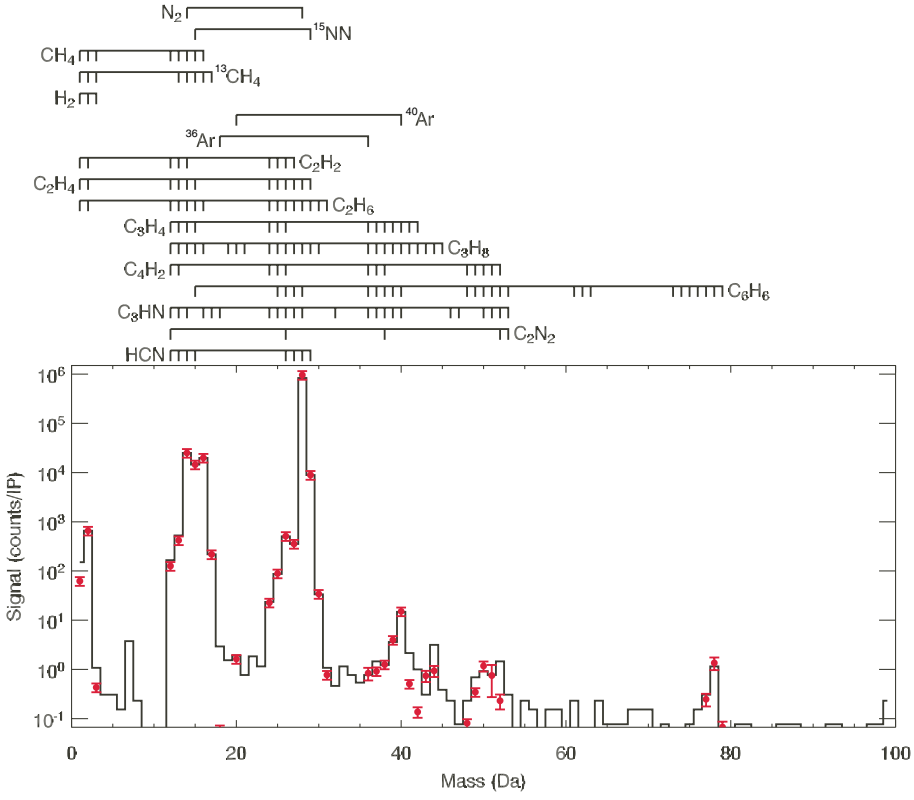

Fig. 1. The average mass spectrum from 1 to 99 daltons measured by INMS on the 26 October flyby (T_A) between the altitudes of 1174 and 1230 km. The average spectrum includes only inbound data where the INMS was pointed along the spacecraft velocity vector. The solid black line represents the measured, background-corrected spectra and the red circles represent the reconstructed spectra using the values of Table 1. The error bars displayed are the larger of the 20% calibration uncertainty or the 1σ statistical uncertainty. counts/IP, counts per integration period. The bars above the graph indicate the mass/charge locations of the ionization and dissociative ionization fragments of the species indicated.

Table 1. Minor species determined from the mass spectral deconvolution with 1σ error. C_6H_6 may represent a contaminant. Data are expressed in values of the mole fraction. C_2H_4 value depends on the value adopted for HCN. The following species were identified at less than 5 ppm: C_3H_8, C_4H_2, HCN, HC_3N, C_6H_6, and C_2N_2.

Species	INMS-derived values	CIRS values (*7*)
CH_4	$2.19 \times 10^{-2} \pm 0.002 \times 10^{-2}$	$1.6 \times 10^{-2} \pm 0.5 \times 10^{-2}$
H_2	$4.05 \times 10^{-3} \pm 0.03 \times 10^{-3}$	Not measured
C_2H_2	$1.89 \times 10^{-4} \pm 0.05 \times 10^{-4}$	$3.3 \times 10^{-6} \pm 0.3 \times 10^{-6}$
C_2H_4	$2.59 \times 10^{-4} \pm 0.70 \times 10^{-4}$ to $5.26 \times 10^{-4} \pm 0.08 \times 10^{-4}$	$1.6 \times 10^{-7} \pm 0.7 \times 10^{-7}$
C_2H_6	$1.21 \times 10^{-4} \pm 0.06 \times 10^{-4}$	$2.3 \times 10^{-5} \pm 0.4 \times 10^{-5}$
C_3H_4	$3.86 \times 10^{-6} \pm 0.22 \times 10^{-6}$	$1.2 \times 10^{-8} \pm 0.3 \times 10^{-8}$

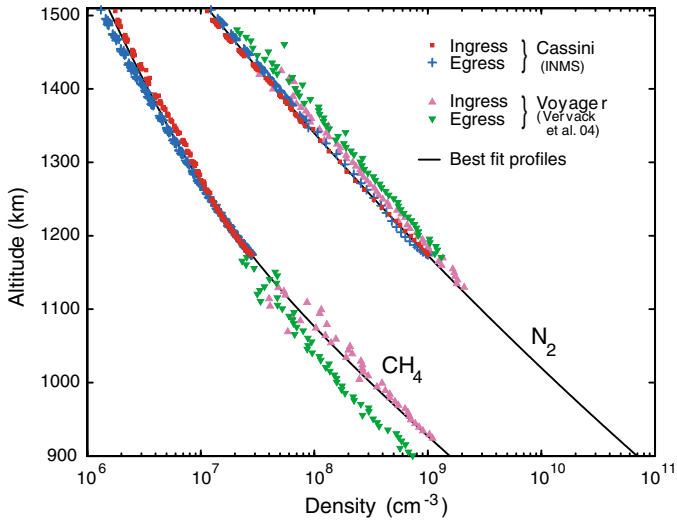

Fig. 2. The INMS-derived densities of methane (mass channel 16) and molecular nitrogen (mass channels 14 and 28) in red (ingress) and blue (egress) from T_A, compared with the Vervack-derived (*4*) values from Voyager ultraviolet spectrometer in pink (ingress) and green (egress). The solid black lines represent the best-fit densities, which correspond to a 149 K isothermal temperature profile. The methane mixing ratio from this modeling fit to the data is 2.7% at 1174 km.

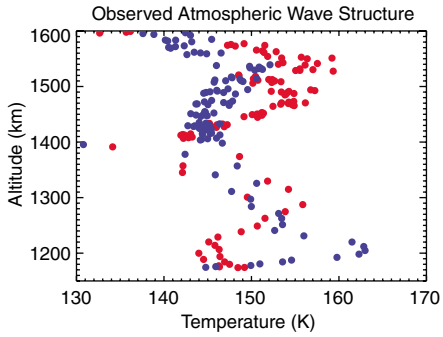

Fig. 3. Vertical profiles of temperature derived from observations of N_2 and CH_4 by INMS during T_A. Red data refer to ingress results and blue to egress.

atmosphere, or they could represent an external source from Saturn's magnetosphere, or both.

Analysis of an average spectra for the altitude range of 1230 to 1174 km near CA allowed us to determine a preliminary list of carbon-nitrile compounds and their abundances. The spectral fit from our deconvolution, discussed above, is shown in Fig. 1, and the resulting list of compounds is provided in Table 1. At this preliminary stage in the analysis, the abundances of molecular species are not well-established because we have not completed a thorough analysis of systematic uncertainties, most notably the interaction of potentially reactive species (such as HCN) with the wall of the antechamber for an impact velocity of ~6 km s^{-1}. However, we are confident in the detection of all species listed in the table.

The spectral analysis procedure also leads to a determination of isotopic ratios for nitrogen ($^{14}N/^{15}N$) and carbon ($^{12}C/^{13}C$), a determination of the ^{40}Ar mixing ratio, and an upper limit on the ^{36}Ar mixing ratio in the upper atmosphere. Because the lowest altitudes sampled by INMS on this first Titan flyby were evidently below the homopause, these volume-mixing ratio values can be used to infer mixing ratios for the well-mixed atmosphere at lower altitudes. The statistical error associated with determining the volume-mixing ratios by this method is on the order of 1%, but the uncertainties associated with the calibration data lead to an overall uncertainty of 20% (Table 2). However, the calibration uncertainties cancel for the isotopic ratios reported so that the only error sources are statistical or systematic errors introduced by the analysis method. Another method was also used to determine the isotopic abundances in which integrated sums of measured abundances (and errors) below 1230 km are used. The results of the two approaches are given in Table 2. There is good agreement between the methods for the carbon ratio, leading us to conclude that systematic errors are small and that statistical errors define the uncertainty. In the case of the nitrogen ratio, the saturation in the mass-28 channel required scaling of the low-sensitivity counter to replace data from the saturated high-sensitivity counter. At this time, the scale factor is not well-determined, resulting in systematic errors that are differential between the two methods. Thus we quote a range of values that define our uncertainty in this regard and we have verified the reported isotopic ratio value at higher altitudes where the N_2 data in channel 28 are not yet saturated.

INMS measurements obtained during the first pass of the Cassini orbiter through Titan's upper atmosphere lead to some important conclusions. A key finding is the apparent stability of the atmosphere over the 25 years since the Voyager flyby, as indicated by the comparison shown in Fig. 2. We suggest that this may be due to the thermostatic control exercised on the upper atmosphere by the infrared active species HCN. Another key result is the location of the homopause at ~1195 km, which is much higher than was expected [table 1 in (*1*)] (*5*). This result indicates that turbulent mixing extends to very high altitudes, and is consistent with the discovery by INMS of large scale–size and large-amplitude atmospheric waves in the upper atmosphere (Fig. 3). The large-scale size of the atmospheric waves was anticipated and is a consequence of atmospheric filtering by wind shears and thermal gradients at lower altitudes, and the large wave amplitude is within the limits of model predictions (*6*).

The existence of heavy hydrocarbon species at altitudes above 1200 km is another possible consequence of the well-mixed atmosphere. An alternative explanation is that previous determinations of the production rates for these chemical species at high altitudes are too small. Most of the observed compounds were identified earlier in the lower atmosphere [table 1 in (*1*)] (*5*). A comparison of INMS-derived high-altitude values with those determined in the lower atmosphere from Cassini Composite Infrared Spectrometer (CIRS) measurements (*7*) is shown in Table 1. Modeling and further analysis of the new atmospheric data will lead to explanations of the large abundance of complex hydrocarbons and nitriles at high altitudes.

The measured isotopic ratios have important implications for the evolution of the Titan atmosphere and interior over geological time. The isotopic ratios for nitrogen ($^{14}N/^{15}N$) and carbon ($^{12}C/^{13}C$) can be used to constrain the role of atmospheric escape and other physical and chemical processes in the Titan system. The $^{14}N/^{15}N$ ratio of 172 to 215 (Table 2) is between that of Mars and Earth, indicating either substantial escape of the atmospheric reservoir of nitrogen since capture or release from the interior or an initial source of nitrogen with an isotopic ratio closer to the solar wind value of 200 ± 55 (*8*, *9*). Comparison of these results with model results of Lunine *et al.* (*10*) is informative. If one assumes that the initial nitrogen isotopic ratios were similar to those of Earth [$^{14}N/^{15}N = 272.0 \pm 0.3$ (*11*)], that the exospheric temperature has remained near 150 K, and that the relative position of the homopause and exobase has remained unchanged over the course of atmospheric evolution, then the formulation of Lunine *et al.* combined with INMS measurements suggests a loss of atmospheric nitrogen over the history of the atmosphere by a factor of 1.7 ± 0.05 to 10 ± 5 from its original levels, depending on the efficiency (0 to 0.6) for dissociative fractionation of the isotopes. This also assumes that the upper end of the INMS measurement range for this ratio (i.e., 215) is representative of the present-day isotopic ratio. Correspondingly, if we use the lower end of the INMS-measured range (172), the range of atmospheric loss factor becomes 2.8 ± 0.2 to 100 ± 75. Clearly, it is hard to constrain the amount of atmospheric loss over geological time with the present data set. The quoted uncertainty is largely due to our imprecise knowledge of the position of the homopause and exobase. However, large uncertainties about the initial Titan isotopic ratio (*8*, *9*) and the role of dis-

Table 2. Key isotopic ratios measured by INMS (uncertainties are quoted as a 95% confidence interval).

Isotopic ratio	Integration method	Deconvolution method	Combined results	Estimated value at surface
$^{14}N/^{15}N$	$188\ ^{+14}_{-16}$	214 ± 1	$172 < {}^{14}N/{}^{15}N < 215$	$168 < {}^{14}N/{}^{15}N < 211$
$^{12}C/^{13}C$	95.6 ± 0.1	93.8 ± 1.9	95.6 ± 0.1	81
^{36}Ar mixing ratio	$<4 \times 10^{-7} \pm 1 \times 10^{-7}$	$<6 \times 10^{-7}$	$<5 \times 10^{-7} \pm 2 \times 10^{-7}$	Not applicable
^{40}Ar mixing ratio	$7.1 \times 10^{-6} \pm 0.1 \times 10^{-6}$	$7.3 \times 10^{-6} \pm 2.1 \times 10^{-6}$	$7.1 \times 10^{-6} \pm 0.1 \times 10^{-6}$	

sociative fractionation limit us to conclude only that the Titan atmosphere was at least 50% denser in the past.

A perplexing aspect of the nitrogen isotopic ratios comes from comparing the INMS-measured molecular nitrogen isotopic ratio value to earlier ground-based determinations of $^{14}N/^{15}N$ in HCN measured in Titan's stratosphere (*12*, *13*). The HCN-derived values show enrichment of the heavier isotope of nitrogen that is more than a factor of 2 larger than the INMS-measured values for the molecular nitrogen isotope ratio. Chemical fractionation is the most likely source of the difference, but estimates so far do not come close to explaining the difference (*14*, *15*).

The heavy isotope enrichment of nitrogen stands in contrast to the carbon isotopic ratio ($^{12}C/^{13}C = 95 \pm 1$). The ratio is well-determined and slightly above the terrestrial value of 89.01 ± 0.38, but certainly within the present constraints of determinations for Jupiter (94 ± 12) and Saturn (89^{+25}_{-18}) (*10*). This suggests that the methane in the atmosphere is being replenished by an interior source at a rate fast enough that escape is not the dominant effect on the isotopic ratio. This is consistent with our understanding of photodissociation rates for methane and the associated deposition of complex hydrocarbons on the surface. This dissociation process acts as the dominant sink for the atmospheric portion of the carbon cycle on Titan. INMS measurements of H_2 outflow can help quantify this process. H_2 is a byproduct of the methane photodissociation, and the measured H_2 escape rate of $6.1 \times 10^9 \pm 0.2 \times 10^9$ cm^{-2} s^{-1} represents a photodissociation rate of 5×10^{27} methane molecules per second and an atmospheric carbon residence time of 5×10^7 years. However, this does not explain the elevated isotopic ratio value indicating an increase of the light ^{12}C isotope relative to the ^{13}C isotope when compared with the terrestrial value of 89.01 ± 0.38 (*11*). Such a light isotope enhancement on Earth of up to ~10% is associated with biology (*16*); on Titan a more likely process involves vapor pressure isotope effects at the surface (*17*). However, using a diffusion model and our present estimate of thermal structure and atmospheric diffusion to propagate the upper atmospheric value to the surface (Table 2), we obtained a surface value of 81, which is below the terrestrial value. Clearly, combining the INMS data with information obtained by the Huygens Gas Chromatograph Mass Spectrometer is necessary to reach closure on this issue.

The volume-mixing ratios of the isotopes of argon can be used to study both interior and accretion processes. ^{40}Ar is likely produced by radioactive decay of ^{40}K, as it is on Earth, and therefore the mixing ratio of ^{40}Ar can be compared to estimates of the radiogenic production and release of potassium in the mantle rocks. The measured ^{40}Ar is $7.081 \times 10^{-6} \pm 0.1 \times 10^{-6}$ as compared with an upper limit of 0.05 to 0.07% set by McKinnon's estimate (*18*). This suggests either that the outgassing of the interior has an efficiency of ~1% or (less likely) that the ^{40}Ar was lost to space at an early phase of atmospheric evolution. On the other hand, the nondetection of ^{36}Ar and ^{38}Ar may suggest that N_2 was not trapped in nebula ices in the form of clathrate hydrates (*19*–*22*). The upper limit of less than 6×10^{-7} by volume set by INMS for the ^{36}Ar abundance ratio leads to the conclusion that the nitrogen in the moon's atmosphere was not brought to Titan as N_2 trapped in clathrates but was likely derived initially from ammonia ice or ammonia hydrate formed in the local Saturn nebulae (*23*) or in the solar nebula (*24*) and subsequently converted to N_2 by photochemical processes (*25*) and/or from high-temperature shock formation of N_2 (*26*).

The first measurements of Titan's neutral composition in the upper atmosphere lead to a number of notable conclusions about the current atmospheric structure and about the evolution of Titan's atmosphere and interior. The atmosphere likely formed from the outgassing after planetesimals composed of silicates, water ice, clathrates of methane, and ammonia hydrates coalesced to form the moon. Subsequent photochemistry and/or shock-induced chemistry likely converted the atmospheric nitrogen into molecular nitrogen. The early atmosphere was 1.6 to 100 times more substantial and was lost through escape over the intervening 4.5 billion years due to the reduced gravity associated with the relatively small mass of Titan. Carbon in the form of methane has likely continued to outgas over time from the interior, given that much of its subsequent photolysis products have been deposited in the form of complex hydrocarbons on the surface (~5×10^{27} s^{-1} as estimated from the H_2 escape rate of $6.1 \times 10^9 \pm 0.2 \times 10^9$ cm^{-2} s^{-1} measured by INMS) and some of it has also been lost to space [2×10^{25} s^{-1} as estimated from modeling of the exospheric loss of carbon (*27*)]. The carbon isotopes in the upper atmosphere appear to be isotopically light due to atmospheric diffusion effects or vapor phase isotope effects at the surface resulting from condensation, evaporation, and sublimation of surface methane.

References and Notes

1. J. H. Waite *et al.*, *Space Sci. Rev.* **114**, 113 (2005).
2. W. K. Kasprzak *et al.*, *Proc. SPIE* **2803**, 129 (1996).
3. W. H. Press, B. P. Flannery, S. A. Teukolsky, W. T. Vetterling, *Numerical Recipes* (Cambridge Univ. Press, Cambridge, 1986).
4. J. R. Vervack, B. R. Sandel, D. F. Strobel, *Icarus* **170**, 91 (2004).
5. A. Coustenis *et al.*, *Icarus* **80**, 54 (1989).
6. D. F. Strobel, B. Sicardy, in *Huygens Science Payload and Mission* (ESA Special Publication SP-1177, Noordwijk, Netherlands, 1997), pp. 299–311.
7. Lower atmosphere values of the hydrocarbon mixing ratios at a pressure of 1.5 to 3.0 mbar and a latitude of 39° were taken from Flaser *et al.* (*28*). The methane value comes from the same reference but at a pressure of 3 to 20 mbar.
8. R. Kallenbach *et al.*, *Astrophys. J.* **507**, L185 (1998).
9. If instead of the solar wind value, we choose initial values close to the newly determined protonebula value (430), determined by Owen *et al.* (*29*), the requirement for escape is much larger than our assumption of a terrestrial initial value of 272.
10. J. I. Lunine *et al.*, *Planet. Space Sci.* **47**, 1291 (1999).
11. B. Fegley, in *Global Earth Physics: A Handbook of Physical Constants*, T. Ahrens, Ed. (American Geophysical Publications, Washington, DC, 1995), pp. 320–345.
12. M. A. Gurwell, *Astrophys. J.* **616**, L7 (2004).
13. T. Hidayat *et al.*, *Icarus* **126**, 170 (1997).
14. One likely mechanism for the enrichment of $HC^{15}N$ is the photoinduced isotopic fractionation effect (PHIFE) proposed by Yung and Miller (*30*). However, a preliminary estimate by Yung (*31*) shows that the magnitude of PHIFE for HCN is not sufficient to account for the observed enrichment.
15. Another possibility is ion-neutral reactions as studied in the case of the interstellar medium by R. Terzieva and E. Herbst (*32*), but such effects have not been examined at Titan temperatures (150 K).
16. M. J. Whiticar, *Chem. Geol.* **161**, 291 (1999).
17. Because methane is near the triple point near the Titan surface, one would expect a heavy isotope depletion of the gas as compared with the liquid or solid due to vapor pressure isotope effects similar to those observed for H_2O on Earth (*33*).
18. William B. McKinnon, personal communication. McKinnon assumes an anhydrous rock mass fraction for Titan of 0.55 ± 05 and a CI carbonaceous [K = 550 parts per million (ppm)] or H chondrite (780 ppm) composition for the rock (*34*). Of a primordial $^{40}K/K = 1.47 \times 10^{-3}$, 9.6% has decayed to ^{40}Ar. Perhaps we shouldn't be surprised by the very low degassing efficiency. If we assume that Titan has a rock core and that core was volcanically active, those magmas would still be erupting at great depths, and at pressures around 2 GPa. There is no thermodynamic incentive for volcanics to degas at such pressures.
19. T. Owen, *Planet. Space Sci.* **30**, 833 (1982).
20. J. I. Lunine, D. J. Stevenson, *Astrophys. J. Suppl. Ser.* **58**, 493 (1985).
21. T. Owen, *Planet. Space Sci.* **48**, 747 (2000).

22. F. Hersant *et al.*, *Space Sci. Rev.* **114**, 25 (2004).
23. J. I. Lunine, D. J. Stevenson, *Icarus* **70**, 61 (1987).
24. O. Mousis *et al.*, *Icarus* **156**, 167 (2002).
25. S. K. Atreya, T. M. Donahue, W. R. Kuhn, *Science* **201**, 611 (1978).
26. C. P. McKay *et al.*, *Nature* **332**, 520 (1988).
27. T. E. Cravens *et al.*, *Planet. Space Sci.* **45**, 889 (1998).
28. F. M. Flasar *et al.*, *Science* **308**, 975 (2005).
29. T. Owen, P. R. Mahaffy, H. B. Niemann, S. Atreya, M. Wong, *Astrophys. J.* **553**, L77 (2001).
30. Y. L. Yung, C. E. Miller, *Science* **278**, 1778 (1997).
31. Y. L. Yung, personal communication.
32. R. Terzieva, E. Herbst, *Mon. Nat. R. Astron. Soc.* **317**, 563 (2000).
33. T. F. Johns, in *Atomic Energy Research Establishment, Harwell: A Brief Guide* (GP/R-2166, Atomic Energy Research Establishment, Harwell, UK, 1957).
34. K. Lodders, B. Fegley, *The Planetary Scientist's Companion* (Oxford Univ. Press, New York, 1999).
35. We thank the Cassini project at NASA/Jet Propulsion Laboratory for financial support through contract #1228303; the flight and instrument teams for many years of dedicated effort; the Cassini Interdisciplinary Scientists T. Owens, D. Gautier, and J. Lunine for many helpful discussions; and several members of the Space Science community, K. Freeman, J. Kasting, R. Dissly, Y. Yung, and W. McKinnon for additional discussions.

3 February 2005; accepted 13 April 2005
10.1126/science.1110652

REPORT

Cassini Measurements of Cold Plasma in the Ionosphere of Titan

J.-E. Wahlund,[1]* R. Boström,[1] G. Gustafsson,[1] D. A. Gurnett,[2] W. S. Kurth,[2] A. Pedersen,[3] T. F. Averkamp,[2] G. B. Hospodarsky,[2] A. M. Persoon,[2] P. Canu,[4] F. M. Neubauer,[5] M. K. Dougherty,[6] A. I. Eriksson,[1] M. W. Morooka,[1] R. Gill,[1] M. André,[1] L. Eliasson,[7] I. Müller-Wodarg[6]

The Cassini Radio and Plasma Wave Science (RPWS) Langmuir probe (LP) sensor observed the cold plasma environment around Titan during the first two flybys. The data show that conditions in Saturn's magnetosphere affect the structure and dynamics deep in the ionosphere of Titan. The maximum measured ionospheric electron number density reached 3800 per cubic centimeter near closest approach, and a complex chemistry was indicated. The electron temperature profiles are consistent with electron heat conduction from the hotter Titan wake. The ionospheric escape flux was estimated to be 10^{25} ions per second.

The giant planet Saturn and its magnetosphere rotate with a period of ~11 hours, which can be inferred from radio measurements (*1*). At the distance of the large moon Titan [20 Saturn radii (R_S)], this corotation causes a magnetospheric plasma flow of several hundred kilometers per second that affects the upper ionized part of the thick atmosphere of Titan. Atoms and molecules in the upper atmosphere are ionized by solar ultraviolet (UV) radiation and by impacts of energetic particles that originate mainly from the magnetosphere. The aeronomic and electrodynamic processes involved in the interaction further produce a complex organic chemistry within the nitrogen- and methane-rich atmosphere of Titan as well as a loss of atmospheric constituents, providing in turn a source of plasma for the magnetosphere of Saturn (*2*).

The two first flybys of Titan (T_A and T_B) on 26 October and 13 December 2004 were very similar. Both occurred at 10.5 Saturn local time (LT) near the front side of Saturn's magnetosphere, and both approached inbound from the sunlit side and through the wake of Titan (Fig. 1). The outbound passes partly traversed a shaded region caused by Titan's thick atmosphere at a latitude of 30° to 40°N.

The structure and thermal state of the ionosphere of Titan were affected by the saturnian magnetosphere all the way down to closest approach (1176 km) during both flybys (Figs. 2 and 3). The general shape of the two main number density maxima near closest approach in Fig. 2 is broadly consistent with photoionization by UV light from the Sun and impact ionization by magnetospheric electrons (*3*, *4*). However, the plasma density was otherwise very structured and could be related to similar structures in the magnetic field data. The density data in Figs. 2 and 3 were collected at a high time resolution (20 samples/s) and are derived from the probe current at a constant bias voltage (~ +10 V), corrected for electron temperature and adjusted to fit the potential sweep data points for density. The LP sensor (*5*) samples the total electron number density surrounding the spacecraft, which includes the naturally occurring plasma electrons as well as a nearly constant level of photoelectrons around the spacecraft. The spacecraft-generated photoelectrons dominated the magnetospheric part of the flyby. According to measurements by the Cassini Plasma Spectrometer (CAPS), the magnetospheric electron density near Titan was just below 0.1 cm^{-3} during T_A (*6*).

The calculated magnetic pressure ($B^2/2\mu_0$) of the magnetosphere and the electron thermal pressure ($n_e k_B T_e$) of the ionosphere (where B is magnetic field strength, μ_0 is magnetic permeability, n_e is electron number density, k_B is the Boltzmann constant, and T_e is electron temperature) were largely of the same order of magnitude during the T_A flyby (Fig. 2B). Both flybys traversed the wake of Titan, and the effect of the magnetospheric dynamic pressure ($n_i m_i v_i^2/2$, where n_i is ion number density, m_i is average ion mass, and v_i is ion ram velocity) should therefore be small near closest approach. The ionopause, the region where the ionospheric thermal pressure balances the magnetospheric pressure, covered an extended region on both the inbound and outbound trajectories (yellow area in Fig. 2). The close relationship between cold plasma density signatures and magnetic field fluctuations and comparable values of ionospheric electron thermal and magnetospheric magnetic field pressures confirms the view that the saturnian magnetosphere is important for the structure and dynamics in Titan's ionosphere.

The Titan wake "neutral" sheet, where the magnetic field sharply rotates and relates to an electrical current, was identified by the Dual-Technique Magnetometer (MAG) near 15:35 UT (*7*). At this time, the RPWS LP detected a sharp peak in both electron number density (850 cm^{-3}) and electron thermal pressure (900 eV/cm^3). The altitude thickness of the compressed plasma sheet was 60 km, which is on the order of the ion gyroradius.

The LP provides estimates of n_e and T_e, but under some circumstances, values can also be obtained for m_i, v_i, n_i, ion temperature (T_i), solar UV intensity, and spacecraft potential. An estimate of the effective ion temperature ($T_{i,eff}$), which is the sum of the thermal random ion temperature and the ram ion directed flow energy [$T_{i,eff} = T_i + (m_i v_i^2/2e)$, expressed

[1]Swedish Institute of Space Physics, Box 537, SE-751 21 Uppsala, Sweden. [2]Department of Physics and Astronomy, University of Iowa, Iowa City, IA 52242, USA. [3]Department of Physics, University of Oslo, NO-0316 Oslo, Norway. [4]Centre d'Etude des Environnements Terrestre et Planétaires/CNRS/Institut Pierre Simon Laplace, 78140 Vélizy-Villacoublay, France. [5]Institute for Geophysics and Meteorology, Köln University, D-50923 Köln, Germany. [6]Blacket Laboratory, Imperial College London, London SW7 2BW, UK. [7]Swedish Institute of Space Physics, Box 812, SE-981 28 Kiruna, Sweden.

*To whom correspondence should be addressed. E-mail: jwe@irfu.se

as electron-volts], can be obtained from the slope of the ion current-bias voltage characteristic. If the total ion current to the LP is dominated by the ram contribution, the ion current for a given bias voltage is proportional to $n_i v_i / m_i$, and $T_{i,eff}$ gives a value of $m_i v_i^2$. Thus, by using the condition that the plasma must be electrically neutral ($n_e = n_i$), it is possible to estimate the ion mass and ram velocity. This method only works if there is an ion current signature to the LP and $T_i \ll m_i v_i^2/2e$. The maximum ion velocity that can be measured with reasonable certainty is 100 km/s, and larger ion ram velocities may become underestimated (gray areas in Figs. 2 and 3).

The ion velocity during T_A (Fig. 2C) decreased from ~100 km/s near 15:14 UT to the spacecraft ram velocity (black line) of ~6 km/s near 15:24 UT. This is the mass-loading region, and the boundary near 15:14 UT [1.7 Titan radii (R_T) from Titan] is called the mass-loading boundary (MLB) (*8*). In the mass-loading region, heavy ions from the ionosphere are accelerated (picked up) downstream by the magnetospheric $\mathbf{v} \times \mathbf{B}$ induced electric field (around 1 to 2 mV/m). At the same time, the magnetospheric ion flow slows down because of the heavy loading of matter by the ionosphere. A corresponding mass-loading region and MLB were detected on the outbound pass between 15:34 and 15:40 UT. Magnetic enhancements (pileup) were detected inside both the MLBs as seen from Titan, which suggests that the magnetic pileup boundary (MPB) (*9*) was colocated with the MLB.

No large asymmetry of the mass-loading region could be detected between the inbound and outbound passes during T_A, in stark contrast to the findings of the Voyager 1 flyby (*10*) and the T_B flyby. An extended pickup region was expected on the side of Titan facing away from Saturn because the gyroradii of the heavy ionospheric ions should be in excess of 1000 km. Gyrating ions would to a large degree be absorbed by collisions in the dense atmosphere of Titan on the side that faces Saturn, thereby causing an asymmetry in the induced magnetosphere around Titan.

During the inbound pass of the T_B flyby (Fig. 3), plasma of ionospheric origin, as indicated by the enhanced number density of 10 to 100 cm^{-3} and slowed ion ram speed, was found as far as 9 R_T (20,000 km) from Titan. Thus, the MLB was located at nearly 9 R_T inbound, whereas a sharp increase in the ion ram velocity occurred closer to Titan on the outbound pass. The RPWS LP data during the T_B flyby therefore confirm the existence of an extensive mass-loading region on the anti-Saturn side of Titan under certain magnetospheric conditions, as suggested from theoretical predictions (*11*, *12*). During other conditions, the ionospheric plasma is concentrated closer to Titan (e.g., 15:18 to 15:40 UT during T_A). Data from further flybys and comparison with data from other instruments are needed to infer the degree of control that the saturnian magnetospheric conditions exert on the structure of the induced space environment around Titan.

The tail or wake region is an outflow region where plasma escapes a planet or moon. A nonmagnetized (or almost nonmagnetized) object such as Titan is directly exposed to the external (corotating magnetospheric or solar wind) flow.

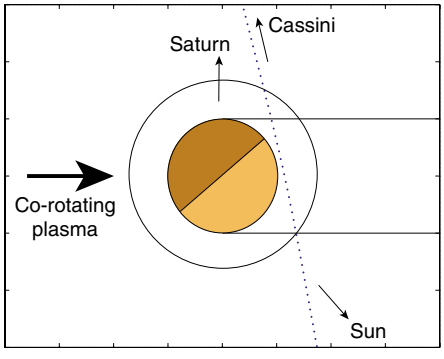

Fig. 1. The T_A flyby trajectory. Titan's surface and approximate ionopause boundary are indicated. The flyby occurred within the magnetosphere at 10.6 Saturn LT. The T_B flyby was similar.

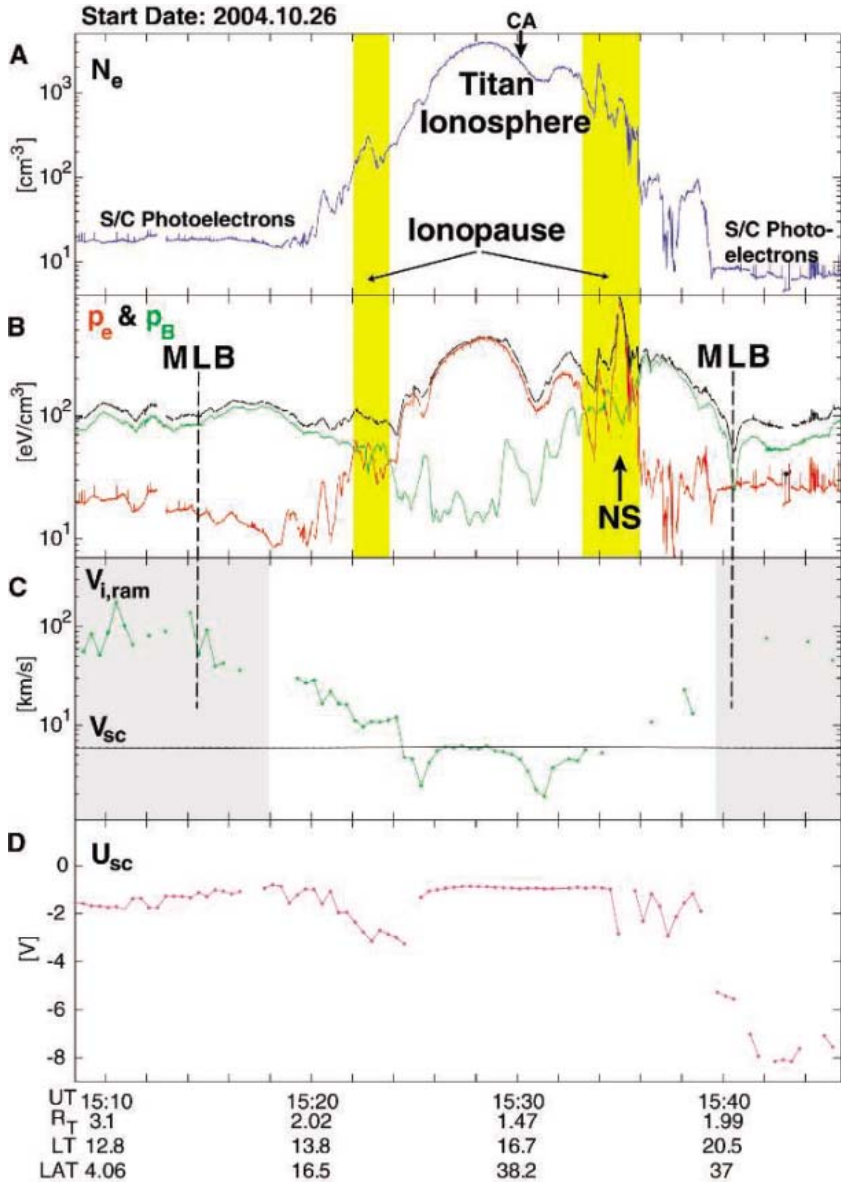

Fig. 2. Cold plasma characteristics during T_A. The data reveal a rather symmetric but dynamic interaction with the magnetosphere of Saturn. The peak in the measured electron number density N_e is shifted inbound from closest approach because Cassini traversed the dayside hemisphere on its inbound pass. The MLBs, magnetic wake neutral sheet (NS), and extended ionopause regions (yellow shading) are indicated. The displayed parameters are (**A**) N_e; (**B**) electron thermal pressure (p_e, red), magnetic pressure (p_B, green), and the sum (black); (**C**) ion ram speed ($v_{i,ram}$) and spacecraft speed (v_{sc}); and (**D**) spacecraft potential (u_{sc}). The gray shaded areas in (C) indicate possibly underestimated ion ram speeds.

Consequently, the erosion of the atmosphere of Titan may be quite substantial. A total plasma outflow of 1.2×10^{24} ions/s was estimated from Voyager 1 observations in the far Titan wake with the use of simple pressure balance considerations (*10*). The RPWS instruments on Cassini are able to monitor the ion outflow (and related processes) more directly. An order of magnitude estimate can be calculated for the ion outflow during T_A (Fig. 2) from the product $n_e v_i$ if we assume that the geometry of the wake region is cylindrical. The density around 15:22 UT was 100 cm^{-3} and the ram velocity was 10 km/s, giving a flux of $\sim 10^{12}$ ions m^{-2} s^{-1}. A similar flux is inferred between 15:18 and 15:24 UT (or over a distance of 1000 km across the tail). For the assumption of a cylindrical geometry, the resulting total escape flux amounts to 10^{25} ions/s. This number will most likely vary with magnetospheric and illumination conditions as well as orbit position of Titan, but it is in rough agreement with theoretical predictions (*13*).

Figure 4 shows the inbound (red) and outbound (black) altitude profiles of the electron density and temperature as well as the averaged ion mass during the T_A flyby. The maximum densities near 1250 km were 3800 cm^{-3} (inbound) and 2000 cm^{-3} (outbound). During T_B the maximum number density was 3200 cm^{-3}. The inbound pass traversed the more sunlit dayside, whereas the outbound pass traversed the shaded region behind the atmospheric terminator. Photoionization and ionization by magnetospheric electrons could explain the overall ionospheric shape (*3*, *4*), whereas the detailed plasma density features most probably were related to the electrodynamic interaction with the magnetospheric flow. The altitudes 1750 km (inbound) and 1400 km (outbound) were associated with changes in ion composition (Fig. 4), whereas at lower altitudes the averaged ion mass stayed above 20 to 30 amu. The ionopause was not sharply defined but rather smeared over an extended region from 1750 to 2150 km (inbound) and from 1400 to 1700 km (outbound). This smearing can be expected in Titan's wake, and it is similar to the ionopause characteristics at Mars (*14*) and in contrast to the sharp ionopause boundary near Venus. On Titan the ionopause will vary, as it did during T_A, with magnetospheric and illumination conditions.

An intriguing result is the sharp increase in averaged ion mass (up to 60 to 70 amu) near closest approach on the outbound pass, which traversed a region that was less illuminated by the Sun. The ion mass is derived under the assumptions that the ion thermal energy is negligible and that quasi-neutrality applies so that $n_i \approx n_e$. If the ion temperature becomes larger than 1 eV, or if negative ions become a fair part of the total plasma number density, then the derived ion mass must be modified accordingly. The CAPS instrument has detected negative ions near Titan (*6*). Therefore, this increase in averaged ion mass might be due to the presence of some negative ions (and/or very hot ions, which seems unlikely in the dense atmosphere that exists here). In any case, it points to a situation where very complex organic ion-molecule chemistry occurs in the lower ionosphere.

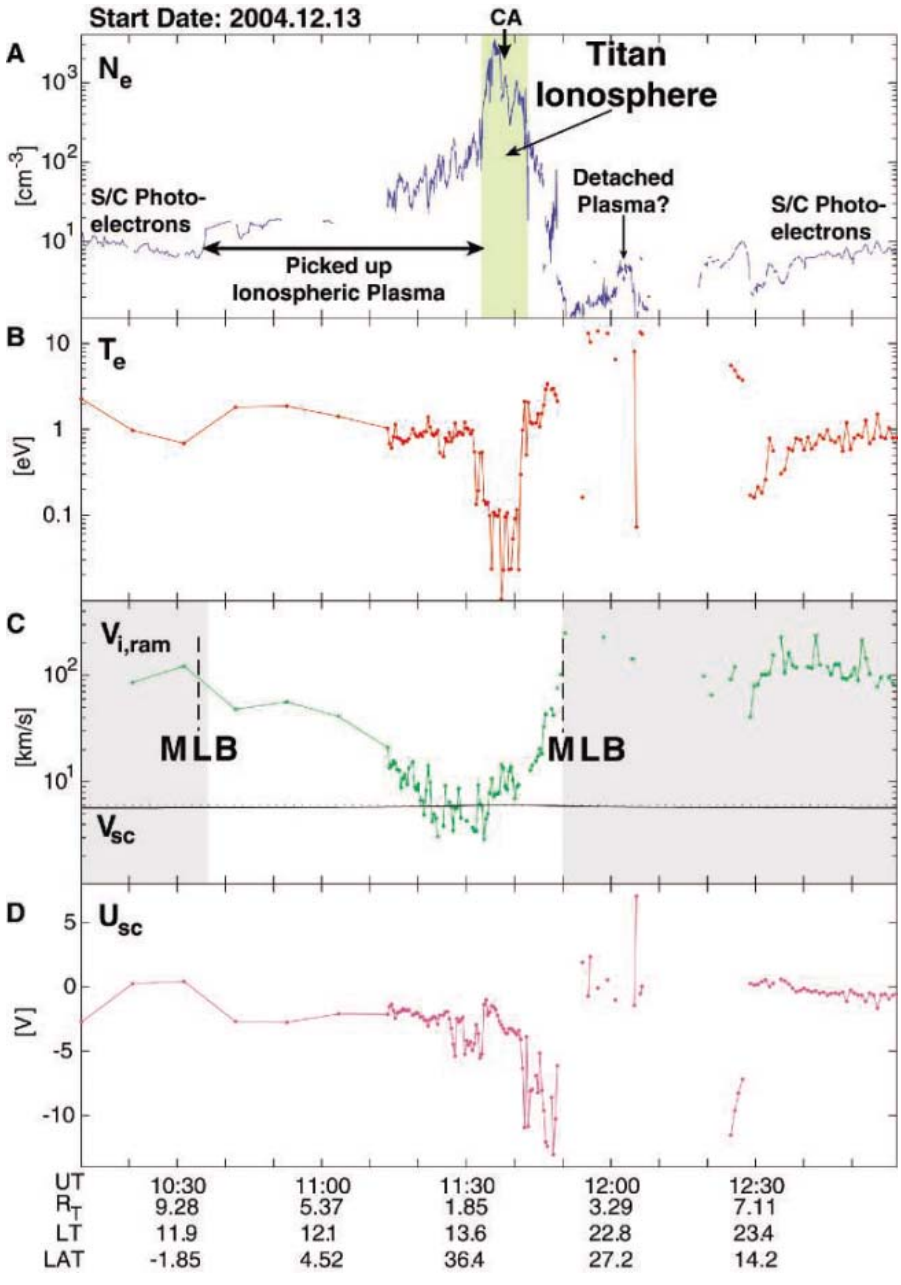

Fig. 3. Cold plasma characteristics during T_B. The data reveal a large and asymmetric interaction where the magnetosphere of Saturn picked up ionospheric plasma as far out as 9 R_S inbound from Titan. The outbound (Saturn-facing) MLB was much closer to Titan and similar to the T_A flyby. The displayed parameters are (**A**) electron number density, (**B**) electron temperature (T_e), (**C**) ion ram speed and spacecraft speed, and (**D**) spacecraft potential. The gray shaded areas in (C) indicate possibly underestimated ion ram speeds.

The closest approach T_A electron temperatures (Fig. 4) were 1200 to 1400 K and increased from these values with altitude. The magnetic geometry was rather complicated during the outbound pass, and it was hard to justify an estimate of the electron heat conduction. However, the magnetic geometry did not change considerably during the inbound pass, and the estimated electron temperature gradient (0.1 to 0.8 meV/km) is more reliable. We conclude that the ionospheric electron energy balance is controlled mostly by electron heat conduction from Titan's wake into the atmosphere, which is in qualitative agreement with theoretical predictions (*15*, *16*). The derived electron temperatures near closest approach during the T_B flyby were lower (110 to 1200 K, Fig. 2). Future studies will use

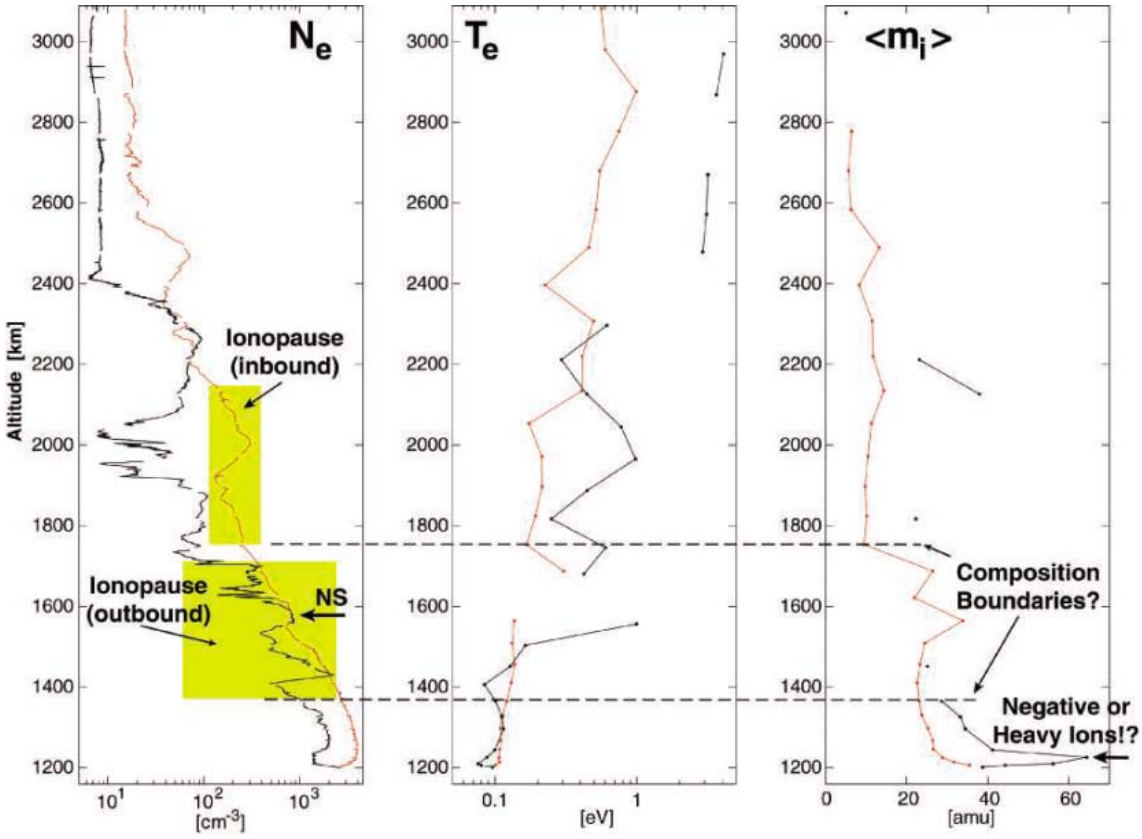

Fig. 4. Altitude profiles of electron number density (N_e), electron temperature (T_e), and mean ion mass ($\langle m_i \rangle$) during the T_A flyby. The ionopause regions and the magnetic wake neutral sheet (NS) are indicated. There seem to be composition boundaries associated with the lower part of the ionopause regions. The RPWS LP also detected signatures below the maximum density signatures, which could be due to substantial amounts of heavy ions (60 to 70 amu) or possibly negative ions.

the LP in a mode that provides better accuracy for low-temperature values.

References

1. D. A. Gurnett *et al.*, *Science* **307**, 1255 (2005); published online 16 December 2004 (10.1126/science.1105356).
2. M. Blanc *et al.*, *Space Sci. Rev.* **104**, 253 (2002).
3. H. Backes *et al.*, paper presented at the American Geophysical Union fall meeting, San Francisco, 2004.
4. T. E. Cravens *et al.*, in preparation.
5. D. A. Gurnett *et al.*, *Space Sci. Rev.* **114**, 395 (2004).
6. A. Coates *et al.*, paper presented at the American Geophysical Union fall meeting, San Francisco, 2004.
7. H. Backes *et al.*, *Science* **308**, 992 (2005).
8. R. Lundin, S. Barabash, *Adv. Space Res.* **33**, 1945 (2004).
9. D. Vignes *et al.*, *Geophys. Res. Lett.* **27**, 49 (2000).
10. D. A. Gurnett, F. L. Scarf, W. S. Kurth, *J. Geophys. Res.* **87**, 1395 (1982).
11. S. A. Ledvina *et al.*, *Adv. Space Res.* **33**, 2092 (2004).
12. E. Kallio *et al.*, *Geophys. Res. Lett.* **31**, L15703 (2004).
13. A. F. Nagy *et al.*, *J. Geophys. Res.* **106**, 6151 (2001).
14. A. F. Nagy *et al.*, *Space Sci. Rev.* **111**, 33 (2004).
15. C. N. Keller, T. E. Cravens, *J. Geophys. Res.* **99**, 6527 (1994).
16. A. Roboz, A. F. Nagy, *J. Geophys. Res.* **99**, 2087 (1994).

14 January 2005; accepted 24 March 2005
10.1126/science.1109807

REPORT

Energetic Neutral Atom Emissions from Titan Interaction with Saturn's Magnetosphere

D. G. Mitchell,[1]* P. C. Brandt,[1] E. C. Roelof,[1] J. Dandouras,[2] S. M. Krimigis,[1] B. H. Mauk[1]

The Cassini Magnetospheric Imaging Instrument (MIMI) observed the interaction of Saturn's largest moon, Titan, with Saturn's magnetosphere during two close flybys of Titan on 26 October and 13 December 2004. The MIMI Ion and Neutral Camera (INCA) continuously imaged the energetic neutral atoms (ENAs) generated by charge exchange reactions between the energetic, singly ionized trapped magnetospheric ions and the outer atmosphere, or exosphere, of Titan. The images reveal a halo of variable ENA emission about Titan's nearly collisionless outer atmosphere that fades at larger distances as the exospheric density decays exponentially. The altitude of the emissions varies, and they are not symmetrical about the moon, reflecting the complexity of the interactions between Titan's upper atmosphere and Saturn's space environment.

Interactions between charged particles and neutral gases are ubiquitous throughout much of the solar system, the Galaxy, and the universe. In the magnetosphere of a magnetized planet, charge exchange between energetic ions and the exosphere of the planet or any of its moons can modify the rate of erosion of the gravitationally bound atmosphere. This process also results in the loss of energy and material from the magnetosphere. A fast ion exchanges charge with a cold neutral atom, becomes an ENA, and freely escapes its previous magnetic confinement as a newly born neutral. Left behind is the former cold neutral gas atom, now a cold ion, which is then typically picked up in the planetary magnetic and electric fields and swept out of the exosphere where it originated.

[1]Applied Physics Laboratory, Johns Hopkins University, Laurel, MD 21042, USA. [2]Centre D'Etude Spatiale Des Rayonnements, 31028 Toulouse, France.

*To whom correspondence should be addressed. E-mail: don.mitchell@jhuapl.edu

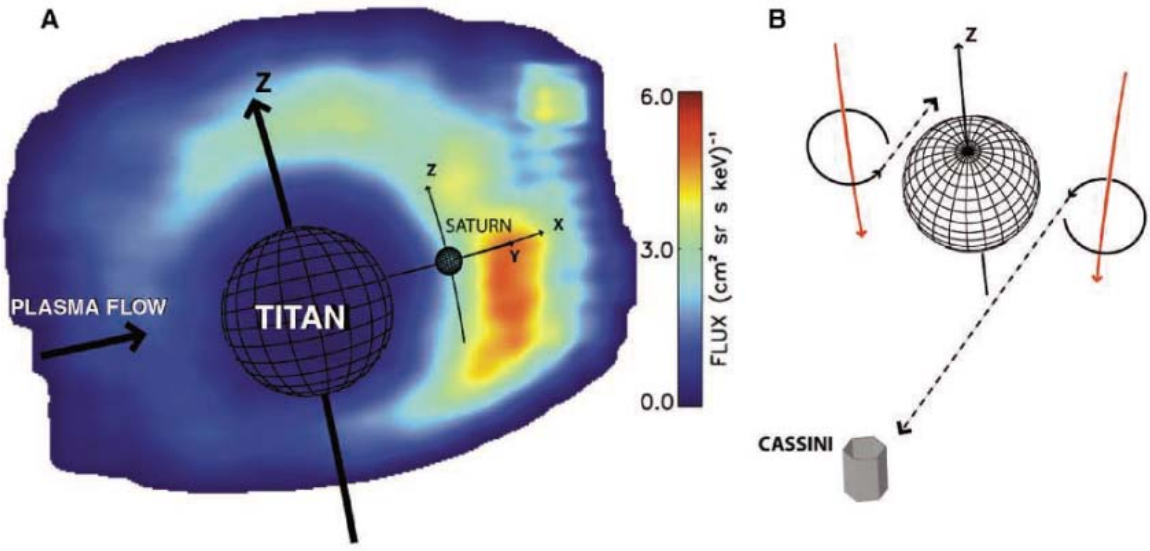

Fig. 1. (**A**) ENA image in 20 to 50 keV H of magnetically trapped protons charge-exchanging in Titan's exosphere. Intensity is color-coded on a linear scale from 0 to 10 ENAs cm^{-2} s^{-1} sr^{-1} keV^{-1}. The limits of the emission are circumscribed by the INCA sensor 90°-by-120° FOV. The latitude-longitude grid locates Titan (north up) at 15:14:25 UT on 26 October 2004, the midpoint of the 8-min image integration. Saturn is shown to the right of Titan. The ENA emission is dominated by the Titan interaction; general Saturnian magnetospheric emission is obscured by Titan's atmosphere. (**B**) Schematic proton gyration in a southward field at Titan. As the magnetic field guiding the proton to the left approached Titan, the right side of its circle of gyration encountered the dense atmosphere (absorbing the proton) before the left side, with the appropriate velocity vector to appear as an ENA at Cassini, reaches the altitude (exospheric density) of maximum likelihood for charge exchange.

The initial close encounter between the Cassini spacecraft and Titan took place on 26 October 2004 as Cassini approached within a few Titan radii of the moon (Titan's radius is 2575 km). This encounter took place as Cassini was inbound on the day side, at 10:30 local time and about 4 hours after the last inbound magnetopause crossing. The first resolved MIMI/INCA (*1*) ENA image of Titan's exosphere (Fig. 1A) confirms some theoretical expectations. The hole in the emission, centered on Titan, was expected and is a result of the absorption of the ambient energetic ions by Titan's dense lower atmosphere (*2*). The crescent shape to the emission region was also anticipated: The left side (upstream side in the corotating plasma flow) is much dimmer than the downstream side. Dandouras *et al*. (*3*) predicted this feature and explained it in terms of shadowing of the ambient magnetically trapped energetic ions. Protons with energies covered by this observation gyrate about the magnetic field, and the sizes of the gyroradii are comparable to Titan's diameter (Fig. 1B). For a nominal magnetospheric magnetic field directed from north to south (downward in the figure), the protons that are converted to ENAs to the left side of Titan may intersect Titan's atmosphere before they reach the point in their gyrating trajectories where they can be efficiently converted to observable ENAs. Protons converted to ENAs on the right side of Titan have trajectories that originate far from Titan's atmosphere, so they are free to complete their gyration about the magnetic field without encountering a high-density neutral gas region. Those particles that are observed after their conversion to ENAs intersect the densest part of the Titan exosphere, close to the region where they are traveling, tangent to constant atmospheric density contours. At the altitude where the exospheric density is such that they begin to have a high probability for conversion to ENA, a bright emission is observed. Above that peak, the emission drops again as the exospheric density falls roughly exponentially (*2*). Oxygen ENAs are also generated in this interaction, but the statistics are insufficient to analyze the images in detail.

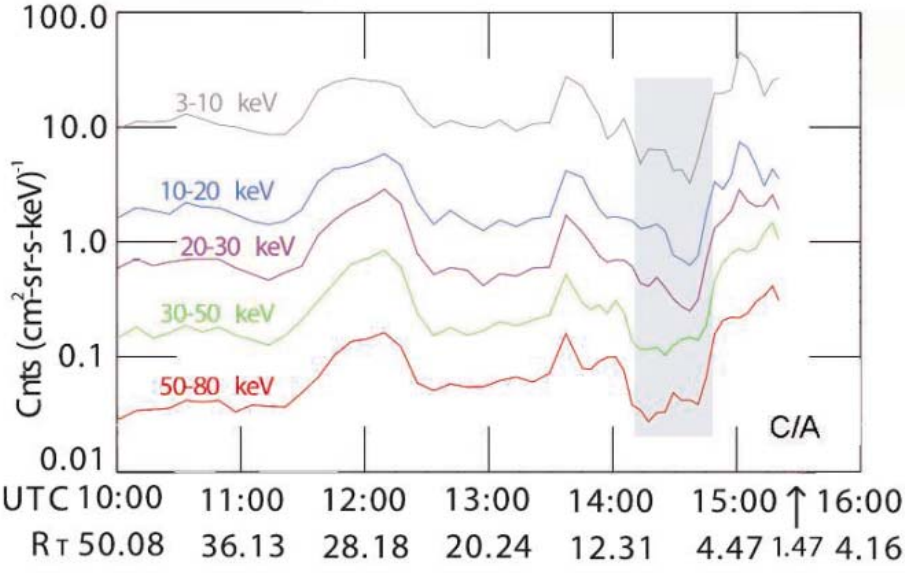

Fig. 2. ENA flux integrated over hydrogen images for specific energy pass bands versus time during the approach to Titan on 26 October 2004. Between 14:10 and 14:40 UT, the Cassini spacecraft reoriented for radar imaging of Titan, removing Titan from the INCA FOV and creating the dip in ENA intensity (shaded area).

The ENA emissions (like those in Fig. 1) varied substantially with time. This is because Titan is 20 planetary radii from Saturn and orbits in the equatorial plane, a region where ion intensity can vary by orders of magnitude over hours or even minutes (*4*). The ENA emission strength varies because the intensity of energetic ions interacting with Titan varies; Titan's atmosphere and exosphere do not vary much on these time scales. Consistent with this supposition, in situ measurements for this flyby as well as for the 13 December flyby showed essentially random ion intensity variations along the Cassini trajectory.

The image-integrated ENA emission from Titan's exosphere is displayed in Fig. 2. For the distances represented in Fig. 2 (between 50 and 2 Titan radii), the entire exospheric emitting region is contained within the INCA field of view (FOV) of 90° by 120°, and a constant emission source would vary in integrated strength by the inverse square law. However, a simple inverse

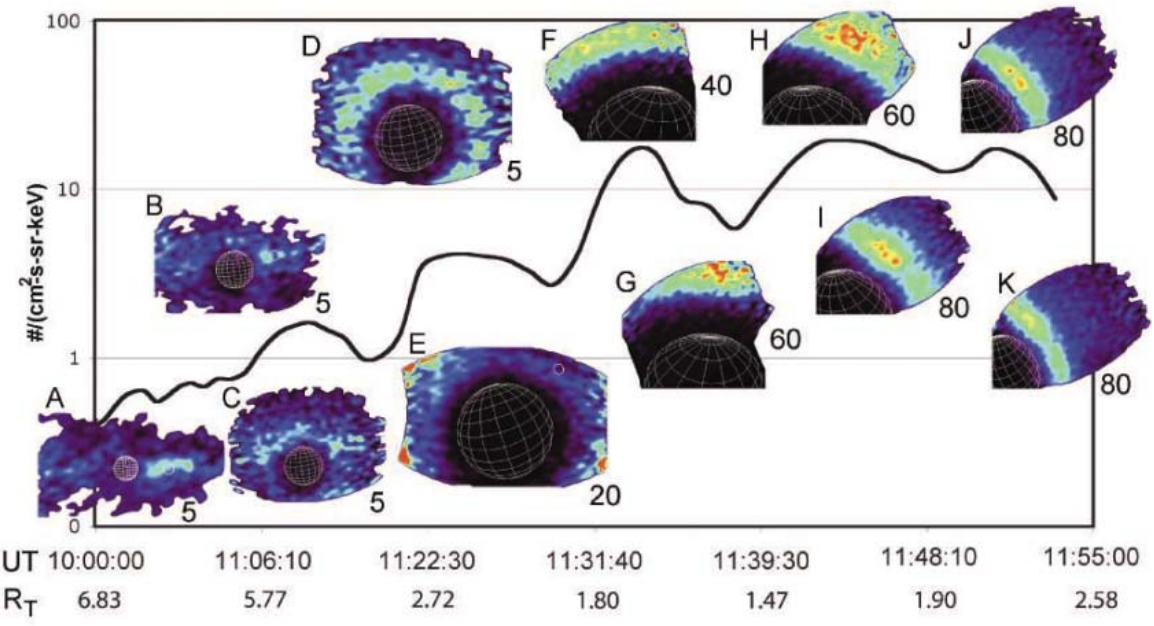

Fig. 3. Energetic hydrogen images in the 20 to 50 keV pass band during the 13 December 2004 encounter. The images are located according to their acquisition time. The timeline is highly nonlinear. Each image is scaled linearly in color (intensity) between 0 and the number immediately to the lower right, in ENAs cm^{-2} s^{-1} sr^{-1} keV^{-1}. R_T indicates Titan radii (2500 km).

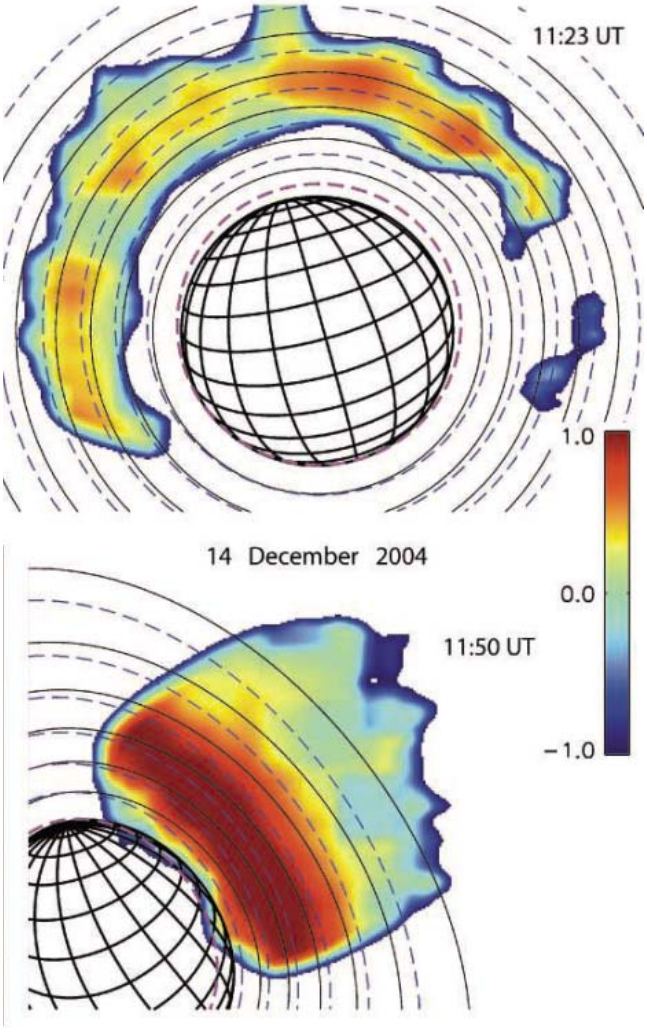

Fig. 4. One-minute exposure images in 50 to 80 keV H during the 13 December 2004 Titan encounter. Intensity is scaled logarithmically between 0.1 and 10 cm^{-2} s^{-1} sr^{-1} keV^{-1}. The latitude-longitude grid represents Titan's position (north up) at the beginning of the image acquisition, whereas the heavy dashed violet line represents Titan's limb at the end of the acquisition. Likewise, the light solid curves locate the intersections of the lines of sight from Cassini to the tangent point of spherical shells about Titan at 500, 1000, 1500, …, 3000 km altitude in the atmosphere at the beginning of image acquisition, whereas the light blue dashed curves locate the same points at the end of acquisition. (**Top**) H ENA emission as it appeared during approach to Titan. (**Bottom**) H ENA emission as it appeared after closest approach, when the low altitude boundary appears to be close to Titan's limb.

square law is not evident. Instead, the emission varied considerably with time, because clouds of magnetically confined ions were swept over Titan and its atmosphere by the rotation of Saturn's magnetic field, which rotates more or less rigidly with the planet about once every 10 hours 45 min. Indeed, a major peak in the ENA flux from Titan was measured almost 4 hours before closest approach. As a precautionary measure against high voltage breakdown in Titan's atmosphere, for this encounter the INCA sensor was turned off before closest approach, so no data are available during or after closest approach.

On 13 December 2004, Cassini made its second close flyby of Titan. The geometry for the second encounter was nearly identical to that for the first (including the fact that Cassini was close to but inside the magnetopause), so we expected to see essentially the same features. Instead, the observed interactions were more complex (Fig. 3). On the approach, the ENA emission associated with the Titan exospheric interaction once again varied strongly with time. However, Titan-associated ENA emission remained low until just before closest approach, when a cloud of trapped ions swept over Titan, lighting up the exosphere in ENA. This time, the ENA emission was relatively symmetric about the moon, with little hint of a crescent shape [(Fig. 3, D and E) Titan is not centered in the FOV, so the circle of emission is cut off to Titan's south]. Unlike the 26 October flyby, INCA remained on until 17 min after closest approach, so the emission was imaged from a variety of positions.

The horizontal axis in Fig. 3 is not linear in time; rather, the time intervals along the axis have been scaled by the reciprocal of the spacecraft distance to Titan. This representation emphasizes the time around closest approach and provides a format through which the associated ENA images can be easily cross-referenced to both time and the variation in flux. The first hour of this 2-hour segment was characterized by no discernable ENA emission from the Titan exosphere (Fig. 3, A

and B). Titan and its atmosphere measurably absorbed the ENA emission from Saturn's magnetosphere (Fig. 3B). In Fig. 3C, which corresponds in time with the first increase in the integrated ENA flux (black curve), a hint of the halo emission seen in the October Titan encounter is evident. Later (Fig. 3D) the characteristic halo emission is quite evident, including the dark region in the lower atmosphere where the neutral density is too high for survival of the magnetically trapped ions (*2*, *3*).

By 11:27 universal time (UT) (Fig. 3E) the peak of the ENA emission was no longer within the 90°-by-120° FOV. The ENA intensity increased all the way to the edge of the FOV. The emission was considerably more intense: The color in this image is scaled to a peak value of 20 cm^{-2} s^{-1} sr^{-1} keV^{-1}, four times the peak in the preceding images.

Beginning in Fig. 3F, the orientation of the INCA FOV relative to Titan changed, and Titan's limb remained in the FOV for the remainder of the observation. The peak intensity in the images also rose (note the rescaling of the color bar). As shown in the last several images, a qualitative change occurred: The peak emission, which in Fig. 3, D to F, remained well above the limb, moved closer and closer to the limb until the time of Fig. 3, I to K, and then it appeared at a much lower apparent altitude.

With the use of the currently accepted range for the Titan exospheric density profile (*5*, *6*), we calculated the altitude at which we expect to find the maximum emissions by using the same approach outlined in Amsif *et al*. (*2*) and Dandouras *et al*. (*3*). Because the density profile was slightly different than that assumed in (*2*) and (*3*), the predicted altitude of the peak was a bit lower (1400 km versus 1700 km). Emissions are expected to fall steeply below that altitude, because the mean free path for the ions and ENAs rapidly shortens in the dense lower atmosphere (scale height of roughly 150 km). The observed peak in emission for the October encounter, at an altitude of ~2000 km for the tangent point of the line of sight, was higher than the predicted ~1400 km. In the 13 December encounter, the peak emission moved from about the same tangent point altitude (~2000 km) to an apparent altitude much lower than can be easily explained (~1000 km) toward the end of the encounter (Fig. 4). The model we used to predict the location of the peak intensity did not include the complex and important physics of the interaction between the ionosphere of Titan and the corotating, magnetized medium in which Titan is immersed. Treated as noninteracting, the magnetic field close to Titan has the same magnitude and direction as the field that intercepts Titan, and the ion interaction with the exosphere can be described by simple geometry (*3*).

In actuality, the highly conducting ionosphere interacts strongly with the flowing, magnetized medium about it, and magnetic flux piles up on the upstream side and drapes about Titan into a long tail on the downstream side, quite analogous to a comet tail in the magnetized solar wind. This Alfvénic interaction creates much higher magnetic field strengths than in the unperturbed medium as well as far different vector directions of the field. The trapped, gyrating ions are controlled by that field close to the moon, executing much more complex motions than those predicted by the simple noninteracting model. Consideration of effects of the actual measured magnetic field on ion trajectories during each flyby suggests that the unexpectedly high altitude for the peak emission during each Titan approach may be explained by the departure of these near-Titan magnetic field characteristics from the model used by Amsif *et al*. (*2*). Images taken after closest approach on 13 December (with the peak ENA emission occurring at anomalously low apparent altitude) will likewise require a more sophisticated treatment.

The energetic neutral atom images of Titan thus have revealed unexpected aspects of the interaction between the trapped energetic plasma and the exosphere of an outer planet moon. As is often the case, simple models are not adequate to describe all of the features found in the images. The Cassini MIMI images reveal the structure of ENA emission from the Saturn magnetosphere–Titan exosphere interaction to be quite complex. The emission is sensitive to quantitative details of the electromagnetic interaction of Titan's atmosphere and ionosphere, with the fast flowing corotating magnetosphere surrounding them. Magnetohydrodynamic and kinetic effects lead to extreme departures of the magnetic field direction and strength from the nominal conditions in the unperturbed medium, and the ENA images affirm that improved models of the interaction are required to represent that complexity.

References and Notes

1. S. M. Krimigis *et al.*, *Space Sci. Rev.* **114**, 233 (2004).
2. A. Amsif, J. Dandouras, E. C. Roelof, *J. Geophys. Res.* **102**, 22169 (1997).
3. J. Dandouras, A. Amsif, *Planet. Space Sci.* **47**, 1355 (1999).
4. S. M. Krimigis *et al.*, *Science* **307**, 1270 (2005).
5. R. J. Vervack, B. R. Sandel, D. F. Strobel, *Icarus* **170**, 91 (2004).
6. R. V. Yelle, *Astrophys. J.* **383**, 380 (1991).
7. The MIMI program at the Johns Hopkins University Applied Physics Lab is supported by the NASA Office of Space Science under task order 003 of contract NAS5-97271 between the NASA/Goddard Space Flight Center and the Johns Hopkins University.

14 January 2005; accepted 16 March 2005
10.1126/science.1109805

REPORT

Titan's Magnetic Field Signature During the First Cassini Encounter

Heiko Backes,[1]* Fritz M. Neubauer,[1] Michele K. Dougherty,[2] Nicholas Achilleos,[2] Nicolas André,[3] Christopher S. Arridge,[2] Cesar Bertucci,[2] Geraint H. Jones,[4] Krishan K. Khurana,[5] Christopher T. Russell,[5] Alexandre Wennmacher[1]

The magnetic field signature obtained by Cassini during its first close encounter with Titan on 26 October 2004 is presented and explained in terms of an advanced model. Titan was inside the saturnian magnetosphere. A magnetic field minimum before closest approach marked Cassini's entry into the magnetic ionopause layer. Cassini then left the northern and entered the southern magnetic tail lobe. The magnetic field before and after the encounter was approximately constant for ~20 Titan radii, but the field orientation changed exactly at the location of Titan's orbit. No evidence of an internal magnetic field at Titan was detected.

We report results from the Cassini magnetometer experiment obtained during the first close encounter [closest approach (CA) altitude: 1174 km] of Cassini with Saturn's moon Titan on 26 October 2004. This was the first opportunity to investigate Titan's environment with in situ measurements since the Voyager 1 flyby in 1980. With its extended neutral atmosphere, Titan orbits Saturn at a distance of 20.3 Saturn radii (R_S) and an orbital period of 15.95 days. For most of its orbit Titan is inside Saturn's magnetosphere (*1*), which is populated by neutral atoms and plasma from several potential sources (Saturn atmosphere and rings, icy satellites, Titan, solar wind) and at least partially corotates with the planet. Because Titan's orbital period is much larger than Saturn's rotational period (10.7 hours),

Titan is embedded in a flow of magnetized plasma with a relative velocity on the order of 100 km/s (*2*). The magnetic field data measured as Voyager 1 flew by Titan placed an upper limit on Titan's internal magnetic field of 4.1 nT at the equatorial surface (*3*), which is approximately equal to the magnetospheric field at Titan's orbit. Thus, the interaction of Titan with Saturn's magnetosphere is of an atmospheric type, like, for example, the interaction of Venus with the solar wind, but has some unique features. At times of high solar wind dynamic pressure, when the magnetopause is pushed toward Saturn, Titan can leave the magnetosphere on the subsolar part of its orbit and interact with magnetosheath plasma or even the solar wind. In addition, the ionospheric properties on the side of Titan that faces the oncoming plasma flow vary with saturnian local time (SLT). The Voyager data also showed that the magnetospheric plasma properties are different from those of other plasmas in the solar system [trans-sonic, trans-Aflvénic, $\beta \approx 10$ (*3*, *4*)].

Cassini's magnetometer experiment is described in (*5*). Throughout the encounter, 32 vectors per second were measured by the flux gate magnetometer. At its first close encounter (T_A), Cassini passed through the northern part (with respect to the equatorial plane) of the streaming plasma wake of Titan, heading toward Saturn (Fig. 1). The closest approach occurred on 26 October 2004 15:30:04 SCET UTC (*6*) at an altitude of 1174 km above Titan. At this time Titan was near the saturnian magnetopause at 10:36 SLT (fig. S1), with the declination of the Sun relative to Titan's orbital plane $\alpha_{sol} = -23{:}23°$ (south summer). At about 12:15 on 25 October and at a radial distance of $\sim 28\ R_S$, Cassini finally crossed the saturnian bow shock and entered the magnetosheath, where strong compressional waves were observed (Fig. 2). The bow shock crossing was closer to Saturn than it was at Saturn orbit insertion (*7*), indicating that the magnetosphere was now more compressed. At about 10:40 on 26 October, 4 hours before CA and at a distance of about 39 Titan radii (R_T), Cassini finally crossed the saturnian magnetopause; thus, Titan was well inside the magnetosphere during T_A (Fig. 2). Cassini observed the magnetic field disturbance generated by Titan's interaction with the magnetospheric plasma between 15:10 and 15:50, centered about CA (15:30:04). The inbound magnetic field ($\vec{B}_{in}$) between 12:20 and 14:50, covering a distance of more than $\sim 20\ R_T$ in Titan's rest frame, was notably steady (Fig. 2), with a mean value of $\vec{B}_{in} = (0.72, 2.38, -5.60)$ nT (*8*), implying that the magnetic field was rotated toward Saturn by an angle of $\theta_{x,in} = 23.8°$. The angle between the Saturn-Sun line and Titan's orbital plane was $\|\alpha_{sol}\| = 23.2°$. The rotation toward Saturn was likely produced by Chapman-Ferraro currents in the near magnetopause. In the period after the encounter from 16:10 to 18:40, the outbound magnetic field ($\vec{B}_{out}$)

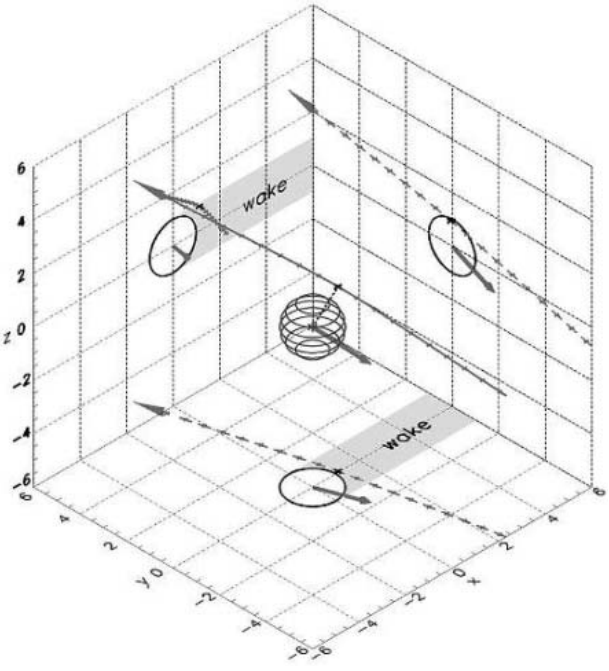

Fig. 1. Geometry of Cassini's T_A encounter. The Titan interaction coordinate system (TIIS) is centered at Titan with the *x* axis pointing in the direction of Titan's orbital motion, the *y* axis pointing toward Saturn, and the *z* axis being perpendicular to the orbital plane. Under ideal conditions, the incident plasma flow is along the *x* direction and the ambient saturnian magnetic field points in the –*z* direction. Cassini's trajectory and the projections on the three planes are shown. The drawn vector with its origin in Titan's center indicates the direction to the Sun. The wake with respect to an ideal corotating plasma flow is also indicated.

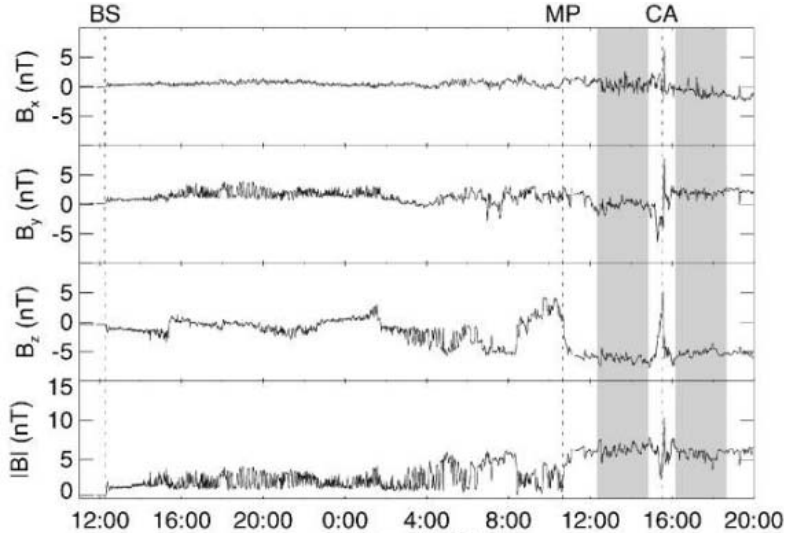

x(KSM)	21.97	21.40	20.80	20.15	19.46	18.71	17.91	17.01	16.06
y(KSM)	-14.91	-13.59	-12.24	-10.86	-9.46	-8.04	-6.58	-5.13	-3.79
z(KSM)	10.43	10.26	10.07	9.86	9.63	9.37	9.08	8.74	8.28
r (R_S)	28.5	27.3	26.1	24.9	23.7	22.4	21.1	19.8	18.5

Fig. 2. MAG data leading up to the Cassini T_A encounter (CA). The coordinates are in the Kronocentric Solar Magnetospheric (KSM) coordinate system (*x* is in the solar direction, *z* is in the plane formed by *x* and the saturnian dipole axis, and *y* completes the system). At 12:15 on 25 October 2004, Cassini crossed the bow shock (BS) at a saturnian distance of about 28 R_S. The magnetic field in the magnetosheath showed strong wave signatures. After several magnetopause crossings, Cassini finally entered the saturnian magnetosphere at 10:40 on 26 October 2004 at a distance of 21.6 R_S from Saturn's center (MP). The shaded areas mark periods of steady field inbound and outbound of the encounter.

[1]Institut für Geophysik und Meteorologie, Universität zu Köln, Albertus Magnus Platz, 50678 Cologne, Germany. [2]Space and Atmospheric Physics, Blackett Laboratory, Imperial College London, Prince Consort Road, London SW7 2AZ, UK. [3]Centre d'Etude Spatiale des Rayonnements, Université Paul Sabatier, Toulouse, France. [4]Jet Propulsion Laboratory, California Institute of Technology, 4800 Oak Grove Drive, Pasadena, CA 91109–8099, USA. [5]Institute of Geophysics and Planetary Physics, University of California, Los Angeles, CA 90095–1567, USA.

*To whom correspondence should be addressed. E-mail: backes@geo.uni-koeln.de

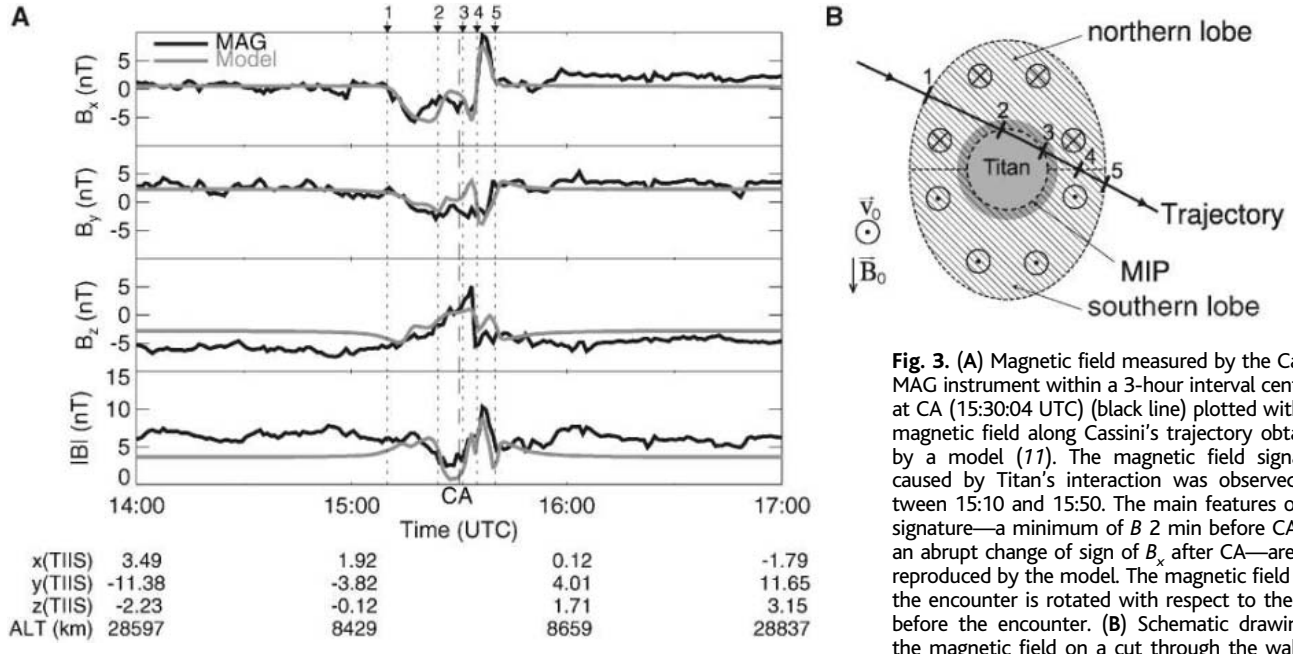

Fig. 3. (**A**) Magnetic field measured by the Cassini MAG instrument within a 3-hour interval centered at CA (15:30:04 UTC) (black line) plotted with the magnetic field along Cassini's trajectory obtained by a model (*11*). The magnetic field signature caused by Titan's interaction was observed between 15:10 and 15:50. The main features of the signature—a minimum of *B* 2 min before CA and an abrupt change of sign of B_x after CA—are well reproduced by the model. The magnetic field after the encounter is rotated with respect to the field before the encounter. (**B**) Schematic drawing of the magnetic field on a cut through the wake as obtained by the model (*11*). Titan is in gray. The hatched oval illustrates the magnetic wake. In the upper (northern) lobe the magnetic field points toward Titan, and in the lower (southern) lobe the field points away from Titan. Cassini's trajectory as it crosses the wake is drawn as a bold line. The numbers along the trajectory mark the borders between different regions traversed by Cassini [the positions are also marked in (A)]. Between positions 1 and 2, Cassini was in the northern lobe with the magnetic field pointing toward Titan $B_x < 0$. Between positions 2 and 3 Cassini dipped into the magnetic ionopause (MIP). In this region the field was at a minimum and the ionospheric electron density was at a maximum (*19*). After entering the northern lobe again for a short time (between positions 3 and 4), the polarity reversal layer (*22*) separating the northern and southern lobe was crossed and Cassini entered the southern lobe with $B_x > 0$ (between positions 4 and 5). The results of the model (*11*) that were used to generate this schematic are shown in the supporting online material (*15*).

was again steady but at a different orientation $\vec{B}_{\text{out}} = (1.99, 3.53, -3.93)$ nT and rotated more toward Saturn ($\theta_{x,\text{out}} = 41.9°$). The magnetic field changed at the position of Titan by $\Delta\vec{B} = (1.59, 1.03, 1.75)$ nT, with the magnitude remaining nearly constant ($\Delta B < 0.6$ nT). It might appear that Titan marks a boundary between two different magnetospheric regions, although no similar feature was observed by Voyager 1, and this feature may be a temporal coincidence.

Titan's large-scale magnetic interaction can be qualitatively described in terms of magnetic field line draping—a feature that has been observed, for example, at the solar wind interaction with comets (*9*). The basic idea is that a magnetized plasma streaming around a conducting obstacle leads to a draping of the frozen-in magnetic field around that obstacle [see figure 3 in (*10*)]. A quantitative description of the magnetic field topology—especially near the obstacle—is quite complicated because it involves details of the incident plasma flow and of the obstacle, which in the case of Titan consists predominantly of the neutral atmosphere and the ionosphere and their interdependence.

A three-dimensional resistive magnetohydrodynamic (MHD) model has been developed to describe Titan's interaction with the saturnian magnetospheric plasma (*11*, *12*). The model includes a static neutral atmosphere consisting of the two major species N_2 and CH_4 with radial distributions following (*13*). Ionospheric plasma is produced by photoionization and impact ionization by photoelectrons and magnetospheric electrons. The incident solar extreme ultraviolet (EUV) flux is parameterized using the EUVAC model (*14*) at solar minimum conditions. Elastic and inelastic collisions of magnetospheric electrons with the neutral gas and heat conduction along the magnetic field lines are included (*15*). The three-dimensional (3D) ionosphere generated has a dayside peak electron density of 7200 cm^{-3} at an altitude of 900 km. The nightside peak density is lower by an order of magnitude and is located at higher altitudes. We applied the model to T_A conditions (*16*) and assumed that the incident plasma properties were similar to the properties deduced from data measured during the Voyager 1 encounter (*3*).

For a comparison with the magnetic field data measured by the Cassini magnetometer (MAG) instrument during T_A, the coordinate system of the model was rotated with respect to the TIIS frame (defined in Fig. 1) in order to obtain the least-mean-square fit of the data by the model between 15:10 and 15:50. This was necessary because in the basic model it was assumed that the incident magnetic field was in the $-z$ direction. In the rotated frame the plasma velocity does not deviate from the ideal corotation direction in the equatorial plane (<1°) but has a small northward component (~10°). During the Voyager 1 encounter, the plasma velocity deviated from corotation by more than 20° in Titan's orbital plane (*17*, *18*). The incident magnetic field is rotated Saturnward (41.7°), which is inside the range between $\vec{B}_{\text{in}}$ and $\vec{B}_{\text{out}}$, and has a small x component (fig. S2). In the rotated frame (where the incident magnetic field is aligned with the $-z$ axis), the trajectory had to be adjusted appropriately. Whereas in TIIS the trajectory has a small northward component, it is southbound in the rotated frame (Fig. 3B). The model reproduces the observed magnetic field structure very well (Fig. 3A).

Titan's magnetic field signature in the interval between 15:10 and 15:40 is explained in terms of results from the model. At 15:10 the magnetic field changed direction and pointed toward Titan ($B_x < 0$ in Fig. 3A). At this point, Cassini entered the northern magnetic tail lobe (Fig. 3B). Two minutes before CA (15:28), the magnitude of the magnetic field as measured by Cassini showed a minimum and the ionospheric electron density, measured by the Langmuir probe of the plasma wave experiment (RPWS) (*19*) onboard the spacecraft, as well as in the model, was at a maximum. There are two reasons for the discrepancy between the location of the plasma density peak and CA: (i) Cassini travels along its trajectory from the dayside to the nightside of Titan. At CA, the optically thick atmosphere has absorbed most of the ionizing EUV. (ii) As predicted by the model, the ionization rate

by magnetospheric electrons is an order of magnitude lower than the photoionization rate. Both effects cause the peak location to shift from CA toward Titan's dayside, i.e., toward times before CA. The reduction of the magnetic field magnitude is a consequence of shielding currents flowing in a layer that we call the magnetic ionopause, which separates the upper magnetized ionosphere from the lower non- or weakly magnetized ionosphere. The presence of this layer has been predicted by 1D models (*20*, *21*) for the side of Titan facing the streaming plasma. Our model (*11*) successfully describes the 3D structure of this layer and explains the observed magnetic field minimum. After the minimum, the magnetic field increased and was orientated toward Titan, indicating that Cassini was still in the northern lobe. About 5 min after CA, B_x changed sign abruptly. This point marks the transition from the northern into the southern magnetic lobe (Fig. 3B), which occurs as a rotation of the magnetic field at nearly constant field magnitude (*22*). Cassini left the southern magnetic lobe at 15:39 and returned into the unperturbed saturnian magnetic field. The good agreement between the modeled (*11*) and measured magnetic field signature of Titan implies that the signature can be explained without imposing any internal magnetic field.

This conclusion is consistent with the upper limit derived from Voyager 1 (*3*). However, the geometry of the T_A trajectory was not favorable for detecting an internal field. In addition, the occurrence of the magnetic field minimum before CA indicates the existence of a magnetic ionopause at Titan, implying that the lower ionosphere is non- or weakly magnetized. The model also shows that the plasma velocity vector derived from the rotation angles in order to obtain the best fit aligns nearly perfectly with the corotation direction in the equatorial plane, with a small northward component. From the similarities between model and MAG data, we suggest that the incident flow plasma conditions were not substantially different from Voyager 1 conditions.

References and Notes

1. A. W. Schardt *et al.*, *Saturn*, T. Gehrels, M. S. Matthews, Eds. (Univ. of Ariz. Press, Tucson, AZ, 1984), pp. 417–459.
2. This velocity was measured by Voyager 1 (*3*). Ideal corotation would imply a velocity of 200 km/s in Titan's restframe.
3. F. M. Neubauer, D. A. Gurnett, J. D. Scudder, R. E. Hartle, *Saturn*, T. Gehrels, M. S. Matthews, Eds. (Univ. of Ariz. Press, Tucson, AZ, 1984), pp. 760–787.
4. Plasma-β: ratio of thermal and magnetic pressure.
5. M. K. Dougherty, *Space Sci. Rev.*, **114**, 331 (2004).
6. Space Craft Event Time (SCET) in the universal time frame (UTC). All times given here are in this time frame.
7. M. K. Dougherty *et al.*, *Science* **307**, 1266 (2005).
8. The coordinate system used is the Titan interaction system (TIIS) defined in Fig. 1.
9. H. Alfvén, *Tellus* **9**, 92 (1957).
10. N. F. Ness, M. H. Acuña, K. W. Behannon, F. M. Neubauer, *J. Geophys. Res.* **87**, 1369 (1982).
11. H. Backes, thesis, Institut für Geophysik und Meteorologie, University of Cologne, Germany (2004).
12. Several models have been developed to explain Titan's interaction with the saturnian plasma (*20*, *21*, *23–27*), which all differ in certain respects.
13. C. N. Keller, T. E. Cravens, L. Gan, *J. Geophys. Res.* **97**, 12117 (1992).
14. P. G. Richards, J. A. Fennelly, D. G. Torr, *J. Geophys. Res.* **99**, 8981 (1994).
15. Materials and methods are available as supporting material on *Science* Online.
16. Conditions at T_A: CA time, 26 October 2004, 15:30:05 UTC; CA altitude, 1174 km; SLT = 10.6; solar declination, −23.23°; angle between ideal corotation direction and Sun-Titan line, 109.2°; flyby through northern tail.
17. R. E. Hartle *et al.*, *J. Geophys. Res.* **87**, 1383 (1982).
18. M. G. Kivelson, C. T. Russel, *J. Geophys. Res.* **88**, 49 (1983).
19. J.-E. Wahlund *et al.*, *Science* **308**, 986 (2005).
20. W.-H. Ip, *Astrophys. J.* **362**, 354 (1990).
21. C. N. Keller, T. E. Cravens, L. Gan, *J. Geophys. Res.* **99**, 6511 (1994).
22. The layer between the northern and the southern lobe can have two configurations: In the first, the magnetic field is at a minimum. In this case, it is called a "neutral sheet." In the second, the magnetic field rotates continuously from the field direction in the northern lobe to the field direction in the southern lobe, while the field magnitude is constant. In this case, the expression "neutral sheet" is not appropriate and we call it "polarity reversal layer" instead.
23. T. E. Cravens, C. J. Lindgren, S. A. Ledvina, *Planet. Space Sci.* **46**, 1193 (1998).
24. S. A. Ledvina, T. E. Cravens, *Planet. Space Sci.* **46**, 1175 (1998).
25. K. Kabin, T. I. Gombosi, D. L. D. Zeeuw, K. G. Powell, P. L. Israelevich, *J. Geophys. Res.* **104**, 2451 (1999).
26. S. H. Brecht, J. G. Luhmann, D. J. Larson, *J. Geophys. Res.* **105**, 13119 (2000).
27. A. F. Nagy *et al.*, *J. Geophys. Res.* **106**, 6151 (2001).

28. We acknowledge the superb work done by the technical and data processing staff of the MAG team. H.B., F.M.N., and A.W. are supported by the DLR (Germany). M.K.D., C.B., C.S.A., and N. Achilleos are supported by PPARC (UK). N. André is supported by CNES (France). This research was performed while G.H.J. held a National Research Council Research Associateship at the Jet Propulsion Laboratory (JPL). The research at the University of California, Los Angeles, was supported by NASA under a grant administered by JPL.

Supporting Online Material

www.sciencemag.org/cgi/content/full/308/5724/992/DC1
SOM Text
Figs. S1 to S3
References

13 January 2005; accepted 10 March 2005
10.1126/science.1109763

Reconstructing the Origin of Andaman Islanders

Kumarasamy Thangaraj,[1] Gyaneshwer Chaubey,[1] Toomas Kivisild,[2] Alla G. Reddy,[1] Vijay Kumar Singh,[1] Avinash A. Rasalkar,[1] Lalji Singh[1]*

The Andaman and Nicobar Islands are inhabited by six indigenous tribal populations. Our previous work (*1*) suggested that Andamanese "Negritos" have closer affinities with Asian than with African populations and that the Nicobarese have close genetic affinities to Southeast Asians. In a parallel study by Endicott *et al.* (*2*), which also suggested Asian affinities for the mitochondrial DNA (mtDNA) lineages of the Andamanese, analyses of museum specimens related the two major lineage groups on the islands with haplogroups M2 and M4, which are found commonly throughout India (*3*–*5*). Analysis of a hypervariable sequence (HVS-I) motif indicated a link with Papuan populations (*1*). These links, however, relied on nucleotide positions in the control region of mtDNA that are known to be hypervariable. To clarify the phylogenetic position of the mtDNA lineages of the Andaman Islanders, we analyzed the complete mtDNA sequence of five Onge, five Great Andamanese, and five Nicobarese individuals.

Analysis of the Onge and Great Andamanese complete mtDNA sequences revealed the existence of two previously uncharacterized clades, which we named M31 and M32 (Fig. 1). Analysis of the complete mtDNA sequences shows that none of the coding region mutations defining these two haplogroups overlap with the known Indian or East Asian mtDNA haplogroups (*1*–*5*). In our survey of ~6500 mtDNA sequences from mainland India, none of the M lineages carried the coding region mutations specific to M31 and M32 (*6*). Furthermore, none of the haplogroup M complete sequences reported so far share any of the mutations that define M31 and M32, suggesting that these two haplogroups are likely to have evolved in situ on these islands.

Our previous studies have shown that all Eurasian and Oceanian founder haplogroups—mitochondrial M, N, and R and Y-chromosomal C, D, and F—coexist in South Asia, suggesting their comigration along the southern coastal route in one wave after the exit of modern humans from Africa (*1*, *3*–*5*). Because the Andaman Negrito populations carry only one mitochondrial founder haplogroup (M) and only one Y-chromosomal haplogroup (D), it is tempting to relate this phylogeographic pattern with a one-haplogroup–one-migration scenario. However, the shallow phylogenetic time depths of M31 and M32 in Onge and Great Andamanese populations (Fig. 1) more likely reflect the effect of genetic drift in these extremely small populations. Therefore, it is not surprising that the founding mtDNA haplogroups N* and R* and Y-chromosomal haplogroups C and F may have completely disappeared from the extant Andaman and Nicobar islanders.

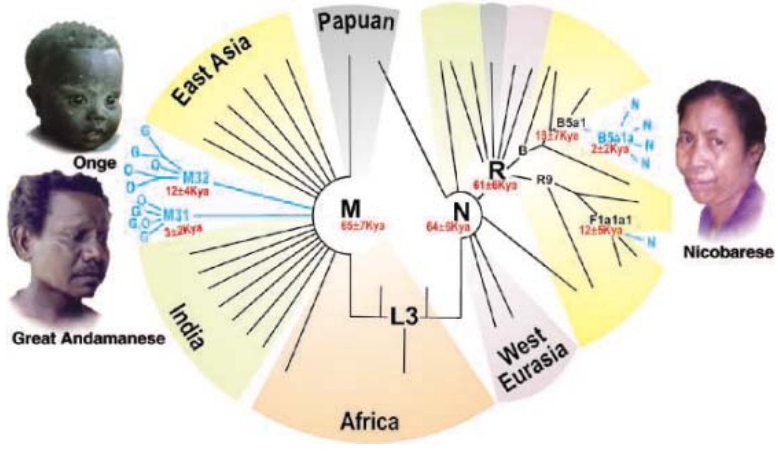

Fig. 1. A tree showing the phylogenetic position of the complete mtDNA sequences of Andaman and Nicobar islanders. O, G, and N represent Onges, Great Andamanese, and Nicobarese lineages, respectively; kya, thousands of years ago. Coalescent times of haplogroups M, N, and R were obtained from Mishmar *et al.* (*10*); a mutation rate of 1.26×10^{-8} was used for other haplogroups estimated from the present data (*7*, *10*).

Most Nicobarese mtDNA lineages belong to either of the two common haplogroups B and F (*1*), which are specific to East Asia. All four Nicobarese B5a sequences clustered together in a branch defined by three coding region substitutions (at nucleotide positions 11881, 13145, and 13395) (fig. S1) (*7*). The low variation observed both in control and coding region sequences implies that these lineages among Nicobarese coalesce to their most recent common ancestor within the past couple of thousand years. The phylogenetic analysis of a Nicobarese F sequence clustered it into haplogroup F1a1a1. This subclade of haplogroup F has been observed in China (*8*), Malaysia, and Thailand (*9*), confirming a Southeast Asian origin of this lineage in Nicobarese. Relatively older coalescence times for the most recent common ancestors of Nicobarese and Southeast Asian B5a1 and F1a1a1 lineages (Fig. 1) are based on only a few samples from Southeast Asia. Therefore, these coalescence times reflect the time of the origin of these lineages in mainland Southeast Asia rather than the time of their migration to the Nicobar Islands.

Our data indicate that two ancient maternal lineages, M31 and M32 in the Onge and the Great Andamanese, have evolved in the Andaman Islands independently from other South and Southeast Asian populations. These lineages have likely been isolated since the initial penetration of the northern coastal areas of the Indian Ocean by anatomically modern humans, in their out-of-Africa migration ~50 to 70 thousand years ago. In contrast, the Nicobarese show a close genetic relation with populations in Southeast Asia, suggesting their recent arrival from the east during the past 18 thousand years.

References and Notes

1. K. Thangaraj *et al.*, *Curr. Biol.* **13**, 86 (2003).
2. P. Endicott *et al.*, *Am. J. Hum. Genet.* **72**, 178 (2003).
3. T. Kivisild *et al.*, *Am. J. Hum. Genet.* **72**, 313 (2003).
4. P. Endicott, V. Macaulay, T. Kivisild, C. Stringer, A. Cooper, *Am. J. Hum. Genet.* **72**, 1590 (2003).
5. M. Metspalu *et al.*, *BMC Genet.* **5**, 26 (2004).
6. K. Thangaraj, unpublished data.
7. Materials and methods are available as supporting material on *Science* Online.
8. Y. G. Yao, Q. P. Kong, H.-J. Bandelt, T. Kivisild, Y. P. Zhang, *Am. J. Hum. Genet.* **70**, 635 (2002).
9. M. Ingman, H. Kaessmann, S. Pääbo, U. Gyllensten, *Nature* **408**, 708 (2000).
10. D. Mishmar *et al.*, *Proc. Natl. Acad. Sci. U.S.A.* **100**, 171 (2003).
11. We thank C. Tyler-Smith and P. M. Bhargava for their comments.

Supporting Online Material

www.sciencemag.org/cgi/content/full/308/5724/996/DC1
Materials and Methods
SOM Text
Fig. S1
References and Notes

19 January 2005; accepted 10 March 2005
10.1126/science.1109987

[1]Centre for Cellular and Molecular Biology, Hyderabad-500 007, India. [2]Estonian Biocenter, Riia 23, Tartu-51010, Estonia.

*To whom correspondence should be addressed. E-mail: lalji@ccmb.res.in

Implementation of the Semiclassical Quantum Fourier Transform in a Scalable System

J. Chiaverini,* J. Britton, D. Leibfried, E. Knill, M. D. Barrett,† R. B. Blakestad, W. M. Itano, J. D. Jost, C. Langer, R. Ozeri, T. Schaetz,‡ D. J. Wineland

We report the implementation of the semiclassical quantum Fourier transform in a system of three beryllium ion qubits (two-level quantum systems) confined in a segmented multizone trap. The quantum Fourier transform is the crucial final step in Shor's algorithm, and it acts on a register of qubits to determine the periodicity of the quantum state's amplitudes. Because only probability amplitudes are required for this task, a more efficient semiclassical version can be used, for which only single-qubit operations conditioned on measurement outcomes are required. We apply the transform to several input states of different periodicities; the results enable the location of peaks corresponding to the original periods. This demonstration incorporates the key elements of a scalable ion-trap architecture, suggesting the future capability of applying the quantum Fourier transform to a large number of qubits as required for a useful quantum factoring algorithm.

Among quantum algorithms discovered up to this time, Shor's method for factoring large composite numbers (*1*) is arguably the most prominent application of large-scale quantum information processing, given that efficient factoring would render current cryptographic techniques based on large composite-number keys vulnerable to attack. The key component of this algorithm is an order-finding subroutine that requires application of the quantum discrete Fourier transform (QFT) to determine the period of a set of quantum amplitudes (*1–4*). The QFT is also an essential part of quantum algorithms for phase estimation and the discrete logarithm (*4*). In fact, the polynomial-time QFT is responsible for most of the known instances of exponential speedup over classical algorithms.

Relative phase information of the output state from the QFT is not required when applied in any of the algorithms mentioned above; only the measured probability amplitudes of each state are used. This allows the replacement of the fully coherent QFT with the semiclassical (or "measured") QFT (*5*), in which each qubit is measured in turn, and prescribed controlled-phase rotations on the other qubits are conditioned on the classical measurement outcomes. This eliminates the need for entangling gates in the QFT protocol, which considerably relaxes the required control of motional states for the trapped-ion implementation. In addition, the semiclassical version is quadratically more efficient in the number of quantum gates when compared with the fully coherent version (*6*), a benefit in any physical implementation of quantum computing. The coherent QFT has been implemented in nuclear magnetic resonance systems (*7–11*) but has not been demonstrated in a scalable system (*12*). Here, we describe an implementation of the measured QFT in an architecture that can be scaled (*13*, *14*).

The QFT is a basis transformation in an N-state space that transforms the state $|k\rangle$ (k is an integer ranging from 0 to $N-1$) according to

$$|k\rangle \rightarrow \frac{1}{\sqrt{N}} \sum_{j=0}^{N-1} e^{i2\pi jk/N} |j\rangle \qquad (1)$$

The action on an arbitrary superposition of states may be written as

$$\sum_{k=0}^{N-1} x_k |k\rangle \rightarrow \sum_{j=0}^{N-1} y_j |j\rangle \qquad (2)$$

where the complex amplitudes y_j are the discrete Fourier transform (*15*) of the complex amplitudes x_k. For three qubits, switching to binary notation, where k_1, k_2, and k_3 are the most to least significant bits, respectively, in the label for the state $|k_1\ k_2\ k_3\rangle = |k_1\rangle \otimes |k_2\rangle \otimes |k_3\rangle$ ($k_i \in \{0,1\}$), the transform can be written as (*4*)

$$|k_1 k_2 k_3\rangle \rightarrow \frac{1}{\sqrt{8}} (|0\rangle + e^{i2\pi[0.k_3]}|1\rangle) \otimes (|0\rangle + e^{i2\pi[0.k_2 k_3]}|1\rangle) \otimes (|0\rangle + e^{i2\pi[0.k_1 k_2 k_3]}|1\rangle) \qquad (3)$$

where $[0.q_1\ q_2\ \ldots q_n]$ denotes the binary fraction $q_1/2 + q_2/4 + \ldots + q_n/2^n$. When written in this form, it can be seen that the QFT is the application to each qubit of a Hadamard transformation $[|0\rangle \rightarrow (1/\sqrt{2})(|0\rangle + |1\rangle)$ and $|1\rangle \rightarrow (1/\sqrt{2})(|0\rangle - |1\rangle)]$ and a z rotation conditioned on each of the less significant qubits, with a phase of decreasing binary significance due to each subsequent qubit, all followed by a bit-order reversal (*4*). The three-qubit quantum circuit, without the bit-order reversal, is shown in Fig. 1A. The simplified circuit for the measured QFT is shown in Fig. 1B.

In the experiment, z rotations are transformed into x rotations, which are more straightforward to implement in our system, and rotations are redistributed to accommodate required spin-echo refocusing pulses (π rotations) which reduce dephasing due to fluctuating magnetic fields (*16–18*), but this does not change the basic protocol. Because of the substitution of $\pi/2$ rotations for Hadamard operations and our choice of conditional-rotation direction, the coherent QFT corresponding to our measured QFT is described by

$$|k_1 k_2 k_3\rangle \rightarrow \frac{1}{\sqrt{8}} (|0\rangle - e^{-i2\pi[0.k_3]}|1\rangle) \otimes (|0\rangle - e^{-i2\pi[0.k_2 k_3]}|1\rangle) \otimes (|0\rangle - e^{-i2\pi[0.k_1 k_2 k_3]}|1\rangle) \qquad (4)$$

The sign differences from Eq. 3 are unimportant, because only the probability amplitudes of the output state are measured; the relative phases of the output-basis states are arbitrary. We have applied this three-qubit QFT to input states of several different periodicities.

The qubits comprise two states of the ground-state hyperfine manifold of $^9Be^+$: the state $|F=1, m_F=-1\rangle$, labeled $|0\rangle$, and the state $|F=2, m_F=-2\rangle$, labeled $|1\rangle$. These states are separated in frequency by 1.28 GHz. Rotations

$$R(\theta,\phi) = \cos\frac{\theta}{2} I - i \sin\frac{\theta}{2} \cos\phi\, \sigma_x - i \sin\frac{\theta}{2} \sin\phi\, \sigma_y \qquad (5)$$

are performed by means of two-photon stimulated-Raman transitions (*19*, *20*). Here, θ is the rotation angle, ϕ is the angle of the

National Institute of Standards and Technology, Boulder, CO 80305, USA.

*To whom correspondence should be addressed. E-mail: john.chiaverini@boulder.nist.gov
†Present address: Physics Department, University of Otago, Dunedin 9001, New Zealand.
‡Present address: Max Planck Institut für Quantenoptik, Garching 85748, Germany.

rotation axis from the x axis in the xy plane of the Bloch sphere (*17*), I is the identity operator, and σ_x and σ_y are the usual Pauli spin operators. The beryllium ions are confined in a linear radio-frequency Paul trap (*21*), similar to that described in (*18*). This trap contains six zones, and the ions can be moved between these zones, together or separately, by means of synchronized variation of the potentials applied to the trap's control electrodes. State determination is made by projection of the qubit state with the use of resonance fluorescence (*19*) (an ion in the $|1\rangle$ state fluoresces, whereas an ion in the $|0\rangle$ state does not). Measurement results were recorded, and laser pulses were applied by means of classical logic to implement conditional operations. The QFT protocol proceeded as depicted in Fig. 2A, with ions located in the multizone trap as shown in Fig. 2B.

Five different states were prepared to test the QFT protocol (Table 1). These states have periods of 1, 2, 4, 8, and approximately 3. The three-qubit state space consists of eight states, labeled $|000\rangle$, $|001\rangle$, …, $|111\rangle$ in binary notation and ordered lexicographically. The periodicity is derived from the recurrence of the quantum amplitudes in a superposition of these eight states.

The period 1 state was generated by applying the rotation $R(\pi/2,-\pi/2)$ to all three ions in the initial state $|111\rangle$. The period 2 state was generated from $|111\rangle$ by physically separating ion 3 from ions 1 and 2, applying a rotation $R(\pi/2,-\pi/2)$ to ions 1 and 2, and then bringing all three ions back together. Similarly, the period 4 state was created by applying the rotation $R(\pi/2,-\pi/2)$ to only the first ion after separating it from ions 2 and 3. The period 8 state was simply the state of the ions after initialization, $|111\rangle$.

The most obvious (approximate) period 3 state in this eight-state space is $|000\rangle + |011\rangle + |110\rangle$ (here and in the following, we omit normalization factors). Because this state's periodicity is not commensurate with the state space, the addition of the next (in a sequence of three) basis state $|001\rangle$ to this superposition also results in an approximate period 3 state, $|\psi_3'\rangle = |000\rangle + |011\rangle + |110\rangle + |001\rangle$. We used a cyclic permutation of $|\psi_3'\rangle$; in particular, adding 3 (mod 8) to each state produces $|\psi_3\rangle = |011\rangle + |110\rangle + |001\rangle + |100\rangle$. This state is the tensor product of $|01\rangle_{1,3} + |10\rangle_{1,3}$ (ions 1 and 3) with $|0\rangle_2 + |1\rangle_2$ (ion 2). Starting from $|111\rangle$, this state can be prepared by entangling the outer two ions (ions 1 and 3) with a geometric phase gate embedded between two rotations—$R(\pi/2,\pi/4)$ and $R(3\pi/2,\pi/4)$—applied to all three ions (*21*, *22*). This was followed by a rotation $R(\pi/2,-\pi/2)$ to all three ions. This state was produced with a fidelity of approximately 0.90 (resulting from the reduced fidelity inherent in multi-qubit entangling operations compared with single-qubit rotations).

Each experiment began with Doppler cooling and Raman-sideband cooling to bring the ions to the ground state of all three axial vibrational modes of the trapping potential and optical pumping to prepare the three ions in the internal state $|111\rangle$ (*13*, *23*). The aforementioned input states were then prepared as described above. For each input state, several thousand implementations of the QFT were performed, each involving: (i) rotation of ion 1,

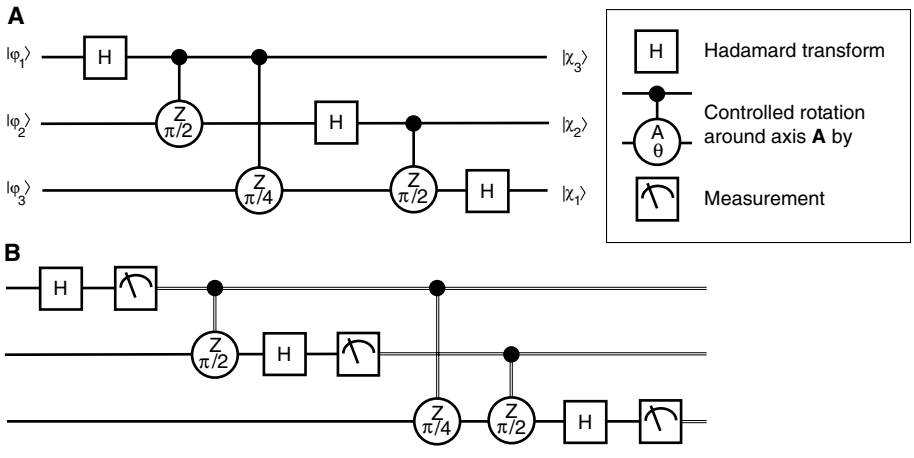

Fig. 1. Circuits for the quantum Fourier transform (QFT) of three qubits. (**A**) The QFT as composed of Hadamard transforms and two-qubit conditional phase gates (*4*). The gate-labeling scheme denotes the axis about which the conditional rotation takes place and, below the axis label, the angle of that rotation. The $|\varphi_i\rangle$ and $|\chi_i\rangle$ are the input and output states, respectively, of qubit i. The most significant qubit corresponds to $i = 1$. This circuit produces the QFT in reverse bit order, so in practice, the qubits are simply read out in reverse order (*4*). (**B**) The semiclassical (or "measured") QFT (*5*). The double lines denote classical information. This circuit can be implemented by means of a single classically controlled quantum operation on each qubit. The protocol is preceded by state preparation (Table 1) of the quantum state to be transformed.

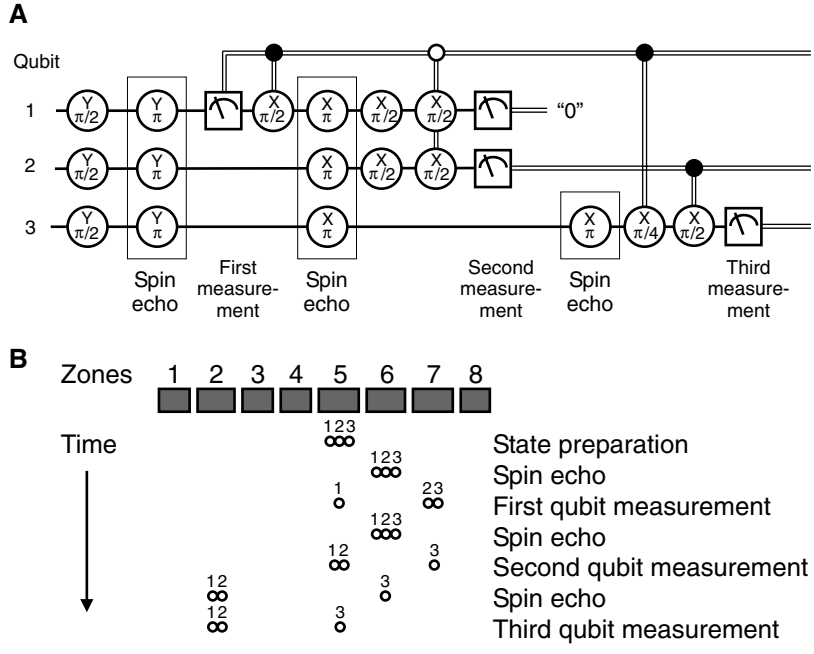

Fig. 2. Circuit for the QFT and locations of the ions in the multizone trap during protocol execution. (**A**) The semiclassical QFT (*5*) as implemented in this Report. The double lines denote classical information. The closed circles on control lines denote rotation conditional on "1"; the open circles denote rotation conditional on "0." The initial conditional rotation of qubit 1 ensures that it is in the nonfluorescing state when the second ion is measured [the second ion is measured in the presence of the first ion, which contributes negligibly to the fluorescence signal during the second measurement (*25*); refer to "Second qubit measurement" in (B)]. This circuit, up to some irrelevant phases, can be obtained from that in Fig. 1B through conjugation of rotations and reordering of some operations. (**B**) The locations of the ions in the multizone trap structure during the QFT protocol as a function of time. Separation of ions and refocusing operations are performed in zone 6, and all other qubit operations are performed in zone 5.

(ii) measurement of ion 1, (iii) rotation of ion 2 conditional on the measurement of ion 1, (iv) measurement of ion 2, (v) rotation of ion 3 conditional on the first two measurements, and (vi) measurement of ion 3. Each experiment required approximately 4 ms after initial cooling, optical pumping, and state preparation.

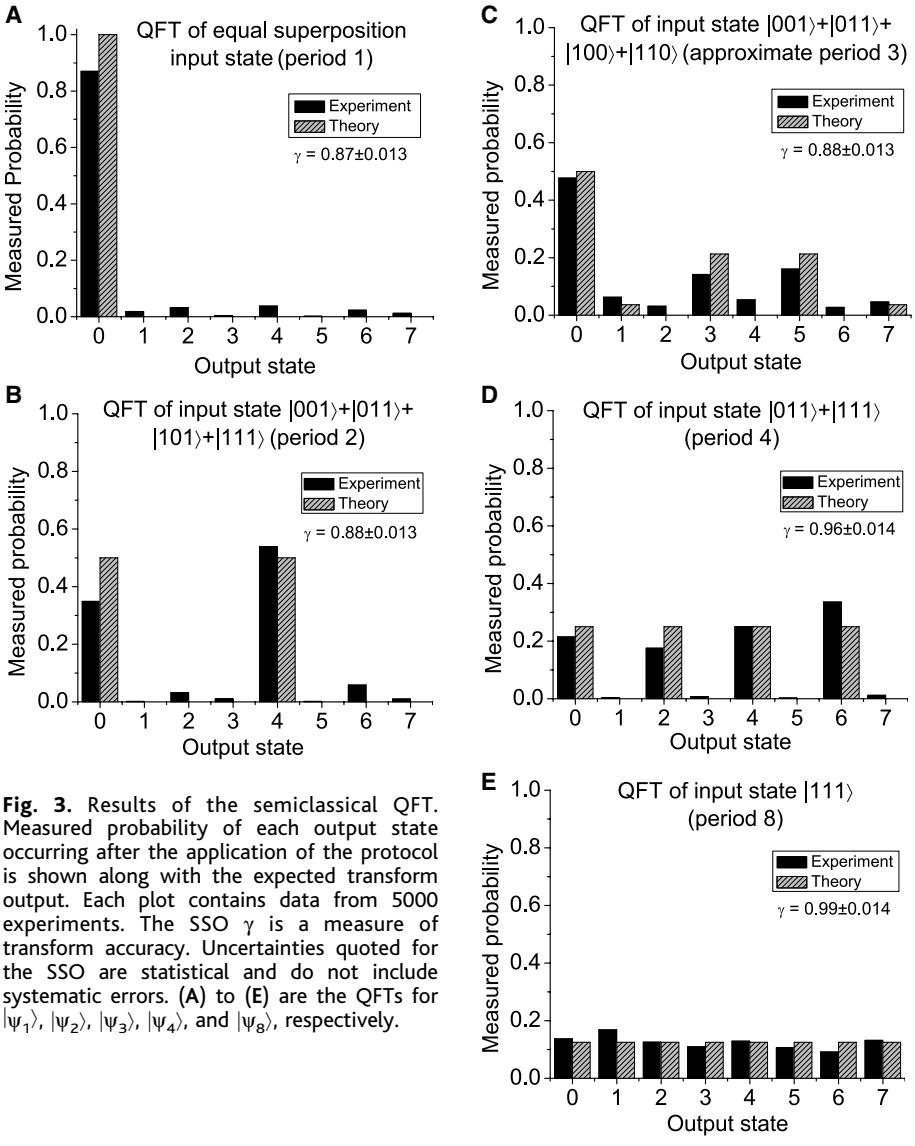

Fig. 3. Results of the semiclassical QFT. Measured probability of each output state occurring after the application of the protocol is shown along with the expected transform output. Each plot contains data from 5000 experiments. The SSO γ is a measure of transform accuracy. Uncertainties quoted for the SSO are statistical and do not include systematic errors. (**A**) to (**E**) are the QFTs for $|\psi_1\rangle$, $|\psi_2\rangle$, $|\psi_3\rangle$, $|\psi_4\rangle$, and $|\psi_8\rangle$, respectively.

The measured output-state probabilities after application of the QFT algorithm are shown in Fig. 3 along with the theoretically expected probabilities for the five different input states. The data generally agree with the theoretical predictions, although the deviations from the predicted values are larger than can be explained statistically and are due to systematic errors in the experiment. These systematic errors are associated with the state preparation (not associated with the QFT protocol) as well as with the separate detections and conditional rotations of the three ions (intrinsic to the QFT protocol). The first, second, and third ions were measured approximately 1.2 ms, 2.4 ms, and 3.5 ms after the beginning of the algorithm. Dephasing due to slow local magnetic-field fluctuations, though mitigated by the refocusing (spin-echo) operations, grows as a function of time during each experiment; the chance that an error occurs because of dephasing grows from approximately 5% for the first ion to approximately 13% for the third ion.

Even with these systematic errors, the results compare well with theory, as can be shown by examining the squared statistical overlap (SSO) [derived from the statistical overlap of (*24*)] of each set of data with the associated predictions. Here, we define the SSO as $\gamma = (\Sigma_{j=0}^{7} m_j^{1/2} e_j^{1/2})^2$, where m_j and e_j are the measured and expected output-state probabilities of state $|j\rangle$, respectively. This is an effective measure of fidelity without regard for relative output phases. The lowest measured SSO for the five prepared states is 0.87, suggesting that peaks can be reliably located to determine periodicities as required for Shor's factorization algorithm. To verify the reliability of the protocol for this task, one should compare the experimental and theoretical values of the measurement probabilities of the output states where peaks are located. For the period 2 state, the measured probability for the output state $|4\rangle = |100\rangle$ (the measurement outcome sufficient to determine the periodicity as 2), was 0.538, an 8% difference from the expected

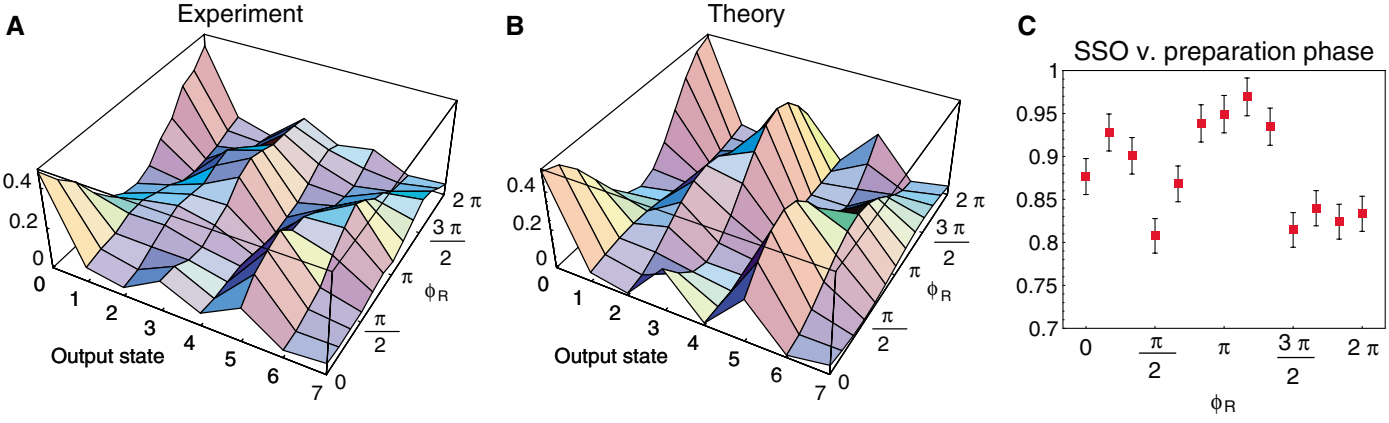

Fig. 4. Semiclassical QFT of nominal period 3 state as a function of preparation phase ϕ_R (Eq. 6). (**A**) The measured probabilities are plotted as a function of the output state and the phase of the state preparation after application of the QFT protocol. The QFT at each phase is based on 2000 experiments. (**B**) The expected probability plotted in the same manner. (**C**) The SSO γ as a function of preparation phase. Error bars represent 1σ statistical uncertainties only.

Table 1. Periodic states prepared to test the semiclassical QFT protocol. Numbers in parentheses indicate experimental uncertainty.

Periodicity	State (normalization omitted)	Preparation fidelity
1	$\|\psi_1\rangle = \|000\rangle + \|001\rangle + \|010\rangle + \ldots + \|111\rangle$	0.98(1)
2	$\|\psi_2\rangle = \|001\rangle + \|011\rangle + \|101\rangle + \|111\rangle$	0.98(1)
~3	$\|\psi_3\rangle = \|001\rangle + \|011\rangle + \|100\rangle + \|110\rangle$	0.90(2)
4	$\|\psi_4\rangle = \|011\rangle + \|111\rangle$	0.98(1)
8	$\|\psi_8\rangle = \|111\rangle$	>0.99(1)

value of 0.5. For the period 3 state, the sum of the measured probabilities for output state $|3\rangle = |011\rangle$ and state $|5\rangle = |101\rangle$ (the states corresponding to the most correct periodicity) was 0.301, a 29% difference from the expected value of 0.426. Notably, the preparation fidelity of this state was not as high as for the others.

One other set of input states was created to demonstrate that the semiclassical QFT protocol is sensitive to relative input phases. All the states of Table 1 had amplitudes (of the basis states in the superpositions) with the same phase. We also prepared a period 3 state with a relative phase between some states in the superposition. By incrementing the phase of the three uniform rotations used in the creation of the period 3 state with respect to the operations in the QFT protocol by a phase ϕ_R [that is, $R(\theta,\phi) \rightarrow R(\theta,\phi + \phi_R)$], we can create the state

$$|\psi_3(\phi_R)\rangle = |001\rangle + e^{i\phi_R}|011\rangle + |100\rangle + e^{i\phi_R}|110\rangle \quad (6)$$

The relative phase between pairs of basis states in this superposition leads to a Fourier transform that depends on ϕ_R. The measured probabilities of the eight output states are plotted in Fig. 4A along with the theoretical values in Fig. 4B. The level of agreement can be seen in Fig. 4C, a plot of the SSO as a function of preparation phase.

These results demonstrate that for small state-spaces, the QFT can be performed semiclassically with a signal-to-noise level sufficient for period-finding in quantum algorithms by means of a system of trapped-ion qubits. Even with input state infidelities as large as 0.10, as in the period 3 state created here, the measured QFT had substantial SSO with the theoretical prediction for the correct input state. Furthermore, the effect of the incommensurability of state periodicity with state space is diminished as the size of the state space increases. Peaks due to similar incommensurate periodicities will be easier to locate in larger state spaces (compared to the case of a period 3 state in an eight-state space). Extension of the technique described here to larger quantum registers (*13*, *14*) is a function only of trap-array size and involves a linear overhead in ion separation and movement. The main source of intrinsic error in our implementation was qubit dephasing resulting from magnetic-field fluctuations. Use of first-order magnetic field–independent qubit transitions (*13*) can mitigate this problem and lead to a high-fidelity method for implementation of the QFT, a necessary step toward large number–factorization applications of quantum computing.

References and Notes

1. P. W. Shor in *Proceedings of the 35th Annual Symposium on Foundations of Computer Science*, S. Goldwasser, Ed. (IEEE Computer Society Press, Los Alamitos, CA, 1994), pp. 124–134.
2. D. Coppersmith, "An Approximate Fourier Transform Useful in Quantum Factoring," (IBM Research Report RC19642, 1994).
3. A. Ekert, R. Jozsa, *Rev. Mod. Phys.* **68**, 733 (1996).
4. M. A. Nielsen, I. L. Chuang, *Quantum Computation and Quantum Information* (Cambridge Univ. Press, Cambridge, 2000).
5. R. B. Griffiths, C.-S. Niu, *Phys. Rev. Lett.* **76**, 3228 (1996).
6. For *n* qubits, the number of quantum gates is $O(n)$ rather than $O(n^2)$.
7. L. M. K. Vandersypen *et al.*, *Phys. Rev. Lett.* **85**, 5452 (2000).
8. Y. S. Weinstein, M. A. Pravia, E. M. Fortunato, S. Lloyd, D. G. Cory, *Phys. Rev. Lett.* **86**, 1889 (2001).
9. L. M. K. Vandersypen *et al.*, *Nature* **414**, 883 (2001).
10. J.-S. Lee, J. Kim, Y. Cheong, S. Lee, *Phys. Rev. A.* **66**, 042316 (2002).
11. Y. S. Weinstein *et al.*, *J. Chem. Phys.* **121**, 6117 (2004).
12. D. G. Cory *et al.*, *Fortschr. Phys.* **48**, 875 (2000).
13. D. J. Wineland *et al.*, *J. Res. Natl. Inst. Stand. Technol.* **103**, 259 (1998).
14. D. Kielpinski, C. Monroe, D. J. Wineland, *Nature* **417**, 709 (2002).
15. G. Arfken, *Mathematical Methods for Physicists* (Academic Press, Orlando, FL, ed. 3, 1985).
16. E. L. Hahn, *Phys. Rev.* **80**, 580 (1950).
17. L. Allen, J. H. Eberly, *Optical Resonance and Two-Level Atoms* (Dover, New York, 1987).
18. M. A. Rowe *et al.*, *Quantum Inf. Comput.* **2**, 257 (2002).
19. C. Monroe *et al.*, *Phys. Rev. Lett.* **75**, 4011 (1995).
20. D. J. Wineland *et al.*, *Philos. Trans. R. Soc. London Ser. A* **361**, 1349 (2003).
21. M. D. Barrett *et al.*, *Nature* **429**, 737 (2004).
22. D. Leibfried *et al.*, *Nature* **422**, 412 (2003).
23. B. E. King *et al.*, *Phys. Rev. Lett.* **81**, 1525 (1998).
24. C. A. Fuchs, thesis, University of New Mexico, Albuquerque, NM (1996); preprint available at http://arxiv.org/abs/quant-ph/9601020.
25. T. Schaetz *et al.*, *Phys. Rev. Lett.* **93**, 040505 (2004).

26. We thank J. J. Bollinger and R. P. Mirin for helpful comments on the manuscript. This work was supported by the U.S. National Security Agency (NSA) and the Advanced Research and Development Activity (ARDA). This manuscript is a publication of NIST and is not subject to U.S. copyright.

27 January 2005; accepted 16 March 2005
10.1126/science.1110335

Picometer-Scale Electronic Control of Molecular Dynamics Inside a Single Molecule

M. Lastapis, M. Martin, D. Riedel, L. Hellner, G. Comtet, G. Dujardin

Tunneling electrons from a low-temperature (5 kelvin) scanning tunneling microscope were used to control, through resonant electronic excitation, the molecular dynamics of an individual biphenyl molecule adsorbed on a silicon(100) surface. Different reversible molecular movements were selectively activated by tuning the electron energy and by selecting precise locations for the excitation inside the molecule. Both the spatial selectivity and energy dependence of the electronic control are supported by spectroscopic measurements with the scanning tunneling microscope. These experiments demonstrate the feasibility of controlling the molecular dynamics of a single molecule through the localization of the electronic excitation inside the molecule.

New concepts have recently emerged in which molecules on surfaces are considered as nanomachines in themselves (*1*). However, the use of a single molecule as a functionalized nanomachine will require the ability to power and control numerous dynamic processes at the atomic scale. Resonant electronic excitation that activates a specific reversible movement of the molecule appears to be the most promising method for controlling the operation of such a molecular nanomachine. Indeed, electronic excitation has, a priori, several advantages over other methods, such as vibrational excitation (*2–4*) or direct scanning tunneling microscope (STM) tip-molecule contact (*5*). In particular, electronic excitation should enable the molecule to be excited into far-from-equilibrium conformations, resulting in very rapid, efficient, and more easily controllable molecular dynamic processes. Such electronic control has been possible only at the macroscopic level for a collection of molecules (*6–8*).

We will show that electronic excitation and the ensuing reversible dynamics can be controlled not only at the single-molecule level but

Laboratoire de Photophysique Moléculaire, Bâtiment 210, Université Paris-Sud, 91405 Orsay, France.

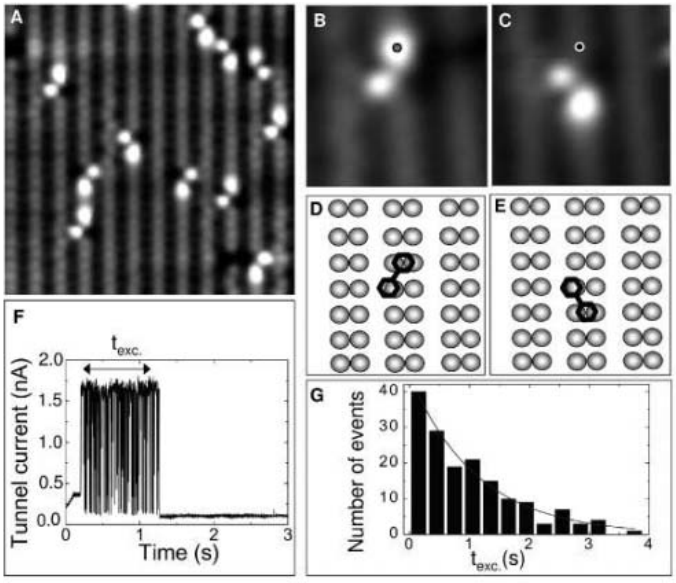

Fig. 1. (**A**) 90 Å by 90 Å STM topography (V_S = –2 V, I = 0.2 nA) of biphenyl molecules on a Si(100) surface at 5 K. (**B**) A zoom (21 Å by 21 Å) showing a single biphenyl molecule in a stable configuration (S_1). The dot indicates the STM tip position during the surface voltage pulse. (**C**) Same as (**B**) after the surface voltage pulse. The biphenyl molecule has switched to its second stable configuration (S_2). (**D**) and (**E**) show schematically the biphenyl molecule in its S_1 and S_2 adsorption configurations, respectively. The large circles represent the silicon atoms of the reconstructed Si(100) surface. (**F**) Tunnel current during the surface voltage pulse at V_S = –2.8V (duration 4 s). (The peaks in the tunnel current before t_{exc} are explained in the discussion of Fig. 3A, curve P_1.) After t_{exc}, the molecule switches, leading to a sudden drop to 0.17 nA. (**G**) Exponential distribution of the time of excitation t_{exc}.

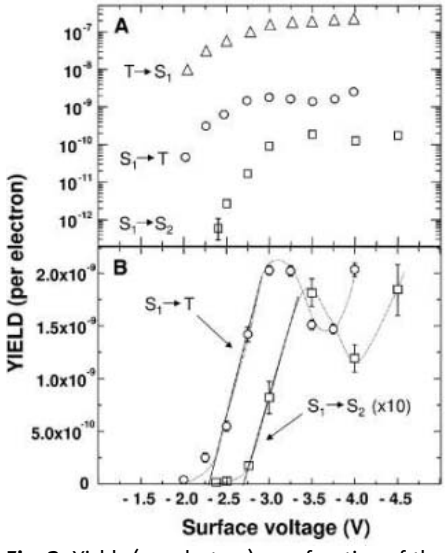

Fig. 2. Yields (per electron) as a function of the surface voltage for molecular switching ($Y_{S1\rightarrow S2}$), moving to ($Y_{S1\rightarrow T}$), and moving from ($Y_{T\rightarrow S1}$) to the transient state. Plot on an (**A**) semi-logarithmic and (**B**) linear scale.

also inside the molecule, in this case a biphenyl molecule adsorbed on a Si(100) semiconductor surface. At low temperatures (5 K), the molecule behaves as a molecular switch that can be reversibly moved either from one stable configuration to the other or into a transient configuration by resonant electronic excitation with tunnel electrons from the STM tip. By selecting precise locations for the excitation inside the molecule with the STM, specific electronically excited states are produced, each associated with a given reversible molecular movement.

A clean Si(100) surface of a p-type B-doped silicon sample with a resistivity of 0.004 to 0.006 ohm·cm is prepared in an ultrahigh-vacuum (UHV) chamber, as described elsewhere (*9*). The Si(100) surface (*9*) was held at room temperature during the exposure to biphenyl molecules, which chemisorb in a bistable configuration at this temperature (*10*). The sample was then rapidly cooled to 5 K and transferred into the UHV low-temperature STM (*9*). The STM topography of a biphenyl molecule is shown in Fig. 1, together with a diagram of the adsorption configuration. The molecule is very stable and has never been observed to move under normal scanning conditions.

To switch the bistable molecule, the STM tip was held at a fixed position over a selected part of the molecule, as indicated in Fig. 1B. After positioning the tip, the feedback loop was switched off and a negative voltage V_S was applied to the surface for a certain time (from 10 ms to 4 min) depending on V_S and the tunnel current. For each manipulation, the tip-to-surface distance was adjusted to obtain a given tunnel current. Immediately after the molecule started to move, the tunneling current I was abruptly switched from 1.7 to 0.17 nA, which resulted in an I_{on}/I_{off} ratio of 10 (Fig. 1F). This drop in I enabled the measurement of the time of excitation t_{exc}.

Afterward, a new STM topography was recorded to check that the molecule moved to the opposite bistable position (Fig. 1C). As previously discussed (*10*), this change of configuration ($S_1 \rightarrow S_2$) is believed to involve a rotation of the molecule around a fixed point, where one phenyl ring (mobile phenyl ring) undergoes a large movement across the surface while the other phenyl ring (fixed phenyl ring) rotates about a fixed point. The distribution of t_{exc} for a given I was obtained by assembling the results in bins of fixed time over a large number of experiments (*11*) (Fig. 1G). An exponential decay fit gives the average value τ of t_{exc} before switching. For each value of V_S, the mean value $I\tau/e$ of the number of electrons necessary for switching the molecule is constant when varying the intensity of the tunnel current I, indicating a one-electron process (*11*).

Further proof of an electronic-excitation mechanism (rather than an electric-field-induced process) is that the switching yield is constant when varying the temperature from 5 to 10 K. The switching yield $Y_{S1\rightarrow S2} = 1/(I\tau/e)$, which is the probability of switching per electron, is shown as a function of the surface voltage V_S in Fig. 2. A threshold energy of –2.7 ± 0.1 eV has been deduced by assuming a linear-threshold law similar to that for single ionization by electron impact of gas-phase atoms and molecules (*12*). This threshold energy suggests that the π orbitals (highest occupied molecular orbitals) of the biphenyl molecule, which are expected to be about 2 to 3 eV below the Fermi level (*13*), are resonantly involved in the excitation mechanism. The electronic-excitation mechanism consists of the resonant transfer of an electron from the biphenyl π orbitals to the STM tip, thus creating a positively charged molecular species (*14*) equivalent to a transient oxidation of the biphenyl.

This resonant electronic excitation markedly differs from other mechanisms that also involve electronic coupling but are "off resonance" (*15*–*17*) or in "pseudoresonance" (*18*). Indeed, in the resonant electronic case, the lifetime and the shape of the potential-energy surface of the electronically excited state would be expected to play a dominant role in the molecular dynamics, whereas they should have little or no influence in the "off resonant" or "pseudoresonant" cases. The reversible switching shown in Fig. 1 is reproducible, and several thousand successive switchings could be performed on the same molecule, despite the high energy (several electron volts) of the excitation. All previously studied electronic excitation processes (*19*–*21*) were associated with irreversible dissociation, desorption, or diffusion of molecules. Here, for all voltages from –2 to –5 V and all tunnel currents from 0.1 to 15 nA, no diffusion, desorption, or fragmentation of the molecule was observed.

The ability of the low-temperature STM to perform experiments with picometer-scale spatial resolution (*22*, *23*) enables the investigation of both the electronic-excitation processes and the ensuing molecular dynamics within a molecule. Step features in the time dependence of the tunnel current measured at three different locations inside the biphenyl molecule (Fig. 3A) correspond to the reversible switching of the molecule between the two S_1 and S_2 stable configurations, as already seen in Fig. 1. The molecule has switched one, three, and nine times when the STM tip is in

position P_1, P_2, and P_3, respectively. From the distribution of the time of excitation before switching, the switching yield has been derived at each position for $V_S = -2.5$ V: $Y_{S1\rightarrow S2}(P_1) = 2.7 \pm 0.5 \times 10^{-12}$, $Y_{S1\rightarrow S2}(P_2) = 2.5 \pm 0.3 \times 10^{-13}$, and $Y_{S1\rightarrow S2}(P_3) = 5.0 \pm 0.6 \times 10^{-11}$. This result shows that the switching yield varies by more than two orders of magnitude simply by moving the STM tip only 4 Å inside the molecule (from P_2 to P_3). Quite unexpectedly, the switching yield is at a maximum when exciting the less mobile part of the molecule (location P_3), as will be discussed below. There are additional features in the tunnel-current curves of Fig. 3A consisting of narrow peaks that are far more scarce in curves P_2 and P_3 as compared with P_1. We assign the narrow features to the movement of the molecule into a transient state (T) located between the two stable states (S_1 and S_2) of the bistable molecule. Transient states can be observed only if their lifetime is longer than ~1 ms, because the frequency bandpass of our tunnel-current detection is limited to about 1.3 KHz. Direct evidence that such a transient molecular state (T) exists was obtained by rapidly scanning the STM tip along the same line scan (Fig. 3C). The bright dashes observed in position T indicate the transient molecular state. Each bright dash in the T state has a corresponding dark dash in either position S_1 or position S_2. Such correlations demonstrate that the narrow peaks in curve P_1 of Fig. 3A are indeed associated with the movement of the molecule into a transient state T. The sequence of narrow peaks in curve P_1 of Fig. 3A were analyzed in more detail (inset). Both the time interval between peaks and the width of the peaks exhibit perfect exponential distributions (Fig. 3B) whose time constants $\tau_{S1\rightarrow T}$ and $\tau_{T\rightarrow S1}$, respectively, are inversely proportional to the tunnel current and do not depend on the temperature, as observed for the molecular switching. This result indicates that the series of peaks observed in curve P_1 (Fig. 3A) corresponds to a succession of $S_1 \rightarrow T$ and $T \rightarrow S_1$ transitions that are both induced by electronic excitation with the STM tip. The corresponding yields $Y_{S1\rightarrow T} = 1/(I\tau_{S1\rightarrow T}/e)$ and $Y_{T\rightarrow S1} = 1/(I\tau_{T\rightarrow S1}/e)$ are given in Fig. 2 as a function of the surface voltage for an STM tip in position P_1. In fact, at any STM tip position, the $Y_{T\rightarrow S1}$ yield is found to be several orders of magnitude larger than the $Y_{S1\rightarrow T}$ yield, which is consistent with the T state being transient compared with the S_1 and S_2 states. Curves P_2 and P_3 of Fig. 3A show less narrow peaks ($S_1 \rightarrow T$ movement) than step features ($S_1 \rightarrow S_2$ switching), as compared with curve P_1. This indicates that the $S_1 \rightarrow T$ movement is less probable than the $S_1 \rightarrow S_2$ switching when the STM tip is in position P_2 and P_3. For example, at $V_S = -2.5$ V, $Y_{S1\rightarrow T}(P_3) = 1.0 \pm 0.5 \times 10^{-11}$ is less than $Y_{S1\rightarrow S2}(P_3) = 5.0 \pm 0.6 \times 10^{-11}$ by a factor of 5. A schematic of the ground-state potential-energy surface of this surface molecular switch (*1*) [biphenyl on Si(100)] is shown in Fig. 3D.

The $Y_{S1\rightarrow T}$ yield for moving the molecule into the T state has a threshold surface voltage at –2.3 ± 0.1 V (see Fig. 2) that is significantly smaller than the threshold (–2.7 V) of the $Y_{S1\rightarrow S2}$ switching yield. We note that the $Y_{S1\rightarrow T}$ and $Y_{S1\rightarrow S2}$ yield curves have similar shapes, in particular that they dip at –3.6 and –4.0 V, respectively. The voltage shift (0.4 V) is the same as the corresponding threshold voltage shift, which indicates that the two observed molecular movements, that is, moving to the transient state ($S_1 \rightarrow T$) and molecular switching ($S_1 \rightarrow S_2$), are both associated with a resonant electronic excitation with the STM tip but involve the excitation of two different

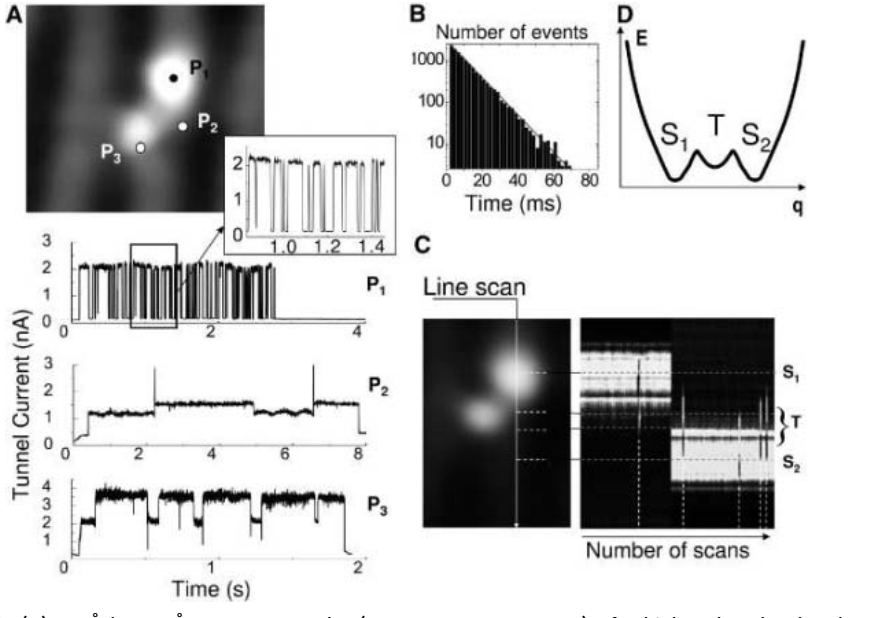

Fig. 3. (**A**) 20 Å by 20 Å STM topography ($V_S = -2$ V, $I = 0.56$ nA) of a biphenyl molecule. The tunnel current during the surface voltage pulse ($V_S = -2.5$ V, duration 10 s) is shown for three different STM tip positions, P_1, P_2, and P_3. (**B**) Exponential distribution of the time interval between peaks of the tunnel-current curve (P_1) in (A). (**C**) On the left, an STM topography of a biphenyl molecule shows the repeatedly scanned line. On the right, the line scan is shown as a function of time ($V_S = -3$ V, $I = 0.1$ nA). The scan speed is 90 nm/s. The bright features, S_1, T, and S_2, indicate the successive positions of the molecule. (**D**) Schematic of the ground-state potential-energy surface of biphenyl on Si(100). *q* is an arbitrary reaction coordinate.

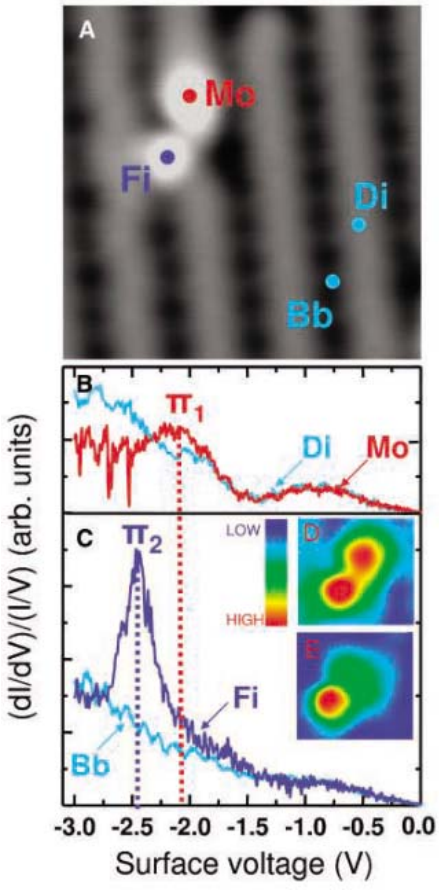

Fig. 4. (**A**) Tunneling spectra have been recorded at the centers of the mobile (Mo) and fixed (Fi) phenyl rings of a biphenyl molecule and at the corresponding locations Di (dangling bonds) and Bb (backbonds) of the clean Si(100) surface. (**B** and **C**) *dI/dV* curves have been recorded with a lock-in amplifier (frequency 930 Hz, voltage modulation 40 mV) when recording the tunnel current *I* as a function of the surface voltage from 0 to –3.0 V. From this, $(dI/dV)/(I/V)$ has been calculated numerically. The narrow peaks in the Mo curve for surface voltages smaller than –2.5 V are due to molecule motion. The π_1 resonance at –2.1 V and the π_2 resonance at –2.5 V are seen in the Mo and Fi curves, respectively. (**D**) STM topography of a biphenyl molecule ($V_S = -2.5$ V, $I = 0.12$ nA). (**E**) Topography of the *dI/dV* signal recorded with the lock-in amplifier at $V_S = -2.5$ V, $I = 0.12$ nA, showing the localization of the π_2 resonance at –2.5 V.

molecular resonances π_1 and π_2, whose energies are –2.3 and –2.7 eV, respectively. These different threshold surface voltages indicate that the two $S_1 \rightarrow T$ and $S_1 \rightarrow S_2$ movements are independent. Similarly, the observation that the $S_1 \rightarrow S_2$ motion is a one-electron process demonstrates that it is a direct process and not just a sequence of $S_1 \rightarrow T$ and $T \rightarrow S_2$ motions. As seen in Fig. 2, the $Y_{T \rightarrow S1}$ yield for moving the molecule from the T to the S_1 state has an even lower threshold voltage than the $Y_{S1 \rightarrow S2}$ and $Y_{S1 \rightarrow T}$ yield curves. This difference most probably originates because, when the STM tip is in position P_1 and activates the $T \rightarrow S_1$ movement, the molecule in the T transient state is no longer under the tip and the electronic excitation process must involve only the transfer of electronic excitations of the silicon substrate (*24*) to the molecule.

Direct evidence of the existence of the two π_1 and π_2 molecular resonances has been obtained by STM *I-V* spectroscopy (Fig. 4) (*25*). When mapping the *I-V* spectroscopy over the entire biphenyl molecule, a resonance at –2.1 eV (with slight variations of ±0.1 eV) was found localized over the mobile phenyl ring (Mo), and a second separate resonance at –2.5 eV (with slight variations of ±0.1 eV) was found localized over the fixed phenyl ring (Fi). This localization probably reflects the relatively weak coupling between the two phenyl groups of the molecule, which interact more strongly with the silicon surface. The slightly lower energies (0.2 eV) of the two π_1 and π_2 resonances observed in tunneling spectroscopy compared with their energies derived from the $Y_{S1 \rightarrow T}$ and $Y_{S1 \rightarrow S2}$ yield thresholds result from the *I-V* spectroscopy method itself (*25*). The observed localization of the π_1 and π_2 resonances (Fig. 4E) correlates well with the localization of the corresponding $Y_{S1 \rightarrow T}$ (π_1) and $Y_{S1 \rightarrow S2}$ (π_2) yields. Indeed, the $Y_{S1 \rightarrow T}$ yield is much higher than the $Y_{S1 \rightarrow S2}$ yield with the tip at position P_1 (Fig. 2). The $Y_{S1 \rightarrow S2}$ yield has a maximum when the STM tip is at position P_3 that rapidly decreased when the STM tip was moved away to positions P_1 and P_2. Thus, depending on the precise location of the STM tip inside the molecule, different electronically excited states (π_1 or π_2 resonances) of the molecular system can be produced, each associated with a specific molecular movement ($S_1 \rightarrow T$ or $S_1 \rightarrow S_2$).

Compared with other molecular quantum-control methods based on the use of photon absorption selection or coherent control rules (*8*), the real-space picometer-scale control method described here has the advantage of working with single molecules and of dealing with a completely different concept based on the selection of a specific electronically excited state through the spatial localization of the excitation inside the molecule. This is a crucial step toward the development of a real quantum technology able to control the internal operation of future mono-molecular machines (*26*).

References and Notes

1. C. Joachim, J. K. Gimzewski, *Struct. Bonding* **99**, 1 (2001).
2. B. C. Stipe, M. A. Rezaei, W. Ho, *Phys. Rev. Lett.* **81**, 1263 (1998).
3. B. C. Stipe, M. A. Rezaei, W. Ho, *Phys. Rev. Lett.* **82**, 1724 (1999).
4. J. I. Pascual, N. Lorente, Z. Song, H. Conrad, H.-P. Rust, *Nature* **423**, 525 (2003).
5. L. Bartels, G. Meyer, K.-H. Rieder, *Phys. Rev. Lett.* **79**, 697 (1997).
6. A. H. Zewail, in *Nobel Lectures, Chemistry 1996–2000*, I. Grenthe, Ed. (World Scientific, Hackensack, New Jersey, 2003), pp. 274–367.
7. S. A. Rice, *Nature* **403**, 496 (2000).
8. H. Rabitz, R. de Vivie-Riedle, M. Motzkus, K. Kompa, *Science* **288**, 824 (2000).
9. D. Riedel, M. Lastapis, M. Martin, G. Dujardin, *Phys. Rev. B* **69**, 121301 (2004).
10. A. J. Mayne *et al.*, *Phys. Rev. B* **69**, 045409 (2004).
11. B. C. Stipe, M. A. Rezaei, W. Ho, *Science* **279**, 1907 (1998).
12. G. H. Wannier, *Phys. Rev.* **90**, 817 (1953).
13. S. Gokhale, *J. Chem. Phys.* **108**, 5554 (1998).
14. K. Stokbro *et al.*, *Phys. Rev. Lett.* **80**, 2618 (1998).
15. A. Yazdani, D. M. Eigler, N. D. Lang, *Science* **272**, 1921 (1996).
16. B. C. Stipe, M. A. Rezaei, W. Ho, *Science* **280**, 1732 (1998).
17. N. Lorente, M. Persson, *Phys. Rev. Lett.* **85**, 2997 (2000).
18. D. Teillet-Billy, J. P. Gauyacq, M. Persson, *Phys. Rev. B* **62**, R13306 (2000).
19. L. Bartels *et al.*, *Phys. Rev. Lett.* **80**, 2004 (1998).
20. L. J. Lauhon, W. Ho, *Surf. Sci.* **451**, 219 (2000).
21. P. A. Sloan, M. F. G. Hedouin, R. E. Palmer, M. Persson, *Phys. Rev. Lett.* **91**, 118301 (2003).
22. X. H. Qiu, G. V. Nazin, W. Ho, *Science* **299**, 542 (2003).
23. B. C. Stipe *et al.*, *Phys. Rev. Lett.* **78**, 4410 (1997).
24. Y. Nakamura, Y. Mera, K. Maeda, *Phys. Rev. Lett.* **89**, 266805 (2002).
25. N. D. Lang, *Phys. Rev. B* **34**, 5947 (1986).
26. C. Joachim, J. K. Gimzewski, A. Aviram, *Nature* **408**, 541 (2000).

27. This work is supported by the European Research and Training Network AMMIST (contract HPRN-CT-2002-00299) and the European STREP NanoMan (contract NMP4-CT-2003-550660). M.M. also acknowledges support from a European Marie Curie fellowship (contract MEIF-CT-2003-502037). The authors thank G. Meyer for invaluable advice.

29 November 2004; accepted 23 March 2005
10.1126/science.1108048

Glacial/Interglacial Changes in Subarctic North Pacific Stratification

S. L. Jaccard,[1] G. H. Haug,[2] D. M. Sigman,[3] T. F. Pedersen,[4] H. R. Thierstein,[1] U. Röhl[5]

Since the first evidence of low algal productivity during ice ages in the Antarctic Zone of the Southern Ocean was discovered, there has been debate as to whether it was associated with increased polar ocean stratification or with sea-ice cover, shortening the productive season. The sediment concentration of biogenic barium at Ocean Drilling Program site 882 indicates low algal productivity during ice ages in the Subarctic North Pacific as well. Site 882 is located southeast of the summer sea-ice extent even during glacial maxima, ruling out sea-ice–driven light limitation and supporting stratification as the explanation, with implications for the glacial cycles of atmospheric carbon dioxide concentration.

Air bubbles trapped in Antarctic ice reveal that the atmospheric concentration of carbon dioxide (CO_2) has varied over ice age cycles, between 280 parts per million by volume (ppmv) during interglacials (including the preindustrial Holocene) and 180 ppmv during peak glacial conditions (such as the last glacial maximum) (*1*). Because the ocean holds 50 times more inorganic carbon than does the atmosphere, the consensus is that changes in ocean/atmosphere exchange drove the CO_2 changes, which in turn amplified climate forcings to yield the large observed amplitude of ice age cycles. However, the specific cause of glacial/interglacial CO_2 change remains elusive.

CO_2 is extracted from the atmosphere by phytoplankton growth in the sunlit surface ocean, and this carbon is then sequestered in the ocean interior by the downward rain of organic matter and its subsequent degradation back to CO_2. This biologically driven sequestration of carbon in the ocean interior is referred to as the "biological pump." In the modern ocean, the efficiency of the biological pump is limited by particular regions of the polar ocean: the Antarctic and the Subarctic North Pacific. In these regions, vertical exchange of water causes deeply sequestered CO_2 to be mixed back into the surface ocean faster than phytoplankton fix it back into organic matter, so that previously deep-sequestered CO_2 is released to the atmosphere. Because either increased phytoplankton growth

[1]Department of Earth Sciences, Sonneggstrasse 5, ETHZ, 8092 Zurich, Switzerland. [2]Geoforschungszentrum Potsdam, Potsdam, Germany. [3]Department of Geosciences, Princeton University, Princeton, NJ, USA. [4]School of Earth and Ocean Sciences, University of Victoria, Victoria, BC, Canada. [5]DFG Research Center for Ocean Margins, Bremen University, Bremen, Germany.

*To whom correspondence should be addressed. E-mail: jaccard@erdw.ethz.ch

or decreased vertical exchange [polar ocean stratification (*2*)] would work to reduce this CO_2 leak, both changes have been proposed to explain the reduction in atmospheric CO_2 during the last ice age (*3*, *4*).

Paleoceanographic data suggest that export production in the Antarctic Zone of the Southern Ocean was lower during glacial times (*2*, *5*–*7*). This argues against increased polar ocean productivity as the driver of lower ice-age CO_2 levels. However, these data do not necessarily rule out polar ocean changes as the cause of glacial/interglacial CO_2 change. If the productivity decrease was driven by increased light limitation during glacial times because of nearly year-round ice coverage, then one would expect Antarctic surface partial pressure of CO_2 to have been higher during glacial times. In this case, the region could not be taken as a driver of lower CO_2 during glacial times unless sea-ice coverage was so pervasive as to prevent gas exchange between the surface ocean and atmosphere (*8*). In contrast, if this decrease in productivity was due to decreased vertical exchange, lowering the supply of nutrients from below (iron probably being the most critical), then the region may indeed have been a driver of lower glacial CO_2, even without limitation of gas exchange by sea-ice coverage (*2*, *9*).

Different paleoceanographic proxies of surface ocean nutrient status have yielded contradictory results and so have not yet convincingly distinguished between these two different scenarios for the observed glacial decrease in polar productivity (*10*). Although efforts are underway to understand paleoceanographic proxies through studies of the modern ocean, this ground-truthing has proven to be difficult. An alternative approach to distinguish among plausible interpretations of ambiguous paleoceanographic data is to take advantage of different coring sites to test the significance of down-core trends; this is the strategy followed here. We combine the measurement of biogenic barium (Ba), a paleoceanographic proxy of export production (*11*), with the use of the open Subarctic North Pacific as an analog to other polar sites (the Antarctic Zone of the Southern Ocean, the Sea of Okhotsk, and the Bering Sea) that differs substantially from these sites only in its history of sea-ice cover.

In sediments retrieved from Subarctic North Pacific Ocean Drilling Program (ODP) site 882 (Fig. 1) (50°21′N, 167°35′E, 3244 m water depth), we measured relative elemental concentrations at submillennial resolution, using the x-ray fluorescence (XRF) core-scanner at Bremen University, Bremen, Germany (*12*). Assuming that sedimentary aluminum (Al) or titanium (Ti) is exclusively of detrital origin, Ba abundance normalized to Al or Ti abundance yields an estimate of the sedimentary concentration of biogenic (or excess) Ba (BioBa). According to the same reasoning, calcium (Ca) normalized to Al or Ti indicates the sedimentary concentration of biogenic calcium carbonate ($CaCO_3$). The records of Al and Ti show almost identical trends and amplitudes, but the XRF signal is better for Al, which is thus used for normalization.

The BioBa record shows a strong climate-related signal (Figs. 2 and 3), with high concentrations during interglacials and lower values during cold stages. The large-scale Ba variations cannot be explained as the result of sulfate reduction and associated barite dissolution, because no significant sulfate reduction is observed in the interstitial water of late Pleistocene sediments of ODP site 882, and sedimentary organic carbon is uniformly low (*13*). Hence, the sedimentary Ba/Al or Ba/Ti ratio is interpreted to indicate lower BioBa accumulation and thus less export of organic matter from the surface ocean during cold periods, with the lowest BioBa concentrations coinciding almost exclusively with the glacial maxima. These data confirm previously reported observations from the Okhotsk Sea (*14*–*16*), the Subarctic Northwest Pacific (*16*, *17*), and the Bering Sea (*18*) indicating that the export production in the Subarctic Pacific is similar to that of the Antarctic Zone of the Southern Ocean in its response to glacial/interglacial cycles.

However, as compared to the Antarctic or the Okhotsk Sea, the modern open western Subarctic Pacific near site 882 is characterized by much higher summertime sea surface temperatures (SSTs), reaching 12°C. SST reconstructions for the region from alkenones (*19*), foraminiferal Mg/Ca, and foraminiferal transfer functions (*20*) all indicate that, even during the coldest times, summertime SSTs never approached freezing. This corroborates evidence that ODP site 882 was located well east and south of the perennial sea-ice extent during glacial maxima (*15*, *21*). As a result, sea-ice cover could not have been a major limitation on the spring/summer growing season during glacial times. Rather, the supply of nutrients must have provided the critical limitation on phytoplankton growth during glacial times. Iron appears to be the limiting nutrient today (*22*), although silicate may limit diatom production in some areas of the Subarctic Pacific during the late summer. The aeolian supply of iron to the region was, if anything, higher during colder times (*23*). Thus, the only clearly plausible mechanism for reducing the nutrient supply to the euphotic zone above site 882, regardless of which nutrient most constrained growth during the

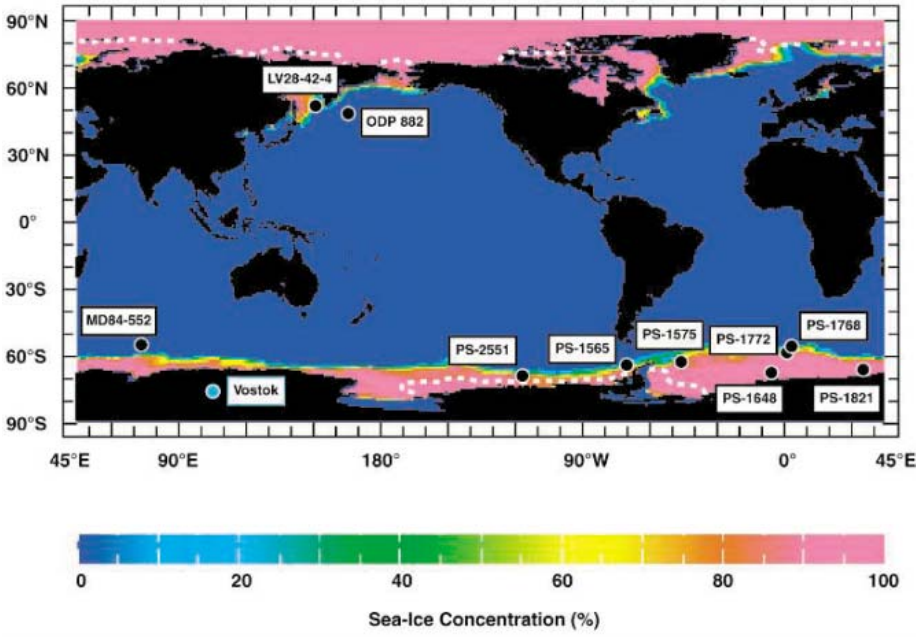

Fig. 1. Global map of annual maximum sea-ice concentration. Black dots represent core sites from the Subarctic North Pacific and the Antarctic Zone of the Southern Ocean in which BioBa records have been measured [ODP 882; LV28-42-4 (*15*); MD84-552 (*2*); PS-1768 and PS-1772 (*24*); PS-1575, PS-1648, and PS-1821 (*25*); and PS-1565 and PS-2551 (*26*)]. The Antarctic sites, which occur over a wide range of latitude, and the record from the Okhotsk Sea show a similar correlation between productivity and climate as measured at North Pacific ODP site 882, with lower BioBa during ice ages. The colors indicate modern wintertime sea-ice extent (February and September for the Northern and Southern Hemisphere, respectively); the white dashed lines indicate modern annual minimum sea-ice extent (80% sea-ice concentration contour, based on satellite data from NASA International Satellite Land Surface Climatology Project Global Data Sets for Land Atmosphere Models). We used the http://ingrid.ldeo.columbia.edu/ Web site to design the map. The blue dot represents the Vostok ice-core site.

last ice age, is a reduction in the nutrient supply from below, as would result from polar stratification during cold periods. As described earlier, a similar correlation between productivity and climate appears to apply at various sites of different latitudes within the Antarctic, with lower BioBa accumulation during ice ages (*2*, *24*–*26*) (Figs. 1 and 3). Given the constraint on the cause of the productivity drop in the open Subarctic Pacific, it follows that the same climate/productivity correlation in the Antarctic most likely arises from a parallel tendency for the Antarctic water column to stratify in cold climates (*2*, *9*).

A strong temporal correlation exists between the Subarctic Northwest Pacific BioBa record and the D/H-derived temperature record from the Vostok ice core (*1*), applying not only to the major climate transitions but also to some of the more subtle climate variations (Figs. 2 and 3). Because the Subarctic Pacific itself is unlikely to have driven the climate changes observed in the Antarctic ice cores, Southern Hemisphere climate must modulate productivity (and, according to the logic above, stratification) in the polar North Pacific. Thus, we propose that deep water formation in the Antarctic during interglacials communicates Southern Hemisphere warming to the polar Northern Hemisphere, destratifying the Subarctic North Pacific, enhancing nutrient supply, and increasing productivity. The pervasive correlation between North Pacific stratification and Antarctic climate argues for a simple connection between polar ocean vertical stability and mean ocean temperature, such as is provided by the dependence of the thermal expansion coefficient of seawater on its absolute temperature (*9*).

The BioBa maxima during peak interglacials in isotope stages 1, 5, 7, 9, and 11 are accompanied by $CaCO_3$ maxima that contain up to 40% biogenic $CaCO_3$ in these otherwise carbonate-free sediments (Fig. 2). The near-absence of $CaCO_3$ in most of the record suggests that seafloor preservation of the $CaCO_3$ rain drives the bimodal character of the $CaCO_3$ record. Thus, we interpret the $CaCO_3$ peaks to indicate times of higher calcite saturation state in bottom water, although changes in the $CaCO_3$ flux may well have affected the peak amplitudes. If the $CaCO_3$ peaks were exclusively associated with deglaciation, they could be explained as the result of previously recognized processes not necessarily associated with the North Pacific (*27*). Specifically, at the end of ice ages, deeply sequestered CO_2 is released from the ocean back into the atmosphere, where it accumulates or is absorbed by the terrestrial biosphere. This causes a transient $CaCO_3$ preservation event in the deep sea that has been broadly observed (*27*). However, the fact that the $CaCO_3$ peaks persist through the interglacials indicates a glacial-to-interglacial increase in the calcite saturation state of the deep North Pacific. Because this saturation state change has not been so clearly observed in the lower-latitude Pacific (*28*), it is best explained as the result of oceanographic changes within the North Pacific region. Indeed, a higher deep ocean saturation state in the region would be the logical result of a weakening of the Subarctic North Pacific halocline, which would accelerate CO_2 escape through the North Pacific surface. This effect would have been magnified if interglacial weakening of the stratification was accompanied by less complete nutrient drawdown at the surface (*10*).

Although previously generated records of temperature- and salinity-related proxies in the North Pacific did not evoke an interpretation of enhanced glacial stratification, those records are not inconsistent with it. A reduction in the halocline during ice ages would have increased planktonic foraminiferal $\delta^{18}O$ by up to 1 per mil (‰) more than dictated by glacial cooling and ice buildup. A sediment core raised near site 882 indicates a remarkably modest glacial-to-interglacial $\delta^{18}O$ decrease

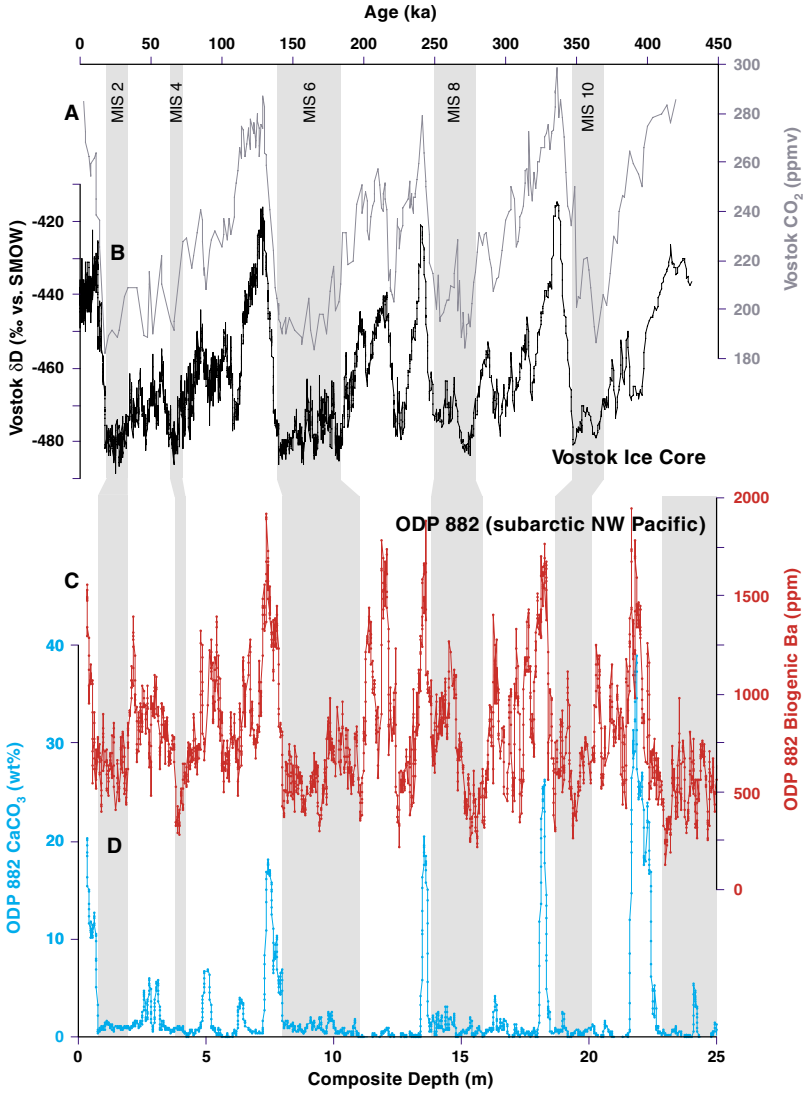

Fig. 2. BioBa and $CaCO_3$ records from Subarctic North Pacific ODP site 882 compared to the Vostok CO_2 and deuterium (δD) records during the past 450,000 years (*1*). (**A** and **B**) Orbitally tuned (*35*) Vostok CO_2 and δD records. SMOW, standard mean ocean water; ppmv, parts per million by volume. (**C**) ODP 882 submillennial BioBa record versus core depth in meters of composite depth [calculated from the Ba/Al ratio (*12*), with a 2-cm sampling interval and data smoothed by a five-point running mean]. The glacial sedimentation rates are probably somewhat higher than the interglacial rates because of ice-rafted debris. However, the linearity of the age-to-depth correlation indicated by comparison of (A) and (B) with (C) does not appear to allow for the concentration signal to be driven by sediment dilution. Moreover, the detailed similarity between the 882 BioBa and the Vostok δD records, the latter reflecting atmospheric change in the Southern Hemisphere, argues against changing ice-rafted debris inputs, the timing of which would follow Northern Hemisphere climate, as the cause of the variations in BioBa concentration. (**D**) ODP 882 wt % $CaCO_3$ (data smoothed by a five-point running mean) calculated from the Ca/Al ratio (*12*).

of ~1.1‰ (*20*), ~0.8‰ of which represents the global ice volume signal (*29*). Thus, there is very little room for glacial cooling, let alone a glacial increase in local surface salinity. Indeed, the strongest indication from extant planktonic foraminiferal $\delta^{18}O$ data is that there was a gradual strengthening of the Subarctic Pacific halocline from the early Holocene to the present (*30*). Given other evidence of climate degradation since the early Holocene, we take this trend as further evidence of a cooling/stratification link. With improved age control for our site 882 BioBa record, we may be able to determine whether this same trend exists within earlier interglacial periods.

Modeling studies have yet to focus on the CO_2 impact of nutrient drawdown and/or stratification in the Subarctic North Pacific. The expectation is that the impact will be modest in comparison to similar changes in the Antarctic (*31*), which appears to ventilate much of the modern deep ocean (*32*). However, the evidence reported here for stratification in the Subarctic North Pacific during cold periods provides strong support for a similar change in the Antarctic, which has long been recognized as a potentially dominant driver of the glacial CO_2 cycles (*3*, *4*, *33*).

We noted previously that the Subarctic North Pacific underwent stratification upon the initiation of Northern Hemisphere glaciation 2.7 million years ago (*34*). Only later did it become clear that this was contemporaneous with similar stratification in the Antarctic (*9*). The bipolar nature of this phenomenon argued for a simple and general connection between climate and polar ocean vertical stability. Symmetrically, the data reported here indicate that the stratification during the late Pleistocene ice ages proposed previously for the Antarctic (*2*–*4*, *10*) also occurred in the Subarctic North Pacific. This only strengthens our conviction that a simple physical mechanism must exist by which a cold climate leads to polar ocean stratification.

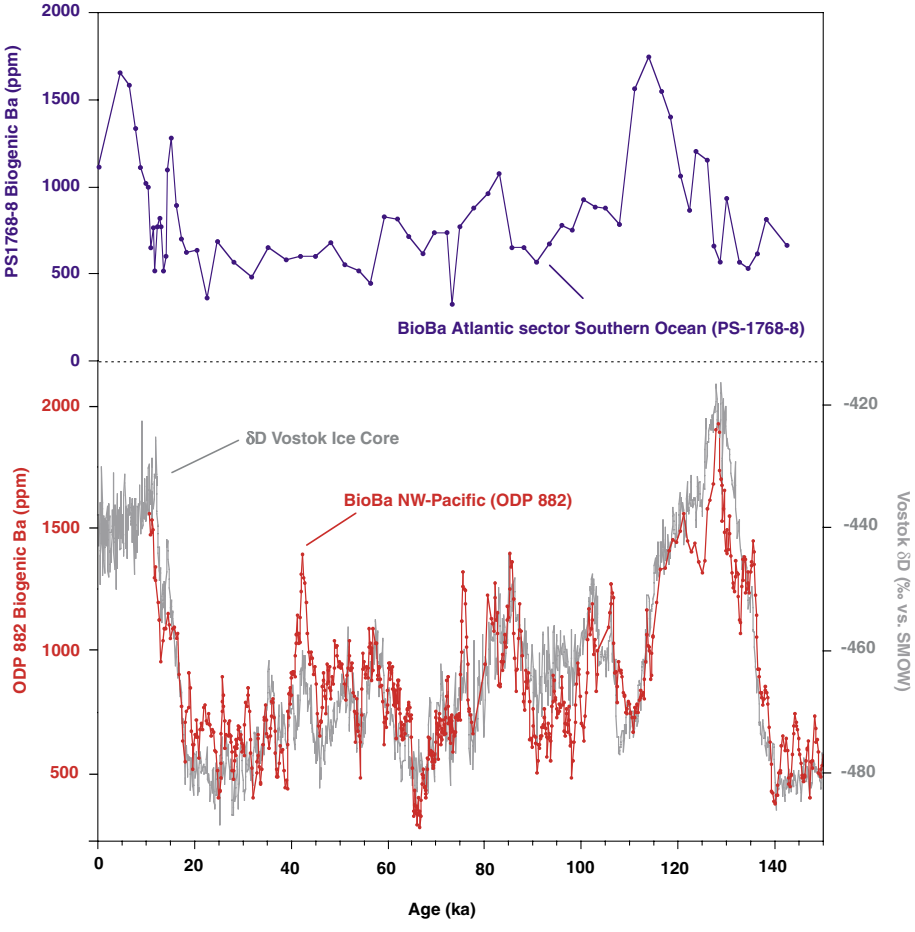

Fig. 3. Detail of Fig. 2, illustrating the strong correlation between the ODP 882 BioBa concentration (red, now plotted versus time) and the Vostok δD record (gray) (*1*) over the past 150,000 years. To improve the correlation with the Vostok record, control points in the ODP site 882 age model have been adjusted from the initial age model (*12*). This model was based on foraminiferal $\delta^{18}O$ data, which provide unambiguous markers of the glacial terminations but do not tightly constrain the age of mid-glacial–stage sediments (*19*). The adjustments to this model represent less than 5000 years in all cases. The BioBa record from Southern Atlantic site PS-1768 (*24*) is shown for comparison (blue; indicated in Fig. 1). The basic glacial/interglacial variations are similar in the Subarctic Northwest Pacific and the Atlantic sector of the Southern Ocean, both in the sense of change and the absolute concentrations of sedimentary BioBa at minima and maxima. The age constraints for Antarctic cores are limited by a lack of preserved foraminifera, which is the likely reason for the poor temporal correlation at the detail level between ODP 882 and PS-1768-8.

References and Notes

1. J.-R. Petit *et al.*, *Nature* **399**, 429 (1999).
2. R. François *et al.*, *Nature* **389**, 929 (1997).
3. J. L. Sarmiento, J. R. Toggweiler, *Nature* **308**, 621 (1984).
4. U. Siegenthaler, T. Wenk, *Nature* **308**, 624 (1984).
5. R. A. Mortlock *et al.*, *Nature* **351**, 220 (1991).
6. N. Kumar *et al.*, *Nature* **378**, 675 (1995).
7. M. Frank *et al.*, *Paleoceanography* **15**, 642 (2000).
8. B. B. Stephens, R. F. Keeling, *Nature* **404**, 171 (2000).
9. D. M. Sigman, S. L. Jaccard, G. H. Haug, *Nature* **428**, 59 (2004).
10. D. M. Sigman, E. A. Boyle, *Nature* **407**, 859 (2000).
11. J. Dymond, E. Suess, M. Lyle, *Paleoceanography* **7**, 163 (1992).
12. Materials and methods are available as supporting material on *Science* Online.
13. D. K. Rea, I. A. Basov, T. R. Janecek, A. Palmer-Julson, in *Introduction to LEG 145: North Pacific Transect* (Proceedings of ODP Initial Reports 145, College Station, TX, 1993), pp. 85–120.
14. M. M. Sato, H. Narita, S. Tsunogai, *J. Oceanogr.* **58**, 461 (2002).
15. D. Nürnberg, R. Tiedemann, *Paleoceanography* **19**, 10.1029/2004PA001023 (2004).
16. H. Narita *et al.*, *Geophys. Res. Lett.* **29**, 22 (2002).
17. S. S. Kienast, I. L. Hendy, J. Crusius, T. F. Pedersen, S. E. Calvert, *J. Oceanogr.* **60**, 189 (2004).
18. T. Nakatsuka, T. Watanabe, N. Handa, E. Matsumoto, E. Wada, *Paleoceanography* **10**, 1047 (1995).
19. G. H. Haug, *Ber. Rep. Geol. Inst. Univ. Kiel* **78**, 1 (1996).
20. T. Kiefer, M. Kienast, *Quat. Sci. Rev.* **24**, 1063 (2005).
21. CLIMAP Project Members, *Geol. Soc. Am. Map Chart Ser. MC-36* (1981).
22. A. Tsuda *et al.*, *Science* **300**, 958 (2003).
23. M. Werner *et al.*, *J. Geophys. Res.* **107**, 4744 (2002).
24. C. C. Nürnberg, G. Bohrmann, M. Schlüter, M. Frank, *Paleoceanography* **12**, 594 (1997).
25. W. J. Bonn, F. X. Gingele, H. Grobe, A. Mackensen, D. K. Füutterer, *Paleogeogr. Paleclimatol. Paleoecol.* **139**, 195 (1998).
26. C.-D. Hillenbrand, thesis, Alfred Wegner Institut, Bremerhaven, Germany (2000).
27. T. M. Marchitto, J. Lynch-Stieglitz, S. Hemming, *Earth Planet. Sci. Lett.* **231**, 317 (2005).
28. N. R. Catubig *et al.*, *Paleoceanography* **13**, 298 (1998).
29. D. P. Schrag, G. Hampt, D. W. Murray, *Science* **272**, 1930 (1996).
30. M. Sarnthein *et al.*, *Quat. Sci. Rev.* **23**, 2089 (2004).
31. J. L. Sarmiento, J. C. Orr, *Limnol. Oceanogr.* **36**, 1928 (1991).
32. W. S. Broecker *et al.*, *J. Geophys. Res.* **103**, 15 (1998).
33. J. R. Toggweiler, *Paleoceanography* **14**, 571 (1999).
34. G. H. Haug, D. M. Sigman, R. Tiedemann, T. F. Pedersen, M. Sarnthein, *Nature* **401**, 799 (1999).
35. M. L. Bender, *Earth Planet. Sci. Lett.* **204**, 275 (2002).

36. We thank R. Francois, M. Frank, and E. Galbraith for discussions and P. Rais (ETHZ) for technical assistance. P. Dulski and G. Schettler (GFZ Potsdam) provided the Inductively Coupled Plasma Mass Spectrometry (ICP-MS) and ICP–Optical Emission Spectroscopy calibration data, respectively. Financial support is provided by the Swiss National Science Foundation, the Deutsche Forschungsgemeinschaft, the U.S. NSF, and the Princeton University Carbon Mitigation Initiative sponsored by British Petroleum and the Ford Motor Company. This research used samples provided by the ODP. The ODP is sponsored by NSF and participating countries under the management of Joint Oceanographic Institutions.

Supporting Online Material

www.sciencemag.org/cgi/content/full/308/5724/1003/DC1
Materials and Methods
Reference

14 December 2004; accepted 24 March 2005
10.1126/science.1108696

Two Chemically Distinct Pools of Organic Nitrogen Accumulate in the Ocean

Lihini I. Aluwihare,[1]* Daniel J. Repeta,[2] Silvio Pantoja,[3] Carl G. Johnson[2]

The chemical dynamics of marine dissolved organic nitrogen (DON), a reservoir featuring surface accumulations even in areas where nitrogen limits productivity, have yet to be resolved. We exploited differences in the acid lability of amide bonds within high-molecular-weight (HMW) DON to show that vertical DON profiles result in part from the presence of two chemically distinct pools of amide. Half of HMWDON in surface waters is present as *N*-acetyl amino polysaccharides. In contrast, nearly all deep-sea HMWDON, and therefore, most HMWDON, is present in amides that resist both chemical hydrolysis and biological degradation.

Low concentrations of inorganic nitrogen (such as nitrates and ammonia) are assumed to limit primary production over wide expanses of the surface ocean. However, in many of these areas, dissolved organic nitrogen (DON) accumulates to measurable quantities (*1*–*3*) despite a demonstrated role in fueling both primary and secondary production (*4*). Given the importance of nitrogen for limiting ocean productivity, mechanisms that regulate DON production and removal could help control both the ocean's N balance and, consequently, the sequestration of atmospheric carbon dioxide.

Processes that lead to DON accumulation in seawater are unclear, but vertical profiles show that upper ocean DON concentrations are enhanced by 30 to 50% over deep water values (*5*). This observation suggests a major source for DON in the upper ocean and is consistent with findings that a large fraction of inorganic N assimilated by marine phytoplankton can be returned to seawater as DON (*6*). However, an important step for explaining DON profiles in the ocean is to identify compositional features that differentiate DON fractions with diverse biological reactivity. Here we report evidence for major structural differences between the DON pools of the surface and the deep ocean.

About 30% of DON occurs as a high-molecular-weight fraction (HMWDON) that can be sampled by ultrafiltration (*6*, *7*). The depth profile of HMWDON is similar to that of total DON, with high near-surface concentrations. Despite a decline in HMWDON concentrations below the mixed layer, nuclear magnetic resonance (NMR) spectra and amino acid analyses imply a homogenous chemical composition throughout the water column (*8*, *9*). Nitrogen-15 NMR (^{15}N-NMR) spectroscopy shows that nearly all HMWDON in the ocean is chemically bound as amide functional groups (*8*). Amides are commonly found in living marine organisms within proteins and biopolymers of *N*-acetyl amino polysaccharides (*N*-AAPs, e.g., chitin and peptidoglycan). However, acid hydrolysis of HMWDON yields only small amounts of amino acids and amino sugars, suggesting that HMWDON is deficient in these polymers (*9*, *10*). However, previous studies have also demonstrated that it is difficult to draw quantitative conclusions from analyses that require depolymerization of HMWDON compounds (*10*).

Rather than relying on a hydrolysis method that efficiently depolymerizes polysaccharides and proteins, we exploited differences in the amide bonds of proteins and *N*-AAPs to quantify the contribution of these biochemicals to marine DON. Amide bonds in proteins are an integral part of the peptide linkage, and amide hydrolysis depolymerizes proteins to yield amino acids (Fig. 1). Amide bonds in *N*-AAPs are not an integral part of the glycosidic linkage, and amide hydrolysis of *N*-AAPs is not directly coupled to depolymerization. Instead, amide hydrolysis de-acetylates the polysaccharide, releasing 1 mole of acetic acid for each mole of amide-N that is hydrolyzed (Fig. 1). Therefore, proteins can be quantified and distinguished from *N*-AAPs by the products of acid hydrolysis (amino acids and acetic acid, respectively). In both cases (proteins and *N*-AAPs), the hydrolysis of the amide bond produces amine-N. We used solid-state (cross-polarization magic-angle spinning) ^{15}N-NMR spectroscopy to follow the hydrolysis of HMWDON amide and quantify the conversion of amide-N to amine-N. Concurrent measurements of acetic and amino acid generation were used to partition HMWDON into proteins and *N*-AAPs. These experiments allowed us to construct a budget of nitrogen-containing biopolymers in marine HMWDON.

High molecular weight dissolved organic matter (HMWDOM) in surface seawater is rich in carbohydrate (60 to 80% of total C) and acetate (5 to 7% of total C), as seen in the ^{1}H-NMR spectrum for Woods Hole surface seawater (Fig. 2A) [carbohydrates, 5.2, 4.5-3.2, and 1.3 parts per million (ppm); acetate, 2 ppm]. Previous studies have shown that the chemical composition of Woods Hole HMWDOM is representative of marine HMWDOM in general (*10*, *11*). The ^{15}N-NMR for this sample (Fig. 2B) shows one major resonance at 124 ppm for amide-N (92% of total N) and a minor resonance at 35 ppm for amine-N (8% of total N). We hydrolyzed

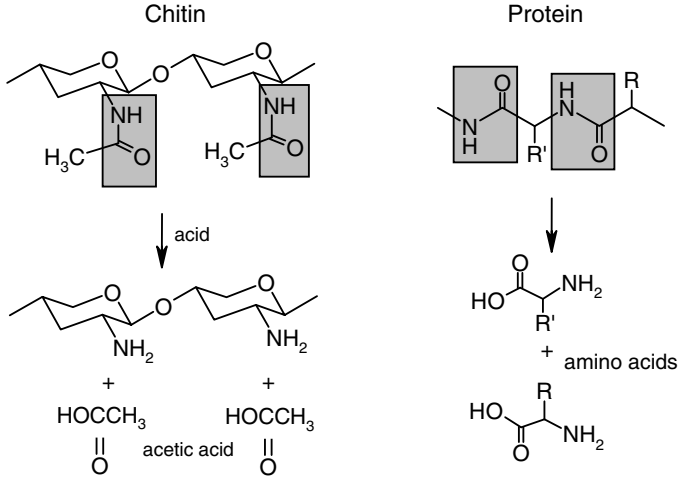

Fig. 1. Schematic showing the effect of mild acid hydrolysis on the amide linkage of proteins and *N*-AAPs (chitin). Mild acid hydrolysis (*13*) completely destroys the amide linkage (gray shaded area) in an *N*-AAP and quantitatively releases acetic acid. However, the glycosidic linkage remains unaffected, and the macromolecule is not depolymerized. Mild acid hydrolysis could likewise destroy the amide linkage in proteins (gray shaded area), thereby depolymerizing the macromolecule to release amino acids. If proteins and *N*-AAPs are the major biochemical components of HMWDON, then the sum of acetic and amino acids recovered after mild acid hydrolysis should equal the amount of amide destroyed during the reaction.

[1]Geosciences Research Division, Scripps Institution of Oceanography, La Jolla, CA 92093, USA. [2]Department of Marine Chemistry and Geochemistry, Woods Hole Oceanographic Institution, Woods Hole, MA 02543, USA. [3]Department of Oceanography and Fondap Copas Center, University of Concepción, Casilla 160-D, Concepción, Chile.

*To whom correspondence should be addressed. E-mail: laluwihare@ucsd.edu

Woods Hole HMWDON using conditions that were considerably milder than those typically employed for peptide bond hydrolysis (*12*) but that quantitatively release acetic acid from *N*-acetyl glucosamine and chitotriose (*13*). As expected in the case of *N*-AAPs, the acid hydrolysis (*13*) removed acetic acid from our samples (Fig. 2C) in quantifiable yield (Table 1) (*14*). Concurrent with the loss of acetic acid, there was a decrease in amide-N from 92% of the total N (7.1 μmol of N) to 35%, and an increase in the amount of amine-N from 8% of the total (0.6 μmol of N) to 65% (5 μmol of N) N (Fig. 2D and Table 1). Amino acid analysis showed that some proteins were hydrolyzed to amino acids that were recovered at 13% (Table 1) of the total N (*15*). The amount of amide-N converted to amine-N during acid hydrolysis, as quantified by ^{15}N-NMR spectroscopy, nearly equaled the molar sum of acetic and amino acids recovered by molecular level techniques (4.4 versus 4.3 μmol) (Table 1). The agreement between NMR spectroscopy and these molecular level analyses confirms that the hydrolyzed amide was originally present in HMWDON as proteins and *N*-AAPs. Under stronger hydrolysis conditions (*12*), we were able to recover 21% (1.6 μmol of N) of the total N in the sample as amino acids.

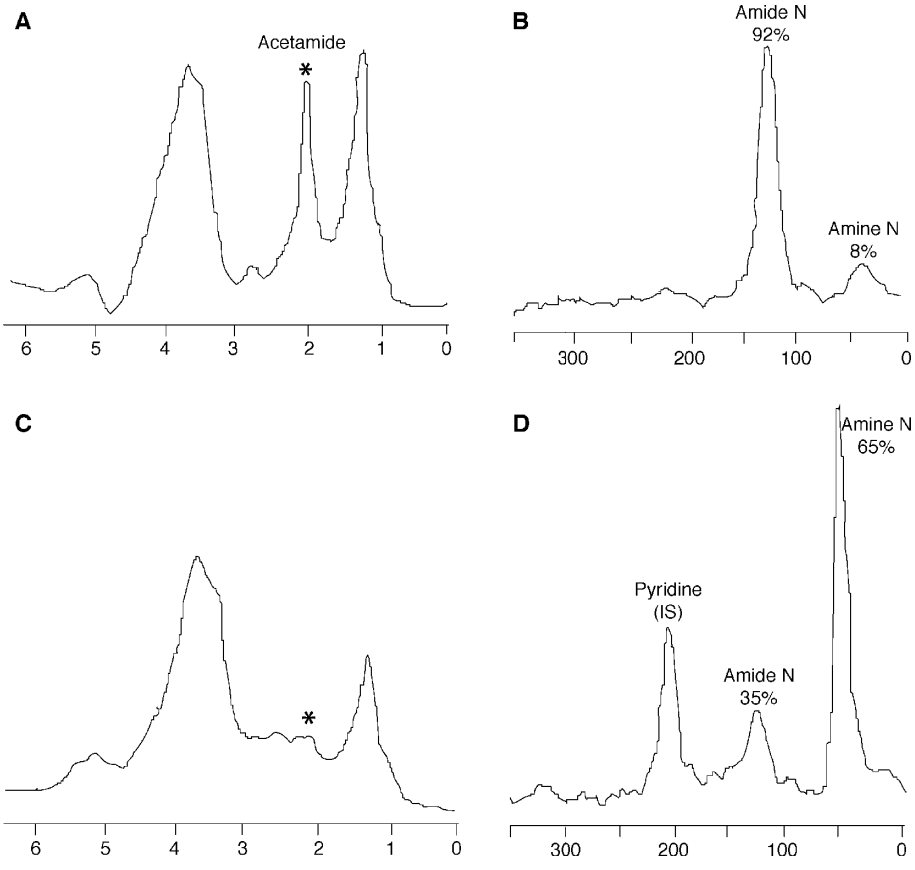

Fig. 2. The effect of mild acid hydrolysis (*13*) on the amide linkages of HMWDON isolated from Woods Hole surface seawater. (**A**) The ^{1}H-NMR spectrum [300 MHz, D_2O, δ (chemical shift in ppm downfield from tetramethylsilane)] shows bound acetic acid (*, 2.0 ppm). (**B**) The ^{15}N-NMR spectrum [400 MHz, solid-state, δ (chemical shift in ppm downfield from liquid NH_3)] before acid hydrolysis shows most nitrogen (92%) bound as amide. (**C**) Mild acid hydrolysis and organic extraction removes acetic acid, demonstrating complete de-acetylation. (**D**) This hydrolysis converts 57% of the amide-N into amine, commensurate with the amount of acetic and amino acids recovered by molecular level analyses (56%) (Table 1) and increases the total amine-N to 65%. Pyridine added to quantify losses during sample processing showed 98% recovery of HMWDON. IS, internal standard.

Using acetic acid as a proxy for *N*-AAPs, our results indicate that HMWDON in surface seawater is 43% *N*-AAPs (Table 1), 21% hydrolyzable protein, and 29% (2.2 μmol of N) nonhydrolyzable amide (*16*). The remaining HMWDON in our Woods Hole sample (8%, 0.6 μmol of N) initially present as amine was not characterized by our analyses but may be present as basic or N-terminal amino acids of proteins or as amino sugars. We obtained a similar agreement between the quantity of N converted from amide to amine and the molar sum of amino acids plus acetic acid recovered by molecular level analyses for HMWDON sampled from the North Pacific Ocean (Table 1); the agreement confirms the ubiquity of *N*-AAPs. Our analyses demonstrate that soluble *N*-AAP biopolymers contribute ~26% of the carbon and 40 to 50% of the nitrogen to surface ocean HMWDOM (*16*).

Peptidoglycan, currently assumed to dominate the oceanic reservoir of HMWDON, is rich in *N*-acetyl glucosamine and *N*-acetyl muramic acid (present in a 1:1 ratio) (*9*). Both sugars contain amide-N and are potential sources for the *N*-AAPs we quantified by our NMR experiment. The presence of acetylated amino sugars in HMWDON has been inferred previously from mass spectrometric data (*17*, *18*), but recoveries of *N*-acetyl glucosamine and *N*-acetyl muramic acid, which make up the amide-rich glycan of peptidoglycan, are low (*10*, *11*, *19*). Even under conditions specific for peptidoglycan hydrolysis (*20*, *21*), we were unable to detect muramic acid in our samples. Glucosamine, though present, contributed <1% of the total carbon, far lower than the ~10% HMWDOM-carbon ex-

Table 1. Change in amide content and yields of acetic and amino acids, upon mild acid hydrolysis of HMWDON. All percentages are expressed relative to total μmol of N.

Sample	Total (μmol N)*	Amide (μmol N)	Δ Amide (μmol N)†	Acetic acid (μmol)	Amino acids (μmol)	Σ Acetic + amino acids (μmol)	Unhydrolyzed amide (μmol N)‡
Woods Hole (5 m)	7.7	7.1 (92%)	–4.4	3.3 (43%)	1.0 (13%)	4.3	2.7 (35%)
MAB (1000 m)	7.7	7.7 (100%)	–1.8	1.3 (17%)	0.8 (10%)	2.1	5.8 (76%)
Hawaii (23 m)	6.2	6.2 (100%)	–3.7	3.3 (53%)	0.5 (8%)	3.8	2.4 (39%)
Hawaii (600 m)	6.2	6.2 (100%)	–3.7	3.4 (55%)	0.4 (6%)	3.8	2.4 (39%)

*Values are expressed per 100 μmol of HMW dissolved organic carbon and calculated based on the C/N ratio of each sample. †Δ Amide is the change in the amount of amide-N after hydrolysis, as quantified by integration of the ^{15}N-NMR spectra. In all cases, hydrolysis resulted in the loss of amide-N. ‡The quantity (μmol of N) of amide remaining in the sample after mild (*13*) hydrolysis, quantified directly by ^{15}N-NMR spectroscopy. Higher concentrations of HCl (*12*) hydrolyzed a greater percentage of the amide-N, leaving slightly less (2.2 and 5.5 μmol) amide-N unhydrolyzed in the Woods Hole and MAB samples, respectively. In order to quantify the amount of amide-N remaining after strong acid hydrolysis the Σacetic acid (mild) + amino acids (strong) was first determined and then subtracted from the initial amide content of the HMWDON sample (before hydrolysis) (*16*). Here, acetic acid is being used as a proxy for *N*-AAPs.

pected if all of the acetic acid in our samples was from peptidoglycan. Possible explanations for the general discrepancy between NMR-derived estimates of *N*-AAPs and molecular-level carbohydrate analyses are incomplete depolymerization of *N*-AAPs and rapid Maillard condensation reactions of hydrolysis products (*22*).

Muramic acid also contains lactic acid, which can be quantitatively released from peptidoglycan without depolymerizing the glycan (*23*). For peptidoglycan, 1 mol of lactic acid will be released for every 2 mol of acetic acid. Concentrations of lactic acid (*14*) in our samples were <0.4% of HMWDOM-carbon, an order of magnitude less than expected if all of the acetic acid we recovered was from peptidoglycan. The low concentration of lactic acid measured in this study and the low concentration of D-amino acids previously reported for HMWDON (*9*) together suggest that peptidoglycan is at best only a minor component of HMWDON. In addition, the D-amino acids in HMWDON so far identified to be present in peptidoglycan (*9*) could be present in a number of compounds synthesized by prokaryotes and eukaryotes (*24*, *25*).

Because *N*-AAPs represent ~40 to 50% of the HMWDON in surface waters, and given that 40 to 50% of HWMDON is removed below the mixed layer (*6*, *8*), we hypothesize that the global decrease in HMWDON with depth in the oceans results from the selective removal of *N*-AAPs. To test this hypothesis, we analyzed HMWDOM collected from a depth of 1000 m in the Middle Atlantic Bight (MAB), which has radiocarbon, ^{1}H-NMR, and molecular-level properties characteristic of deep-sea HMWDOM (*10*). In agreement with previous ^{15}N-NMR spectra of deep sea HMWDON (*8*), the ^{15}N-NMR spectrum of our sample shows one major resonance characteristic of amide-N (100% of total N) (Fig. 3A). Mild acid hydrolysis (*13*) decreased amide-N from 100% to 76% of total N and increased amine-N from undetectable levels to 24% of total N (Fig. 3B and Table 1). After acid hydrolysis, acetic acid was released from HMWDOM, as were amino acids, which increased from undetectable levels to 10% of total N. The sum of acetic plus amino acids (2.1 μmol) in the hydrolysis products was similar to the increase in amine-N (1.8 μmol of N) observed with ^{15}N-NMR spectroscopy. Molecular-level analyses after strong acid hydrolysis showed deep-sea HMWDON was 17% *N*-AAPs (Table 1), 12% hydrolyzable protein, and 71% nonhydrolyzable amide (5.5 μmol of N) (*16*). Despite the surface water abundance, a large fraction of *N*-AAPs are lost during mixing into the deep ocean. Proton NMR spectra of numerous deep-sea samples showed a sharp decrease in acetate below the mixed layer, confirming the loss of *N*-AAPs with depth (Fig. 4). The loss in *N*-AAPs and the relative increase in nonhydrolyzable amides will not result in any change to the ^{15}N-NMR spectrum (*8*).

The lack of amines in marine HMWDON implies that amine-N is more labile than amide-N. Many marine microorganisms have cell surface–bound deaminases that are capable of extracting amine-N from a variety of organic compounds (*26*). These enzymes could render HMW amine-N more biologically available by allowing organisms to bypass polymer hydrolysis or uptake. The eventual depth-dependent loss of *N*-AAPs from HMWDON suggests either that *N*-AAP compounds are labile or that organisms have developed a mechanism to access the nitrogen in *N*-AAPs without complete hydrolysis of the polymer (perhaps through cell surface–bound acetamidases). Although we were unable to depolymerize *N*-AAPs using acid hydrolysis, the capacity to enzymatically degrade *N*-AAPs may be widespread among marine microbes. In particular, the ability to hydrolyze chitin [β (1→ 4)-(*poly*) *N*-acetyl D-glucosamine] is notable in members of the marine α-proteobacteria and the *Cytophaga-Flavobacter* cluster (*27*, *28*). The widespread occurrence of chitinase activity and the ubiquity of chitinase genes in marine bacteria (*29*) imply that chitin-like biopolymers are important substrates in the marine environment, consistent with the abundance of *N*-AAPs in HMWDON. The presence of specialized bacteria could explain the ultimate removal of *N*-AAPs from the marine environment.

More than 90% of DON is sequestered in the deep sea, and most deep-sea HMWDON

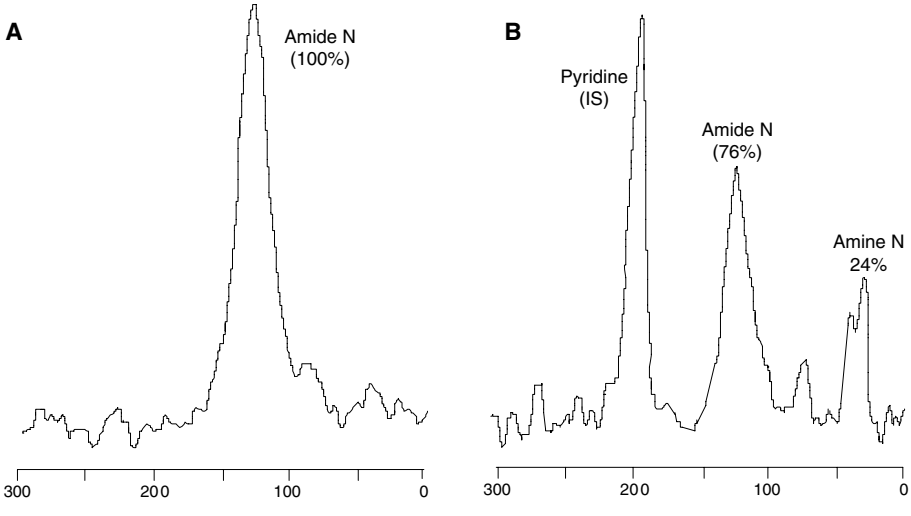

Fig. 3. The effect of mild acid (*13*) hydrolysis on the amide linkage of deep-sea HMWDON. (**A**) The ^{15}N-NMR spectrum of HMWDON shows only one resonance for amide-N [400 MHz, solid state δ (chemical shift in ppm downfield from liquid NH_3)]. (**B**) Treatment of the sample with mild acid converts 24% of the nitrogen to amine but does not affect most (76%) of the nitrogen. Pyridine (IS), added as an internal recovery standard, showed >98% N recovery through the hydrolysis procedure. Deep-sea HMWDON may also include some (<13% total N) contribution from pyrrole- and indole-N, which resonate between 130 and 215 ppm and overlap with the amide region in our ^{15}N-NMR spectrum.

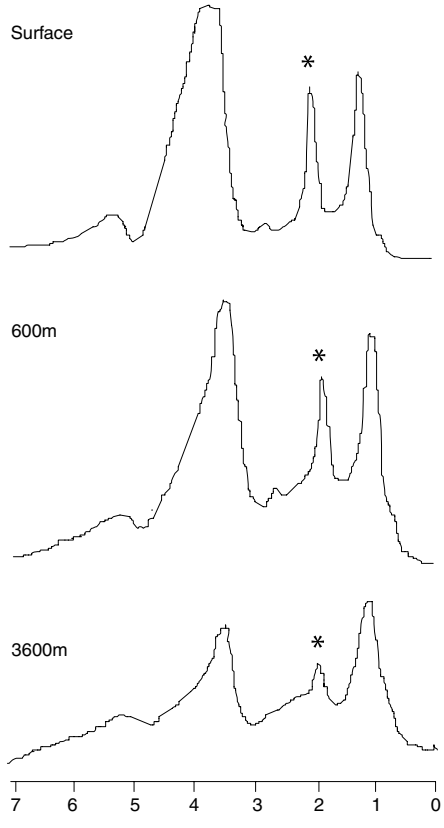

Fig. 4. The ^{1}H-NMR spectra [400 MHz, D_2O, δ(ppm)] of HMWDOM isolated from several depths (surface, 600 m, and 3600 m) in the Pacific Ocean (31°N, 159°W; the total water column depth was 5770 m). The peak at 2.0 ppm (*) arises from acetate, which is presumed to be present in *N*-AAPs. The clear decrease in the relative amount of acetate with depth is interpreted as a depth-dependent loss of *N*-AAPs.

is not hydrolyzed by treatment with strong acids (Table 1). Hydrolysis-resistant amides have been observed in marine particulate matter and sediments, where the resistance to chemical hydrolysis has been attributed to physical sorption and encapsulation (*30*). Amide-N in DON is not physically protected, but previous experiments have shown that the biodegradation rate of labile compounds such as proteins is substantially reduced by abiotic complexation within marine DOM (*31*). Long-term protein-DOM interactions may lead to structural modifications that render proteins resistant to chemical hydrolysis and unavailable to bacteria. This mechanism could lead to the sequestration of nitrogen in the dissolved phase (*32*) and give rise to the hydrolysis-resistant amide-N observed by ^{15}N-NMR.

Our data show that two chemically distinct pools of organic nitrogen accumulate in the ocean. The higher concentration of HMWDON in the mixed layer (relative to deep ocean values) largely reflects the presence of *N*-AAPs, which degrade on time scales of upper ocean mixing. These newly added biopolymers are chemically distinct from the refractory HMWDON pool that exists throughout the water column. If we assume the proportion of *N*-AAPs, protein, and nonhydrolyzable amide measured in our samples is representative of global HMWDON, then as much as 80% of the decrease in HMWDON with depth involves the removal of *N*-AAPs. The abundance of amide-N throughout the water column suggests amides are more biologically recalcitrant than other forms of organic-N. The ubiquity of amide linkages in HMWDON is not surprising, given that most organic nitrogen in phytoplankton is protein. However, the important contribution of *N*-AAPs to upper ocean HMWDOM, and the resistance of amides in deep sea HMWDOM to chemical and biological degradation, are unexpected results that help elucidate the currency of DON in the marine nitrogen cycle.

References and Notes

1. J. Abell, S. Emerson, P. Renaud, *J. Mar. Res.* **58**, 203 (2000).
2. M. J. Church, H. W. Ducklow, D. M. Karl, *Limnol. Oceanogr.* **47**, 1 (2002).
3. P. Libby, P. Wheeler, *Deep-Sea Res.* **44**, 345 (1997).
4. N. J. Antia, P. J. Harrison, L. Oliveira, *Phycologia* **30**, 1 (1991).
5. T. Berman, D. A. Bronk, *Aquat. Microb. Ecol.* **31**, 279 (2003).
6. D. A. Bronk, in *Biogeochemistry of Marine Dissolved Organic Matter*, D. A. Hansell, C. A. Carlson, Eds. (Academic Press, San Diego, CA, 2002), pp. 163–247.
7. HMWDON is defined here as the fraction of DON retained by an ultrafiltration membrane with a pore size of 1 nm. This fraction is expected to have a nominal molecular weight of >1 kD.
8. M. D. McCarthy, T. Pratum, J. I. Hedges, R. A. Benner, *Nature* **390**, 150 (1997).
9. M. D. McCarthy, J. I. Hedges, R. A. Benner, *Science* **281**, 231 (1998).
10. L. I. Aluwihare, D. J. Repeta, R. F. Chen, *Deep-Sea Res. II* **49**, 4421 (2002).
11. L. I. Aluwihare, D. J. Repeta, R. F. Chen, *Nature* **387**, 166 (1997).
12. S. Henrichs, P. M. Williams, *Mar. Chem.* **17**, 141 (1985).
13. De-acetylation of HMWDON samples was performed in 1 N HCl. Samples were heated overnight at 90°C under an atmosphere of N_2. The acetic acid produced during the hydrolysis was extracted from a weighed aliquot of the hydrolysate into either ethyl ether or dichloromethane. After extraction, the presence of acetic acid in the organic fraction was confirmed by solution-state ^{1}H-NMR before low molecular weight acids (e.g., acetic acid) were quantified. The aqueous fraction of the hydrolysate was lyophilized and, as shown in the ^{1}H-NMR (Fig. 2C), no longer contained acetamide. Changes in C and N were assessed with solid-state ^{13}C- and ^{15}N-NMR spectroscopy. Under these hydrolysis conditions, no muramic acid (de-acetylated) or amino sugar monomers were detected.
14. D. B. Albert, C. S. Martens, *Mar. Chem.* **56**, 27 (1997).
15. M. Zhao, J. L. Bada, *J. Chromatogr. A.* **690**, 55 (1995).
16. The percentage of N in each sample represented by *N*-AAPs, hydrolyzable protein, and nonhydrolyzable amide was calculated as follows: Because 1 mol of *N*-AAP sugar is de-acetylated for every mole of acetic acid released, we assumed that μmoles of acetic acid were equal to μmoles of N in *N*-AAPs; hydrolyzable protein N was calculated on the basis of the recoveries of amino acid N after strong acid hydrolysis (*12*); nonhydrolyzable amide was determined after strong acid hydrolysis (Table 1). Higher amino acid yields were obtained when HMWDON was hydrolyzed with strong acid. As a result, after strong acid hydrolysis, only 2.2 (29% of total N) and 5.5 μmol (71% of total N) of amide-N remained unhydrolyzed in the Woods Hole and MAB samples, respectively. In order to quantify the amount of amide-N remaining after strong acid hydrolysis, the sum Σacetic acid (mild) + amino acids (strong) was first determined and then subtracted from the initial amide content of the HMWDON sample (before hydrolysis). In all cases, percentages are expressed relative to total N in each sample. We calculated the amount of *N*-AAP carbon with the C/N ratio in HMWDOM (Table 1) and assumed 8 μmol of C per μmol of *N*-AAP (e.g., *N*-acetyl glucosamine).
17. J. J. Boon, V. A. Klap, T. I. Eglinton, *Org. Geochem.* **29**, 1051 (1998).
18. J. A. Leenheer, T. I. Noyes, C. E. Rostad, M. L. Davisson, *Biogeochemistry* **69**, 125 (2004).
19. K. Kaiser, R. Benner, *Anal. Chem.* **72**, 2566 (2000).
20. D. L. Popham, J. Helin, C. E. Costello, P. Setlow, *J. Bacteriol.* **178**, 6451 (1996).
21. We modified the method provided in (*20*) and hydrolyzed samples (in 4 N HCl) overnight at 90°C. We recovered no muramic acid and only small amounts of glucosamine and galactosamine from surface samples. This modified hydrolysis method was tested on chitin oligomers, peptidoglycan (from *Bacillus subtilus*), and bacterial cells (mixed laboratory culture) to ensure the quantitative (>90%) recovery of glucosamine and de-acetylated muramic acid. We assessed amino sugar recoveries by high-performance liquid chromatography and fluorescence detection of *o*-phthaldialdehyde-derivatized samples (*15*) or gas chromatography after derivatizing to alditol acetates (*10*).
22. J. I. Hedges *et al.*, *Org. Geochem.* **31**, 945 (2000).
23. O. Hadja, *Anal. Biochem.* **60**, 512 (1974).
24. Y. Nagata, T. Fujiwara, K. Kawaguchinagata, Y. Fukumori, T. Yamanaka, *Biochim. Biophys. Acta* **1379**, 76 (1998).
25. J. S. Martinez *et al.*, *Science* **287**, 1245 (2000).
26. B. Palenik, S. E. Henson, *Limnol. Oceanogr.* **42**, 1544 (1997).
27. M. T. Cottrell, D. L. Kirchman, *Appl. Environ. Microbiol.* **66**, 1692 (2000).
28. A. L. Svitil, D. L. Kirchman, *Microbiol.* **144**, 1299 (1998).
29. M. T. Cottrell, D. N. Wood, L. Yu, D. L. Kirchman, *Appl. Environ. Microbiol.* **66**, 1195 (2000).
30. H. Knicker, P. G. Hatcher, *Naturwissenschaften* **84**, 231 (1997).
31. R. G. Keil, D. L. Kirchman, *Mar. Chem.* **45**, 187 (1994).
32. E. Tanoue, S. Nishiyana, M. Kamo, A. Tsugita, *Geochim. Cosmochim. Acta* **59**, 2643 (1995).

33. We thank A. Beilecki, then at Brüker Instruments, for assistance with ^{15}N-NMR spectroscopy; M. Pullin and D. Albert for assistance in the determination of acetic acid; and the staff at the Natural Energy Laboratory in Kona, Hawaii, and E. Smith for assistance in sample collection. Supported by the Chemical and Biological Oceanography Programs at the National Science Foundation; the Carbon Sequestration Program at the U.S. Department of Energy; the Rhinehart Coastal Research Center of the Woods Hole Oceanographic Institution; and the Fundación Andes, Chile.

20 December 2004; accepted 9 March 2005
10.1126/science.1108925

Assessing Methane Emissions from Global Space-Borne Observations

C. Frankenberg,[1] J. F. Meirink,[2] M. van Weele,[2] U. Platt,[1] T. Wagner[1]

In the past two centuries, atmospheric methane has more than doubled and now constitutes 20% of the anthropogenic climate forcing by greenhouse gases. Yet its sources are not well quantified, introducing uncertainties in its global budget. We retrieved the global methane distribution by using space-borne near-infrared absorption spectroscopy. In addition to the expected latitudinal gradient, we detected large-scale patterns of anthropogenic and natural methane emissions. Furthermore, we observed unexpectedly high methane concentrations over tropical rainforests, revealing that emission inventories considerably underestimated methane sources in these regions during the time period of investigation (August through November 2003).

Methane (CH_4) is, after carbon dioxide (CO_2), the second most important anthropogenic greenhouse gas (*1*). It also has an indirect effect on climate through chemical feedbacks (*1*, *2*). More than 50% of present-day global methane emissions are anthropogenic, the largest contributors being fossil fuel production, ruminants, rice cultivation, and waste handling (*3*). The natural source strength of CH_4, mainly constituted by wetlands, is particularly uncertain, because these emissions vary considerably in time and space (*4*, *5*) and available ground-based measurements are sparse, albeit precise, and limitedly representative at larger scales. Better knowl-

[1]Institute of Environmental Physics, University of Heidelberg, INF 229, 69120 Heidelberg, Germany. [2]Section of Atmospheric Composition, Royal Netherlands Meteorological Institute, Post Office Box 201, 3730 AE De Bilt, Netherlands.

edge of the methane distribution and emissions is indispensable for a correct assessment of its impact on global change (*1*). Observations from space now allow the global detection of spatial and temporal variations in atmospheric methane concentrations, thereby enabling identification of known sources and discovery of new ones, particularly in regions that are poorly sampled by existing surface measurement networks.

The SCIAMACHY (scanning imaging absorption spectrometer for atmospheric chartography) instrument (*6*) on board the European Space Agency (ESA)'s environmental research satellite ENVISAT records the intensity of solar radiation, reflected from the Earth surface or the atmosphere, in more than 8000 spectral channels between 240 and 2390 nm. From these measurements, atmospheric trace gas concentrations (e.g., BrO, OClO, H_2O, SO_2, NO_2, CH_2O, O_3, N_2O, CO, CH_4, and CO_2) can be derived (*7*, *8*). The near-infrared spectrometers are used for global measurement of total columns of carbon monoxide and greenhouse gases carbon dioxide and methane. ENVISAT operates in a nearly polar, sun-synchronous orbit at an altitude of 800 km, crossing the equator at 10:00 a.m. local time. SCIAMACHY offers a variety of measurement geometries. For column retrievals, we chose the nadir mode in which the instrument points down almost perpendicular to the earth's surface, detecting reflected sunlight. The spatial extent of the ground pixels considered in this study is 60 km (east-west) by 30 km (north-south). Global coverage is achieved every 6 days.

CO_2 and CH_4 not only absorb thermal radiation from the Earth system, causing radiative forcing, but also solar radiation in the near-infrared. Hence, these molecules can be measured by means of the proven method of differential optical absorption spectroscopy (*9*) (DOAS). To account for peculiarities of spectrometry in the near-infrared (*10*, *11*), we implemented a new modified iterative algorithm (IMAP-DOAS) (*12*) that enables precise and unbiased determination of vertical column densities (VCDs, the vertically integrated concentrations from surface to top of atmosphere) of methane and carbon dioxide. The negligibility of Rayleigh scattering proves to be a major advantage in the near-infrared: In the absence of clouds and aerosols, most photons recorded by the instrument have thus been reflected at the Earth's surface, thereby having traversed the entire atmospheric column twice. This renders the measurements sensitive to the lower troposphere, which is a prerequisite for the detection of near-ground methane sources. In contrast, thermal-infrared sounders, which have also been used to measure CH_4 (*13*), exhibit a lack of sensitivity near the ground. However, they could derive methane abundances in the free troposphere and stratosphere, thus yielding more accurate information about the lower troposphere when synergistically combined with near-infrared retrievals.

Two main points affecting the retrieval in the near-infrared have to be considered: First, the VCD of a well-mixed gas scales linearly with the total column of all atmospheric constituents, thus with surface pressure. Hence, we need a proxy for surface pressure to convert columns into mixing ratios. Second, clouds and aerosols can substantially alter the light path of the recorded photons. CO_2 exhibits only very small variations in its total columns, and the retrieval window (1562 to 1585 nm) is spectrally close to the CH_4 retrieval window (1630 to 1670 nm). Thus, it is well suited as a proxy for both surface pressure (or, in the presence of clouds, cloud top pressure) and changes in the light path due to partial cloud cover and aerosols. Consequently, we can derive the column-averaged dry (no water vapor included) volume mixing ratio (VMR) of CH_4 in the atmosphere from the ratio of the CH_4 VCD (V_{CH_4}) and the CO_2 VCD (V_{CO_2}), scaled by the global and annual mean of the CO_2 column-averaged mixing ratio [370 parts per million (ppm)], i.e., $VMR(CH_4) \approx V_{CH_4}/V_{CO_2} \cdot \overline{VMR}(CO_2)$. Care should be taken not to confuse column-averaged VMRs with surface VMRs. Surface VMRs have a stronger response to emissions, whereas column-averaged mixing ratios exhibit less variation and are slightly lower because of reduced methane VMRs in the stratosphere.

A retrieval bias is introduced by assuming a constant column-averaged VMR(CO_2), whereas in reality it varies globally and seasonally over a range (minimum to maximum) of about 11 ppm by volume or 3% (*14*). This bias will be largest in Eurasia and North America north of 40°N. However, south of 40°N the bias can be assumed to be within 1.5% (*14*). Methane enhancements may be masked by our method in cases of sources leading to similar relative enhancements of V_{CO_2} and V_{CH_4} (e.g., biomass burning for certain fire types).

In the next step, we discard all measurements exhibiting substantial cloud cover at altitudes substantially above the ground, because we are primarily interested in variations in the lower troposphere. Figure 1A demonstrates how we extracted appropriate measurements: Highest CO_2 column observations show strong anticorrelation with surface altitude, illustrating the sensitivity to the boundary layer and being a first proof of the quality of the measurements. Strongly reduced column retrievals can be attributed to the shielding effect of clouds. We used a lower threshold of V_{CO_2} (red line) to obtain a suitable subset of measurements (gray pixels) representing the lower troposphere. A scatter plot of V_{CO_2} and V_{CH_4} underlines the close correlation of both measurements in this subset (Fig. 1A). The deviations from the strictly linear correlation bear the actual information, i.e., the variations of the CH_4 column with respect to the CO_2 column, which is determined by the length of the light path and an only slightly varying CO_2 VMR.

By using only the aforementioned measurement subset, we averaged the CH_4 VMRs from August through November 2003 on a horizontal grid (1° by 1°) as shown in Fig. 2. The latitudinal gradient in the methane VMRs can be seen, with strongest gradients, as expected, across the Intertropical Convergence Zone (ITCZ). Apart from this gradient, large-scale and strong methane enhancements are observed in various parts of the world. The largest abundances are found in the Gangetic plains of India, Southeast Asia, and parts of China. According to current emission inventories (fig. S1) (*3*), the sources can be mostly attributed

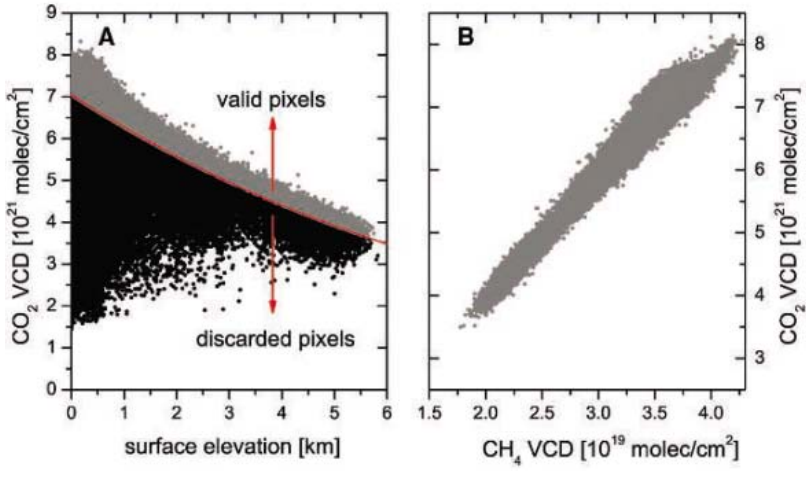

Fig. 1. (**A**) A scatter plot of the retrieved CO_2 VCDs versus surface altitude (August to September 2003). For further evaluations, only pixels above the threshold indicated by the red line are considered (corresponding to an effective cloud top height of 1 km). (**B**) A scatter plot of the retrieved vertical column densities of CH_4 and CO_2 for all valid pixels. The slight deviations from the strictly linear correlation between both VCDs can be mostly explained by variations in the CH_4 VMRs.

to rice cultivation in this time period and, to a lesser extent, to domestic ruminants. Wetlands presumably caused the observed high abundances in central Africa and Manchuria in China. Fossil fuel production can be associated with enhanced CH_4 VMRs over the industrialized Yellow river basin in China and the Appalachian basin (coal mining) in the eastern United States. Waste treatment–related emissions are likely to add to these in populated areas.

To substantiate our findings, we compared the measurements with methane concentration fields simulated with use of a global chemistry-transport model (TM3) (*15*) that takes current emission inventories (*16*, *17*) into account (fig. S1). The modeled enhancements in the United States and Asia as well as the north-south gradient (Fig. 3) strongly resemble the methane VMRs retrieved by SCIAMACHY in magnitude and spatial extent (Fig. 2). Additionally, persistent long-range transport features are observed, most clearly over the Pacific east of Japan (movie S1 and Fig. 2). In principle, the model enables discrimination of emissions and transport, e.g., evident in November 2003, with Africa strongly influenced by methane transported from South Asia (movie S1).

Although the general agreement between the measurements and the model is very good (fig. S2), there are discrepancies in India and in the tropics (Fig. 3B). The measured abundances over India are lower than that simulated by the model. This indicates that the rice emissions used in our model runs (amounting to 80 Tg $year^{-1}$) were probably overestimated. In contrast, SCIAMACHY retrievals in the tropics are up to 4% [70 parts per billion (ppb)] higher than predicted by the model.

We verified that this discrepancy cannot be attributed to a retrieval error dependent on solar zenith angle, light-path changes, or albedo [Supporting Online Material (SOM) Text]. A model bias, such as an underestimate of the stratospheric methane abundances or large errors in the modeled distribution of OH radicals, can also be excluded (SOM Text). The higher methane VMRs of the measurement compared with the model can thus be explained either by tropical methane emissions not considered in the model, a regional CO_2 depression relative to the annual global mean, or some combination of both. Although CO_2 flux estimates in the tropical land masses are uncertain (*18*), the required depression in the CO_2 column (3 to 4%) would have an improbably high magnitude (*14*). Hence, we conclude that tropical CH_4 sources in our model are underestimated.

The underestimate may be related to biogenic methane emissions, because there is a strong spatial correlation between the discrepancies and the presence of broadleaf evergreen forest (fig. S3) (*19*). Model simulations indicate that an additional tropical methane source of around 30 Tg over the considered time period (August through November) is needed if the discrepancy is fully assigned to methane sources. For comparison, the tropical source in our model is 45 Tg (table S1). Potential candidates for the enhanced source include wetlands, biomass burning, termites, cattle breeding in pastures, or a hitherto unknown methane source that might be directly related to the broadleaf evergreen forest. Wetland emissions, in particular in the Amazon, appear to be underestimated in our model [e.g., Melack *et al.* (*20*) estimate an annual source of 29 Tg of CH_4 for the Amazon, whereas we used 8 Tg], but the investigated period coincides with the dry season in most of the tropics, when wetland emissions are supposed to be lowest (*20*, *21*). However, in the dry season unaccounted biomass burning can also contribute to the discrepancy. Tropical fires are characterized by a molar CH_4/CO_2 ratio (*22*) that is more than twice the ratio of their respective background concentrations. Hence, our measurements are sensitive to these fires. Lastly, termites constitute a substantial but poorly constrained tropical methane source (*23*). Further validation measurements and process-based investigations for the considered

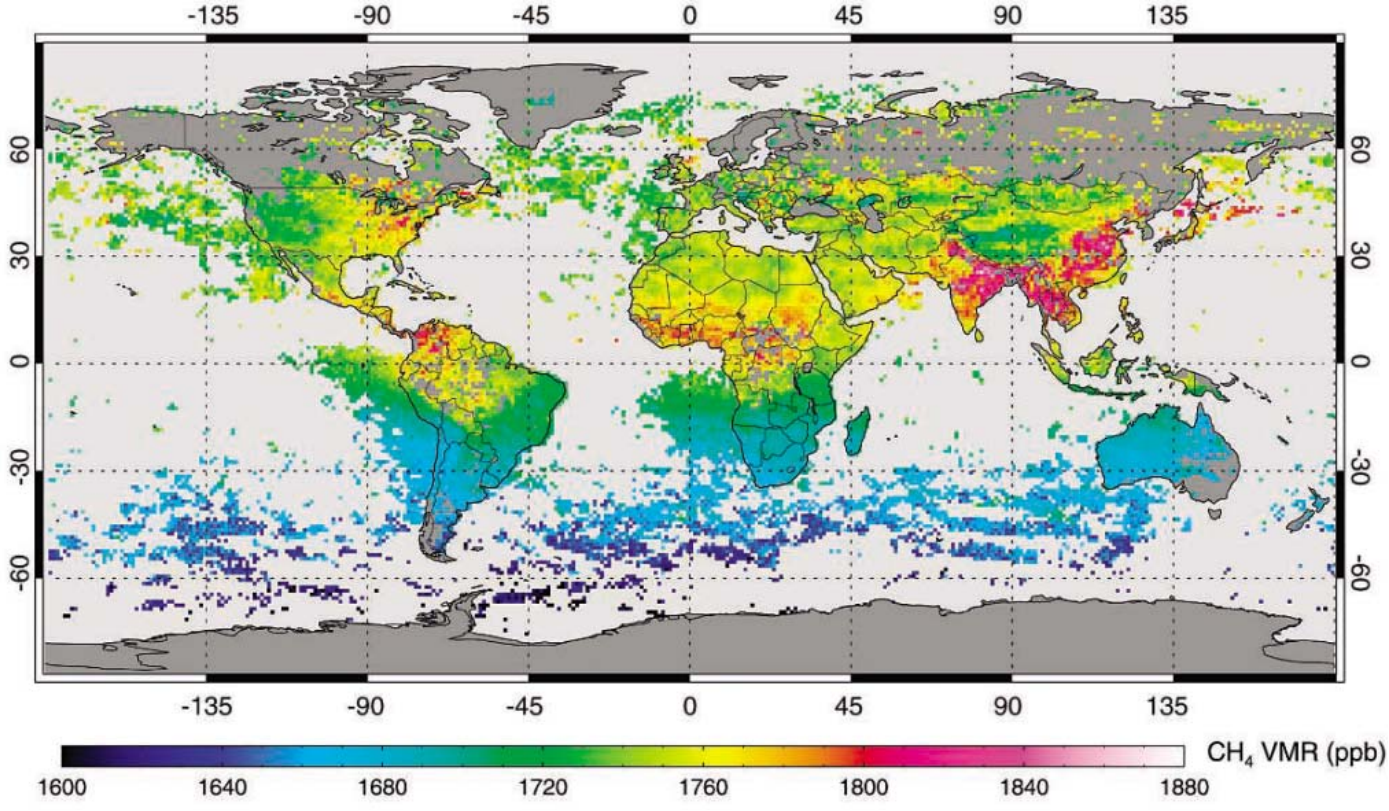

Fig. 2. SCIAMACHY measurements of column-averaged methane VMR in ppb units. The measurements are averaged over the time period of August through November 2003 on a 1° by 1° horizontal grid. At least 5 (and up to 150) measurements are taken for each grid cell. Only few observations are available over the ocean, because low ocean reflectivity substantially reduces the quality of the retrieval, leading in turn to unreliable measurements (standard deviation of the fit residual above 0.5%) that are discarded. Occasionally, sun glint or clouds at low altitudes allow measurement over the ocean.

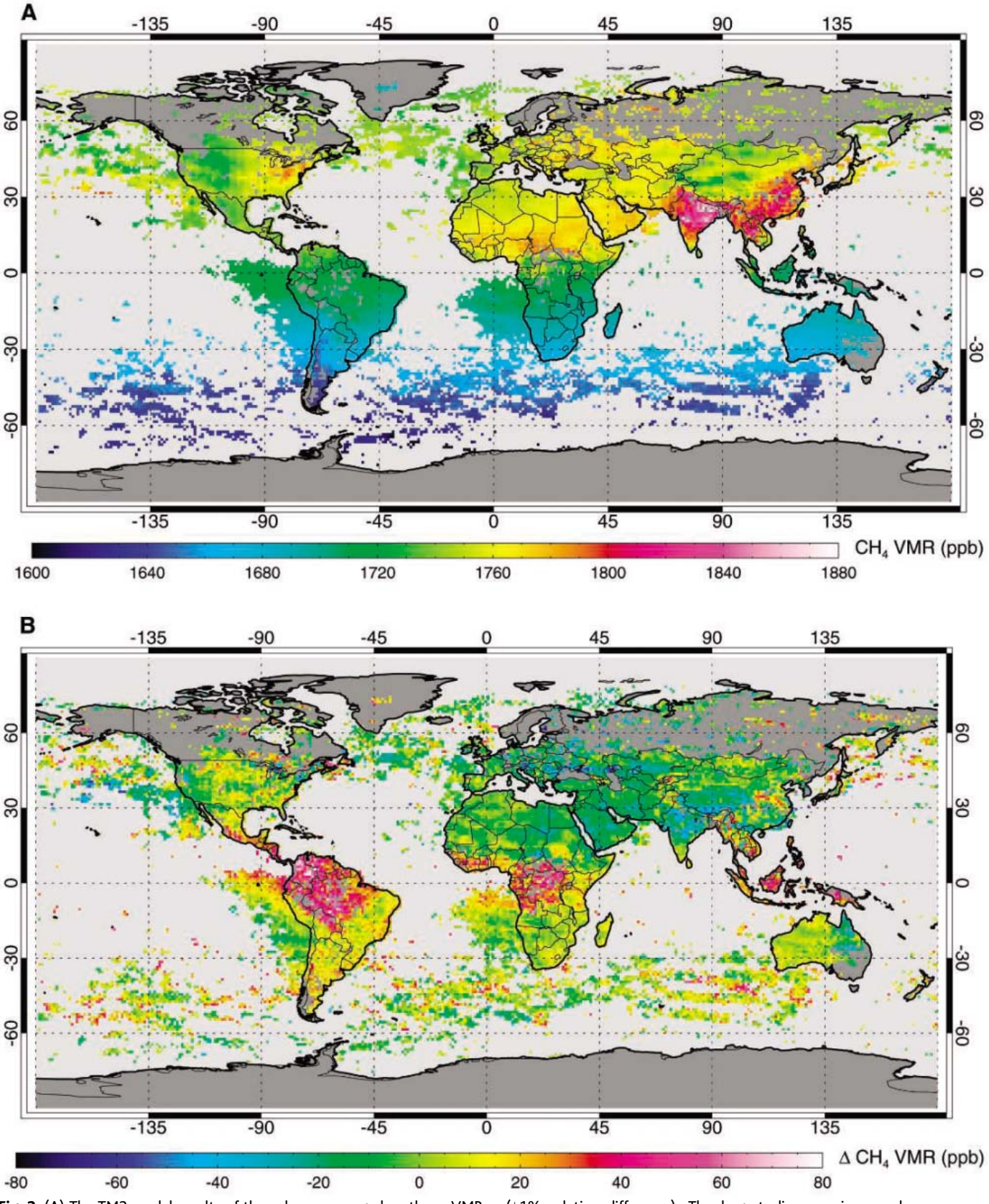

Fig. 3. (**A**) The TM3 model results of the column-averaged methane VMR in ppb for the time period of August through November 2003. Only modeled values that are colocated in space and time with the respective SCIAMACHY measurements are used for the averaging. (**B**) The difference between the SCIAMACHY measurements and the TM3 model results (Δ). The results are displayed in ppb, ranging in most pixels from –20 to 20 ppb (±1% relative difference). The largest discrepancies can be seen over tropical broadleaf evergreen forests in South America, central Africa, and Indonesia. In these areas, measured values are persistently higher than predicted by the model. Prevailing wind directions cause transport of these discrepant concentrations over the oceans (e.g., northwest of South America or west of Africa).

season in the evergreen forests of tropical South America, Africa, and Indonesia are needed to conclude which source type is responsible for the observed discrepancy and to what extent this discrepancy is caused by an underestimated or hitherto unknown methane source. In addition, investigations of satellite data for longer time periods are necessary to estimate the annual methane excess and to constrain the source attribution.

An additional methane source of 30 Tg in 4 months is large but can be accommodated by the uncertainty in the global budget, which is estimated to be 50 to 100 Tg $year^{-1}$ (*1*). Further, surface observations (*24*) are not in disagreement with a large additional tropical source. Methane emitted in the tropics is generally rapidly uplifted by convection, so that the surface stations, which are located in remote ocean sites, are sensitive to these emissions only to a limited extent. Inverse modeling studies based on ground-based measurements (*25*, *26*) have also indicated higher tropical emissions than those estimated from bottom-up inventories. However, this evidence has been rather indirect and uncertain. The present satellite measurements over the tropical land masses are sensitive to the entire atmospheric column, thus directly reflecting enhancement patterns.

Global measurement from space has proven feasible for detection of CH_4 emissions. The satellite's ability to sense sources globally is unique and opens a new window for the analysis of the biogeochemical cycle of methane and anthropogenic impacts. With SCIAMACHY hopefully in operation for several years to come, we should be able to examine the temporal and spatial variations of CH_4 over longer time periods. The integration of these measurements with atmospheric models and precise ground-based observations should greatly reduce uncertainties in the methane source strength, helping to draw a consistent picture of the global methane budget. This will be a high priority for climate research.

References and Notes

1. J. Houghton *et al.*, Eds., *Climate Change 2001: The Scientific Basis* (Cambridge Univ. Press, Cambridge, 2001).
2. J. Lelieveld, P. J. Crutzen, F. J. Dentener, *Tellus* **B50**, 128 (1998).
3. J. G. J. Olivier, J. J. M. Berdowski, in *The Climate System*, J. J. M. Berdowski, R. Guicherit, B. J. Heij, Eds. (A. A. Balkema/Swets and Zeitlinger, Lisse, Netherlands, 2001), pp. 33–78.
4. L. A. Morrissey, G. P. Livingston, *J. Geophys. Res.* **97**, 16661 (1992).
5. B. P. Walter, M. Heimann, *Global Biogeochem. Cycles* **14**, 745 (2000).
6. H. Bovensmann *et al.*, *J. Atmos. Sci.* **56**, 127 (1999).
7. J. P. Burrows *et al.*, *J. Atmos. Sci.* **56**, 151 (1999).
8. T. Wagner *et al.*, *Monitoring of Trace Gas Emissions from Space: Tropospheric Abundances of BrO, NO_2, H_2Co, SO_2, H_2O, O_2 and O_4 as Measured by GOME in Air Pollution X* (WIT Press, Southampton, UK, 2002).
9. U. Platt, *Differential Optical Absorption Spectroscopy (DOAS) in Air Monitoring by Spectroscopic Techniques* (Wiley, New York, 1994).
10. M. Buchwitz, V. Rozanov, J. Burrows, *J. Geophys. Res.* **105**, 15231 (2000).
11. D. M. O'Brien, P. J. Rayner, *J. Geophys. Res.* **107**, 4354 (2002).
12. C. Frankenberg, U. Platt, T. Wagner, *Atmos. Chem. Phys.* **5**, 9 (2005).
13. C. Clerbaux, J. Hadji-Lazaro, S. Turquety, G. Mégie, P. Coheur, *Atmos. Chem. Phys.* **3**, 1495 (2003).
14. S. C. Olsen, J. T. Randerson, *J. Geophys. Res.* **109**, 10.1029/2003JD003968 (2004).
15. F. Dentener, M. van Weele, M. Krol, S. Houweling, P. van Velthoven, *Atmos. Chem. Phys* **3**, 73 (2003).
16. S. Houweling *et al.*, *J. Geophys. Res.* **105**, 8981 (2000).
17. J. A. Van Aardenne, F. J. Dentener, J. G. J. Olivier, C. G. M. Klein Goldewijk, J. Lelieveld, *Global Biogeochem. Cycles* **15**, 909 (2001).
18. K. Gurney *et al.*, *Nature* **415**, 626 (2002).
19. R. S. DeFries, J. R. G. Townshend, *Int. J. Remote Sens.* **15**, 3567 (1994).
20. J. M. Melack *et al.*, *Global Change Biol.* **10**, 530 (2004).
21. A. H. Devol, J. E. Richey, B. R. Forsberg, L. A. Martinelli, *J. Geophys. Res.* **95**, 16417 (1990).
22. M. O. Andreae, P. Merlet, *Global Biogeochem. Cycles* **15**, 955 (2001).
23. M. G. Sanderson, *Global Biogeochem. Cycles* **10**, 543 (1996).
24. Information about the Climate Monitoring and Diagnostics Network (CMDL) can be found online at www.cmdl.noaa.gov/ccgg.
25. R. Hein, P. J. Crutzen, M. Heimann, *Global Biogeochem. Cycles* **11**, 43 (1997).
26. S. Houweling, T. Kaminski, F. J. Dentener, J. Lelieveld, M. Heimann, *J. Geophys. Res.* **104**, 26,137 (1999).

27. Most importantly the authors thank all scientists and engineers involved in the ESA's ENVISAT/SCIAMACHY mission, especially J. P. Burrows and H. Bovensmann from the University of Bremen, as well as the space agencies of Germany [German Aerospace Center (DLR)], Netherlands [Netherlands Agency for Aerospace Programmes (NIVR)], and Belgium [Belgian User Support and Operations Center (BUSOC)]. We also thank R. Washenfelder and G. Toon from Jet Propulsion Laboratory for the updated methane spectral database; S. Sanghavi for proofreading the manuscript; and the Netherlands SCIAMACHY Data Center, in particular A. J. M. Piters and J. van de Vegte from [Royal Netherlands Meteorological Institut (RNMI)], for invaluable assistance in handling the SCIAMACHY data format. We acknowledge the European Commission for supporting the 5th Framework Programme RTD project EVERGREEN (contract number EVG1-CT-2002-00079) and A. P. H. Goede, EVERGREEN project coordinator.

Supporting Online Material

www.sciencemag.org/cgi/content/full/1106644/DC1
Materials and Methods
SOM Text
Figs. S1 to S4
Movie S1

22 October 2004; accepted 9 March 2005
Published online 17 March 2005;
10.1126/science.1106644
Include this information when citing this paper.

A Hydrogen-Rich Early Earth Atmosphere

Feng Tian,[1,2]* Owen B. Toon,[2,3] Alexander A. Pavlov,[2] H. De Sterck[4]

We show that the escape of hydrogen from early Earth's atmosphere likely occurred at rates slower by two orders of magnitude than previously thought. The balance between slow hydrogen escape and volcanic outgassing could have maintained a hydrogen mixing ratio of more than 30%. The production of prebiotic organic compounds in such an atmosphere would have been more efficient than either exogenous delivery or synthesis in hydrothermal systems. The organic soup in the oceans and ponds on early Earth would have been a more favorable place for the origin of life than previously thought.

It is generally believed that the existence of prebiotic organic compounds on early Earth was a necessary step toward the origin of life. Biologically important molecules can be formed efficiently in a highly reducing atmosphere (CH_4- and/or NH_3-rich) (*1*, *2*). They can also be produced efficiently in a weakly reducing atmosphere (*3*–*5*), where one important factor influencing the efficiency of production is the ratio of hydrogen to carbon (*6*–*8*). However, our current understanding of the composition of early Earth's atmosphere suggests it was neither strongly reducing nor hydrogen-rich. The concentrations of CH_4 and NH_3 are thought to have been low (*9*), and the hydrogen mixing ratio is believed to be of the order of 10^{-3} or smaller (*10*). Because it is difficult to produce organics in the atmosphere, two directions of research into the origin of life on Earth have become dominant: synthesis of organic compounds in hydrothermal systems, and exogenous delivery of organic compounds to early Earth (*11*). Here we reexamine the theory of diffusion-limited escape of hydrogen and show that hydrogen escape from early Earth's atmosphere was not as rapid as previously assumed. Hydrodynamic escape should be the dominant mechanism of escape, implying a hydrogen-rich early Earth atmosphere in which organic molecules could be produced efficiently.

The assumption that the escape of hydrogen is limited by diffusion into the hetero-

[1]Astrophysical and Planetary Science Department, [2]Laboratory for Atmospheric and Space Physics, [3]Program in Atmospheric and Oceanic Science, University of Colorado, Boulder, CO 80309, USA. [4]Department of Applied Mathematics, University of Waterloo, Waterloo, Ontario, N2L 3G1, Canada.

*To whom correspondence should be addressed. E-mail: tian@colorado.edu

sphere from below is applicable only when the escape is efficient. For Jeans escape to be efficient, the exobase temperature must be high. This condition is satisfied in the current Earth's atmosphere, where exobase temperatures exceed 1000 K as a result of the efficient absorption of solar ultraviolet (UV) radiation by atomic oxygen. The prebiotic Earth's atmosphere was anoxic and probably contained substantial amounts of CO_2 (*12*), similar to modern Venus or Mars. CO_2 absorbs UV, but unlike oxygen, it can effectively radiate energy back to space and keep the exobase temperatures low. The CO_2-rich venusian and martian exobases have temperatures of 275 K and 350 K, respectively (*13*). In the anoxic early Earth's atmosphere with low exobase temperature (*14*), Jeans escape of hydrogen would have been inhibited. For present-day Earth and Mars atmospheres, which have low hydrogen concentrations, the relatively low hydrogen escape rates caused by nonthermal processes are comparable to the Jeans escape rate (*15*, *16*). It is important to consider how the nonthermal escape rate might increase in an atmosphere with large hydrogen abundance. For an H_2O-rich early venusian atmosphere, the maximum limit of the nonthermal hydrogen escape rate (caused by the saturation of ionization of hydrogen atoms, which occurs when the homopause hydrogen mixing ratio reaches 2×10^{-3}) is $\sim 10^{10}$ cm^{-2} s^{-1} (*17*). The maximum nonthermal escape rate on early Earth should be similar to that on Venus (*18*). Given the low Jeans and nonthermal escape rates, the total hydrogen escape rate would not have been in balance with the volcanic H_2 outgassing rate on early Earth (*10*) at the previously suggested hydrogen mixing ratio of 10^{-3}. Instead, hydrogen would have been one of the major constituents in the ancient atmosphere.

H_2 can absorb extreme ultraviolet (EUV), as can O_2 and CO_2, but cannot effectively radiate energy back to space. However, H_2 can escape because of its low molecular weight and thereby carry energy away to space in a hydrodynamic hydrogen escape flow. When hydrogen is the major gas in the heterosphere and the major absorber of EUV, the escape of hydrogen would not be diffusion-limited but would be controlled by the solar EUV flux available to drive the escape flow (energy-limited), which would produce an escape rate smaller than the diffusion-limited escape rate.

In this report, we describe the application of a hydrodynamic escape model, which was recently developed to study transonic hydrogen hydrodynamic escape (*14*), to a hydrogen-rich early Earth's atmosphere. Because the solar EUV radiation level could have been much stronger during the Archean era than today (*19*), EUV radiation levels $\times 1$, $\times 2.5$, and $\times 5$ that of today were used in the simulations for sensitivity studies.

The velocity distributions in the high-energy input cases ($\times 2.5$ and $\times 5$) (Fig. 1A) level off and converge near the upper boundary of the model where the sound speed is exceeded (supersonic flow). Transonic points in the higher-energy input cases ($\times 2.5$ and $\times 5$) are near 10 Earth radii (*14*). Near the upper boundary of the model, the flow velocity is comparable to the escape velocity from the planet. Escape velocity is exceeded by the combination of the flow velocity and the thermal velocity at an altitude below the transonic points. In the $\times 1$ EUV level case, the energy absorbed is not adequate to drive supersonic flow, but escape still occurred. Figure 1B shows the temperature profiles in the correspond-

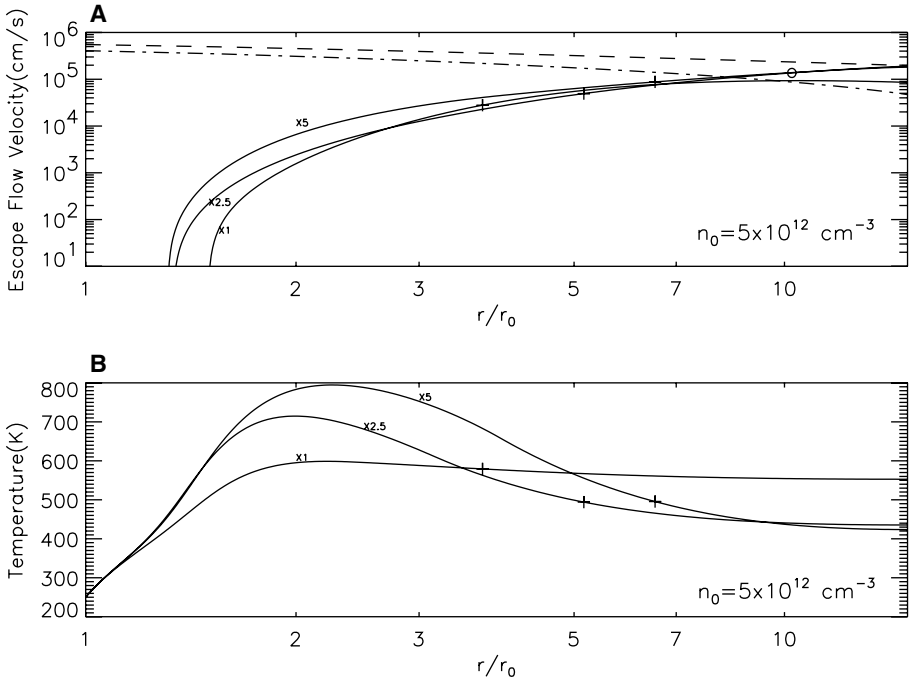

Fig. 1. (**A**) Flow velocity profiles in hydrodynamic escape of hydrogen under solar EUV levels $\times 1$, $\times 2.5$, and $\times 5$ that of today. r_0 is the distance between the lower boundary and the center of Earth. The homopause hydrogen density is 5×10^{12} cm^{-3} , corresponding to a mixing ratio of 50%. The dashed curve represents the escape velocity from Earth. The transonic point is marked approximately by a circle. The dash-dotted curve shows the difference between the escape velocity and the thermal velocity. The exobases are marked by crosses. (**B**) Temperature profiles in the corresponding cases. Although the peak temperatures are in the range of 700 to 800 K, the temperature at the exobases (marked by crosses) is low (500 to 600 K).

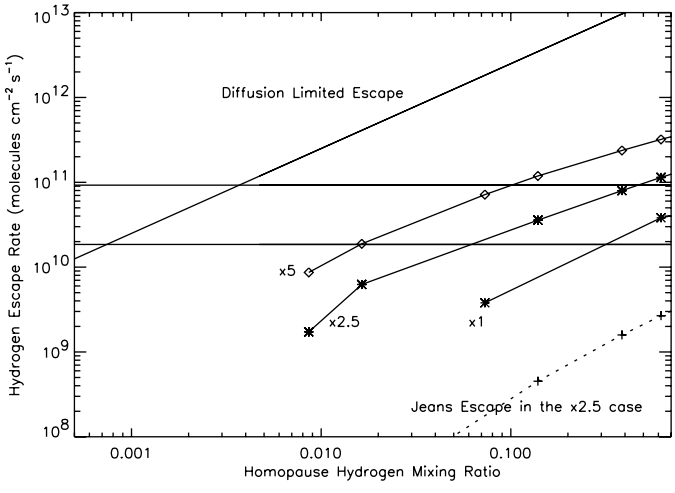

Fig. 2. Calculated hydrogen escape rate from early Earth's atmosphere as a function of the homopause hydrogen mixing ratio. The homopause air composition is assumed to be the same as that of today, except for the higher hydrogen concentration and lack of oxygen. The diffusion-limited escape rates, previously assumed to apply, are one or two orders of magnitude greater than the hydrodynamic escape rates because of overestimated exobase temperature. The dotted curve shows the Jeans escape rate as a function of homopause hydrogen mixing ratio under the $\times 2.5$ energy input level for the exobase temperatures that are likely to have been present for early Earth. The lower horizontal line represents the volcanic outgassing rate of hydrogen from the interior of Earth today ($\sim 1.8 \times 10^{10}$ hydrogen molecules cm^{-2} s^{-1}) (*29*). The upper horizontal line is the estimated outgassing rate of hydrogen from the interior of early Earth (~ 5 times the outgassing rate today) (*30*).

ing cases. Although the peak temperatures are 700 to 800 K in the high-energy input cases, the temperatures at the exobases (marked by crosses) are in the range of 500 to 600 K because of adiabatic cooling associated with the hydrodynamic escape.

Figure 2 illustrates our calculated escape rates for varying hydrogen homopause mixing ratios. The Jeans escape rates computed for the exobases are more than one order of magnitude smaller than the corresponding hydrodynamic escape rates because of the low exobase temperatures. If the solar EUV radiation level was 2.5 times that of today and the volcanic hydrogen outgassing rate was 5 times that of today ($\sim 9.25 \times 10^{10}$ hydrogen molecules cm^{-2} s^{-1}), a hydrogen mixing ratio of more than 30% could have been maintained everywhere below the homopause by balancing the volcanic hydrogen outgassing with the hydrodynamic escape of hydrogen (Fig. 2). By increasing the solar EUV radiation level to 5 times that of today, the hydrogen mixing ratio could still have been maintained at ~10%. These mixing ratios are two orders of magnitude greater than the 10^{-3} hydrogen concentration, considering the diffusion-limited hydrogen escape rate. A hydrogen-rich early Earth's atmosphere could be maintained even for the modest hydrogen outgassing rates appropriate if the oxidation state of Earth's mantle 3.9 billion years ago were the same as it is today.

The hydrodynamic escape rate increases nearly linearly as the solar EUV radiation level increases (Fig. 3), which reflects the energy-limited nature of the hydrodynamic escape. The slope depends on the hydrogen density at the homopause (*20*).

An early Earth's atmosphere with high hydrogen concentration has important consequences for the origin and evolution of life. Endogenous sources of prebiotic organics, such as production by lightning or photochemistry, are dominant in a reducing early Earth's atmosphere, whereas exogenous sources, such as delivery from space or production in hydrothermal systems, become major contributors in an atmosphere of an intermediate oxidation state (*1*). To provide more specific examples of the influence of high hydrogen concentration, we consider two organic molecule formation mechanisms, realizing that these are not the only prebiotic organic molecule formation mechanisms that are affected by the high hydrogen concentration.

Both H_2 and CO_2 are uniformly mixed below the homopause (*21*, *22*), where we have shown that the hydrogen mixing ratio could have been greater than 30%. Most photochemistry of interest occurs well below the homopause. Because the CO_2 concentration is likely to be less than 30%, H_2/C ratios in early Earth's atmosphere could have been greater than 1 throughout the chemically interesting part of the atmosphere. The formation of certain prebiotic organic compounds in an atmosphere of CO_2 or CO by electric discharge is almost as productive as that in an atmosphere of CH_4, when $H_2/C \geq 1$ (*7*, *8*). The conservative estimate of amino acid production rate by electric discharge is 10^7 kg/year when $H_2/C \geq 1$ (*23*). Although early Earth's atmosphere might have been dominated by CO_2 immediately after the heavy bombardment period, as continents formed on early Earth, the atmospheric CO_2 concentration would decline because of weathering, and the H_2/C ratio would become suitable for efficient formation of prebiotic organic compounds through electric discharge. Formation of prebiotic organic compounds by electric discharge at this conservative rate in a hydrogen-rich early Earth's atmosphere would have created an ocean with a steady-state amino acid concentration $\sim 10^{-6}$ mol/liter (*24*), which is orders of magnitude greater than the amino acid concentration estimated for a hydrogen-poor early Earth's atmosphere (*25*). This amino acid concentration is highly uncertain because neither the production rate nor the destruction rate is well known. In addition, organic films may have formed at the ocean surface, leading to higher concentrations of organic compounds than in the bulk sea water (*26*).

Because the magnitude of energy deposition from electric discharge in the ancient atmosphere is poorly understood, it is difficult to predict the exact production rate of organic materials from these sources. Alternatively, organics can be formed through photolysis of methane by Lyman-α (Ly-α) photons with subsequent polymerization. The rate of photochemical haze production is critically dependent on the CH_4/CO_2 ratio (*27*). A similar dependence on the CH_4/CO_2 ratio has been found for hydrogen cyanide (HCN) formation in an atmosphere with N_2, CO_2, and CH_4 (*5*). We used a one-dimensional photochemical model to study the organic production rate in a hydrogen-rich early Earth's atmosphere (*14*). Figure 4 shows that the production rate of hydrocarbons is enhanced by about three orders of magnitude (from $<10^7$ kg/year to 10^{10} kg/year) when the hydrogen concentration in early Earth's atmosphere changes from 10^{-3} to 30%. Hence, the atmospheric production rate of organics through UV photolysis would have been orders of magnitude greater than the rate of either the synthesis of organic compounds in hydrothermal systems or the exogenous delivery of organic compounds to early Earth (*28*).

On the basis of our new model of hydrodynamic hydrogen escape, we conclude that diffusion-limited escape theory does not apply to a hydrogen-rich early Earth atmosphere. Rather, the escape of hydrogen was energy limited. Hydrogen mixing ratios greater than 30% could have been maintained in the atmosphere of prebiotic Earth without either invok-

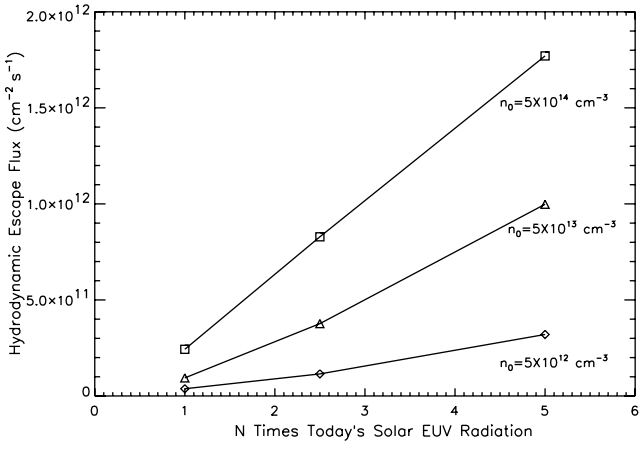

Fig. 3. The hydrogen escape rate increases nearly linearly as the solar EUV level increases. The slope is regulated by the homopause hydrogen density n_0.

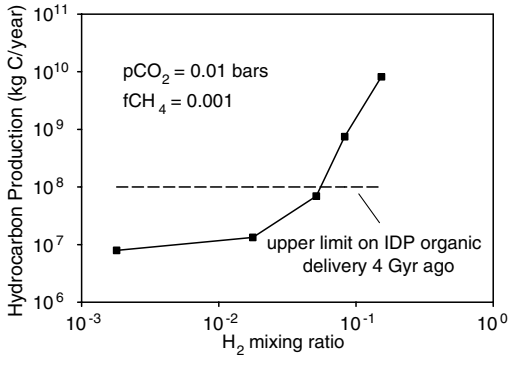

Fig. 4. Hydrocarbon production rate increases rapidly as the hydrogen concentration increases, and exceeds the delivery of organics by interplanetary dust particles (IDPs) for H_2 mixing ratios above 10%. pCO_2 is the partial pressure of CO_2 and fCH_4 is the mixing ratio of CH_4.

ing huge volcanic hydrogen outgassing rates or assuming a reduced mantle. The efficient production of organics in a hydrogen-rich early Earth's atmosphere would have led to an organic soup in the oceans and ponds on the early Earth. The world ocean could have been the birthplace of life (*14*).

References and Notes

1. C. F. Chyba, C. Sagan, in *Comets and the Origin and Evolution of Life* (Springer, New York, 1997), pp. 147–173.
2. S. L. Miller, *Science* **117**, 528 (1953).
3. J. P. Pinto, G. R. Gladstone, Y. L. Yung, *Science* **210**, 183 (1980).
4. P. H. Abelson, *Proc. Natl. Acad. Sci. U.S.A.* **55**, 1365 (1966).
5. K. J. Zahnle, *J. Geophys. Res.* **91**, 2819 (1986).
6. V. M. Canuto, J. S. Levine, T. R. Augustsson, C. L. Imhoff, M. S. Giampapa, *Nature* **305**, 281 (1983).
7. G. Schlesinger, S. L. Miller, *J. Mol. Evol.* **19**, 376 (1983).
8. R. Stribling, S. L. Miller, *Orig. Life* **17**, 261 (1987).
9. Both CH_4 and NH_3 in the atmosphere of early Earth would have been subject to rapid loss driven by solar UV radiation. It is unlikely that the volcanic outgassing rate of CH_4 or NH_3 could have been adequate to maintain high concentrations of these gases.
10. The hydrogen concentration is determined by the balance between the volcanic outgassing rate of hydrogen and the escape of hydrogen to space. The modern volcanic hydrogen outgassing rate is $\sim 1.8 \times 10^{10}$ hydrogen molecules cm^{-2} s^{-1} (*29*). Because of higher heat flow in the past, the overall outgassing rate of gases, and hydrogen in particular, might have been ~5 times greater on ancient Earth (*30*). In the present Earth's atmosphere, oxygen is dominant at the exobase level (defined as the boundary beyond which rapidly moving molecules may escape without collision). The current exospheric temperature is high (1000 to 2500 K) because of the efficient absorption of solar UV radiation by oxygen. If the exospheric temperature on the early Earth were as high as it is today, Jeans escape of hydrogen from the atmosphere would have been efficient, and the diffusion of hydrogen through the background gases to the homopause level would have been the limiting process. The rate of diffusion-limited escape can be expressed as $F(H_2) = 2.5 \times 10^{13} f_{total}$ molecules cm^{-2} s^{-1}, with f_{total} defined as the total mixing ratio of hydrogen (in all chemical forms) at the homopause (*31*). By balancing the diffusion-limited escape rate of hydrogen with the hydrogen outgassing rate, the hydrogen mixing ratio up to the homopause in early Earth's atmosphere should be of the order of 10^{-3} or below (*21*, *31*), unless the oxidation state of Earth's mantle was more reduced than its current oxidation state. But Earth's mantle has been suggested to be in a similar oxidation state to that of today for the past 3.96 billion years (*32*). The common consensus among planetary scientists for the past 30 years has been that early Earth's atmosphere had a low hydrogen concentration.
11. However, experiments to date generate only methane or formate in realistic hydrothermal-like systems (*33*). The exogenous flux of organic materials at about 4 billion years ago (Ga), primarily interplanetary dust particles (IDPs), may be less than 150 times the present value (*34*), although the interpretations of the Akilia rocks are debatable (*35*).
12. J. C. G. Walker, *Orig. Life* **16**, 117 (1985).
13. I. de Pater, J. J. Lissauer, in *Planetary Sciences* (Cambridge Univ. Press, Cambridge, 2001), pp 66–71.
14. Materials and methods are available as supporting material on *Science* Online.
15. H. Lammer *et al.*, *Icarus* **165**, 9 (2003).
16. D. M. Hunten, *Planet. Space Sci.* **30**, 773 (1982).
17. S. Kumar, D. M. Hunten, J. B. Pollack, *Icarus* **55**, 369 (1983).
18. Nonthermal escape from a hydrogen-rich early Earth has not been studied in detail. Although a similar upper limit of nonthermal hydrogen escape rate should apply to early Earth, it is important to note that nonthermal hydrogen escape processes may also be rather different for Earth than for Venus because of the presence of a strong magnetic field on Earth. Future work should include these processes in escape models to make more accurate estimates.
19. J. D. Dorren, E. F. Guinan, *Astrophys. J.* **428**, 805 (1994).
20. Assuming that the linear relation between escape flux and EUV still holds for even higher solar EUV input, the hydrogen escape flux would be about 7.5×10^{12} cm^{-2} s^{-1} for a solar EUV level 100 times that of today if the homopause hydrogen density is kept at $\sim 5 \times 10^{12}$ cm^{-3}. This escape rate is still slower than the diffusion-limited escape rate ($>1 \times 10^{13}$ cm^{-2} s^{-1}) for the same homopause hydrogen density. Hence, the diffusive flux does not become limiting except for extreme EUV input.
21. J. F. Kasting, *Science* **259**, 920 (1993).
22. H_2 is not a chemically reactive gas. So in the steady state, hydrogen has a virtually constant mixing ratio all the way from the surface to the homopause, as does CO_2 (*21*). Therefore, the homopause mixing ratio of hydrogen is representative of the whole homosphere.
23. The amino acid production rate is found to be ~0.4 nmol cm^{-2} $year^{-1}$ (*8*) in electric discharge experiments when $H_2/CO_2 = 4$, equivalent to 2×10^8 kg/year assuming a mean molecular weight of 100. This estimate is based on an annual electric discharge rate $\sim 2 \times 10^{19}$ J/year, which is ~20 times the contemporary electric discharge rate, $\sim 1 \times 10^{18}$ J/year (*36*). If the electric discharge rate on early Earth is the same as that of today, the rate of amino acid production by electric discharge would be 1×10^7 kg/year when $H_2/CO_2 = 4$. Extrapolating the contemporary data back to early Earth faces large uncertainty. So here the conservative estimate (1×10^7 kg/year) of the amino acid production rate by electric discharge is taken.
24. Assuming the ocean volume is 1.4×10^{21} liters and that there is no loss of organics within the ocean, the amino acid concentration in the ocean can reach 7×10^{-8} kg/liter (equivalent to 7×10^{-7} mole/liter, assuming a mean molecular weight of 100) in 10 million years, which is the time scale for the entire ocean to circulate through submarine vents at 300°C, potentially destroying the organics (*25*).
25. E. Pierazzo, C. F. Chyba, *Meteorit. Planet. Sci.* **34**, 909 (1999).
26. C. M. Dobson, G. B. Ellison, A. F. Tuck, V. Vaida, *Proc. Natl. Acad. Sci. U.S.A.* **97**, 11864 (2000).
27. A. A. Pavlov, J. F. Kasting, J. L. Eigenbrode, K. H. Freeman, *Geology* **29**, 1003 (2001).
28. It is difficult to estimate accurately how much organic material was delivered to early Earth by comets because of the large uncertainty in the impact record (*37*). The delivery of organic compounds by IDPs is more definitive, although still debatable. For the present Earth, the mass flux of all IDPs with particle mass lower than 10^{-6} g is 10^7 kg/year (*38*). It is suggested that the IDP flux at 4 Ga could be up to ~150 times that of today (*34*), although the interpretation of the geological record leading to this suggestion is debatable. Bearing that in mind, a reasonable estimate of the organic delivery rate by IDP at 4 Ga is in the order of $\sim 10^8$ kg/year, assuming 10% of the mass is organic (*1*). The formation rate of prebiotic organic compounds in hydrothermal vents is also in the order of 10^8 kg/year (*39*). Therefore, the production of prebiotic organic compounds by UV in a hydrogen-rich atmosphere is ~2 orders of magnitude greater than the delivery of organic compound from outer space or the synthesis of organic compounds in hydrothermal systems at 3.8 Ga.
29. H. D. Holland, *Geochim. Cosmochim. Acta* **66**, 3811 (2002).
30. D. L. Turcotte, *Earth Planet. Sci. Lett.* **48**, 53 (1980).
31. J. C. G. Walker, *Evolution of the Atmosphere* (Macmillan, New York, 1977).
32. J. W. Delano, *Orig. Life Evol. Biosph.* **31**, 311 (2001).
33. T. M. McCollom, J. S. Seewald, *Geochim. Cosmochim. Acta* **65**, 3769 (2001).
34. A. D. Anbar *et al.*, *J. Geophys. Res.* **106**, 3219 (2001).
35. M. A. Zuilen, A. Lepland, G. Arrhenius, *Nature* **418**, 627 (2002).
36. C. F. Chyba, C. Sagan, *Orig. Life* **21**, 3 (1991).
37. G. Ryder, *J. Geophys. Res.* **107**, 5022 (2002).
38. S. G. Love, D. E. Brownlee, *Science* **262**, 550 (1993).
39. P. Ehrenfreund *et al.*, *Rep. Prog. Phys.* **65**, 1427 (2002).

40. We thank two anonymous reviewers and J. F. Kasting for valuable comments. This study was supported by the NASA Astrobiology Institute.

Supporting Online Material

www.sciencemag.org/cgi/content/full/1106983/DC1
Materials and Methods
SOM Text
References

1 November 2004; accepted 24 March 2005
Published online 7 April 2005;
10.1126/science.1106983
Include this information when citing this paper.

Lichen-Like Symbiosis 600 Million Years Ago

Xunlai Yuan,[1] Shuhai Xiao,[2]* T. N. Taylor[3]

The fossil record of fungi and lichens is scarce. Here we report the discovery of lichen-like fossils, involving filamentous hyphae closely associated with coccoidal cyanobacteria or algae, preserved in marine phosphorite of the Doushantuo Formation (between 551 and 635 million years old) at Weng'an, South China. These fossils indicate that fungi developed symbiotic partnerships with photoautotrophs before the evolution of vascular plants.

Fungi are a major eukaryote kingdom and perform critical ecological roles in nutrient recycling. Many living fungi maintain facultative or obligate interactions with marine and terrestrial photoautotrophs (*1*, *2*). However, the fossil record of fungi is poor and includes Ordovician [460 million years ago (Ma)] glomaleans (*3*) and microfossils interpreted as probable fungi dating to >720 Ma (*4*). Fossil evidence for fungal interactions (such as cyanolichenization, mycoparasitism, and vesicular arbuscular mycorrhizal symbiosis) with other organisms comes from the ~400-million-year-old Rhynie chert in Scotland, which also preserves a diverse

[1]Nanjing Institute of Geology and Palaeontology, Nanjing 210008, China. [2]Department of Geosciences, Virginia Polytechnic Institute and State University, Blacksburg, VA 24061, USA. [3]Department of Ecology and Evolutionary Biology, University of Kansas, Lawrence, KS 66045, USA.

*To whom correspondence should be addressed. E-mail: xiao@vt.edu

fungal assemblage, including chytridiomycetes and ascomycetes (*5*). In addition, some Ediacara fossils (575 to 542 Ma) have been interpreted, on the basis of taphonomic observations, as fungi (*6*) and lichens (*7*).

Here we describe three specimens of lichen-like fossils occurring in thin sections of two phosphorite samples from the upper Doushantuo Formation at Weng'an, South China (*8*) (fig. S1). The samples were collected from a 0.5- to 5-m-thick unit of black bituminous phosphorite immediately above a karstification surface in the middle Doushantuo Formation (*9*). This unit was probably deposited in a shallow subtidal environment and contains abundant algal fossils (*10*, *11*). The Doushantuo Formation in the Yangtze Gorges area is bracketed by U-Pb ages between 635 ± 1 and 551 ± 1 Ma (*12*), and direct Pb-Pb dating of upper Doushantuo phosphorite at Weng'an indicates that the fossils described here are probably 599 ± 4 million years old (*13*); however, Condon and colleagues argue that the fossiliferrous upper Doushantuo Formation may be between 580 and 551 million years old (*8*, *12*).

The lichen-like fossils are completely phosphatized. They consist of two closely associated components: coccoidal cells and thin filaments (Figs. 1 and 2). The coccoid cells are 6 to 15 μm in diameter (average = 9 μm, SD = 2 μm, n = 25 cells) and are usually clustered (Figs. 1A, 2A, and 2C). They typically consist of an opaque central body surrounded by a hyaline envelope 1 to 2 μm thick (Fig. 2E). In some, the remains of organic sheaths are visible in the hyaline envelope. These coccoidal cells are interpreted as sheathed cyanobacteria (similar to modern *Gloeocapsa*, *Entophysalis*, *and Chroococcus*) or possibly green algae (similar to modern colonial chlorococcaleans).

The filaments are about 0.5 to 0.9 μm wide (average = 0.6 μm, SD = 0.1 μm, n = 20 filaments). They are up to 50 μm long, although they may be longer, because the 30-μm-thick thin section captures only a segment of the filaments. It is unclear whether they are septate, because they are opaque. Some filaments branch dichotomously (Fig. 2, E and G). Many bear opaque, pyriform terminal structures (Fig. 2, B and D to F) that are smaller than the coccoidal cells described above, about 3 to 6 μm in maximum dimension (average = 5 μm, SD = 1 μm, n = 6 terminal structures) and 2 to 4 μm in minimum dimension (average = 3 μm, SD = 1 μm, n = 6 terminal structures). Some terminal structures show evidence of possible transverse splits (Fig. 2, D to E). A number of filaments appear to envelop coccoidal cells or are arranged in loops (Fig. 2C). In some cases, a single filament connects two pyriform structures, or a single pyriform structure is connected to multiple filamentous appendages. The filaments lack hyaline sheath-like envelopes that characterize filamentous cyanobacteria, and can be distinguished from pseudoparenchymatous multicellular algae preserved in the same deposit (Fig. 3) (*10*, *11*). In one specimen (Fig. 1A), which was probably fragmented during post-phosphatization reworking, the filaments can be found throughout the entire specimen. In another (Fig. 1B), the filaments occur on only one side of the specimen. However, because the specimens were found in thin sections, it remains impossible to reconstruct the three-dimensional structure of the coccoid/filament association.

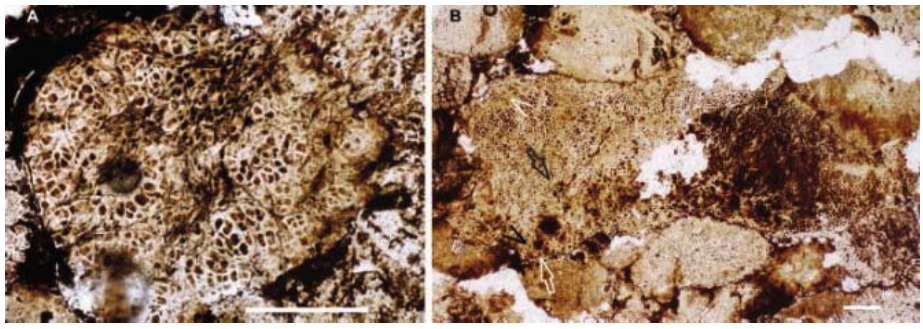

Fig. 1. Thin-section photomicrographs of two better-preserved specimens. (**A**) Coccoidal thallus divided by dense filaments in the middle. Further compartmentalization of coccoidal thallus by less densely packed filaments is visible at higher magnification (Fig. 2, A to C). (**B**) Coccoidal thallus with filaments (not discernable at this magnification; see magnified views of arrowed areas in Fig. 2, D to G) in the left part, but not the right part, of this specimen. Scale bars, 100 μm.

We interpret these filaments as fungal hyphae and the pyriform terminal structures as resting spores, reproductive structures, or some type of fungal vesicle. Alternative interpretations (such as filamentous cyanobacteria) are inconsistent with the combination of morphological features (thin filaments, dichotomous branching, pyriform terminal structures, and absence of sheaths). The diameter of the hyphae may have been reduced during phosphatization (*14*), but modern marine fungal hyphae can be <1 μm in diameter (*1*). The pyriform terminal structures are similar to, although smaller than, modern and fossil glomalean spores or vesicles (*2*, *3*, *15*). Furthermore, glomalean (such as *Entrophospora*) hyphae can bear terminal sporiferous saccules and lateral spores (*2*), which are similar to those illustrated in Fig. 2E (white arrowheads).

It is unlikely that the fungal hyphae were saprophytic or were accidentally preserved with the coccoidal cells. In all three specimens, the hyphae are associated only with coccoidal thalli; they do not occur in pseudoparenchymatous red algae in the same deposit (Fig. 3A) (*10*, *11*), which would be expected if they were saprophytic. Furthermore, the coccoidal cells would be expected to show a greater degree of decomposition if the fungal hyphae were saprophytic; instead, the preservation of coccoidal cells is not inferior to that of the fungal hyphae. Third, the hyphae appear to be structurally (and not accidentally) associated with the cyanobacterial coccoids; the coccoid clusters are distinctly compartmentalized and surrounded by abundant hyphae (Figs. 1A, 2A, and 2C) similar to the hyphal nets described in the Devonian cyanolichen (*16*, *17*). This structural association make the coccoidal clusters appear different from structures described as "cell islands" in Doushantuo multicellular algae (*10*); cell islands (Fig. 3B) are surrounded by ellipsoidal cells rather than hyphae. In addition, some hyphae are in close contact with coccoid cells (Fig. 2, C and G), suggesting that there was direct physiological interaction between them.

The association between coccoidal cells and fungal hyphae is interpreted to be symbiotic, not parasitic. The coccoidal thalli show no evidence of host reaction to mycoparasitism. Neither do the coccoid cells in contact with hyphae show morphological abnormality. On the other hand, there are numerous similar coccoidal thalli in the same deposit that are not associated with fungal hyphae (Fig. 3B). Thus, the coccoidal thalli may have functioned as facultative photobionts that could form loose lichen-like or lichenoidal (*1*) association with filamentous mycobionts.

Terrestrial lichens, involving ascomycetes or basidiomycetes as mycobionts and cyanobacteria or chlorophytes as photobionts, have affected global weathering since the Devonian (*5*). Modern marine fungi (mostly ascomycetes) also form a wide range of interactions with cyanobacteria, chlorophytes, phaeophytes, and rhodophytes. These interactions can be loose lichenoidal association with microscopic photobionts, mycophycobiosis with macroscopic algae, mycoparasitism, or obligate lichen association (*1*). Lichenized fungi are phylogenetically widespread within the Dikaryomycota (Ascomycota + Basidiomycota), which suggests that fungal lichenization may have evolved multiple times (*18*–*20*). However, the broadly defined symbiotic life-style (including arbuscular mycorrhizal symbiosis) has a broader phylogenetic distribution and characterizes the Symbiomycota (Glomeromycota + Dikaryomycota) (*21*, *22*). Although most glomerocycetes are arbuscular mycorrhizal fungi with vascular plants,

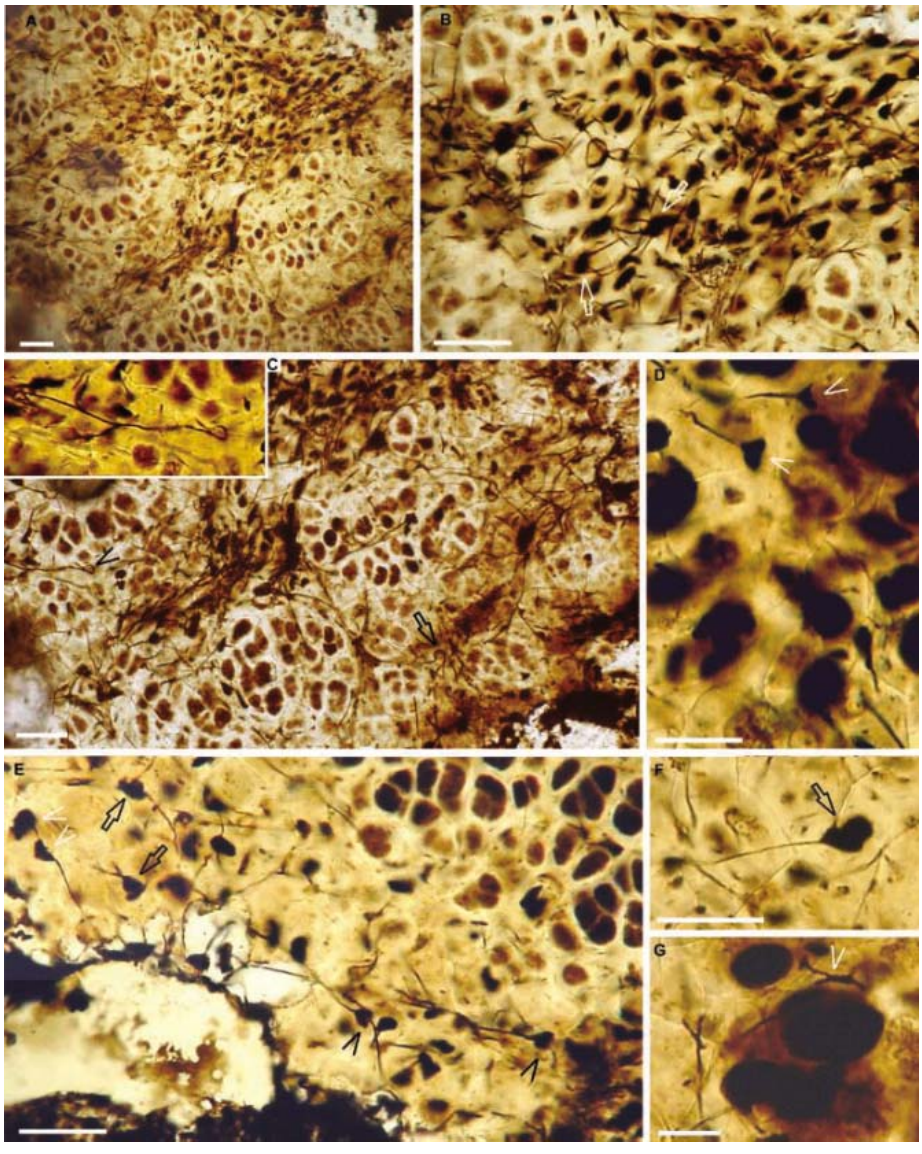

Fig. 2. (**A**) Detail of the upper center part of Fig. 1A. (**B**) Detail of the upper right quarter of (A), showing filament tract. Several filamentsh have dark swollen terminal structures. Arrows indicate terminal structures with multiple filamentous appendages. (**C**) Detail of the center part of (A). Two packets of coccoidal cells (center and lower center) are surrounded by a few filaments. The arrow points to a filament that appears to envelop a coccoidal cell. The arrowhead indicates a filament with a terminal loop (close-up in inset). (**D**) Detail (white arrow in Fig. 1B) showing hyphae with funnel-shaped terminal structures (arrowheads), the distal parts of which were probably dehisced along a transverse split. (**E**) Detail (white arrowhead in Fig. 1B) showing funnel-shaped terminal structures (black arrowheads), clustered coccoidal cells with hyaline envelopes (upper right quarter), dark terminal structures connected to multiple or branching filaments (black arrows), and a filament with a terminal structure and a laterally borne intercalary vesicle (white arrowheads). (**F**) Detail (black arrow in Fig. 1B) showing terminal structure (arrow) with subtending filament. (**G**) Detail (black arrowhead in Fig. 1B) showing branching filament (arrow) in close association with coccoidal cells. Scale bars, 20 μm.

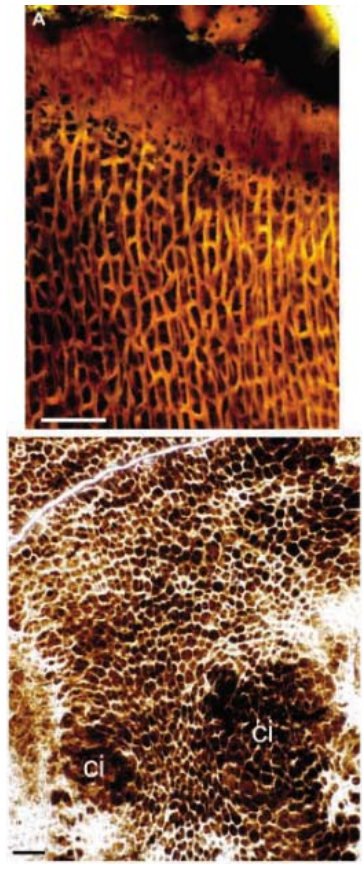

Fig. 3. Doushantuo algal thalli with no filamentous symbionts. (**A**) Pseudoparenchymatous red alga (*Thallophyca corrugata*) from the same horizon (*9*, *11*). (**B**) Thallus from the same thin section where lichen-like fossils were found. Emerging cell islands (ci) are indicated. Scale bars, 20 μm.

Geosiphon pyriforme (a basal glomeromycete) is symbiotic with cyanobacteria (*23*). The ease with which symbionts can be gained, lost, and switched in fungal/photoautotroph associations (*24*, *25*), the fungal phylogenetic tree that is basally populated by aquatic chytrids (*22*), and probably fungal fossils from Proterozoic marine deposits (*4*) indicate that the early steps toward fungal/photoautotroph symbiosis may have begun as facultative interactions with aquatic cyanobacteria or algae. The Doushantuo lichenoidal fossils suggest that these early steps may have occurred long before the colonization of land by vascular plants, in a shallow marine ecosystem where a large number of free-living cyanobacteria, algae, and fungi were in close association—a necessary step in the evolution of symbiosis. Thus, this and other fossil evidence (*4*) join molecular data (*26*, *27*) to support a deep history of fungi and lichen-like symbiosis.

References and Notes

1. J. Kohlmeyer, E. Kohlmeyer, *Marine Mycology: The Higher Fungi* (Academic Press, New York, 1979).
2. C. J. Alexopoulos, C. W. Mims, M. Blackwell, *Introductory Mycology* (Wiley, New York, ed. 4, 1996).
3. D. Redecker, R. Kodner, L. E. Graham, *Science* **289**, 1920 (2000).
4. N. J. Butterfield, *Paleobiology* **31**, 165 (2005).
5. T. N. Taylor *et al.*, *Trans. R. Soc. Edinb. Earth Sci.* **94**, 457 (2004).
6. K. J. Peterson, B. Waggoner, J. W. Hagadorn, *Integr. Comp. Biol.* **43**, 127 (2003).
7. G. J. Retallack, *Paleobiology* **20**, 523 (1994).
8. Stratigraphic information is available as supporting material on *Science Online*.
9. Y. Zhang, L. Yin, S. Xiao, A. H. Knoll, *Paleontol. Soc. Mem.* **50**, 1 (1998).
10. Y. Zhang, *Lethaia* **22**, 113 (1989).
11. S. Xiao, A. H. Knoll, X. Yuan, C. M. Pueschel, *Am. J. Bot.* **91**, 214 (2004).
12. D. Condon *et al.*, *Science* **308**, 95 (2005); published online 24 February 2005 (10.1126/science.1107765).
13. G. H. Barfod *et al.*, *Earth Planet. Sci. Lett.* **201**, 203 (2002).
14. A. H. Knoll, S. Golubic, *Precambrian Res.* **10**, 115 (1979).
15. T. N. Taylor, W. Remy, H. Hass, H. Kerp, *Mycologia* **87**, 560 (1995).
16. T. N. Taylor, H. Hass, W. Remy, H. Kerp, *Nature* **378**, 244 (1995).
17. T. N. Taylor, H. Hass, H. Kerp, *Am. J. Bot.* **84**, 992 (1997).

18. A. Gargas, P. T. Depriest, M. Grube, A. Tehler, *Science* **268**, 1492 (1995).
19. F. Lutzoni, M. Pagel, V. Reeb, *Nature* **411**, 937 (2001).
20. Y. J. Liu, B. D. Hall, *Proc. Natl. Acad. Sci. U.S.A.* **101**, 4507 (2004).
21. A. Schüßler, D. Schwarzott, C. Walker, *Mycol. Res.* **105**, 1413 (2001).
22. A. Tehler, D. P. Little, J. S. Farris, *Mycol. Res.* **107**, 901 (2003).
23. H. Gehrig, A. Schüßler, M. Kluge, *J. Mol. Evol.* **43**, 71 (1996).
24. P. T. DePriest, *Annu. Rev. Microbiol.* **58**, 273 (2004).
25. M. Wedin, H. Döring, G. Gilenstam, *New Phytol.* **164**, 459 (2004).
26. M. L. Berbee, J. W. Taylor, in *The Mycota: A Comprehensive Treatise on Fungi as Experimental Systems for Basic and Applied Research*, D. J. McLaughlin, E. G. McLaughlin, P. A. Lemke, Eds. (Springer-Verlag, Berlin, 2001), pp. 229–245.
27. D. S. Heckman *et al.*, *Science* **293**, 1129 (2001).
28. This research was supported by the National Natural Science Foundation of China, U.S. NSF, Chinese Academy of Sciences, and Chinese Ministry of Science and Technology. We thank M. Kowalewski, S. E. Scheckler, C. M. Zhou, and four anonymous reviewers for valuable comments.

Supporting Online Material
www.sciencemag.org/cgi/content/full/308/5724/1017/DC1
SOM Text
Fig. S1
References

22 February 2005; accepted 29 March 2005
10.1126/science.1111347

The Structure of a pH-Sensing Mycobacterial Adenylyl Cyclase Holoenzyme

Ivo Tews,[1]*† Felix Findeisen,[1]* Irmgard Sinning,[1] Anita Schultz,[2] Joachim E. Schultz,[2] Jürgen U. Linder[2]†

Class III adenylyl cyclases contain catalytic and regulatory domains, yet structural insight into their interactions is missing. We show that the mycobacterial adenylyl cyclase Rv1264 is rendered a pH sensor by its N-terminal domain. In the structure of the inhibited state, catalytic and regulatory domains share a large interface involving catalytic residues. In the structure of the active state, the two catalytic domains rotate by 55° to form two catalytic sites at their interface. Two α helices serve as molecular switches. Mutagenesis is consistent with a regulatory role of the structural transition, and we suggest that the transition is regulated by pH.

Adenylyl cyclases (ACs) synthesize the universal second messenger 3′,5′-cyclic adenosine monophosphate (cAMP) (*1*). Most ACs belong to class III, such as all mammalian and many bacterial enzymes (*2*), and are multidomain proteins (*2*, *3*). In the genome of the bacterium *Mycobacterium tuberculosis* (*4*), 15 putative class III ACs (*5*) with eight different domain compositions have been identified. For comparison, the similarly sized genome of *Escherichia coli* contains a single AC gene, and even in the human genome only 10 AC genes have been identified (*6*, *7*). This suggests that mycobacteria can respond to changing extra- and intracellular conditions by cAMP formation.

The mycobacterial AC Rv1264 is autoinhibited by its N-terminal domain (*8*). A knockout of the single *Streptomyces* AC, which has an identical domain composition to Rv1264, abolishes the bacterial response to an acidic milieu that affects differentiation processes (*9*). Because *M. tuberculosis* must counteract acidification of phagolysosomes during host invasion for intracellular survival (*10*, *11*), we examined the pH sensitivity of Rv1264 (Fig. 1A) (*12*). At pH 8, AC activity was 3 nmol of cAMP•mg^{-1}•min^{-1} at 0.5 mM adenosine triphosphate (ATP) with a maximal velocity (V_{max}) of 34 nmol of cAMP•mg^{-1}•min^{-1} and a substrate affinity (SC_{50}) of 1.5 mM ATP. At pH 6, AC activity increased almost 40-fold to 115 nmol and V_{max} increased 12-fold to 420 nmol of cAMP•mg^{-1}•min^{-1}. The substrate affinity increased slightly to 0.8 mM ATP. The Hill coefficient of 1.9 was unaffected. In contrast, the isolated catalytic domain ($Rv1264_{211-397}$) displayed uniformly high AC activity between pH 5.5 and 8 (Fig. 1A). Thus, in Rv1264, pH sensitivity is mediated by a distinct regulatory domain, and the activation by far exceeds the usual pH dependence of an enzyme. Biochemically, Rv1264 qualifies as a pH-sensing AC and is a likely candidate for mycobacterial pH sensing.

To understand the molecular mechanism of pH sensing and AC regulation, two crystal forms of Rv1264 were analyzed (*12*). Anisotropic crystals in a hexagonal space group with a diffraction limit of 3.3 Å were grown from Li_2SO_4, and the resulting model was designated the active form of Rv1264 (Fig. 2A); the 2.3 Å resolution structure obtained from monoclinic crystals grown from polyethylene glycol was designated the inhibited

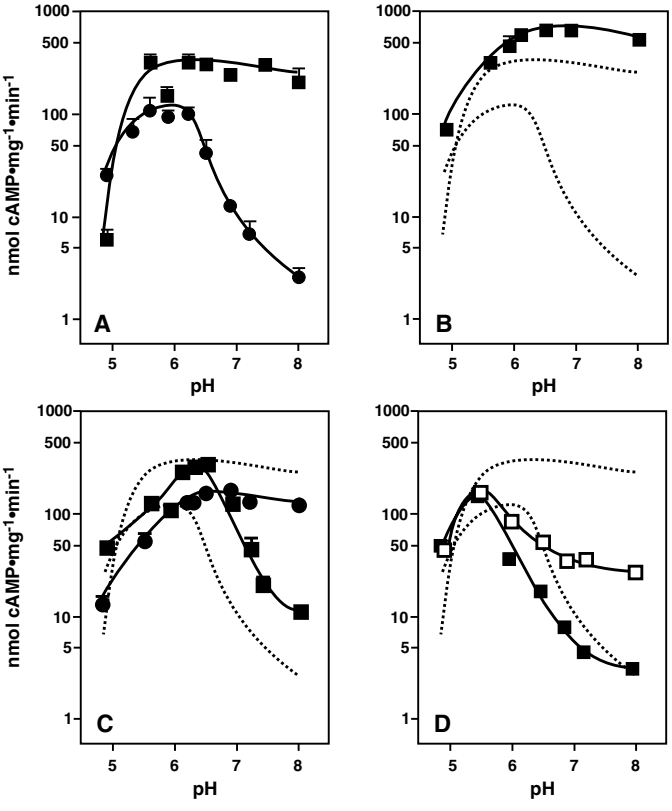

Fig. 1. The pH dependence of the AC activity of the Rv1264 wild type and mutants. AC activities of purified recombinant enzymes were measured from pH 4.8 to 8.0, with 0.5 mM ATP as a substrate. Standard deviation (SD) is given by error bars, if they exceed the size of the symbols. The symbol size itself corresponds to an SD of 10%. (**A**) Rv1264 catalytic domain ($Rv1264_{211-397}$) (■) and holoenzyme (●). To facilitate comparisons, these curves are included as dotted lines in the other panels. (**B**) Rv1264 M193P/M194P (■). (**C**) Rv1264 R309A (●) and E195A (■). (**D**) Rv1264 H192A (■) and H192E (□).

[1]Biochemiezentrum der Universität Heidelberg, Im Neuenheimer Feld 328, 69120 Heidelberg, Germany. [2]Pharmazeutisches Institut, Pharmazeutische Biochemie, Morgenstelle 8, 72076 Tübingen, Germany.

*These authors contributed equally to this work.
†To whom correspondence should be addressed. E-mail: ivo.tews@bzh.uni-heidelberg.de (I.T.); juergen.linder@uni-tuebingen.de (J.U.L.)

form (Fig. 2B and table S1). The designation was based on the structural and ensuing mutagenic analysis (*13*). Both structures have three discrete segments, a rigid N-terminal domain (amino acids 14 to 191), a flexible linker region (amino acids 192 to 213) (Fig. 2, red), and the C-terminal catalytic domain (amino acids 214 to 377).

We determined the structures using molecular replacement techniques with the dimer of N-terminal domains as a search model (determined previously to 1.6 Å resolution) (*14*). In all three structures, the N-terminal dimer comprises 20 α helices and has a disc-like shape of 80 by 50 by 20 $Å^3$, with an internal contact surface of 5500 $Å^2$. Dimerization involves a crossover of protein chains by threading of the αN10 helix of one monomer through the central coiled coil of the other monomer (helices αN4, αN7, αN8, αN9, and αN10) (Fig. 2, A and B). This results in a domain arrangement for Rv1264 in which the regulatory domain of monomer A contacts the catalytic domain of monomer B and vice versa (Figs. 2 and 3A). Residues 60 to 191 of the regulatory domain are essentially identical in both states of the holoenzyme and can be superimposed with a root mean square deviation (rmsd) of 1.42 Å over 264 Cα positions.

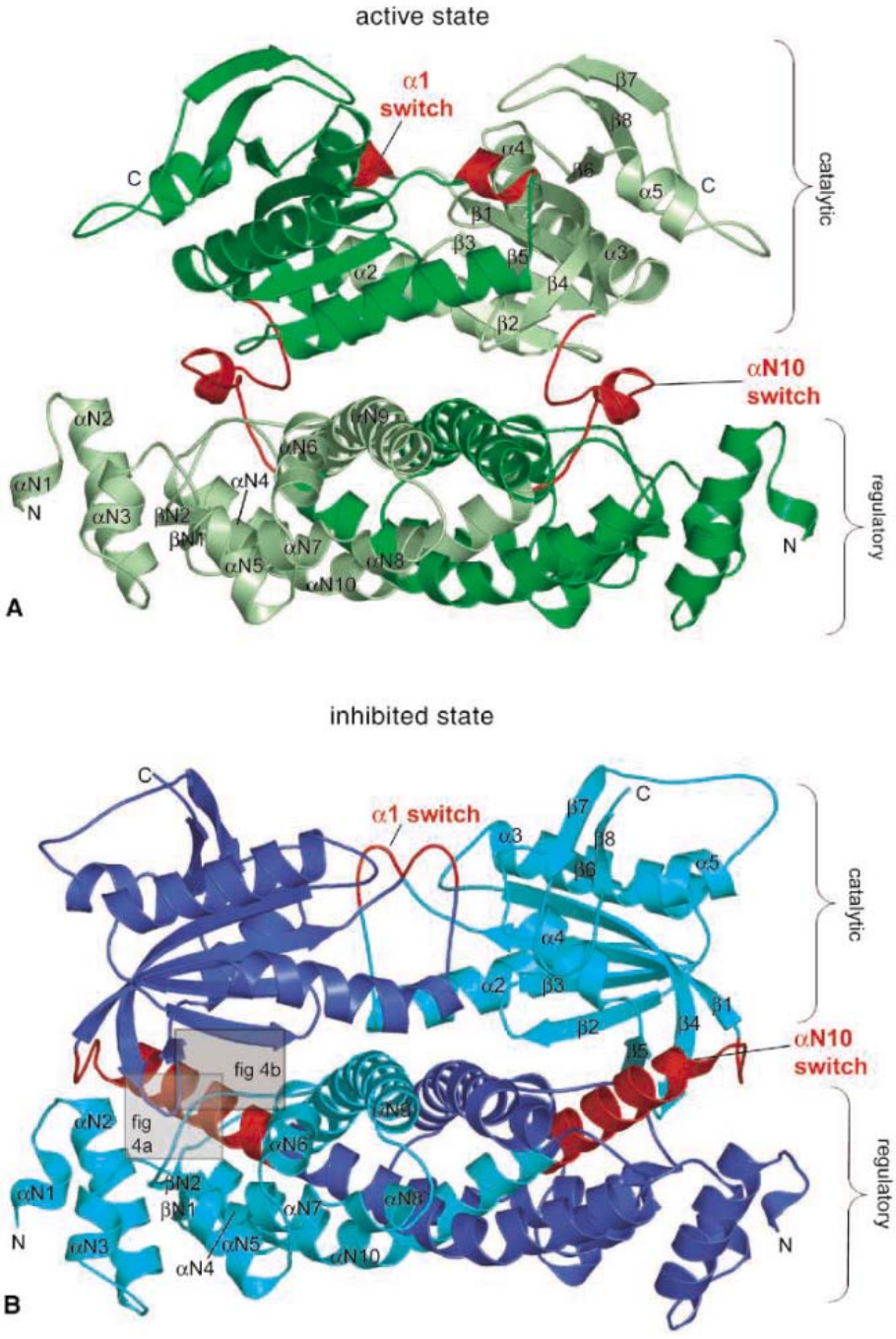

Fig. 2. Overall structure of Rv1264 in the active and inhibited states. (**A**) The active dimer, green, and (**B**) the inhibited dimer, blue. Monomers are distinguished by dark and light colors. The regulatory domains remain essentially unchanged upon enzyme activation, but the interface with the catalytic domains differs substantially. Secondary structure elements are labeled in the ribbon diagrams (for one monomer); C- and N termini are also indicated. Structural switch regions, red, are found in the linker region and in the catalytic dimer. The boxed regions are shown in detail in Fig. 4. Ribbon diagrams in all figures were drawn with PyMOL (*22*).

The catalytic domains in the active state (Fig. 2A) are arranged head-to-tail in the wreath-like quaternary structure known from the C_2 homodimer of rat AC type II (*15*) (fig. S1), as well as from the G protein–activated heterodimer of canine AC type V C_1 and rat AC type II C_2 catalytic domains (*16*). Although sequence identities between the Rv1264 and mammalian catalytic domains were low, with 22% to canine C_1 and 25% to rat C_2, the catalytic dimer of Rv1264 superimposes well with the mammalian heterodimer (rmsd of 1.76 Å over 256 out of 324 Cα positions). It is more compact than the mammalian catalytic domain because of several slightly shortened loops (fig. S2). A 7–amino acid gap obliterating the so-called dimerization arm (*2*, *8*, *16*) (fig. S2) is the major reason for a reduction of the interface from 3800 $Å^2$ in the mammalian heterodimer to 1900 $Å^2$ in the Rv1264 active-state homodimer. The known catalytic residues of class III ACs (*2*, *17*, *18*) in Rv1264 (Asp^{222}, Lys^{261}, Asp^{265}, Arg^{298}, Asp^{312}, Asn^{319}, and Arg^{323}) (Fig. 3, B and C, and fig. S2) are in almost identical positions to those in the mammalian heterodimer (*19*). A superposition of these residues of one active site gave an rmsd of 0.69 Å over the Cα positions and 1.17 Å over all atoms (Fig. 3B). The phosphate-coordinating residues Arg^{298} and Arg^{323} in Rv1264 bind to a sulfate ion located in the position of the β phosphate of the substrate ATP, as confirmed by modeling ATP into the active site of Rv1264 by superposition with noncylizable adenosine 5′-(1-thiotriphosphate) (ATPαS-R_p) from the mammalian heterodimeric structure (*19*). Taken together, these data demonstrate that the Rv1264 structure shown in Fig. 2A represents the active state of the enzyme.

The inhibited state of Rv1264 is characterized by a disassembled active site (Fig. 3C). The transition from the active to the inhibited state is accompanied by a marked change in tertiary structure (Fig. 2). Each of the two catalytic domains is rotated by 55° and translated by 6 Å with respect to the fixed regulatory domains (Fig. 3A and movie S1). The catalytic residues move by up to 25 Å during this transition (Fig. 3C). In the inhibited state, residues from a single active site were ~40 Å apart. Additionally, the

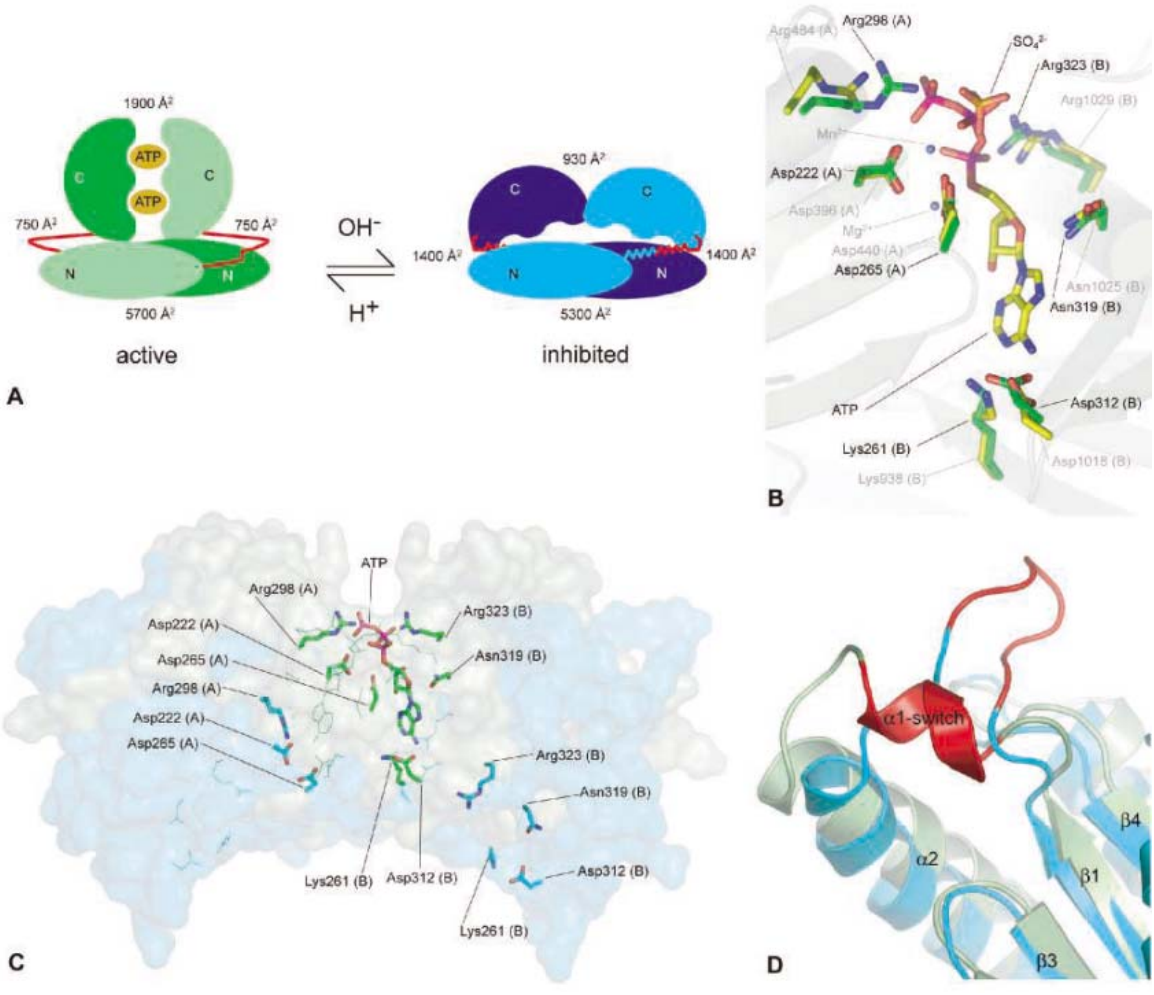

Fig. 3. Active site formation of Rv1264. (**A**) Schematic diagram of domain rearrangements upon activation. Regulatory and catalytic domains are labeled N and C, respectively. Numbers in Å^2 refer to buried surface areas between domains. (**B**) Superposition of the active sites of Rv1264 (active conformation, green with black labels) and a mammalian AC (*19*) (1CJK, yellow with gray labels). ATP was modeled into Rv1264 by superposition with ATPαS-R_p of 1CJK. The side chains of seven key residues, ATP, and sulfate are shown in stick representation with oxygen, red; nitrogen, blue; phosphate, mauve; sulfur, orange; and Mg^{2+} and Mn^{2+}, light blue. (A) and (B) after residue names refer to the two monomers. (**C**) Surface representation of the catalytic domains of Rv1264 in the inhibited (blue) and active (green) states. Active-site residues for one active site are shown in stick representation. For clarity, residues from the second of the two identical active sites are shown as lines. (**D**) Detailed view of the α1-switch region (red) from a superposition of the catalytic domains of the active (green) and inhibited (blue) states of Rv1264 (rmsd of 1.66 Å over 157 out of 163 Cα atoms).

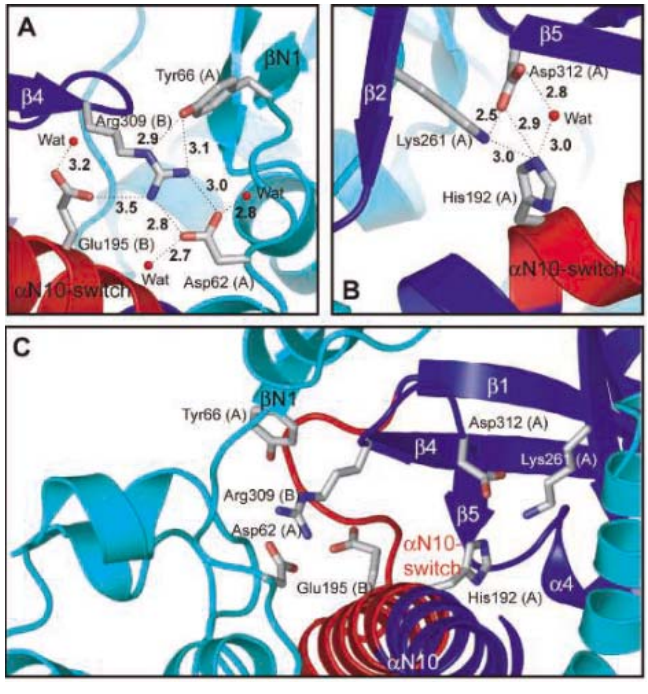

Fig. 4. Detailed view of two interaction sites of the αN10-switch helix with the catalytic domain in the inhibited state. Water atoms are indicated as red spheres; distances between polar atoms are given in Å. (A) and (B) after residue names refer to the two monomers, distinguished by dark and light blue colors; the αN10-switch helix is shown in red. The positions of these interaction sites within the holoenzyme are indicated in Fig. 2B. (**A**) Site around Arg^{309} involving Asp^{62}, Tyr^{66}, and Glu^{195}. (**B**) Site around His^{192} involving Asp^{312} and Lys^{261}. (**C**) View along the αN10-switch helix showing the interactions of this helix with the catalytic domain.

interface between the two catalytic domains was reduced from 1900 Å^2 in the active state to 930 Å^2 in the inhibited state, whereas that between regulatory and catalytic domains was increased from 1500 Å^2 in the active state to 2800 Å^2 in the inhibited state.

Two regions, called switch elements, undergo major structural changes (Fig. 2, red). The α1-switch helix (residues 226 to 231), located within the catalytic domain (Figs. 2A and 3D), is also present in the mammalian structures and contributes to binding of the β/γ-phosphates (*18*). There, the α1-switch helix and the adjacent loop to α2 form the binding site for the heterotrimeric G protein subunits $G_s\alpha$ and $G_i\alpha$ that regulate the activity of mammalian ACs (*15*). In the active state of Rv1264, the α1-switch is in a helical conformation as in the mammalian enzymes. However, in the inhibited state, it changes into a random coil with the Cα atoms moving by up to 11 Å (Fig. 3D).

The second switch element, the αN10 switch, comprises residues 192 to 206 in the linker region and undergoes the most noticeable changes between the two states (Fig. 2).

In the active state, it assumes a random coil conformation with a short helical segment (residues 202 to 206) (Fig. 2A) loosely connecting regulatory and catalytic domains. High B factors in this region are consistent with a high mobility that allows the catalytic domains to assemble both active sites. In the inhibited state, this segment forms an α helix with low B values, extending the αN10-helix of the regulatory domain by 24 Å or four turns (Fig. 2B) to keep the catalytic domains apart. The newly formed helical turns participate in the interface between regulatory and catalytic domains. To test whether the integrity of the helical segment is a prerequisite of pH regulation, two consecutive prolines were introduced at the beginning of the αN10-switch. Because of their restricted Φ and Ψ-values, this was not compatible with an α-helical conformation (*20*). In the M193P/M194P double mutant, pH regulation was lost, and the activity of the mutant holoenzyme over the pH range of 5.5 to 8 is similar to that of activated wild-type protein at pH 5.5 (Fig. 1B). Thus, the extension of the αN10 switch helix is a determinant of the inhibited state.

Two residues in the αN10-switch helix, identified by mutagenesis, are important for the interaction between the regulatory and catalytic domains (Fig. 4C). One site of interaction comprises Asp^{62}, Tyr^{66}, Glu^{195}, and Arg^{309} (Fig. 4A). The arginine points into a crevice in the regulatory domain and organizes the other residues through formation of hydrogen bonds. An R309A mutation renders the holoenzyme active and unregulated (Fig. 1C). The same mutation in the isolated catalytic domain ($Rv1264_{211\text{-}397}$R309A) has no effect (*21*). Additionally, an E195A mutation partially relieves the inhibition, results in a fourfold increase in activity at pH 8.0, and shifts the pH optimum from pH 5.8 to pH 6.5 (Fig. 1C). A further site of interaction at the beginning of the αN10-switch helix forms around His^{192} (Fig. 4B). The catalytic residues Lys^{261} and Asp^{312} are held 14 Å and 21 Å away from their respective positions in the active state by an interaction with His^{192} (Figs. 3C and 4B). A H192A mutant shows the wild-type phenotype at pH 8, but the slope of activation is shifted by 0.5 pH units toward the acidic pH (Fig. 1D). At acidic pH, His^{192} is expected to be protonated, and the positive charge may result in electrostatic repulsion of Lys^{261}. Similarly, a H192E mutant has a 10-fold higher activity at pH 8.0 than the wild-type protein, indicating that a negative charge at this position interferes with Asp^{312} (Fig. 1D). The data indicate that there is no designated, single amino acid residue that acts as a pH receptor, but that a network of hydrogen and ionic bonds in the interface between catalytic and regulatory domains mediate pH sensitivity and responsiveness.

Because of the structural similarities between the catalytic domains of both AC Rv1264 and mammalian ACs, the α1 and the αN10 switch regions may be prototypical regulatory elements for class III ACs. In the active state of Rv1264, the catalytic domains align even in the absence of bound nucleotide, whereas the regulatory domains effectively impede this alignment in the inhibited state. The comparison with mammalian enzymes shows that, in all class III ACs, activity is tuned by the alignment of the catalytic dimer. The mode of interaction may differ, but the repositioning of catalytic domains organized by a common structural switch may prove to be a general principle as more AC holoenzyme structures become available.

References and Notes

1. O. Barzu, A. Danchin, *Prog. Nucleic Acid Res. Mol. Biol.* **49**, 241 (1994).
2. J. U. Linder, J. E. Schultz, *Cell. Signal.* **15**, 1081 (2003).
3. D. A. Baker, J. M. Kelly, *Mol. Microbiol.* **52**, 1229 (2004).
4. S. T. Cole *et al.*, *Nature* **393**, 537 (1998).
5. L. A. McCue, K. A. McDonough, C. E. Lawrence, *Genome Res.* **10**, 204 (2000).
6. W. F. Simonds, *Trends Pharmacol. Sci.* **20**, 66 (1999).
7. D. M. F. Cooper, *Biochem. J.* **375**, 517 (2003).
8. J. U. Linder, A. Schultz, J. E. Schultz, *J. Biol. Chem.* **277**, 15271 (2002).
9. U. Süsstrunk, J. Pidoux, S. Taubert, A. Ullmann, C. J. Thompson, *Mol. Microbiol.* **30**, 33 (1998).
10. S. Sturgill-Koszycki *et al.*, *Science* **263**, 678 (1994).
11. K. Pethe *et al.*, *Proc. Natl. Acad. Sci. U.S.A.* **101**, 13642 (2004).
12. Materials and methods are available as supporting material on *Science* Online.
13. The inhibited form of Rv1264 was determined from a crystal grown at pH 5.5 and the active form from a crystal grown at pH 7.5. These pH values are in contrast to the activity assays. A discrepancy between crystallization conditions and activity assays is not unusual, however; the structure of the $G_s\alpha$-activated mammalian AC (1CJK) (*16*) has been crystallized at pH 5.4, two units below the pH of both the in vivo environment of the enzyme and the in vitro activity assay. Rv1264 exists in equilibrium between active and inhibited states that are governed by pH in our in vitro assay (Fig. 1A). For crystallization, other factors such as the different dielectric constants (PEG400 versus Li_2SO_4) can override the effect of pH on this equilibrium. Indeed, both the active and inhibited states of Rv1264 crystallize at the same pH: The needle-shaped crystals of the active state are obtained over a pH range from pH 5.4 to pH 7.5. These crystals all have the same distinctive morphology, which strongly suggests that they all represent the enzyme in the active state, and are easily distinguished from those crystals of the enzyme in the inhibited state. The needle-shaped crystals are usually 1 to 5 μm in diameter and not suitable for diffraction analysis, but one crystal grown to a diameter of ~20 μm at pH 7.5 diffracted to 3.3 Å at the beamline ID13 in Grenoble.
14. F. Findeisen *et al.*, unpublished data.
15. G. Zhang, Y. Liu, A. E. Ruoho, J. H. Hurley, *Nature* **386**, 247 (1997).
16. J. J. Tesmer, R. K. Sunahara, A. G. Gilman, S. R. Sprang, *Science* **278**, 1907 (1997).
17. W.-J. Tang, J. H. Hurley, *Mol. Pharmacol.* **54**, 231 (1998).
18. J. J. Tesmer *et al.*, *Biochemistry* **39**, 14464 (2000).
19. J. J. Tesmer *et al.*, *Science* **285**, 756 (1999).
20. K. T. O'Neil, W. F. DeGrado, *Science* **250**, 646 (1990).
21. I. Tews *et al.*, unpublished data.
22. W. L. DeLano (DeLano Scientific, San Carlos, CA, 2002), available at www.pymol.org.

23. Data collection was performed at beamlines ID13 and ID14-4 (European Synchrotron Radiation Facility, Grenoble). Supported by the Deutsche Forschungsgemeinschaft (grant nos. TE368/1-1 and LI928/2-1). Structure coordinates have been deposited in the Protein Data Bank under accession codes 1Y10 (inhibited state) and 1Y11 (active state).

Supporting Online Material

www.sciencemag.org/cgi/content/full/308/5724/1020/DC1
Materials and Methods
Figs. S1 and S2
Table S1
References and Notes
Movie S1

17 November 2004; accepted 1 March 2005
10.1126/science.1107642

Structural Basis of Energy Transduction in the Transport Cycle of MsbA

Jinhui Dong, Guangyong Yang, Hassane S. Mchaourab*

We used site-directed spin-labeling and electron paramagnetic resonance spectroscopy to characterize the conformational motion that couples energy expenditure to substrate translocation in the multidrug transporter MsbA. In liposomes, ligand-free MsbA samples conformations that depart from the crystal structures, including looser packing and water penetration along the periplasmic side. Adenosine triphosphate (ATP) binding closes the substrate chamber to the cytoplasm while increasing hydration at the periplasmic side, consistent with an alternating access model. Accentuated by ATP hydrolysis, the changes in the chamber dielectric environment and its geometry provide the likely driving force for flipping amphipathic substrates and a potential exit pathway. These results establish the structural dynamic basis of the power stroke in multidrug-resistant ATP-binding cassette (MDR ABC) transporters.

ABC transporters transduce the energy of ATP binding and hydrolysis into the mechanical work of substrate translocation across cell membranes (*1*–*3*). The functional unit consists of two nucleotide binding and hydrolysis domains (NBDs), each coupled to a

transmembrane domain (TMD) that encodes the determinants of substrate specificity and provides a pathway through the membrane. A subclass of ABC transporters, including P-glycoprotein (P-gp) and LmrA, consists of lipid efflux pumps that have been implicated in multidrug resistance (*4*–*7*). MsbA, an ABC *E. coli* transporter, transports lipid A across the inner membrane (*8*, *9*), and its adenosine triphosphate hydrolysis activity (ATPase) is stimulated by cytotoxic molecules (*10*). A prevalent mechanistic model of MDR ABC transporters links alternating ATP hydrolysis by each NBD domain to substrate transport through changes in orientation and affinity of the substrate-binding site(s) (*11*).

Two crystal structures of ligand-free MsbA define the molecular architecture of MDR ABC transporters (*12*, *13*). Obtained in detergent micelles, one structure consists of two monomers organized in an open conformation where the two TMDs pack asymmetrically to form a large V-shaped chamber open to the cytoplasm and the inner bilayer leaflet (Fig. 1A). In each monomer, the NBD and TMD are bridged by an intracellular domain (ICD). In the second structure, referred to as the closed conformation (Fig. 1C), rigid-body motion of the TMD and NBD occludes the chamber to the cytoplasm.

Although the two structures portray a flexible molecule and provide snapshots of the large conformational motion possible, the absence of ligands in the crystals does not allow interpretation of the structural differences in the context of the transport cycle. Furthermore, these static structures are not easily reconcilable with a body of biochemical and cross-linking studies of homologous proteins (*14*–*18*). The crystallization in two conformations and the discrepancies with solution constraints suggest that apo-MsbA is in a conformeric equilibrium.

We have investigated the structure of apo-MsbA in liposomes and mapped conformational changes during the ATPase cycle by electron paramagnetic resonance (EPR) analysis of 112 spin-labeled mutants (*19*) (Fig. 1A) trapped in four intermediate states. Spin-label mobilities, collisions with the paramagnetic reagents nickel(II) ethylenediaminediacetate (NiEDDA) and molecular oxygen, and spin-spin interactions were interpreted as constraints on the local steric environment, the accessibility to the bilayer and aqueous phases, and proximities between identical sites in the MsbA dimer, respectively (*20*).

The accessibility (*21*) data set of apo-MsbA, shown in Fig. 1B, defines the location and orientation of transmembrane helices and maps regions of aqueous solvation in the chamber and the periplasmic loops (labeled EC1 and EC3). We observed distinct patterns of oxygen accessibility [$\Pi(O_2)$], consisting of 3.6 residue periodicity with an amplitude gradient, that reflects the transmembrane orientation of helices 2 and 5 and their direct contact with the bilayer. In contrast, the lack of such a pattern along helix 6 suggests that this helix does not have a lipid-interacting surface. Supporting this conclusion is the restricted motion of the spin label at sites predicted to be exposed to the bilayer by the crystal structures (Fig. 2A). At the periplasmic side of the transporter, evidence of a loose structure includes an increase in $\Pi(O_2)$ and mobile line shapes (residues 271 and 274 in Fig. 2B) at the helix 5 C-terminal end and the adjacent EC3 loop, where monomer-monomer contacts occur in the crystal structures. Little if any broadening due to spin-spin interactions was detected at these sites.

The gradient of decreasing NiEDDA accessibility [Π(NiEDDA)], starting at chamber-facing residues in the ICD and the cytoplasmic ends of the helices, is in agreement with the spatial disposition of the monomers and the progressive narrowing of the chamber in the open

Department of Molecular Physiology and Biophysics, Vanderbilt University, Nashville, TN 37232, USA.

*To whom correspondence should be addressed. E-mail: hassane.mchaourab@vanderbilt.edu

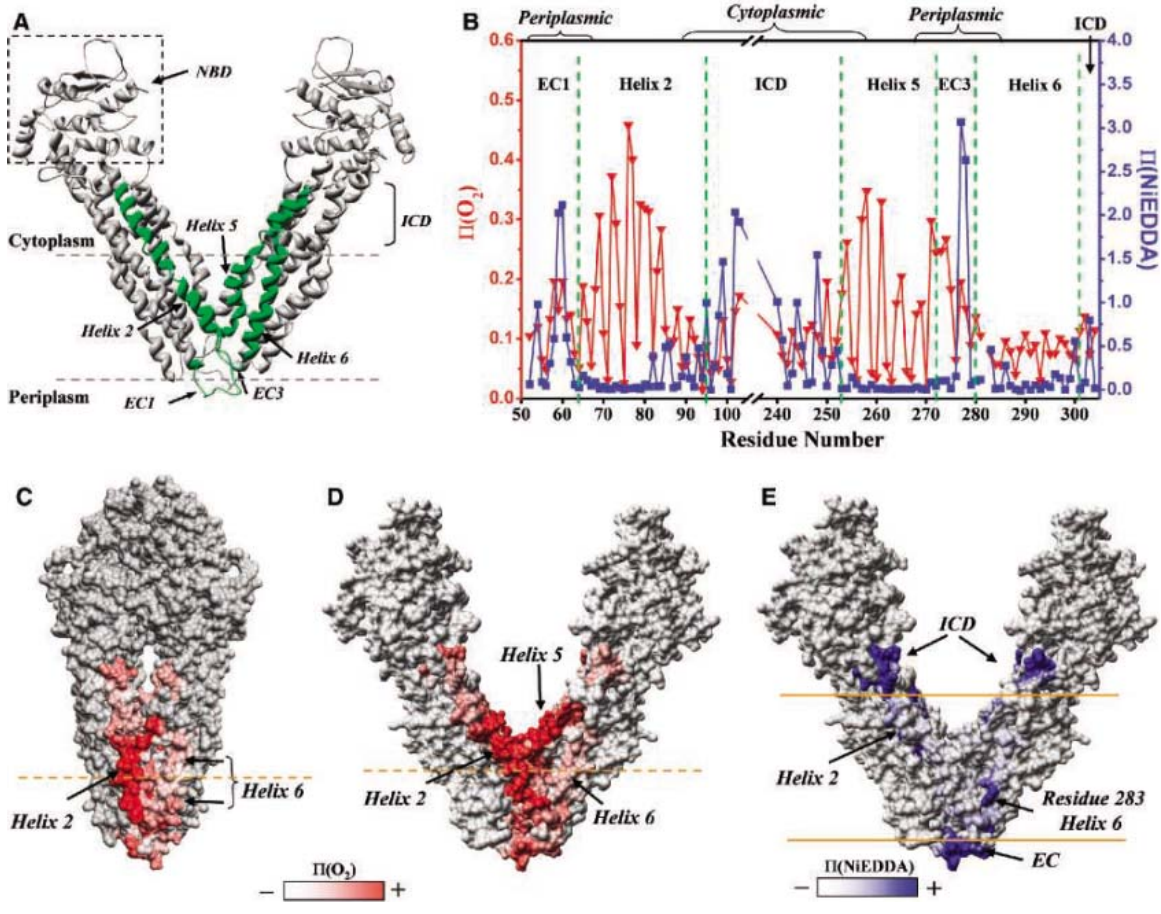

Fig. 1. (**A**) Ribbon representation of the structure of MsbA in the open state. Highlighted in green are the segments in a monomer subjected to cysteine substitution and spin labeling. (**B**) Accessibility profiles of apo-MsbA. Red, $\Pi(O_2)$; blue, Π(NiEDDA). The dotted green lines indicate the boundaries of the helices and loops on the basis of the crystal structure assignment. (**C** and **D**) $\Pi(O_2)$ mapped onto a surface rendering of the closed and open states, respectively. The dashed line through residue 76 defines the middle of the bilayer. (**E**) Π(NiEDDA) mapped onto a surface rendering of the open state. The solid orange lines represent the boundaries of the bilayer deduced from the onset of in-phase oscillations of $\Pi(O_2)$ and Π(NiEDDA) along helix 2. Surface representations were produced with Chimera (*34*).

structure (Fig. 1, A and B). Significant NiEDDA accessibility continues into the transmembrane domain including residues such as 82, one turn away from the middle of the bilayer defined by the absolute maximum in $\Pi(O_2)$ at residue 76.

The trend of looser packing at the periplasmic side of the transporter corresponds with significant NiEDDA accessibility along the N-terminal end of helix 6 (e.g., residues 283, 286), EC3, and to a lesser extent the 271 to 274 stretch, all of which are predicted by the crystal structures to be within the confines of the bilayer. Patterns of Π(NiEDDA) and proximities in EC1 also suggest deviations from the open and closed states. For instance, strong spin-spin interactions at residue 57 (Fig. 2C) and, to a lesser extent, at residues 52 and 58 (*22*) do not reflect the pattern of relative proximities observed in the crystal structures. Multiple conformations of this loop are implied by the composite nature of the EPR spectrum at site 57.

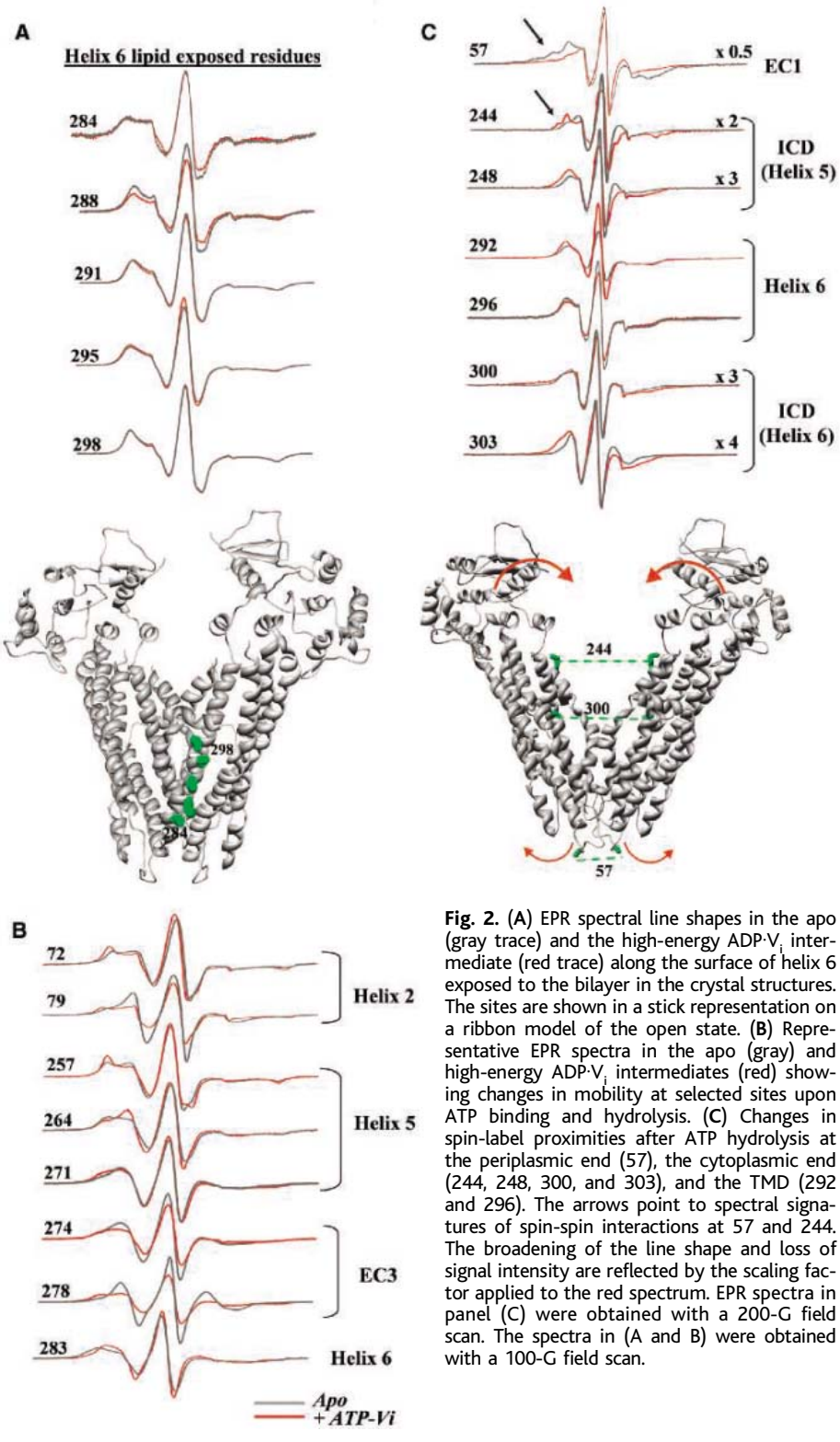

Fig. 2. (**A**) EPR spectral line shapes in the apo (gray trace) and the high-energy ADP·V_i intermediate (red trace) along the surface of helix 6 exposed to the bilayer in the crystal structures. The sites are shown in a stick representation on a ribbon model of the open state. (**B**) Representative EPR spectra in the apo (gray) and high-energy ADP·V_i intermediates (red) showing changes in mobility at selected sites upon ATP binding and hydrolysis. (**C**) Changes in spin-label proximities after ATP hydrolysis at the periplasmic end (57), the cytoplasmic end (244, 248, 300, and 303), and the TMD (292 and 296). The arrows point to spectral signatures of spin-spin interactions at 57 and 244. The broadening of the line shape and loss of signal intensity are reflected by the scaling factor applied to the red spectrum. EPR spectra in panel (C) were obtained with a 200-G field scan. The spectra in (A and B) were obtained with a 100-G field scan.

To evaluate the compatibility of the EPR constraints with the crystal structures, the accessibility parameters were mapped onto the open and closed conformations (Fig. 1, C, D, and E). Extensive NiEDDA accessibility and lack of spin-spin interactions support a dominant openlike conformation or ensemble of conformations at the cytoplasmic end, whereas along the periplasmic side, where crystal contacts occur, the data set indicates a more open structure and the presence of hydrated regions in the membrane. Aqueous solvation in the transmembrane part of the chamber was also deduced from accessibility studies of LmrA (*23*) and P-gp (*24*). Our data disagree with the conclusion of Buchaklian *et al*. (*25*) that the MsbA chamber is not accessible to water. The source of this discrepancy may be their limited sampling of the chamber, as they examined the accessibility of only two sites.

In the TMD, $\Pi(O_2)$ and the mobility pattern (fig. S1A) of helix 2 are in general agreement with its peripheral location and orientation relative to the bilayer, although its NiEDDA-exposed surface appears to be rotated away from the chamber and in contact with a neighboring helix (Fig. 1E). A similar phase-shift along helix 5 results in the maxima of $\Pi(O_2)$ (residues 257 and 258) partly facing the chamber. The most intriguing discrepancy occurs in a region of helix 6 (residues 283 to 290), where the EPR constraints are incompatible with the extensive bilayer contact of this helix in both crystal structures. The simplest model implied by the EPR constraints has helix 6 displaced toward the interior of the dimer, where it is in tertiary contacts with neighboring helices. This model is supported by spin-spin interactions at sites 292 and 296 (Fig. 2C), which are not predicted by the open conformation and the uniformly restricted mobilities of the spin label along the helix (*22*).

An alternative model that resolves these inconsistencies is based on a recent crystal structure of MsbA that shows the binding of a lipid A molecule at the surface of helix 6 (*26*). Specific contacts with a substrate molecule may explain the immobilized line shapes and the lower oxygen accessibility but not the spin-spin interaction pattern. The substrate in our samples could be a lipid A molecule copurified with the transporter, or the binding site may be occupied by phosphatidylethanolamine, a component of our reconstitution mixture that was shown to be transported by MsbA (*27*).

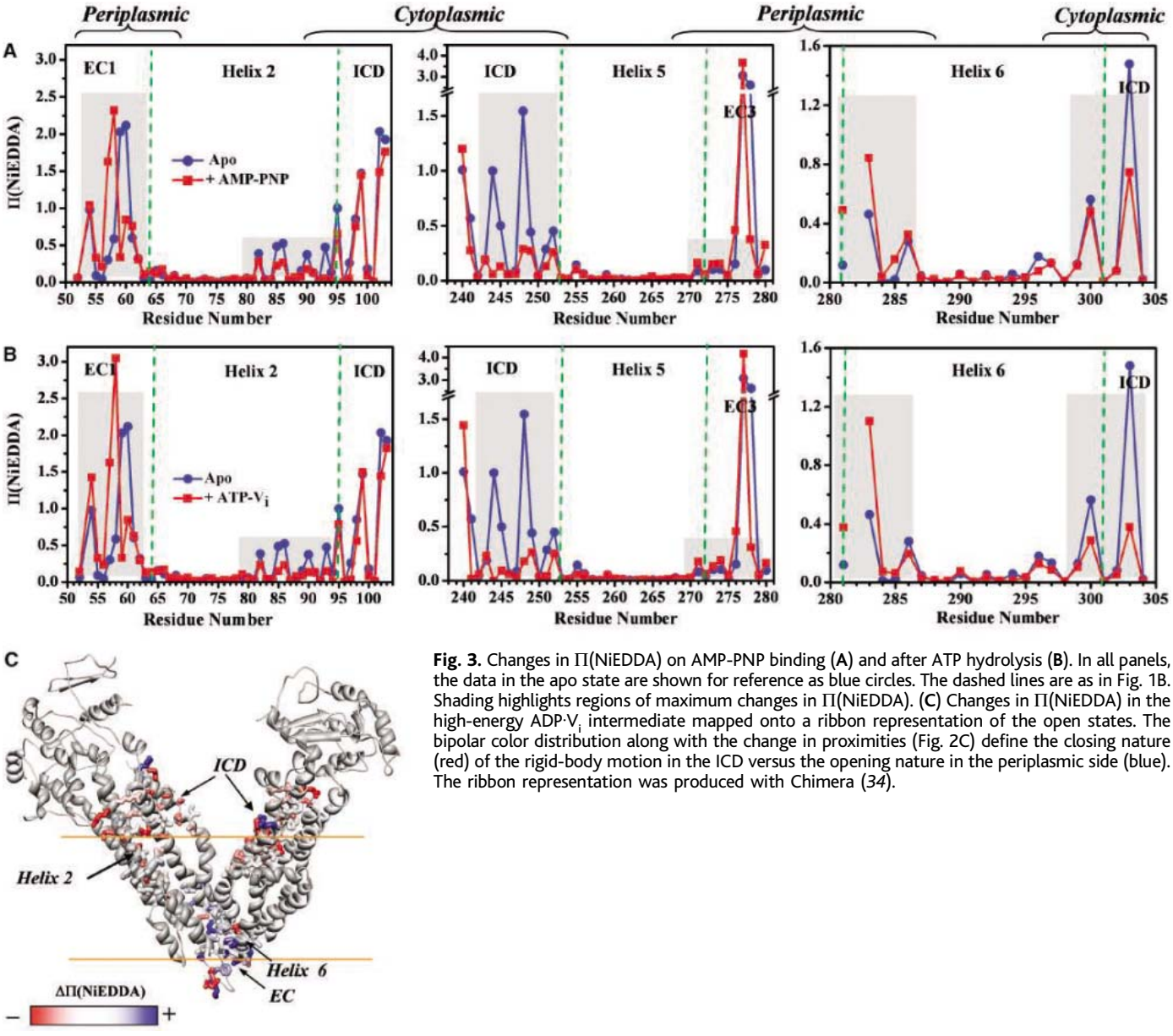

Fig. 3. Changes in Π(NiEDDA) on AMP-PNP binding (**A**) and after ATP hydrolysis (**B**). In all panels, the data in the apo state are shown for reference as blue circles. The dashed lines are as in Fig. 1B. Shading highlights regions of maximum changes in Π(NiEDDA). (**C**) Changes in Π(NiEDDA) in the high-energy ADP·V_i intermediate mapped onto a ribbon representation of the open states. The bipolar color distribution along with the change in proximities (Fig. 2C) define the closing nature (red) of the rigid-body motion in the ICD versus the opening nature in the periplasmic side (blue). The ribbon representation was produced with Chimera (*34*).

Overall, our analysis reinforces the model that apo-MsbA is in an equilibrium that includes conformers besides the two crystallized so far. Indeed, the extent of opening at the periplasmic side in these conformers may be understated by the averaging of the NiEDDA accessibilities over a heterogeneous ensemble. Although the EPR data set is not indicative of a highly populated closed state in the ensemble, the averaging may also understate this population in our analysis. The dynamic partitioning of MsbA among these conformers may account for the phase differences in the accessibility of helices.

The trajectory of the average structure and the corresponding shifts in the conformeric equilibrium during the functional cycle have been captured by the changes in the EPR parameters in three nucleotide-bound intermediates (*11*, *28*, *29*). The ATP-bound state is trapped by binding of the nonhydrolyzable analog AMP-PNP. Two post hydrolysis states, i.e., adenosine diphosphate (ADP)–bound states, were stabilized by inorganic vanadate (V_i) addition after either ATP or ADP binding. V_i acts as a γ-phosphate analog and, along with ADP, forms a complex mimicking the transition state of ATP hydrolysis. Studies of the ABC transporters P-gp and MalK demonstrate that a high-energy ADP-bound intermediate is more readily trapped by V_i after ATP hydrolysis than by direct ADP addition (*28*, *29*).

Changes in Π(NiEDDA) upon nucleotide binding are shown in Fig. 3 and fig. S2. Parallel reduction along the ICD and cytoplasmic ends of helices 2, 5, and 6 reveals a global, conformational change upon AMP-PNP binding that occludes the substrate chamber. Occlusion is maintained and accentuated in the post hydrolysis state populated by adding V_i and ATP. Concomitant nucleotide-induced increase in spin-spin interactions at multiple sites in the ICD regions (Fig. 2C) indicates that reduced chamber accessibility is due to rigid-body motion that moves the spin labels into close proximity (less than 15 Å). The pattern of proximity change is in overall agreement with the direction of the domain movement observed in the closed state, although the relative strengths of spin-spin interactions are not.

The opposite pattern of accessibility and proximity changes are observed at the periplasmic side of the transporter. The two EC1 loops undergo conformational changes that increase the distance between residues 57 (Fig. 2C) and 58 from different subunits and alter the NiEDDA accessibility in the 57 to 61 stretch (Fig. 3A). The loop movement allows increased NiEDDA accessibility at the periplasmic sides of helix 5 (C terminus),

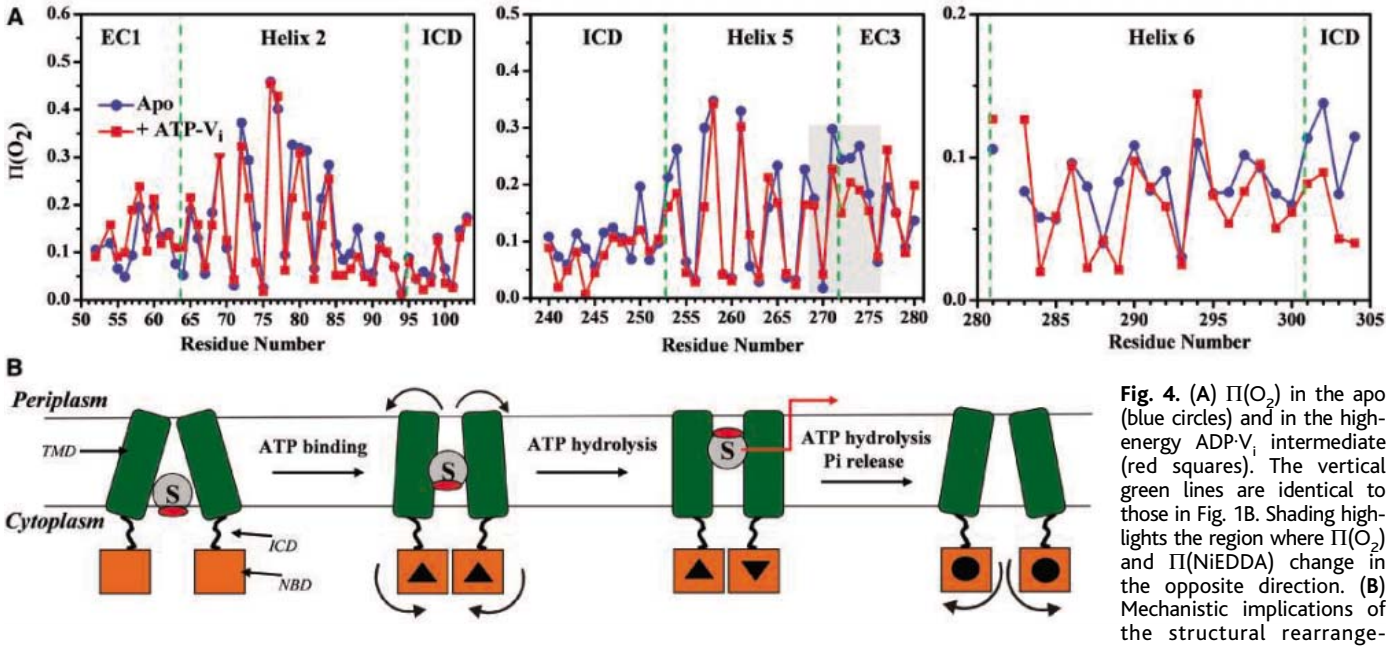

Fig. 4. (**A**) Π(O$_2$) in the apo (blue circles) and in the high-energy ADP·V$_i$ intermediate (red squares). The vertical green lines are identical to those in Fig. 1B. Shading highlights the region where Π(O$_2$) and Π(NiEDDA) change in the opposite direction. (**B**) Mechanistic implications of the structural rearrangements. From an ensemble dominated by open-like conformers, ATP binding occludes the chamber, presumably through NBD dimerization, and increases water penetration at the periplasmic side. ATP hydrolysis accentuates the preference for closed-chamber conformations. At this stage, the amphipathic substrate senses equivalent dielectric environments at either side of the chamber and can partition to the bilayer or aqueous phases. The schematic shows the turnover of a single ATP molecule as implied by LmrA and P-gp biochemical studies. These studies also show that an intermediate with APD and P$_i$ bound at a single NBD can rebind ATP and carry out another power stroke. In the low-energy ADP-bound state, chamber accessibility is restored, which allows the binding of another substrate molecule. ▲ Mg ·ATP; ▼ Mg ·ADP ·P$_i$; ● Mg ·ADP; S, substrate.

helix 6 (N terminus), and their interhelical loop (Fig. 3, A and B), areas of steady-state hydration in apo-MsbA. The changes in accessibility, accompanied by changes in mobilities along the 277 to 285 stretch, indicate extensive repacking (Fig. 2B).

Accessibilities and mobilities of the cytoplasmic region in the form populated by direct ADP and V$_i$ addition are more similar to those obtained in the apo state (fig. S2). MsbA binds ADP as evidenced by the inhibition of ATP turnover (*22*). Therefore, the slow formation of the high-energy intermediate by addition of ADP and V$_i$ demonstrates the presence of two post hydrolysis intermediates with different free energies.

The rigid-body movement that reduces the chamber accessibility does not change the phase of the oxygen accessibility patterns of helices 2 and 5, consistent with the absence of large-angle rigid helix rotation (Fig. 4A). Localized changes in Π(O$_2$) amplitude associated with mobility changes (e.g., residues 72, 79, 83, 257, and 264 in Fig. 2B) indicate rearrangements in the backbone or tilting and translational motion relative to neighboring helices. In the 271 to 275 segment, ATP hydrolysis reduces O$_2$ accessibility (Fig. 4A, shaded region) and concomitantly increases NiEDDA accessibility (Fig. 3B), the types of changes anticipated as a result of increased hydration. Bending of helix 6 around a hinge provides a feasible model for the opposite change in distance at residue 292 versus residues 300 and 303 in the high-energy intermediate.

From the changes in the EPR constraints in trapped intermediates, we can reconstruct the protein rearrangements that mediate transition to a transport-competent state. The changes in Π(NiEDDA) mapped onto the open structure in Fig. 3D reveal simultaneous closing of the chamber and loosening of the periplasmic region initiated by ATP binding. Parallel changes in proximity establish the rigid-body nature of the underlying movement. The pattern of changes agrees with the model of alternate chamber exposure to each side or leaflet (*11*, *30*, *31*).

Correlation of the conformational cycle described here with previous biochemical data provides a plausible outline for the mechanism of transport (Fig. 4B). Substrate binding must precede chamber occlusion, i.e., it occurs before ATP binding, consistent with structural changes observed in two-dimensional crystals of P-gp (*32*). Crystal structures of isolated NBDs demonstrate that ATP binding drives NBD dimerization to form the ATP sandwich (*33*). The free energy of ATP is harnessed to close the chamber, which thereby traps the substrate, and the conformational changes are propagated to reconfigure the periplasmic side. ATP hydrolysis widens the periplasmic opening such that the ends of helices 5 and 6 at opposite sides of the transporter have similar levels of NiEDDA accessibility. The symmetrization of the chamber dielectric environment may act as a driving force for flipping and translocation of the amphipathic substrate (*12*, *13*). Hydrolysis of the second ATP molecule and inorganic phosphate (P$_i$) release move the NBDs apart, which restores chamber accessibility for another cycle.

Evidence of spectral heterogeneity in the EPR data set is consistent with shifts in the conformational equilibrium during the functional cycle. Starting from an ensemble of structures, ATP binding and hydrolysis shift the equilibrium toward states that have a closed chamber and a looser packing at the periplasmic side, although in none of the intermediates do the EPR constraints suggest a pure crystallographic closed state. The incremental nature of the structural changes on ATP hydrolysis suggests that ATP binding may provide the power stroke for transport. Although further analysis will be required to interpret the equilibrium data in terms of distinct conformers, the results provide a perspective on the flexibility of MDR ABC transporters and the conformational cycle that underlies their function.

References and Notes

1. C. F. Higgins, *Annu. Rev. Cell Biol.* **8**, 67 (1992).
2. C. F. Higgins, *Res. Microbiol.* **152**, 205 (2001).
3. H. Nikaido, J. A. Hall, *Methods Enzymol.* **292**, 3 (1998).
4. C. F. Higgins, R. Callaghan, K. J. Linton, M. F. Rosenberg, R. C. Ford, *Semin. Cancer Biol.* **8**, 135 (1997).
5. M. M. Gottesman, T. Fojo, S. E. Bates, *Nat. Rev. Cancer* **2**, 48 (2002).
6. H. W. van Veen, W. N. Konings, *Biochim. Biophys. Acta* **1365**, 31 (1998).
7. H. W. van Veen, W. N. Konings, *Adv. Exp. Med. Biol.* **456**, 145 (1998).
8. Z. Zhou, K. A. White, A. Polissi, C. Georgopoulos, C. R. Raetz, *J. Biol. Chem.* **273**, 12466 (1998).
9. W. T. Doerrler, C. R. Raetz, *J. Biol. Chem.* **277**, 36697 (2002).

10. G. Reuter *et al.*, *J. Biol. Chem.* **278**, 35193 (2003).
11. H. W. van Veen, C. F. Higgins, W. N. Konings, *Res. Microbiol.* **152**, 365 (2001).
12. G. Chang, C. B. Roth, *Science* **293**, 1793 (2001).
13. G. Chang, *J. Mol. Biol.* **330**, 419 (2003).
14. C. F. Higgins, K. J. Linton, *Science* **293**, 1782 (2001).
15. T. W. Loo, D. M. Clarke, *J. Biol. Chem.* **271**, 27482 (1996).
16. T. W. Loo, D. M. Clarke, *J. Biol. Chem.* **276**, 31800 (2001).
17. M. Seigneuret, A. Garnier-Suillerot, *J. Biol. Chem.* **278**, 30115 (2003).
18. D. R. Stenham *et al.*, *FASEB J.* **17**, 2287 (2003).
19. Starting with a cysteine-less MsbA background where the two native cysteines were replaced with alanines, we constructed 116 single-cysteine mutants. Only four mutations resulted in either weak or no expression (51, 53, 282) or slow aggregation after reaction with the spin label (78). MsbA mutants were spin labeled after Ni affinity chromatography, purified by size-exclusion chromatography (SEC) and then reconstituted in unilamellar vesicles. Details of the structural and functional analysis of the mutants are in the supporting material available on *Science* Online.
20. W. L. Hubbell, H. S. Mchaourab, C. Altenbach, M. A. Lietzow, *Structure* **4**, 779 (1996).
21. The collision frequency with paramagnetic reagents was deduced from the analysis of the saturation behavior of the spin label at each site. Power saturation curves were obtained under nitrogen gas, in the presence of 20% oxygen, or under nitrogen and in the presence of 50 mM NiEDDA. Distinct patterns of oxygen accessibility are expected for transmembrane segments, whereas exposure to the aqueous environments results in high NiEDDA accessibility. Spin-label mobility was estimated from the inverse of the central line width.
22. J. Dong, H. S. Mchaourab, unpublished observations.
23. G. J. Poelarends, W. N. Konings, *J. Biol. Chem.* **277**, 42891 (2002).
24. T. W. Loo, M. C. Bartlett, D. M. Clarke, *Biochemistry* **43**, 12081 (2004).
25. A. H. Buchaklian, A. L. Funk, C. S. Klug, *Biochemistry* **43**, 8600 (2004).
26. C. L. Reyes, G. Chang, *Science* **308**, 1028 (2005).
27. W. T. Doerrler, H. S. Gibbons, C. R. Raetz, *J. Biol. Chem.* **279**, 45102 (2004).
28. A. L. Davidson, *J. Bacteriol.* **184**, 1225 (2002).
29. I. L. Urbatsch, G. A. Tyndall, G. Tombline, A. E. Senior, *J. Biol. Chem.* **278**, 23171 (2003).
30. P. Mitchell, *Nature* **180**, 134 (1957).
31. P. Mitchell, *Res. Microbiol.* **141**, 286 (1990).
32. M. F. Rosenberg *et al.*, *EMBO J.* **20**, 5615 (2001).
33. P. C. Smith *et al.*, *Mol. Cell* **10**, 139 (2002).
34. E. F. Pettersen *et al.*, *J. Comput. Chem.* **25**, 1605 (2004).
35. We thank D. Piston, A. Beth, C. Cobb, H. Koteiche, and R. Nakamoto for critically reading the manuscript. This work was supported by a discovery grant from Vanderbilt University.

Supporting Online Material
www.sciencemag.org/cgi/content/full/308/5724/1023/DC1
Materials and Methods
Figs. S1 and S2
Table S1
References and Notes

21 October 2004; accepted 22 February 2005
10.1126/science.1106592

Structure of the ABC Transporter MsbA in Complex with ADP·Vanadate and Lipopolysaccharide

Christopher L. Reyes and Geoffrey Chang*

Select members of the adenosine triphosphate (ATP)–binding cassette (ABC) transporter family couple ATP binding and hydrolysis to substrate efflux and confer multidrug resistance. We have determined the x-ray structure of MsbA in complex with magnesium, adenosine diphosphate, and inorganic vanadate ($Mg{\cdot}ADP{\cdot}V_i$) and the rough-chemotype lipopolysaccharide, Ra LPS. The structure supports a model involving a rigid-body torque of the two transmembrane domains during ATP hydrolysis and suggests a mechanism by which the nucleotide-binding domain communicates with the transmembrane domain. We propose a lipid "flip-flop" mechanism in which the sugar groups are sequestered in the chamber while the hydrophobic tails are dragged through the lipid bilayer.

Multidrug resistance is an alarming and rapidly growing obstacle in the treatment of infectious diseases, human immunodeficiency virus (HIV), malaria, and cancer (*1*). Drug-resistant bacterial strains that cause gonorrhea, pneumonia, cholera, and tuberculosis are widespread and difficult to treat (*2*). In humans, a similar drug efflux mechanism is a major reason for the failure of several chemotherapeutics in the treatment of cancers. Found ubiquitously in both bacteria and humans, ABC transporters have been implicated in both antibiotic and cancer drug resistance and represent key targets for the development of agents to reverse multidrug resistance (*3*, *4*). Several MDR ABC efflux pumps have been shown to extrude both lipids and drug molecules, which suggests a common transport mechanism for amphipathic compounds across the cell membrane (*5*, *6*).

Department of Molecular Biology, The Scripps Research Institute, 10550 North Torrey Pines Road CB105, La Jolla, CA 92137, USA.

*To whom correspondence should be addressed. E-mail: gchang@scripps.edu

MsbA is an essential bacterial ABC transporter that transports lipid A and lipopolysaccharide (LPS) to the outer membrane (*7–10*) and that has been shown to have overlapping substrate specificity with the multidrug-resistant ABC (MDR ABC) transporter LmrA and with human P-glycoprotein (P-gp) (*11*). MsbA adenosine triphosphatase (ATPase) hydrolysis is stimulated by LPS and lipid A and also shows vanadate-inhibited activity (*12*). LPS makes up the outer leaflet of the outer membrane in Gram-negative bacteria and potently activates the mammalian innate immune system in response to bacterial infections; it can cause septic shock (*13–15*). ABC transporters are minimally composed of two transmembrane domains (TMDs) that encode substrate specificity and a pair of nucleotide-binding domains (NBDs) with conserved structural features. Comparison of the x-ray structures of MsbA and the vitamin B_{12} ABC importer, BtuCD, suggests that differences in substrate specificities are a consequence of structurally divergent TMDs (*16–18*). These structures, along with those derived from electron microscopy (EM) of other MDR ABC transporters, reveal that large conformational changes are possible in both the TMDs and NBDs (*19–23*).

Despite attempts to model the structural changes of MsbA and other MDR ABC transporters, a detailed view of conformational rearrangements during ATP hydrolysis and substrate translocation has remained elusive (*24*). What are the conformational changes of the TMDs during the catalytic cycle? What residues are involved in substrate binding and release? And what specific role does nucleotide binding and hydrolysis play during the catalytic cycle? To address these questions, we describe the structure of MsbA from *Salmonella typhimurium* in complex with adenosine 5′-diphosphate and inorganic vanadate ($ADP{\cdot}V_i$), Mg^{2+}, and rough-chemotype (Ra) lipopolysaccharide (Ra LPS). The structure provides evidence for an intermediate after ATP hydrolysis and a molecular basis for coupling ATP hydrolysis with amphipathic substrate transport.

Crystals of MsbA in complex with $Mg{\cdot}ADP{\cdot}V_i$ and Ra LPS were grown using detergent-solubilized protein incubated with Ra LPS purified from *S. typhimurium*. ATP, Mg^{2+}, and boiled sodium orthovanadate were added to favor the transition state conformation before crystallization (*25*). Mass spectrometry on washed crystals indicated the presence of Ra LPS, nucleotide, and vanadate. The structure was determined by single-wavelength anomalous dispersion (SAD), and the electron density maps were improved by using noncrystallographic symmetry averaging to a resolution of 4.2 Å (see table S1) (*26*). The asymmetric unit revealed two dimers of MsbA with clear electron density corresponding to a nucleotide and Ra LPS. The TMDs in each dimer exhibit a 30° torque relative to the molecular two-fold axis and an extensive interdigitation of the helices (Fig. 1, A and B). A chemical model with good geometry was built with R_{cryst} of 28% and R_{free} of 33%.

In this structure, each dimer contains two bound LPS molecules located at the protein-

membrane interface on the outer membrane leaflet side with the sugar head groups roughly parallel to the axis of the elbow helix (residues 10 to 24) (Fig. 1C). Electron density was observed for only one nucleotide per dimer in the active site position (Fig. 1D). To confirm the positioning of the ADP at this resolution, we replaced ATP with a 2′-brominated ATP analog (*27*) and collected anomalous diffraction data at the bromine edge (λ = 0.9198 Å). Anomalous difference Fourier synthesis using experimental protein phases yielded only one bromine peak (~5 σ) per NDB dimer corresponding to the observed electron density for the nucleotide at the 2′ position (Fig. 1D). The position of the vanadium was confirmed by anomalous Fourier synthesis from diffraction data collected at the vanadium edge (λ = 2.2608 Å). The vanadium peak (~4 σ) corresponds to the position predicted on the basis of the Mg·ADP·V_i structure of myosin (*28*). At this resolution, we have not included either the coordinated oxygen atoms of the vanadate ion or Mg^{2+} in the model described here.

Previous structures have shown MsbA in open and closed conformations in the absence of nucleotide. In the open conformation, the two TMDs interact at the extracellular ends of the membrane-spanning helices to form an inverted V-shaped molecule with NBDs distant from each other. In the closed apo conformation, both the TMDs and the NBDs are closely packed. In addition, a large internal chamber accessible from the cytoplasm is formed between the interacting TMDs (Fig. 2A). The two structures suggest a highly dynamic sampling of conformational space by the protein in the absence of nucleotide with respect to the TMD interactions, lipid bilayer arrangements, and the folding of the NBDs. Electron paramagnetic resonance (EPR) studies also indicate that movements in the TMD are dramatic (*29*, *30*).

Changes in the TMD interactions provide insight into the pathway of substrate efflux. In comparison with the apo closed conformation of MsbA, this structure exhibits a large rigid-body rotation and translation that result in a ~15 Å opening toward the periplasmic ends and a ~15 Å closing of the NBD-associated intracellular domain helices (ICD1; residues 111 to 121), which allow accessibility to an internal chamber from the periplasm but not from the cytoplasm (Fig. 2B). The third extracellular loops (EC3) mediate the internal contact between the two monomers while placing the periplasmic ends of the TM5 helices close together. This causes the periplasmic opening of the internal chamber to be pinched and divides the opening of the cavity into two lobes adjacent to TM6, which corresponds to drug-binding sites observed for LmrA (*31*) and human P-gp (*32*). In this structure, TM5 forms extensive intermolecular interactions with TM2 and TM3. Because the ICD1 is formed between TM2 and TM3, this interaction suggests a probable pathway for transmitting conformational changes caused by ATP hydrolysis to the substrate-binding sites.

Besides affecting the interactions between TMDs, substrate binding and ATP hydrolysis also drive changes in the intermolecular helical packing of the TMDs. Although the TM1 to TM4 helices are arranged in an overall architecture similar to both the open and closed apo conformations, TM5 and TM6 reveal significant rearrangements [root mean square deviation (RMSD) on Cα of 2.1 Å (open) and 1.9 Å (closed)] (Fig. 2C). In both apo structures, a conserved residue (Ile^{257} of *S. typhimurium* MsbA) is located near a helical bulge that characterizes TM5. In this structure, this region has moved toward the interior of the TMD, which facilitates intermolecular contacts within the dimer. Similarly, the periplasmic end of TM6 has moved out of the interior, contributing to a >7 Å shift in EC3 between the apo and post hydrolysis intermediate conformation. The consequence of these intermolecular movements is a concerted movement of TM1, TM6, and the elbow helix toward the cell membrane.

A critical question is how substrate specificity is shared within the subfamily of MDR ABC flippases. In this structure, we observe bound LPS on the outer membrane leaflet side of MsbA forming extensive contacts with TM1 and TM6 from one monomer and with TM2 from the other monomer (Fig. 2D). The hy-

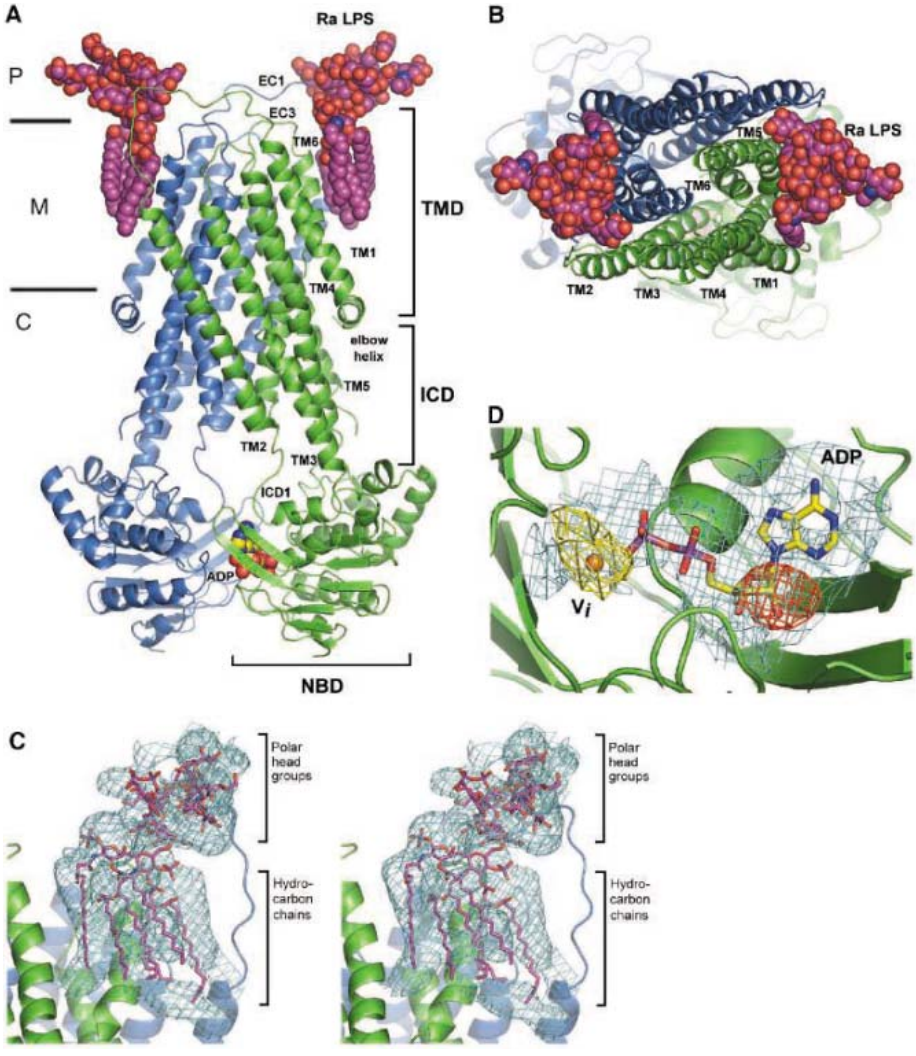

Fig. 1. Structure of MsbA with Mg·ADP·Vi and LPS. (**A** and **B**) The MsbA homodimer is shown in two orthogonal orientations, within the plane of the bilayer and down the two fold, respectively. Green and blue indicate the two monomers. The TMDs span the lipid bilayer matrix (M), and the NBD forms an extensive homodimeric interface within the cytoplasm (C). Two Ra lipopolysaccharide (LPS) molecules (carbon shown in magenta, oxygen in red, nitrogen in blue) are bound on the periplasmic side (P) of the TMDs. A single ADP molecule (carbon shown in yellow, oxygen in red, nitrogen in blue, phosphate in purple) is sequestered within the NBD composite active site. (**C**) Experimental electron density map (1.0 σ) corresponding to bound LPS. (**D**) Experimental electron density map in blue (1.0 σ) surrounding ADP with anomalous difference maps shown in red (4.0 σ) corresponding to the 2′-ADP position for Br and in orange corresponding to the vanadate position (4.0 σ). The images were created with PyMol (*37*).

drocarbon chains of the LPS interact with apolar residues on this interface, and the head groups interact with polar residues near the periplasmic side of the TMD, which includes the first extracellular loop, EC1 (residues 54 to 68). Interestingly, several conserved residues between MsbA and P-gp map to the binding interface of the LPS, which suggests that this region could be a general binding site for other amphipathic compounds. These residues are localized on the elbow helix, TM1, and TM6. Conserved residues specific to the MsbA subfamily also map to the EC1 loop, which interacts with the LPS sugar head groups from opposing monomers, and to the elbow helix (Fig. 2D).

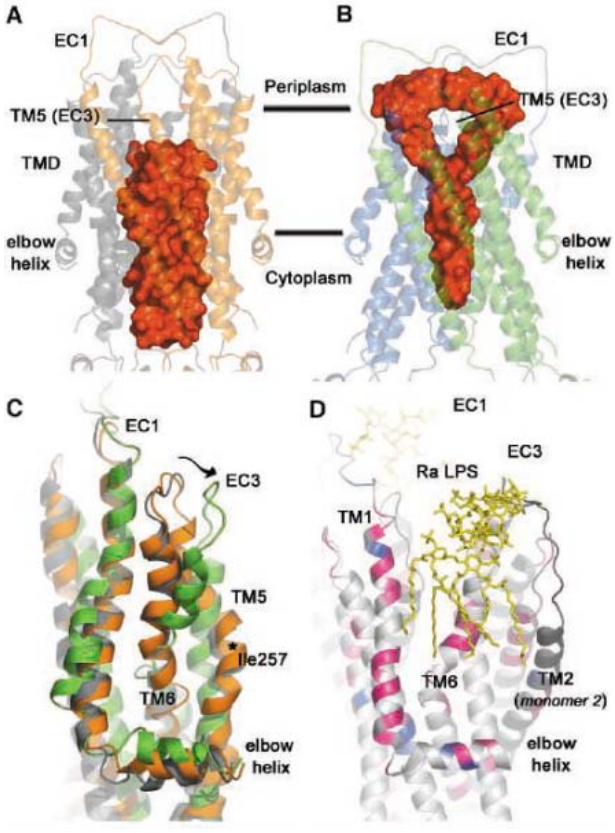

Fig. 2. Transmembrane domain rearrangements and specificity. (**A**) Solvent-filled internal chamber (red) for the closed apo structure of MsbA (monomers in orange and gray). (**B**) Solvent-filled internal chamber for MsbA complexed with LPS and ADP·V_i (monomers in green and blue). (**C**) Superimposed TMDs from open apo (gray), closed apo (orange), and post hydrolysis conformation of MsbA (green) show the movement of TM5, TM6, and EC3 (as indicated by arrow). The helical bulge near residue Ile^{257} is indicated by an asterisk. (**D**) Position of conserved residues shared by MsbA and P-gp (pink) and conserved residues specific to the MsbA subfamily (blue) mapped onto the structure of MsbA (white). The LPS is shown in yellow.

The architecture of the NBDs observed in this model is reminiscent of the dimer sandwich structures of the ABC transporters BtuCD and MJ0796 (*33*) with the P loop and the "LSGGQ" signature motif anchoring two subdomains of the NBD (Fig. 3, A and B). In the ATP-bound form of the MJ0796 NBD dimer, the two motifs from opposing NBDs align to orient the bound ATP molecules and to form a composite active site. In this structure, a nucleotide is observed in only one of the active sites. In addition, the signature motif from opposing NBDs disengages from the P loop and bound nucleotide. We interpret this to imply a post hydrolysis conformation, and it is likely that the nucleotide from the empty binding site has already dissociated.

Interaction between the NBDs and the TMDs involves two conserved motifs. The Q loop contains a conserved glutamine that coordinates Mg^{2+} and the proposed nucleophilic water (*34*), and the short conserved ICD1 helix mediates the contacts with the proximal NBD and the TMD. In the apo structure of BtuCD, the ICD1-equivalent helix (termed the L loop) does not contact the conserved glutamine (Gln^{80}) in the Q loop (Fig. 3C). However, in the structure described here, the amino end of the ICD1 (residues 111 to 121) is in position to interact with the glutamine from the Q loop and fits

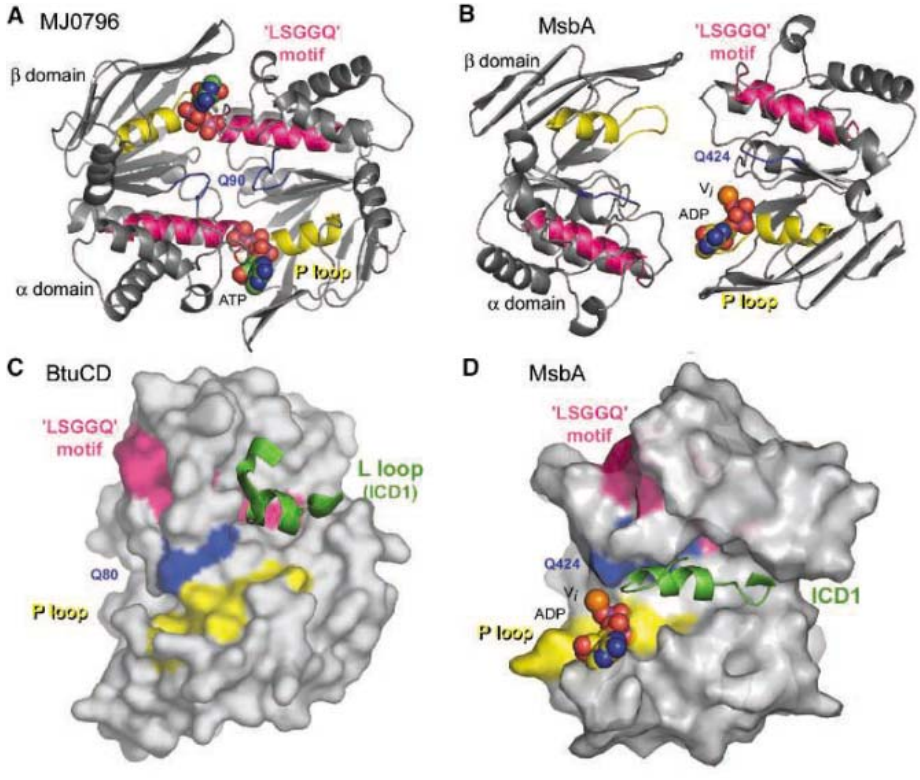

Fig. 3. The composite catalytic site of the NBDs with substrate and conserved sequence motifs. (**A**) Two bound ATP molecules (carbon shown in green, oxygen in red, nitrogen in blue, phosphate in purple) are sandwiched between the P loop (yellow) and LSGGQ (pink) moieties in the composite active site from MJ0796. The Q loop is shown in blue. (**B**) Architecture of interacting NBDs from MsbA post hydrolysis intermediate showing one bound ADP (carbon shown in yellow, oxygen in red, nitrogen in blue, phosphate in purple) molecule and one vanadate (orange) per dimer. The nucleotide is bound to the P loop (yellow) and disengaged from the conserved LSGGQ signature motif from the opposing monomer (pink). The Q loop is shown in blue. (**C**) Surface view of a single NBD from the apo structure of BtuCD shows no interaction between the L loop and the conserved glutamine (Gln^{80}) (blue) that is proposed to coordinate the nucleophilic attacking water (L loop is the ICD1 equivalent, shown in green). (**D**) Post hydrolysis intermediate MsbA shows the ICD1 helix (green) from the TMD positioned to interact with conserved glutamine (Gln^{424}) (blue).

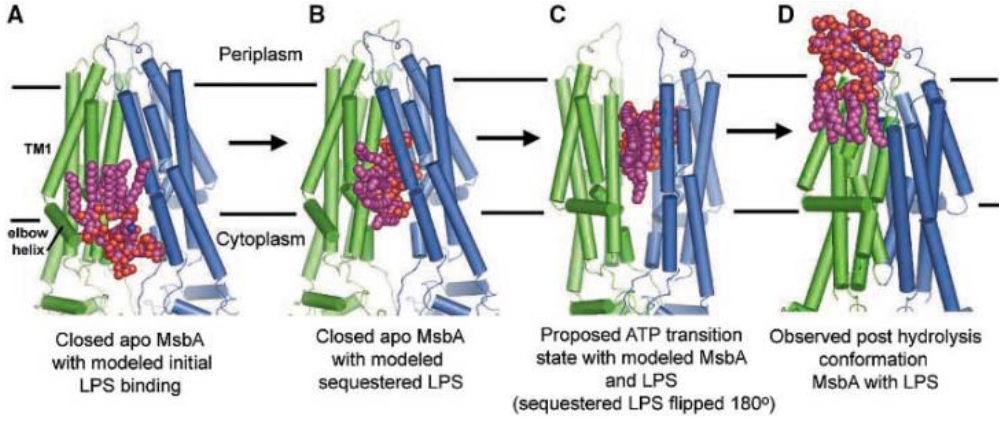

Fig. 4. Proposed model for sequestering polar sugar head group of the LPS in internal chamber of MsbA (only one LPS shown for clarity). (**A**) LPS initially binds to the elbow helix as modeled onto the closed apo structure. (**B**) Lipid head groups are modeled to insert into the chamber of the apo closed structure. (**C**) As the transporter undergoes conformational changes related to binding and hydrolysis of ATP, the head group is flipped within the polar chamber while the LPS hydrocarbon chains are freely exposed and dragged through the lipid bilayer. Both LPS and MsbA conformations are modeled. (**D**) LPS is presented to the outer leaflet of the membrane as observed in this structure.

within an elongated groove on the TMD-exposed NBD surface (Fig. 3D). As ICD1 is the only structural motif from the TMD to interact with the active site of the NBD, it seems likely that a reorientation of the ICD1 helix to contact with the Q loop could depend on the catalytic status of the γ-phosphate.

Together with previously described MsbA structures, the model described here provides a framework for interpreting functional data concerning MDR ABC transporters. Substrate recognition by the TMD and nucleotide binding by the NBD change the conformation of the molecule and thus promote the formation of the NBD dimer in an arrangement competent to hydrolyze ATP. This dimerization of the NBDs and hydrolysis of ATP together are the "power stroke" of the transport cycle and drive the transport of the lipid substrate from the inner to the outer membrane leaflet through conformational changes in the TMDs. In the post hydrolysis conformation structure described here, only one ADP is trapped per dimer, which suggests that the two NBDs act to hydrolyze ATP alternately. This would support the model of alternating catalytic sites proposed for P-gp (*35*) and LmrA (*36*). However, the presence of two LPS molecules on the outer leaflet side of the membrane suggests two substrate molecules may be transported per power stroke.

We propose a structurally based mechanism of LPS flipping whereby the sugar head groups are sequestered and "flipped" in the internal chamber while the hydrophobic tail of the lipid is dragged through the bilayer. We have observed a titratable high-affinity binding site for several cationic heavy metals such as 2-chloromercuri-4-nitrophenol and ethyl mercury chloride located at the interface of the elbow helix and TM1 (*25*). We propose that this region, which contains a locus of conserved residues across this subfamily of MDR ABC transporters, may point to an initial high-affinity surface binding site for LPS and other cationic hydrophobic compounds similar in chemical structure to most anticancer chemotherapeutics. In our proposal, LPS initially binds near the elbow helix (Fig. 4A). During the power-stroke step, the sugar head groups are sequestered within the chamber and flipped to the outer membrane leaflet by the rigid-body shearing of the TMDs while the hydrophobic tails of the LPS are dragged through the lipid bilayer (Fig. 4, B and C). The result is an energetically favorable "flip-flop" in the orientation of the lipid in the bilayer and the presentation of LPS sugar head groups on the periplasmic side of the membrane (Fig. 4D), as observed in this structure.

The size of the chamber is large enough to accommodate the sugar groups from two Ra LPS molecules. The head group size of various LPS and related molecules affects the stimulation of MsbA ATPase activity. A larger stimulatory effect on ATP activity is observed for Re LPS, which has a shorter head group than that for Ra LPS. This might be an effect of steric hindrance inside the cavity to accommodate the sugar head groups. Our model could also extend to other molecules with cationic/hydrophobic properties, such as most chemotherapeutic drugs associated with multidrug resistance. A mechanism where export could occur more exclusively through the chamber for less hydrophobic molecules is certainly possible. The model described constitutes a general molecular basis for export by MDR ABC flippases and the structural characterization of a $Mg{\cdot}ADP{\cdot}V_i$ post hydrolysis conformation of MsbA, which provides an excellent springboard for further studies.

References and Notes

1. R. C. Moellering Jr., *Clin. Infect. Dis.* **27** (suppl. 1), S135 (1998).
2. M. Ouellette, D. Legare, B. Papadopoulou, *J. Mol. Microbiol. Biotechnol.* **3**, 201 (2001).
3. M. Dean, R. Allikmets, *J. Bioenerg. Biomembr.* **33**, 475 (2001).
4. H. W. van Veen, C. F. Higgins, W. N. Konings, *Res. Microbiol.* **152**, 365 (2001).
5. V. Ling, *Cancer* **69**, 2603 (1992).
6. Y. Raviv, H. Pollard, E. P. Bruggermann, I. Pastan, M. M. Gottesman, *J. Biol. Chem.* **265**, 3975 (1990).
7. M. Karow, C. Georgopoulos, *Mol. Microbiol.* **7**, 69 (1993).
8. A. Polissi, C. Georgopoulos, *Mol. Microbiol.* **20**, 1221 (1996).
9. Z. Zhou, K. A. White, A. Polissi, C. Georgopoulos, C. R. Raetz, *J. Biol. Chem.* **273**, 12466 (1998).
10. G. Reuter *et al.*, *J. Biol. Chem.* **278**, 35193 (2003).
11. W. T. Doerrler, H. S. Gibbons, C. R. Raetz, *J. Biol. Chem.* **279**, 45102 (2004).
12. W. T. Doerrler, C. R. Raetz, *J. Biol. Chem.* **277**, 36697 (2002).
13. R. Medzhitov, C. A. Janeway, *Cell* **91**, 295 (1997).
14. J. A. Hoffmann, F. C. Kafatos, C. A. Janeway, R. A. Ezekowitz, *Science* **284**, 1313 (1999).
15. C. R. Raetz, C. Whitfield, *Annu. Rev. Biochem.* **71**, 635 (2002).
16. G. Chang, C. B. Roth, *Science* **293**, 1793 (2001).
17. K. P. Locher, A. T. Lee, D. C. Rees, *Science* **296**, 1091 (2002).
18. G. Chang, *J. Mol. Biol.* **330**, 419 (2003).
19. M. F. Rosenberg, R. Callaghan, S. Modok, C. F. Higgins, R. C. Ford, *J. Biol. Chem.* **280**, 2857 (2005).
20. A. Ferreira-Pereira *et al.*, *J. Biol. Chem.* **278**, 11995 (2003).
21. J. Y. Lee, I. L. Urbatsch, A. E. Senior, S. Wilkens, *J. Biol. Chem.* **277**, 40125 (2002).
22. M. Chami *et al.*, *J. Mol. Biol.* **315**, 1075 (2002).
23. M. F. Rosenberg *et al.*, *EMBO J.* **20**, 5615 (2001).
24. C. F. Higgins, K. J. Linton, *Nat. Struct. Mol. Biol.* **11**, 918 (2004).
25. Materials and methods are available as supporting material on *Science* Online.
26. C. R. Reyes, G. Chang, unpublished observations.
27. M. Gruen *et al.*, *Protein Sci.* **8**, 2524 (1999).
28. C. A. Smith, I. Rayment, *Biochemistry* **35**, 5404 (1996).
29. J. Dong, G. Yang, H. S. Mchaourab, *Science* **308**, 1023 (2005).
30. A. H. Buchaklian, A. L. Funk, C. S. Klug, *Biochemistry* **43**, 8600 (2004).
31. G. F. Ecker *et al.*, *Mol. Pharmacol.* **66**, 1169 (2004).
32. T. W. Loo, D. M. Clarke, *J. Biol. Chem.* **276**, 14972 (2001).
33. P. C. Smith *et al.*, *Mol. Cell* **10**, 139 (2002).
34. K. P. Hopfner *et al.*, *Cell* **101**, 789 (2000).
35. A. E. Senior, D. C. Gadsby, *Semin. Cancer Biol.* **8**, 143 (1997).
36. H. W. van Veen, A. Margolles, M. Muller, C. F. Higgins, W. N. Konings, *EMBO J.* **19**, 2503 (2000).
37. W. L. Delano, www.pymol.org (2002).

38. We thank P. Wright, D. C. Rees, R. Stroud, I. Urbatsch, W. Balch, R. Milligan, and R. H. Spencer for discussion and comments on the manuscript, as well as O. Pornillos, Y. Yin, and A. Ward. We also thank the Stanford Synchrotron Radiation Laboratory, Advanced Light Source, and Advanced Photon Source for the tremendous support and access. C.L.R. was supported by a NSF Minority Postdoctoral Fellowship. This work was supported by NIH grant GM61905, Beckman Young Investigators Grant, Fannie E. Rippel Foundation, Baxter Foundation, and The Skaggs Institute for Chemical Biology. Coordinates have been deposited in the Protein Data Bank (accession code 1Z2R).

Supporting Online Material

www.sciencemag.org/cgi/content/full/308/5724/1028/DC1
Materials and Methods
Table S1
References and Notes

19 November 2004; accepted 11 March 2005
10.1126/science.1107733

Human Mpp11 J Protein: Ribosome-Tethered Molecular Chaperones Are Ubiquitous

Heather A. Hundley,[1,2]* William Walter,[1] Shawn Bairstow,[2] Elizabeth A. Craig[1]†

The existence of specialized molecular chaperones that interact directly with ribosomes is well established in microorganisms. Such proteins bind polypeptides exiting the ribosomal tunnel and provide a physical link between translation and protein folding. We report that ribosome-associated molecular chaperones have been maintained throughout eukaryotic evolution, as illustrated by Mpp11, the human ortholog of the yeast ribosome-associated J protein Zuo. When expressed in yeast, Mpp11 partially substituted for Zuo by partnering with the multipurpose Hsp70 Ssa, the homolog of mammalian Hsc70. We propose that in metazoans, ribosome-associated Mpp11 recruits the multifunctional soluble Hsc70 to nascent polypeptide chains as they exit the ribosome.

In the crowded cellular environment, folding of newly synthesized polypeptides into their active three-dimensional conformations requires the action of a class of proteins called molecular chaperones. These chaperones bind unfolded polypeptides by interacting with hydrophobic regions that are normally sequestered in the interior of a protein, thereby preventing aggregation and promoting folding (*1*, *2*). Because partially synthesized nascent chains are particularly prone to aggregation, the presence of specialized molecular chaperones that interact directly with the ribosome near the polypeptide exit tunnel provides an important direct link between translation and protein folding (*3*). Such ribosome-tethered chaperones, only identified in microorganisms, are structurally divergent. Trigger factor, a member of the peptidyl-prolyl isomerase family, is found ubiquitously in bacteria (*1*). In contrast, the yeast ribosome-associated chaperone machinery is of the Hsp70:J protein type: Both the J protein Zuo and its Hsp70 partner Ssb independently associate with ribosomes (*4*, *5*). In such systems, both a J protein and an Hsp70 are obligatory; the J protein serves to recruit the Hsp70 to substrate polypeptides as well as to stimulate Hsp70's adenosine triphosphatase (ATPase) activity, thus stabilizing Hsp70's interaction with the substrate (*6*, *7*).

Identification of ribosome-associated chaperones in unicellular but not multicellular organisms raises the question of whether early involvement by molecular chaperones at the ribosome to prevent aggregation of nascent polypeptides is universally important (*8*, *9*). As a candidate for a metazoan ribosome-associated chaperone, we chose the human protein, Mpp11, which is orthologous to the yeast ribosome-associated J protein Zuo and is present in a wide variety of eukaryotes (*10*, *11*). In addition to having 45% identity in their J domains—the region of J proteins critical for functional interaction with Hsp70—Zuo and Mpp11 are 42% identical in a 80–amino acid region required for ribosome-association of Zuo (*4*).

To determine whether Mpp11 is ribosome associated, we separated lysates of human tissue culture cells by sucrose density gradient centrifugation and probed for Mpp11 (*12*). Mpp11 cosedimented with human ribosomal protein L10 (Rpl10) (Fig. 1A). Because Mpp11 is so highly conserved, we used rabbit reticulocyte lysate (RRL) to further assess ribosome association. After centrifugation of RRL through a sucrose cushion, the Mpp11 and Rpl10 cross-reactive proteins were quantitatively found in the pellet fraction (Fig. 1B). Because RRL has a high concentration of nontranslating ribosomes, this cofractionation suggested that Mpp11 interacts directly with the ribosome and does not require a nascent polypeptide chain for association. To test this idea more directly, ribosomes purified from RRL and stripped of endogenous Mpp11 by treatment with high salt were incubated with purified Mpp11 (Fig. 1C). When added at a stoichiometry of approximately 1:1, most Mpp11 sedimented with ribosomes; at a ratio of 2:1, Mpp11 distributed equally between the supernatant and pellet, consistent with the idea that Mpp11 bound directly to mammalian ribosomes.

Because both Mpp11 and Zuo associate with ribosomes, we asked if Mpp11 could substitute for Zuo when expressed in yeast. Mpp11 partially rescued the cation hypersensitivity of a *Δzuo* strain (*13*), as demonstrated by enhanced growth in the presence of NaCl or paromomycin (Fig. 2A and fig. S1). To assess whether Mpp11 was ribosome associated in the heterologous yeast system, lysates prepared from the *Δzuo* strain expressing Mpp11 were subjected to centrifugation through a sucrose cushion. Ribosomes were present in the pellet fraction, as was the vast majority of Mpp11 (Fig. 2B). The resuspended pellet was subjected to centrifugation through a sucrose density gradient. The distribution of Mpp11 in the gradient closely coincided with that of ribosomes, even after treatment with ribonuclease A (RNase A) caused ribosomes to migrate as 80*S* monosomes. Thus, nearly all of Mpp11 was associated with yeast ribosomes.

Because of the sequence similarity between Mpp11 and the region of Zuo required for ribosome association, we asked whether the two proteins interacted similarly with ribosomes. Ribosomes from wild-type cells and Δ*zuo* cells expressing Mpp11 were incubated with various concentrations of KCl. The endogenous Zuo and heterologous Mpp11 showed similar salt sensitivities, with most of the protein

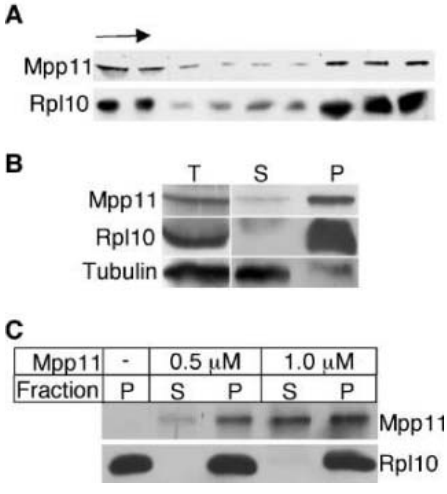

Fig. 1. Ribosome association of mammalian Mpp11. (**A**) Cell lysate from human embryonic kidney cells (HEK293) centrifuged through a sucrose gradient of 5 to 47%. Arrow denotes direction of the gradient. Fractions were collected and subjected to immunoblot analysis with antibodies directed against human Mpp11 or human Rpl10. (**B**) Ribosomes from RRL were isolated by centrifugation through a sucrose cushion. Equivalent amounts of supernatant (S) and ribosomal-containing pellet (P) from centrifugation of 5 μl of RRL (T) were subjected to immunoblot analysis with the indicated antibodies. (**C**) Indicated concentrations of purified Mpp11 were incubated in the presence of high salt–washed ribosomes (~0.5 μM). Samples were centrifuged and the supernatant (S) and pellet (P) fractions were analyzed as described above with the use of the indicated antibodies.

[1]Department of Biochemistry, 433 Babcock Drive, University of Wisconsin–Madison, Madison, WI 53706, USA. [2]Graduate Program in Biomolecular Chemistry, University of Wisconsin–Madison, Madison, WI 53706, USA.

*Present address: Department of Biochemistry and Howard Hughes Medical Institute, University of Utah, Salt Lake City, UT 84132, USA.

†To whom correspondence should be addressed. E-mail: ecraig@wisc.edu

being released from ribosomes after treatment with 200 mM KCl (Fig. 2C). To test the idea that the two proteins bind to the same site on the ribosome, we performed a competition assay. Ribosomes stripped of endogenous Zuo by treatment with high salt were incubated with approximately equimolar amounts of Zuo and increasing concentrations of Mpp11 (Fig. 2D). In the absence of Mpp11, nearly all of the Zuo was found in the pellet after centrifugation, indicative of its ribosome association. When Mpp11 was present in threefold excess, less than 20% of the added Zuo was ribosome associated, indicating that binding of Mpp11 and Zuo was mutually exclusive, consistent with the idea that Mpp11 and Zuo occupy the same, or overlapping, sites on the yeast ribosome.

Interaction of J proteins with the ATPase domain of their partner Hsp70 occurs through the highly conserved J domain. To ascertain whether Mpp11 functioned as a J protein in yeast, we exploited the fact that within the J domain of all known J proteins, there is a histidine, proline, aspartic acid tripeptide (HPD motif) that is critical for this interaction (*14*). We constructed a *MPP11* mutant, $MPP11_{H\text{-}Q}$, that replaced the histidine of its HPD motif with glutamine, an alteration that has been shown to inactivate many J proteins by rendering them incapable of functioning with Hsp70 (*15*, *16*). As expected, $Mpp11_{H\text{-}Q}$ was unable to rescue the cation hypersensitivity of a *Δzuo* strain (Fig. 2A and fig. S2).

Because J proteins function only in partnership with an Hsp70, we sought to establish the yeast Hsp70 partner of Mpp11. Ssb is the endogenous Hsp70 partner of Zuo (*17*, *18*). However, no known orthologs of Ssb exist outside of fungi (*19*). Zuo and Ssb have coevolved to form a specialized Hsp70:J protein ribosome-associated pair (*4*). Ssa, on the other hand, is homologous to the abundant, soluble cytosolic Hsc70 of higher eukaryotes. We predicted that human Mpp11 may function in the yeast cytosol by partnering with Ssa, rather than Ssb. To test this hypothesis, we first expressed Mpp11 in a strain lacking Zuo and Ssb, which has the same phenotype as a strain lacking only Zuo (consistent with the evidence that activity of this type of chaperone machinery requires both a J protein and an Hsp70) (*4*). Mpp11 rescued cells lacking Ssb and Zuo (Fig. 3A) as well as cells lacking only Zuo (Fig. 2A). Thus, Mpp11 does not require Ssb as an Hsp70 partner to function in yeast.

Ssa is an essential Hsp70. Thus, we could not directly test whether it is required for Mpp11 to functionally substitute for Zuo (*20*). Instead, we asked whether the ability of Mpp11 to function in yeast was enhanced by increased expression of Ssa. As expected, the presence of a plasmid expressing *SSA1* had no effect on the ability of cells lacking Zuo and Ssb to grow in the presence of cations. However, when plasmids expressing both Mpp11 and *SSA1* were present, growth was improved compared with the strain expressing only Mpp11 (Fig. 3B). This enhancement required a func-

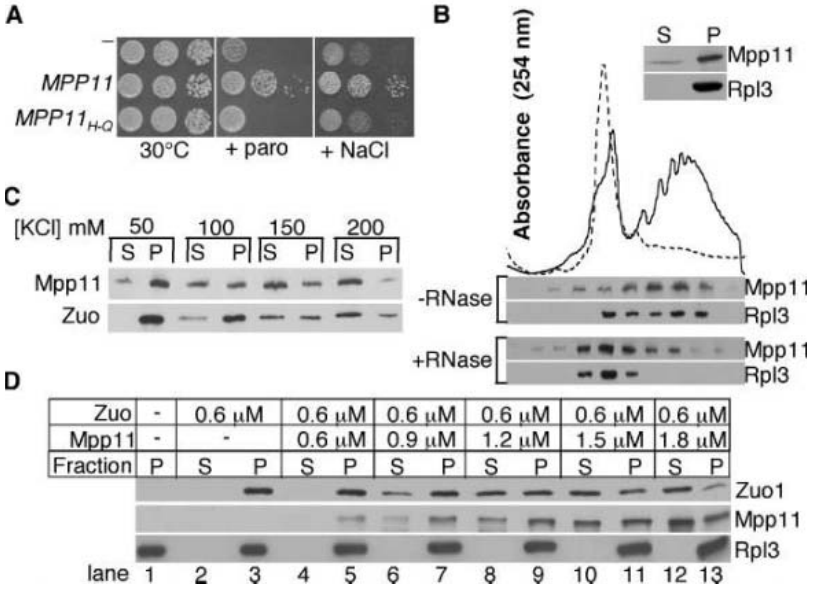

Fig. 2. Characterization of Mpp11 function in yeast cells lacking Zuo. (**A**) Serial dilution of *Δzuo* cells expressing Mpp11 or $Mpp11_{H\text{-}Q}$, which were spotted on minimal media in the presence or absence of paromomycin (paro) (250 μg/ml) and incubated at 30°C (3 days) or 1 M NaCl (5 days). (**B**) (Inset) Lysate of *Δzuo* cells expressing Mpp11-HA was centrifuged through a sucrose cushion separating the ribosome-containing pellet (P) from the supernatant (S). Equivalent amounts of each fraction were subjected to electrophoresis and immunoblot analysis with hemagglutinin (HA)– or Rpl3-specific antibodies. The main panel shows the resuspended pellet, which was incubated in the presence (+) or absence (–) of RNase and centrifuged through a sucrose gradient of 5 to 47%. Optical density (OD_{254}) was monitored (top); fractions were collected and subjected to immunoblot analysis as described above (bottom). (**C**) Ribosome-containing pellets of *Δzuo* cells expressing Mpp11-HA (top) or wild-type cells (bottom) were incubated in the presence of the indicated concentrations of KCl for 30 min at 30°C and then centrifuged through sucrose cushions containing the same salt concentration. Equivalent amounts of the supernatant (S) and pellet (P) fractions were subjected to electrophoresis and immunoblot analysis with HA- or Zuo-specific antibodies. (**D**) Indicated concentrations of purified Zuo and Mpp11 were incubated in the presence of high salt–washed ribosomes (0.6 μM). Samples were centrifuged and the supernatant (S) and pellet (P) fractions were analyzed as described above with the use of the indicated antibodies.

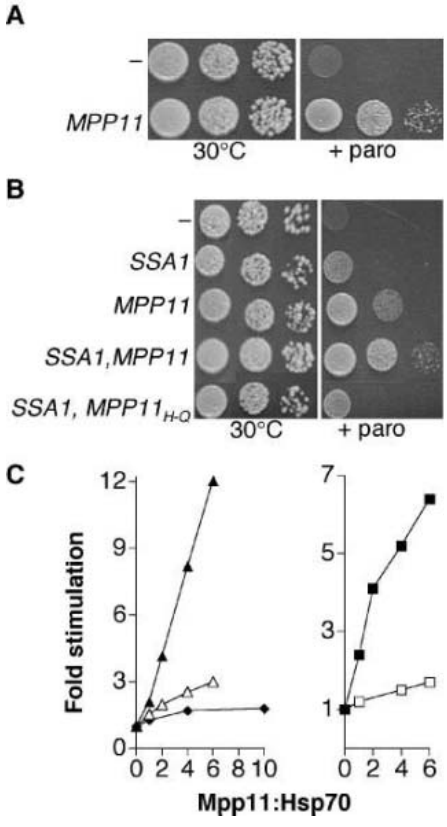

Fig. 3. Mpp11 substitutes for Zuo in the absence of Ssb. (**A**) Yeast strain HH6 expressing *MPP11* was diluted in a 10-fold series, spotted on minimal media and incubated at 30°C (3 days) in the presence and absence of paromomycin (paro) (250 μg/ml). (**B**) HH6 was transformed with control vector plasmids and plasmids expressing *MPP11*, *SSA1*, and both the *SSA1* and either *MPP11* or $MPP11_{H\text{-}Q}$. The resulting strains were diluted in a 10-fold series and incubated at 30°C (3 days) in the presence and absence of paromomycin (150 μg/ml). (**C**) Hsp70:ATP-[^{32}P] complexes were incubated in the presence of various concentrations of wild-type Mpp11 or $Mpp11_{H\text{-}Q}$ and the rate of hydrolysis of ATP determined. Fold stimulation over the basal rate is plotted. (Left) Mpp11 and Ssa (solid triangles) or Ssb (solid diamonds); $Mpp11_{H\text{-}Q}$ and Ssa (open triangles). (Right) Hsc70 and Mpp11 (solid squares) or $Mpp11_{H\text{-}Q}$ (open squares).

tional J domain, because no suppression was observed when the mutant $Mpp11_{H-Q}$ rather than wild-type Mpp11 was expressed.

The in vivo results described above suggest that Mpp11 functions as the J-protein partner of Ssa, not Ssb. To test this idea biochemically, we asked if Mpp11 could stimulate the ATPase activity of Ssa. Such stimulation, the result of interaction of the J domain with Hsp70's ATPase domain, converts Hsp70 to the adenosine 5′-diphosphate (ADP)–bound form that has high affinity for substrate polypeptides (*6*, *7*). A complex between Hsp70 and radiolabeled ATP was isolated, and the rate of ADP formation was determined upon incubation in the presence of increasing concentration of Mpp11. Mpp11 stimulated the ATPase activity of Ssa 12-fold under the conditions tested, whereas the ability of $Mpp11_{H-Q}$ was severely compromised, as expected of an inactive J protein (Fig. 3C). In contrast, Mpp11 did not substantially stimulate the ATPase activity of Ssb, even when present at a 10-fold molar excess. Thus Mpp11 acts as a J-protein partner of Ssa. If in metazoans, Mpp11 partners with the Ssa homolog, Hsc70, Mpp11 should efficiently stimulate the ATPase activity of human Hsc70. Indeed, Mpp11 stimulated Hsc70's ATPase activity (Fig. 3C). Additional support for such a partnership comes from the identification of *Drosophila* Zuo/Mpp11 ortholog as an interaction partner with *Drosophila* Hsc70 in a genome-wide two-hybrid study (*21*).

We conclude that Mpp11, an ortholog of yeast Zuo, is a human ribosome-associated J protein. We propose that in metazoans, ribosome-associated Zuo and Mpp11 orthologs recruit the multifunctional soluble cytosolic Hsc70 to short ribosome-bound nascent chains as they exit the ribosome. Consistent with this idea, Hsc70 is not only associated with newly synthesized polypeptide chains recently released from ribosomes, but also with ribosome-associated chains (*22*, *23*). Such recruitment is reminiscent of other cases in which particular J proteins determine the site of action of Hsp70s (*24*, *25*).

References and Notes

1. F. Hartl, M. Hayer-Hartl, *Science* **295**, 1852 (2002).
2. B. Bukau, E. Deuerling, C. Pfund, E. A. Craig, *Cell* **101**, 119 (2000).
3. E. A. Craig, H. C. Eisenman, H. A. Hundley, *Curr. Opin. Microbiol.* **6**, 157 (2003).
4. W. Yan *et al.*, *EMBO J.* **17**, 4809 (1998).
5. C. Pfund *et al.*, *EMBO J.* **17**, 3981 (1998).
6. D. Wall, M. Zylicz, C. Georgopoulos, *J. Biol. Chem.* **269**, 5446 (1994).
7. A. Szabo *et al.*, *Proc. Natl. Acad. Sci. U.S.A.* **91**, 10345 (1994).
8. A. Horwich, *Nature* **431**, 520 (2004).
9. V. Albanese, J. Frydman, *Nat. Struct. Biol.* **9**, 716 (2002).
10. N. Matsumoto-Taniura, F. Pirollet, R. Monroe, L. Gerace, J. M. Westendorf, *Mol. Biol. Cell* **7**, 1455 (1996).
11. J. M. Stuart, E. Segal, D. Koller, S. K. Kim, *Science* **302**, 249 (2003).
12. Materials and methods are available as supporting material on *Science* Online.
13. S.-Y. Kim, E. A. Craig, *Eukaryot. Cell* **4**, 82 (2005).
14. P. Walsh, D. Bursac, Y. C. Law, D. Cyr, T. Lithgow, *EMBO Rep.* **5**, 567 (2004).
15. J. Tsai, M. G. Douglas, *J. Biol. Chem.* **271**, 9347 (1996).
16. P. D. D'Silva, B. Schilke, W. Walter, A. Andrew, E. A. Craig, *Proc. Natl. Acad. Sci. U.S.A.* **100**, 13839 (2003).
17. H. Hundley *et al.*, *Proc. Natl. Acad. Sci. U.S.A.* **99**, 4203 (2002).
18. M. Gautschi, A. Mun, S. Ross, S. Rospert, *Proc. Natl. Acad. Sci. U.S.A.* **99**, 4209 (2002).
19. C. Pfund, P. Huang, N. Lopez-Hoyo, E. Craig, *Mol. Biol. Cell* **12**, 3773 (2001).
20. M. Werner-Washburne, D. E. Stone, E. A. Craig, *Mol. Cell. Biol.* **7**, 2568 (1987).
21. L. Giot *et al.*, *Science* **302**, 1727 (2003).
22. R. P. Beckmann, L. Mizzen, W. Welch, *Science* **248**, 850 (1990).
23. J. Frydman, E. Nimmesgern, K. Ohtsuka, F. U. Hartl, *Nature* **370**, 111 (1994).
24. W. Barouch, K. Prasad, L. Greene, E. Eisenberg, *Biochemistry* **36**, 4303 (1997).
25. J. L. Brodsky, R. Schekman, *J. Cell Biol.* **123**, 1355 (1993).

26. This work was supported by American Heart Association grant 0410032Z to H.H. and NIH grant R01GM031107 to E.C. We thank E. Lund, J. Warner, and C. Wiese for antibodies; R. Morimoto for Hsc70; and P. Huang, C. Pfund, C. Wiese, and A. Ansari for helpful comments. Molecular interaction data have been deposited in the Biomolecular Interaction Network Database under accession code 215373.

Supporting Online Material
www.sciencemag.org/cgi/content/full/1109247/DC1
Materials and Methods
Figs. S1 and S2
References

29 December 2004; accepted 23 February 2005
Published online 31 March 2005;
10.1126/science.1109247
Include this information when citing this paper.

Single, Rapid Coastal Settlement of Asia Revealed by Analysis of Complete Mitochondrial Genomes

Vincent Macaulay,[1]* Catherine Hill,[2] Alessandro Achilli,[3] Chiara Rengo,[3] Douglas Clarke,[2] William Meehan,[2] James Blackburn,[2] Ornella Semino,[3] Rosaria Scozzari,[4] Fulvio Cruciani,[4] Adi Taha,[5] Norazila Kassim Shaari,[6] Joseph Maripa Raja,[6] Patimah Ismail,[6] Zafarina Zainuddin,[7] William Goodwin,[8] David Bulbeck,[9] Hans-Jürgen Bandelt,[10] Stephen Oppenheimer,[11] Antonio Torroni,[3] Martin Richards[12]*

A recent dispersal of modern humans out of Africa is now widely accepted, but the routes taken across Eurasia are still disputed. We show that mitochondrial DNA variation in isolated "relict" populations in southeast Asia supports the view that there was only a single dispersal from Africa, most likely via a southern coastal route, through India and onward into southeast Asia and Australasia. There was an early offshoot, leading ultimately to the settlement of the Near East and Europe, but the main dispersal from India to Australia ~65,000 years ago was rapid, most likely taking only a few thousand years.

The traditional "out of Africa" model for modern human origins posits an ancestry in sub-Saharan Africa, followed by a dispersal via the Levant ~45,000 years ago (*1*, *2*). However, the suggestion of an earlier "southern route" dispersal from the Horn of Africa ~60,000 to 75,000 years ago, along the tropical coast of the Indian Ocean to southeast Asia and Australasia (*3*, *4*), has recently gained ground (*5*–*8*). Part of its rationale has been the presence of a number of "relict" populations in southern India and southeast Asia; it has been suggested that these populations might be the descendants of such an earlier dispersal, along with Papuans and Aboriginal Australians (*9*).

Following the work of Vigilant *et al.* (*10*), Watson *et al.* (*11*) provided evidence from mitochondrial DNA (mtDNA) patterns for a single dispersal from Africa, although not distinguishing between a northern or southern route. More recently, the existence of a southern route has been supported by analyses of mtDNA restriction enzyme data from New Guinea (*12*) and control region sequences from main-

[1]Department of Statistics, University of Glasgow, Glasgow G12 8QQ, Scotland, UK. [2]Department of Chemical and Biological Sciences, University of Huddersfield, Huddersfield HD1 3DH, UK. [3]Dipartimento di Genetica e Microbiologia, Università di Pavia, 27100 Pavia, Italy. [4]Dipartimento di Genetica e Biologia Molecolare, Università "La Sapienza," 00185 Roma, Italy. [5]National Museum of Kuala Lumpur, 50566 Kuala Lumpur, Malaysia. [6]Department of Biomedical Science, Universiti Putra Malaysia, 43400 Serdang, Selangor, Malaysia. [7]Department of Forensic Medicine and Science, University of Glasgow, Glasgow G12 8QQ, Scotland, UK. [8]Department of Forensic and Investigative Science, University of Central Lancashire, Preston PR1 2HE, UK. [9]School of Archaeology and Anthropology, Australian National University, Canberra, ACT 0200, Australia. [10]Department of Mathematics, University of Hamburg, 20146 Hamburg, Germany. [11]Department of Anthropology, University of Oxford, Oxford OX1 2JD, UK. [12]Schools of Biology and Computing, University of Leeds, Leeds LS2 9JT, UK.

*To whom correspondence should be addressed. E-mail: vincent@stats.gla.ac.uk; m.b.richards@leeds.ac.uk

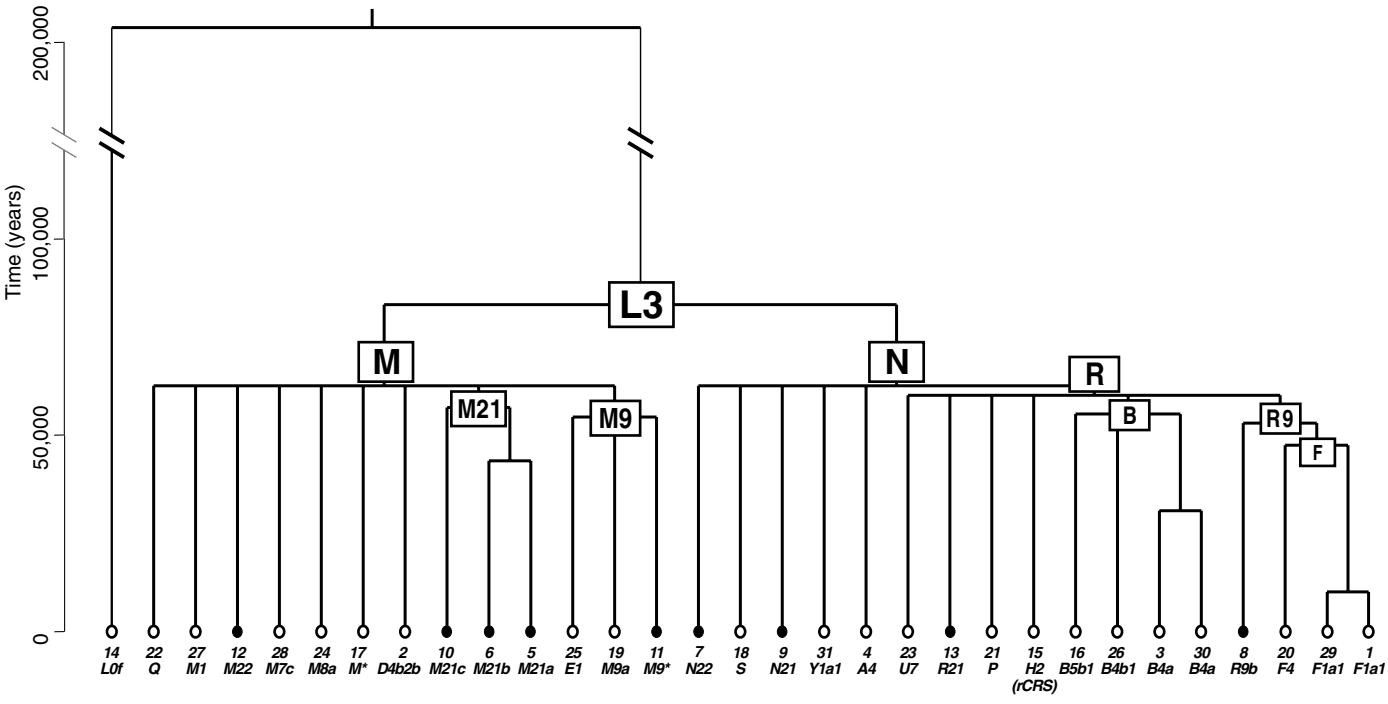

Fig. 1. Reconstructed phylogeny of 31 mtDNA coding region sequences. mtDNAs from the Malay Peninsula are indicated by solid circles at the tips of the tree.

land India and the Andaman Islands (*13*–*16*). Meanwhile, archaeological evidence has been found for the occupation of the coast of Eritrea ~125,000 years ago—the oldest known indication of human exploitation of marine resources (*17*).

However, the published genetic data remain sufficiently ambiguous for some geneticists to reject the very existence of a southern route (*18*), and the question of single versus multiple dispersals also remains in dispute. What is needed to distinguish between the different dispersal hypotheses are well-resolved sequence data from the relict populations themselves. Here, we test the possible dispersal routes with a maximum likelihood analysis of complete mtDNA genomes from the Orang Asli—the aboriginal inhabitants of Malaysia and the principal relict group in southeast Asia (*19*)—in the context of other eastern Eurasian and Australasian lineages.

We sampled 260 maternally unrelated Orang Asli, including (i) Semang, who live (or lived until recently) in small, nomadic hunter-gatherer groups in the lowland rainforests; (ii) Senoi, who are traditionally swidden agriculturalists; and (iii) Aboriginal Malays, horticulturalists and fishers who most resemble physically the majority *Melayu* Malays. It is widely agreed that the Orang Asli, especially the Semang, are aboriginal inhabitants of the Malay Peninsula (*19*, *20*). Moreover, there is a well-documented archaeological record of continuous occupation by hunter-gatherers throughout the Holocene, and an essentially continuous hunter-gatherer record from at least 40,000 (perhaps 70,000) years ago (*21*).

A reconstructed phylogeny of eastern Eurasian mtDNA genomes is shown in Fig. 1 (see fig. S1 for branch labels); ages of the principal nodes in the tree are shown in table S3. This analysis yields a time to the most recent common ancestor of all humans (TMRCA) of ~200,000 years ago, in close agreement with Mishmar *et al*. (*22*). Haplogroup L3 (the African clade that gave rise to the two basal non-African clades, haplogroups M and N) is ~84,000 years old, and haplogroups M and N themselves are almost identical in age at ~63,000 years old, with haplogroup R diverging rapidly within haplogroup N ~60,000 years ago. This agrees quite well with the similarity of ages of M and N noted by Forster *et al*. (*12*) [see also (*23*)] and with the ages of both autochthonous R lineages in India (*24*) and the three major haplogroups in China (*25*).

Three possible hypotheses can be distinguished using these data. If modern non-Africans are descendants of populations that dispersed along both northern and southern routes, then mtDNA lineages belonging to relict populations (including Orang Asli, Papuans, and Aboriginal Australians) should diverge from founder types that are distinct from those leading to the main continental Eurasian groups. If there were just a single dispersal, then all non-African populations should diverge from the same set of founders, which would coalesce to ~45,000 to 50,000 years ago if the Levantine corridor model were correct, or ~60,000 to 75,000 years ago if they were all the result of the proposed earlier single southern route (*4*). At this time, a northern passage was most likely blocked by desert and semi-desert (*26*).

We assessed the distribution of mtDNAs present in the Orang Asli (table S2) by searching for their associated control region motifs in the worldwide mtDNA database (*27*). Several are shared with other southeast Asian populations, and these most likely indicate Holocene introgression (*25*, *28*). However, most are virtually unique to the Orang Asli and are therefore likely to be indigenous. This strongly supports the suggestion that the Orang Asli harbor "relict" mtDNA lineages with time depths of ~44,000 to 63,000 years (*27*). Their restricted distribution makes it very likely that these lineages diverged around that time within mainland southeast Asia. Although caution is warranted given the time depths involved, this conclusion is plausible on environmental grounds. Forests would have flourished on the lowlands abutting the Malaysian Peninsula throughout the last glacial period (*21*), which implies that this region acted as a glacial refuge where populations survived and genetic diversity was maintained. Although it is likely that waves of replacement occurred during the late Holocene to the north of the peninsula and on the coasts, it appears that they did not take place in the interior rainforest—or at least that the ancestors of the Orang Asli survived, albeit in low numbers, in Malaysia (*20*).

Furthermore, examination of recently published complete mtDNA genomes from Papuans and Aboriginal Australians (*29*) shows an analogous situation in which the lineages are predominantly unique to Australasia but diverge from the base of all three founder haplogroups. Both the indigenous Malaysian mtDNAs and those of Australasia are de-

rived from the three major Eurasian founder haplogroups, M, N, and R, which are also found alongside one another to the west in the Indian subcontinent (*15*) as well as throughout continental Asia (*25*, *28*).

The very similar ages of haplogroups M, N, and R indicate that they were part of the same colonization process [see (*23*)]. This most likely involved the exodus of a founding group of several hundred individuals (*27*) from East Africa, some time after the appearance of haplogroup L3 ~85,000 years ago, followed by a period of mutation and drift during which haplogroups M, N, and R evolved and the ancestral L3 was lost. Although the details of this period remain to be elucidated, the next stage is much clearer. The presence in each region of the same three founder haplogroups, but differentiated into distinct subhaplogroups, indicates that there was a rapid coastal dispersal from ~65,000 years ago around the Indian Ocean littoral and on to Australasia. Firm minimum archaeological age estimates are somewhat more recent—~50,000 years for Australia (*30*) and ~45,000 years for southeast Asia (*31*)—but early evidence may have been lost to sea level rises. Moreover, human populations may then have diffused from the coast into the continental interiors more gradually, leaving a greater archaeological signature on the landscape as they grew in size.

This evidence suggests that this coastal trail was likely the only route taken during the Pleistocene settlement of Eurasia by the ancestors of modern humans, and that the primary dispersal process, at least from India to Australasia, was very rapid. A founder analysis of western, southern, and eastern Eurasian and Australasian complete mtDNAs suggested a shallow gradient of arrival times, from ~66,000 years ago in India to ~63,000 years ago in Australasia (table S4). Assuming a distance of ~12,000 km, this allowed us to estimate a dispersal rate of ~4 km/year from point estimates, a little lower than estimates for the more recent expansion into the Americas (*32*). An approximate lower bound on the dispersal rate is ~0.7 km/year, comparable to the recolonization of Europe after the ice age (*33*).

By contrast with South Asians, eastern Eurasians, and Australasians, western Eurasians have a high level of haplogroup-level diversity within haplogroups N and R, but lack haplogroup M almost entirely (*34*). The colonization of western Eurasia has usually been thought to have been the result of a "northern route" dispersal out of Africa, through North Africa and the Levant (*4*), but the close similarity of the mtDNA founder age to that of India (table S4) suggests that it was most likely the result of an early offshoot of colonization along the southern route, followed by a lengthy pause until the climate improved (*26*) and the ancestors of western Eurasians were able to enter the Levant and Europe. This implies that the subsequent Upper Paleolithic "revolution" in western Eurasia was one regional indication of the emergence of modern humans, rather than a radical break with the past (*35*).

References and Notes

1. C. B. Stringer, P. Andrews, *Science* **239**, 1263 (1988).
2. F. Prugnolle, A. Manica, F. Balloux, *Curr. Biol.* **15**, R159 (2005).
3. L. L. Cavalli-Sforza, P. Menozzi, A. Piazza, *The History and Geography of Human Genes* (Princeton Univ. Press, Princeton, NJ, 1994).
4. M. M. Lahr, R. Foley, *Evol. Anthropol.* **3**, 48 (1994).
5. L. Quintana-Murci *et al.*, *Nat. Genet.* **23**, 437 (1999).
6. N. Maca-Meyer, A. M. González, J. M. Larruga, C. Flores, V. M. Cabrera, *BMC Genet.* **2**, 13 (2001).
7. M. Tanaka *et al.*, *Genome Res.* **14**, 1832 (2004).
8. R. Lewin, R. A. Foley, *Principles of Human Evolution* (Blackwell, Oxford, ed. 2, 2004).
9. M. Nei, A. K. Roychoudhury, *Mol. Biol. Evol.* **10**, 927 (1993).
10. L. Vigilant, M. Stoneking, H. Harpending, K. Hawkes, A. C. Wilson, *Science* **253**, 1503 (1991).
11. E. Watson, P. Forster, M. Richards, H.-J. Bandelt, *Am. J. Hum. Genet.* **61**, 691 (1997).
12. P. Forster, A. Torroni, C. Renfrew, A. Röhl, *Mol. Biol. Evol.* **18**, 1864 (2001).
13. P. Endicott *et al.*, *Am. J. Hum. Genet.* **72**, 178 (2003).
14. P. Endicott, V. Macaulay, T. Kivisild, C. Stringer, A. Cooper, *Am. J. Hum. Genet.* **72**, 1590 (2003).
15. T. Kivisild *et al.*, *Am. J. Hum. Genet.* **72**, 313 (2003).
16. M. Metspalu *et al.*, *BMC Genet.* **5**, 26 (2004).
17. R. C. Walter *et al.*, *Nature* **405**, 65 (2000).
18. R. Cordaux, M. Stoneking, *Am. J. Hum. Genet.* **72**, 1586 (2003).
19. P. Bellwood, *Asian Perspect.* **32**, 37 (1993).
20. P. Bellwood, *Prehistory of the Indo-Malaysian Archipelago* (Univ. of Hawaii Press, Honolulu, 1997).
21. D. Bulbeck, in *Under the Canopy: The Archaeology of Tropical Rain Forests*, J. Mercader, Ed. (Rutgers Univ. Press, New Brunswick, NJ, 2003), pp. 119–160.
22. D. Mishmar *et al.*, *Proc. Natl. Acad. Sci. U.S.A.* **100**, 171 (2003).
23. P. Forster, *Philos. Trans. R. Soc. London Ser. B* **359**, 255 (2004).
24. M. G. Palanichamy *et al.*, *Am. J. Hum. Genet.* **75**, 966 (2004).
25. Q.-P. Kong *et al.*, *Am. J. Hum. Genet.* **73**, 671 (2003); erratum, *Am. J. Hum. Genet.* **75**, 157 (2004).
26. T. H. van Andel, P. C. Tzedakis, *Quat. Sci. Rev.* **15**, 481 (1996).
27. See supporting data on *Science* Online.
28. Y.-G. Yao, Q.-P. Kong, H.-J. Bandelt, T. Kivisild, Y.-P. Zhang, *Am. J. Hum. Genet.* **70**, 635 (2002).
29. M. Ingman, U. Gyllensten, *Genome Res.* **13**, 1600 (2003).
30. C. S. M. Turney *et al.*, *Quat. Res.* **55**, 3 (2001).
31. G. Barker *et al.*, *Proc. Prehist. Soc.* **68**, 147 (2002).
32. L. Hazelwood, J. Steele, *J. Archaeol. Sci.* **31**, 669 (2004).
33. R. A. Housley, C. S. Gamble, M. Street, P. Pettitt, *Proc. Prehist. Soc.* **63**, 25 (1997).
34. M. Richards *et al.*, *Am. J. Hum. Genet.* **67**, 1251 (2000).
35. S. McBrearty, A. S. Brookes, *J. Hum. Evol.* **39**, 453 (2000).

36. Supported by United Productions and the Discovery Channel, the British Academy, the Royal Society, the University of Huddersfield, the Wellcome Trust, the Italian Ministry of the University (Progetti Ricerca Interesse Nazionale 2003), Progetto CNR-MIUR Genomica Funzionale-Legge 449/97, Grandi Progetti di Ateneo (Università La Sapienza), the Muzium Negara Malaysia (Kuala Lumpur), and the Universiti Putra Malaysia. We thank the Malaysian participants for providing cheek-swab samples and J. Clegg and A. S. Sofro for Indonesian samples.

Supporting Online Material

www.sciencemag.org/cgi/content/full/308/5724/1034/DC1
Materials and Methods
Fig. S1
Tables S1 to S4
References

14 January 2005; accepted 24 March 2005
10.1126/science.1109792

Induction of Protein Secretory Pathway Is Required for Systemic Acquired Resistance

Dong Wang, Natalie D. Weaver, Meenu Kesarwani,* Xinnian Dong†

In plants, systemic acquired resistance (SAR) is established as a result of NPR1-regulated expression of pathogenesis-related (*PR*) genes. Using gene expression profiling in *Arabidopsis*, we found that in addition to controlling the expression of *PR* genes, NPR1 also directly controls the expression of the protein secretory pathway genes. Up-regulation of these genes is essential for SAR, because mutations in some of them diminished the secretion of PR proteins (for example, PR1), resulting in reduced resistance. We provide evidence that NPR1 coordinately regulates these secretion-related genes through a previously undescribed cis-element. Activation of this cis-element is controlled by a transcription factor that is translocated into the nucleus upon SAR induction.

SAR is a plant immune response that is induced after a local infection and confers resistance throughout the plant to a broad spectrum of pathogens (*1*). Induction of SAR requires accumulation of the endogenous signaling molecule salicylic acid (SA), which activates gene expression mediated by the master regulator protein NPR1 [Nonexpressor of pathogenesis-related (*PR*) genes 1, also known as NIM1] (*2*). Exogenous application of SA triggers the translocation of NPR1 into the nucleus. Once in the nucleus, NPR1 interacts with TGA transcription factors to mediate gene expression.

Developmental, Cell and Molecular Biology Group, Department of Biology, Post Office Box 91000, Duke University, Durham, NC 27708, USA.

*Present address: Massachusetts General Hospital, Department of Surgery, Boston, MA 02114, USA.
†To whom correspondence should be addressed. E-mail: xdong@duke.edu

Treatment of plants with SA alters the expression of a large array of genes (*3*–*5*). Among these, only some are regulated by NPR1 and therefore specific to SAR. The most-studied NPR1 targets are *PR* genes, which encode small, secreted or vacuole-targeted proteins with antimicrobial activities (*6*).

To identify additional NPR1 target genes, we used the *35S::NPR1-GR* transgenic line generated in the *npr1-3* mutant (*7*). In this transgenic plant, nuclear translocation of NPR1-GR (GR, glucocorticord receptor) requires not only SA but also dexamethasone (Dex). Treating *35S::NPR1-GR* plants first with SA and then with Dex specifically activates NPR1 target genes. With the use of a known NPR1 primary target, *PR1*, experimental conditions were optimized with the inclusion of the translation inhibitor cycloheximide (Chx) to achieve maximal induction of NPR1 target genes in the absence of de novo protein synthesis (fig. S1).

Using Affymetrix GeneChips (8200 genes), we identified putative NPR1 primary target genes by comparing transcriptional profiles of *npr1* and *npr1*/*35S::NPR1-GR* that were both treated with SA and then Chx/Dex (fig. S1). Duplicate experiments were performed independently and the data were analyzed with both MAS5.0 and dChip programs. Genes that showed a consistent difference in their pattern of expression (induction or repression) and low *P*-values (<0.05) in both replicates were considered for further analysis (table S1). Many of the induced genes can be classified into groups according to their known or deduced functions. One group (Table 1) contains genes known to be involved in defense, including several *PR* genes. Another group encodes members of the protein secretory pathway (9 of the 49 genes with >2-fold induction or 18 of the 120 genes with >1.6-fold induction), most of which are endoplasmic reticulum (ER)–localized proteins (*8*, *9*). These secretion-related genes include those encoding the Sec61 translocon complex, which provides a channel for proteins to cross the ER membrane, and a signal recognition particle (SRP) receptor, which directs proteins with a signal peptide to the translocon complex. NPR1 also regulates many genes encoding ER-resident chaperones, such as BiP2 and glucose regulated protein 94 (GRP94), as well as co-chaperones including defender against apoptotic death 1 (DAD1) (*10*), calnexins (CNXs), calreticulins (CRTs), and protein disulfide isomerases (PDIs). These proteins function in the cotranslational folding and modification (e.g., disulfide bond formation and glycosylation) of nascent polypeptides destined for the apoplast or various organelles. Other genes in this group encode a Golgi-associated membrane trafficking protein; a clathrin, which is involved in packaging secretory proteins into small vesicles; and a vacuolar sorting receptor.

Taken as a group, the secretion-related genes showed statistically significant up-regulation in both experiments using a mixed-model analysis of variance (ANOVA) (P = 0.003) (*11*). Furthermore, the induction of many of these genes by SA via the endogenous NPR1 was confirmed by RNA blot analysis, real-time reverse transcription–polymerase chain reaction (RT-PCR) (fig. S2), and with data from public microarray databases, such as the Stanford Microarray Database (*12*).

Although several previous studies have noted the induction of a few individual secretion-related genes by plant defense elicitors, the importance of this induction has only been speculated on (*13*–*17*) and the regulatory mechanism is not known. During SAR, there is a massive buildup of PR proteins in vacuoles and the apoplast. The basal activity of the protein secretory pathway may not be sufficient to accommodate the marked increase in PR protein synthesis. Therefore, we hypothesized that a coordinated up-regulation in the protein secretory machinery is required to ensure proper folding, modification, and transport of PR proteins. Consistent with this hypothesis, the ER-resident gene, *BiP*, was shown to be induced before the accumulation of PR1 (fig. S3) (*16*).

To provide genetic evidence that the up-regulation of the secretion-related genes is essential for SAR, we identified knockout mutants in five secretion-related genes from the Salk Institute transferred DNA (T-DNA) insertion collection (*18*). Mutants of a *calnexin* (Salk_044381; At5g07340) and a *PDI* (Salk_046705; At2g47470) gene showed no significant change in induced resistance. Because the *Arabidopsis* genome contains six calnexin and the related calreticulin genes, and more than 20 *PDI* genes, the lack of a phenotype in these mutants is likely due to functional redundancy. On the other hand, T-DNA insertions in *BiP2* (Salk_047956), *DAD1* (Salk_046070), and *SEC61α* (Salk_034604) all compromised the plant's ability to efficiently secrete PR1 after treating with benzothiadiazole *S*-methylester (BTH, an SA analog) (Fig. 1A). The reduction in PR protein secretion directly correlates with impaired resistance against the bacterial pathogen *Pseudomonas syringae* pv. *maculicola* ES4326 (Fig. 1B). In the *sec61α bip2* and *dad1 bip2* double mutants, less PR1 was secreted and more pathogen growth was detected compared with the single mutants. Thus, an intact and responsive protein secretory pathway is required for SAR.

Table 1. A partial list of primary target genes of NPR1 identified in the microarray experiments. Data from two independent biological replicates are presented. Fold changes (F. C.) and *P*-values were calculated with the MAS 5.0 package, and similar results were obtained with dChip (*21*). Both groups of genes are shown to be significantly induced by a mixed-model ANOVA test with $P = 7.6 \times 10^{-14}$ for the defense genes and $P = 0.003$ for the secretory pathway genes.

Gene description	Locus	Replicate 1		Replicate 2	
		F. C.	*P*-value	F. C.	*P*-value
Defense					
PR-1	At2g14610	42.2	1.0×10^{-6}	256.0	0
PR-5	At1g75040	14.9	0	2.6	0
Endochitinase	At2g43570	2.1	1.8×10^{-4}	2.5	0
Putative disease resistance protein	At4g12010	6.1	5.2×10^{-3}	2.6	2.4×10^{-4}
Disease resistance protein RPP8	At5g43470	2.5	9.2×10^{-5}	2.0	0
Beta-1,3-glucanase	At4g34480	2.0	9.9×10^{-5}	2.8	1.0×10^{-6}
Chitinase	At2g43570	2.1	1.8×10^{-4}	2.5	0
Peroxidase	At5g64120	2.1	4.7×10^{-5}	2.6	0
Endoxyloglucan transferase	At5g57550	3.5	1.1×10^{-5}	29.9	0
Protein folding and secretion					
Signal recognition particle receptor	At2g45770	4.9	3.1×10^{-5}	6.1	0
Sec61α subunit	At2g34250	2.1	5.4×10^{-5}	1.5	0
Sec61β subunit	At2g45070	1.4	4.0×10^{-2}	1.3	1.0×10^{-2}
BiP2	At5g42020	3.2	7.0×10^{-6}	2.5	0
GRP94	At4g24190	7.5	0	2.3	0
DAD1	At1g32210	3.0	1.0×10^{-6}	2.0	0
Protein disulfide-isomerase (PDI)	At2g47470	3.2	3.1×10^{-5}	2.0	1.0×10^{-6}
Protein disulfide-isomerase (PDI)	At3g54960	1.6	8.0×10^{-4}	3.0	1.0×10^{-6}
Calreticulin 3	At1g08450	4.0	0	2.3	0
Calreticulin	At1g09210	4.3	1.0×10^{-6}	3.1	0
Calnexin1	At5g61790	6.1	4.3×10^{-5}	2.6	0
Calnexin 2	At5g07340	1.4	5.0×10^{-6}	2.1	1.2×10^{-5}
Ribophorin I	At2g01720	3.7	8.0×10^{-6}	1.5	1.0×10^{-6}
Tetratricoredoxin	At4g22670	3.2	0	1.9	0
Cyclophilin	At2g47320	4.0	2.0×10^{-6}	1.4	7.9×10^{-5}
Clathrin-coat assembly protein	At1g10730	3.7	5.8×10^{-2}	2.0	4.7×10^{-5}
Transmembrane trafficking protein	At1g14010	4.3	2.2×10^{-4}	2.0	1.0×10^{-6}
Vacuolar sorting receptor	At1g30900	7.0	1.0×10^{-5}	3.5	0

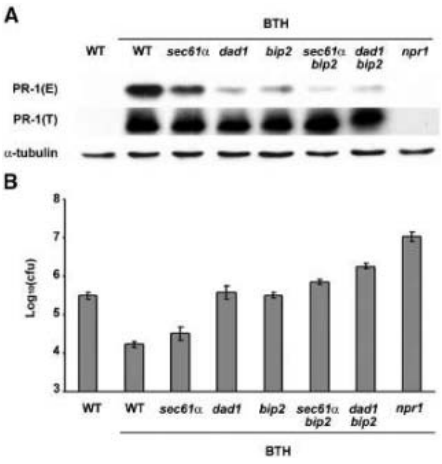

Fig. 1. Effects of mutations in secretion-related genes on PR1 protein secretion and resistance against *Pseudomonas syringae* pv. *maculicola* ES4326 (*Psm* ES4326). (**A**) Immunoblot of PR1 protein in the secretion-related gene mutants. Intercellular wash fluid (IWF) was collected from equal amounts of plant tissue treated with BTH or untreated. As a control, total protein was extracted. Secreted (E) and total (T) PR1 was examined using separate immunoblots with an antibody raised against this protein. An antibody against α-tubulin was then used to probe the total protein blot to confirm equal loading of the samples. The same antibody was also used to probe the IWF blot to demonstrate that no intracellular protein (α-tubulin) leaked out of the cell during IWF preparation (*21*). This experiment was repeated three times with similar results. (**B**) Growth of *Psm* ES4326 in the secretion-related gene mutants after BTH induction. Plants were induced with 60 μM BTH 24 hours before infiltration with *Psm* ES4326 (optical density at 600 nm = 0.001). Uninduced WT plants were infiltrated at the same time. Bacterial growth was monitored 2 days after infection (*27*). Error bars represent 95% confidence limits of log-transformed data from eight independent samples. cfu, colony-forming units.

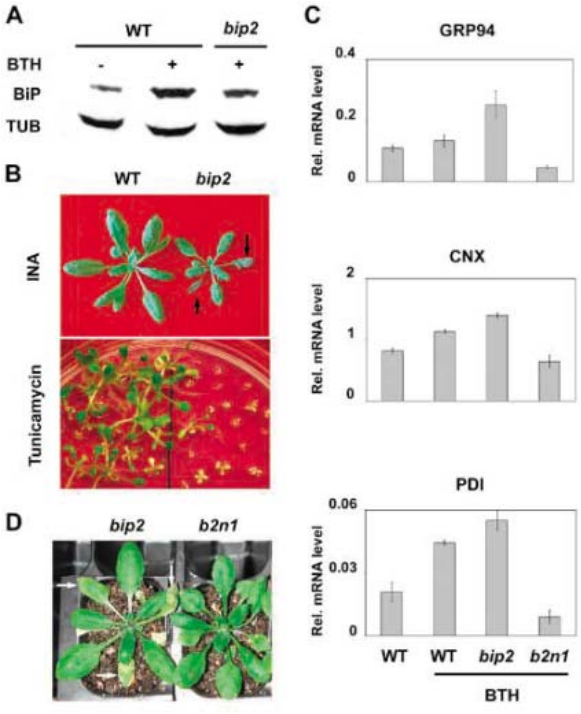

Fig. 2. UPR in the *bip2* mutant after BTH, INA, and tunicamycin treatment. (**A**) Total BiP protein levels in WT and the *bip2* knockout mutant after BTH treatment. BiP protein was detected with a polyclonal antibody (anti-BiP, Santa Cruz Biotechnology) and α-tubulin (TUB) was probed as a loading control. (**B**) Upper panel: Leaf collapse, marked by arrows, observed overnight after INA treatment. Lower panel: Three-week-old seedlings treated with tunicamycin (0.3 μg ml^{-1}) for 5 days during germination. (**C**) Induction of UPR marker genes in *bip2* and *bip2 npr1* (*b2n1*). Real-time RT-PCRs were performed to examine the relative mRNA levels (Rel. mRNA level) of *GRP94*, *CNX* (At5g61790), and *PDI* (At1g21750) normalized to that of ubiquitin. Error bars represent standard deviations from three PCR results. (**D**) Rescue of the BTH-induced leaf collapse phenotype in *bip2* by *npr1*.

The importance of this coordinated induction of *PR* and secretion-related genes by NPR1 was further demonstrated by additional characterization of the *bip2* mutant. In *Arabidopsis*, there are three *BiP* genes (*19*, *20*). Knocking out the NPR1-regulated *BiP2* gene resulted in reduced accumulation of total BiP protein after BTH induction (to ~50% of the wild-type level) (Fig. 2A). As a result, the *bip2* mutant is not only impaired in BTH-induced resistance (Fig. 1B), but also is hypersensitive to treatment of BTH or 2,6-dichoroisonicotinic acid (INA, another SA analog). Application of these chemicals at high concentrations to the *bip2* mutant resulted in a rapid tissue collapse not seen in wild-type (WT) or untreated mutant (Fig. 2B) (*21*). We believe that in the *bip2* plants, the increased PR protein synthesis is not accompanied by a sufficient increase in BiP protein, causing intracellular accumulation of unfolded proteins, leading to an acute unfolded protein response (UPR) in the form of cell death. In mammalian cells, free BiP binds the UPR sensor Ire1 (a kinase and endonuclease on the ER membrane) and prevents it from dimerizing and activating the UPR. When unfolded proteins accumulate, BiP dissociates from Ire1 and binds the unfolded proteins, thus freeing Ire1 to activate UPR (*22*). Indeed, in the *bip2* mutant, several UPR marker genes, which are also NPR1-responsive, are hyperactivated after BTH treatment (Fig. 2C). The *bip2* mutant plants are also more sensitive to inducers of UPR, such as tunicamycin, which causes misfolding of proteins by inhibiting glycosylation (*23*). Whereas WT plants recovered from tunicamycin treatment, *bip2* plants failed to do so (Fig. 2B).

To determine whether the UPR observed in *bip2* was caused by insufficient processing of PR proteins, we introduced the *bip2* mutation into the *npr1* background, in which BTH-induced *PR* gene expression is blocked. Both BTH-induced UPR marker gene expression and cell death were diminished in the *bip2 npr1* double mutant (Fig. 2, C and D). These genetic data clearly illustrate the detrimental effects that can occur when SAR is induced in plants without a sufficient increase in protein folding and secretion capability.

Because the entire protein secretory pathway is coordinately up-regulated by NPR1 during SAR, the regulatory mechanism may involve common elements. To search for such elements, we focused on the 13 ER-resident genes listed in Table 1 and analyzed their promoter regions (1 kb upstream of the start codon) using the MEME program (*24*). A consensus sequence, designated *TL1* (CTGAAGAAGAA), was overrepresented in the promoter regions of all 13 NPR1-responsive ER-resident genes surveyed (Fig. 3A) (P = 0.02), but was absent from related genes not up-regulated by NPR1, such as the other *DAD* (At2g35520) and *Sec61α* (At1g78720).

In an electrophoretic mobility shift assay (EMSA), the *TL1* element was shown to have a specific protein-binding activity, which was completely abolished with changes in the core sequence (*m1*, *m2*, and *TLm* in Fig. 3B). When whole-cell extracts were used, this binding activity was not affected by SA treatment in either WT or *npr1* mutants (Fig. 3C; only *npr1-1* is shown). When nuclear extracts were used instead, the specific binding was enhanced in SA-treated samples, suggesting that the *TL1*-binding protein translocates into the nucleus upon SAR induction (Fig. 3D). Moreover, this translocation was facilitated by NPR1, as indicated by a less profound enhancement of *TL1* binding after SA treatment in *npr1*. Because the induced binding was not completely abolished in *npr1*, we do not exclude the possibility that NPR1 also controls the activation of the *TL1*-binding protein. All of these data are consistent with the facts that the induction of secretion-related genes does not require de novo protein synthesis and that NPR1 is also translocated to the nucleus after SAR induction.

To demonstrate the biological activity of *TL1*, we generated reporter constructs in which the coding sequence of β-glucuronidase (*GUS*) is driven by either the WT *BiP2* promoter or mutant constructs with changes in each of the promoter's three *TL1* elements (Fig. 3E; Sites 1, 2, and 3). These constructs were transformed into WT plants, and the effect of each mutation on promoter activity was analyzed through a GUS assay. As expected, the reporter driven by the WT *BiP2* promoter showed a 4.8-fold

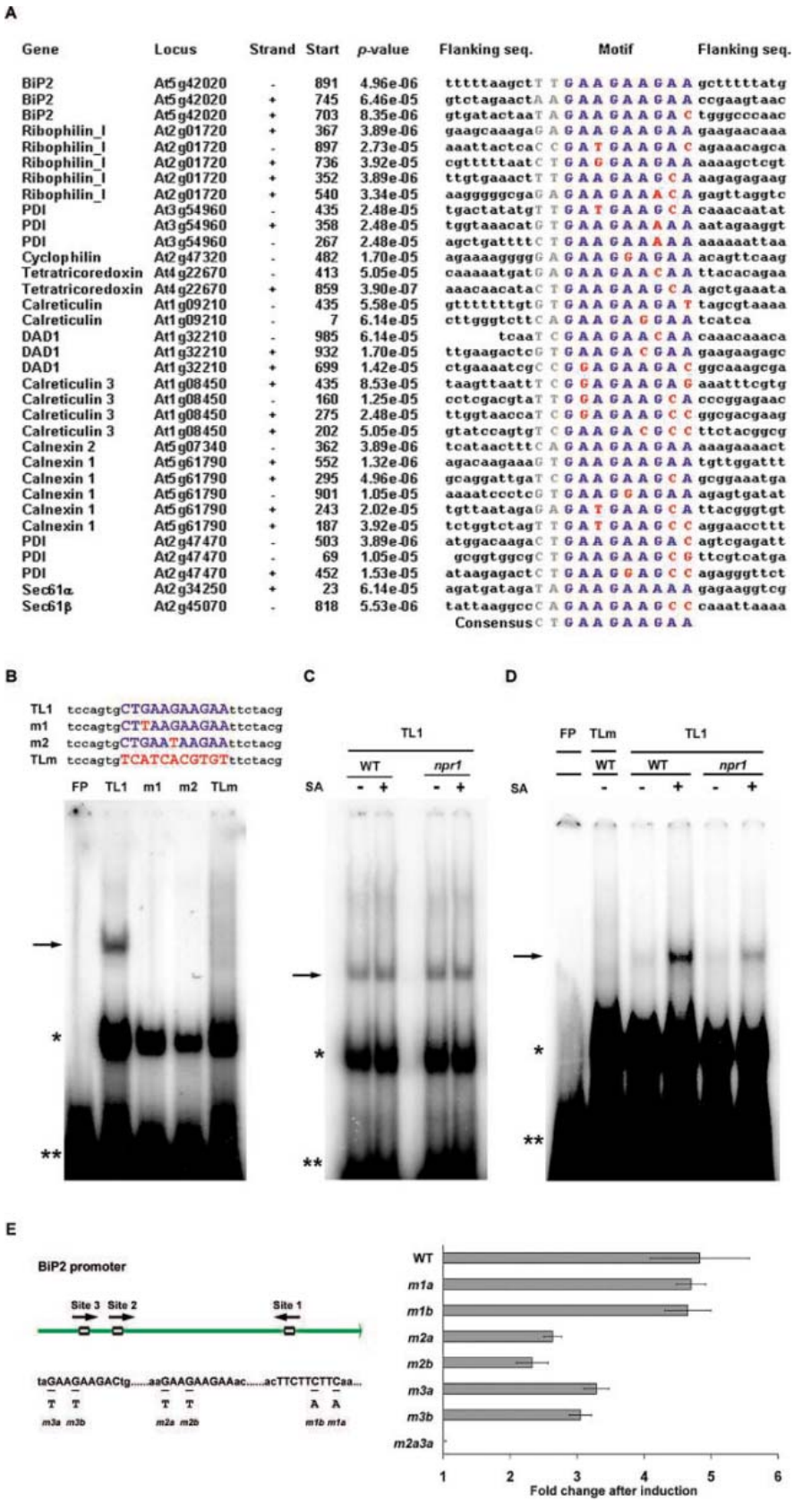

Fig. 3. Characterization of the *TL1* element. (**A**) Discovery of a conserved sequence (*TL1*) in the promoters of all 13 NPR1-regulated ER-resident protein genes (1 kb upstream of the translation start codon) using MEME (*24*). Blue and gray letters represent highly and moderately conserved nucleotides identified by the program, respectively. Variations from the consensus sequence are marked in red. (**B**) EMSA using whole-cell protein extracts and ^{32}P-labeled oligonucleotides *TL1*, *m1*, *m2*, and *TLm*. The arrow indicates the specific DNA-protein band, the single asterisk marks a nonspecific band, and double asterisks indicate the free probes. FP, free probe without protein extract. (**C**) EMSA of *TL1* using whole-cell extracts prepared from WT and *npr1-1* with and without SA induction. (**D**) EMSA of *TL1* using nuclear extracts prepared from WT and *npr1-1* with and without SA treatment. (**E**) Mutant analysis of the *BiP2* promoter. The three putative *TL1* elements found in the *BiP2* promoter (Sites 1, 2, and 3) are indicated by small rectangles and their orientations shown by black arrows. The coding sequence is on the right (green arrow). WT and mutant (*m1a*, *m1b*, *m2a*, *m2b*, *m3a*, *m3b*, and *m2a3a*; the altered nucleotides are underlined) *BiP2* promoters were cloned upstream of the *GUS* coding sequence and transformed into plants. Eight independent T_2 lines were pooled for each construct, and the inducibility of the promoter by INA was measured by quantitative GUS assay. Fold changes were determined using GUS activity ratios between induced and uninduced samples. Error bars represent standard deviations of three measurements.

increase in expression after treatment with INA. When transformed into *npr1*, the WT *BiP2* promoter::GUS reporter showed no induction by INA, consistent with the result from the RNA blot analysis (fig. S2) (*21*). Whereas mutations in Site 1 had little effect on the inducibility of the promoter, mutations in Sites 2 and 3 significantly reduced the induction of the *GUS* gene. Because Sites 2 and 3 are adjacent (30 base pairs apart) (Fig. 3E), we examined whether they can function cooperatively to confer full induction of *BiP2*. Indeed, when both sites were mutated, the reporter showed no induction after INA treatment (Fig. 3E, *m2a3a*).

Taken together, our microarray analysis, EMSA, and promoter mutagenesis data suggest that *TL1* is indeed a cis-element involved in SA induction of secretion-related genes via NPR1. The transcription factor that controls *TL1* is unlikely a TGA factor because *TL1* is distinct from the TGA-binding *as-1* element. Furthermore, in a *tga2 tga5 tga6* triple mutant, the induction of *PR* genes is diminished (*25*), whereas secretion-related genes are still induced (fig. S4). Therefore, we believe that NPR1 regulates secretion-related and *PR* genes through different transcription factors and cis-elements.

Our finding sheds new light on the induction mechanism of SAR by demonstrating that NPR1 not only directly induces the *PR* genes but also prepares the cell for secretion of the *PR* proteins by first making more secretory machinery components. A similar phenomenon is also observed in mammals in which the secretory machinery in B cells is up-regulated before the B cells start secreting antibodies (*26*). Further study may clarify whether this commonality reflects any conserved regulatory mechanisms.

References and Notes

1. W. E. Durrant, X. Dong, *Annu. Rev. Phytopathol.* **42**, 185 (2004).
2. X. Dong, *Curr. Opin. Plant Biol.* **7**, 547 (2004).
3. K. Maleck *et al.*, *Nat. Genet.* **26**, 403 (2000).
4. J. Glazebrook *et al.*, *Plant J.* **34**, 217 (2003).
5. Y. Tao *et al.*, *Plant Cell* **15**, 317 (2003).

6. L. C. Van Loon, E. A. Van Strien, *Physiol. Mol. Plant Pathol.* **55**, 85 (1999).
7. M. Kinkema, W. Fan, X. Dong, *Plant Cell* **12**, 2339 (2000).
8. A. Vitale, J. Denecke, *Plant Cell* **11**, 615 (1999).
9. E. S. Trombetta, A. J. Parodi, *Annu. Rev. Cell Dev. Biol.* **19**, 649 (2003).
10. J. Fu, G. Kreibich, *J. Biol. Chem.* **275**, 3984 (2000).
11. T. M. Chu, B. Weir, R. Wolfinger, *Math. Biosci.* **176**, 35 (2002).
12. http://genome-www5.stanford.edu
13. H. Walther-Larsen, J. Brandt, D. B. Collinge, H. Thordal-Christensen, *Plant Mol. Biol.* **21**, 1097 (1993).
14. J. Denecke *et al.*, *Plant Cell* **7**, 391 (1995).
15. P. Wick *et al.*, *Plant Physiol.* **132**, 343 (2003).
16. E. P. Jelitto-Van Dooren, S. Vidal, J. Denecke, *Plant Cell* **11**, 1935 (1999).
17. M. Petersen *et al.*, *Cell* **103**, 1111 (2000).
18. J. M. Alonso *et al.*, *Science* **301**, 653 (2003).
19. B. L. Lin *et al.*, *Cell Stress Chaperones* **6**, 201 (2001).
20. S. J. Noh, C. S. Kwon, D. H. Oh, J. S. Moon, W. I. Chung, *Gene* **311**, 81 (2003).
21. D. Wang, N. D. Weaver, M. Kesarwani, X. Dong, data not shown.
22. C. Patil, P. Walter, *Curr. Opin. Cell Biol.* **13**, 349 (2001).
23. I. M. Martinez, M. J. Chrispeels, *Plant Cell* **15**, 561 (2003).
24. T. L. Bailey, C. Elkan, *Proc. Int. Conf. Intell. Syst. Mol. Biol.* **2**, 28 (1994).
25. Y. Zhang, M. J. Tessaro, M. Lassner, X. Li, *Plant Cell* **15**, 2647 (2003).
26. E. van Anken *et al.*, *Immunity* **18**, 243 (2003).
27. H. Cao, S. A. Bowling, S. Gordon, X. Dong, *Plant Cell* **6**, 1583 (1994).

28. We thank P. Benfey, W. Durrant, J. Siedow, T. P. Sun, D. Thiele, and L. Tyler for critical readings of the manuscript and helpful discussion and X. Li for providing the *tga2 tga5 tga6* triple mutant. This project is supported by a NSF 2010 grant and a grant from the U.S. Department of Agriculture.

Supporting Online Material

www.sciencemag.org/cgi/content/full/308/5724/1036/DC1
Materials and Methods
Figs. S1 to S4
Table S1
References and Notes

16 December 2004; accepted 25 February 2005
10.1126/science.1108791

On the Origin of Leprosy

Marc Monot,[1]* Nadine Honoré,[1]* Thierry Garnier,[1] Romulo Araoz,[1] Jean-Yves Coppée,[2] Céline Lacroix,[2] Samba Sow,[3] John S. Spencer,[4] Richard W. Truman,[5] Diana L. Williams,[5] Robert Gelber,[6] Marcos Virmond,[7] Béatrice Flageul,[8] Sang-Nae Cho,[9] Baohong Ji,[10] Alberto Paniz-Mondolfi,[11] Jacinto Convit,[11] Saroj Young,[12] Paul E. Fine,[12] Voahangy Rasolofo,[13] Patrick J. Brennan,[4] Stewart T. Cole[1]†

Leprosy, a chronic human disease with potentially debilitating neurological consequences, results from infection with *Mycobacterium leprae*. This unculturable pathogen has undergone extensive reductive evolution, with half of its genome now occupied by pseudogenes. Using comparative genomics, we demonstrated that all extant cases of leprosy are attributable to a single clone whose dissemination worldwide can be retraced from analysis of very rare single-nucleotide polymorphisms. The disease seems to have originated in Eastern Africa or the Near East and spread with successive human migrations. Europeans or North Africans introduced leprosy into West Africa and the Americas within the past 500 years.

Comparative genomics enables us to establish solid genealogical relationships with greater precision than ever before. Leprosy (*1*) has plagued human populations for thousands of years and puzzled scientists since the identification of its etiological agent, *Mycobacterium leprae*, by Hansen in 1873 (*2*). The main difficulties of working with *M. leprae* are that it cannot be grown in axenic culture and that its doubling time in tissue is slow, nearly 13 days (*3*). It was only when it was discovered that the nine-banded armadillo, *Dasypus novemcinctus*, could be infected (*4*) that sufficient quantities of *M. leprae* were obtained for biological and immunological analysis. Comparison of the genome sequence of the armadillo-passaged strain of *M. leprae* from Tamil Nadu, India (TN strain) with that of the close relative *Mycobacterium tuberculosis* (*5*), led to a major breakthrough (*6*). *M. leprae* was shown to have embarked upon a path of reductive evolution in which the genome underwent downsizing and accumulated more than 1130 pseudogenes. The concomitant loss of catabolic and respiratory functions appears to have resulted in severe metabolic constraints (*6*, *7*).

To establish whether all strains of *M. leprae* had undergone similar events and to determine their level of relatedness, we used technological approaches that have successfully detected polymorphic regions in the *M. tuberculosis* complex (*8*–*10*). First, genomic DNA, prepared from seven different strains of leprosy bacilli (Table 1), was hybridized to microarrays corresponding to the complete genome of the TN strain, but no evidence for further gene loss was uncovered in these isolates (fig. S1). Second, to establish whether differences existed in the copy number of insertion-sequence-like, dispersed repetitive sequences, quantitative polymerase chain reaction was performed to target the repetitive sequences RLEP, REPLEP, LEPREP, and LEPRPT (*11*). Again, within the limits of sensitivity of this approach, no differences were detected between the TN strain and the other isolates (fig. S2).

A major source of variability in tubercle bacilli is the mycobacterial interspersed repetitive unit (MIRU), which serves as the basis of a robust typing system that exploits differences in the variable number of the tandem repeats

[1]Unité de Génétique Moléculaire Bactérienne, Institut Pasteur, Paris, France. [2]PF2, Génopole, Institut Pasteur, Paris, France. [3]Centre National d'Appui à la lutte Contre la Maladie, Bamako, Mali. [4]Department of Microbiology, Immunology, and Pathology, Colorado State University, Fort Collins, Colorado 80523–1682, USA. [5]National Hansen's Disease Program, DHHS/HRSA/BPHC, Lousiana State University, Baton Rouge, Lousiana 70894, USA. [6]Leonard Wood Memorial Center for Leprosy Research, Cebu, Philippines. [7]Instituto Lauro de Souza Lima, Bauru, São Paulo, Brazil. [8]Hôpital Saint-Louis, Paris, France. [9]Yonsei University College of Medicine, Seoul, Republic of Korea. [10]Bactériologie-Hygiène, Faculté de Médecine Pitié-Salpêtrière, Paris, France. [11]Instituto de Biomedicina, Caracas, Venezuela. [12]London School of Hygiene and Tropical Medicine, London, UK. [13]Institut Pasteur de Madagascar, Antananarivo, Madagascar.

*These authors contributed equally to this work.
†To whom correspondence should be addressed: E-mail: stcole@pasteur.fr

Table 1. Strains of armadillo-derived *M. leprae* and VNTR profile.

Strain	Patient's country of origin	Source	3-Hexa	21-TTC	9-GTA	14-AT	15-AT	17-AT	18-AT
Tamil Nadu*	India	IP	3	21	9	14	15	17	18
Africa	Ethiopia	IP	3	29	8	14	19	13	13
India 2	India	IP	3	15	11	18	14	13	9
Br4923	Brazil	NHDP	3	12	12	20	20	15	18
NHDP98	Mexico	CSU/NHDP	3	10	9	22	14	11	12
Thai-53	Thailand	CSU/NHDP	3	15	9	16	17	10	13
NHDP63	USA	CSU/NHDP	3	10	10	18	18	13	16

*Numbers refer to the repeat copy number for the Tamil Nadu strain (*11*), whereas numbers in the rest of the table are the copy numbers found in the respective isolates. IP, Institut Pasteur; NHDP, National Hansen's Disease Program; CSU, Colorado State University.

(VNTR) that make up this repetitive element (*12*). Unlike *M. tuberculosis,* none of the 20 MIRU loci in the TN strain contains tandem repeats of the element (*11*) and, on examination of the additional strains, no copy number differences were detected. Furthermore, the 20 MIRUs were of identical sequence in all seven strains studied (Table 1). Seven other VNTR, with two to six base-pair (bp) repeats, were also targeted, because some of them have proved useful for tracking strains over short epidemiological distances (*13*–*16*). No variation was seen in a hexanucleotide repeat situated within the coding sequence of the *sigA* (*rpoT*) gene (*17*), whereas on examination of two trinucleotide repeats and four dinucleotide repeats, located in pseudogenes or noncoding regions of the genome, extensive differences were seen in copy number (Table 1). However, as expected for such sequences, which are highly prone to slipped-strand mispairing during replication (*18*), the level of variability was too great to allow patterns to be detected.

Although these results rule out the existence of the most likely insertion and deletion events, they are less informative about genome topology and global organization. These features were surveyed by fingerprinting and end-sequencing 1466 cosmids from a library of a second Indian strain of *M. leprae*, leading to an integrated genome map that showed perfect cocircularity with that of the TN strain (*19*, *20*). To increase the likelihood of detecting single-nucleotide polymorphisms (SNPs), selected genes, noncoding regions, and pseudogenes were sequenced from a Brazilian strain, Br4923 (table S1). This strain was chosen for two reasons: the relative geographic remoteness of the country and the severity of the disease burden in Brazil, which is second highest worldwide after India (*1*). By this means, five SNPs were revealed in 142 kb of sequenced DNA, one in an apparently noncoding region and four in pseudogenes. When all seven strains were analyzed, only three of the SNPs were found in two or more of the strains tested (Fig. 1A), whereas the remaining two were restricted to the TN strain of *M. leprae.* Overall, the SNP frequency observed in *M. leprae* of ~1 per 28 kb was significantly less than that seen in other human pathogens, such as the tubercle bacilli (*8*, *9*, *21*, *22*), *Salmonella typhi* (*23*), and *Helicobacter pylori* (*24*) (Table 2). Taken together, these findings indicate that the *M. leprae* genome is exceptionally well conserved and that the leprosy bacillus is highly clonal (*25*).

To gain insight into the worldwide distribution of the *M. leprae* SNPs, we sought the three informative SNPs in a total of 175 clinical and laboratory specimens from 21 countries and all five continents. We discovered that of a possible 64 permutations only 4 occurred (Table 3 and table S2), referred to as SNP types 1 to 4. When the VNTR panel was probed, extensive variability was found for six VNTRs (table S2), but no particular VNTR pattern was associated with a given SNP type. In contrast, a correlation exists between the geographical origin of the leprosy patient and the SNP profile, because type 1 occurs predominantly in Asia, the Pacific region, and East Africa, type 4 in West Africa and the Caribbean region, and type 3 in Europe, North Africa, and the Americas. SNP type 2 is the rarest and has only been detected in Ethiopia, Malawi, Nepal/North India, and New Caledonia.

Ancient texts describe the existence of leprosy in China, India, and Egypt in about 600 BC, and skeletal remains bearing hallmarks of the disease have been found in Egypt (*26*). Leprosy is believed to have originated in the Indian subcontinent and to have been introduced into Europe by Greek soldiers returning from the Indian campaign of Alexan-

Table 2. Comparison of SNP frequency in other bacterial pathogens.

Pathogen	SNP frequency/bp	Reference
M. leprae	1 in 28,400	This work
M. tuberculosis complex	1 in ~3,000	(*21*, *22*)
S. typhi	1 in 1,112	(*23*)
H. pylori	1 in 3.2	(*24*)

Table 3. SNP analysis of *M. leprae* from different countries.

Country	SNP type 1	SNP type 2	SNP type 3	SNP type 4
New Caledonia	3	1	3	
Philippines	19		2	
Korea	3		2	
Thailand	1			
Nepal/North India	23	5		
South India	4			
Madagascar	6			
Ethiopia		2		
Malawi	4	6		
Mali				31
Ivory Coast				6
Guinea				1
Senegal				2
Morocco			2	
France			2	
Brazil			12	2
French West Indies	4		2	14
Venezuela			5	
Mexico			1	
United States			3	
WARM*			4	
Total	67	14	38	56

*Wild armadillos from Louisiana, USA.

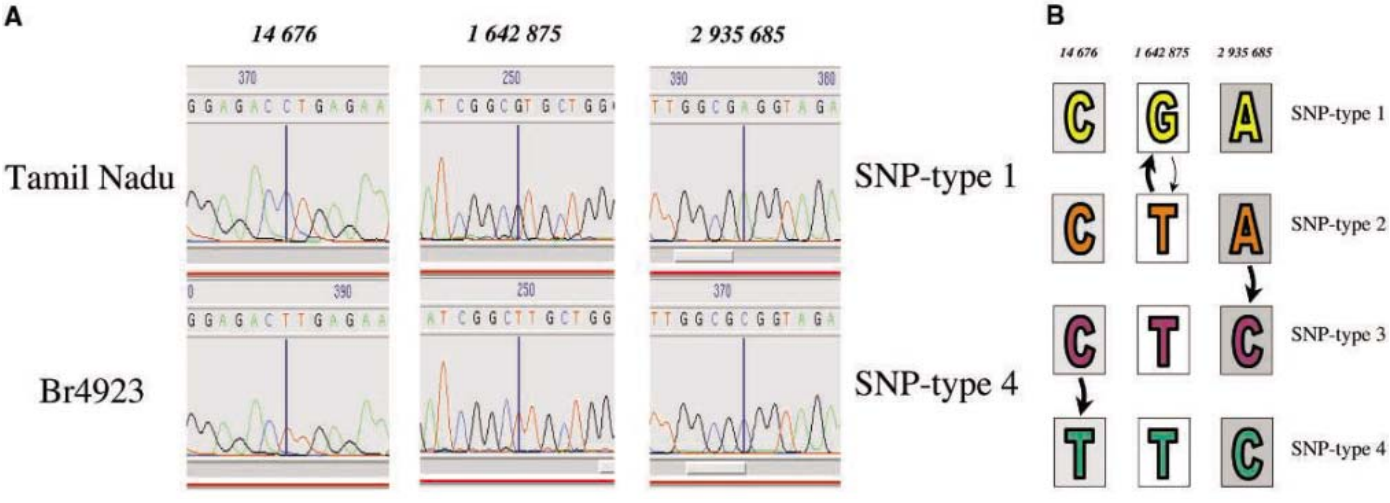

Fig. 1. SNP analysis of isolates of different geographical origin and parsimony. (**A**) Comparison of polymorphic sites in the genomes of the TN and Br4923 strains by automated DNA sequencing. Coordinates are the position in the genome of the TN strain, and the vertical bar indicates the polymorphic base. (**B**) The most parsimonious route to account for the four SNP types. Bold arrows indicate the most likely direction, based on historical and geographic considerations; the faint arrow denotes an alternative route.

der the Great (*26*). From Greece, the disease is thought to have spread around the Mediterranean basin, with the Romans introducing leprosy into the Western part of Europe. Little is known about its presence in sub-Saharan Africa except that the disease was present prior to the colonial era. From India, leprosy is thought to have spread to China and then to Japan, reaching Pacific Islands like New Caledonia as recently as the 19th century.

Our results provide evidence for a general evolutionary scheme for *M. leprae* and, on the basis of our interpretation of the SNP data, offer two alternative conclusions for the global spread of leprosy that differ from classic explanations. Two equally plausible evolutionary scenarios are possible (Figs. 1B and 2). In the first, SNP type 2, from East Africa/Central Asia, preceded type 1, which migrated eastward, and type 3, which disseminated westward in human populations, before giving rise to type 4. In the second scenario, type 1 was the progenitor of type 2, with SNP types 3 and 4 following in that order.

Leprosy was most likely introduced into West Africa by infected explorers, traders, or colonialists of European or North African descent, rather than by migrants from East Africa, because SNP type 4 is much closer to type 3 than to type 1 (Fig. 1B). West and southern Africa are thought to have been settled >50,000 years ago by migrants from East Africa before the arrival of humans in Eurasia (*27*, *28*). It seems unlikely that early humans brought leprosy into West Africa with them unless that particular bacterial clone has since been replaced. From West Africa, leprosy was then introduced by the slave trade in the 18th century to the Caribbean islands, Brazil, and probably other parts of South America, because isolates of *M. leprae* with the same SNP type, 4, are found there as in West Africa.

The strain of *M. leprae* responsible for disease in most of the Americas is closest to the European/North African variety (Fig. 1B), which indicates that colonialism and emigration from the old world most probably contributed to the introduction of leprosy into the new world. For instance, in the 18th and 19th centuries, when the midwestern states of the United States were settled by Scandinavian immigrants, many cases of leprosy were reported and, at that time, a major epidemic was under way in Norway (*26*). Further support for this hypothesis is provided by the finding that wild armadillos from Louisiana, which are naturally infected with *M. leprae*, harbor the European/North African SNP type 3 strain, indicating that they were contaminated by human sources. Although most mycobacteria occur in the soil, there is no convincing evidence for an environmental reservoir of *M. leprae* and, apart from armadillos, which have limited geographical distribution and only very recently became infected, there is no known animal source of the pathogen. Although an ancient zoonotic origin cannot be excluded, insect bites may also have been a possible route of early human infection, particularly as recent studies show that *M. ulcerans*, a related pathogen with many pseudogenes, appears to be transmitted by aquatic insects (*29*).

In conclusion, *M. leprae,* with its exceptionally stable genome, is a helpful marker for tracking the migration of peoples and retracing the steps that led to modern human populations. In this respect, it complements *H. pylori,* which is considerably more diverse and thus allows finer understanding of the ethnic origin of humans (*30*). It is noteworthy that the greatest variety of SNP types in the leprosy bacillus is found in islands such as the French West Indies and New Caledonia (Fig. 2), reflecting the passage of, and settlement by, different human populations. Finally, the remarkable clonality seen in isolates of *M. leprae* indicates that genome decay occurred prior to the global spread of leprosy and that it has not accelerated substantially since.

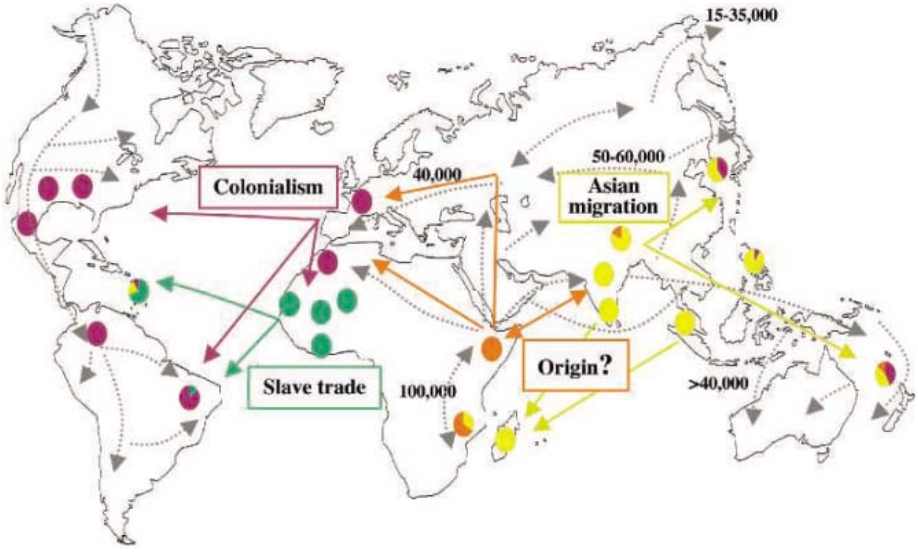

Fig. 2. Dissemination of leprosy in the world. The circles indicate the country of origin of the samples examined and their distribution into the four SNP types, which are color coded as in Fig. 1B. The colored arrows indicate the direction of human migrations predicted by, or inferred from, our SNP analysis; gray arrows correspond to the migration routes of humans derived from genetic, archaeological, and anthropological studies, with the estimated time of migration in years (*27*, *28*).

References and Notes

1. W. J. Britton, D. N. J. Lockwood, *Lancet* **363**, 1209 (2004).
2. G. H. A. Hansen, *Norsk Mag. Laegervidenskaben* **4**, 1 (1874) (supplement).
3. C. C. Shepard, D. H. McRae, *J. Bacteriol.* **89**, 365 (1965).
4. W. K. Kirchheimer, E. E. Storrs, *Int. J. Lepr.* **39**, 693 (1971).
5. S. T. Cole *et al.*, *Nature* **393**, 537 (1998).
6. S. T. Cole *et al.*, *Nature* **409**, 1007 (2001).
7. K. Eiglmeier *et al.*, *Lepr. Rev.* **72**, 387 (2001).
8. R. Brosch, A. S. Pym, S. V. Gordon, S. T. Cole, *Trends Microbiol.* **9**, 452 (2001).
9. R. Brosch *et al.*, *Proc. Natl. Acad. Sci. U.S.A.* **99**, 3684 (2002).
10. P. Supply *et al.*, *Mol. Microbiol.* **36**, 762 (2000).
11. S. T. Cole, P. Supply, N. Honoré, *Lepr. Rev.* **72**, 449 (2001).
12. E. Mazars *et al.*, *Proc. Natl. Acad. Sci. U.S.A.* **13**, 1901 (2001).
13. Y. C. Shin, H. Lee, G. P. Walsh, J. D. Kim, S. N. Cho, *J. Clin. Microbiol.* **38**, 4535 (2000).
14. R. Truman, A. B. Fontes, A. B. de Miranda, P. Suffys, T. Gillis, *J. Clin. Microbiol.* **42**, 2558 (2004).
15. N. A. Groathouse *et al.*, *J. Clin. Microbiol.* **42**, 1666 (2004).
16. S. K. Young *et al.*, *J. Clin. Microbiol.* **42**, 4931 (2004).
17. M. Matsuoka *et al.*, *Int. J. Lepr. Mycobact. Dis.* **68**, 121 (2000).
18. S. T. Lovett, *Mol. Microbiol.* **52**, 1243 (2004).
19. K. Eiglmeier, S. Simon, T. Garnier, S. T. Cole, *Lepr. Rev.* **72**, 462 (2001).
20. K. Eiglmeier, N. Honoré, S. A. Woods, B. Caudron, S. T. Cole, *Mol. Microbiol.* **7**, 197 (1993).
21. R. D. Fleischmann *et al.*, *J. Bacteriol.* **184**, 5479 (2002).
22. T. Garnier *et al.*, *Proc. Natl. Acad. Sci. U.S.A.* **100**, 7877 (2003).
23. C. Kidgell *et al.*, *Infect. Genet. Evol.* **2**, 39 (2002).
24. D. Falush *et al.*, *Science* **299**, 1582 (2003).
25. J. M. Smith, N. H. Smith, M. O'Rourke, B. G. Spratt, *Proc. Natl. Acad. Sci. U.S.A.* **90**, 4384 (1993).
26. S. G. Browne, in *Leprosy*, R. C. Hastings, Ed. (Churchill Livingstone, Edinburgh, 1985).
27. P. A. Underhill *et al.*, *Nat. Genet.* **26**, 358 (2000).
28. L. L. Cavalli-Sforza, M. W. Feldman, *Nat. Genet.* **33** (suppl.), 266 (2003).
29. L. Marsollier *et al.*, *Appl. Environ. Microbiol.* **68**, 4623 (2002).
30. T. Wirth *et al.*, *Proc. Natl. Acad. Sci. U.S.A.* **101**, 4746 (2004).

31. We thank S. Brisse, R. Brosch, S. V. Gordon, R. Davies, and C. Morey for their help, advice, and encouragement, and the patients and staff of the various leprosy clinics for their invaluable participation. The DNA sequences of SNP-containing regions have been deposited at GenBank with accession numbers AY960580 to AY960582. This work received the financial support of the Institut Pasteur, the Association Française Raoul Follereau, Lepra, the Consortium National de Recherche en Génomique (RNG program), and the NIH National Institute of Allergy and Infectious Diseases (grant RO1-AI47197-01A1 and contract NO1-AI25469).

Supporting Online Material

www.sciencemag.org/cgi/content/full/308/5724/1040/DC1
Materials and Methods
Figs. S1 and S2
Tables S1 to S3

13 January 2005; accepted 22 March 2005
10.1126/science/1109759

Obesity and Metabolic Syndrome in Circadian *Clock* Mutant Mice

Fred W. Turek,[1,3] Corinne Joshu,[3,4*] Akira Kohsaka,[3,4*] Emily Lin,[3,4*] Ganka Ivanova,[2,4] Erin McDearmon,[3,5] Aaron Laposky,[3] Sue Losee-Olson,[3] Amy Easton,[3] Dalan R. Jensen,[6] Robert H. Eckel,[6] Joseph S. Takahashi,[1,3,5] Joseph Bass[2,3,4,†]

The CLOCK transcription factor is a key component of the molecular circadian clock within pacemaker neurons of the hypothalamic suprachiasmatic nucleus. We found that homozygous *Clock* mutant mice have a greatly attenuated diurnal feeding rhythm, are hyperphagic and obese, and develop a metabolic syndrome of hyperleptinemia, hyperlipidemia, hepatic steatosis, hyperglycemia, and hypoinsulinemia. Expression of transcripts encoding selected hypothalamic peptides associated with energy balance was attenuated in the *Clock* mutant mice. These results suggest that the circadian clock gene network plays an important role in mammalian energy balance.

Major components of energy homeostasis, including the sleep-wake cycle, thermogenesis, feeding, and glucose and lipid metabolism, are subjected to circadian regulation that synchronizes energy intake and expenditure with changes in the external environment imposed by the rising and setting of the sun. The neural circadian clock located within the hypothalamic suprachiasmatic nucleus (SCN) orchestrates 24-hour cycles in these behavioral and physiological rhythms (*1*–*3*). However, the discovery that clock genes can regulate circadian rhythmicity in vitro in other central as well as peripheral tissues, including those involved in nutrient homeostasis (e.g., mediobasal hypothalamus, liver, muscle, and pancreas), indicates that circadian and metabolic processes are linked at multiple levels (*4*–*9*). The recent finding that changes in the ratio of oxidized to reduced nicotinamide adenine dinucleotide phosphate control the transcriptional activity of the basic helix-loop-helix (bHLH) protein NPAS2—a homolog of a primary circadian gene, *Clock*—suggests that cell redox may couple the expression of metabolic and circadian genes (*10*). Mice harboring a mutation in *Clock* show profound changes in circadian rhythmicity (*11*) and offer an experimental genetic model to analyze the link among circadian gene networks, behavior, and metabolism in vivo.

Positional cloning and transgenic rescue of normal circadian phenotype identified *Clock* as a member of the bHLH Per-Arnt-Sim (PAS) transcription factor family (*12*, *13*). Relative to wild-type mice, the most pronounced alteration in circadian phenotype in *Clock* mutants is a 1-hour increase in the free-running rhythm of locomotor activity in heterozygous mice in constant darkness (DD) and a 3- to 4-hour increase (i.e., period = 27 to 28 hours in DD) in circadian period in homozygous mice, which is often followed by a total breakdown of circadian rhythmicity (i.e., arrhythmicity) after a few weeks in DD.

Although previous studies that used running wheel behavior as a marker of locomotor activity did not reveal major differences between homozygous *Clock* mutant and wild-type mice maintained on a light-dark (LD) cycle, use of infrared beam crossing to monitor total activity revealed a significant increase in activity during the light phase and a change in the temporal pattern of total activity during the dark phase (Fig. 1A) (*14*). In particular, wild-type mice showed two pronounced peaks of activity—one occurring after lights off, the other before lights on—whereas these peaks were attenuated in *Clock* mutant mice. Surprisingly, despite there being a clear (but dampened) diurnal rhythm in locomotor activity in *Clock* mutant mice (Fig. 1B), the diurnal rhythm in food intake was severely altered in these

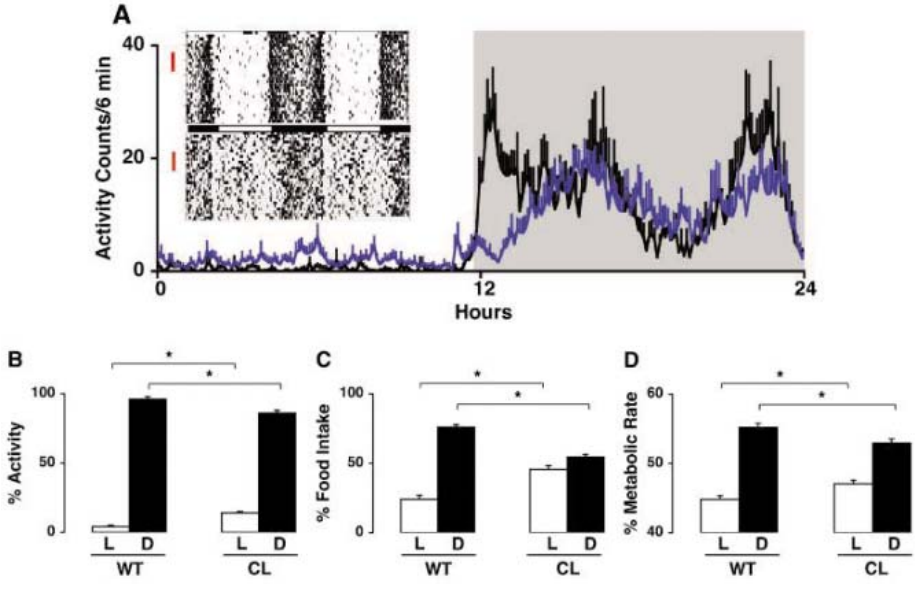

Fig. 1. Altered diurnal rhythms in locomotor activity, feeding, and metabolic rate in *Clock* mutant mice. (**A**) Activity counts over the 24-hour cycle during light (unshaded) and dark (shaded) periods [wild-type, $n = 5$, black line; *Clock*, $n = 9$, blue line]. Inset: Actograms showing locomotor activity over a 30-day period in representative adult wild-type (top) and *Clock* mutant (bottom) mice individually housed in 12:12 LD (at 23°C) and provided food and water ad libitum. Activity bouts were analyzed using ClockLab software in 6-min intervals across 7 days of recording (selected days are indicated by red vertical lines to the left of the actograms). (**B**) Diurnal rhythm of locomotor activity for mice in (A). Activity counts were accumulated over the 12-hour light and 12-hour dark periods and are expressed in each period as a percentage of total 24-hour activity (*$P < 0.05$). Total activity over the 24-hour period was similar between wild-type (WT) and *Clock* mutant (CL) genotypes. (**C**) Diurnal rhythm of food intake. Different groups of adult WT ($N = 7$) and *Clock* mutant ($N = 5$) mice were maintained on a regular diet (10% kcal/fat), and food intake (in grams) was measured during light and dark periods. Results shown are average food intake during light and dark periods as a percentage of total food intake (*$P < 0.001$). (**D**) Diurnal rhythm of metabolic rate. Metabolic rate was determined in additional groups of WT ($N = 7$) and *Clock* mutant ($N = 9$) mice by indirect calorimetry under 12:12 LD conditions over a 3-day continuous monitoring period (*$P < 0.05$). Results shown are average metabolic rates during the light and dark periods as a percentage of total metabolic rate. All results shown are expressed as group means ± SEM.

[1]Department of Neurology and [2]Department of Medicine, Feinberg School of Medicine, [3]Department of Neurobiology and Physiology, Northwestern University, Evanston, IL 60208, USA. [4]Evanston Northwestern Healthcare (ENH) Research Institute, Evanston, IL 60208, USA. [5]Howard Hughes Medical Institute, Chevy Chase, MD 20815, USA. [6]Department of Medicine, University of Colorado at Denver and Health Sciences Center, Aurora, CO 80045, USA.

*These authors contributed equally to this work.
†To whom correspondence should be addressed. E-mail: j-bass@northwestern.edu

mice (Fig. 1C): Only 53% of the food intake occurred during the dark phase in *Clock* mutant mice, versus 75% in wild-type mice. In a preliminary analysis, we found that the diurnal rhythm of food intake was already attenuated in 3-week-old mice before an increase in weight (fig. S1). Similarly, the rhythm in energy expenditure, as measured by respiratory gas analysis, was attenuated in the *Clock* mutant mice (Fig. 1D). Overall there was a net 10% decrease in energy expenditure in the mutants.

Clock mutant mice fed either a regular or high-fat diet showed a significant increase in energy intake and body weight (Fig. 2, A and B). In *Clock* mutant and wild-type adult mice fed either a control or high-fat diet for a period of 10 weeks beginning at 6 weeks of age (Fig. 2C), the increase in body weight was 24% in wild-type and 29% in *Clock* mutant mice fed a regular diet, versus 38% in wild-type and 49% in *Clock* mutant mice fed a high-fat diet. Comparison of somatic growth and solid organ mass did not reveal genotype-specific differences. Instead, the marked weight gain in *Clock* mutants fed a regular diet was attributable to a 65% increase in lean mass and a 35% increase in fat mass, whereas in mutants fed a high-fat diet, the weight gain was due to a 25% increase in lean mass and a 75% increase in fat mass relative to wild-type control mice (fig. S2).

Because the *Clock* mutation could affect early fetal growth and development, we analyzed the body weights of *Clock* and littermate pups throughout the first 8 weeks of life. Body weights were similar in *Clock* mutant and wild-type mice during the first 5 weeks, but by 6 weeks of age *Clock* mutant mice were consistently heavier (Fig. 2D), which suggests that the mutation did not affect fetal growth or nutrition.

We next investigated whether the *Clock* mutation altered the adipose–central nervous system (CNS) axis that regulates feeding and energy expenditure. Histological analysis revealed adipocyte hypertrophy and lipid engorgement of hepatocytes with prominent glycogen accumulation (fig. S3A) in *Clock* mice fed a high-fat diet relative to wild-type controls; these are hallmarks of diet-induced obesity in wild-type mice. At 6 to 7 months of age, *Clock* mutant mice also had hypercholesterolemia, hypertriglyceridemia, hyperglycemia, and hypoinsulinemia (Table 1). In addition, serum leptin levels increased during the light phase in *Clock* mutant mice fed a regular diet; this increase was enhanced in mice fed a high-fat diet (fig. S3B). These markers of metabolic dysregulation were not due to an increase in glucocorticoid production, because levels of corticosterone were lower in the *Clock* mutant mice across the 24-hour LD cycle (wild-type, 5.5 ± 1.4 μg/dl; *Clock* mutant, 2.6 ± 0.4 μg/dl; $P < 0.05$). Thus, the *Clock* mutant mice developed a spectrum of tissue and biochemical abnormalities that are hallmarks of metabolic disease.

To explore whether the *Clock* mutation affects expression of neuropeptides involved in appetite regulation and energy balance, we analyzed transcripts corresponding to selected orexigenic and anorexigenic neuropeptides expressed in the mediobasal hypothalamus (MBH). We studied the orexin transcript because the orexinergic system is involved in both feeding and sleep-wake regulation (*15*, *16*); we also studied the transcripts for ghrelin and CART (cocaine- and amphetamine-regulated transcript) because the corresponding genes contain CLOCK-responsive E-box elements (*17*, *18*). In addition, we examined the expression of a second circadian clock gene, *Per2*, which has a diurnal rhythm of expression in the retrochiasmatic area. The expression levels of *Per2*, *orexin*, and *ghrelin* mRNA were markedly reduced in *Clock* mutant mice at virtually all time points of the 12L:12D cycle (Fig. 3). A small but significant decrease in the expression level of *CART* in *Clock* mutant mice occurred at the beginning and end of the 12-hour light phase (Fig. 3).

These broad effects of the *Clock* gene mutation on nutrient regulation reveal an unforeseen role for the circadian clock system in regulating more than just the timing of food intake and metabolic processes. The effect of

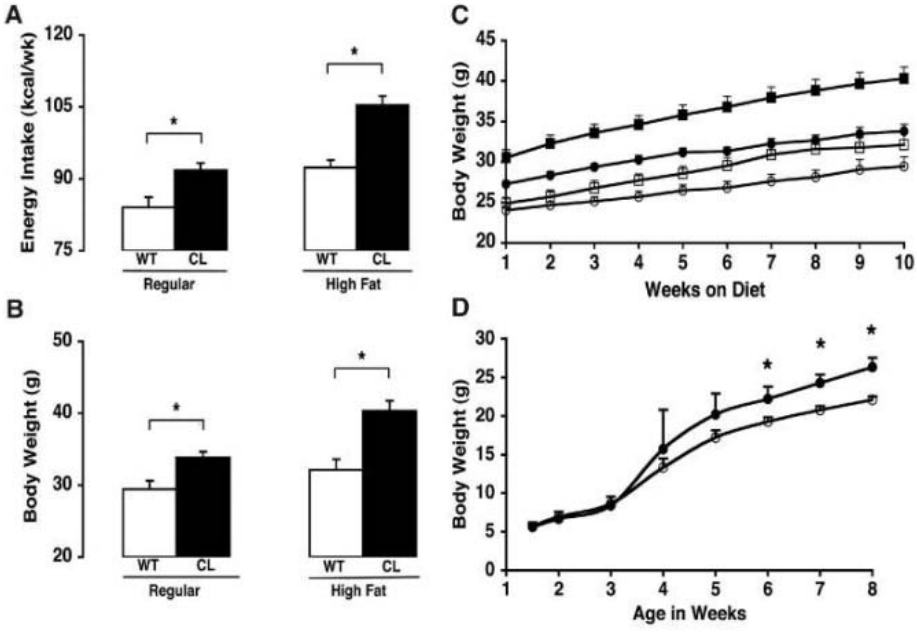

Fig. 2. Obesity in *Clock* mutant mice. (**A**) Average caloric intake over a 10-week period in male WT and *Clock* mutant mice. WT and *Clock* mutant mice were provided ad libitum access to regular (10% kcal/fat; WT, $n = 8$; *Clock*, $n = 10$) or high-fat chow (45% kcal/fat; WT, $n = 7$; *Clock*, $n = 11$) for 10 weeks beginning at 6 weeks of age. Weekly food intake was analyzed in the two groups (*$P < 0.01$). (**B**) Body weights for the mice in (A) after the 10-week study (*$P < 0.01$). (**C**) Body weights of WT (open symbols) and *Clock* mutant (solid symbols) mice over the 10-week study for mice in (A) fed either regular (circles) or high-fat (squares) diets. (**D**) Body weight of mice after weaning, from 10 days to 8 weeks of age. Growth curves in WT (open circles) and *Clock* mutant (solid circles) mice on regular chow were obtained by weekly weighing. Significant differences did not appear until 6 weeks of age (*$P < 0.05$). All values represent group means ± SEM.

Table 1. Metabolic parameters in WT and *Clock* mutant mice. Serum triglyceride, cholesterol, glucose, insulin, and leptin concentrations were determined in 7- to 8-month-old WT and *Clock* mutant mice fed a regular diet ad libitum ($n = 4$ to 8 mice per group). For measurement of glucose, insulin, and leptin, blood was collected at 4-hour intervals over a 24-hour time period via an indwelling catheter (40 μl per blood sample), and the data were pooled to provide an overall mean (±SEM) value. For triglyceride and cholesterol measurement, a single blood sample (160 μl) was collected at zeitgeber time 0.

Metabolic parameter	WT	*Clock*	*P* value
Triglyceride (mg/dl)	136 ± 8	164 ± 8	<0.05
Cholesterol (mg/dl)	141 ± 9	163 ± 6	<0.05
Glucose (mg/dl)	130 ± 5	161 ± 7	<0.01
Insulin (ng/ml)	1.7 ± 0.3	1.1 ± 0.1	n.s.
Leptin (ng/ml)	3.4 ± 0.4	4.6 ± 0.3	<0.05

the *Clock* mutation on body weight in mice fed a regular diet was similar in magnitude to the effect of a high-fat diet in wild-type mice (Fig. 2). In addition, when *Clock* mutant mice were fed a high-fat diet, the combined effect of the diet plus mutation led to the most severe alteration in body weight and markers of metabolism (Fig. 2). Note that the weight gain in the *Clock* mutant mice is similar to that observed in a number of metabolic mutants (*19*, *20*).

Alterations in fuel metabolism in animals carrying a mutant circadian *Clock* gene could emerge from a cascade of neural events initiated by an alteration in circadian rhythms under the direct control of the SCN (*21*), in particular the feeding rhythm, which is greatly attenuated in *Clock* mutant mice. Thus, the misalignment of food intake and/or the near-loss of feeding rhythmicity could create metabolic instabilities that lead to hyperphagia and associated obesity and lipid/glucose irregularities. On the other hand, because circadian clock genes are also expressed in nearly all CNS and peripheral tissues, alterations in metabolism could be due to cell-autonomous effects associated with altered expression of *Clock* in CNS feeding centers and/or peripheral tissues involved in metabolism (*5*, *22*). The observation that mRNAs of selected energy-regulatory peptides are altered in both diurnality and absolute expression level in the MBH supports the idea of a molecular coupling between circadian and metabolic transcription networks. These results are consistent with the recent finding that in addition to regulating the timing of many genes, the circadian clock regulates the absolute expression levels of approximately 3 to 10% of transcripts (*23*–*25*).

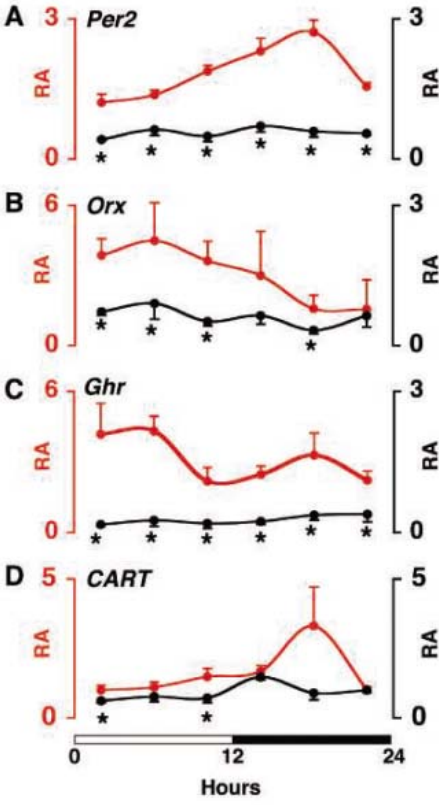

Fig. 3. *Clock* mutant mice display altered diurnal rhythms and abundances of *Per2* mRNA (**A**) and mRNAs encoding selected hypothalamic peptides involved in energy balance (**B** to **D**). Real-time PCR was used to determine transcript levels as they varied across a 12:12 LD cycle (indicated by bar at bottom). Values for WT (red line) and *Clock* mutant (black line) mice are displayed as relative abundance (RA; mean ± SEM) after normalization to glyceraldehyde-3-phosphate dehydrogenase (GAPDH) expression levels in the same sample. Note that for visual clarity the RA scales vary for the different transcripts and vary between genotypes for orexin (*Orx*) and ghrelin (*Ghr*). Brains of four WT and four *Clock* mutant mice were collected at 4-hour intervals across the 12:12 LD cycle. At each time point, genotype comparisons were made by independent-sample *t* tests (*$P < 0.05$). *CART*, cocaine- and amphetamine-regulated transcript.

Clues to the effects of the *Clock* mutation on energy balance may be derived from the emerging map of SCN projections to critical energy centers within the hypothalamus. For example, SCN projections form synapses directly on lateral hypothalamic area neurons that express orexins (*26*), as well as indirectly via the subparaventricular nuclei (SPV). Additional evidence suggests that connections between the SCN and neurons within the MBH may have important effects on cell and molecular functions. Specifically, recent analyses from several groups have indicated that the growth hormone agonist ghrelin, originally discovered as an incretin hormone within the stomach, may also be produced within the MBH/SPV (*27*, *28*). Our real-time polymerase chain reaction (PCR) results provide further support for expression of *ghrelin* within the MBH. Remarkably, we find that *ghrelin* mRNA is greatly reduced in the MBH from *Clock* mutant mice, which suggests that signaling from SCN neurons and/or expression of the *Clock* gene within the MBH may play a critical role in transcriptional control of target genes within the MBH. Similarly, we found that *orexin* levels were lower in *Clock* mutant than wild-type mice, and the normal diurnal variation in expression was abolished.

Previous transcriptome analysis in the SCN and liver of *Clock* mutant mice has uncovered global changes in metabolic pathways, including those encoding enzymes of glycolysis, mitochondrial oxidative phosphorylation, and lipid metabolism (*23*). The connection between metabolism and circadian rhythmicity is particularly intriguing in view of the finding that genes involved in mitochondrial redox metabolism account for a large fraction of the circadian transcriptome in most tissues (*10*). Although these earlier results indicated that cell redox flux can alter the molecular circadian core machinery, our results in *Clock* mutant mice indicate that alterations in this molecular clock may alter cell metabolism as well.

References and Notes

1. E. Van Cauter, F. W. Turek, in *Handbook of Physiology, Section 7: The Endocrine System*, B. S. McEwen, Ed. (Oxford Univ. Press, New York, 2000), pp. 313–330.
2. S. M. Reppert, D. R. Weaver, *Nature* **418**, 935 (2002).
3. J. S. Takahashi, F. W. Turek, R. Y. Moore, Eds., *Handbook of Behavioral Neurobiology* (Kluwer Academic/Plenum, New York, 2001), vol. 12, pp. 770.
4. A. Balsalobre, F. Damiola, U. Schibler, *Cell* **93**, 929 (1998).
5. K. A. Stokkan, S. Yamazaki, H. Tei, Y. Sakaki, M. Menaker, *Science* **291**, 490 (2001).
6. K. Yagita, F. Tamanini, G. T. van Der Horst, H. Okamura, *Science* **292**, 278 (2001).
7. M. Abe *et al.*, *J. Neurosci.* **22**, 350 (2002).
8. S. H. Yoo *et al.*, *Proc. Natl. Acad. Sci. U.S.A.* **101**, 5339 (2004).
9. R. D. Rudic *et al.*, *PLoS Biol.* **2**, e377 (2004).
10. J. Rutter, M. Reick, L. C. Wu, S. L. McKnight, *Science* **293**, 510 (2001).
11. M. H. Vitaterna *et al.*, *Science* **264**, 719 (1994).
12. D. P. King *et al.*, *Cell* **89**, 641 (1997).
13. M. P. Antoch *et al.*, *Cell* **89**, 655 (1997).
14. Male mice were used in all studies.
15. J. T. Willie, R. M. Chemelli, C. M. Sinton, M. Yanagisawa, *Annu. Rev. Neurosci.* **24**, 429 (2001).
16. S. Taheri, J. M. Zeitzer, E. Mignot, *Annu. Rev. Neurosci.* **25**, 283 (2002).
17. K. Yamada *et al.*, *Int. J. Obes. Relat. Metab. Disord.* **26**, 132 (2002).
18. N. Kanamoto *et al.*, *Endocrinology* **145**, 4144 (2004).
19. D. J. Burks *et al.*, *Nature* **407**, 377 (2000).
20. J. C. Bruning *et al.*, *Science* **289**, 2122 (2000).
21. S. E. la Fleur, A. Kalsbeek, J. Wortel, M. L. Fekkes, R. M. Buijs, *Diabetes* **50**, 1237 (2001).
22. Y. Kitamura, D. Accili, *Rev. Endocr. Metab. Disord.* **5**, 143 (2004).
23. S. Panda *et al.*, *Cell* **109**, 307 (2002).
24. R. A. Akhtar *et al.*, *Curr. Biol.* **12**, 540 (2002).
25. K. F. Storch *et al.*, *Nature* **417**, 78 (2002).
26. C. B. Saper, T. C. Chou, J. K. Elmquist, *Neuron* **36**, 199 (2002).
27. M. A. Cowley *et al.*, *Neuron* **37**, 649 (2003).
28. B. Bodosi *et al.*, *Am. J. Physiol. Regul. Integr. Comp. Physiol.* **287**, R1071 (2004).

29. Supported by NIH grants AG18200, DK02675, AG11412, HL75029, HL59598, and DK26356. We thank the Northwestern University Robert H. Lurie Comprehensive Cancer Center Pathology Core Faculty for their assistance. All animal procedures were performed at Northwestern University following institutional guidelines. J.S.T. is a cofounder of, has equity in, and is a member of the scientific advisory board of Hypnion Inc., which develops sleep-related pharmaceuticals. He is also on the scientific advisory boards of NutraGenomics Inc. and the Allen Institute for Brain Science. F.W.T. is a cofounder of and has equity in Slowave Inc., which develops sleep-related pharmaceuticals, and is on the board of directors of the National Sleep Foundation. Additional paid consulting relationships are disclosed in the SOM.

Supporting Online Material
www.sciencemag.org/cgi/content/full/1108750/DC1
Materials and Methods
Figs. S1 to S3
Conflicts of Interest Disclosure

16 December 2004; accepted 23 February 2005
Published online 21 April 2005;
10.1126/science.1108750
Include this information when citing this paper.

Freedom and Rules: The Acquisition and Reprogramming of a Bird's Learned Song

Timothy J. Gardner,[1,2*] Felix Naef,[2,3,4] Fernando Nottebohm[1]

Canary song is hierarchically structured: Short stereotyped syllables are repeated to form phrases, which in turn are arranged to form songs. This structure occurs even in the songs of young isolates, which suggests that innate rules govern canary song development. However, juveniles that had never heard normal song imitated abnormal synthetic songs with great accuracy, even when the tutor songs lacked phrasing. As the birds matured, imitated songs were reprogrammed to form typical canary phrasing. Thus, imitation and innate song constraints are separate processes that can be segregated in time: freedom in youth, rules in adulthood.

The songs of adult songbirds consist of stereotyped units, called syllables, acquired by imitation and arranged in sequences characteristic of each species. An understanding of how syllables are sequentially arranged to form songs is of general interest because the learning and reordering of stereotyped motor patterns is the basis of speech and may underlie other aspects of motor control (*1*, *2*). The neural basis of vocal production in songbirds is beginning to be understood (*3*–*6*), but the mechanisms that program the sequential order of syllables remain unknown.

The typical song of the canary (*Serinus canaria*) consists of tonal whistles ("syllables") that differ in duration and frequency modulation. Each syllable is repeated many times, forming a "phrase" (Fig. 1). Phrases are produced in variable order. Young canaries reared in the presence of singing adults will closely imitate the song of the latter (*7*), a process that takes 6 to 8 months; in these birds, incipient phrasing is already present by 60 days of age (*8*). However, canary-like syllables and phrase structure also develop in the absence of imitation and even in the absence of hearing, although under these conditions the repertoire of syllables is uncommonly small (*7*, *9*, *10*). Normal phrased song can be rapidly induced in very young, isolated male canaries by exposing them to adult levels of testosterone. This rapid emergence of adult-like song is shown in Fig. 1.

We wondered whether young canaries would imitate songs that lacked phrasing and violated a key "rule" of canary song. To address this question, we synthesized two kinds of songs that never occur in the repertoire of an adult canary (*11*) and exposed young canaries to these songs while isolating them from exposure to natural canary song. We built the first abnormal tutor song by generating a 30-s "random walk" through a space of syllable shapes comparable to that of normal canary song (Fig. 2A). Each syllable in the song contained a modulated tone with harmonics, filtered to create a timbre similar to that normally produced by the birds themselves (*12*). However, the overall sequence was unlike the phrases in normal adult canary song, because each syllable in the sequence differed slightly from the preceding and following one in shape and duration. The second synthetic song designed for this study was based on three repeats of a 5-s "glissando"; in a glissando, the same basic syllable occurs in descending frequency steps. These synthetic songs are illustrated in sonogram form and can be heard as sound files (*11*).

The canaries of the Belgian Waterslager strain that we used were born in soundproof chambers and were reared solely by their mothers, which at that time did not sing. At 25 days of age, males were transferred to individual soundproof chambers, where they heard a playback of a tutor song every 2 hours during the daylight photoperiod, which followed the natural outdoor cycle. Ten birds were exposed to the random walk, and six to the glissando; this exposure was continued for the duration of the experiment. Sound was recorded continuously and automated tools were used to detect and extract songs, discarding brief calls and other cage noises. Thus, we had for each bird a complete record of its vocal ontogeny.

In contrast to normal song ontogeny where phrase structure is apparent already in early plastic song (as in Fig. 1B), for these birds the earliest imitations contained long sequences of dissimilar sounds. In the random-walk group, six of 10 birds achieved remarkably accurate imitations of the first 10 s of the tutor song. These juvenile imitations, exemplified in Fig. 2B, demonstrate that juvenile canaries can accurately memorize and imitate atypical

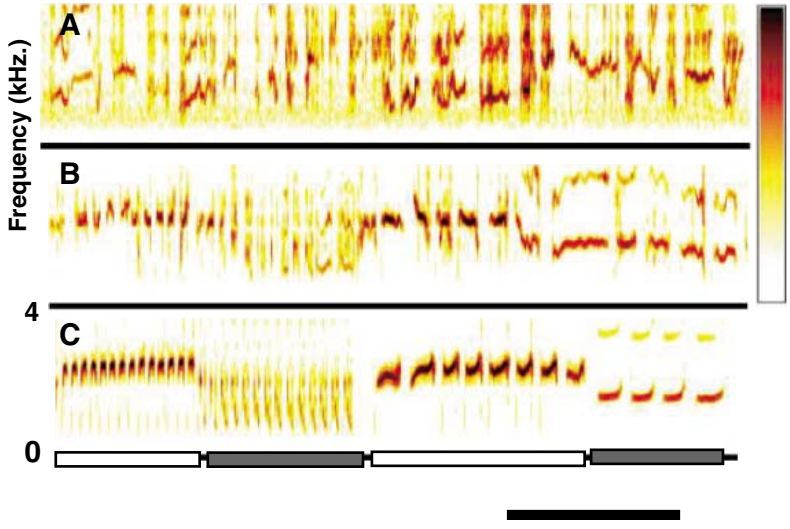

Fig. 1. A canary reared in social isolation develops normal syllable and phrase structure. The normal time course for song learning is 6 to 8 months, but an implant of testosterone at 2 months of age induced development of normal adult song structure over the course of a single week. The changes that took place during this week recapitulate song ontogeny in accelerated form and are illustrated with time-frequency sonograms (scale bar at bottom, 1 s). (**A**) The first stage, recorded at 75 days of age, is highly variable, with no evidence of stereotyped syllables and only the faintest suggestion of phrase structure. (**B**) At 80 days, most of the syllables that the bird will use as an adult already appear in a recognizable if still variable manner, organized in emerging phrases (*13*). (**C**) At 82 days, 1 week after testosterone implant, the variability of syllable structure is reduced, forming adult-like song. White and black rectangles indicate phrases consisting of repeats of stereotyped units, the syllables of adult song. Syllables are 20 to 200 ms in duration, and phrases are typically 1 s in length. The color scale presents the loudest sound in each panel as dark brown.

[1]Laboratory of Animal Behavior, [2]Laboratory of Mathematical Physics, Rockefeller University, New York, NY 10021, USA. [3]Swiss Institute for Experimental Cancer Research, CH-1066 Epalinges, Switzerland. [4]Swiss Institute of Bioinformatics, CH-1066 Epalinges, Switzerland.

*To whom correspondence should be addressed. E-mail: tgardner@mit.edu

songs that lack phrasing. This 10-s imitation represents a considerable achievement, because the summed duration of all unique sounds (not counting repetitions) produced in aviary-raised Belgian Waterslager canaries is on average 2.7 s (*8*). The result of this tutoring experiment indicates that song imitation in juvenile canaries can be remarkably unconstrained. However, song development did not end there, because our training had delayed but not eliminated the use of phrases (see below).

Between 150 and 250 days of age (i.e., in late fall and early winter), six of the 10 birds tutored with the random-walk model achieved a clearly recognizable imitation; there was considerably less imitation in the other four, and we did not follow their song thereafter. In pilot work, we had noticed that after birds achieved a clear imitation of the random-walk model, the approach of the breeding season brought a gradual change toward the typically phrased song of aviary-reared juveniles. This change occurred more slowly or rapidly and with varying degrees of completeness in different individuals. Therefore, beginning in January, we exposed two of the six birds that imitated the random-walk model to a more abrupt change in photoperiod, and additionally gave them a testosterone implant to overcome any factors that might slow the transition to a full breeding condition. Recall that in isolated juveniles, the change from early plastic song to phrased adult song was induced by this kind of forced transition to adult breeding status (Fig. 1).

The two testosterone-treated birds displayed a marked rearrangement in song structure. The nature of this change is shown in Fig. 2, C and D. In the early imitated songs, the birds had retained the syllable order as it appeared in the tutor song (Fig. 2C). In the transition to adulthood, a subset of the imitated sounds was serially repeated to form phrases, and in successive songs these phrases occurred in different orders (fig. S2), as in the song of aviary-reared birds. Because the transition from the imitated random-walk song to phrased song involved some of the original imitated syllables, we refer to this change as "reprogramming," a term that implies a reordering of existing material. For the bird whose imitated song is pictured in Fig. 2C, an automated survey (*11*) of all songs produced in the month of March yielded no match to the tutor sequence; the song with the best residual similarity to the tutor is illustrated in Fig. 2D. For this bird, the inferred innate rules forced a complete reprogramming of the imitated song. This reprogramming occurred in the absence of any exposure to normal canary song and in the presence of continued tutoring with the random-walk model.

In the four birds exposed to natural lengthening of days and spared the testosterone implant, the transition to phrased song occurred more gradually. All birds that achieved detailed copies of the tutor song in the juvenile period reprogrammed their songs as they approached sexual maturity.

Each bird's record of song development included 5000 to 30,000 songs, and therefore it was necessary to develop an automated methodology for comparing each song to the tutor (*11*). This method recognized something we have all experienced: A given word can be spoken faster or slower or at higher or lower pitches, and the same is true for canary song. The similarity score was based on the well-defined pitch contours of syllables (*13*), with the use of dynamic time warping to find the best match between two sounds (*14*, *15*). The alignment algorithm (Fig. 3A) shows how the extent of similarity with the tutor model changed over time in the six birds that imitated the random-walk model. This similarity started very low, increased as the tutor model was mastered, and then declined as the birds approached breeding condition. In parallel with the late decline in match to the tutor, there was an increase in phrased repetition (*11*), quantified in Fig. 3B.

In addition to the emergence of syllable repetition, the transition to adulthood involves a change in the distribution of syllable shapes that are most commonly used in song. This change includes reduction of variability in some syllables as well as attrition of other syllables, resulting in songs built from a small subset of stereotyped syllable forms. This change is shown in Fig. 3, C to F, by density plots of syllable mean pitch and duration. At the peak of imitation, the distributions indicate a broad range of syllable characteristics. One month later, after exposure to breeding conditions, the distributions indicate a transition toward a more categorical syllable distribution comparable to that of aviary-raised adult canaries (fig. S4).

The transition from juvenile imitation to adult song included, for all birds, a period when both the imitated song and phrased song coexisted. Most of the six birds that imitated the random-walk model maintained some capacity to produce the juvenile imitations in adulthood. Intact fragments of up to 6 s of the juvenile imitation were occasionally integrated into adult songs consisting of phrased repetitions (fig. S1). When a bird produced both song types in adulthood, some of the same imitated syllables could be found in both song types. We infer that the order of these syllables was determined sometimes by imitation and at other times by an innate phrase-forming program. Moreover, the switch between these two states of serial ordering occurred over short periods of time and even within the same song (fig. S2).

The capacity to produce both song types throughout adulthood was more pronounced in

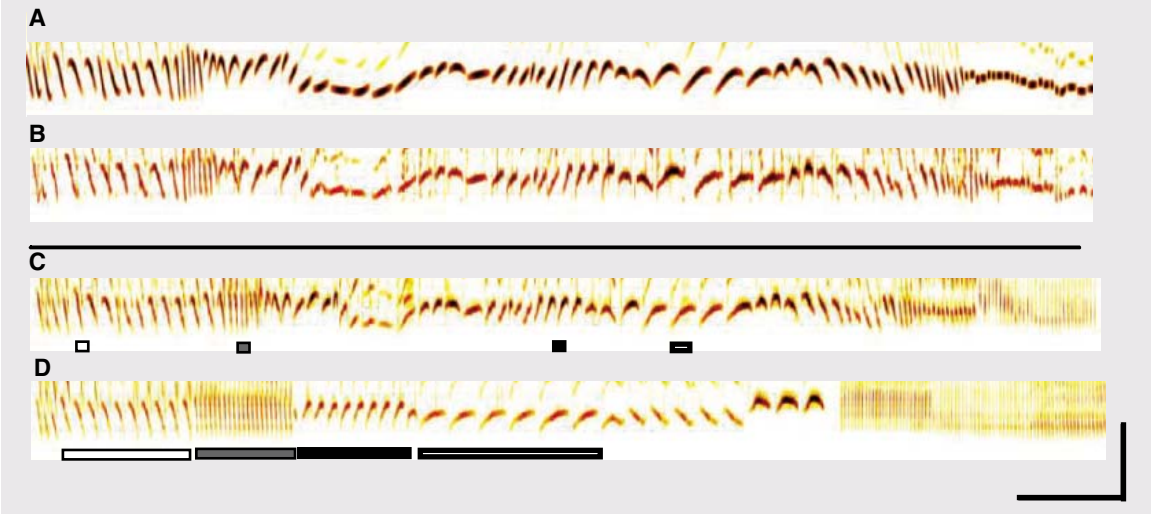

Fig. 2. Canaries achieve detailed imitations of an unnatural "random walk" song but reprogram these imitations in the transition to adulthood. (**A**) Synthetic tutor song. (**B**) Example of the best imitation achieved by 200 days of age. (**C**) Imitation produced by another bird at 250 days. (**D**) An automated survey (*11*) revealed that by 300 days, the bird whose song is pictured in (C) produces only phrased song. In the phrased song, a subset of the imitated syllables [small rectangles in (C)] are produced in phrased repetitions [stretched rectangles in (D)]. Scale bars at lower right: time, 1 s; frequency, 3 kHz.

the group of birds exposed to the glissando song (Fig. 4). In this group, accurate imitations achieved in the juvenile period were preserved throughout adulthood (fig. S3), even after exposure to exogenous testosterone. In adulthood, glissando imitations were produced side by side with phrased songs; these phrased songs consisted of syllables apparently drawn from the glissando song as well as of improvised syllables that the bird had not heard before. As for the first group, the switch from imitated sequence to phrased song and back could occur within a single song (Fig. 4, B and C) (fig. S3), which suggests that imitated syllables could be accessed by two different programs.

We have established the following: (i) Juvenile canaries can accurately perceive, memorize, and imitate long, atypical sequences of unique sounds arranged in a single linear order. (ii) As these birds approach sexual maturity, they produce a subset of these sounds as serial repetitions in the phrased manner typical of adults. (iii) Adults that produce both unphrased and phrased song can switch from one to the other over short time scales. Such quick reprogramming is reminiscent of the

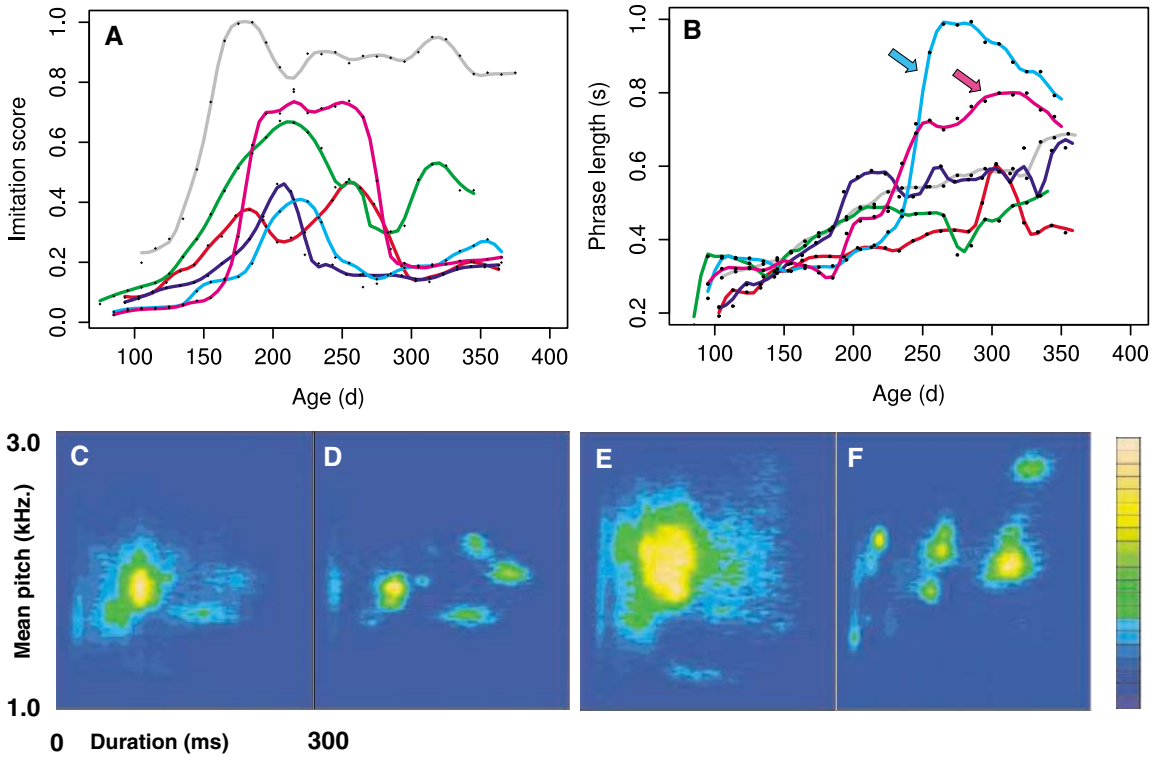

Fig. 3. (**A**) Time course of model imitation using the alignment algorithm (*11*). Every pupil's song is scored on the length and acoustic match of the best fragment that can be aligned to the tutor song. For each week, the scores of the best imitations, defined as the 90th percentile by rank (i.e., the typical best imitation, not the very best that the bird can do), are plotted after smoothing with a running average over 30 days. This plot is essentially unchanged when plotting percentiles in the range 90 to 100%. Each color represents one of six birds. (**B**) Average phrase length increases over time (*11*). The two birds with the sharpest increase in phrase length (light blue and magenta traces, arrows) received exogenous testosterone treatment starting at 210 and 180 days, respectively. (**C** to **F**) Density plots (*11*) illustrate a transition in how the two testosterone-treated birds apportioned their singing time in terms of syllable characteristics. Each panel is calculated from the durations and mean pitches of 60,000 syllables selected from random times in the month of peak imitation [(C) and (E)] and in the subsequent month [(D) and (F)]. Colors are normalized separately for each panel, with yellow indicating the highest concentration of singing time. At the peak of imitation, singing time is still distributed across a range of duration and pitch characteristics. In adulthood, this distribution becomes fragmented into distinct clusters; each cluster in the density plot is typically populated by multiple syllable types that have similar duration and mean pitch values. Patterns in (D) and (F) are qualitatively similar to those obtained from colony-reared canaries singing adult song (fig. S4).

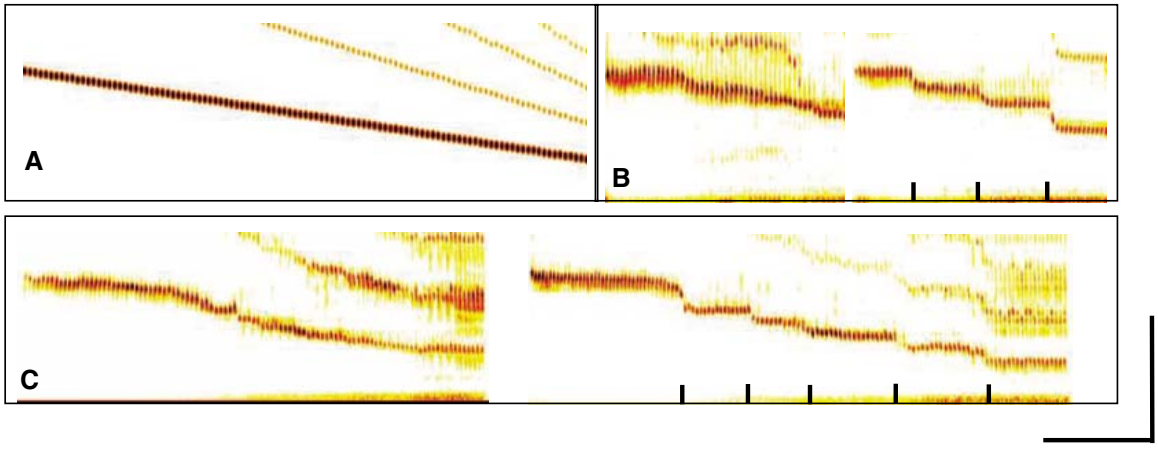

Fig. 4. Canaries imitate an extremely unnatural "glissando song." In adulthood, the birds rapidly alternate between imitation of the glissando and songs that reprogram a subset of the glissando syllables to form phrases (phrase boundaries are indicated by tick marks.) (**A**) Tutor song. (**B**) Glissando imitation and phrased structure produced in the same song by an 8-month-old canary after 2 months of testosterone treatment. (**C**) Example of glissando imitation and phrased structure produced in the same song by another adult, age 11 months, after 2 months of testosterone treatment. Sound files in (B) and (C) were adjusted with a running amplitude normalization to better illustrate loud and quiet syllables in the same color scale. Scale bars: time, 1 s; frequency, 3 kHz.

flexibility of phoneme rearrangement in human speech and is an aspect of vocal prowess in birds that had not been described before. Given the many parallels in the ways in which birds and humans go about vocal learning (*16*–*18*), there may also be common neural mechanisms underlying the ways in which they can access and sequence the learned vocal units.

Classical ethologists have remarked on the fact that, among songbirds that learn their song but are not usually thought of as mimics, model imitation is usually restricted to conspecific models. Imitations of other species, which occur rarely during the juvenile stage, are usually expunged by sexual maturity (*19*–*21*) and thus do not compromise a species' "song universals" (*22*). It has been known, too, that some songbirds master as juveniles more songs than they will sing as adults (*21*, *23*, *24*). These are examples of how selective attrition of juvenile song can lead to the final repertoire of adults.

Our work with canaries sheds light on this editing process. Normally, the rules of adult canary song guide vocal ontogeny, so that phrasing is already in evidence in early juvenile song, even in the absence of external models (Fig. 1). However, this mechanism for developmental guidance is separate from the ability to learn a song, and the two can be temporally uncoupled. During the first half of their juvenile life, our canaries were free to imitate sounds that violated the rules of normal canary song. As the breeding season approached, this material was reorganized both by attrition of some syllable variants and by imposing a new syntax, so that it now conformed with the rules of adult song. This order of occurrence—freedom to learn followed by rules of expression—may tell us something important. Vocal learning may have evolved not just by relaxing innate programs for vocal ontogeny and linking them to external models and auditory feedback, but also by delaying the onset of adult strictures, allowing for a period of vocal experimentation and play. A glimpse of this early evolutionary step may be found in young birds learning their song.

References and Notes

1. K. S. Lashley, in *Cerebral Mechanisms in Behavior*, L. A. Jeffress, Ed. (Wiley, New York, 1951), pp. 112–136.
2. A. M. Graybiel, *Neurobiol. Learn. Mem.* **70**, 119 (1998).
3. E. T. Vu, M. E. Mazurek, Y. C. Kuo, *J. Neurosci.* **14**, 6924 (1994).
4. A. C. Yu, D. Margoliash, *Science* **273**, 1871 (1996).
5. E. T. Vu, M. F. Schmidt, M. E. Mazurek, *J. Neurosci.* **18**, 9088 (1998).
6. R. H. Hahnloser, A. A. Kozhevnikov, M. S. Fee, *Nature* **419**, 65 (2002).
7. P. Marler, M. S. Waser, *J. Comp. Physiol. Psychol.* **91**, 8 (1977).
8. F. Nottebohm, M. E. Nottebohm, L. Crane, *Behav. Neural Biol.* **46**, 445 (1986).
9. H. R. Guttinger, *Z. Tierpsychol.* **56**, 323 (1981).
10. F. Nottebohm, T. M. Stokes, C. M. Leonard, *J. Comp. Neurol.* **165**, 457 (1976).
11. See supporting data and sound files on *Science* Online.
12. T. Gardner, G. Cecchi, M. Magnasco, R. Laje, G. B. Mindlin, *Phys. Rev. Lett.* **87**, 208101 (2001).
13. O. Tchernichovski, P. P. Mitra, T. Lints, F. Nottebohm, *Science* **291**, 2564 (2001).
14. L. Rabiner, B. Juang, *Fundamentals of Speech Recognition* (Prentice-Hall, Englewood Cliffs, NJ, 1993).
15. S. E. Anderson, A. S. Dave, D. Margoliash, *J. Acoust. Soc. Am.* **100**, 1209 (1996).
16. P. Marler, *Am. Sci.* **58**, 669 (1970).
17. L. Wan-Chun, T. J. Gardner, F. Nottebohm, *Proc. Natl. Acad. Sci. U.S.A.*, in press.
18. A. J. Doupe, P. K. Kuhl, *Annu. Rev. Neurosci.* **22**, 567 (1999).
19. W. H. Thorpe, *Ibis* **97**, 247 (1955).
20. W. H. Thorpe, *Ibis* **100**, 535 (1958).
21. P. Marler, S. Peters, *Dev. Psychobiol.* **15**, 369 (1982).
22. P. Marler, in *Nature's Music*, P. Marler, H. Slabbekoorn, Eds. (Elsevier, San Diego, CA, 2004), pp. 1–37.
23. P. Marler, S. Peters, *Science* **213**, 780 (1981).
24. P. C. Mundinger, *Anim. Behav.* **50**, 1491 (1995).

25. Supported by U.S. Public Health Service grants MH18343 and MH63132, the Mary Flaggler Cary Charitable Foundation, the Nell and Herbert Singer Foundation, and the Phipps Family Foundation. F. Naef was supported by a Bristol Meyers-Squibb fellowship. We thank G. Mindlin and S. Ribeiro for discussions that influenced experimental design; B. Olveczky for comments on the manuscript; the Center for Physics and Biology at Rockefeller University for computing resources and advice; D. Jackson, S. Sepe, and H. Ecklund for excellent care of our birds; and the staff of the Rockefeller University Field Research Center.

Supporting Online Material

www.sciencemag.org/cgi/content/full/308/5724/1046/DC1
Materials and Methods
Figs. S1 to S4
Sound Files S1 to S11

2 December 2004; accepted 8 March 2005
10.1126/science.1108214

New Products

http://science.labvelocity.com

Automated Cloning System

High-throughput (HT) cloning methods are used in thousands of experiments performed by research labs with the aim of improving their drug development process and gaining insights into complete genetic interactions. Invitrogen's Gateway HT cloning system is simple compared with other systems, but still involves polymerase chain reaction, DNA isolation, incubation, transformation, gel loading, and gel imaging steps, which are repetitive and time-consuming. However, the system can be automated using Hamilton's Microlab Star liquid handling workstation, equipped with monitored air displacement pipetting technology. The system eliminates the use of tubing, pumps, or system liquids, thus significantly reducing the risk of cross-contamination. Plating of the transformed bacteria is done on the workstation. The eight-well plates containing the bacterial colonies are later picked by the EasyPick integrated colony picker.

Hamilton Life Science Robotics For information 800-648-5950 www.hamiltonrobotics.com

Proteomics Analysis

The SPRimagerII detection system is designed to make proteomics analysis faster, easier, and more reliable. It is a complete system for label-free analysis of protein and other molecular arrays. Detection is achieved using surface plasmon resonance, so molecular labels such as fluorescent tags are not required for detection. It can be used to monitor not only protein–protein interactions, but also interactions involving DNA, RNA, carbohydrates, and ligands. Applications include measurement of antibody–antigen affinities, monitoring transcription factor binding to DNA elements, and functional characterization of receptors on cell surfaces.

GWC Technologies For information 608-441-2722 www.gwctechnologies.com

Magnetic Cell Separation

The BD IMag Cell Separation System is based on a simple yet effective direct magnet technology that allows for the rapid positive and/or negative selection of cell populations without the use of magnetic separation columns. The system can supply excellent purities and recoveries of specific leukocyte subpopulations in a few short steps.

BD Biosciences For information 877-232-8995 www.bdbiosciences.com

Monoclonal Antibody Purification

MabSelect Xtra and MabSelect SuRe are two new products designed to offer the highest purity and most time- and cost-efficient chromatography media for the industrial purification of monoclonal antibodies. MabSelect Xtra is a recombinant protein A-based chromatography medium that captures antibodies with improved efficiency and economy. It is engineered to give 30% higher dynamic binding capacity than other commercially available protein-A based media. MabSelect SuRe is a chromatography medium based on a novel alkali-stabilized protein A-derived ligand engineered to provide greater stability than conventional protein A-based media in the alkaline conditions used in cleaning-in-place protocols.

GE Healthcare For information +44 (0) 1494 498 068 www.gehealthcare.com

Electrophoresis Kit

The GelAmp Electrophoresis Kit resolves high molecular-weight DNA, eliminating the need for expensive pulsed-field gel electrophoresis equipment. The all-inclusive kit contains high-strength agarose, running buffer, and a proprietary polymer additive that allows for superior resolution and separation of high molecular weight DNA. The kit is suitable for plasmid preparation, cosmid DNA, genomic DNA, and more. It can resolve up to 50 kb DNA fragments using standard horizontal electrophoresis equipment. The high resolution and sharp banding allow the user to achieve high-quality photo documentation.

Amresco For information 800-448-4442 www.amresco-inc.com

Thermal Cycler

The MultiGene II personal-sized thermal cycler features precise temperature control, excellent uniformity, and fast temperature change, making it useful for a wide range of applications, from DNA amplification to constant temperature incubations. There are two models available, for 16 0.5-ml tubes and 25 0.2-ml tubes. Ninety-nine protocols can be stored in memory for later use or modification. Peltier technology allows for fast heating and cooling in the range from 4°C to 99°C. The auto-adjusting heated lid adapts to the height of the sample tubes, eliminating the need for an oil overlay.

Labnet International For information 877-521-8001 www.labnetlink.com

Tips for Deep Labware

New P50 Tips are narrow-length tips that enable pipetting from the bottom of deep labware, for maximum retrieval of valuable samples. They work with Biomek 3000, NX, and FX and Multimek liquid handlers. The disposable, non-conductive P50 Tips are suitable for work in both 96- and 384-well formats, in applications such as compound library profiling and assay development, matrix-assisted laser desorption ionization–time of flight plate spotting, sample pooling, plate replication, and hit picking. The tips pipette a volume of 50 μl with barrier and are certified to be free of ribonuclease and deoxyribonuclease.

Beckman Coulter For information 800-742-2345 www.beckmancoulter.com

Literature

Qbiogene 2005/2006 Catalog includes products for sample preparation, polymerase chain reaction, cloning and transformation, enzymes, nucleic acid purification, transfection, gene expression, yeast kits, growth media, plant culture and specialty media, and bacterial growth media. The catalog also contains sections on proteomic tools; electrophoresis and hybridization; apoptosis, oncology, and fluorescence in situ hybridization; laboratory tools; and custom services.

Qbiogene For information 800-854-0530 www.qbiogene.com

Newly offered instrumentation, apparatus, and laboratory materials of interest to researchers in all disciplines in academic, industrial, and government organizations are featured in this space. Emphasis is given to purpose, chief characteristics, and availability of products and materials. Endorsement by *Science* or AAAS of any products or materials mentioned is not implied. Additional information may be obtained from the manufacturer or supplier by visiting www.science.labvelocity.com on the Web, where you can request that the information be sent to you by e-mail, fax, mail, or telephone.

ScienceCcareers.org

Classified Advertising

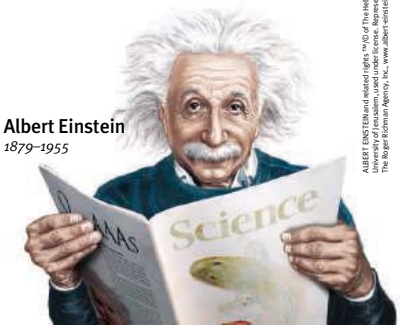

Albert Einstein
1879–1955

For full advertising details, go to **www.sciencecareers.org** and click on **How to Advertise,** or call one of our representatives.

United States & Canada

E-mail: advertise@sciencecareers.org
Fax: 202-289-6742

JILL DOWNING
(CT, DE, DC, FL, GA, MD, ME, MA, NH, NJ, NY, NC, PA, RI, SC, VT, VA)
Phone: 631-580-2445

KRISTINE VON ZEDLITZ
(AK, AZ, CA, CO, HI, ID, IA, KS, MT, NE, NV, NM, ND, OR, SD, TX, UT, WA, WY)
Phone: 415-956-2531

KATHLEEN CLARK
Employment: AR, IL, LA, MN, MO, OK, WI, Canada; Graduate Programs; Meetings & Announcements (U.S., Canada, Caribbean, Central and South America)
Phone: 510-271-8349

EMNET TESFAYE
(Display Ads: AL, IN, KY, MI, MS, OH, TN, WV; Line Ads)
Phone: 202-326-6740

BETH DWYER
(Internet Sales Manager)
Phone: 202-326-6534

Europe & International

E-mail: ads@science-int.co.uk
Fax: +44 (0) 1223-326-532

TRACY HOLMES
Phone: +44 (0) 1223-326-525

HELEN MORONEY
Phone: +44 (0) 1223-326-528

CHRISTINA HARRISON
Phone: +44 (0) 1223-326-510

JASON HANNAFORD
Phone: +81 (0) 52-789-1860

To subscribe to *Science*:
In U.S./Canada call 202-326-6417 or 1-800-731-4939
In the rest of the world call +44 (0) 1223-326-515

Science makes every effort to screen its ads for offensive and/or discriminatory language in accordance with U.S. and non-U.S. law. Since we are an international journal, you may see ads from non-U.S. countries that request applications from specific demographic groups. Since U.S. law does not apply to other countries we try to accommodate recruiting practices of other countries. However, we encourage our readers to alert us to any ads that they feel are discriminatory or offensive.

POSITIONS OPEN

FACULTY POSITION
Department of Structural and Cellular Biology

The Department of Structural and Cellular Biology is seeking applications for one tenure-track appointment at the **ASSISTANT PROFESSOR** level. Candidates must have an earned Doctorate in a relevant field of study and at least two years of productive postdoctoral research experience. The candidate must have the potential for competing for extramural research funding, and an active, transferable grant is highly desirable. Preferred areas of research should be consistent with the departmental focus on neuroscience. Successful candidates will be expected to participate in both graduate and medical student (histology and neuroscience) teaching. Prior experience in teaching is desirable. Submit applications including curriculum vitae, summary of research interests, summary of teaching philosophies, funding history, and names of three references to: **Dr. Richard Harlan, Department of Structural and Cellular Biology, SL49, Tulane University Health Sciences Center, 1430 Tulane Avenue, New Orleans, LA 70112** by September 30, 2005. *Tulane University is an Affirmative Action/Equal Opportunity Employer.*

MICROBIOLOGIST
GS-12, Salary Range of $61,000 to $80,260

Department of Health and Human Services, Centers for Disease Control and Prevention (CDC), National Center for Infectious Diseases, Division of Viral Diseases, Viral and Rickettsial Zoonoses Branch is seeking a permanent, full-time **RESEARCH SCIENTIST** with demonstrated expertise in molecular virology to serve as a team member in the investigation of rabies. The laboratory is located at CDC's Roybal campus in Atlanta, Georgia. The incumbent will be responsible for multiple aspects of laboratory's research, including detection, characterization, and molecular epidemiology of lyssaviruses from outbreaks or sporadic cases, as well as training and liaison duties with countries in the former Soviet Union. Candidates should have a Ph.D. or equivalent degree in virology, microbiology, biology, chemistry, biochemistry, genetics, or a closely related field, with at least two years postdoctoral experience and linguistic skills in English and Russian. Salary is commensurate with experience. Excellent benefits and federal retirement plan.

For further information, contact: **Dr. Charles Rupprecht** at **telephone: 404-639-1050** or by **e-mail: cyr5@cdc.gov.** Additional information about the position and application procedure can be obtained via the CDC **website: http://www.cdc.gov** or at the Office of Personnel Management **website: http://www.usajobs.opm.gov.** Interested persons should apply under announcement number DE2-05-3132. The application period will open on May 3, 2005, and will run until May 23, 2005. *HHS/CDC is an Equal Opportunity Provider and Employer.*

FACULTY POSITION
Burnett College of Biomedical Sciences

Molecular Cardiovascular Biology: To conduct research on the role of chemokines on heart disease. This is a nontenure-track position. However, opportunities will be provided to get NIH funding and compete for tenure-track positions in this field that will be available in this rapidly expanding college. Please send curriculum vitae, and the names and contact information of three or more references to: **Dr. P. E. Kolattukudy, Dean, 4000 Central Florida BoulevardBoulevard, BMS 136, University of Central Florida, Orlando, FL 32816-2364** or via **e-mail: pk@mail.ucf.edu.**

The University of Central Florida is an Affirmative Action/Equal Opportunity Employer. As a member of the Florida State University System, all application materials and selection procedures are available for public review.

POSITIONS OPEN

LAB HEAD POSITIONS
BIOLOGICAL SCIENCES
Shanghai

Shanghai Institutes for Biological Science (SIBS), established in July 1999, is the largest life science research organization in Chinese Academy of Sciences. Currently there are seven research institutes in SIBS (including Institute of Biochemistry and Cell Biology, Institute of Neuroscience, Institute of Materia Medica, Institutes of Plant Physiology and Ecology, Health Science Center, Institute of Nutritional Science, and Institute of Pasteur), and a large number of faculty positions are available for application.

(1) Research fields: neuroscience, protein science, bioinformatics, epigenetics, rnaomics, stem cell research, cell biology, molecular immunology, virology, developmental biology, pharmaceutics, molecular pharmacology, pharmaceutical analysis, medicinal chemistry, structure biology, plant functional genomics, insect science, photosynthesis, metabolism and metabolomics, symbiotic nitrogen fixation, phytopathology, biomass and biofuels, industrial microbiology, biotechnology, nutrition, essential medicinal.

(2) Applicants should have Ph.D. degree and postdoctoral experience and are under the age of 45. Those who are **ASSISTANT PROFESSOR** or in equivalent position are preferred. Applicants should have the ability to lead an independent research group in SIBS.

(3) Application form should include a copy of curriculum vitae, list of publication, three to five papers published in past five years, the future research plan, three reference letters, a copy of Ph.D. diploma and other relevant certificates.

(4) Salary and other personal benefits: negotiable.

(5) Application should be sent to: **Mr. Weijun Wang, Shanghai Institutes for Biological Sciences, 320 Yue-yang Road, Shanghai 200031, China. Fax: 0086-21-54920078. Telephone: 0086-21-54920027. E-mail: wjwang@sibs.ac.cn.**

SENIOR RESEARCH FELLOW

The Pain Research Center of Harvard Medical School at the Brigham and Women's Hospital invites applications for the position of Senior Research Fellow. Applicants must have postdoctoral experience and are expected to work independently on existing projects on inflammatory, neuropathic, or post-operative pain, using demonstrated skills in electrophysiology, molecular biology, or cell biology, in collaboration with Principle Investigators of the Center. The salary is $50,000 per year (plus benefits) for a minimum two-year appointment.

Send curriculum vitae, statement of interest, and names and contact information of three references to:

Professor Gary R. Strichartz, Director
Pain Research Center
Brigham and Women's Hospital
75 Francis Street, MRB611
Boston, MA 02115

Women and minorities are particularly encouraged to apply. Brigham and Women's Hospital and Harvard Medical School are Equal Opportunity/Affirmative Action Employers.

FACULTY POSITION
Burnett College of Biomedical Sciences

Tuberculosis: To identify new targets for novel antimycobacterial drugs using molecular genetic and cell biological approaches. This is a nontenure-track position. However, opportunities will be provided to get NIH funding and compete for tenure-track positions that will be available in this field in this rapidly expanding college. Please send curriculum vitae, and the names and contact information of three or more references to: **Dr. P. E. Kolattukudy, Dean, 4000 Central Florida Boulevard, BMS 136, University of Central Florida, Orlando, FL 32816-2364** or via **e-mail: pk@mail.ucf.edu.**

The University of Central Florida is an Affirmative Action/Equal Opportunity Employer. As a member of the Florida State University System, all application materials and selection procedures are available for public review.

The Gerstner Sloan-Kettering Graduate School of Biomedical Sciences offers the next generation of basic scientists a program to study the biological sciences through the lens of cancer — while giving students the tools they will need to put them in the vanguard of research that can be applied in any area of human disease.

PhD Program in Cancer Biology

An Internationally Recognized Research Faculty in:

- Cancer genetics
- Genomic integrity
- Cell signaling and regulation
- Structural biology
- Immunology
- Chemical biology
- Developmental biology
- Computational biology
- Experimental therapeutics
- Experimental pathology
- Imaging and radiation sciences
- Oncology
- Genomics
- Animal models of disease

An Innovative, Integrated Curriculum Provides a Fundamental Understanding of:

- The nature of genes and gene expression
- Cellular organization
- Tissue and organ formation
- Cell-cell interactions
- Cellular response to the environment
- Enzyme activity

Student Support and Services:

Students receive a fellowship package that includes a stipend, tuition, textbook allowance, and health insurance. Students also have access to affordable housing within easy reach of the school.

Please visit our Web site to learn how to apply, for application deadlines, and for more information about our PhD program.

www.sloankettering.edu

gradstudies@sloankettering.edu | 646.888.6639

Gerstner Sloan-Kettering
Graduate School of Biomedical Sciences

New York City

Positions @ NIH

THE NATIONAL INSTITUTES OF HEALTH

For students, recent graduates, and postdoctoral, research, and clinical fellows.

Your on-line guide to training with the best at the world's largest biomedical research institution.

In Bethesda, Maryland, and at other NIH laboratories.

Office of Intramural Training and Education
Bethesda, Maryland
20892
800.445.8283

opportunity *clicks*

www.training.nih.gov

NIDDK

NATIONAL INSTITUTE OF DIABETES AND DIGESTIVE AND KIDNEY DISEASES

POSTDOCTORAL FELLOWSHIP
Molecular Genetics

National Institutes of Health (NIH), National Institute of Diabetes and Digestive and Kidney Diseases (NIDDK), in Phoenix, Arizona. We are working to identify and characterize novel genes that cause type 2 diabetes and obesity in humans. Applicants must have a PhD. or M.D. degree obtained within the past 5 years, with research experience in molecular biology.

Please send curriculum vitae to:

Leslie Baier, Ph.D.
National Institute of Diabetes and Digestive and Kidney Diseases
National Institutes of Health
Phoenix, AZ 85016

For further information, please contact Dr. Baier by email: lbaier@phx.niddk.nih.gov

NATIONAL HEART, LUNG, AND BLOOD INSTITUTE (NHLBI)

Deputy Director

The NHLBI is seeking exceptional candidates for the position of Deputy Director, NHLBI, to provide leadership with the Director for a national research program in diseases of the heart, blood vessels, lung and blood; blood resources; sleep disorders; and administrative management of the NIH Women's Health Initiative. This position offers a unique opportunity for the right individual to share responsibility with the Director in providing strong and visionary leadership to an organization dedicated to uncovering new knowledge and technologies, both basic and clinical, as well as ensuring that rigorous science guides the appropriate use of more conventional treatments. Applicants must possess an M.D., Ph.D., or equivalent degree and senior-level research experience and knowledge of research programs in one or more scientific areas related to diseases of the heart, blood vessels, lung, and blood; blood resources; and sleep disorders. They should be known and respected within their profession, both nationally and internationally, as distinguished individuals of outstanding scientific competence. Salary is commensurate with experience and a full package of Civil Service benefits is available including retirement, health and life insurance, long term care insurance, leave and savings plan (401K equivalent).

CV, bibliography, and two letters of recommendation must be received by **September 1, 2005**. Application package should be sent to National Institutes of Health, attn:

Mr. Barry Rubinstein
Building 31, Room 5A28
31 Center Drive, MSC 2490
Bethesda, MD 20892-2490.

For further information, please contact Mr. Rubinstein by email: **Rubinstb@nhlbi.nih.gov or telephone 301-496-2411.**

With nationwide responsibility for improving the health and well being of all Americans, the Department of Health and Human Services oversees the biomedical research programs of the NIH. The NIH encourages the application and nomination of qualified women, minorities, and individuals with disabilities.

WWW.NIH.GOV

NATIONAL CANCER INSTITUTE

Be an NCI Cancer Prevention Fellow

The Cancer Prevention Fellowship Program provides training for individuals from the health professions and biomedical sciences to become leaders in the field of cancer prevention and control. The Program is sponsored by the Department of Health and Human Services, the National Institutes of Health, the National Cancer Institute (NCI), and the Division of Cancer Prevention.

What will I get out of the program?

- Master of Public Health (M.P.H.) degree
- NCI Summer Curriculum in Cancer Prevention
- Mentored research opportunities t the NCI or at the Food and Drug Administration (FDA)
- Professional development and leadership training

What areas of cancer prevention research are available?

- Chemoprevention
- Clinical cancer prevention
- Development and research-related review of drugs, biologics, or medical devices
- Epidemiology (environmental, genetic, molecular, nutritional)
- Ethics and evidence-based decision making
- Laboratory-based research
- Screening and early detection
- Social and behavioral research
- Statistical methodology

Am I eligible?

You must have a doctoral degree (M.D., Ph.D., J.D., or equivalent). Foreign education must be comparable to that received in the United States.

You must also be a citizen or permanent resident of the United States at the time of application (September 1).

How long is the program?

The typical duration is 3 years (year 1: M.P.H.; years 2-3: NCI Summer Curriculum in Cancer Prevention and mentored research).

How do I obtain more information?

Visit our website **http://cancer.gov/prevention/pob** or request a catalog.

To receive a catalog*, contact:

Douglas L. Weed, M.D., M.P.H., Ph.D.
Director, Cancer Prevention Fellowship Program
National Cancer Institute
6130 Executive Boulevard (EPN)
Suite 321, MSC 7361
Bethesda, MD 20892-7361

** Please provide home address, telephone, e-mail, and where you heard about the Program.*

How do I apply?

Apply online at **http://cancer.gov/prevention/pob** or send your application materials directly to the Cancer Prevention Fellowship Program Director, as described on our website and in our catalog.

When are applications due?

Applications are due September 1 for entry into the Program the following July 1.

Further inquiries:

Program Coordinator
Cancer Prevention Fellowship Program
Phone (301) 496-8640
Fax (301) 402-4863
E-mail: cpfpcoordinator@mail.nih.gov

DHHS, NIH, AND NCI ARE EQUAL OPPORTUNITY EMPLOYERS

Selection for these positions will be based solely on merit, with no discrimination for non-merit reasons, such as race, color, gender, national origin, age, religion, sexual orientation, or physical or mental disability. NIH provides reasonable accommodations to applicants with disabilities. If you need reasonable accommodation during any part of the application and hiring process, please notify us. The decision on granting reasonable accommodation will be handled on a case-by-case basis.

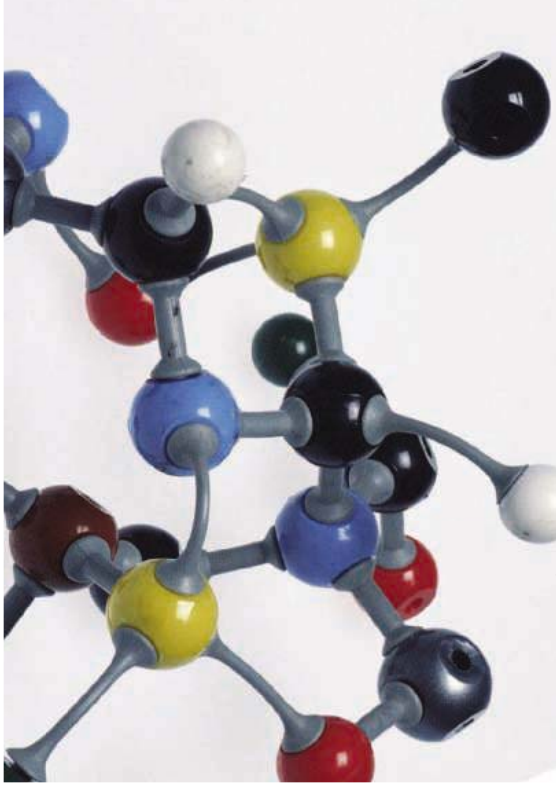

Postdoctoral Research Training at NIH

Launch a career to improve human health

Work in one of 1250 of the most innovative and well-equipped biomedical research laboratories in the world

Explore new options in interdisciplinary and bench-to-bedside research

Develop the professional skills essential for success

Earn an excellent stipend and benefits

Click on www.training.nih.gov

Office of Intramural Training and Education

EMBL

The European Molecular Biology Laboratory (EMBL) is an international research organisation with Units in the Headquarters Laboratory in Heidelberg, Germany and additional Units in Hinxton (the European Bioinformatics Institute, EBI), Grenoble and Hamburg (Structural Biology, X-ray and Neutron Beamline facilities for Life Sciences) and Monterotondo (Mouse Biology). In Heidelberg, four scientific Units (Cell Biology and Biophysics, Developmental Biology, Gene Expression and Structural and Computational Biology) interact closely to tackle problems at multiple levels of biological organisation, from the molecule to the organism.

EMBL is searching for the Structural and Computational Biology unit:

GROUP LEADER IN ELECTRON MICROSCOPY/CELLULAR ELECTRON TOMOGRAPHY S 05/44

The Candidate should lead an independent research group in the Structural and Computational Biology Unit. The Unit has recently acquired an electron microscope featuring a helium stage and energy filter. This microscope can provide high resolution images of cells and cellular structures. The final goal of the Structural and Computational Biology Unit is to bridge the gap between light microscopic cellular imaging and atomic structures. In addition to the EM facility with currently three research group leaders and a service team, there is complementary experience within the unit and EMBL that provides a stimulating environment for various collaborations on cellular and structural topics.

TEAM LEADER POSITION IN CHEMICAL BIOLOGY S 05/45

The Candidate should lead an independent research Team in the Structural and Computational Biology Unit. Scientists in the Unit use different structure determination techniques (X-ray, NMR, EM) and various computational approaches. The integration of small molecules into protein research should enable systemic approaches for an understanding of cellular processes and, in the context of structural biology, should give a better understanding pf protein-ligand interactions at a large scale. We are looking for scientists with experience in protein complex purification and chemical proteomics who are open to our vision of an atomic resolution of a cell.

Candidates should possess a PhD in an appropriate field of science with a strong publication record and exciting research plans.

Further information about EMBL can be obtained at http://www.embl.org/ and on the positions from the Heads of Structural and Computational Biology, Peer Bork and Luis Serrano (bork@embl.de) (serrano@embl.de)

To apply for either of these posts, please send a curriculum vitae quoting ref. no. S/05/44 or S/05/45 with a concise description of research interests and future plans.

Personnel, EMBL, Postfach 10.2209, D-69012 Heidelberg, Germany. Fax: +49 6221 387555. http://www.embl.org

University of Oxford

Life and Environmental Sciences Division

The Life and Environmental Sciences Division at the University of Oxford is a highly interdisciplinary organisation, bringing together academic departments representing diverse disciplines but sharing common thematic interests. Units within the Division are the Departments of Biochemistry, Plant Sciences and Zoology and the Schools of Archaeology, Anthropology and Geography and the Environment.

University Lecturership in Human Geography in association with St Catherine's College

The Department of Geography proposes to appoint a University Lecturer in Human Geography. The post is tenable from 1st October 2005 or as soon as possible thereafter. The successful candidate will be offered a Fellowship at St Catherine's College. The combined College and University salary will be according to age on a scale up to £45,707 p.a. (as at 1st August 2004).

The University and the College are seeking candidates with a proven record of scholarship and research in human geography and a track record of attracting research funding. The appointee will be required to engage in research which will contribute to the Department's research reputation; to teach, supervise and examine undergraduate and graduate students; and to contribute to administration in College and the Department.

Further particulars are available from http://www.admin.ox.ac.uk/fp/ or from Professor G Clark, Head of the School, to whom informal enquiries may be addressed (e-mail Gordon.clark@ouce.ox.ac.uk).

Applications (eight copies except from candidates overseas who need send only one), including a curriculum vitae, a list of principal publications, and the names of two referees, should be sent to Professor Gordon L Clark, Head, School of Geography and the Environment, Mansfield Road, Oxford OX1 3TB for receipt not later than 1st June 2005.

RCUK Academic Fellowship Scheme

Applications are invited for four 5-year fellowships which will lead to a permanent academic post on the successful completion of a probationary period. Fellowships tenable from 1st August 2005 are available in the following subject areas:

Biomathematics: in the Department of Zoology, with research interests in behaviour or development

Motivations and Means of Global Migration: in the Institute of Social and Cultural Anthropology

Chromosomes and Development: in the Department of Biochemistry

Archaeological Science (Tephrochronology): in the Research Laboratory for Archaeology and the History of Art

The Academic Fellowship Scheme is a national initiative funded by the Research Councils to provide a structured path into an academic career for contract research staff and other suitably qualified individuals. Applicants should have guaranteed research funding from a source other than the Academic Fellowship for at least part of the five-year fellowship period; the scheme is open to researchers supported on any type of grant funding and to holders of current fellowship awards. In the case of cell cycle and development, departmental funds are available to help support returners or other researchers without current research support.

Academic Fellows will:

- take up their appointments on 1st August 2005
- be able to develop their expertise in both research and teaching
- take part in outreach to schools
- have an academic mentor and full access to the University's staff development provision, including the opportunity to take the University's postgraduate diploma in learning and teaching
- be appointed to a permanent academic post, subject to satisfactory performance, at the end of the five-year fellowship period
- be paid on the research support scales during the fellowship period according to experience and stage of academic career.

Further particulars for the posts together with details of the Academic Fellowship Scheme are available on the University website at http://www.admin.ox.ac.uk/fp/ or from Dr M S Edwards, Secretary of the Life and Environmental Sciences Division, 9 Parks Road, Oxford OX1 3PD. The closing date for applications is 1st June 2005.

The University is an Equal Opportunities Employer.

Our client is the Swiss based headquarter of one of the world most prominent lifescience companies, ranking in the top ten of pharmaceutical enterprises worldwide. We are seeking the

Director Pharmacokinetics/ADME

In this role, you will develop and implement the vision of early pharmacokinetics within the research organisation of the enterprise. Together with your group and in close collaboration with the discovery project teams and the global chemistry organisation, your task is to secure the PK aspects for the advancement of the discovery of high quality drug candidates. Based on your experience both in the drug discovery process and in people management, you ensure a smooth transition at drug candidate nomination in close interaction with the development department. With your

leadership charisma

you attract high potential talent to the group. In order to successfully fill this position, you are a confident self starter, used to working under high pressure with a strategic and result oriented approach. Fluency in English is a must, good knowledge of German is wishable. If you have a PhD degree in pharmacology, biochemistry, chemistry or related with many years of experience in pharmaceutical industry and strong knowledge of the drug discovery process, and if you have acquired several years of direct line management experience, please send in your application with CV and testimonials to:

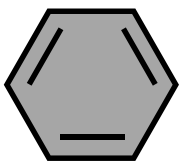

PP PHARMA PLANING
Bergauer + Partner AG
International Health Care Recruitment

attn. Mr Dieter Hubmann, PhD,
direct dial: +41-61-261 94 64,
Gerbergässlein 41,
CH 4051 Basel (Switzerland),
Tel. +41-61-261 94 93
e-mail: d.hubmann@pp-pharma-plan.com

www.pp-pharma-plan.com
www.pharma-career-box.com

Your application will be treated with strict confidentiality.

POSTDOCTORAL POSITIONS AVAILABLE

AMERICAN SOCIETY FOR MICROBIOLOGY AND NATIONAL CENTER FOR INFECTIOUS DISEASES

2006 POSTDOCTORAL RESEARCH PROGRAM

Up to ten positions will be awarded for full-time research on infectious diseases which cause significant public health problems. Fellows will perform research in residence at the National Center for Infectious Diseases (NCID) which is headquartered at the Centers for Disease Control and Prevention (CDC) in Atlanta, GA. In addition to Atlanta, NCID operates laboratories in Ft. Collins, CO, Anchorage, AK, and San Juan, Puerto Rico.

Eligible fields of study include:
- Bacterial and Mycotic Diseases
- Viral and Rickettsial Infections
- Nosocomial Infections
- HIV/AIDS
- Vector-borne Infectious Diseases
- Sexually Transmitted Diseases
- Parasitic Diseases

Positions are limited to individuals who either earned their doctorate degree (Ph.D., Sc.D., M.D., D.V.M., or D.D.S.) or have completed a primary residency within three years of their proposed start date. The program provides an annual stipend of $35,800, up to $500 relocation expenses, up to $3,000 health care benefits package and up to $2,000 for professional development. The fellowship is for 2 years.

The application deadline is **November 15, 2005**. For more information, visit **http://www.asm.org/Education/index.asp?bid=15497**. The brochure and application are available on line.

ASM
American Society for Microbiology

CDC/NCID
Centers for Disease Control and Prevention/National Center for Infectious Diseases

The University of Oklahoma
HEALTH SCIENCES CENTER

Post-doctoral Opportunities in Cancer Research
The University of Oklahoma Cancer Center

The University of Oklahoma Cancer Center is located on The University of Oklahoma Health Sciences Center Campus (OUHSC) and includes researchers from The Oklahoma Medical Research Foundation (OMRF) and The Dean McGee Eye Institute (DMEI).

The OU Cancer Center has several post-doctoral opportunities available with the following investigators:
- **Doris Benbrook, Ph.D.** – Drug Development for Ovarian Cancer – Ob/Gyn/ OUHSC; **http://w3.ouhsc.edu/benbrooklab/**
- **Brian Ceresa, Ph.D.** – Growth Factor Receptor Signaling – Cell Biology/OUHSC; **http://w3.ouhsc.edu/cell_biology/faculty/ceresafacultytext.html**
- **Gary Gorbsky, Ph.D.** – Mitosis and Chromosome Instability – Molecular, Cell, and Developmental Biology/ OMRF; **http://www.omrf.org/OMRF/Research/06/GorbskyG.asp**
- **Marie Hanigan, Ph.D.** – Protein Glycosylation Cancer and Cancer Therapy – Cell Biology/OUHSC; **http://w3.ouhsc.edu/cell_biology/faculty/haniganfacultytext.html**
- **Robert Hurst, Ph.D.** – Tumor Microenvironment and Systems Biology – Urology/OUHSC; **http://w3.ouhsc.edu/UrolLab**
- **Ricardo Saban, D.V.M., Ph.D.** – Bladder Transcriptome in Response to BCG Therapy and Mouse Models of Bladder Cancer – Physiology/OUHSC; **http://ouhscphysio.org/saban/**
- **Lurdes Queimado, M.D., Ph.D.** – WNT signaling and DNA repair – Otorhinolaryngology/OUHSC; **http://www.okcotorhinolaryngology.com/Aao/aao476/me.get?WEB.websections.show&AAO476_477125**

More information about the Principal Investigators and their research can be found on his/her lab website. Successful candidates will have a Ph.D. or M.D./Ph.D. in the biological sciences. Please send a C.V. with a brief history of research experience, a statement of research interests, and the names and email addresses of three references: **OU Cancer Center Post-doc Position, OU Cancer Center, 920 Stanton L. Young Blvd, WP-2080 Oklahoma City, OK 73104**. *OUHSC is an Equal Opportunity Employer.*

University of Texas M.D. Anderson Cancer Center

Postdoctoral positions are available for highly motivated individuals to study the roles of: (1) MTA family members using mouse models; (2) PAK1 and its novel effector substrates in cancer cells; (3) Estrogen receptor signaling and coregulators in cytoplasmic and nuclear functions in breast and endometrial cancer cells. Prior publications and direct experience in molecular cell biology and mouse disease models will be useful. See recent publications from the laboratory *NCB* **3:**30, 2001; *Nature* **418:**654, 2002; *NCB* **4:**681, 2002; *EMBO J.* **21:**5437, 2002; *Cell* **113:**142, 2003; *JCB* **161:** 583, 2003; *MCB* **24:**6581, 2004; *Cancer Cell* **5:**575, 2004; *Development* Aug 2004; *EMBO Rep.* 2005.

For immediate consideration, please send your CV and contact information of three references to: **Rakesh Kumar, Professor and Deputy Chair, M. D. Anderson Cancer Center-108, 1515 Holcombe Boulevard, Houston, Texas 77030. E-mail: rkumar@mdanderson.org**.

The University of Texas M. D. Anderson Cancer Center is an EOE Employer and does not discriminate on the basis of race, color, national origin, gender, sexual orientation, age, religion disability or veteran status, except where law requires such distinction. All positions at M.D. Anderson are considered security sensitive; drug screening and thorough background checks will be conducted. The University of Texas M.D. Anderson Cancer Center values diversity in its broadest sense. Diversity works at M. D. Anderson. Smoke-free environment.

LESLIE DAN FACULTY OF pharmacy University of Toronto

Canada Research Chairs
Pharmaceutical Chemistry and Molecular Medicine/ Molecular Pharmacology
Leslie Dan Faculty of Pharmacy
University of Toronto

Applications are invited for two tenure-stream positions at the rank of Assistant, Associate or Full Professor in the areas of **Pharmaceutical Chemistry** and **Molecular Medicine/Molecular Pharmacology**. The successful candidates will be expected to establish independent and externally funded research programs, to supervise graduate students and to teach at the graduate and undergraduate levels. Upon their appointment, they will be nominated for two Canada Research Chairs (**www.chairs.gc.ca**), one of which will be Tier 1 (senior) and the other Tier 2 (junior). Canada Research Chairs have been established by the Government of Canada to foster research of the highest quality at Canadian universities.

We seek individuals whose scientific activities will complement existing strengths within the Faculty. While some areas are of particular interest, the selection will be based in large measure on the originality and quality of recent and proposed research. For the Chair in Pharmaceutical Chemistry, we encourage applicants whose work is based in physical chemistry and focused on the molecular properties of materials in the solid state. Related areas of investigation within the Faculty include drug delivery, controlled release and polymeric delivery systems. For the Chair in Molecular Medicine/Molecular Pharmacology, we encourage applicants who plan to combine biochemical, biophysical, computational or imaging approaches to investigate processes of cellular signaling. It is expected that there will be a general focus on questions of structure and mechanism at the molecular level; areas of specific interest could include neurotransmitter and hormone receptors, ion sensors and other drug targets or signaling elements.

The University of Toronto and its affiliated teaching hospitals and research institutes maintain a strong presence in the physical, biological and medical sciences. Collaboration is encouraged and supported through cross-appointments, joint courses and various multidisciplinary programs. Opportunities also exist for interactions with pharmaceutical companies in the Toronto area. The Leslie Dan Faculty of Pharmacy offers excellent facilities for both research and teaching, and it is a partner in the Terrence Donnelly Centre for Cellular and Biomolecular Research (**http://ccbr.med.utoronto.ca**). The Faculty is presently undergoing an expansion that has included a substantial increase in research and in enrolment within its Graduate Department of Pharmaceutical Sciences (**www.utoronto.ca/pharmacy/graduate**). To accommodate this expansion, the Faculty will move to a new building in late 2005 (**www.greatspaces.utoronto.ca/projects/pharmacy.htm**).

Interested individuals are asked to forward a covering letter of application, a curriculum vitae, a statement of current and proposed research, a summary of teaching experience and philosophy, and three letters of reference to: **The Chair, Search Committee, Leslie Dan Faculty of Pharmacy, University of Toronto**, at **phmsearch@utoronto.ca**. Please apply electronically, using Microsoft Word or Adobe Acrobat (pdf) format. Letters of reference may be sent electronically or addressed to the above Committee at **19 Russell St., Toronto, Ontario, Canada M5S 2S2**. Evaluation of applications will begin on **1 July 2005**, and applications will be considered until the positions are filled.

The University of Toronto is strongly committed to diversity within its community. The University especially welcomes applications from visible minority group members, women, Aboriginal persons, persons with disabilities, members of sexual minority groups and others who may contribute to further diversification of ideas. All qualified candidates are encouraged to apply; however, Canadians and permanent residents will be given priority.

Drexel University College of Medicine
In the tradition of Woman's Medical College of Pennsylvania and Hahnemann Medical College

Chair, Department of Pharmacology and Physiology

Drexel University College of Medicine (formerly MCP-Hahnemann University) invites applications and nominations for the position of Professor and Chair of the Department of Pharmacology and Physiology (**http://www.drexel.edu/med/pharmacology_physiology/**). The department has primary teaching responsibility for teaching Pharmacology and Physiology to medical students. The department has 16 faculty and a flourishing PhD graduate program. Current major research strengths are in cell signaling and neuropharmacology. We are seeking an individual with leadership and administrative skills and a distinguished record of research accomplishments whose interests will complement existing strengths in the College of Medicine and University. The major responsibilities of the Chair are: (1) to promote the scholarly development of the faculty and students in the department; (2) to provide leadership in creating and implementing a vision to enhance existing and build new programs; and (3) to oversee teaching and research within the department. The Chair will work closely with other Chairs and senior leadership of the College to promote excellence in all missions. Resources will be made available for the recruitment of additional faculty.

Drexel University College of Medicine is the nation's largest private medical school. The Department of Pharmacology and Physiology is conveniently located in Center City Philadelphia and offers a collegial and stimulating environment with many opportunities for collaboration. Drexel University has 17,000 students and more than 1,300 faculty members. Drexel's annual budget exceeds $500 million, and the university is among the top 100 universities in federal grant and contract expenditures.

Applicants should provide a letter of application, curriculum vitae, and names of three references via email to **hhaberle@drexelmed.edu** or by mail to: **Jane Clifford, PhD, Chair, Search Committee, Chair, Dept. of Biochemistry and Molecular Biology, 245 N. 15th Street, M.S. 497, Philadelphia, PA 19102**.

Drexel University College of Medicine is an Equal Opportunity Institution.

Lecturer with Potential for Security of Employment
University of California, San Diego
Division of Biological Sciences
http://biology.ucsd.edu/

The Division of Biological Sciences at the University of California, San Diego seeks outstanding applicants for an opening as Lecturer with Potential for Security of Employment in Biochemistry and Molecular Biology, and Microbiology. All interested parties are encouraged to apply, including minorities and women.

The Lecturer will teach lecture and laboratory courses relevant to each area of study (including Structural Biochemistry, Biochemical Techniques Laboratory, Recombinant DNA Techniques Laboratory, or Microbiology Laboratory) and be responsible for curriculum development including new laboratory offerings and participation in efforts to secure extramural funding for educational program development. *The Lecturers will also be expected to teach introductory biology major and non-major biology lecture courses when needed.* In addition the successful candidate will be responsible for training of new laboratory Teaching Assistants *and provide service to the University by participating in committees and recruitment and outreach efforts.*

A Ph.D. in a relevant field of science is required. Applicants must have a strong record of excellence and innovation in teaching, along with strong interpersonal, writing and computer skills. The position will be a nine-month appointment. Salary will be commensurate with background and experience and based on University of California pay scale. A Lecturer-PSOE position closely parallels that of an assistant professor on track for tenure.

Complete applications received by **May 31, 2005** will be assured consideration. Applicants should send a curriculum vitae, publication list, synopsis of professional goals, and three letters of reference (forwarded separately) to: **Lecturer Search Committee, c/o Shiwan Tribbett – Mail Code 0355 - A, University of California, San Diego, 9500 Gilman Drive, La Jolla, CA 92093-0355.**

UCSD is an Equal Opportunity-Affirmative Action Employer with a strong institutional commitment to the achievement of diversity among its faculty and staff.

EUROPEAN INSTITUTE OF ONCOLOGY

Giancarla Vollaro Foundation

The European Institute of Oncology (IEO) and the Vollaro Foundation are launching a new program in **"Cancer Stem Cells and Innovative Treatment Modalities"** with emphasis on breast cancer and leukemias**.** Research will be performed at IEO. The IEO is a comprehensive cancer center not only offering the most modern and effective treatments and diagnostic services for many of the major cancers, but also committed to basic research, clinical trials, cancer prevention, training and education. The basic research facilities of IEO are located within the recently created IFOM-IEO Campus (www.ifom-ieo-campus.it). Our new campus will host up to 500 researchers and it is home to a newly created international PhD program (www.semm.it). Central services include the Animal Facility, Imaging, DNA and tissue microarrays, Antibodies, DNA sequencing, Bioinformatics. Open structure laboratories foster communication between groups. We are calling for applications for the position of:

Staff Scientist Position

We are seeking excellent candidates for entry at the level of staff scientist for the coordination of clinical and laboratory activities, in the context of our program on "Cancer Stem Cells and Innovative Treatment Modalities". Suitable candidates should have an MD degree and experience in cancer stem cell research or related areas; several years of postdoctoral research and a proven track-record based on publications in high-ranking journals.

Two Post-doctoral Positions

The candidates are expected to perform research in the area of leukemia stem cells. We encourage anyone with a strong background in molecular biology, cell biology, mouse genetics to apply. Preference will be given to MDs with prior experience in both clinical and experimental hematology.

Technician Position

We are seeking candidates for entry at the level of Senior Technician. Suitable candidates should have strong experience in mouse work, molecular and cellular biology.

DEADLINE FOR APPLICATIONS: June 15th, 2005. Applications should be sent by e-mail only to prof. Pier Giuseppe Pelicci (chairman.office@ieo-research.it) and should include: CV, publication list, statement of research interests (max. 2 pages), names and e-mail addresses of 2-3 referees.

the City College of New York

Deputy Director for Photonics Programs and Centers

The Deputy Director for Photonics Programs & Centers will oversee and manage the scientific and administrative aspects of photonics-funded research centers at the City College of New York. S/he will report directly to the Director and will interact closely with Centers' administrators and multidisciplinary, multi-campus photonics research groups.

Responsibilities: include overseeing research projects, Centers' administration, reporting and budgets; coordination of presentations, meetings, events, grant proposal preparation and student recruitment; and providing support for the CUNY Photonics Initiative.

Qualifications: Ph.D. degree or equivalent research experience in physics or engineering preferred, with strong experience in various areas of photonics. Bachelor's degree required. Min. 8 years combined experience in senior-level program administration, including project, budget and staff management, and senior-level research in a photonics field. Excellent writing, verbal, organizational, interpersonal, computer, and proposal writing skills. Proven ability to take initiative, work independently and troubleshoot.

Salary: $61k - $81k, commensurate with experience; vacation and full benefits package.

To apply, send resume, cover letter & name and contact information of 3 references to: **Prof. Robert R. Alfano, Director, Photonics Programs & Centers, PVN# MP-10481, The City College/CUNY, 160 Convent Ave., New York, NY 10031, Attn: Mr. Daniel Moy, or e-mail to: dmoy@sci.ccny.cuny.edu.** Applications accepted until position is filled.

For more details, see CCNY website: http://www2.ccny.cuny.edu/positions/.

The City College/CUNY is an EEO/AA/IRCA/ADA Employer.

CITY COLLEGE IS CUNY

Max Planck Institute for Demographic Research
Directors: Prof. James W. Vaupel - Prof. Jan M. Hoem

National Centre for Statistical Ecology
Director: Prof. Byron J. T. Morgan

The Max Planck Institute for Demographic Research (MPIDR) and The National Centre for Statistical Ecology (NCSE) are seeking to appoint to a

PhD position

in the

Statistical Analysis of Age-specific Survival Rates

The National Centre for Statistical Ecology (NCSE) is a new joint venture between the Universities of Cambridge, Kent and St. Andrews, funded under the EPSRC multidisciplinary critical mass in Mathematics initiative. It links the research groups in statistical ecology at the three universities. This particular position will principally involve collaboration between the University of Kent and the Biodemography research programme of the MPIDR. It will involve spending time both in Germany (Rostock) and in the United Kingdom (Canterbury). In Rostock, the successful candidate will complement an existing research team of 19 staff, including a number of recently recruited evolutionary ecologists. The team aims to gain a fundamental understanding of how age-specific demographic processes are shaped by evolution. In Canterbury, the student will form part of a thriving group, working on many different aspects of statistical ecology, biometry in general, and other areas of applied and theoretical statistics. The group involves PhD students and post-doctoral research workers. As a member of the National Centre for Statistical Ecology, the student will also come into close contact with related work in the Universities of Cambridge and St. Andrews, which host similar research groups. The successful candidate will work towards their doctorate through structured coursework, focused workshops and seminar programmes as well as through their main research project on new statistical methods for modeling how survival rates of organisms change with age. We anticipate that mark-recapture data, mostly from bird and mammal populations, will be the main material used in the development of these methods.

We are seeking able graduate scientists with strong academic track records in quantitative disciplines. Applications should be addressed to the Executive Director of the MPIDR, Prof. James W. Vaupel and Director NCSE, Prof. Byron J. T. Morgan, and should include a CV with a statement of academic interests and relevant experience, qualifications (details of all grades for exams, projects, and coursework), and the contact details of 3 referees. Details of any publications should be listed. Material should be e-mailed to: **MPIDR-NCSE-Age-Models@demogr.mpg.de** by latest 15th June 2005. See **www.demogr.mpg.de**, **http://www.ncse.org.uk/** and **http://www.kent.ac.uk/ims/groups/statistics/index.htm** for more information.

The Max Planck Society and the University of Kent wish to increase the share of women in areas where they are underrepresented, and strongly encourage women to apply.

The Max Planck Society and the University of Kent are committed to employing more handicapped individuals and especially encourage them to apply.

MAX PLANCK SOCIETY

ETH

Eidgenössische Technische Hochschule Zürich
Swiss Federal Institute of Technology Zurich

The Department of Earth Sciences and the Center for Earth, Environment, and Natural Resources at the Swiss Federal Institute of Technology (ETH) in Zurich intend to strengthen their research and teaching activities in the general area of Earth surface systems and invite applications for two faculty positions.

Professor of Sedimentology

We are seeking a scientist with a strong background in the investigation of Earth surface processes. Areas of expertise and interest include, but are not limited to: physical sedimentology and sediment transport; evolution of landscapes and sediment routing systems; quantification of longterm relationships between erosion, sediment transport, climate and tectonics; physical processes linking the surface, atmosphere, hydrosphere, and cryosphere. The appointment will also be at the Faculty of Science of the University of Zurich (MNF). The new professor and his or her staff will contribute to the Earth science teaching curricula at ETH and MNF, including field-based courses at the Bachelor's and Master's levels. Courses at the Master's level may be taught in English. He or she will supervise graduate and undergraduate students in the areas of sedimentology, quantitative stratigraphy and basin analysis, mapping and field observation, and regional geology (in particular the Alps).

Assistant Professor (Tenure Track) of Biogeoscience

We seek a scientist with a strong Earth science background who will be working at the interface between bio- and geosciences. Areas of interest include but are not restricted to: environmental geomicrobiology, molecular geobiology, ecosystem biogeochemistry, origin and evolution of life, microbial geochemistry, and bioremediation. Potential candidates will use multiple analytical and modeling approaches in their work. In addition to developing a broad interdisciplinary biogeoscience research program, the successful candidate and his or her staff will contribute to the Earth science teaching programs at the Bachelor's and Master's levels and supervise graduate students in the areas of geology, contaminant biogeochemistry, and geobiology. Courses at the Master's level may be taught in English.

We expect the new professors to develop innovative research groups that interface with research programs at ETH, MNF, and at the national and international level.

Please submit your application with a detailed curriculum vitae, a publication list, a statement of research interests, and the names of three potential referees **to the President of ETH Zurich, Prof. Dr. O. Kuebler, ETH Zentrum, CH-8092 Zurich, no later than June 30, 2005**. ETH Zurich specifically encourages female candidates to apply with a view towards increasing the proportion of female professors.

Careers in Biotechnology & Pharmaceuticals

A *Science* Advertising Supplement

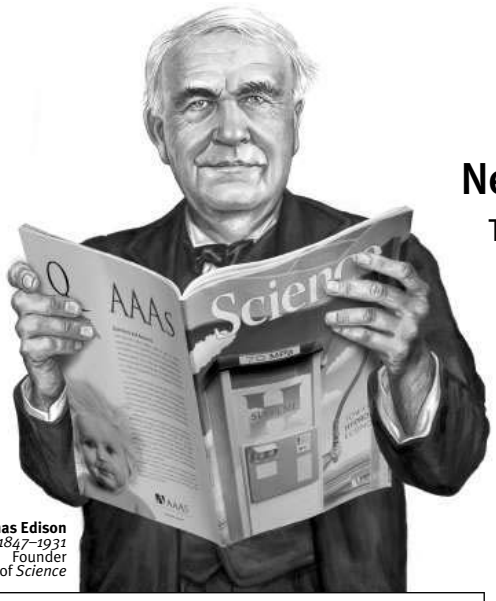

Thomas Edison
1847–1931
Founder
of *Science*

Need to attract great scientists?

Then talk to someone who knows science.

Issue date 10 June 2005
Reserve ad space by 24 May 2005

25% discount for multiple insertions

Run your ad again in any of these issues at a 25% discount.

1 July — 125th Anniversary issue
15 July — Immunology/Infectious Disease Research Careers
29 July — Careers in Drug Discovery

Qualified circulation of 129,590[1]

plus our pass-along readers brings total global weekly readership to over 710,000.[2] Copies of this issue will be distributed to:

- BIO 2005, 19–22 June, Philadelphia, PA
- BIO Career Fair, 19 June, Philadelphia, PA

ScienceCareers.org postings available — 7 websites for the price of one!

Your print recruitment ad can be placed on our website, ScienceCareers.org, for a nominal fee. Ads posted are also searchable on the following websites:

- Biocompare
- National Postdoctoral Association (NPA)
- Stanford University School of Medicine
- *Science*'s Signal Transduction Knowledge Environment (STKE)
- *Science*'s Aging Knowledge Environment (SAGE)
- *Science*'s Next Wave.

1 *Science* June 2004 BPA Publisher's Statement.
2 *Science* June 2004 circulation as applied to 14 January 2000 Harvey Readership Survey and 2002 Harvey Cumulative Report, publisher's own data.

To advertise contact:

U.S. Daryl Anderson
Phone: (202) 326-6543
E-mail: advertise@sciencecareers.org

Europe and International
Tracy Holmes
Phone: +44 (0) 1223 326 500
E-mail: ads@science-int.co.uk

Japan Jason Hannaford
Phone: +81 (0) 52 789-1860
E-mail: jhannaford@sciencemag.jp

ScienceCareers.org
We know science AAAS

POSITIONS OPEN

CURATOR
The American Society for Cell Biology
Image and Video Library

The American Society for Cell Biology (ASCB) seeks a skilled and dedicated cell biologist to serve as Curator to guide the launch of the ASCB Image and Video Library. The Library will offer an accessible, searchable, comprehensive electronic database of high-quality images and movies demonstrating molecular and functional organization of healthy and diseased cells.

The Curator will build and maintain the Library, assisted by technology and archiving staff, and in partnership with a Scientific Advisory Board.

Requirements include broad training in cell biology. Expertise in microscopy preferred.

Apply to:

The American Society for Cell Biology
8120 Woodmont Avenue, Suite 750
Bethesda, MD 20814-2762
E-mail: president@ascb.org

FACULTY POSITIONS
Cancer Nanomedicine
The Cleveland Clinic Foundation

The Cleveland Clinic Foundation is establishing a new Cancer Nanotechnology Center, a joint enterprise between the Department of Biomedical Engineering (BME) and the Taussig Cancer Center. We are seeking highly qualified individuals for faculty positions in the Center, including a mid-career scientist to assume a project programmatic leadership role. Target technologies include detection, imaging, and drug delivery. Diseases of current emphasis include genitourinary cancers (prostate, bladder), haematological cancers (leukemia, lymphoma), and melanoma.

These individuals would have joint appointments in two vibrant departments in an institution that values collaboration between basic science and clinical medicine. The BME Department is located in the Lerner Research Institute where more than 1,000 faculty and staff in nine departments are dedicated to biomedical investigation. The Taussig Cancer Center consists of 70 faculty and additional support and technical staff focused on clinical and translational research in specific tumor types and anticancer drug discovery and development. We invite applications for positions at the **ASSISTANT** or **ASSOCIATE STAFF (PROFESSOR)** levels. The successful candidate will have a Ph.D. and/or M.D. degree(s) in an area appropriate to the applicant's field of specialization, a strong record of, or potential for, independent extramural funding, and a high quality publication record in peer-reviewed journals.

Applicants should submit a letter of application, complete curriculum vitae, a statement of current and future research goals, and details of three references to:

Peter R. Cavanagh, Ph.D., D.Sc./
Derek Raghavan M.D., Ph.D.
Joint Chairs of the Search Committee
Department of Biomedical Engineering, ND 20
The Lerner Research Institute
The Cleveland Clinic Foundation
9500 Euclid Avenue, ND-20
Cleveland, OH 44195
E-mails: cavanap@ccf.org and **raghavd@ccf.org**

More information about the BME Department, the Taussig Cancer Center, the Research Institute, and the Cleveland Clinic can be found at **websites: http://www.lerner.ccf.org/bme/, http://www.clevelandclinic.org/cancer/, http://www.lerner.ccf.org/,** and **http://www.clevelandclinic.org/.**

The Cleveland Clinic Foundation is an Equal Opportunity/Affirmative Action Employer.

POSITIONS OPEN

The **University of Cincinnati College of Medicine** seeks outstanding M.D., M.D./Ph.D., or Ph.D. **FACULTY** through its Millennium Scholars Program in the areas of infectious diseases, immunology, or inflammation. Specific areas of interest include the immunology of HIV, microbial pathogenesis, host defense related to pulmonary infections transplantation. We also seek individuals interested in the development and maintenance of inflammatory responses. Individuals whose research is translational in nature are particularly attractive to this program as are investigators seeking to establish and develop multi-investigator interdisciplinary research programs. To qualify as a Millennium Scholar, investigators are expected to have ongoing substantial extramural grant support from federal institutions. Generous startup packages and competitive salaries are provided to those selected as Millennium Scholars. Faculty appointment will be granted in the appropriate department. Rank and track will be commensurate with education and experience. All curriculum vitae should be addressed to: **George S. Deepe, Chair, Infection/Inflammation Millennium Scholars Program, Division of Infectious Diseases, University of Cincinnati College of Medicine, Cincinnati, OH 45267-0560** or **e-mail: george.deepe@uc.edu.** Review of applications will commence upon receipt. *Women and members of underrepresented groups are especially encouraged to apply. The University of Cincinnati is an Affirmative Action/Equal Opportunity Employer.*

POSTDOCTORAL POSITION
Duke University, Durham, North Carolina

A Postdoctoral position is available immediately for independent and highly motivated individuals to conduct research in ultrasound-targeted gene delivery and activation in the Therapeutics Research Laboratory (TRL) at Duke University. We foster a multidisciplinary and collaborative environment between the School of Engineering and Duke University Medical Center. Candidates with a recent Ph.D. or M.D./Ph.D. degree and a strong molecular and cell biology or gene therapy background are encouraged to apply. Experiences in gene delivery in small animal models, surgery, and pathology are highly desirable. Applicants should send their curriculum vitae and a list of three references to: **Pei Zhong, Ph.D.** via **e-mail: pzhong@duke.edu** or **fax: 919-660-8963.**

TRAINING PROGRAM IN CELL AND MOLECULAR DERMATOLOGY

POSTDOCTORAL FELLOWSHIPS available in NIH-funded Training Program in Cell and Molecular Dermatology. Training opportunities available in basic science and translational research. Areas of focus include cancer biology (melanoma and non-melanoma skin cancer), psoriasis genetics, and photoaging. *While trainees must be a U.S. citizen or permanent resident, additional unrestricted positions are available in individual laboratories.* Send curriculum vitae and references to: **Dr. James T. Elder, 3312 CCGC, University of Michigan, Ann Arbor, MI 48109-0932. Fax: 734-763-4575; e-mail: jelder@umich.edu.** *An Equal Opportunity/Affirmative Action Employer.*

Ashland University–ASSISTANT PROFESSOR, cell biology/physiology. Full-time, one-year, nontenure-track appointment, beginning August 2005. Qualifications include Ph.D. and teaching courses in cell biology, human anatomy, physiology, and general introductory courses for majors and nonmajors. Undergraduate teaching experience desired. Facilities available for directing undergraduate research. Send letter of application, statement of teaching philosophy, curriculum vitae, transcripts, and three letters of recommendation to: **Cell Biology Search, Department of Biology/Toxicology, Ashland University, Ashland, OH 44805. Website: http://www.ashland.edu.** Applications should be received by June 15, 2005. *Ashland University is an Equal Opportunity Employer and is committed to diversity in the workplace.*

POSITIONS OPEN

USDA ARS Agricultural Research Service

The U.S. Department of Agriculture (USDA), Agricultural Research Service (ARS), Food Science Research Unit is seeking a permanent full-time **MICROBIOLOGIST** (GS-12/13) to develop a program of basic and applied research related to the genetic and physiological responses of sequenced lactic acid bacteria and acid-tolerant food pathogens to low pH, organic acids, and food preservatives. The position is located in the Department of Food Science at North Carolina State University, Raleigh, North Carolina. Salary range of $60,576 to $93,643. For details and application directions, see **website: http://www.afm.ars.usda.gov/divisions/hrd.** See announcement no. ARS-X5S-0177. To have a printed copy mailed or for specific application information, contact: **Susan Davis** at **telephone: 919-515-2731** or **e-mail: susan_davis@ncsu.edu.** *U.S. citizenship is required.* Announcement closes July 8, 2005. Visit the ARS **website: http://www.ars.usda.gov.** *USDA/ARS is an Equal Opportunity Employer and Provider.*

FACULTY POSITIONS:
ASSOCIATE OR FULL PROFESSOR
Chief Scientist of Laboratory of
Stem Cell Biology
Institute of Biochemistry and Cell Biology
Shanghai Institutes for Biological Sciences
Chinese Academy of Sciences

Institute of Biochemistry and Cell Biology (IBCB), Shanghai Institutes for Biological Sciences (SIBS), Chinese Academy of Sciences (CAS) has begun an initiative to complement and strengthen existing programs (**website: http://www.sibcb.ac.cn**), aiming at developing an internationally renowned institution in life sciences. As part of this initiative, we invite applications for the position of Professor and Chief Scientist of Laboratory of Stem Cell Biology. Candidates should have a Ph.D. or an equivalent degree, demonstrated excellence in research, and possess strong leadership qualities.

We also invite applications for up to ten faculty positions at the rank of Associate or Full Professor. We seek motivated individuals with established world-class research in any of, but not limited to, the following areas: protein science, bioinformatics, epigenetics, RNAomics, stem cell research, cell biology, immunology, and developmental biology. The positions require a doctoral or an equivalent degree, postdoctoral experience, and evidence of outstanding research potential. The successful candidates will be expected to develop vigorous, independently funded research programs and to contribute to graduate and postdoctoral training programs. The positions come with excellent laboratory space and substantial startup funds. Competitive salary, housing subsidy, and fringe benefit package will be commensurate with experience.

IBCB has long-standing expertise in biochemistry, molecular biology, cell biology, and protein science and provides a highly interactive and dynamic research environment, state-of-the-art research support facilities, and one of the best Ph.D. graduate programs in China. Opportunities for participation in intra- and inter-institute collaborative and interdisciplinary research are excellent. The IBCB campus is located in downtown Shanghai with easy access to many social, cultural, and sports opportunities.

Applicants should send curriculum vitae with a complete list of publications, a concise summary of past research accomplishments and future research plans, and three letters of references to: **Mr. Banghe Mao, Faculty Search Committee, Institute of Biochemistry and Cell Biology, Shanghai Institutes for Biological Sciences, Chinese Academy of Sciences, 320 Yue-Yang Road, Shanghai 200031, China** or electronically to **e-mail: bhmao@sibs.ac.cn** (**telephone: 086-21-54921006** and **fax: 086-21-54921011**). Applications will be accepted until positions are filled. Interviews may be conducted at any time upon arrangement. *IBCB is an Equal Opportunity Employer.*

Chief Executive Officer
FEDERATION OF ANIMAL SCIENCE SOCIETIES (FASS)
Administrative Office, Savoy, IL and Scientific Liaison Office, Washington, DC

FASS is seeking candidates for Chief Executive Officer. A complete position announcement and additional information on FASS can be found at **http://www.fass.org/positions.asp**. Requirements are a PhD, PhD/DVM, or equivalent degree in an animal science related field and the appropriate experience and ability to be an effective leader and science policy advocate for animal agriculture. The CEO is expected to have an excellent understanding of and appreciation for science and scientific publishing.

FASS (a 501 (c) (3) nonprofit organization) was founded by the Poultry Science Association, the American Society of Animal Science, and the American Dairy Science Association to serve as the single, scientific advocacy voice for animal agriculture. The CEO has overall responsibility to implement and administer the vision, mission, and strategic plan of FASS under direction of the FASS Board of Directors.

Application materials (see web site for details) should be submitted in electronic format to: **Dr. Mary M. Beck, Chair, FASS CEO Search Committee, Department of Animal Sciences, University of Nebraska-Lincoln; mbeck1@unl.edu.**

Application Deadline: **July 1, 2005**

Assistant Professor
Director of Transgenic Mouse and Knock-out Core Facilities

NYU School of Medicine
Skirball Institute of Biomolecular Medicine

The Skirball Institute and Cancer Institute of NYU School of Medicine invite applications for a non-tenure track position at the Research Assistant Professor level to serve as Director for their heavily utilized Transgenic Mouse and Knock-out Core Facilities. These facilities will offer a range of services including ES cell gene targeting, generation of chimeric mice, pronuclear microinjection of conventional and BAC transgenes, as well as cryogenic preservation. In addition, the successful applicant will be expected to implement new mouse genetic technologies and to work with Information Technology on database development and management. Broad financial support will be provided for this endeavor on a recurrent basis.

The candidate will have the opportunity to work with a broad range of investigators in designing and producing a wide range of transgenic mice. In addition, they will be expected to expand and update the existing infrastructure for transgenic and ES cell technologies. The qualified candidate will have a PhD and/or MD, and have experience in ES cell and transgenic mouse procedures, as well as excellent interpersonal skills. Salary and benefits will be highly competitive and commensurate with experience.

Applicants should submit a C.V., and arrange for three letters of reference to be sent by June 15, 2005 to: **Nan McKeown, HR Coordinator, Skirball Institute, 3rd floor, NYU School of Medicine, 540 First Avenue, New York, NY 10016 or email: mckeown@saturn.med.nyu.edu**. We are an equal opportunity employer and provide a drug free workplace.

SCHOOL OF MEDICINE
NEW YORK UNIVERSITY

MICHIGAN STATE UNIVERSITY

Department of Biochemistry and Molecular Biology
John A. Hannah Distinguished Professorship in Gene Regulation

Michigan State University invites applications and seeks nominations for a John A. Hannah Professorship in Gene Regulation. The position is intended to complement a strong gene regulatory research presence at MSU, including structural, biochemical, genetic, and bioinformatic studies in animal, plant and microbial systems. The individual selected will bring innovative and multidisciplinary approaches to bear on central questions in gene regulation, including but not restricted to analysis of regulatory networks, structural analysis of higher order complexes, and dynamics of molecular complexes in live cells. It is anticipated that the candidate will contribute to the highly collaborative research atmosphere on campus and take a leadership role in enhancing training and research in the area of gene regulation.

This tenured research and teaching position comes with significant operating funds provided annually for program support. The primary appointment will be based in the Department of Biochemistry and Molecular Biology, with possible joint appointments in related departments.

The John A. Hannah Professorships were established in 1969, and are awarded to exceptional scholars to honor Hannah's 25 years as president of the University. Applications will be received until a suitable candidate is identified. For more information, please visit our website **www.bch.msu.edu**. Send applications, including c.v. and statement of current/future research interests to:

David Arnosti
Hannah Chair Search Committee
Biochemistry and Molecular Biology
Michigan State University
East Lansing, MI 48824-1319
arnosti@msu.edu

Women and minorities are encouraged to apply.

VCU
Virginia Commonwealth University

Director of Introductory Biology

The Department of Biology invites applications for the position of Director of Introductory Biology. The Director will coordinate departmental instruction of introductory biology courses for majors and non-majors. This individual will have primary responsibility for the coordination and development of course content and objectives, development and implementation of instructional methods, course assessment, and other aspects of instruction associated with the introductory biology program. A major focus of the responsibilities of this position will be the coordination of departmental activities to improve student learning outcomes and success in introductory biology courses. Teaching responsibilities will be six credits of introductory biology courses per semester. Responsibilities in the summer will focus on curriculum development.

This is a continuing 12-month, collateral faculty position that will commence in the summer or fall semester 2005. A Ph.D. in Biology or Biological Education is required, as is experience in teaching introductory biology courses and curriculum development.

Information on the Biology Department, which has 950 undergraduate majors and 33 faculty members, can be found at **www.has.vcu.edu/bio**

Submit vitae, statement of pertinent experience, and three letters of reference by June 10, 2005 to: **Stephanie Millican, Department of Biology, Virginia Commonwealth University, Richmond, VA 23284-2012.**

Virginia Commonwealth University is an equal opportunity/affirmative action employer. Women, minorities and persons with disabilities are encouraged to apply.

POSITIONS OPEN

FACULTY RESEARCH POSITIONS

The Department of Surgery, Indiana University School of Medicine is seeking applicants for two **ASSISTANT/ASSOCIATE PROFESSOR** research positions in the surgical research arena. Candidates must have either a Ph.D. in basic science or an M.D. degree. A minimum of five years of laboratory research experience or two years postdoctoral research experience/study, preferably with emphasis in cancer research, academic teaching experience at the university/college level are also required. These are tenure-track positions. Good communication and manuscript writing skills are also preferred. In addition to responsibilities in cancer research, successful candidates will assist in laboratory training of graduate students and surgery residents. Please send current curriculum vitae to:

Eric A. Wiebke, M.D.
Director, General Surgery
Department of Surgery
545 Barnhill Drive, EH 242
Indianapolis, IN 46202
Telephone: 317-274-4990
Fax: 317-274-0241
E-mail: ewiebke@iupui.edu

Indiana University is an Equal Employment Opportunity/Affirmative Action Employer, Minorities/Females/Persons with Disabilities.

MEDICAL GENETICS

The American University of the Caribbean (AUC), a 25-plus-year-old accredited medical school, with over 3,000 graduate physicians is pleased to announce an opening for a Medical Geneticist, Ph.D. and/or M.D., with postdoctoral training. Rank is commensurate with experience.

We seek an individual with experience and expertise, who both enjoys and is dedicated to teaching. The course includes transmission genetics, molecular genetics, inborn errors of metabolism, cancer genetics; and represents the full spectrum of the major forms of human genetics.

Individuals familiar with U.S. medical education and evaluation systems are encouraged to apply. All lectures are in English. Teamwork is encouraged; the majority of the basic science faculty being drawn from North America and the European Union, with clinical clerkships in the United States, United Kingdom, and Ireland.

AUC (**website: http://www.aucmed.edu**) is in a new, up-to-date facility on the delightful island of St. Maarten in the Netherlands Antilles, some three hours by air from Miami, Florida.

Interested parties should send their curriculum vitae, and the names of three references, with coordinates, via e-mail to: **James D. Regan, Ph.D., Chairman, Department of Genetics** at **e-mail: reganauc@hotmail.com.**

TENURE-TRACK FACULTY POSITION
MOLECULAR ONCOLOGY
Department of Medicine
Washington University, St. Louis

The Division of Oncology invites applications for full-time, tenure-track appointment at the rank of **ASSISTANT PROFESSOR.** Candidates must have a Ph.D., M.D., or equivalent degree, relevant postdoctoral experience, and a strong record of research accomplishment. We are seeking candidates with an interest in basic molecular oncology using innovative approaches in developmental, molecular, or cell biology, biochemistry, or biophysics. The successful candidate will be expected to establish and maintain a vigorous, independently funded research program. Competitive salary, ample startup packages, and first-class laboratory space will be provided.

Please provide (1) current curriculum vitae, list of publications, and grant support, (2) a brief statement of research interests, and (3) contact information for three references. Send applications to: **Dr. Lee Ratner, Chair of the Search Committee, Division of Oncology, Campus Box 8069, 660 S. Euclid Avenue, Washington University, St. Louis, MO 63110,** or **e-mail: lratner@im.wustl.edu.**

UNIVERSITY OF DENVER
1864

RESEARCH ASSISTANT PROFESSOR, RESEARCH ASSOCIATE PROFESSOR, OR RESEARCH PROFESSOR
(depending on qualifications)

Founded in 1961, The Eleanor Roosevelt Institute (ERI) has pioneered basic biomedical research in an effort to unlock the mysteries of human health and disease. ERI's research has earned it an international reputation in Down syndrome research as well as in the fight against cancer, amyotrophic lateral sclerosis (Lou Gehrig's disease), autism, Alzheimer's disease, obesity, and Type II diabetes.

ERI is now recruiting several new faculty positions. ERI seeks to recruit scientists in the early or mid stages of their careers, but talented candidates at all levels will be considered. Candidates must have completed postdoctoral training with a strong record of research accomplishment and should be prepared to develop a vigorous, independently funded research program in an area of basic biomedical science. We are particularly interested in recruiting candidates with scientific backgrounds or established programs in Alzheimer's disease, neuroendocrine disorders including diabetes, and Down syndrome, especially with a focus on relationships between these conditions. Successful candidates will be provided with startup packages, competitive compensation and benefits, laboratory space, and access to state-of-the-art core facilities.

Appointees will be eligible for tenure-track appointments in the Department of Biological Sciences and will be part of an expansion of the molecular life sciences program within the University, which will include participation in the graduate and undergraduate curriculum.

To apply for this position please visit our **website: http://www.dujobs.org** and complete an online application and attach the following documents: cover letter, complete curriculum vitae, the names of four references, and a statement of research interests and plans. If you do not have these additional documents saved electronically, please send them via regular mail to: **Dr. David Patterson, Director, Eleanor Roosevelt Institute, University of Denver, Denver, CO 80208 (e-mail: dpatter2@du.edu).** Review of applications will begin on 15 June 2005 and continue until the positions are filled.

BIOCHEMIST/MOLECULAR BIOLOGIST
Davis Heart and Lung Research Institute
The Ohio State University

A position is available for a **POSTDOCTORAL RESEARCHER** with experience related to nitric oxide synthase to study substrate, co-factor, and protein interactions of the enzyme in cardiovascular disease.

Salary commensurate with experience. Please send curriculum vitae to: **Jay L. Zweier, M.D., 473 W. 12th Avenue, Room 110, Columbus, OH 43201. E-mail: zweier-1@medctr.osu.edu.**

The Ohio State University is an Equal Opportunity/Affirmative Action Employer. Qualified women, minorities, Vietnam era veterans, and individuals with disabilities are encouraged to apply.

POSTDOCTORAL POSITION
Molecular Microbiology

A position is available to study respiratory microbial pathogens relevant to occupational health. Studies will involve genomic library construction, denaturing gradient gel electrophoresis, fluorescent in situ hybridisation, and real-time quantitative polymerase chain reaction among other molecular and microbiological techniques. Apply to: **Jagjit S. Yadav, Ph.D., Department of Environmental Health, University of Cincinnati Medical Center, Cincinnati, OH 45267. Telephone: 513-558-4806; fax: 513-558-4397; e-mail: jagjit.yadav@uc.edu.**

PENN STATE CAPITAL COLLEGE
Harrisburg Campus

Penn State Capital College is accepting applications for an **ASSOCIATE** or **FULL PROFESSOR** of sustainable engineering available 2005–2006. Exceptional candidates will be considered for Professor and the endowed "Quentin Berg University Chair in Engineering." Candidate must have an outstanding record of interdisciplinary environmental practice, teaching, and research; experience in one or more areas of sustainable engineering systems, green engineering, pollution prevention, and/or industrial ecology; and leadership of environmental initiatives and coordination of green engineering research and teaching. Teaching responsibilities include undergraduate courses in green engineering, graduate courses in specialty areas, and other related engineering and environmental subjects. Candidates must have experience in developing an externally funded research program and supervising diverse groups of majors, including engineering, science, and business students. Ph.D. with at least one earned degree in engineering or a related discipline required. Acceptable backgrounds could include environmental, civil, architectural, mechanical, chemical, or electrical engineering with sustainable engineering as the primary research and teaching focus. Additional information can be found at the Penn State Harrisburg **website: http://www.hbg.psu.edu/epc.**

Applicants should submit curriculum vitae, three references, and a research and teaching statement to: **Quentin Berg Professor Search Committee, c/o Mrs. Dorothy Guy, Director of Human Resources, Penn State Capital College, Box SCIENCE, 777 West Harrisburg Pike, Middletown, PA 17057-4898.** Direct e-mail applications to: **Mrs. Dorothy Guy** at **e-mail: djg1@psu.edu.** Nominations are welcome. Applicant review will begin in September 2005 and will continue until the position is filled. *Penn State is committed to Affirmative Action/Equal Opportunity, and the diversity of its workforce.*

FACULTY POSITION: IMMUNOLOGIST
Microbiology, Immunology, and Molecular Genetics

The Department of Microbiology, Immunology, and Molecular Genetics, College of Medicine, University of Kentucky, seeks candidates for full-time tenure-track **ASSISTANT PROFESSOR** in immunology with interests including host-parasite interactions, vaccines, autoimmunity, innate immunity, and immunoregulation. Special consideration will be given to candidates with interests in select agents. Applicants should have a Ph.D. and/or M.D., or equivalent degree, and postdoctoral experience. Successful candidates are expected to develop/maintain an innovative, externally funded research program as well as participate in graduate and medical student teaching. This is an excellent opportunity to join a department with strong predoctoral and postdoctoral training programs, and research programs in microbial pathogenesis, eukaryotic molecular biology, molecular and cellular immunology, and molecular virology. Excellent startup funds, state-funded salary commensurate with experience, and modern research facilities will be provided. Applications should include curriculum vitae, representative reprints, a summary of past experience, a statement regarding research interests and future plans, as well as three letters of recommendation. All material should be sent to:

Chair, Faculty Search Committee
Department of Microbiology and Immunology and Molecular Genetics
MS409, Medical Center
University of Kentucky
Lexington, KY 40536-0298
Telephone: 800-462-5257
Fax: 859-257-8994

The University of Kentucky is an Equal Opportunity/Affirmative Action Employer and has an affirmative duty to reasonably accommodate otherwise qualified individuals with a disability.

POSITIONS OPEN

POSTDOCTORAL POSITION
U.S. Food and Drug Administration
Department of Health and Human Services

A Postdoctoral position in the area of genomic diversity among enteric pathogens is available in the Division of Molecular Biology of the Center for Food Safety and Applied Nutrition. Applicants should be familiar with DNA microarray techniques and data analysis currently being used for genotyping and gene expression studies in prokaryotes. The candidate must have a Ph.D., or equivalent, in the field of molecular biology or a related field. The position is for one year, but may be extended for up to three years.

The position offers a unique research opportunity as part of a multidisciplinary team to develop strategies for identifying and understanding genomic diversity of bacterial pathogens. The candidate will develop novel methods for genomic analysis of bacterial pathogens such as Escherichia coli, Shigella, and Salmonella that may contaminate the nation's food supply, as part of collaboration between the Food and Drug Administration and the Department of Homeland Security.

The facility is located at the Muirkirk Research Complex in Laurel, Maryland, near Washington, D.C. Salary is very competitive. Interested applicants should send curriculum vitae and three letters of recommendation to: **Thomas A. Cebula, Ph.D., Center for Food Safety and Applied Nutrition (HFS-025), 8301 Muirkirk Road, Laurel, MD 20708,** or **e-mail: thomas.cebula@fda.hhs.gov.**

TWO POSTDOCTORAL FELLOW POSITIONS
Available Immediately
Molecular Pathobiology of Atherosclerosis

A Postdoctoral Fellowship is available immediately to work on a project in The Wake Forest and Harvard Center for Botanical Lipids, one of five NIH National Center for Complementary and Alternative Medicine funded Centers in the United States. The focus of the project is to investigate the molecular mechanisms by which botanical oils, compared to fish oil, influence plasma lipid metabolism, inflammation, and atherosclerosis. A Postdoctoral Fellowship is also available to investigate the molecular mechanisms by which tissue specific expression of ABCA1 will affect high density lipoprotein metabolism and atherosclerosis. The successful candidate will use a multidisciplinary approach that includes transgenic/gene-targeted mouse models, molecular biology, biochemistry, and vascular wall biology. Background in molecular and cellular biology is necessary and experience in vascular wall biology and use of mouse models is desirable. Applicants should send a cover letter stating goals and curriculum vitae with reference contacts to: **Dr. John Parks, Department of Pathology, Wake Forest University School of Medicine, Medical Center Boulevard, Winston-Salem, NC 27157. E-mail: jparks@wfubmc.edu.** *Affirmative Action/Equal Opportunity Employer.*

POSTDOCTORAL POSITION

Laboratory of **Michael Rosenblatt,** Department of Physiology, Tufts University School of Medicine. Project: A novel animal model of human cancer cell metastasis to human bone to study "osteotropism" utilizing gene expression profiling.

Our laboratory offers interdisciplinary training in a premier research environment.

Send curriculum vitae, summary of research experience, copies of publications, and contact information for three references to: **Michael Rosenblatt, M.D., Office of the Dean, Tufts University School of Medicine, 136 Harrison Avenue, Boston, MA 02111. Telephone: 617-636-6565; fax: 617-636-0375; e-mail: michael.rosenblatt@tufts.edu.**

POSITIONS OPEN

ASSISTANT PROFESSOR

The Institute of Human Virology, University of Maryland Biotechnology Institute, has an immediate opening for a nontenure-track faculty, to conduct scientific research in the molecular basis of neurotropism of HIV-1; regulation of HIV-1 receptor and co-receptor of CD4 independent entry; immune-mediated pathways of not productive HIV-1 infection, that may foster new vaccine design and/or improved understanding of HIV-1/AIDS pathogenesis. Will perform research and contribute to the field of neurovirology in the Latin American countries by building their research capacity, infrastructure and programs, developing societies in the field of virology and neurosciences on a national and international level.

Candidate must have an M.D. and/or Ph.D. in virology, neuroscience, with at least three years postdoctoral experience. Must have a record of outstanding publications in neurovirology or immunology, with substantial evidence of innovation. Salary is commensurate with experience and qualifications. Please send a letter of application (referencing 300589), current resume, and names and telephone numbers of three references to the following address: **Dr. C. David Pauza, Institute of Human Virology, 725 West Lombard Street, Baltimore, MD 21201** and/or **e-mail: pauza@umbi.umd.edu.** Review of applications will begin immediately, and continue until a suitable candidate is selected. *The University of Maryland Biotechnology Institute is an Equal Opportunity/Affirmative Action Employer. Women, minorities, veterans, and candidates with disabilities are encouraged to apply.*

POSTDOCTORAL/RESEARCH ASSOCIATE POSITION

The Molecular Cardiology and Neuromuscular Institute, a not-for-profit laboratory associated with the Department of Physiology and Biophysics-Robert Wood Johnson Medical School, has a position in cardiovascular research. Applicant must have experience in cardiomyocite culture, fluorescent/confocal imaging, spectrophotometric analysis of enzymes activity, and modern molecular and biochemical techniques. Excellent communication skills. *Must be U.S. citizen or permanent resident.* Write or e-mail to:

Jose Marin, M.D., Director
Molecular Cardiology and Neuromuscular Institute
75 Raritan Avenue
Highland Park, NJ 08904
E-mail: tmci@att.net

POSTDOCTORAL POSITION
Davis Heart and Lung Research Institute
The Ohio State University

A position is available for a scientist with experience in cardiac physiology to study free radical and nitric oxide formation and related mechanisms of post ischemic injury. Experience with isolated heart and in vivo models desired. Salary commensurate with experience. Please send curriculum vitae to: **Jay L. Zweier, M.D., 473 W. 12th Avenue, Room 110, Columbus, OH 43201. E-mail: zweier-1@medctr.osu.edu.** Please reference PA08 in your application.

The Ohio State University is an Equal Opportunity/Affirmative Action Employer. Qualified women, minorities, Vietnam era veterans, and individuals with disabilities are encouraged to apply.

Additional job postings not featured in this issue can be viewed online at **website: http://www.sciencecareers.org.** New jobs are added daily!

Manage your job search more effectively by creating an account at **website: http://www.sciencecareers.org.** You can post your resume (open or confidentially) in our database and use it to apply to multiple jobs simultaneously. Track the jobs you have applied to in special tracking folders. Plus, you can create Job Alerts that will e-mail you notification of jobs that match your search criteria.

POSITIONS OPEN

POSTDOCTORAL AND CLINICAL FELLOWSHIPS
at the
National Institutes of Health
U.S. Department of Health and Human Services

Website: http://www.training.nih.gov

NIH is dedicated to building a diverse community in its training and employment programs.

POSTDOCTORAL CHEMIST METABOLOMICS

A Postdoctoral Chemist, preferably with experience in nuclear magnetic resonance spectroscopy and analytical chemistry is needed for a metabolomics project, which will use both clinical and animal models. This is a chance to participate in systems biology research and to interact closely with biologists and computer scientists. Training towards an independent career in biomedical science will be provided. To apply (including curriculum vitae and three reference letters) or for more information please contact: **Dr. Giovanni Paternostro (e-mail: giovanni@burnham.org) at the Burnham Institute, 10901 North Torrey Pines, La Jolla, CA 92037.**

The Burnham Institute (**website: http://www.burnham.org**) is one of the major biomedical research centers in the United States, located close to the Salk Institute, Scripps, and the University of California, San Diego.

RESEARCH ASSISTANT PROFESSOR: Nontenure-track, full-time research faculty position available in the Department of Medicine, Division of Gastroenterology and Hepatology at the University of Alabama at Birmingham (UAB). Applicant should have molecular biology experience with HIV-1 and cytomegalovirus and cellular transport mechanisms. Experience in mucosal immunology, particularly working with dendritic cells, is preferred.

Contact: **Phillip D. Smith, M.D., Division of Gastroenterology and Hepatology, Department of Medicine, University of Alabama at Birmingham, 703 19th Street South, ZRB 633, Birmingham, AL 35294. Fax: 205-934-8493, e-mail: pdsmith@uab.edu.**

Applicants must comply with the Immigration and Control Act. *UAB is an Equal Opportunity/Affirmative Action University.*

POSTDOCTORAL POSITION

NIH-funded position to study signaling pathways underlying cancer cell behavior involving Ras and Rho family proteins. Experience in molecular biology or biochemistry required. Candidates must have Ph.D. or M.D. and *reside in the United States.* Send curriculum vitae with three references to: **Dr. Rachel Buchsbaum, Molecular Oncology Research Institute, Tufts-New England Medical Center, 750 Washington Street, Boston, MA 02111. E-mail: rbuchsbaum@tufts-nemc.org.**

COURSES AND TRAINING

GRADUATE STUDENTS AND POSTDOCTORAL SCIENTISTS

Are you Seeking Information on:
Career Opportunities?
Scientific Presentations?
Grant Writing?
Teaching Strategies?
American Society for Microbiology is accepting applications for the
Graduate and Postdoctoral Summer Institute in Preparation for Careers in Microbiology
July 30 to August 3, 2005
University of Connecticut, Storrs
Applications are available at **website: http://www.asmgap.org**
Application deadline: June 15, 2005

REQUEST FOR APPLICATIONS AVAILABLE

Philip Morris USA Inc. and Philip Morris International announce the availability of their 2005 Request for Applications booklet for the Philip Morris External Research Program. The broad range of research interests includes the following scientific areas: Exposure/ Biomarkers/Dosimetry, Epidemiological Research, Clinical and Model Systems Research, and Tobacco Smoke and Smoking Behavior. Letters of intent are due by **July 1, 2005**. Applications must be received by **August 15, 2005**.

For more information or a copy of the 2005 Request for Applications booklet, please call or write Research Management Group, coordinator for the Philip Morris External Research Program.

Research Management Group
Attn: Research Manager
1099 Winterson Road, Suite 280
Linthicum Heights, Maryland 21090-2216 USA
Telephone: 1-410-684-3782
Fax: 1-410-684-3729
Email: rmgroup2000@aol.com

AWARDS

RANBAXY RESEARCH AWARDS 2004

RESEARCH FOR LIFE
RANBAXY
SCIENCE FOUNDATION

Nominations are invited from Heads of Research Institutions, Universities and Medical & Pharmaceutical Colleges, for the **Ranbaxy Research Awards-2004.** There are four Awards of Rs. 1 lakh each, for excellence in original research, in Medical and pharmaceutical Sciences.

Medical Sciences

One Award each for Basic Research, Medical Research and Clinical Research.

Pharmaceutical Sciences

One Award

The sponsored work of Indian scientists, both in India and abroad, together with their bio-data, research achievements, awards received in the past and papers published, may be forwarded (in 12 bound sets) to the Ranbaxy Science Foundation by July 1,2005.

Details of the procedure are being circulated to nominators and are also available from the office of the Foundation and on our Website. A panel of judges, comprising eminent scientists, will review the research work. Non-resident Indian scientists are also eligible for these awards.

Dr. O.P. Sood
Member-Governing Council
RANBAXY SCIENCE FOUNDATION
77B, Sector 18, IFFCO Road, Udyog Vihar Industrial Area, Gurgaon-122 015 (Haryana) India
Phone : 91-124-2341477 (D) 2342001-10, 5012501-10
Fax : 91-124-2342018, 2342017
E-mail : omprakash.sood@ranbaxy.com
Website : http://www.ranbaxyscienfoundation.com

WORKSHOPS

Cold Spring Harbor Laboratory Workshop

Schizophrenia & Related Disorders
July 6 - 19, 2005

Applications due May 20, 2005

Relaxing on the CSHL beach

Recent progress in genetics, developmental neurobiology and systems neuroscience presents an unprecedented opportunity to study the biological basis of this class of elusive diseases.
Main themes in this two week workshop include:

Clinical Background: History, Symptoms, Treatments
Moderator: Jeffrey Lieberman, Columbia University
Speakers: Joseph Coyle, Terry Goldberg, Stephan Heckers, Peter Jones, Shitij Kapur, Marc Laruelle, David Lewis, Daniel Weinberger

Genetics, Genomics, and Epigenetics
Moderators: Paul Harrison, University of Oxford, UK
Daniel Weinberger, National Institute of Mental Health
Speakers: David Cox, Douglas Falls, Ralph Greenspan, Maria Karayiorgou, Amar Klar, Steve McKnight, Karoly Mirnics, Mick O'Donovan, Arturas Petronis, David Porteous, David Skuse, Richard Straub, Michael Wigler

Development and Function of Neural Circuits
Moderator: Josh Huang, Cold Spring Harbor Laboratory
Speakers: Ken Davis, Ron McKay, Pat Levitt, Pasko Rakic, Judith Rapoport, Lorna Role

Neural Systems, Cognition, and Psychosis
Moderator: John Lisman, Brandeis University
Speakers: Curtis Bell, Judith Ford, Michael Frank, Dan Javitt, Marcel Kinsbourne, Phillip McGuire, Earl Miller, Patricio O'Donnell, Sukhi Shergill, Chris Walsh

Cold Spring Harbor Laboratory
Meetings & Courses Program
1 Bungtown Road, Cold Spring Harbor, NY 11724
Phone 516 367 8346 Fax 516 367 8845
Email meetings@cshl.edu http://meetings.cshl.edu

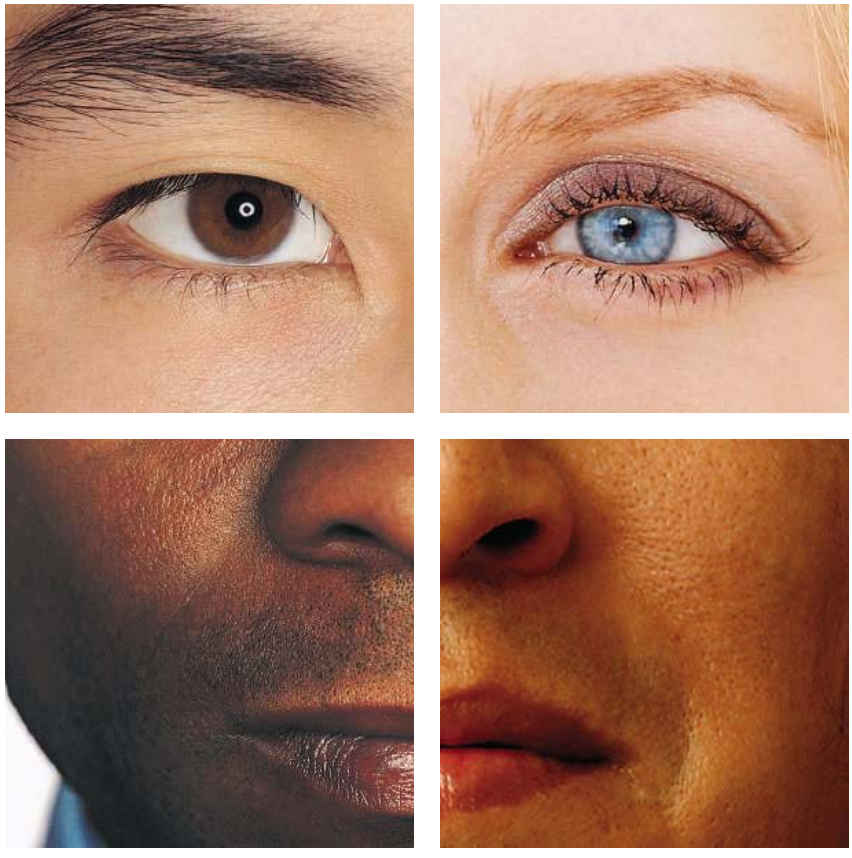

Successful research is important to all of us.

Use Clonetics® Melanocyte Cell Systems.

Clonetics® Melanocyte Cell Systems contain normal human epidermal neonatal melanocytes *(shown on left)* and optimized media for their growth. Each system can quickly generate melanocyte cultures for the study of pigmentation (melanogenesis), cellular differentiation, viral-induced transformation, antigen expression and cell adhesion. Clonetics Melanocyte Cell Systems are convenient and easy to use, allowing the researcher to focus on results.

Normal Human Epidermal Melanocyte Cell System NEW

- Cells are >90% functional based on verification of melanocyte conversion of L-dopa into dopa-melanin.
- New optimized media kit for melanocyte proliferation is superior to existing commercial media products.
- Guaranteed purity of >85% using immunofluorescent labeling of Mel-5.
- Cells, medium and reagents are quality tested together and guaranteed to give optimum performance as a complete "cell system".

Cambrex, the source for Clonetics® and Poietics™ Cell Systems, BioWhittaker™ Classical Media, SeaPlaque® and NuSieve® Agarose, and PAGEr® *Precast Gels.*

For more information contact us at:
www.cambrex.com/prod.NHEM
U.S. **800-638-8174** | Europe **32 (0) 87 32 16 11**

Cambrex Bio Science Walkersville, Inc.
8830 Biggs Ford Road | Walkersville, MD 21793

CAMBREX
Innovation. Experience. Performance.